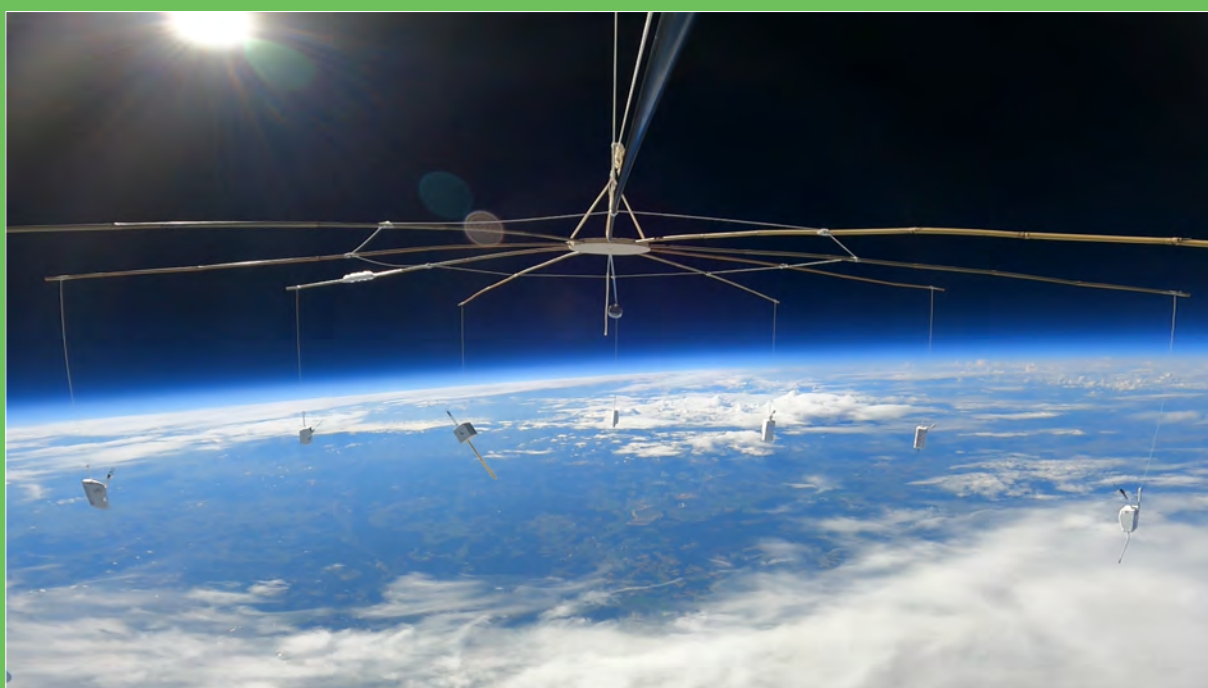


Report of WMO's 2022 Upper-Air Instrument Intercomparison Campaign



WORLD
METEOROLOGICAL
ORGANIZATION

Report of WMO's 2022 Upper-Air Instrument Intercomparison Campaign

Ruud Dirksen¹, Alexander Haefele², Frédéric P.A. Vogt²,
Michael Sommer¹, Christoph von Rohden¹, Giovanni Martucci²,
Gonzague Romanens², Christian Felix², Luca Modolo², Holger Vömel³,
Tzvetan Simeonov¹, Peter Oelsner¹, David Edwards⁴, Tim Oakley⁴,
Tom Gardiner⁵, Mohd. Imran Ansari⁶

¹ Lindenberg Meteorological Observatory, Deutscher Wetterdienst, 15848 Tauche, Germany

² Federal Office of Meteorology and Climatology MeteoSwiss, 1530 Payerne, Switzerland

³ National Center for Atmospheric Research, Boulder, CO 80301, USA

⁴ Met Office, Exeter, Devon, EX1 3PB, United Kingdom

⁵ National Physical Laboratory, Teddington, Middlesex, TW11 0LW, United Kingdom

⁶ India Meteorological Department, New Delhi 110003, India



WORLD
METEOROLOGICAL
ORGANIZATION

Instruments and Observing Methods Report No. 143

© **World Meteorological Organization, 2024**

The right of publication in print, electronic and any other form and in any language is reserved by WMO. Short extracts from WMO publications may be reproduced without authorization, provided that the complete source is clearly indicated. Editorial correspondence and requests to publish, reproduce or translate this publication in part or in whole should be addressed to:

Chairperson, Publications Board
World Meteorological Organization (WMO)
7 bis, avenue de la Paix
P.O. Box 2300
CH-1211 Geneva 2, Switzerland

Tel.: +41 (0) 22 730 84 03
Fax: +41 (0) 22 730 80 40
E-mail: publications@wmo.int

NOTE

The designations employed in WMO publications and the presentation of material in this publication do not imply the expression of any opinion whatsoever on the part of WMO concerning the legal status of any country, territory, city or area, or of its authorities, or concerning the delimitation of its frontiers or boundaries.

The mention of specific companies or products does not imply that they are endorsed or recommended by WMO in preference to others of a similar nature which are not mentioned or advertised.

The findings, interpretations and conclusions expressed in WMO publications with named authors are those of the authors alone and do not necessarily reflect those of WMO or its Members.

This publication has been issued without formal editing.



Figure 1: Group photo of UAII 2022 participants during the field campaign phase. See Appendix P for the list of persons involved.

FOREWORD

The WMO Technical Commission for Observation, Infrastructure and Information Systems (INF-COM), through its Standing Committee on Measurement, Instrumentation and Traceability (SC-MINT), coordinates intercomparisons that enable to characterize the quality of measurements from various observing systems.

Upper-air measurements are very important for a number of application areas and are core to the WMO Global Basic Observing Network. A significant part of these observations is provided by radiosonde systems which represent large operational costs for WMO Members. WMO Members need information on the performance of those systems, and of alternative approaches to meet their requirements. They also need information on approaches that could help them improve the environmental sustainability of their overall observing systems.

WMO upper-air instrument intercomparisons have had a long history (UK 1984, USA 1985, the former USSR 1989, Japan 1993, USA/Russian Federation 1995-7, Brazil 2001, Mauritius Island 2005, China, 2010 and now Germany 2022) and were conducted on a more or less regular basis. This intercomparison was conducted after an unusually long time since the last intercomparison, partly because of the COVID pandemic.

The aim of this intercomparison was to test the performance of operational radiosonde systems and to provide guidance on their performance, as well as to evaluate the current capabilities of a number of other observing systems (remote-sensing instruments in particular), in a robust manner, which was extremely ambitious.

The intercomparison was conducted in an innovative manner. It allied a laboratory and a field phase. Independent operators were in charge of operating the radiosonde systems during the field phase. The data evaluation was conducted in a robust manner, making use of GCOS Reference Upper-Air Network (GRUAN) data products that have well characterized uncertainties as reference, and assessing whether the different systems are meeting the user requirements that are provided in the OSCAR/Surface database for a several application areas. Furthermore, the data evaluation methodology and software are fully documented publicly available which ensures transparency on the approach that was used, and can facilitate the organization of follow-up intercomparisons.

This report includes a wealth of information. It will help WMO Members in selecting observing systems that meet their requirements. Readers are encouraged to familiarize themselves with the report overall rather than to draw conclusions only from the summary tables, which represent only part of the outcomes.

This intercomparison also proved to be a valuable capacity development activity as the independent radiosonde operators had the opportunity to gain knowledge on different systems, and on the conduct of a radiosonde intercomparison which is a rare opportunity.

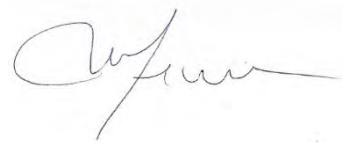
I wish to express my sincere thanks to MeteoSwiss and Deutscher Wetterdienst for taking the lead in organizing and conducting this intercomparison, which represents a large commitment in terms of both human and financial resources. I would also like to thank more personally the project Co-Leads, Ruud Dirksen and Alexander Haefele and their teams for conducting the project in such a smooth manner and for the professionalism of the analysis and of the report, and the expert of the SC-MINT Task Team on Upper-Air Instrument Intercomparison for their contribution to the planning and support of the intercomparison. I would also like to thank the independent operators for their contribution to the project and the management of the National Meteorological

and Hydrological Services from which they come for their support to their participation in the campaign. Finally, I would like to thank all the manufacturers who participated in this campaign, for their trust and collaborative contribution to the success of this project.

The quality of the data has always been critical, and as we move into an increasingly data driven world, feeding machine learning and AI approaches, the quality of the data will remain a priority. I trust that this report will be extremely useful not only to many WMO Members, but also to the manufacturers to further improve their systems. It also points out a number of activities that will have to be considered by INFCOM in the future.

Finally, I would like to encourage the research community, or any interested expert, to make further use of the intercomparison dataset from which lots of additional knowledge could be drawn.

Michel Jean

A handwritten signature in black ink, appearing to read 'Michel Jean', written in a cursive style.

President of the Infrastructure Commission

CONTACTING THE PROJECT TEAM

Any inquiry about the content of this report should be sent to the World Meteorological Organization (WMO):

Website: <https://wmo.int>
Email: wmo@wmo.int

ACKNOWLEDGEMENTS

The Upper-Air Instrument Intercomparison (UAI) 2022 has been supported by numerous individuals, groups and institutions and the authors wish to extend their thanks to:

- The board of directors of Deutscher Wetterdienst (DWD) and MeteoSwiss (MCH) for the strong material and immaterial support to the campaign.
- The technical staff at Lindenberg Meteorological Observatory – Richard Assmann Observatory (MOL-RAO) (Tatjana Naebert, Rico Tietz, Susanne Körner, Helge Friedrich, and Marion Fiedler-Krüger) for their tireless support with building and operating the experimental setups and carrying out numerous measurements as basis for the GRUAN RS41 data product development.
- Bassem Lajnef, Josette Jhabeemissur, Nontobeko Langa, Norman Duri, Quyen Nguyen Thi, Savitri Gangadeen, Sonny Pajarilla, Sven Körner, Wayne Pene and Zeinab Sayed Fahmy for their reliable service as radiosonde operators during the field campaign.
- Azista Industries Pvt. Ltd., Aerospace Newsky Technology Co., Ltd., Graw Radiosondes GmbH & Co. KG, Diel Met Systems (Pty) Ltd. trading as InterMet, Meisei Electric Co., Ltd., Meteomodem, Vikram Sarabhai Space Center, Indian Space Research Organisation, Tianjin Huayuntianyi Special Meteorological Sounding Tech. Co., Ltd., Vaisala Oyj, and Weathex for their constructive collaboration during the laboratory and the field campaign and their valuable feedback for the final report.
- Erik Andersson for reviewing an early version of the statistical methodology presented in Appendix J, and the anonymous WMO-mandated reviewers for their constructive feedback on the content of this report.
- Stella Dietze (FU Berlin) for her dedicated support in various activities during the field campaign.
- The remote sensing specialists at MOL-RAO (Volker Lehmann, Ronny Leinweber, and Christine Knist) for providing the remote sensing data, for scientific discussions and for reviewing the report.
- The WMO secretariat, and in particular Isabelle Rüedi, for the excellent support and guidance given throughout the entire activity.
- The Totex Corporation, for providing the TX1500 meteorological balloons used during the campaign.
- Meisei Electric Co., Ltd. and Vaisala Oyj for providing the radiosondes used as GRUAN Data Product (GDP) during the field campaign.
- Deutscher Wetterdienst (DWD), Egyptian Meteorological Authority, Fiji Meteorological Service, Philippine Atmospheric Geophysical and Astronomical Services Administration (PAGASA), Seychelles Meteorological Authority, South African Weather Service, Trinidad and Tobago Meteorological Service, National Institute of Meteorology (INM) Tunisia, Vietnam Meteorological and Hydrological Administration (VNMHA), Meteorological Services Department of Zimbabwe for allowing their staff to participate as operator in the campaign.
- Wettermuseum Lindenberg for inviting the operators to visit their exhibition.
- June Wang (University Albany, USA), initial member of TT-UAI, for her contribution to the campaign in its early phase.
- The radiosonde hunters for their assistance in recovering campaign rigs.

ABSTRACT

Upper air instrument intercomparisons (Upper-Air Instrument Intercomparison) are important to periodically assess the performance of upper air measurement systems, in particular radiosondes, and to support WMO Members in the design of their upper air networks. The focus of the WMO Upper-Air Instrument Intercomparison 2022 (UAI 2022) was set on upper air systems with operational maturity. These are ideally used by national meteorological services to send data to the Global Telecommunication System (GTS). The UAI 2022 took a new approach to such intercomparisons to obtain results of best possible general validity:

1. A laboratory campaign for radiosondes complemented the field campaign and provided valuable insight in the behaviour of radiosondes under laboratory conditions;
2. The use of a well characterised working measurement standard based on GCOS Reference Upper Air Network (GRUAN) data products and a fully documented and objective data analysis yields transparent and traceable results;
3. Independent operators for the radiosondes make the results representative for operational use and allowed the assessment of user friendliness as an added value;
4. Besides radiosondes, UAI 2022 includes a suite of surface based remote sensing upper air systems to give a more complete picture of the performance of upper air systems.

Radiosonde models from manufacturers based in China (2), Finland (1), France (1), Germany (1), India (2), Japan (1), South Africa (1), and Republic of Korea (1) participated in the UAI 2022. The participating radiosonde models represent almost half of the radiosonde data exchanged on the GTS at the time of writing. Due to the conflict between the Russian Federation and Ukraine, no manufacturers from the Russian Federation participated in the intercomparison.

Upper-Air Instrument Intercomparison 2022 was co-hosted by Deutscher Wetterdienst (Deutscher Wetterdienst) and MeteoSwiss (MeteoSwiss), with DWD's Lindenberg Meteorological Observatory as campaign site. The field campaign was performed during a mid-latitude summer offering an atmospheric temperature range of -65°C to 33°C . The main dataset (on which the conclusions are based) consists of data collected from a total of 79 balloon soundings during the field campaign. Taking into account the measurement uncertainty of the working measurement standard, the upper air systems are evaluated against the uncertainty requirements defined in WMO's OSCAR database for various application areas. This approach yields a detailed assessment of the performance of the different systems and is of added value to WMO Members.

For numerical weather prediction and related applications, very good performance is observed for temperature and wind: most systems meet the respective breakthrough requirements. Good performance is observed for humidity: most systems meet the respective threshold requirements. OSCAR requirements for climate applications are the most stringent ones and are challenging to meet. This particularly applies to humidity measurements, where there is a large gap between current systems' capabilities and the OSCAR requirements.

Despite a careful analysis methodology, the readers of this report should be aware of the limitations of the presented results. The GRUAN data products are objectively a good choice for the working measurement standard, in particular because their measurement uncertainties are well characterised. And although they are the community's best-effort for providing reference observations, they are not guaranteed to represent the absolute truth. Furthermore, although the field campaign allowed the sampling of a wide range of atmospheric temperatures, it did not cover the more extreme atmospheric conditions found in tropical or polar regions.

TABLE OF CONTENTS

I	WMO’s 2022 Upper-Air Instrument Intercomparison	1
1	Introduction	3
1.1	Purpose of the campaign	3
1.2	Novelties with respect to previous campaigns	4
1.3	Organisation	6
1.3.1	Governance and timeline	6
1.3.2	DWD-MCH cooperation	6
1.3.3	UAII Project and Task Team memberships	7
1.3.4	Participant selection	7
1.4	Covid-19	8
1.5	Conventions	9
1.6	The UAII 2022 Supplementary Material	10
2	Layout of campaign	11
2.1	Laboratory experiments	11
2.2	Field campaign	13
2.3	Data policy	14
3	Participating radiosonde systems	15
3.1	ATMS-3710 from Azista Industries Pvt. Ltd.	18
3.2	CF-06-AH from Aerospace Newsky Technology Co., Ltd.	19
3.3	DFM-17 from Graw Radiosondes GmbH & Co. KG	20
3.4	HT-GTS(U)2-1 from Tianjin Huayuntianyi Special Meteorological Sounding Tech. Co., Ltd.	21
3.5	iMet-54 from Diel Met Systems (Pty) Ltd. trading as InterMet	22
3.6	iMS-100 from Meisei Electric Co., Ltd.	23
3.7	M20 from Meteomodem	24
3.8	PS-B3 from Vikram Sarabhai Space Center, Indian Space Research Organi- sation	25
3.9	RS41-SG from Vaisala Oyj	26
3.10	WxR-301D from Weathex	27
4	Implementation of the campaign	29
4.1	Local site – the Lindenberg Meteorological Observatory	29
4.1.1	The observatory – general overview	29
4.1.2	Geographical location and local climatology	29
4.1.3	Site description	30
4.1.4	Laboratories	32
4.1.5	Balloon hangar	33
4.1.6	Antenna array	35
4.1.7	Launch site	35
4.1.8	Surface observations	36
4.2	Laboratory strategy and schedule	36
4.2.1	Strategy	36
4.2.2	Schedule	38
4.3	Sounding strategy and schedule	39
4.3.1	Independent operators	39
4.3.2	Sounding strategy and rig configuration	40
4.3.3	Launch schedule	42
4.3.4	Summary of rig construction	44
4.3.5	Standard rig configuration	45
4.3.6	Frequency allocation	46
4.3.7	Main steps in conducting a sounding during the campaign	47

4.3.8	Manufacturer independent ground check in Standard Humidity Chamber (SHC)	48
4.3.9	Selection of the GRUAN Data Products (GDPs)	49
4.3.10	GRUAN Data Product (GDP) soundings	49
4.3.11	Reference measurement of stratospheric humidity (CFH)	51
4.3.12	Data handling and campaign progress monitoring	52
4.4	Remote sensing systems	53

II Laboratory campaign 57

5	Humidity sensor performance at room conditions (LABH)	59
5.1	Introduction	59
5.2	Experimental setup	60
5.2.1	Calibration of the reference temperature sensors	61
5.2.2	Establishing reference levels for relative humidity with SHC	62
5.3	Measurements and results	62
5.3.1	Measurement plan	62
5.3.2	Analysis	64
5.3.3	Relative Humidity	66
5.3.4	Temperature	71
5.4	Conclusions	73
6	Humidity and temperature sensor performance at low temperature	75
6.1	Introduction	75
6.1.1	Time lag measurement	76
6.1.2	Low temperature calibration assessment	77
6.2	Experimental setup	77
6.3	Measurements and Results	79
6.3.1	Quantification of humidity sensor response time (TLAG)	79
6.3.2	Assessment of temperature sensor calibration at low temperature (LOWT)	85
7	Radiation sensitivity of air temperature measurement (RADI)	89
7.1	Introduction	89
7.2	Experimental setup	90
7.3	Measurements and Results	91
7.3.1	Measuring programme	91
7.3.2	Measurements	92
7.3.3	Data evaluation	93
7.3.4	Results	94

III Field Campaign 99

8	Flight statistics	101
8.1	Overview	101
8.2	Selection of valid flights and profiles	106
8.2.1	Attempted ascents with no data	108
8.2.2	Ascents with insufficient data	108
8.2.3	Profiles with invalid data	108
8.2.4	Operational mishaps	108
8.2.5	Early start detections and erroneous geopotential heights	109
8.3	Data availability statistics	109
8.3.1	Radiosondes	109
8.3.2	GNSS IWV	111
8.3.3	Satellite overpasses	111

9	Data analysis methodology	113
9.1	Scope	113
9.1.1	Geophysical variables	113
9.1.2	Flight categories	113
9.1.3	Atmospheric layers	114
9.2	The combined working measurement standards	116
9.3	Assessing upper-air instrument performances with respect to OSCAR	118
9.3.1	ORUCs: definition and selection	118
9.3.2	The ORUC assessment function	121
9.4	dvas: the analysis software for the UAI 2022	123
9.4.1	The dvas diagrams	123
9.4.2	The dvas NetCDF datafiles	123
9.5	Radiosondes	125
9.5.1	The GDP datafiles	125
9.5.2	The MDP datafiles	125
9.5.3	Profile synchronisation	127
9.6	Remote sensing observations	129
9.6.1	Lindenberg Remote Sensing Suite (LRSS): principles and limitations	129
9.6.2	Profile synchronisation	131
9.6.3	The Remote Sensing Data Product (RSDP) datafiles	131
9.6.4	Software analysis for the REMote sensing Intercomparison (REMI)	132
9.6.5	Limitations of the REMote sensing Intercomparison (REMI)	132
10	Results	135
10.1	Radiosondes	135
10.1.1	UTC measurement times	135
10.1.2	Launch detection	136
10.1.3	Missing data	137
10.1.4	BUFR files	138
10.1.5	ORUC assessment profiles Δ	143
10.1.6	Twin soundings	161
10.1.7	Cloud exits	169
10.1.8	In-clouds behaviours	171
10.1.9	Model-specific observations	173
10.2	Remote sensing	177
10.2.1	Missing data	177
10.2.2	ORUC assessment functions (Δ)	178
10.2.3	Instrument-specific observations	178
IV	Outcomes	187
11	Discussion	189
11.1	Radiosondes	189
11.1.1	Fitness-for-purpose with respect to OSCAR	189
11.1.2	User friendliness	198
11.1.3	Forcing of relative humidity measurements in the stratosphere	201
11.2	Remote sensing observations	202
11.2.1	Limitations of the REMote sensing Intercomparison (REMI)	202
11.2.2	Fitness-for-purpose with respect to OSCAR	202
11.2.3	Added value of remote sensing measurements	209
12	Conclusions	215
12.1	Summary of the results and recommendations	215
12.1.1	Radiosondes	215
12.1.2	Remote sensing	217
12.1.3	Other results	217
12.2	Lessons learned for future UAIs	218

Appendix	221
A Selection rules for participants	223
A.1 Questionnaire for manufacturers	223
B UAII 2022 Confidentiality and Code of Conduct	225
B.1 Confidentiality agreement	225
B.2 Code of conduct	226
C UAII 2022 Data Policy	227
C.1 Definitions	227
C.2 Principles	227
D UAII 2022 Data Formats	229
D.1 Overview	229
D.2 Special UAII 2022 ASCII text file formats	229
D.2.1 Base format of UAII 2022 ASCII text files	229
D.2.2 Data variables and meta data of UAII 2022 ASCII text files	230
D.2.3 UAII 2022 ASCII Text Sounding file	233
D.2.4 UAII 2022 ASCII Text Laboratory file	234
D.3 WMO BUFR files	236
D.4 Original Sounding Archive Files (often proprietary)	236
E Templates of protocols used in the UAII 2022	237
F Supplement to implementation of the campaign	239
F.1 Supplement to description of observatory	239
F.1.1 Aerological observation and testing site	239
F.1.2 GRUAN Lead Centre	239
F.1.3 Ground-based remote sensing	240
F.1.4 Boundary layer measurements	240
F.1.5 Radiation processes – national and regional radiation measurement centre	240
F.1.6 Historical milestones of Lindenberg observatory	241
F.2 Sunrise and sunset	242
F.3 String length	242
F.3.1 Experimental investigations	242
F.3.2 Practical considerations	243
F.4 Daily schedule	245
G Manufacturer interactions	247
H List of satellite overpasses	249
I Mathematical description of the CWSs assembly	261
I.1 Introduction	261
I.2 GDP uncertainties	261
I.3 Assessing the statistical compatibility of GDPs	263
I.4 Statistical combination of GDPs into CWSs	264
I.4.1 The Jacobian matrix	266
I.4.2 The covariance matrix and Combined Working measurement Stan- dard (CWS) variance	267
J Assessment of upper-air instruments with respect to ORUCs	269
J.1 Introduction	269
J.2 OSCAR requirement uncertainty criteria	269
J.2.1 Scalar variables	269
J.2.2 Wind (horizontal) vector	272
K Derivation of the ORUC values for humidity	275

L Individual $\Lambda_{c,\ell}$ diagnostic diagrams	279
L.1 ATMS-3710	279
L.2 CF-06-AH	286
L.3 DFM-17	293
L.4 GTH3	300
L.5 iMet-54	307
L.6 iMS-100	314
L.7 M20	321
L.8 PS-B3	328
L.9 RS41	335
L.10 WxR-301D	342
M Combined $\Lambda_{c,\ell}$ performance diagrams	349
N Rig Construction Guide	353
N.1 Preparation	354
N.2 Preparing the surface of the plywood plates	354
N.3 Attaching the bamboo rods and finishing the work on the main rig	355
N.4 Attaching the strings and stabilising the rig	357
N.5 Attaching the balloon attachment cord	358
N.6 Balancing the rig during launch preparation	358
N.7 Launch procedure	361
O Photo gallery of the UAI 2022	365
P Persons involved in the UAI	371
Nomenclature	375
Acronyms	377
Bibliography	379

Part I

WMO's 2022 Upper-Air Instrument Intercomparison

1 INTRODUCTION

It is with great pleasure that we present the final report on the WMO's Upper-Air Instrument Intercomparison (UAI) 2022 campaign. Upper-Air Instrument Intercomparison (UAI) 2022 took place twelve years after the previous WMO Commission for Instruments and Methods of Observation (CIMO) radiosonde intercomparison campaign was held in Yangjiang (China) in 2010. This significant time gap is due to a number of factors, including the global SARS-Covid-19 pandemic.

WMO radiosonde intercomparison campaigns are organised to provide an overview of the performance of the various contemporary operational radiosonde systems. Such campaigns provide important information to National Meteorological and Hydrological Services (NMHS), who partly base the selection of an operational radiosonde system for their network on the results of these campaigns. Furthermore, these campaigns contribute to improving the quality and cost-effectiveness of upper air observing systems by providing recommendations on system performances, improvements of instruments and methods of observation and suitable working references, to WMO Members and instrument manufacturers.

The first international WMO radiosonde intercomparison was organised in 1951 in Payerne (Switzerland), in preparation for the international geophysical year (*Imfeld et al., 2021*). The first intercomparison in its modern form took place in Bracknell in 1984, with a procedure that has been repeated at other locations at more or less regular intervals of a few years since then. After Yangjiang (China) in 2010, the next campaign was initially set to take place in Payerne (Switzerland). For logistical reasons, it was however decided in 2017 that MeteoSwiss (MCH) and Deutscher Wetterdienst (DWD) would jointly organise the campaign, with MOL-RAO (Lindenberg, Germany) as the campaign site. This collaboration was consolidated during project meetings held in Payerne in February 2019 and in Lindenberg in December 2019, where the objectives, rules and underlying philosophy of the campaign were discussed and documented.

The sudden and unexpected emergence of SARS-Covid-19, and the ensuing restrictions with far-reaching consequences for daily life on a global scale, made it impossible to carry out the campaign in 2021 as originally planned. After a delay of 12 months, the call for participation was re-issued, and the final selection of the participants was repeated in August 2021. The new start date for the laboratory phase was set in December 2021. The persistent SARS-Covid-19 situation caused a further three-month delay, such that all lab campaign activities were carried out between February 2022 and January 2023, while the field campaign part of UAI 2022 took place in August-September 2022.

The fruitful cooperation between DWD and MCH resulted not only in the successful organisation and execution of the campaign, but also in the implementation of several innovations, some of which may be of lasting benefit to the wider community. These include, for example, the use of a common reference based on GCOS Reference Upper-Air Network (GRUAN) data products, the GRUAN-inspired laboratory assessment of the radiosondes, the assessment of remote sensing data, the presence of independent operators carrying out the soundings during the field campaign, and a fully transparent data analysis, relying on the use of custom-built open source software (*dvas*). All these elements are discussed in detail in this report.

1.1 PURPOSE OF THE CAMPAIGN

The main objective of the WMO Upper-Air Instrument Intercomparison 2022 is to test the performance of operational radiosonde systems and to provide guidance on their performance relative to each other, as well as to evaluate the current capabilities of surface-based and space-based remote sensing instruments, and aircraft-based observations. Its results shall help WMO Members in selecting observing systems according to their requirements and will allow them to evaluate the potential offered by remote sensing instruments to complement the in situ information provided by the radiosondes. The focus is set on the following geophysical parameters:

- Geopotential height above mean sea level, in m

- Atmospheric temperature, in K
- Relative humidity, in %RH
- Atmospheric pressure, in hPa
- Wind (horizontal) direction, in ° East-of-North
- Wind (horizontal) speed, in m s^{-1}

The list of primary goals of the campaign is defined in the project plan ([WMO, 2020](#)):

1. To test and evaluate as many operational radiosonde systems as possible at the same location and time.
2. To characterize the individual radiosondes with respect to their reproducibility and to determine the uncertainty of the different measured parameters.
3. To compare the different radiosonde systems to characterised reference systems employed in the GCOS Reference Upper Air Network (GRUAN).
4. To characterize measurement errors and uncertainties of radiosonde sensors under laboratory conditions.
5. To demonstrate the added-value of surface-based remote-sensing systems for upper-air measurements and to develop a methodology to compare the measurements of radiosondes with remote-sensing instruments.
6. To evaluate the capability of each system participating in the intercomparison to reach the uncertainty targets as defined in OSCAR.

with secondary goals being:

1. To include and conduct a basic analysis of operational aircraft-based observations, as a component of the intercomparison.¹
2. To include and conduct a basic analysis of a selected set of satellite observations, as a component of the intercomparison.²
3. To evaluate the performance of the operational radiosonde products by comparing them with NWP model fields.
4. To evaluate the user-friendliness of radiosonde systems.
5. To document the environmental impact of the radiosonde models.³

Primary goal number 1 reflects the wish to assemble a group of participants that is representative of the various types of radiosonde employed in the global radiosonde network, expanded with manufacturers from emerging markets. In order to achieve this global representation in the campaign, a successful effort was made to include manufacturers from China, Russian Federation and India. However, the Russian manufacturer withdrew its participation following the conflict between Russian Federation and Ukraine, that broke out in February 2022. Another manufacturer from China also withdrew its participation, resulting in a total of 10 radiosonde manufacturers participating in the campaign (Table 3.1).

The other goals are linked to novelties of the campaign, with core underlying aims to perform the intercomparison in a fair and transparent manner, to provide useful feedback to the participating manufacturers for the further development of their radiosondes, and to provide the community a solid framework for future intercomparison campaigns. These different elements will be discussed in more detail in Section 1.2.

1.2 NOVELTIES WITH RESPECT TO PREVIOUS CAMPAIGNS

The fact that the GRUAN Lead Centre (LC) resides at MOL-RAO led to a natural synergy between GRUAN and the UAI 2022 campaign, with the adoption of several GRUAN practices. For example,

¹This analysis is not included in the report, but data are available upon request.

²This analysis is not included in the report, but is intended to be released as a separate study. A list of satellite overpasses during the field campaign is available in Appendix H.

³This analysis is not included in the report.

this led to the implementation of a separate laboratory campaign (participation was compulsory), during which each participating radiosonde's measurement errors and uncertainties were investigated via dedicated setups. The different experiments were designed to investigate the known, dominant error sources such as heating of the temperature sensor by solar radiation and relative humidity-sensor time lag at low temperatures. Essentially, the laboratory measurement programme of the UAI 2022 represents a scaled-down version of the extensive characterisation process that is normally used to develop correction algorithms for GRUAN Data Products (GDPs). The UAI 2022 lab programme was designed to provide essential information on the radiosonde performance to help understand and interpret the results of the sounding campaign, while also directly benefiting the manufacturers by providing them with new insights on potential areas of improvement for their radiosonde systems.

In previous campaigns, the data from each radiosonde were compared to an ad hoc reference, composed of the profiles of the other participants. This approach was motivated by the lack of an established independent reference instrument. In recent years however, chilled mirror instruments like the Cryogenic Frost point Hygrometer (CFH) have become an established reference for water vapour measurements. They are employed in international networks like GRUAN and the Network for the Detection of Atmospheric Composition Change (NDACC). Furthermore, GRUAN has put considerable effort in developing well-characterised reference data products for radiosondes. Cost and payload-mass considerations essentially prohibits the inclusion of a CFH on each rig of the UAI 2022 field campaign. GRUAN data products are used instead to provide the independent reference for assessing the performance of the participating radiosondes during UAI 2022. Specifically, each payload includes two radiosondes for which a GDP is available, that forms the basis for a Combined Working measurement Standard (CWS). The GDPs used during the UAI 2022 field campaign are generated from the RS41-SGP and the iMS-100 radiosondes (see Section 9.2). Although both radiosonde models are also participants in the campaign, it must be stressed that the CWS is independent from the participating radiosondes: the GDPs are provided by separate, additional radiosondes, rather than being derived from a parallel processing of the data recorded by the iMS-100 and RS41 "participant" radiosondes. In other words, additional RS41-SGP and iMS-100 radiosondes are attached to each rig, and it is the independently processed data from those additional sondes that provide the GDPs from which the CWS is derived. Doing so prevents a systematic covariance between the GDPs/CWS and the manufacturer product data (MDPs), given that the GRUAN data processing is independent from the manufacturer's processing, and in fact is distinctly different for several parameters.

Another GRUAN influence in the UAI 2022 field campaign lies in the use of the so-called Standard Humidity Chamber (SHC) to perform a manufacturer-independent ground check of radiosondes prior to launch. The SHC, further discussed in Section 5.1, creates a stable environment with known humidity and temperature that can be used to verify that a radiosonde is working properly. It can also provide additional information on the uncertainty of the temperature and humidity sensors. At the time of writing, SHCs are employed at various GRUAN sites as part of the standard operational procedure for reference radiosoundings.

During the UAI 2022 field campaign, the different radiosonde systems were operated by independent operators to enable an independent and transparent data collection. Doing so implies that all soundings during the campaign were performed without any involvement of (nor any interaction with) the manufacturers. The systems were operated strictly and exactly following the manufacturer-defined operational procedures. As an added benefit, the feedback gathered from the independent operators can be used to evaluate the user-friendliness of the different radiosonde systems. The implementation of the independent operator concept, including the selection of the operators themselves, is described in Section 4.3.1.

In contrast to previous radiosonde intercomparison campaigns, the results of the UAI 2022 campaign are not presented in the form of a ranking or a scoring of the participating radiosondes, but rather as a table listing the fitness-for-purpose for different application areas based on the Observing Systems Capability Analysis and Review Tool (OSCAR) requirements. The advantage of presenting the fitness-for-purpose for different application areas is that it will help NMHSs to assess the systems that meet the requirements for their specific application (e.g. numerical weather prediction) without being distracted by information on the performance in areas that are not directly relevant to the envisaged application.

The specific analysis methodology developed to assess upper-air instruments against OSCAR

requirements is described exhaustively in this Report, with full mathematical formalism. Doing so ensures that the results provided in this Report are transparent, traceable, and reproducible, with no ambiguity. It also opens up the possibility for this analysis methodology to be re-used in future intercomparison campaigns with similar goals. A dedicated open-source Python package, known as *dvas*, was purposely build by the UAI Project Team to implement the analysis methodology in a manner that would allow the UAI 2022 results to be easily reproduced by motivated readers.

1.3 ORGANISATION

1.3.1 Governance and timeline

The first idea of a successor to the 2010 Yangjiang intercomparison campaign took shape around 2014, with Payerne as the envisaged local organiser and campaign site. In 2017 it became clear that hosting and organising the campaign was too large a logistical challenge for one observatory, and on work-level an agreement was reached between MOL-RAO and Payerne to join forces and co-host the campaign, with MOL-RAO as campaign site. This cooperation was endorsed in 2018 by the board of directors of both DWD and MCH, cemented in an Memorandum of Understanding (MoU), and resulted in an offer to WMO to host the campaign. In 2018, a concept note was submitted to CIMO, outlining the plans, goals and objectives for the campaign, and which later formed the basis for the Project plan ([WMO, 2020](#)). Based on the concept note, WMO-CIMO assigned the local organisation of the campaign to DWD and MCH. At the Payerne meeting in February 2019, core teams from both observatories and CIMO representatives convened to further shape the plans for the organisation and implementation of the campaign. In addition, an expert team was proposed with the task of drafting key documents such as the project plan, sounding schedule, data policy and selection of participants. The expert team met in Lindenberg in December 2019 for this purpose, and after the completion of the project plan, the expert team was dissolved. It was replaced by the Task Team UAI, under the authority of the new WMO Infrastructure Commission, which is responsible for the governance and oversight of the campaign, whereas the actual implementation is the responsibility of the project team, which is mainly composed of staff from MOL-RAO and Payerne.

The campaign was originally planned for 2021 but had to be postponed to 2022 due to the unexpected advent of Covid-19, as discussed in Section 1.4. The laboratory campaign stretched from February 2022 to January 2023 as a series of seven two-week campaign slots at roughly four week-intervals, positioned before and after the field campaign that took place in August-September 2022. Following the completion of the field campaign, the project team's effort were focused on analysing the campaign data and writing the report. In July 2023, a partially completed draft-version of the report was shared with the manufacturers for review. Video calls were held between the project leads and individual manufacturers to clarify questions from manufacturers before their comments were submitted. The deadline for manufacturer comments was 31 August 2023. The project team took these into consideration while finalising the report for submission to WMO in December 2023.

The above-mentioned dates and events are summarised in Table 1.1.

1.3.2 DWD-MCH cooperation

DWD and MCH have co-organised the UAI 2022 with the following responsibilities:

- DWD** Campaign lead, local host of laboratory and field campaign, laboratory, radiosounding and remote sensing operations, data analysis of laboratory campaign, co-authorship of final report.
- MCH** Campaign co-lead, analysis of radiosounding and remote sensing data, co-authorship of final report.

Table 1.1: Relevant events and dates related to the organisation and governance of the campaign.

Date	Event
2017	Work-level agreement MOL-RAO -Payerne for cooperation
July 2018	Endorsement by DWD board
2018	Concept note
Feb 2019	Payerne meeting
Jun 2019	Official announcement at the Meteorological Technology World Expo
Sep 2019	MoU DWD-MCH
Dec 2019	Expert-team meeting in Lindenberg drafting Project plan and other documentation
2020-2021	Covid-19
Feb 2022	Start of the laboratory campaign
Aug-Sep 2022	Field campaign
Jan 2023	Conclusion of the laboratory campaign
July 2023	Draft version of the campaign report sent to manufacturers
Dec 2023	Submission of final report to WMO

1.3.3 UAII Project and Task Team memberships

The members of the UAII Task Team (TT) and of the UAII Project Team are shown in Table 1.2.

1.3.4 Participant selection

The aim of the selection procedure is to select a group of radiosondes that is representative for the global operational network, and at the same time provide opportunities for manufacturers from emerging markets. The number of systems that could be admitted to the campaign was limited to 12, which is the maximum number of systems that MOL-RAO can realistically support during the laboratory campaign.

Following the official announcement of the campaign at the Meteorological Technology World Expo (Metexpo) in June 2019 (Section 1.3.1), a total of 22 manufacturers expressed their interest in participating in an upcoming radiosonde intercomparison campaign. The official call for participants was issued in June 2020. The application procedure involved submitting a questionnaire on the candidate system's specifications before 12 July 2020. The initial response included only 11 manufacturers. This lower number was attributed to the uncertain situation related to recent advent of SARS-Covid-19. After an extension of the deadline, the number of applications increased to 18. However, the subsequent evolution of the SARS-Covid-19 pandemic and the ensuing restrictions for travelling and on daily life, eventually lead the UAII Project Team to postpone the campaign for 12 months, as is discussed in more detail in Section 1.4.

As a consequence, the Project Team decided to repeat the call in order to base the selection of participants on current information. The call was re-issued in May 2021, using the same method for application, which required submitting an online questionnaire, with the deadline set in June 2021. This call yielded 18 applicants, whose responses were ranked using a metric based on different parameters, including the global market share, product maturity, and information on the environmental impact of the radiosonde. An over-arching requirement for admission to the campaign was that prototypes are not allowed. The radiosounding system must also be

Table 1.2: Members of the UAI Project and Task teams.

Name	Project Team	Task Team
Ansari, Mohd. Imran ⁶	No	Yes
Dirksen, Ruud ¹	Yes	Yes
Edwards, David ⁴	No	Yes
Gardiner, Tom ⁵	No	Yes
Felix, Christian ²	Yes	Yes
Haefele, Alexander ²	Yes	Yes
Martucci, Giovanni ²	Yes	Yes
Oakley, Tim ⁴	No	Yes
Romanens, Gonague ²	Yes	Yes
von Rohden, Christoph ¹	Yes	Yes
Simeonov, Tzvetan ¹	Yes	No
Sommer, Michael ¹	Yes	Yes
Vogt, Frédéric ²	Yes	Yes
Vömel, Holger ³	No	Yes

¹Lindenberg Meteorological Observatory, Deutscher Wetterdienst, 15848 Tauche, Germany

²Federal Office of Meteorology and Climatology MeteoSwiss, 1530 Payerne, Switzerland

³National Center for Atmospheric Research, Boulder, CO 80301, USA

⁴Met Office, Exeter, Devon, EX1 3PB, United Kingdom

⁵National Physical Laboratory, Teddington, Middlesex, TW11 0LW, United Kingdom

⁶India Meteorological Department, New Delhi 110003, India

compatible with the infrastructural limitations of the Lindenberg site, which for example means that the transmission frequency must be in the 400 MHz band, and that radar-based systems are excluded. The complete selection rules document and the accompanying questionnaire are included in Appendix A.

Unexpectedly, Lockheed-Martin, that participated in Yiangjiang 2010, and represented a market share of 9%, did not apply for the campaign because of the company's decision to terminate radiosonde production.

From the 18 applications, the project team selected 12 participants for the campaign. This group of participants does represent the radiosondes used in the global observation network and also includes manufacturers from emerging markets, as is shown by the list of participants in Table 3.1.

The 12 manufacturers were officially notified by WMO about their admission as participant to the UAI 2022. Following the withdrawal of Shanghai Changwang Meteotech Corp. for unknown reasons, and JSC "Radi" as a result of the conflict between the Russian Federation and Ukraine, a total of 10 manufacturers ultimately participated in the UAI 2022 campaign.

1.4 COVID-19

The global SARS-Covid-19 pandemic, with first cases of the disease reported in December 2019, was classified by the World Health Organization as a public health emergency of international concern, lasting from 30 January 2020 to 5 May 2023. SARS-Covid-19 had a profound impact on

everyday life worldwide, and consequently also on the planning and execution of the UAI 2022 campaign, ultimately causing the UAI campaign to be postponed for one year.

The early stage of the pandemic, around spring 2020, saw the world trying to cope with this unprecedented challenge on a global scale, resulting in a wide range of safety measures and restrictions to curb the spread of the virus, and to protect the population. As a consequence of lockdowns, several radiosonde manufacturers experienced supply chain problems and had to adjust the production process, and/or had to reduce production capacity.

Although the restrictions in Germany were not as severe as in other countries, these still meant a considerable limitation of work-related activities and of daily life. These measures also included entry regulations for visitors from abroad, with compulsory quarantine for travellers from certain countries. With no signs of the pandemic abating, the restrictions persisted in the fall of 2020 and beyond, such that it became evident that it would not be feasible to conduct the campaign as scheduled in 2021. For example, the policy by the German government by the end of 2020 / beginning of 2021 stipulated that travellers from so-called high-risk countries had to remain in quarantine for 1-2 weeks before being allowed to enter Germany. As a result of this, each visit to MOL-RAO, for the laboratory as well as for the sounding campaign, could bear the additional burden of spending in total up to four weeks in quarantine. Furthermore, there was the constant threat of a general lockdown in case of rising incidence rates, with regulations requiring instant isolation of any person testing positive: all with the added probability of a fast infection spread given the confined spaces associated with the UAI 2022 activities.

Faced with this rapidly evolving and uncertain situation, the UAI 2022 Task Team judged that the risk of a SARS-Covid-19-related interruption, which would have severe impact on the planning of the campaign, was too high. Therefore, the Project Team decided in August 2020, with endorsement of WMO's Standing Committee on Measurements, Instrumentation and Traceability (SC-MINT), to postpone the laboratory campaign for 12 months and to move it to the end of 2021, after the field campaign. It was also decided that the situation would then be re-assessed in January 2021 to decide on the planning and execution of the field campaign. With no signs of the pandemic abating, the project team decided in January 2021 to postpone the field campaign to August/September 2022, restoring the original order of laboratory and field campaign. Altogether, the SARS-Covid-19 pandemic led to a one-year delay of the campaign, and (as described in Section 1.3.4) a repeat of the selection of participants.

Due to the success of national inoculation programmes around the globe, that reduced both the spread of the virus and the severity of an infection, the pandemic sufficiently eased off in the course of 2021 to make it possible to perform the campaign in 2022. Due to a temporary rise in incidence rates in Germany, the start of the laboratory campaign was delayed for another three months to February 2022, but the planning of the field campaign was not affected by this. As a consequence, it was no longer possible to perform all laboratory activities prior to the field campaign, as originally intended, and some slots were rescheduled after the field campaign. In the end, an additional laboratory campaign slot was organised in January 2023 to accommodate a manufacturer who was affected by lockdown-related travel restrictions in China.

During the laboratory campaign, a special hygiene protocol was adopted to reduce the risk of SARS-Covid-19 infection. This included the obligation to wear face masks, and logistical measures to minimise contact between the two manufacturer teams present at MOL-RAO during UAI laboratory campaign slots. Each manufacturer team was also assigned their own support-team of MOL-RAO staff. During the field campaign, incidence rates were low and there were no restrictions for those involved in the campaign, manufacturers and organisers alike, although MOL-RAO staff not involved in the campaign refrained from contact with the campaign team during the first five days after the arrival of the manufacturers and the operators on-site.

1.5 CONVENTIONS

Whenever we refer to geopotential heights, we imply geopotential heights above mean sea level. Unless otherwise specified, dates follow the International Organization for Standardization (ISO) format "YYYY-MM-DD".

The assessment and quantification of the performance of the radiosondes is reported in accordance with metrological terminology (as set out in [JCGM, 2012](#)).

Key terms used in this document, together with their definitions, are as follows:

- *Measured quantity value*: quantity value representing a measurement result.
- *Measurement error*: measured quantity value minus a reference quantity value.
- *Reference quantity value*: quantity value used as a basis for comparison with values of quantities of the same kind.
- *Systematic measurement error*: component of measurement error that in replicate measurements remains constant or varies in a predictable manner.
- *Measurement bias*: estimate of a systematic measurement error.
- *Random measurement error*: component of measurement error that in replicate measurements varies in an unpredictable manner.
- *Measurement uncertainty*: non-negative parameter characterising the dispersion of the quantity values being attributed to a measurand, based on the information used.

The terms accurate or accuracy are only used in a descriptive, qualitative sense.

Following WMO recommendation, relative humidity is reported over liquid water, including at temperatures below freezing.

Following the definitions in (Chapter 7 and Annex 7B of [WMO-No.8-Vol.I, 2021](#), (CIMO guide)), "radiation" can imply a process or apply to multiple quantities.

1.6 THE UAII 2022 SUPPLEMENTARY MATERIAL

This report is self-contained, in the sense that all Tables and Figures necessary to support its conclusions are included in the present document, either as part of the main text or in the Appendices.

This report is complemented by the so-called "UAII 2022 Supplementary Material": a series of datasets archived and publicly accessible online via the following Digital Object Identifier (DOI): [10.5281/zenodo.10160683](https://doi.org/10.5281/zenodo.10160683)

This Supplementary Material is comprised of a series of distinct datasets, which serve different purposes. These include:

- **original radiosonde datasets**, allowing to reproduce the analysis presented in this Report via the *dvas* processing software (also publicly available; see Section 9.4);
- **synchronized radiosonde profiles** in the form of Network Common Data Format (NetCDF) files, allowing motivated users to perform their own extended analysis without the need to cleanup the data first;
- **detailed diagnostic diagrams**, allowing study of the behaviour of each radiosonde on a flight-by-flight and variable-by-variable basis;
- **a diagram explorer tool**, designed to easily navigate among these numerous diagnostic diagrams;
- **pictures and movies**, documenting various technical and human aspects of the campaign for legacy purposes.
- **The measurement values extracted from the supervisor and operator protocols.**

A series of dedicated README files are included in the Supplementary Material. However, the datasets it contains are very much intended to be exploited and perused alongside this Report, the reading of which will be required to properly understand their nature.

2 LAYOUT OF CAMPAIGN

As mentioned in Section 1.2, several novel methods are introduced in the campaign. In this chapter we discuss in more detail how these are implemented and how they shape the campaign. A method with probably the most far-reaching impact on the planning and organisation of the campaign is without doubt the introduction of the laboratory campaign, with the result that the campaign consists of two major groups of activities, the laboratory and the radiosounding (or field) campaign, each with their specific requirements for preparation.

The purpose of the laboratory campaign is to get a good overview of the performance and measurement errors of the temperature and humidity sensors of each of the participating radiosondes model. This is useful information for the manufacturers for improving their products, and at the same time helps to interpret and understand differences observed during the radiosonde campaign. A compact measurement program under laboratory conditions was defined that can be executed within a timespan of two weeks for two manufacturers in parallel. The laboratory campaign was planned to be performed in various two-week slots prior to the field campaign. Participation in the laboratory campaign was compulsory for all manufacturers. As a result of the SARS-Covid-19 epidemic (see Section 1.4), the planning of laboratory campaign had to be adjusted, with approximately half of the laboratory slots occurring prior to the field campaign, and the remaining ones occurring after. The campaign timeline is illustrated schematically in Figure 2.1.

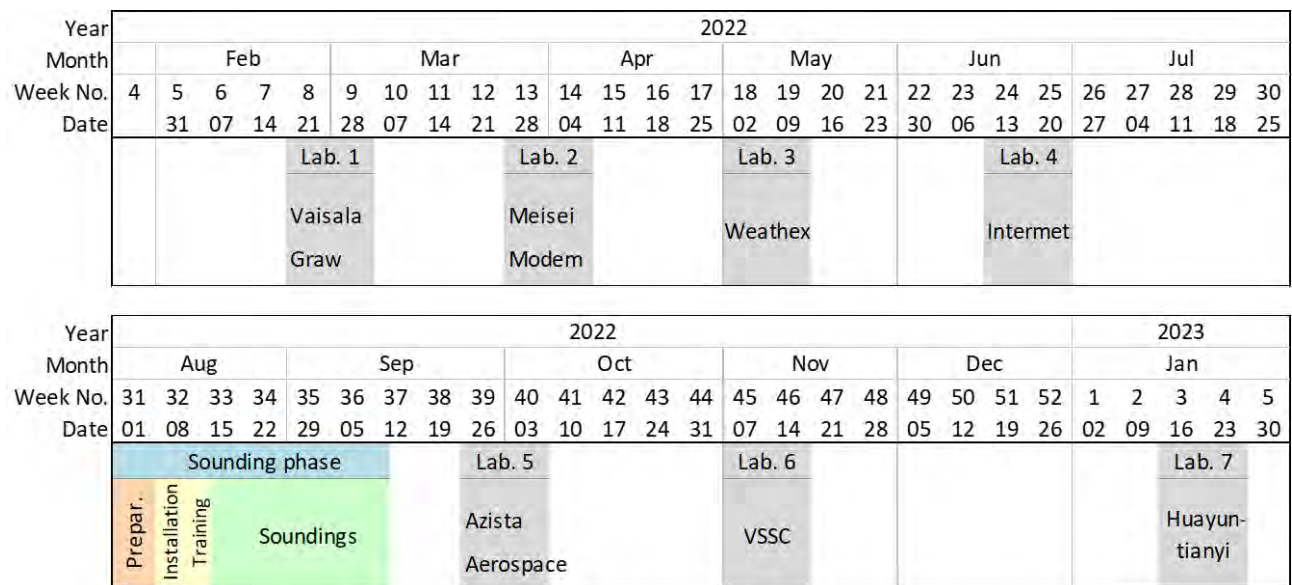


Figure 2.1: Timeline of the UAI 2022 campaign activities at MOL-RAO. The grey blocks represent the laboratory test phases together with the name of the manufacturer(s) present. The coloured block represents the field campaign. In the first week of August MOL-RAO staff performed the final preparations (orange). Manufacturer staff was present on-site during the lab phases, and from 2022-08-08 to 2022-08-16 to set up their systems for the field campaign and train the independent operators (yellow). The campaign soundings were carried out from 2022-08-16 to 2022-09-13 (green). This graph is the same as the one shown in Figure 4.10.

2.1 LABORATORY EXPERIMENTS

The purpose of the laboratory tests is to characterise the most important measurement and calibration errors, and uncertainties of the radiosonde’s sensors. This can help in understanding and interpreting the differences observed between the radiosonde models in flight. The benefit of the

laboratory tests is that these provide an independent assessment of the errors and uncertainties, which is a valuable addition to the radiosonde intercomparison, that provides uncertainties/biases of radiosondes with respect to each other. Furthermore, the results of the laboratory test campaign allow the manufacturers to identify issues with their radiosonde and enable them to improve their products in the future. However, it was not permitted to use the results of the laboratory tests to change the hardware or software of the radiosonde systems for the field campaign, as this would constitute an unfair advantage for the manufacturers scheduled in an early laboratory slot compared to those scheduled after field campaign. This is clearly stipulated in the UAI 2022 Code of Conduct (Appendix B.2).

MOL-RAO has well-equipped laboratory facilities for testing and characterising radiosondes under various conditions, ranging from typical surface conditions to those encountered at 35 km altitude (see Section 4.1.4). In the setups, relevant experimental parameters such as temperature, pressure, water vapour content, ventilation speed and actinic flux can be controlled and monitored, allowing for the investigation of the measurement uncertainty of the radiosonde's sensors.

The laboratory tests focus on the following three topics, which are the dominant sources of error for radiosondes and can readily be investigated under laboratory conditions:

- Calibration uncertainty of the temperature and relative humidity sensor(s).
- Timelag of the relative humidity sensor at low temperatures.
- Radiation-induced error of the temperature sensor.

It is the purpose of the laboratory campaign to assess the performance of the sensors themselves. It is therefore essential to record the calibrated raw data without any corrections (such as for timelag, radiation or otherwise) having been applied. In this regard, it is paramount to realise that a large measurement error on the raw sensor data does not automatically yield bad product data, as the ability of the sounding system's software to correct for the measurement errors is not being assessed here.

The laboratory tests were performed during a condensed program that extended from February 2022 to January 2023, organised as individual two-week measurement blocks (laboratory phases) wrapped around the main sounding campaign which took place in August/September 2022. Section 4.2 provides more information on the motivation and execution of the laboratory measurements as well as a detailed timeline.

The laboratory campaign was compulsory for all manufacturers that participated in the intercomparison campaign. The measurement data are treated confidentially in view of the potential commercial and strategic sensitivity of these data for the manufacturers. Throughout this report, the results of the laboratory measurements are presented anonymously to ensure that these are not traceable to the respective radiosonde model. Instead of using the model name, anonymous labeling ('A', 'B', 'C', etc...) is used to refer to the individual models in plots and tables, with different coding for the different experimental setups.

In short, the goals of the laboratory campaign are:

- a GRUAN-inspired approach to understand and characterise measurement errors and uncertainties.
- Help to understand and interpret differences observed during radiosounding campaign.
- Help radiosonde manufacturers to improve their (future) products.

The following rules were applied for the execution of the laboratory campaign:

- Radiosonde systems are operated by manufacturer's technicians/engineers.
- Calibrated raw data are recorded.
- Data analysis is performed by the project team.
- Two receiving systems are used to allow for parallel data recording.
- Measurement program including preparation and testing is carried out over two consecutive weeks (see Section 4.2.2).

Furthermore, the key data policy/confidentiality for the laboratory campaign includes the following elements:

- Raw measurement data are stored in the campaign database.
- The raw measurement data are accessible to the manufacturer and to the campaign's organisers.
- Data are not shared with other participants, nor distributed globally.
- Anonymous presentation of the results in the campaigns report, i.e. the radiosondes are not identified in plots, tables etc.

The complete (binding) text of the data policy document is included in Appendix C.

2.2 FIELD CAMPAIGN

MOL-RAO has extensive experience with performing balloon soundings with extended rigs and various payloads for aerological research, which was of direct benefit for the UAI 2022 field campaign.

The radiosoundings for the field campaign were performed in a four-week period from 2022-08-16 to 2022-09-14. During this time, a total of 79 balloon ascents were performed, resulting in at least 18 daytime and 16 nighttime soundings for each of the 10 participating radiosonde models, which fulfils the prior defined goal of 15 daytime/nighttime soundings to enable a statistically sound analysis of the campaign data.

As mentioned in Section 1.2 and discussed in detail in Section 9.2, the Combined Working measurement Standard (CWS) provides the campaign reference and is derived from two GRUAN Data Products (GDPs) assembled using the RS41-SGP and iMS-100 radiosondes, that are included to each rig. Together with the need to perform twin flights for participating radiosondes, the presence of GDP-related radiosondes on each rig implies that two distinct balloons are required to accommodate all 10 participant systems. For logistical reasons, the two ascents required for a complete "set of profiles" were separated by a few hours. This contributed to preventing interference from the radio signals between the rigs.

The system's reproducibility (campaign goal #2) was tested by mounting two identical radiosondes on the same rig. For this purpose, all manufacturers had to supply two radiosonde receiving systems for parallel operation. With one exception related to the critical failure of one of the ground system, each participant system performed at least four daytime and three nighttime twin soundings.

Prior to each sounding, the GRUAN-adopted practice of an additional manufacturer-independent ground check was performed. This involved inserting the radiosondes in a Standard Humidity Chamber (SHC) with a stable 100 %RH atmosphere and recording its readings for several minutes.

During the field campaign the receiving systems were operated by independent operators, with no involvement from the manufacturers, to ensure independent and transparent data acquisition, and also to assess the operability of the systems. The operators were recruited from WMO Members, and trained by manufacturer-staff to operate two systems with which they had no prior experience. The setting up of the radiosounding systems and the subsequent training of the operators by the manufacturers took place from 2022-08-09 to 2022-08-15. Before the start of the field campaign soundings, the manufacturers left the campaign site, and communication was only allowed with the project leads.

The measurements from the remote sensing instruments at MOL-RAO are compared to the radiosonde profiles from the CWS in a generic manner for the various measurement techniques, without judging the performance of the specific instruments.

The climate at MOL-RAO is mid-latitude continental, with a typical tropopause temperature of approximately -65°C in summer, which is warmer than the temperatures encountered at the tropical tropopause (-85°C). As a result, the combination of humidity and temperature conditions typical for the tropical UTLS was not accessible during the UAI 2022 field campaign; the same applies to other extreme atmospheric conditions, such as those encountered in the winter-time arctic stratosphere. On the other hand, the important impact of solar irradiance on daytime stratospheric temperature measurements can readily be assessed with soundings performed at MOL-RAO.

The weather conditions during the field campaign ranged from a hot summer with surface temperature exceeding 30 °C in August, to the onset of fall with 13 °C surface temperature by the end of the campaign. Sunny "blue sky" days were spread throughout the field campaign, with other periods of rain and even occasional thunderstorms. As such, a suitably large range of humidity conditions in the summertime troposphere was observed during the campaign.

An inevitable drawback of any intercomparison campaign of this scale and size is that the sounding activity is restricted to a relatively short period of time due to obvious limitations on available personal resources. As a result, the performance of the participating radiosondes is assessed for one time of the year only.

2.3 DATA POLICY

The main points of the data policy are summarised below; the complete (binding) text of the data policy document is included in Appendix C.

- The field campaign dataset will be published on a website and assigned a DOI after the publication of the Final Report.
- The results of the laboratory tests will be presented anonymously in the report.
- The Project Team members may use preliminary results and material (photos, etc.) of the intercomparison for communication and scientific publications before the end of the intercomparison, provided this is authorised by the Project Co-Leads and that the participating instruments remain anonymous in that material/publication.
- Following approval of the Project Co-Leads, the campaign dataset may be provided to other parties for scientific studies prior to the publication of the Final Report. Publication of these studies within five years after the publication of the Final Report requires the agreement of the data providers.
- Publications on the intercomparison dataset and/or results, that include the names of other manufacturers, shall not be used for commercial or promotional purposes in any way. Manufacturers shall avoid qualitative assessment of their radiosonde system in comparison with any other participant's system(s).
- Any publication based on the intercomparison data and/or results must acknowledge the source of the information and comply with the WMO copyright provisions.
- Raw radiosounding data from the field campaign are not disclosed, unless permission is granted by the manufacturer in question.

3 PARTICIPATING RADIOSONDE SYSTEMS

The list of manufacturers selected to participate in the 2022 UAI and the name of the radiosonde model is presented in Table 3.1. Due to the withdrawal of two manufacturers, as discussed in Chapter 1, only 10 manufacturers participated in the campaign. Table 3.2 summarises the main properties of the participating radiosondes including their temperature T , humidity U and pressure p sensors. Information on the calibration of the temperature and humidity sensors is presented in Table 3.3. Further details on the characteristics and ground systems are given separately in the subsequent sections for each of the 10 radiosonde models. The models are listed in alphabetical order.

Table 3.1: List of manufacturers selected to participate in the 2022 UAI. The first column lists the full names of the participating manufacturers, the ‘model’ column lists the full names of the radiosonde models, with the short names that are used in the report in parenthesis (if applicable).

Manufacturer	Country	Model	Participated
Azista Industries Pvt. Ltd.	India	ATMS-3710	yes
Aerospace Newsky Technology Co., Ltd.	China	CF-06-AH	yes
Graw Radiosondes GmbH & Co. KG	Germany	DFM-17	yes
Tianjin Huayuntianyi Special Meteorological Sounding Tech. Co., Ltd.	China	HT-GTS(U)2-1 (GTH3)	yes
Diel Met Systems (Pty) Ltd. trading as InterMet	South Africa	iMet-54	yes
Meisei Electric Co., Ltd.	Japan	iMS-100	yes
Meteomodem	France	M20	yes
Vikram Sarabhai Space Center, Indian Space Research Organisation	India	PS-B3	yes
Vaisala Oyj	Finland	RS41-SG (RS41)	yes
Weathex	Rep. of Korea	WxR-301D	yes
JSC “Rady”	Russian Fed.	MRZ-N1	no
Shanghai Changwang Meteotech Corp.	China	GTS3	no

All photos shown in this chapter are published as part of the supplementary material (see Section 1.6).

Table 3.2: Overview of the main properties of the 10 participating radiosonde models.

Radiosonde	Humidity (U) sensor	Temperature (T) sensor	Pressure (p) sensor	GNSS module	Transmission	Weight	Comment
ATMS-3710	Capacitive thin-film polymer	Platinum resistor	MEMS ^a piezo-resistive	GPS, L1 C/A, 167 ch.	bw ^b = 75 kHz, tp ^c = 100 mW, dlr ^d = 2.4 kbit s ⁻¹	77 g	-
CF-06-AH	Capacitive thin-film polymer	Thermistor	No	Multi-GNSS	bw = 15 kHz, tp = 100 mW, dlr = 2.4 kbit s ⁻¹	101 g	U -sensor with embedded T -sensor
DFM-17	Capacitive thin-film polymer	Thermistor	No	Multi-GNSS (L1; GPS, GLONASS, Beidou)	bw = <12 kHz, tp = 100 mW, dlr = 1.25 kbit s ⁻¹	65 g	Heated U -sensor with embedded T -sensor
GTH3	Capacitive thin-film polymer	Thermistor	MEMS piezo-resistive	Beidou	bw = 50 kHz, tp = 100 mW, dlr = 2.4 kbit s ⁻¹	138 g	-
iMet-54	Capacitive thin-film polymer	Thermistor	No	Multi-GNSS (D-GPS, GLONASS), 99 ch.	bw = 5 kHz, tp = 150 mW, dlr = 4.8 kbit s ⁻¹	84 g	Heated U -sensor with embedded T -sensor
iMS-100	Capacitive thin-film polymer	Thermistor	No	Code correlated D-GPS, 66 ch.	bw = 15 kHz, tp = 100 mW, dlr = 1.2 kbit s ⁻¹	43 g	U -sensor with embedded T -sensor
M20	Capacitive thin-film polymer	Thermistor	MEMS piezo-resistive; not used in MDP	GPS, L1 C/A	bw = 10.2 kHz, tp = 150 mW, dlr = 4.8 kbit s ⁻¹	37 g	Heated U -sensor with embedded T -sensor
PS-B3	Capacitive thin-film polymer	Thermistor	No	GPS	bw = 12 kHz, tp = 50 mW, dlr = 768 bit s ⁻¹	122 g	-
RS41	Capacitive thin-film polymer	Platinum resistor	No	D-GPS, L1 C/A	bw = 8.1 kHz, tp = 70 mW, dlr = 4.8 kbit s ⁻¹	80 g	Heated U -sensor with embedded T -sensor
WxR-301D	Capacitive thin-film polymer	Dual thermistor	No	GPS	bw = 25 kHz, tp = 100 mW, dlr = 4.8 kbit s ⁻¹	71 g	T -sensors with different coatings ('black' & 'white')

^a Micro-Electro-Mechanical Systems (MEMS)^b band width (bw)^c transmission power (tp)^d downlink rate (dlr)

Table 3.3: Information on temperature (T) and humidity (U) sensor calibration for the participating radiosondes provided by manufacturers.

Sonde model	Cal. range T -sensor (°C)	Manufacturer of U -sensor	Cal. range U -sensor (%RH)	Operational T -range U -sensor (°C)	Cal. temperature of U -sensor (°C)	T -dependence of U -sensor (%RH K ⁻¹)	Vapour pressure equation
ATMS-3710	-60 to 60	IST	10 to 95	-80 to 150	27	T -characteristics from manufacturer	N/A
CF-06-AH	-90 to 50	Aerospace Newsky	10 to 95	-80 to 40	23	0.064 (-30 °C; -23 °C)	Hyland and Wexler (1983)
DFM-17	-80 to 40	E+E	0 to 90	-80 to 60	23	T -characteristics from E+E	Hyland and Wexler (1983)
GTH3	-90 to 50	E+E	0 to 100	-90 to 50	23	0.12	Goff and Gratch (1946)
iMet-54	-68 to 30	E+E	0 to 97	-100 to 60	30	T -characteristics from E+E	Wexler (1977) modified by Hardy (1998) for ITS-90
iMS-100	-85 to 40	Meisei	15 to 95	-90 to 60	25	Kizu et al. (2018a) (GRUAN-TD-5)	Hyland and Wexler (1983)
M20	-85 to 40	UPSI	0 to 100	-100 to 60	-75, -55, -40, -20, -10, 0, 20, 40	0.26	Sonntag (1990)
PS-B3	-80, -40, 25 (three-point cal.)	Honeywell	20 to 90	-40 to 60	35	T -characteristics from manufacturer	Bolton (1980)
RS41	-100 to 60	Vaisala	0 to 100	-100 to 60	-90 to 60	0 to 0.042	Wexler (1977) modified by Hardy (1998) for ITS-90
WxR-301D	-70 to 30	E+E	10 to 90	N/A	20	T -characteristics from E+E	Buck (1981)

3.1 ATMS-3710 FROM AZISTA INDUSTRIES PVT. LTD.

Technical details of the radiosonde ATMS-3710 and the associated ground system from the manufacturer Azista Industries Pvt. Ltd. are listed in Table 3.4. Pictures of the radiosonde, the sensor boom, the antenna and the team during the laboratory campaign are shown in Figure 3.1.

Table 3.4: Azista Ascending Telesonde System ATMS-3710 from Azista Industries Pvt. Ltd.

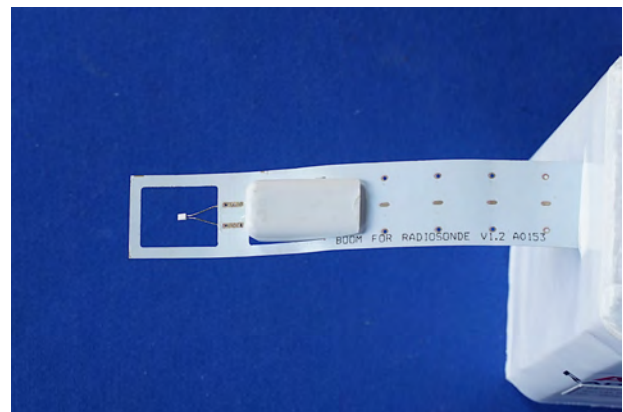
Sonde		Sensors		Transmission		Ground system	
<i>Weight</i>	77 g	<i>T</i>	Platinum resistor Pt1000	<i>Band width</i>	75 kHz	<i>Receiver</i>	ASAC-5750
<i>Body size (H/D/W)</i>	(123/46/55) mm	<i>U</i>	Capacitive polymer	<i>Transm. power</i>	100 mW	<i>Antenna</i>	QFH and Monopole
<i>Boom length</i>	≈ 88 mm	<i>p</i>	MEMS piezo-resistive	<i>Downlink rate</i>	2.4 kbit s ⁻¹	<i>Ground GNSS</i>	N/A
<i>Housing</i>	Styrofoam	<i>GNSS</i>	GPS, L1 C/A, 167 ch.	<i>Freq. band</i>	(400–406) MHz	<i>Check tool</i>	No ground check

Remarks

No ground check is done before launch. The humidity sensor is protected from solar radiation and direct contamination with water/ice by a cover/shield.



(a) Radiosonde ATMS-3710



(b) Sensor boom of ATMS-3710



(c) Antennas, position 4



(d) Manufacturer & host team during lab campaign at the climate chamber



(e) Hanging sonde

Figure 3.1: Azista photos

3.2 CF-06-AH FROM AEROSPACE NEWSKY TECHNOLOGY CO., LTD.

Technical details of the radiosonde CF-06-AH and the associated ground system from the manufacturer Aerospace Newsky Technology Co., Ltd. are listed in Table 3.5. Pictures of the radiosonde, the sensor boom, the antenna and the team during the laboratory campaign are shown in Figure 3.2.

Table 3.5: CF-06-AH GNSS Radiosonde and GPSTK Sounding System from Aerospace Newsky Technology Co., Ltd.

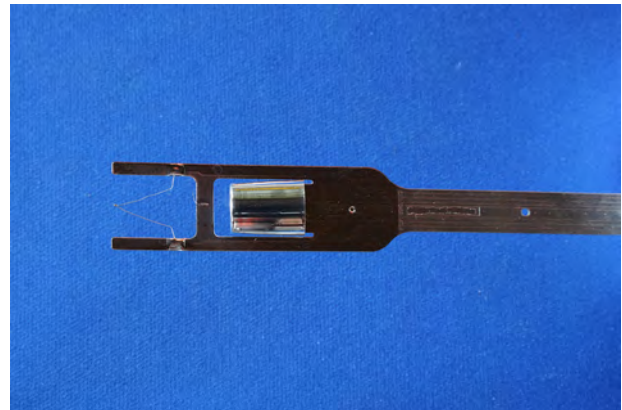
Sonde		Sensors		Transmission		Ground system	
<i>Weight</i>	101 g	<i>T</i>	Bead thermistor	<i>Band width</i>	15 kHz	<i>Receiver</i>	CFL-GPS-JS Ground Receiver
<i>Body size (H/D/W)</i>	(152/50/59) mm	<i>U</i>	Capacitive thin-film polymer + thermistor	<i>Transm. power</i>	100 mW	<i>Antenna</i>	CF-GPD-TX01 Omni-directional (UHF)
<i>Boom length</i>	≈ 116 mm	<i>p</i>	No (calculated by GPS height)	<i>Downlink rate</i>	2.4 kbit s ⁻¹	<i>Ground GNSS</i>	Global Positioning System (GPS), L1, Compass B1
<i>Housing</i>	Styrofoam	<i>GNSS</i>	Multi-GNSS	<i>Freq. band</i>	(400–406) MHz	<i>Check tool</i>	CF-GPS-JC Ground Check set (with Pt1000)

Remarks

The humidity sensor is reconditioned during the manufacturer-prescribed pre-flight ground-check by controlled heating. The humidity sensor is protected from solar radiation and direct contamination with water/ice by a cover/shield.



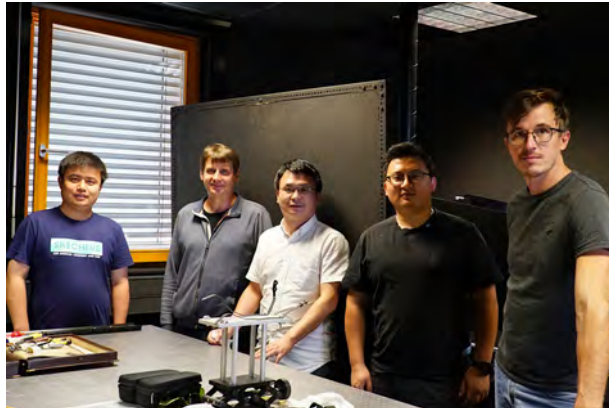
(a) Radiosonde CF-06-AH



(b) Sensor boom of CF-06-AH



(c) Antennas, position 8



(d) Manufacturer & host team during lab campaign in the radiation lab



(e) Hanging sonde

Figure 3.2: Aerospace Newsky photos

3.3 DFM-17 FROM GRAW RADIOSONDES GMBH & CO. KG

Technical details of the radiosonde DFM-17 and the associated ground system from the manufacturer Graw Radiosondes GmbH & Co. KG are listed in Table 3.6. Pictures of the radiosonde, the sensor boom, the antenna and the team during the laboratory campaign are shown in Figure 3.3.

Table 3.6: DFM-17 Multi-GNSS PTU Radiosonde and Groundstation GS-E from Graw Radiosondes GmbH & Co. KG

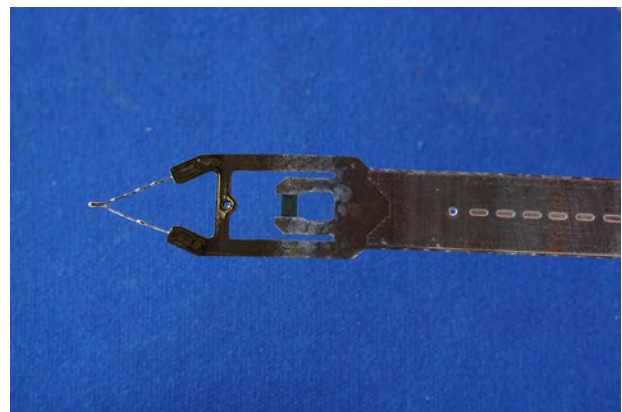
Sonde		Sensors		Transmission		Ground system	
<i>Weight</i>	65 g	<i>T</i>	Thermistor	<i>Band width</i>	<12 kHz	<i>Receiver</i>	GS-E Groundstation
<i>Body size (H/D/W)</i>	(99/45/68) mm	<i>U</i>	Heated capacitive thin-film polymer + <i>T</i> -sensor	<i>Transm. power</i>	100 mW	<i>Antenna</i>	Omni-directional
<i>Boom length</i>	≈ 128 mm	<i>p</i>	No (calculated by GNSS height)	<i>Downlink rate</i>	1.25 kbit s ⁻¹	<i>Ground GNSS</i>	GPS
<i>Housing</i>	Styrofoam	<i>GNSS</i>	Multi-GNSS, (L1; GPS, GLONASS, Beidou)	<i>Freq. band</i>	(400–406) MHz	<i>Check tool</i>	Ground check through sonde; no separate tool

Remarks

The humidity sensor is reconditioned during the manufacturer’s ground-check by controlled heating. The humidity sensor is heated during flight. The sonde is equipped with an additional temperature sensor which measures the temperature of the humidity sensor. There is no cover/shield on the humidity sensor.



(a) Radiosonde DFM-17



(b) Sensor boom of DFM-17



(c) Antennas, position 9



(d) Manufacturer & host team during lab campaign in the humidity lab



(e) Hanging sonde

Figure 3.3: Graw photos

3.4 HT-GTS(U)2-1 FROM TIANJIN HUAYUNTIANYI SPECIAL METEOROLOGICAL SOUNDING TECH. CO., LTD.

Technical details of the radiosonde HT-GTS(U)2-1 (GTH3 for short) and the associated ground system from the manufacturer Tianjin Huayuntianyi Special Meteorological Sounding Tech. Co., Ltd. are listed in Table 3.7. Pictures of the radiosonde, the sensor boom, the antenna and the team during the laboratory campaign are shown in Figure 3.4.

Table 3.7: HT-GTS(U)2-1 GNSS Radiosonde and HT03G-1U GPS sounding system from Tianjin Huayuntianyi Special Meteorological Sounding Tech. Co., Ltd.

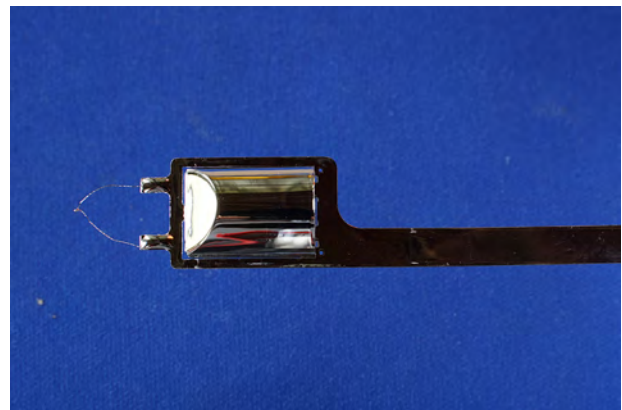
Sonde		Sensors		Transmission		Ground system	
<i>Weight</i>	138 g	<i>T</i>	Thermistor	<i>Band width</i>	50 kHz	<i>Receiver</i>	GTC2
<i>Body size (H/D/W)</i>	(152/61/63) mm	<i>U</i>	Capacitive thin-film polymer	<i>Transm. power</i>	100 mW	<i>Antenna</i>	Omni-directional
<i>Boom length</i>	≈ 127 mm	<i>p</i>	MEMS piezo-resistive	<i>Downlink rate</i>	2.4 kbit s ⁻¹	<i>Ground GNSS</i>	Beidou
<i>Housing</i>	Styrofoam	<i>GNSS</i>	Beidou	<i>Freq. band</i>	(401–406) MHz	<i>Check tool</i>	HT-GTC2-SS-JC Ground Check set

Remarks

The humidity sensor is protected from solar radiation and direct contamination with water/ice by a cap/shield.



(a) Radiosonde GTH3



(b) Sensor boom of GTH3



(c) Antennas, position 2



(d) Manufacturer & host team during lab campaign at the climate chamber



(e) Hanging sonde

Figure 3.4: Huayuntianyi photos

3.5 IMET-54 FROM DIEL MET SYSTEMS (PTY) LTD. TRADING AS INTERMET

Technical details of the radiosonde iMet-54 and the associated ground system from the manufacturer Diel Met Systems (Pty) Ltd. trading as InterMet are listed in Table 3.8. Pictures of the radiosonde, the sensor boom, the antenna and the team during the laboratory campaign are shown in Figure 3.5.

Table 3.8: iMet-54 GPS Radiosonde and iMet-3400 Sounding System from Diel Met Systems (Pty) Ltd. trading as InterMet

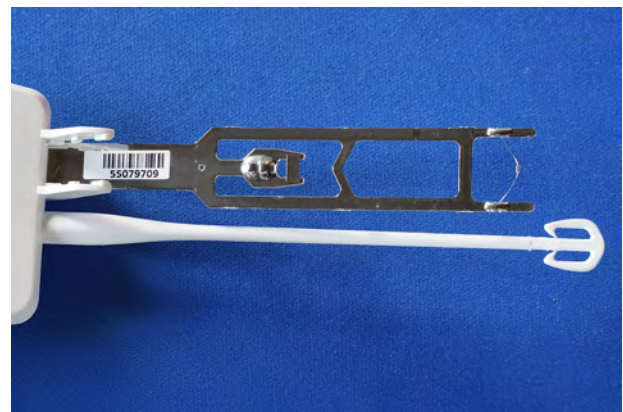
	Sonde		Sensors		Transmission		Ground system
<i>Weight</i>	84 g	<i>T</i>	Glass bead thermistor	<i>Band width</i>	5 kHz	<i>Receiver</i>	iMet-3400 Receiver
<i>Body size (H/D/W)</i>	(122/30/66) mm	<i>U</i>	Heated capacitive thin-film polymer + <i>T</i> -sensor	<i>Transm. power</i>	150 mW	<i>Antenna</i>	iMet-3400 omni-directional
<i>Boom length</i>	≈ 105 mm	<i>p</i>	No (derived by GNSS height)	<i>Downlink rate</i>	4.8 kbit s ⁻¹	<i>Ground GNSS</i>	N/A
<i>Housing</i>	Compostable bioplastic resin	<i>GNSS</i>	Multi-GNSS (D-GPS, GLONASS)	<i>Freq. band</i>	(400–406) MHz	<i>Check tool</i>	Ground Check Unit (GCU)

Remarks

The humidity sensor is dynamically heated during flight. The sonde is equipped with an additional temperature sensor which measures the temperature of the humidity sensor. There is no cover/shield on the humidity sensor.



(a) Radiosonde iMet-54



(b) Sensor boom of iMet-54



(c) Antennas, position 1



(d) Manufacturer & host team during lab campaign in the radiation lab



(e) Hanging sonde

Figure 3.5: InterMet photos

3.6 IMS-100 FROM MEISEI ELECTRIC CO., LTD.

Technical details of the radiosonde iMS-100 and the associated ground system from the manufacturer Meisei Electric Co., Ltd. are listed in Table 3.9. Pictures of the radiosonde, the sensor boom, the antenna and the team during the laboratory campaign are shown in Figure 3.6.

Table 3.9: iMS-100 GPS Radiosonde and Ground System RD-18 from Meisei Electric Co., Ltd.

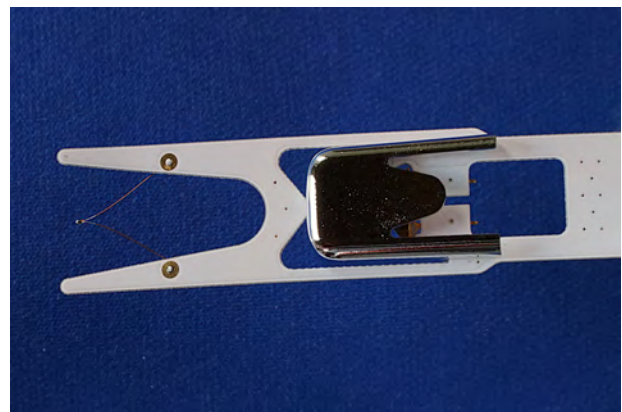
Sonde		Sensors		Transmission		Ground system	
<i>Weight</i>	43 g	<i>T</i>	Glass bead thermistor	<i>Band width</i>	15 kHz	<i>Receiver</i>	Ground system RD-18
<i>Body size (H/D/W)</i>	(131/53/55) mm	<i>U</i>	Capacitive thin-film polymer + <i>T</i> -sensor	<i>Transm. power</i>	100 mW	<i>Antenna</i>	Yagi
<i>Boom length</i>	≈ 87 mm	<i>p</i>	No	<i>Downlink rate</i>	1.2 kbit s ⁻¹	<i>Ground GNSS</i>	GPS
<i>Housing</i>	Bio-degr. corn-based material	<i>GNSS</i>	D-GPS, 66 ch.	<i>Freq. band</i>	(400–406) MHz	<i>Check tool</i>	Baseline Checker

Remarks

The sonde is equipped with an additional temperature sensor which measures the temperature of the humidity sensor. The humidity sensor is protected from solar radiation and direct contamination with water/ice by a cover/shield.



(a) Radiosonde iMS-100



(b) Sensor boom of iMS-100



(c) Antennas, position 3



(d) Manufacturer & host team during lab campaign in the humidity lab



(e) Hanging sonde

Figure 3.6: Meisei photos

3.7 M20 FROM METEOMODEM

Technical details of the radiosonde M20 and the associated ground system from the manufacturer Meteomodem are listed in Table 3.10. Pictures of the radiosonde, the sensor boom, the antenna and the team during the laboratory campaign are shown in Figure 3.7.

Table 3.10: M20 GPS Radiosonde and SR10 System from Meteomodem

Sonde		Sensors		Transmission		Ground system	
<i>Weight</i>	37 g	<i>T</i>	Thermistor	<i>Band width</i>	10.2 kHz	<i>Receiver</i>	SR10 Receiver
<i>Body size (H/D/W)</i>	(97/42/62) mm	<i>U</i>	Heated capacitive thin-film polymer + <i>T</i> -sensor	<i>Transm. power</i>	150 mW	<i>Antenna</i>	Omni-directional
<i>Boom length</i>	≈ 110 mm	<i>p</i>	piezo-resistive, not used in MDP	<i>Downlink rate</i>	4.8 kbit s ⁻¹	<i>Ground GNSS</i>	GPS
<i>Housing</i>	EPS ^a	<i>GNSS</i>	GPS, L1 C/A	<i>Freq. band</i>	(400–406) MHz	<i>Check tool</i>	Ground check device

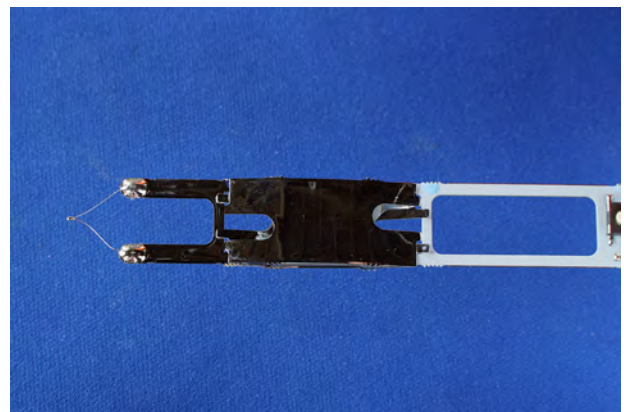
Remarks

The sonde is equipped with an additional temperature sensor which measures the temperature of the humidity sensor. The humidity sensor is protected from solar radiation and direct contamination with water/ice by a cover/shield.

^a Expanded Polystyrene (EPS)



(a) Radiosonde M20



(b) Sensor boom of M20



(c) Antennas, position 5



(d) Manufacturer & host team during lab campaign in the humidity lab



(e) Hanging sonde

Figure 3.7: Modem photos

3.8 PS-B3 FROM VIKRAM SARABHAI SPACE CENTER, INDIAN SPACE RESEARCH ORGANISATION

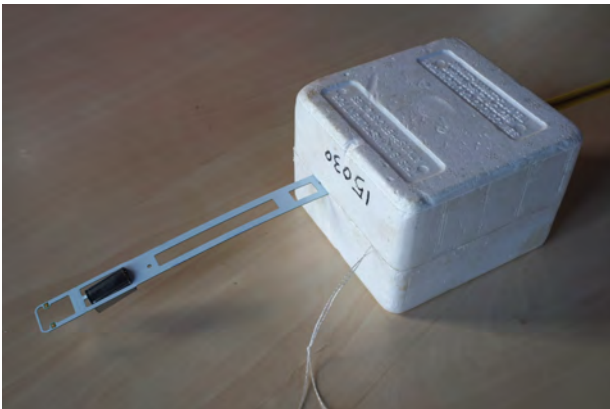
Technical details of the radiosonde PS-B3 and the associated ground system from the manufacturer Vikram Sarabhai Space Center, Indian Space Research Organisation are listed in Table 3.11. Pictures of the radiosonde, the sensor boom, the antenna and the team during the laboratory campaign are shown in Figure 3.8.

Table 3.11: PS-B3 GPS Radiosonde and Pisharoty Sonde system from VSSC, ISRO

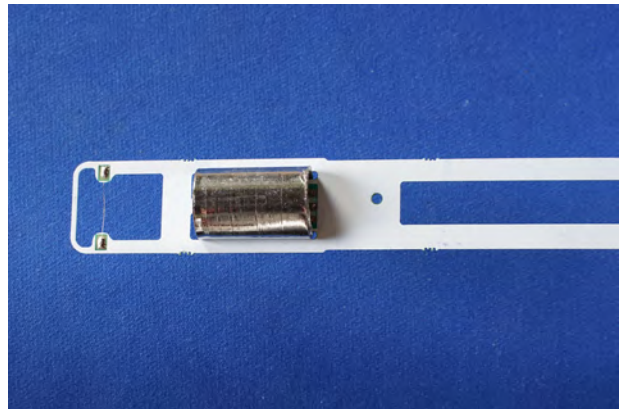
Sonde		Sensors		Transmission		Ground system	
<i>Weight</i>	122 g	<i>T</i>	Bead thermistor	<i>Band width</i>	12 kHz	<i>Receiver</i>	Pisharoty Sonde Receiver
<i>Body size (H/D/W)</i>	(120/90/115) mm	<i>U</i>	Capacitive thin-film polymer	<i>Transm. power</i>	50 mW	<i>Antenna</i>	Monopole and QuadriFilar Helix (QFH)
<i>Boom length</i>	≈ 278 mm	<i>p</i>	No	<i>Downlink rate</i>	768 bits s ⁻¹	<i>Ground GNSS</i>	N/A
<i>Housing</i>	EPS	<i>GNSS</i>	GPS	<i>Freq. band</i>	(400–406) MHz	<i>Check tool</i>	Ground Reference Unit

Remarks

The humidity sensor is protected from solar radiation and direct contamination with water/ice by a cover/shield. The attached sonde body is inclined at a certain angle during flight. The radio antenna is relatively large.



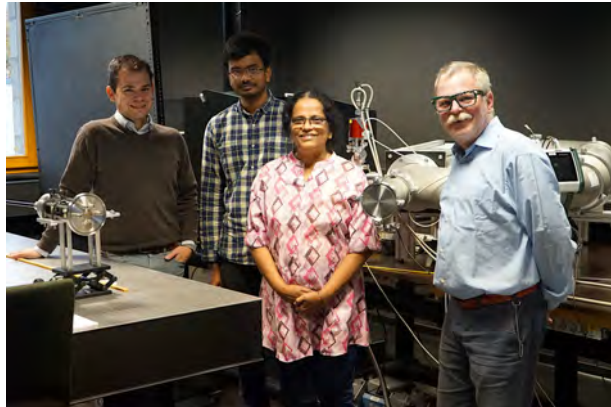
(a) Radiosonde PS-B3



(b) Sensor boom of PS-B3



(c) Antennas, position 10



(d) Manufacturer & host team during lab campaign in the radiation lab



(e) Hanging sonde

Figure 3.8: VSSC photos

3.9 RS41-SG FROM VAISALA OYJ

Technical details of the radiosonde RS41-SG (RS41) and the associated ground system from the manufacturer Vaisala Oyj are listed in Table 3.12. Pictures of the radiosonde, the sensor boom, the antenna and the team during the laboratory campaign are shown in Figure 3.9.

Table 3.12: RS41-SG GPS Radiosonde and Sounding System MW41 from Vaisala Oyj

Sonde		Sensors		Transmission		Ground system	
<i>Weight</i>	80 g	<i>T</i>	Platinum resistor Pt1000	<i>Band width</i>	8.1 kHz	<i>Receiver</i>	Sounding System MW41
<i>Body size (H/D/W)</i>	(155/46/63) mm	<i>U</i>	Heated capacitive thin-film polymer + <i>T</i> (Pt1000)	<i>Transm. power</i>	70 mW	<i>Antenna</i>	Directional (UHF)
<i>Boom length</i>	111 mm	<i>p</i>	No	<i>Downlink rate</i>	4.8 kbit s ⁻¹	<i>Ground GNSS</i>	GPS
<i>Housing</i>	EPS	<i>GNSS</i>	D-GPS, L1 C/A	<i>Freq. band</i>	(400–406) MHz	<i>Check tool</i>	Ground check device RI41

Remarks

The humidity sensor is reconditioned during the ground check by controlled heating. The humidity sensor is permanently heated during flight. The sonde is equipped with an additional temperature sensor which measures the temperature of the humidity sensor. There is no cover on the humidity sensor.



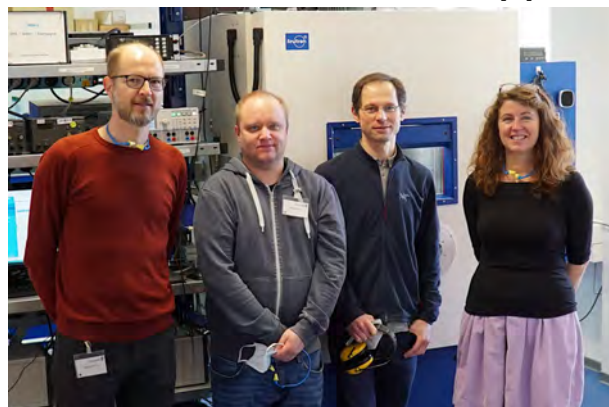
(a) Radiosonde RS41



(b) Sensor boom of RS41



(c) Antennas, position 7



(d) Manufacturer & host team during lab campaign at the climate chamber



(e) Hanging sonde

Figure 3.9: Vaisala photos

3.10 WXR-301D FROM WEATHEX

Technical details of the radiosonde WxR-301D and the associated ground system from the manufacturer Weathex are listed in Table 3.13. Pictures of the radiosonde, the sensor boom, the antenna and the team during the laboratory campaign are shown in Figure 3.10.

Table 3.13: WxR-301D GPS Radiosonde and GPSTK Sounding System from Weathex

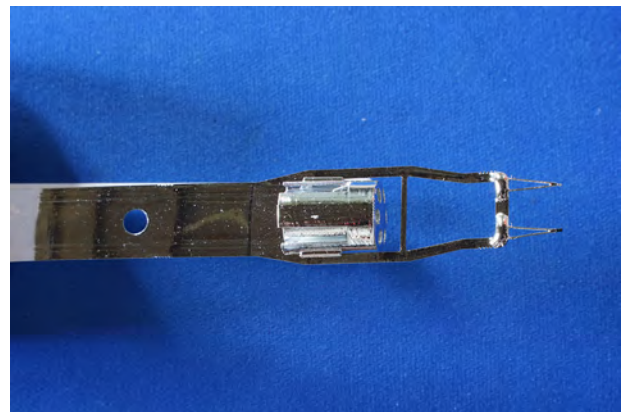
Sonde		Sensors		Transmission		Ground system	
<i>Weight</i>	71 g	<i>T</i>	Dual NTC thermistor	<i>Band width</i>	25 kHz	<i>Receiver</i>	WxRE-401 Ground Receiver
<i>Body size (H/D/W)</i>	(95/42/64) mm	<i>U</i>	Capacitive thin-film polymer	<i>Transm. power</i>	100 mW	<i>Antenna</i>	WxAS-501 Full-wave Quadrifilar Helix
<i>Boom length</i>	≈ 121 mm	<i>p</i>	No	<i>Downlink rate</i>	4.8 kbit s ⁻¹	<i>Ground GNSS</i>	GPS
<i>Housing</i>	Styrofoam, Plastic	<i>GNSS</i>	GPS	<i>Freq. band</i>	(400–406) MHz	<i>Check tool</i>	Ground Checker

Remarks

The sonde has a dual temperature sensor with a “white” (aluminium coated) and a “black” (dark-coated) sensor for direct estimation of the radiation error. The humidity sensor is protected from solar radiation and from contamination by water or ice by a cover.



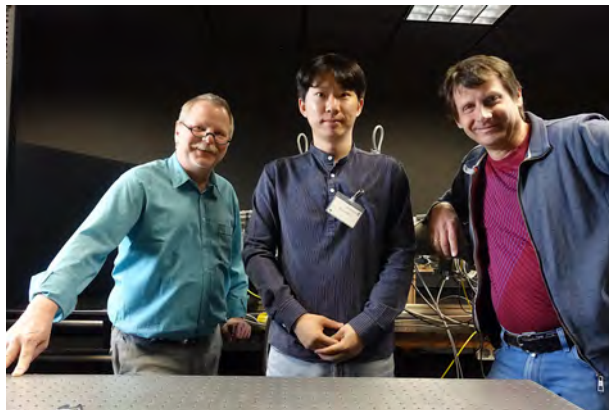
(a) Radiosonde WxR-301D



(b) Sensor boom of WxR-301D



(c) Antennas, position 6



(d) Manufacturer & host team during lab campaign in the radiation lab



(e) Hanging sonde

Figure 3.10: Weathex photos

4 IMPLEMENTATION OF THE CAMPAIGN

4.1 LOCAL SITE – THE LINDENBERG METEOROLOGICAL OBSERVATORY

4.1.1 The observatory – general overview

The Lindenberg Meteorological Observatory – Richard Assmann Observatory (MOL-RAO) is one of two research observatories operated by DWD¹ within its *Research and Development* department. MOL-RAO was founded in 1905 as the Royal Prussian Aeronautical Observatory by Richard Assmann, who is also known as the inventor of the aspiration psychrometer and as discoverer of the stratosphere together with the French scientist Teisserenc de Bort.

For over 100 years, the activities at the observatory mainly focused on the vertical profiling of the atmosphere (aerology). In the beginning this was done using captive balloons and kites, from the 1930s onwards using radiosondes and, for the last 30 years, increasingly with the help of ground-based remote sensing methods such as radar and lidar. The current world high altitude record of 9750 m Above Mean Sea Level (AMSL) for kite ascents was established at the observatory on 1 August 1919.

Other current research activities at MOL-RAO are focused on measurement programmes for the study of solar and terrestrial radiation, and on the processes involved in the interaction between the Earth's surface and the atmosphere. The data collected by the observatory's measurement programmes are used to produce a reference data set, the 'Lindenberg Column', for characterising the vertical structure of the atmosphere from the surface up to the stratosphere.

The observatory participates in various international and national scientific programmes and partnerships. In the context of international programmes, the data obtained in Lindenberg make a significant contribution to the monitoring of the earth's climate and are also used to calibrate satellite sensors and to verify weather prediction and climate models. Scientists at the observatory also test new sensors and observing systems in view of their potential operational deployment in the DWD's observation network.

Further information on the fields of work and research (aerology, ground based remote sensing, atmospheric boundary layer processes, solar and terrestrial irradiance measurements) as well as on the GCOS Reference Upper-Air Network (GRUAN), whose Lead Centre is located at the observatory, can be found in the Appendix F.1.

4.1.2 Geographical location and local climatology

Lindenberg observatory ($\phi = 52^{\circ}13' \text{ N}$, $\lambda = 14^{\circ}7' \text{ E}$) is located in central Europe in the Northeastern part of Germany (see map in Figure 4.1) approximately 50 km south-east of the Berlin Metropolitan area. Lindenberg, part of the municipality of Tauche, lies on the federal road B246, between the towns Storkow and Beeskow. The observatory and the weather station are on the northern edge of the village, situated around a small hill which forms the highest elevation in the area. The top of the hill reaches an altitude of 122 m Above Mean Sea Level (AMSL), whereas the weather station resides at 98 m AMSL. The landscape around Lindenberg is characterised by undulating plateaus formed by terminal moraines at the end of the last glacial period. The elevation varies between 40 m to 130 m AMSL and tends to slope downwards to an altitude of 40 m AMSL towards the South and West. These lower lying areas harbour lakes (Scharmützelsee, Kossenblatter See), and further east are lowlands formed by the Spree river. Lindenberg lies in the inland lowland area, far from the coast with predominantly continental influence.

OSCAR/Surface (Observing Systems Capability Analysis and Review Tool) can be used to get further standardised information on this site².

¹German weather service: <https://www.dwd.de>

²<https://oscar.wmo.int/surface/#/search/station/stationReportDetails/0-20008-0-LIN>



Figure 4.1: Location of the Lindenberg Meteorological Observatory (Germany) in Europe (modified based on [https://commons.wikimedia.org/wiki/File:Germany_in_Europe_\(relief\).svg](https://commons.wikimedia.org/wiki/File:Germany_in_Europe_(relief).svg), TUBS, CC BY-SA 3.0 <https://creativecommons.org/licenses/by-sa/3.0>, via Wikimedia Commons)

The monthly mean surface temperature (1961 to 1990) varies between -1.2°C (January) and 17.9°C (July), and the mean annual precipitation is 563 mm. The annual precipitation has a primary maximum in summer and a secondary maximum in December while the minima are in February and October. A climate diagram of MOL-RAO is shown in Figure 4.2.

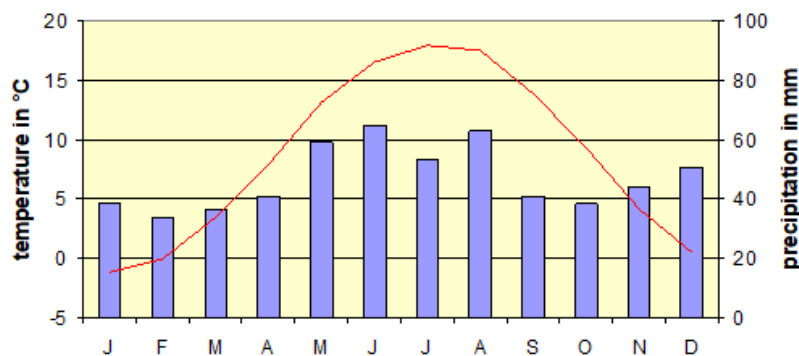


Figure 4.2: Climate diagram for Lindenberg, surface temperature (red trace) and precipitation (blue bars). Climate reference period: 1961 to 1990.

An overview of the vertical atmospheric profile over Lindenberg and its seasonal cycle up to the middle of the stratosphere is shown in Figure 4.3. It shows a time series of monthly means of nighttime temperature and relative humidity on a 1 km vertical grid for the last 6 years based on RS41 radiosonde data (GRUAN Data Product). Both plots show that during the campaign summer 2022 the conditions in the free atmosphere were similar to previous years, with no striking anomalies.

The typical profile over Lindenberg in August-September is characterised by a daytime surface temperature of 25°C (298 K), a -60°C (213 K) cold tropopause at approximately 12 km altitude and a temperature of -40°C (233 K) at 35 km.

4.1.3 Site description

Various buildings and measurement sites are present on the MOL-RAO grounds; those relevant to the campaign are indicated in Figure 4.4.

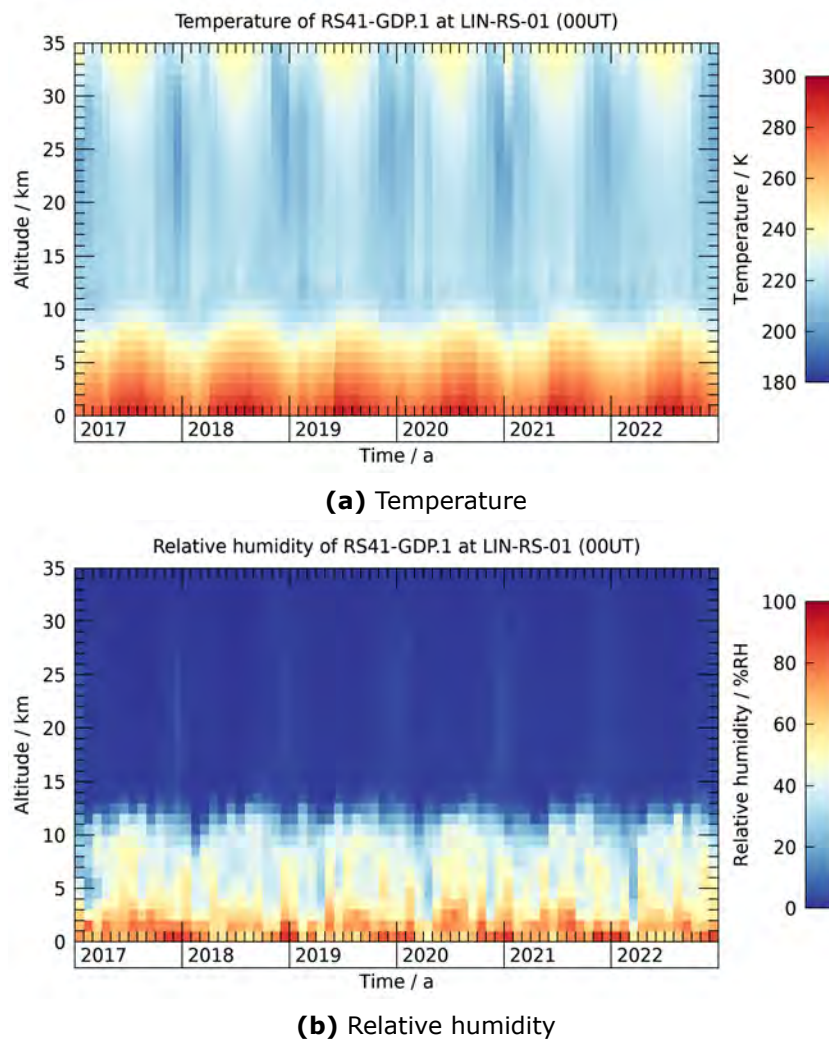


Figure 4.3: Vertically gridded (1 km) monthly means (00 Coordinated Universal Time (UTC)) of temperature and relative humidity profiles (RS41-GRUAN Data Product) at Lindenberg for the period 2017 to 2022.

During the field campaign, meetings were held in the conference room in building ①, which was also used for taking meals. A second room in the same building was used as working space for data processing, preliminary analysis, and monitoring of the campaign's progress and statistics. The training sessions preceding the start of the actual sounding period took place in various rooms of building ① as well as in the neighbouring office building.

During the field campaign, the balloon hangar ② was used as the central facility for all operations with regard to sonde and rig preparations and flight monitoring (Section 4.1.5). The radiosonde antenna array ③ and the actual launch site ④ were located close to the hangar (Sections 4.1.6 and 4.1.7). The ground systems of the GDP radiosondes were located and operated in a separate building ⑦, where also Lindenberg's operational radiosoundings are performed. The historic winch house (round building on the map in Figure 4.4) on the top of the hill is a monument for the more than 100-year long history of aerology in Lindenberg.

The laboratory facilities used during the laboratory campaign are located in the buildings ⑤ and ⑥ (more details in Section 4.1.4). Other relevant measuring instruments (e.g. remote sensing) are indicated by ⑧ and ⑨, among others (see also Section 4.4).

Figure 4.5 shows an aerial photo of the observatory grounds during the field campaign. In the foreground, from left to right, are the radiation building (housing the radiation laboratory), the historical winch house, another radiation measurement platform, the launch site, the antenna array, and the balloon hangar. In the background, the building for operational routine and GDP sonde preparation can be seen in front of the village on the left, and to the right the building



Figure 4.4: Map of the observatory grounds. Numbered marks indicate facilities involved in the campaign: ① conference hall, ② balloon hangar, ③ antenna field, ④ launch site with launch pad and ground weather station, ⑤ building with laboratory facilities for humidity and climate chamber tests, ⑥ radiation measurement building with laboratory for radiation experiments, ⑦ station for operational radiosoundings; preparation of GDP radiosondes, ⑧ LIDAR building, ⑨ wind profiler.

housing the humidity laboratory and the climate chamber.

4.1.4 Laboratories

The observatory hosts extensive laboratory facilities for different research areas. In connection to GRUAN activities, several laboratory setups have been developed to characterise radiosonde sensors under controlled conditions. These setups, including a humidity laboratory, a climatic chamber, and one for radiation tests, were used extensively to assess the performance of the participating radiosondes during the laboratory phase of the campaign. A brief description of the setups is given in the following subsections.

4.1.4.1 Humidity laboratory

The humidity laboratory (located in building ⑤) focuses on assessing the performance of the radiosonde's humidity sensors. The measurements are performed at room temperature and pressure, and use Standard Humidity Chambers (SHCs) to generate a stable humidity environment at six well-defined levels in the range of 0 %RH to 100 %RH. The humidity levels are created by utilising fundamental physical-chemical properties of certain salts, eliminating the need for using humidity generators precise measurement instruments (see Chapter 5).

4.1.4.2 Climatic chamber laboratory

The climatic chamber, located in building ⑤, was used for measurements at low temperatures. The climatic chamber setup was used to determine the response time (time lag) of the humidity



Figure 4.5: Aerial view of the observatory site towards southwest at the time of the campaign.

sensors to sudden changes in humidity at temperatures between -75°C and room temperature, and to assess the calibration uncertainty of the temperature sensors. See Chapter 6 for a detailed description of the measurements and the setup.

4.1.4.3 Radiation laboratory

The Simulator for Investigation of Solar Temperature Error of Radiosondes (SISTER) setup to investigate the sensitivity of the temperature sensor to shortwave radiation (Chapter 7) is located in building ⑥. SISTER is designed as a 2 m large wind tunnel in which the radiosonde to be tested is installed. With this set up it is possible to simulate radiation, pressure, and ventilation conditions that a sonde is exposed to during ascents at altitudes between the surface and 35 km; a Xenon-arc light source provides a beam of artificial Sunlight. This setup was used to develop the radiation correction applied in the GRUAN Data Product for the RS41 radiosonde ([von Rohden et al., 2022](#)).

4.1.5 Balloon hangar

The balloon hangar was originally built after foundation of the observatory and served as preparation and storage space for meteorological kites (building ② in Figure 4.4). According to the space required for the work with the kites, the hangar was built large (approx. 24 m \times 10 m wide and >7 m high). Nowadays it is used to fill balloons and for the preparation of payloads for all kinds of balloon sounding activities at the observatory. Using the available space and the central location close to the launch site, most of the activities during the field campaign took place in the balloon hangar.

Figure 4.6 shows the layout of the work environment inside the balloon hangar (floor altitude 110.5 m AMSL). The ground systems of all manufacturers were set up in the left part (see markings ① to ⑩). Each manufacturer was assigned a workplace for operating two sounding systems (altitude of the top of the worktables 111.2 m AMSL). After the end of the soundings, the profile data were downloaded from the sounding computers (without network connection) by the operators, handed over to the campaign team using colour-coded USB³ sticks that each were assigned to a specific system, and subsequently uploaded to the data collection terminal

³Universal Serial Bus (USB)

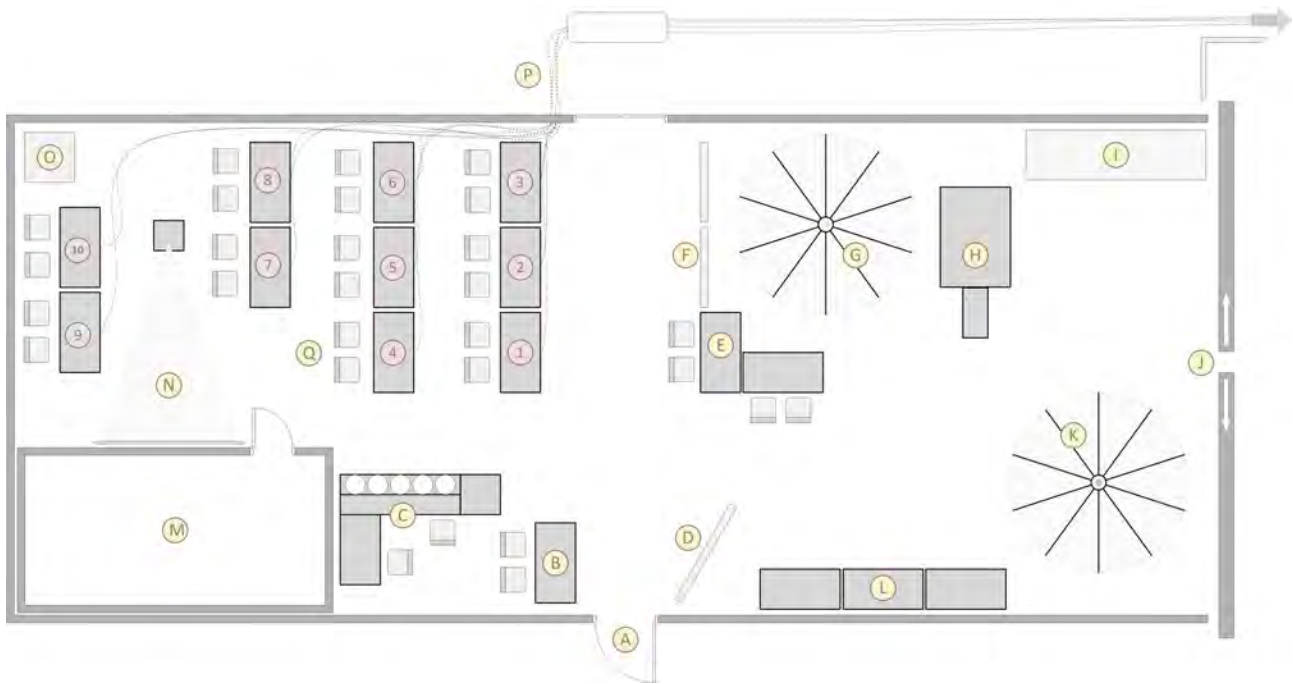


Figure 4.6: Design of the interior of the balloon hangar during the campaign (approx. 24 m × 10 m wide and >7 m height), with markings and descriptions of the relevant objects and setups: ① to ⑩ – Working tables for participants with space for 2 ground systems each; ① – Entrance; ② – Supervisor station; ③ – Set of five SHCs to perform independent ground checks at 100 %RH; ④ – Large screen for current information (e.g. briefings, flight data); ⑤ – Central terminal for data collection; ⑥ – General information boards; ⑦ – Rig preparation area 1 (with stand); ⑧ – Balloon filling system; ⑨ – Rig storage (up to ten); ⑩ – Hangar doors (gate for ready-to-fly balloon rigs); ⑪ – Rig preparation area 2 (suspended from the ceiling by hook and line); ⑫ – Small storage and shelf for tools and aids; ⑬ – Balloon storage and preparation compartment (incl. oven, refrigerator and GNSS signal repeater amplifier); ⑭ – Projector for displaying current measurement values of SHCs; ⑮ – Uninterruptible Power Supply (UPS); ⑯ – Incoming cables from antenna array (max. 100 m); ⑰ – GNSS signal repeater antenna.

⑤. ③ denotes a linear arrangement of five Standard Humidity Chambers (SHCs) to perform independent ground checks of the radiosondes' humidity sensors at 100 %RH relative humidity. A pressure sensor (PTB330) was installed at the same height as the SHCs (111.8 m AMSL) to provide air pressure measurements during the launch preparation. The supervisor desks were next to the entrance (②). The supervisors were in charge of the shifts and directed and managed all activities. The campaign rigs were prepared and balanced at ⑦ and ⑪. A limited supply of rigs was stored in the balloon hangar, lasting for the next two to three sounding days (⑨). The balloons were stored in ⑬, and prepared and inflated at the filling table ⑧.

The entire electrical system in the balloon hangar was buffered by a central Uninterruptible Power Supply (UPS) (⑮). The manufacturers' receiving systems and computers were by default disconnected from the internet to guarantee independent data collection. However, internet access was granted in special cases by the campaign leads to enable troubleshooting of malfunctioning systems (see Appendix G). Permanent (secured) network access was available for the supervisors' computers and for the data transfer computer.

To support Global Navigation Satellite System (GNSS) signal reception in the balloon hangar, a repeater system was installed at the beginning of the phase of system setup and operator training (see Figure 4.10) and was in use for all soundings between 2022-08-09 10:15 UTC and the end of the sounding phase. The frequency response was optimised for the GPS frequency band L1. The main repeater system components included an active GNSS signal receiving antenna (Vaisala GPS Antenna GA31) mounted on an observation tower approx. 26.5 m above the ground next to the balloon hangar (see Figure 4.5), a low-noise signal amplifier (KUHNE KU LNA 1575-50) supplied with a voltage of 7 V at 70 mA current, and a downward directed repeating antenna (Vaisala GA45015) inside the hangar approximately 5 m above the floor (115.5 m AMSL), see

markings (M) and (Q) in Figure 4.6. The GNSS signal was forwarded from the receiving antenna via a 130 m coaxial antenna cable (Vaisala CBL210400) and a signal splitter (ETL Systems Ltd. COM02S1P-2599-N5N5) to the amplifier, and the amplified signal passed a 10 m coaxial cable (type Aircell 7) to the repeater antenna. The output level of the GPS repeater was adjusted to prevent positive feedback from the receiving antenna in the tower.

4.1.6 Antenna array

An array of manufacturer antenna systems was set up for the duration of the field campaign. It was located on a 20 m long stretch along the footpath from the balloon hangar to the winch house ((3) in Figure 4.4). The top end of the antenna array was approximately at the same height as the launch pad ((4)). The array was divided into 10 equally sized sections of approx. 2 m × 2 m. The sections were numbered from 1 to 10, starting on top close to the launch pad. Each participant was assigned per lot one of the sections for setting up, anchoring, and grounding their antennas for radiosonde telemetry and GNSS. The antenna cables were led on the ground into the balloon hangar by a cable route ((P) in Figure 4.6). The largest distance between the hangar and the top of the antenna array was less than 100 metres.

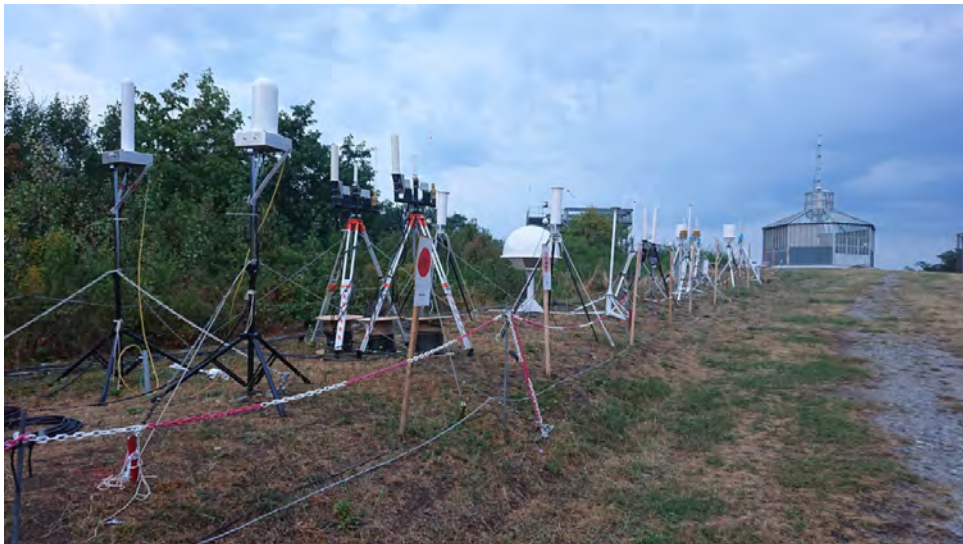


Figure 4.7: Antenna array

4.1.7 Launch site

A 2 m pole was installed at the launch site ((4)). On the top of the pole a horizontal 30 cm diameter disc was mounted, on which the rigs were placed for launch. This was to ease the attachment of the radiosondes to the rig and to ease the launch procedure, and to ensure a fixed, well-defined launch altitude for all flights during the field campaign. The rigs were secured with removable clamps, and the disc could be rotated, to accommodate changing wind direction.

With the rig firmly and stably fixed on the launch pad, the radiosondes could comfortably be tied to the rig using already attached strings. As will be discussed extensively in Appendix F.3 the string length was such that the temperature sensor of the radiosondes was 70 cm below the tip of the rod. In this position, the altitude of the radiosondes was 120 m AMSL.

After removing the clamps, the rig was ready for launch. During launch, the released balloon lifted the rig from launch pad, without being held by an operator. With a string length of 70 cm the separation between the radiosonde and the ground was approximately 1 m, which was generally sufficient to prevent the radiosondes from touching the ground during launch. There were one or two launches under special (unusual) conditions where some of the radiosondes came into contact with the ground (see Section 8.2.4).



(a) Day flight



(b) Night flight

Figure 4.8: Rigs on the launching pad ready for the launch

4.1.8 Surface observations

The information on surface weather during the field campaign was obtained from manual observations of the manned weather station at the observatory (⑦ in Figure 4.4) and from data of an Automatic Weather Station (AWS) for the measurement of atmospheric state variables next to the launch site (see Figure 4.9). Continuous AWS readings as well as time-fixed surface observations at launch time were provided to the operators in the balloon hangar and to the GDP operators using an internal website.

The AWS sensors for temperature, humidity, wind direction and wind speed were mounted on a mast about 10 m southwest of the launch site at a height of 2 m to 2.5 m above ground (sloping terrain). The AWS-sensor for barometric pressure was located on a second mast about 15 m from the launch site in the same direction and at a height 70 cm lower than the launch pad, also 120 m AMSL. This height corresponded to about the position of the radiosondes on the rig at launch. The time resolution of the AWS was 1 Hz.

Manual observation according to WMO guidelines included cloud cover and horizontal visibility at launch time, as well as continuous detection of weather events.

A control software handled automated data retrieval from the AWS via a local area network and allowed manual entry of coded manual observations via web pages. After the official launch time was set by the sounding supervisor, collected AWS data and manual observations were time-assigned and published as surface weather for the respective sounding.

4.2 LABORATORY STRATEGY AND SCHEDULE

4.2.1 Strategy

As mentioned in Section 2.1, laboratory testing is compulsory for all participating radiosondes and constitutes an integral part of the UAI campaign. Factors that may lead to substantial systematic errors in radiosonde measurements, and that can be investigated with reasonable effort under laboratory conditions during the campaign, are the sensor calibration, the sensor behaviour at low temperatures, and short-wave (solar) radiation. Each radiosonde model was subjected to standardised tests in each of four distinct experiments using three setups:

LABH⁴ Performance and calibration of the humidity sensor at room conditions (Chapter 5),

LOWT⁵ Calibration of the temperature sensor at atmospheric temperatures (Chapter 6),

TLAG⁶ Response behaviour of the humidity sensor with focus on low temperature conditions (Chapter 6),

⁴Humidity sensor performance at room conditions (LABH)

⁵Temperature sensor performance at low temperatures (LOWT)

⁶Time lag behaviour of the humidity sensors (TLAG)

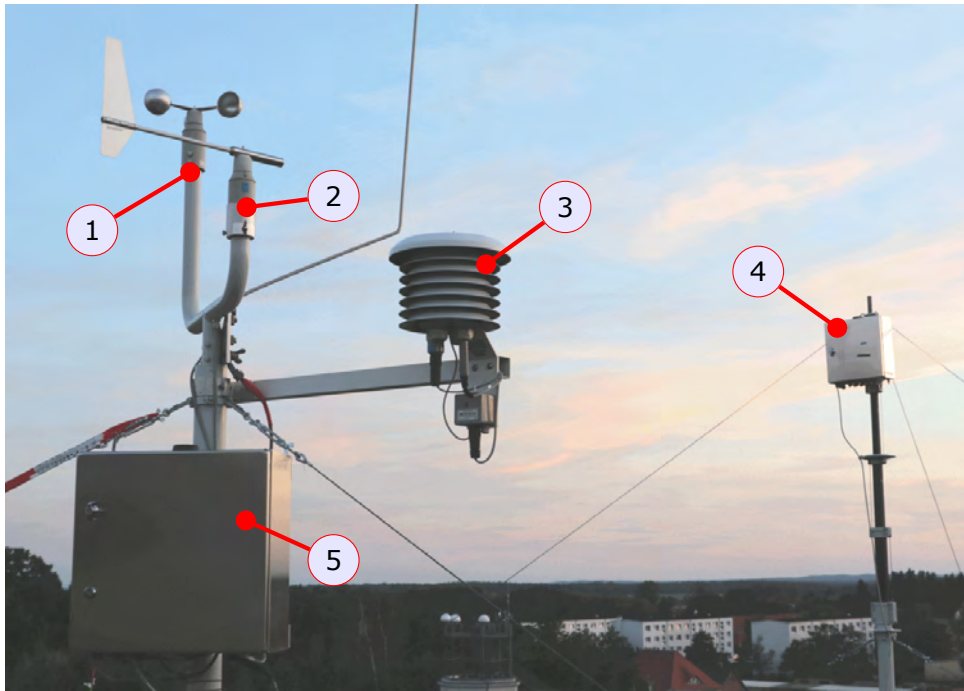


Figure 4.9: Automatic Weather Station main components: ①+② – Wind speed and wind direction sensors of the series “Classic” (Adolf Thies GmbH & Co. KG), ③ – temperature sensor PT100 (Theodor Friedrichs & Co. Meteorologische Geräte und Systeme GmbH) and humidity sensor HMP45D (Vaisala) in a lamellar shelter LAM 630 (Eigenbrodt GmbH & Co. KG.), ④ – barometric pressure sensor PTB330 (Vaisala) in a non-sealed housing and ⑤ – data logger CR1000X (Campbell Scientific Ltd.) in an enclosure.

RADI⁷ Sensitivity of the air temperature measurement to solar irradiance (Chapter 7), where the LOWT and TLAG tests were performed with the same radiosonde units in one pass within the same setup. Standardisation means that measurements with selected but equal measurement parameter settings and conditions are set up as mandatory minimum program for all radiosondes.

The experimental facilities for radiosonde testing and sensor characterisation are located in separate laboratories at the Lindenberg site (see Figure 4.4). These facilities and test setups were developed over the last decades as part of the routine activities for data quality assurance, and became increasingly important in the framework of GRUAN, whose basic ideas include the evaluation of data quality based on independent instrument characterisation, metrological traceability, and comprehensive evaluation of measurement uncertainties. More details on the motivation as well as descriptions of the setups and implementation of the test procedures are given in the respective chapters 5-6.

Due to time restrictions a compact measurement program was defined, that could be performed for all participants alike within a reasonable amount of time in the framework of the campaign. Consequently, this limited test program does not constitute a full characterisation of the radiosonde, but it serves to provide a first assessment of the radiosonde’s sensors. It is important to note that in all experiments only calibrated raw data without any corrections or further processing are evaluated. The results are suitable for providing an overview of the sensor/sonde behaviour under the conditions realised during the experiments. The results may be useful for the manufacturers with regard to understanding or confirming the characteristics, and they will help with the evaluation of the atmospheric profiles taken during the sounding part of the campaign.

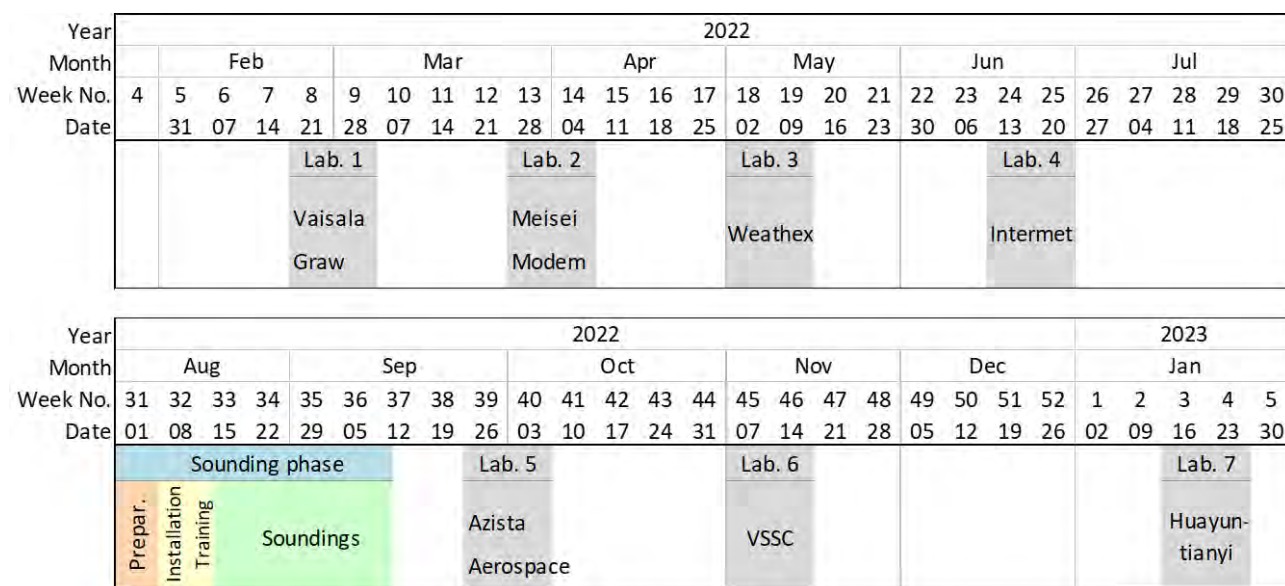


Figure 4.10: Timeline of the campaign activities in Lindenberg. The grey blocks represent the laboratory test phases together with the name of the manufacturer(s) present. The coloured block represents the field campaign. In the first week of August Lindenberg staff performed the final preparations (orange). Manufacturer staff was present during the lab phases and from 8 to 16 August to set up their systems for the field campaign and to train the operators (yellow). The campaign soundings were carried out from 16 August to 13 September, 2022 (green).

4.2.2 Schedule

The original intention was to carry out the laboratory tests for the 10 participating manufacturers independent of, and before the actual field campaign phase, in five blocks of two-week duration each, with two participants in parallel. Due to SARS-Covid-19 related travel restrictions and quarantine regulations in Germany and the home countries of the manufacturers, this schedule had to be adapted. As a result, seven laboratory slots were carried out: three with two manufacturers on site in parallel, and the remaining four with only one manufacturer. Three slots were took place after the field campaign, so that the lab activities extended over the period from February 2022 to January 2023. The actual time sequence of the laboratory activities is shown in Figure 4.10.

The manufacturer teams operating their radiosonde systems consist of up to three members. The lab activities are supported and supervised by (at least) a technician and a scientist of the UAII team in all experiments, who also operate the laboratory systems.

Within the blocks of 10 working days, the first day is foreseen for unpacking, material and system checks by the manufacturers. Subsequently, three days are allocated for the experiments in each of the three laboratories. The experiments are carried out alternately if two manufacturers are present at the same time. The first day in each experiment is in general reserved for experiment specific preparation (e.g. sonde installation in the setups) end testing activities. Measurements following the mandatory program are usually carried out during the second day, and continued on the third day, if necessary. Once the mandatory (standard) program is completed, further tests can be carried out in consultation with the manufacturers if time is available. Deviations from this scheme can be agreed with the manufacturers as long as the completion of the mandatory program is ensured. Table 4.1 summarises the basic schedule of a two-week laboratory experiment phase in the presence of two manufacturers.

⁷Radiation sensitivity of air temperature measurement (RADI)

Table 4.1: Typical sequence of a two-week laboratory phase with two manufacturers in parallel.

Day	Topic	Manufacturer 1	Manufacturer 2
Mo	Welcome & Setup	Setup & test	Setup & test
Tu	Preparation 1	LABH	RADI
We	Experiment 1 (day 1)	LABH	RADI
Th	Experiment 1 (day 2)	LABH	RADI
Fr	Preparation 2	TLAG & LOWT	LABH
Mo	Experiment 2 (day 1)	TLAG & LOWT	LABH
Tu	Experiment 2 (day 2)	TLAG & LOWT	LABH
We	Preparation 3	RADI	TLAG & LOWT
Th	Experiment 3 (day 1)	RADI	TLAG & LOWT
Fr	Experiment 3 (day 2)	RADI	TLAG & LOWT

4.3 SOUNDING STRATEGY AND SCHEDULE

4.3.1 Independent operators

One explicit goal of the Lindenberg Upper-Air Instrument Intercomparison, contrary to previous WMO intercomparisons, was to enable an evaluation of the participating radiosonde systems independent of the manufacturers. Thus radiosonde manufacturers were asked to set up and test their systems and then to leave the campaign site for the remainder of the field campaign. Instead the systems were operated by independent operators, who were selected by the project team following a call by WMO inviting Members to nominate candidates. The operators were trained by the radiosonde manufacturers at the beginning of the field campaign and operated the systems independently and without involvement of the manufacturers. Therefore, this campaign was conducted as a blind intercomparison.

Out of 49 nominations, ten operators were selected by WMO and the project team. Selection criteria included basic meteorological technician training, previous experience with at least one radiosonde system, sufficient English language skills, and the ability to stay at Lindenberg for the duration of the campaign. WMO recognised that this campaign served as international capacity building and preference was given to nominations of operators from developing countries.

Nine operators were able to travel to Lindenberg to support the operations of the intercomparison. One operator, who had been selected, had to be replaced on very short notice by a backup operator from the staff of the Lindenberg observatory. Countries represented by operators (see Appendix P) were

- Egypt
- Fiji
- Germany (backup recruited from staff of Lindenberg Observatory)
- Philippines
- Seychelles
- South Africa
- Trinidad and Tobago
- Tunisia
- Vietnam
- Zimbabwe

All operators had previous experience with one or several of the participating soundings systems. However, all operators were assigned to manufacturers with which they had no prior experience. This assignment was done to allow an evaluation of the usability of sounding systems that was not affected by the operator's previous experience with their systems. All operators worked with two different systems, one of which had participated in a previous intercomparison or had international market share and another, which typically had not previously participated.

During the first week of the campaign, manufacturers set up their systems, installed telemetry and GNSS antennas on the designated spots within the antenna field (Section 4.1.6), and configured their receiving systems. This week also provided time for the manufacturers to train the operators assigned to their systems. All operators received written instruction material and in person instructions on the operations of the soundings systems, including some basic troubleshooting procedures in case unexpected issues were to arise during the sounding phase of the field campaign. In addition to the WMO selected operators, some staff members of Lindenberg Observatory and some project team members were also trained in case backup operators were needed to substitute any of the primary operators.

The staff of Aerospace Newsky Technology Co., Ltd. (China) arrived late at Lindenberg due to unexpected travel delays, missing most of the first week. To prevent delay of the campaign schedule, the task team member who was overseeing the operator training took care of parts of the operator training in this case.

At the end of the setup and training period, the project team confirmed that all manufacturers were satisfied with the level of expertise of the operators. The project team also confirmed that all operators were satisfied with the training they had received. Communication channels were established to handle unexpected system malfunctions during the blind phase of the intercomparison. These communication channels involved the project team to guarantee the ongoing blind intercomparison.

All manufacturers departed Lindenberg prior to the beginning of the formal intercomparison. This phase of the campaign was conducted entirely by the independent WMO operators. The manufacturers received only the sounding data from their own systems and were asked to verify proper operation and to contact the project leads in case of issues. Apart from the manufacturer-interactions listed in Appendix G no serious concerns regarding the independent operation of the systems were raised during the field campaign.

This novel approach guaranteed a blind evaluation of the sounding systems where the performance of the systems was determined by the setup and configuration of the systems, and associated documentation.

4.3.2 Sounding strategy and rig configuration

In the practical implementation, the soundings were designed according to the following criteria.

- Measurements of the same atmospheric column using different radiosonde models at the same time under virtually identical conditions, separately for the relevant parameters.
- In parallel, independent measurements with fully characterised instruments whose data products are transparent, and in this sense considered as references.
- Equal treatment of all participant radiosondes.
- Appropriate number of soundings for a data set as representative as possible and valid statistics.
- Estimation of measurement repeatability for each participant radiosonde,
- Comparable number of profiles at day and night time.

Radiosonde models for which a GRUAN Data Product (GDP) exists were used as reference instruments for all parameters measured with radiosondes (Sections 4.3.9 and 4.3.10).

As stipulated in Chapter 12.8.1 of *WMO-No.8-Vol.I (2021)*, the radiosondes to be compared shall ascend simultaneously, suspended from the same balloon, so that the same air is sampled by all radiosondes under virtually the same conditions. For this purpose, rigs were designed ensuring a uniform way of suspending the radiosondes. However, several requirements and practical aspects

had to be taken into account for the design of the rigs and also for the sounding strategy (number and sequence of flights):

- The weight of the entire balloon chain including payload and balloon should not exceed 4 kg according to the specifications of the air traffic control in Lindenberg.
- The physical size of the rigs is limited for reasons of manageability and stability.
- The behaviour of the radiosondes attached to the rig should be as similar as possible to that of operational individual soundings, and at the same time the measurements should be influenced as little as possible by the rig (contamination).
- Enough separation between the individual radiosondes to prevent collisions in flight and to reduce the risk of radio interference between radiosondes
- The implementation of twin soundings for repeatability studies requires simultaneous operation of a second receiver system.

In the months before the UAI 2022 field campaign, various rig prototypes were built and tested. The final design was a star-shaped construction with 10 arms made of bamboo sticks of 180 cm length, connected to a common central wooden disc (see Section 4.3.4). As a result, the diameter of such a rig was about 360 cm. The radiosondes were attached to the end of the rods with 70 cm long strings. With this configuration, free rotation and swinging of the radiosondes was ensured, and the horizontal distance between the radiosondes was large enough to make collisions of neighbouring radiosondes unlikely. It was not possible to test in advance the electromagnetic compatibility of the participating radiosondes, but the separation between neighbouring radiosondes on the rig is similar to that for the regular research and intercomparison soundings that are performed in Lindenberg, and for which no issues with interference occur. The suspension length was sufficient to keep the contamination risk from the bamboo rods low (see Appendix F.3).

The rigs provided a good compromise between the number of radiosondes that could be launched together, and the practical manageability during preparation and launch. Given the original number of 12 manufacturers selected for the campaign, and in addition up to three independent GDP radiosondes attached to the same rig as the participating radiosondes, it was clear that the soundings had to be distributed over two rigs. This fact did not change with the task team's decision to use only two GDPs (Section 4.3.9), and with the final number of 10 manufacturers reduced to ten before the start of the campaign. As a consequence, the rigs consisted of:

- Two slots for GDP radiosondes.
- Five slots for radiosondes to be tested (called "DEFAULT").
- Up to three (optional) slots for doubling selected radiosondes (called "TWIN").

Empty slots were filled with dummy weights to balance the rig, if necessary.

The fact that not all radiosondes could be flown on the same rig was accounted for by the concept of comparison with the same GRUAN reference radiosondes. Alternate doubling of selected participant radiosondes on a rig ("TWIN") was done for the investigation of calibration stability and uncertainty (repeatability), using the second ground system provided by the manufacturers for the doubled radiosonde models.

The Cryogenic Frost point Hygrometer (CFH) was launched as stratospheric water vapour (humidity) reference instrument once per week under its own balloon at the scheduled time but instead of a normal campaign flight of participant radiosondes, on a special rig together with the same two GDP sonde models as for participant soundings. Due to its weight and special rig construction, the CFH could not be combined with the radiosondes setups. The limited number of CFH soundings is justified with the efforts and costs of recovery, which is required because of the financial value and re-usability of the instrument. The CFH setup was called "RESEARCH" (Section 4.3.11).

Main goal: The campaign aimed at completing at least 15 successful daytime and 15 successful nighttime flights for each participating radiosonde model. This number represents a practical compromise to achieve sufficient statistical validity with the available resources and time during the campaign.

4.3.3 Launch schedule

The considerations on setting up a daily sounding regime took into account the following aspects:

- Duration of a sounding.
- The (changing) radiation in the planning of daytime and nighttime soundings.
- Parallel soundings of more than one balloon chain.
- Aim at equal ratio of daytime and nighttime soundings.
- Scheduling of rest breaks for staff.
- Division of the campaign team into day and night shifts.
- Criteria for cancelling flights.

These questions will be discussed one by one in the following.

Duration of a radiosounding

Following steps were taken into account:

- Briefing of the team – 15 min.
- Preparation by the operators incl. attachment of the radiosondes to the rig – 45 min.
- Ascent part of sounding (until the burst point) – ca. 90 min.
- Descent part of sounding (after burst point until landing) – ca. 60 min.
- Follow-up incl. data handover – 30 min.

In total, this results in a duration of approximately 240 minutes or 4 hours for a complete sounding. If soundings are not to overlap (limited availability of radio-frequencies) and no breaks are required in between, then a maximum of 6 flights per day (24 h) would in principle be feasible.

In addition, a specific planning time for the supervisor was required every 12 hours, which lasted 60 minutes.

Daytime and nighttime conditions

Both the times of sunset and sunrise shifted in opposite directions by more than one hour over the targeted period of the sounding campaign. Daytime hours decreased from more than 15 h to less than 13 h, meaning that in the first part the time available for nighttime flights was increasing, but still significantly shorter than for daytime flights. It should be noted that the light conditions (solar elevation, sunset, sunrise) at the actual position of the ascending balloon chain will differ to some extent from those at the launch site because of the horizontal drift and in particular the quick rise. That is, for example, a radiosonde launched shortly after sunset at the launch site may still be illuminated later during the flight. For this reason, it was ensured that the Sun was at least 5° to 6° below the horizon after sunset at the time (and site) of launch, and at least 5° to 6° above the horizon after sunrise.

Table F.1 summarises these considerations for the time of the campaign. To achieve parity, and also in terms of a reasonable workload, two daytime and two nighttime flights within 24 h were scheduled throughout the campaign.

Parallel soundings with more than one rig

In principle, the number of available frequency slots was sufficient to carry out soundings with 20 radiosondes simultaneously. This means that, in order to save time or increase the number of soundings, two rigs with the maximum possible ten radiosondes each could be launched simultaneously. However, there is a number of limiting factors that led to the decision that, in practice, soundings were only carried out with one rig (≤ 10 radiosondes) at a time. These factors

include that the transmission frequencies of some radiosondes could not be freely set to arbitrary values. Furthermore, selected (and variable) frequency ranges could not be used because they were reserved for other purposes, e.g. routine soundings in Lindenberg and neighbouring stations in Germany and Poland, or military. Narrow frequency ranges also increase the risk of interference effects due to the very different bandwidths of the various sonde models, especially before and during the launch phase. This could not be fully tested in the run-up to the campaign. Another important aspect is limited available personnel for preparation of the radiosondes and operation of the sounding systems, in particular if two (different) systems are to be operated simultaneously.

Break management

During day shifts (see next paragraph), a regular lunch break was arranged. During night shifts, no distinct break was agreed for the sake of more flexibility and the possibility to shorten the shift according to the actual progress of the sounding activities.

During a campaign day intensive and less intensive phases alternate. The preparation phase, the launch, and the subsequent first phase of the ascent are more intense, followed by a quieter phase until balloon burst or landing (if data record extended to descent). Another rather busy phase starts with the completion of the sounding and the download, check, and submission of the data. In summary, there was enough space to divide the time and also to use "free" times as a break.

The aim was to follow the official DWD working time rules so that all people involved should be on duty for at most 10 hours a working day. The weekends (Saturday and Sunday) were "in principle free". However, they were reserved (and in parts used) as alternative working days to meet the campaign targets as far as possible in case previous soundings had to be cancelled during the week.

Day and night shifts

Due to the specification of two day and two night soundings within 24 h, a two-shift working time system was set up. Each shift was performed by a team of at least 11 members, with the following distribution of tasks.

- Supervisor – Overview of all activities, briefings, decision maker.
- Assistant of supervisor – Supervisor support, management of SHC ground checks.
- Rig manager – Rig preparation, incl. balancing, transport to launch site, radiosonde attachment.
- Balloon manager – Preparation and handling of the balloon.
- GDP operator – Preparation of the two GDP radiosondes.
- Five independent operators – Preparation of one or two participant radiosondes.
- Data manager – Monitoring of data delivery, consistency checks.

In order to achieve as equal a number of flights as possible with each participant sonde over the entire campaign, the aim was to maintain a balance during each day and night shift. This should ensure equal treatment even in the case of potential flight cancellations and avoid the situation where more than two participant radiosondes of the same type have to be flown on one rig. To achieve this, the 10 participating radiosondes were divided into two groups of 5 radiosondes each, and these two rigs were launched during each shift. Accordingly, the 10 operators were trained to operate systems for two sonde types.

Other members of the team were trained in specific tasks beside the regular responsible parties so that at least to a certain degree backup personnel were available in cases of unexpected absence of campaign team members. This was important in particular for the participant sonde systems, where in addition to the two designated operators two other team members were trained for these systems.

Criteria for cancellation of flights

The following criteria, situations, or predictions analysed in advance of a launch could lead to the decision to cancel or postpone individual soundings.

- Weather conditions at the time of launch:
 - Thunderstorm
 - Strong surface wind ($\geq 7 \text{ m s}^{-1}$)
 - Heavy rainfall or hail (work safety and high contamination risk)
- Predicted trajectory, in particular predicted landing coordinates:
 - Metropolitan area of Berlin
 - Berlin International Airport (BER)
 - Landing in other major cities
 - (Landing in areas with high density of transport infrastructure)
- Availability of personnel.

The short-term weather forecasts, as well as information about the current and previous hours' wind at the station (especially gustiness), were used by the supervisor for short-term planning. The long-term planning for a week was carried out in core team meetings and based on long-term weather forecasts. It has proven to be very beneficial to have an expert for weather forecasts available, especially for the supervisor's long-term planning decisions.

The prediction of the trajectories and the landing coordinates is in general relatively accurate for routine single soundings or research flights in Lindenberg. The agreement between actual and predicted ascent rate and burst point essentially determines the quality of the predicted landing point. Experience with rigs of the size used during the campaign was scarce and only gained in the course of the soundings, so there were occasional major deviations. This was especially the case for the ascents launched at rainy conditions.

4.3.4 Summary of rig construction

In Lindenberg, in preparation for this campaign, various constructions for a large rig capable of carrying 8 to 12 radiosondes were planned, constructed and tested over the course of several years.

The ready-to-start rigs should meet the following general specifications:

- Capacity to carry 10 radiosondes.
- Suspension of the sonde allows free rotation.
- Sufficient distance between radiosondes to minimise the risk of radio-frequency interference.
- Low risk of collisions of radiosondes (avoid damage).
- Construction and materials should have negligible influence on the measurements (e.g. moisture on rods).
- Construction in a way that air flow conditions are similar for all attached radiosondes to ensure comparability of the results.
- Total weight of the whole chain (incl. rods, parachute, balloon and radiosondes) less than 4 kg (air traffic regulation).
- Can be safely launched by 2 to 3 people.
- Can be launched even at moderate wind speed of 5 m s^{-1} to 7 m s^{-1} .
- Total size less than 4 m.

Various prototypes were developed, tested, and optimised. The above requirements led to the rotational (star-shaped) symmetry of the rig construction (see e.g. the figures presented in Section N). Care was taken to ensure that the materials were easily available and as affordable as

possible. At the same time it was important to use biodegradable materials as far as possible since there was no guarantee that all the rigs would be recovered. A regular recovery by the campaign team was not feasible (too much logistical effort). Some rigs were found by chance, and a considerable amount was even actively and voluntarily collected (and disposed of) by interested people (the community of the so called 'radiosonde hunters').

One important part of the rig configuration is the length of the strings with which the radiosondes are to be suspended to the rig. The results of experimental tests of a potential influence of the rig on the measurements (contamination) and a possible variation with string length are presented in the Appendix F.3.

A guide describing the rig construction for a parallel ascent of up to 10 radiosondes suspended to one balloon, which was used in the UAI 2022, can be found in Appendix N.

4.3.5 Standard rig configuration

The participating radiosondes were divided into two groups with five models each (Table 4.2). In the composition of the two groups, care was taken to mix sonde models with different global market shares and technical designs. The two GDP radiosondes were attached to both rigs.

Table 4.2: Grouping of participating radiosondes

Group 1	Group 2
RS41	iMS-100
DFM-17	M20
HT-GTS(U)2-1	WxR-301D
ATMS-3710	iMet-54
PS-B3	CF-06-AH

With overall 10 slots on a rig including two GDP radiosondes and five regular participant radiosondes, there was room to double up to three participant radiosondes. In most flights, only one sonde was doubled (as "TWIN"). Doubling of participant radiosondes was done in a cycle with the aim to achieve approximately the same number of double soundings for each sonde during the campaign.

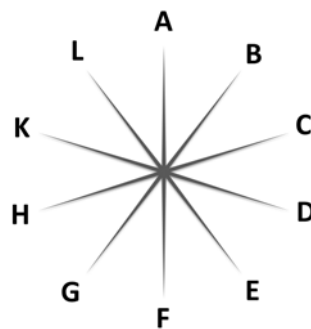


Figure 4.11: Rig with ten named slots

Once the sonde models for a flight had been finally determined, including dual radiosondes, the positioning of the radiosondes on the rig was planned. The different weights of the radiosondes and also of the bamboo rods that made up the rig meant that each rig had to be individually balanced so as not to create any misalignment during launch and flight (see also Appendix N.6). For this, dummy weights corresponding to the different radiosonde models have been used. The arrangement of the radiosondes was varied accordingly and documented for each flight. For the sonde positions at the ends of the rods, letters were assigned in a fixed sequence, see scheme in Figure 4.11.

Depending on the total weight of the rig, and taking into account the weather situation and the predicted trajectory, an appropriate parachute was chosen, and the amount of He-gas for the balloon (filling weight) was determined by the supervisor. The aim was always to achieve an ascent speed of 5 to 6 m s⁻¹ and a descent speed on landing of the rig of less than 5 m s⁻¹.

A fixed balloon size (1500 g) was used during the sounding campaign. The helium gas filling varied between 3200 g and 5700 g, depending on a combination of factors like balloon size, quality of the balloons, payload, as well as expected environmental conditions such as humidity, precipitation, potential ice formation, wind regime, daytime, etc. The amount of gas to be used to achieve the desired ascend speed of about 5 m s⁻¹ to 6 m s⁻¹, under consideration of all these factors, cannot exactly be pre-calculated and was therefore to certain degree based on experience gained over the course of the campaign. Ascent speeds generally between about 4 m s⁻¹ and 6 m s⁻¹ were achieved, with a few flights ascending with lower rates (see Figure 8.1). The lowest (undesired) ascents occurred under very humid and rainy surface conditions, where water and ice formation on the balloon and rig during flight may have increased the overall weight of the chain significantly. Special attention should be paid to this aspect in future campaigns.

Three different parachute types of two sizes were used (290 cm and 160 cm). The larger led to very low descent rates on landing. The smaller was used with smaller payloads, but tended to cause (too) high descent speeds. From this can be learned that also the choice of type and size of the parachute should be adequately considered, in particular if descent data are important (which was less the case in this campaign).

In order to ensure the required distance of approximately 60 m between the balloon and the rig, robust 60 m unwinders were used in case of ground conditions with stronger winds, or, at low winds, the balloon was slowly raised by hand to 60 m with an unwound string connected to the rig and then released to launch the rig.

4.3.6 Frequency allocation

The WMO has allocated different frequency bands within the radio service of meteorological aids (MetAids). The frequency band officially made available in Europe for radiosoundings ranges from 400.15 MHz to 406.0 MHz. The WMO acknowledges that radiosonde operations in the 400.15 MHz to 402.0 MHz is not feasible due to sharing with Satellite Services. This means that in Lindenberg the frequency band from 402.0 MHz to 406.0 MHz could basically be used during the campaign. However, there were a number of other, partly varying restrictions regarding individual frequencies or frequency ranges that had to be taken into account in the frequency planning:

- Routinely used frequencies (operational sounding programme) at MOL-RAO (high priority: clear distinction from campaign frequencies).
- Other neighbouring sounding stations.
- Military usage (402 MHz to 403 MHz).
- Other local emitters.
- Satellite communication.

The frequency band was divided into 0.1 MHz steps. All permanently and sporadically blocked frequency ranges have been marked. For both groups of participating radiosondes (group 1 and group 2), 5 frequencies each were selected for the 5 sonde models. In addition, two further frequencies were defined in each case for the doubling of radiosondes ("TWIN"). The radiosondes' capabilities for frequency adjustment have been taken into account. Care was taken to ensure that the frequency spacing between the radiosondes attached to the same rig was at least 0.2 MHz, and that spacing of at least 0.1 MHz was also maintained between consecutive launches. In addition to the frequencies of the participant radiosondes, frequencies (including alternate frequencies) were defined for the two GDP radiosondes. A total of about 20 frequencies was defined for use during the campaign.

The following information was taken into account in the compilation and assignment of the individual frequencies to the radiosondes:

- Default (initial) frequency used by the radiosonde after switching on.
- Frequency setting capabilities and options of the radiosondes, e.g.

- resolution of adjustable frequencies (e.g. 0.01, 0.1 and 0.5 MHz)
- usable frequency range.
- Quality and shape of the receivable spectrum at the set transmission frequency (tests are highly recommended; relying on technical documentation may be not sufficient):
 - Band width (e.g. 0.01, 0.05 and 0.1 MHz),
 - Occurrence of "side lobes"
 - Frequency stability,
- Potential interference effects in presence of other radio-transmitters:
 - shielding
 - side effects when other nearby radiosondes are transmitting.

Additional provisions to avoid frequency related issues

About half of the radiosonde models immediately started transmitting at manufacturer preset frequencies after being switched on. This could lead to interference if this frequency was already in use by another system. This was managed by first switching on the radiosondes with preset frequency and then change the transmission frequency before switching on and configuring the other radiosondes.

During ground preparation before the actual launch, some radiosonde models were transmitting with intentionally attenuated signal strength. This could lead to a loss of reception from these radiosondes by interference from other radiosondes transmitting at nearby frequencies with full strength, in particular if the bandwidth was rather large.

In the case of recovering rigs from completed soundings, it was important to switch off the radiosondes at the first opportunity.

Routine and non-routine activities with regard to the preparation or conduction of radiosoundings at the campaign site in parallel to the intercomparison campaign, e.g. preparation of operational ozone soundings, had to be taken into account in the actual frequency allocation planning.

4.3.7 Main steps in conducting a sounding during the campaign

The procedure in conducting a campaign sounding is divided into a series of steps with people responsible for the steps (*emphasised*):

1. Assessment of the current weather conditions and the forecast, with special attention on surface wind and (potential) thunderstorms; assessment of the predicted trajectory (landing area) – *supervisor, meteorological advisor*
2. Planning the rig-configuration, incl. grouping of radiosondes, duplicates ('TWIN'), assigned frequencies, positions on the rig, use of unwinder or not, selection of parachute, desired ascent speed, balloon lift, etc. – *supervisor*
3. Briefing during which supervisor communicates these decisions to the shift – *whole team*
4. Start preparation of balloon, parachute, and rig (incl. balancing) – *balloon and rig managers* (see Appendix N, e.g. Section N.6)
5. Prepare SHCs – *assistant* (see Section 4.3.8)
6. Initialisation and preparation of the radiosondes, filling out protocols (participants and GDPs) – *operators, GDP operators* (see Section 4.3.10 for GDP)
7. Transfer the rig to the launch site – *rig manager* (see Appendix N, e.g. Section N.7)
8. [optional] Lay out the string (if no unwinder is used) – *rig or balloon manager* (see Appendix N, e.g. Section N.7)
9. Perform additional manufacturer-independent ground check in the SHCs – *operators, assistant, GDP operator* (see Section 4.3.8)

10. Transfer the ready-to-flight radiosondes to the launch site and attach to the rig – *operators, GDP operator, rig manager* (see Appendix N, e.g. Section N.7)
11. Finalise preparation of balloon, attach parachute, transfer to the launch site and attach to the rig – *balloon manager* (see Appendix N, e.g. Section N.7)
12. Perform the launch procedure (incl. releasing the balloon) – *balloon and rig manager, supervisor* (see Appendix N, e.g. Section N.7)
13. Read weather conditions at time of launch, enter in sounding software – *operators, GDP operator* (see Section 4.1.8)
14. Monitor the sounding until burst point (or until landing) – *whole team*
15. Finalise recording of the soundings, complete protocols, generate and export sounding data files (see Appendix E), etc. – *operators, GDP operators*
16. Collect, validate and transfer data files – *operators, data manager, supervisor* (see Section 4.3.12)
17. Collect and check protocols – *supervisor*

4.3.8 Manufacturer independent ground check in Standard Humidity Chamber (SHC)

All radiosondes on a rig, including the GDPs radiosondes, were subjected to an additional ground check at 100 % relative humidity immediately before launch, which was independent from default procedures and tools of manufacturers. The checks were carried out in Standard Humidity Chambers (SHCs) after the manufacturer-prescribed preparation, initialisation and ground check. The purpose of the SHC check is to check whether and how well the radiosondes are able to measure at this humidity level. The checks are analysed in Section 10.1.8, where the results are also compared with the in-flight behaviour of the radiosondes during cloud passage, in which measurement values of 100 % are expected.

The SHC is developed to provide a well-defined and stable test environment with regard to relative humidity. The humidity level of 100 % is created by the fact that slowly cooled moist air gets saturated with water vapour in a closed volume over a surface of (beforehand slightly heated) liquid water. Taking advantage of this physical principle, reference conditions can be achieved by relatively simple means without the need for instrumental verification. The SHCs are also equipped with reference temperature sensors to record the air temperature inside the chamber which is used for a parallel single point check of the radiosonde temperature sensor. The 100 %RH SHC check is routinely performed in this way for all operational radiosoundings in Lindenberg (see also Chapter 5).

Figure 4.12 shows a photograph of the set of five SHCs that were used in parallel in the balloon hangar during the field campaign (see © in Figure 4.6). For logistical and technical reasons, there was a fixed assignment between the radiosonde models and the chamber number over the course of the campaign. The SHCs were operated and maintained by the supervisor's assistant.

Prior to use, the SHCs are bottom-heated for 10 minutes, causing the temperature of the thin water layer to rise approximately 2 K above ambient. After the heating phase, a waiting time of 10 minutes allows the permanently ventilated air volume above the water layer to saturate. After completing this preparation, the fan is switched off, and the operators are invited to perform the SHC check with their radiosonde.

The check procedure is similar to that employed during the laboratory humidity experiments described in Chapter 5. The radiosondes are installed in the SHC using custom-made air-tight adaptors through the top cover, with the entire sensor boom vertically inserted into the closed air volume. After insertion, the fan is switched on again. The angular orientation is such that the airflow around the sensor boom inside the SHC is similar to that in flight. The radiosonde remains in the SHC for up to 8 minutes, while data recording by the sounding system continues.

At the end of this period, the operators enter the temperature and humidity values indicated by the radiosonde in the protocol, together with the reference temperature inside the SHC. The reference temperatures in all SHCs were displayed during the check period on a large screen located at (N) in Figure 4.6. Subsequently, the fan is switched off and the radiosonde is removed from the SHC and ready to be attached to the rig.



Figure 4.12: Set of five 100 %RH SHCs with the manufacturer-independent ground check running in four of them.

The results and analysis of the independent ground checks are presented in Section 10.1.8.

4.3.9 Selection of the GRUAN Data Products (GDPs)

The radiosonde GDPs are fundamental components of the UAI 2022 field campaign, as they serve as the working measurement standards (see Section 1.2 and Chapter 9). The selection of the specific radiosonde GDPs took place in June 2022, prior to the start of the field campaign. The UAI Task Team⁸ approved the following selection, following a proposal from the UAI Project Team⁹ based on recommendations from the GRUAN Lead Centre:

GDP selection for the UAI 2022 field campaign

iMS-100 GDP version 2 and RS41 GDP version 1

This selection was made from the list of radiosonde GDPs that were GRUAN certified or pre-certified at the time. These included: the Vaisala RS92 GDP version 2, the Vaisala RS41 GDP version 1, the Meisei iMS-100 GDP version 2 and the Meisei RS-11G GDP version 1.

The UAI 2022 project plan specifies that up to three, but no less than two radiosonde GDPs are to be used as working measurement standards during the field campaign. The RS92 GDP version 2 was not selected, as the RS92 is no longer in production. The iMS-100 GDP version 2 was selected over the older RS-11G GDP version 1 because the iMS-100 radiosonde has the same temperature and relative humidity sensors as the RS-11G radiosonde, but with an additional, dedicated thermometer for the humidity sensor (*Kizu et al., 2018b; Hoshino et al., 2022*).

4.3.10 GRUAN Data Product (GDP) soundings

The preparation of the GDP radiosondes during the campaign took place in parallel to the participant radiosondes, but in the separate building of the Lindenberg radiosonde station (⑦ in Figure 4.4). The preparation was not carried out by independent operators but by members of the campaign team assigned for this purpose (GDP operators). The spatial separation of the

⁸see Section 1.3.3 for the list of members.

⁹see Section 1.3.3 for the list of members.

GDP radiosondes from the participant radiosonde preparation should help to avoid any technical and operator-related interference during all activities until the radiosondes are attached to the sounding rigs.

In contrast to the Vaisala radiosonde model RS41-SG that took part in the comparison as a candidate, the RS41-SGP model with integrated pressure sensor was used as the GDP reference radiosonde to enable full GRUAN data processing. The Vaisala ground system consisted of:

- MW41 sounding software (version 2.15) running on a standard Windows®-PC.
- Sounding Processing Subsystem SPS311G including a GPS module, connected to the PC over LAN.
- Radiosonde telemetry antenna RB31-UHF.
- GPS antenna GA31-GPS.
- RI41-B radiosonde interface equipped with a pressure reference sensor for sonde initialisation and ground checks.

The Meisei ground system consisted of:

- MGPS2 sounding software (version 3.9.9) running on a standard Windows®-PC laptop.
- Radiosonde ground check and communication device (Ground Checker, GC) connected to the laptop via USB and using IrDA for communication with the radiosonde; comparison with reference sensors (Meisei MES-39535 for temperature, Meisei TU-CONV for relative humidity) at laboratory conditions.
- Receiver/antenna unit RD-18 connected to the PC over Local Area Network (LAN).

The Meisei receiver/antenna unit and the Vaisala antenna were permanently installed on the roof platform of the radiosonde station building (⑦ in Figure 4.4).

The radio frequencies for both GDP radiosondes were predefined to 405.3 MHz for the RS41 and 405.6 MHz for the iMS-100. Alternate frequencies were selected if required, e.g. in case of foreseeable overlaps with frequency bands of the UAI participant radiosondes or if inferences with external signals of other radiosondes in the region were detected.

Both GDP radiosondes were prepared according to the GRUAN specifications. That means, after initialisation and manufacturer prescribed ground checks, both radiosondes were checked one after the other in a 100 % relative humidity SHC at laboratory temperature. The SHC device was separate from those SHCs used in the balloon hall for ground checks of the participating radiosondes. The duration of the check was 3 minutes for the RS41 and 8 minutes for the iMS-100, respectively. A check of the temperature measurement was done in parallel using a Pt100 sensor installed in the SHC.

After finishing the preparation phase, both GDP radiosondes were brought to the launch site and suspended to the rig at the same time as the participating radiosondes for the forthcoming comparison sounding. After launch, the actual ground weather information was entered by hand into the sounding software. The data recording of the GDP radiosondes was usually extended over a period that includes the recordings of all participant radiosondes. The documentation and logging was done in parallel on paper and in digital logs according to the protocol template shown in Appendix E.

4.3.10.1 Usage of operational GRUAN data flow

Since the MOL-RAO is a GRUAN site, the normal operational GRUAN data flow could be used for processing the measurements of the GDP radiosondes. A detailed description of the data flow, from data submission to processing and storage, can be found in Chapter 7.6 "Data management in GRUAN" of the GRUAN Technical Document 8 ([Sommer et al., 2023](#)).

The campaign team initiated the proper submission of the GDP field campaign flights as GRUAN soundings. This started the GRUAN data flow for each sounding. Most of the GRUAN data management steps including archiving, conversion, and provision, are done by the GRUAN Lead Centre, which is located in Lindenberg.

The GRUAN processing takes place at so-called "Processing Centres". These are assigned to spe-

cific radiosondes in GRUAN. The processing centre for the Meisei radiosonde IMS-100 is located at the GRUAN site Tateno (Tateno Aerological Observatory, Japan). The processing centre for the Vaisala radiosonde RS41 is located at the GRUAN station Lindenberg.

For the RS41, the complete processing is described in detail in Chapter 7 “GRUAN Data Product (GDP)” in [Sommer et al. \(2023\)](#). For the IMS-100, this will be found in the upcoming version 2 of [Kizu et al. \(2018b\)](#) (under revision).

After successful processing, the final GDP files were made available by GRUAN to the campaign team.

4.3.11 Reference measurement of stratospheric humidity (CFH)

The Cryogenic Frost point Hygrometer (CFH) employs the chilled mirror technique to perform accurate in-situ measurements of water vapour. This measurement technique relies on controlling the temperature of the mirror surface such that a thin and constant condensate layer is maintained. Under this condition, the mirror temperature equals the frost (or dew) point of the air flowing over the mirror, which is directly related to the water vapour pressure via the Clausius-Clapeyron equation. The reflectivity of the mirror, which is a proxy for the layer thickness, is measured continuously, and used as feedback for a Proportional Integral Derivative (PID) controller to adjust the temperature of the mirror. The mirror is connected to a cryogenic liquid, providing conductive cooling. The mirror temperature is controlled by heating against this cold sink, using a heating wire at the back of the mirror. It is the job of the PID controller to steer the heating power and to balance the competing processes of cooling and heating so that the mirror remains at frost/dew point temperature and the condensate layer is maintained. The considerable cooling power of the cryogen and the available heating power allow for fast heating and cooling of the mirror, yielding fast response times (below 20 s in the stratosphere).

The cryogen (R23 - Trifluoromethane) has a boiling point of $-80\text{ }^{\circ}\text{C}$ at sea level and $-100\text{ }^{\circ}\text{C}$ in the stratosphere, which is able to keep the mirror temperature well below the frostpoint temperature of the ambient air in this altitude range. The CFH can measure water vapour concentrations from 1 ppmv to 30 000 ppmv with a relative uncertainty of 2 % to 3 %, and is therefore able to accurately measure the low water vapour concentration in the stratosphere (which is approximately 4 ppmv, frostpoint below $-80\text{ }^{\circ}\text{C}$), which is at or below the detection limit of the polymer sensors used by operational radiosondes. The measurement uncertainty of the CFH is determined by the uncertainty of the frostpoint measurement (i.e. the mirror temperature) which is approximately 0.2 K.

The CFH, and related chilled mirror instruments like NOAA’s¹⁰ Frost Point Hygrometer (FPH), or Meisei’s Skydew instrument, are employed within GRUAN as reference instruments for water vapour observations. Originally conceived to measure water vapour in the stratosphere, the altitude range of the CFH has been extended to include the entire profile from surface to the burst point, and apart from monitoring the stratospheric water vapour content it is used as a reference to validate operational radiosondes.

Above information is based on [Vömel et al. \(2007\)](#); [Vömel and Jaennet \(2013\)](#), further information on other chilled mirror instruments is given by e.g. [Sugidachi \(2014\)](#); [Hurst et al. \(2011\)](#).

The CFH, and other chilled mirror instruments, are not equipped with a radiotransmitter so that an additional radiosonde is needed to downlink the data, and to provide measurements of air temperature, pressure and position data. Chilled mirror instruments are sophisticated research instruments that are produced in low numbers, and therefore are considerably more expensive than operational radiosondes. Furthermore, the preparation and handling of CFHs is more elaborate and complicated than for routine radiosondes, because it requires the application of cryogen. As a result of this, they are typically launched at 1 to 2 month intervals.

In summary, the advantages of CFH (and other chilled mirror instruments) are:

- low measurement uncertainty (2 % to 3 %)
- sensitivity (1 ppmv to 30 000 ppmv)
- reference instrument

¹⁰National Oceanic and Atmospheric Administration (NOAA)

- operational range (surface to 30 km)
- fast response time

and the CFH's disadvantages are

- cost
- handling (cryogen).

For the reference soundings, the CFH was flown together with the GDP radiosondes (RS41 and iMS-100) on the same rig. The GDP radiosondes were attached with a 70 cm string, identical to the regular soundings; an additional RS41 was attached to the CFH for data transmission. A sketch of this rig configuration is shown in Figure 4.13.

During the campaign, one reference sounding was performed per week, yielding 2 daytime and 2 nighttime flights.

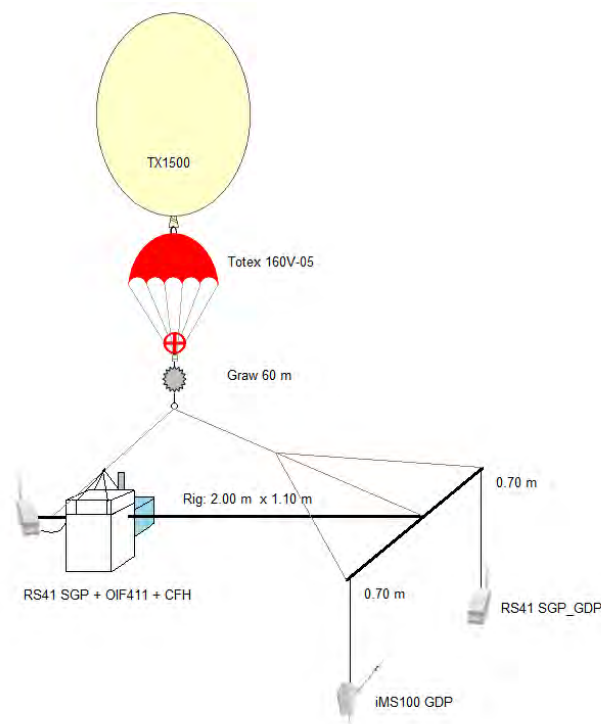


Figure 4.13: Schematic drawing of the rig-configuration of a research payload.

4.3.12 Data handling and campaign progress monitoring

The sounding data from the systems present on a given rig were collected manually by their respective operators and handed over (via system-dedicated, colour-coded USB sticks) to the shift's Data Manager upon the termination of a given flight (either at balloon burst or at the end of the descent phase, as specified by the shift coordinator). The Data Manager was responsible for loading the individual datasets onto the dedicated *central terminal for data collection* (located at (E) in Fig 4.6).

A first custom-built Python script was used by the Data Manager to verify the completeness of each dataset after each upload, including its correct placement within the local storage infrastructure. A second Python script was used to plot the profile data from each system (without any treatment whatsoever), to enable a rapid inspection and verification of the profile validity. A third Python script was then used to automatically transfer all the verified datasets onto the *Data Store*, a central storage area hosted on a dedicated (private) online server with strict remote access control. The datasets from each system were eventually made available to the respective system manufacturers directly from this Data Store, within 24 hours from each flight. It must be stressed

that manufacturers were given access to the data from their own sounding system only, and never to that from other systems or GDPs.

GDP datafiles were transferred onto the Data Store separately from those of the participating systems, after they became available through the dedicated GRUAN processing cascades. The Data Visualization and Analysis Software (dvas) Python code (see Section 9.4) was used to process each flight individually as soon as the necessary GDP files would become available. This preliminary processing with dvas was used to monitor the progress of the field campaign with respect to its statistical goals (see Section 4.3.2). The preliminary dvas processing of the data was particularly useful to identify problematic flights and profiles that would need repeating (see Section 8.2 for a detailed discussion of each case).

Daily data briefings were held every afternoon during the second part of the field campaign. These 30 minutes-long briefings, gathering all the campaign team members present on-site, were used to monitor the progress of the campaign based on the preliminary dvas analysis. They were also used to discuss specific topics and interesting results/observations detected in the data after its preliminary processing following a concise plot-of-the-day approach.

4.4 REMOTE SENSING SYSTEMS

In Sections 9.6, 10.2 and 11.2, the data and the retrievals obtained from a selection of remote sensing instruments installed at the MOL-RAO are used to analyse the performances of each instrument of the so-called Lindenberg Remote Sensing Suite (LRSS) in the framework of the comparison with the radiosondes at the time of the UAI 2022 field campaign. The LRSSs counts five remote sensing instruments, three based on active emission and two on passive reception (see ⑧ and ⑨ in Figure 4.4). They include:

- a Radar Wind Profiler (RWP) operating in two different (high and low) modes (Ultra High Frequency (UHF), 62 cm wavelength),
- two infrared Doppler Wind Lidar (DWL), which will be referred to as “WindLidar1” and “WindLidar2” (1.5 μm wavelength), and
- two Micro-Wave Radiometer (MWR), which will be referred to as “MWR-MF” and “MWR-SMZ” (0.5 cm to 1.6 cm).

The detailed technical specifications of the MWRs are listed in Table 4.3, those of the DWLs are in Table 4.4, and those of the RWPs are in Table 4.5.

In the period from 8th of August to 16th September 2022, both DWLs measured continuously in a Velocity Azimuth Display (VAD) configuration at 75° elevation. The WindLidar1 performed measurements with 50 m Line Of Sight (LOS) resolution at 10 kHz Pulse-Repetition Frequency (PRF). The systems are overall similar in performance, but the pulse duration of the WindLidar2 is almost twice as long as the WindLidar1’s.

The temporal averaging of the RWP data is about 15 min for each mode. The RWP is configured in such a way that it sequentially measures about 13 min exclusively low mode, then 14 min exclusively high mode. So both low and high mode data are reported every 30 min, but the (independent) averaging of low and high mode is 30 min.

Table 4.3: Parameters of Micro-Wave Radiometers (MWRs)

System	MWR-MF, MWR-SMZ
Measurement principle	scanning microwave radiometer
Latitude / Longitude / z_{surface}	52.209 278°/14.128 768°/104 m AMSL, 52.209 278°/14.128 768°/125 m AMSL
Receiver 1 (R1)	water vapour and liquid water absorption
Frequencies (R1), GHz	22.24, 23.04, 23.84, 25.44, 26.24, 27.84, 31.40
Channel band-widths (R1), MHz	230, 230, 230, 230, 230, 230, 230
Optical Resolution (R1) (HPBW)	3.3° to 3.7°
Temporal Resolution	1 s to 2 s
Receiver 2 (R2)	oxygen absorption
Frequencies (R2), GHz	51.26, 52.28, 53.86, 54.94, 56.66, 57.30, 58.00
Channel band-widths (R2), MHz	230, 230, 230, 230, 600, 1000, 2000
Optical Resolution (R2) (HPBW)	2.2° to 2.5°
Pointing Resolution (R2)	0.6° (elevation), 0.1° (azimuth)
Side-lobe level	< -30 dB
Infrared pyrometers	11.1 μm , 12.0 μm , systematic measurement error maximum value of 1.0 K

Table 4.4: Parameters of Doppler Wind Lidars (DWLs)

System	WindLidar1	WindLidar2
Measurement principle	heterodyne Doppler	heterodyne Doppler
Laser wavelength	1.5 μm	1.5 μm
Pulse Duration (τ_p)	201 ns	384 ns
Pulse Repetition Frequency (PRF)	10 kHz	10 kHz
Latitude / Longitude / z_{surface}	52.209 278° / 14.128 768° / 104 m	52.209 278° / 14.128 768° / 104 m
Scan / No. directions / elevation/ filter	VAD / 24 / 75° / consensus	VAD / 24 / 75° / consensus
Time window (can be reprocessed)	30 min	30 min
Vertical range	96 m to 14 300 m	23 m to 11 568 m
Vertical range gate distance	48 m	46 m
Radial resolution ($c \cdot \text{pulse width}/2$)	30 m	58 m
Vertical resolution	29 m	56 m
Horizontal diameter of VAD circle	52 m to 7600 m	12 m to 6200 m
Comments	In Lindenberg since 2021, model upgrade in Sep 2021	In Lindenberg since 2012, model upgrade in Nov 2016

Table 4.5: Parameters of 482 MHz Radar Wind Profiler (RWP)

Mode	Low mode	High mode
Carrier Frequency	482.0078 MHz	
Pulse Duration (τ_p)	1000 ns (Low mode)	2175 ns (High Mode)
Inter Pulse Period (IPP)	81 μ s	179 μ s
Latitude / Longitude / z_{surface}	52.209 674° / 14.128 926° / 104 m	
Scan / No. directions / elevation	DBS / 4 / 74.8°	
Time window	13 min (5 DBS cycles)	14 min (5 DBS cycles)
Vertical range	448 m to 9378 m	5488 m to 16 182 m
Vertical range gate distance	94 m	315 m
Radial resolution (c* pulse width/2)	150 m	330 m
NCI	60	22
NPTS	512	512
NSPEC	16	21
NCODE	0	10
Doppler spectrum estimation	FFT w/ Hanning window + overlap, DC filter	
Ground clutter suppression	Riddle	
Intermittent clutter suppression	Gabor-filtering on I/Q	ICRA (statistical spectral avg.)
Moment estimation	FM w/ thresholds, Consensus	
Noise estimation	Hildebrand-Sekhon	

Part II

Laboratory campaign

5 HUMIDITY SENSOR PERFORMANCE AT ROOM CONDITIONS (LABH)

5.1 INTRODUCTION

The general introduction to the laboratory campaign, including the motivation, the objectives, as well as various general definitions, can be found in Sections 2.1 and 4.2. It is recommended to read these sections before the specific chapters of the laboratory experiments.

Modern radiosondes are intended for one-time use, and are designed for ease-of-use in routine operations. Still, a pre-flight check to verify that the sensors are working properly and to validate the sensor readings is indispensable to make sure that the radiosonde is working according to the manufacturer's specifications, and to apply corrections to the sensor readings, if necessary. For that purpose, most manufacturers provide ground check equipment that is used in the standard pre-flight operational procedure.

Lindenberg Observatory identified the need of an independent ground check that is routinely applied in addition to the standard manufacturer-prescribed check. This led to the development of the Standard Humidity Chamber (SHC) more than 20 years ago. As the name suggests, the main purpose of the SHC is to check the performance of the radiosonde's humidity sensor. The chamber creates a stable environment with a well-defined relative humidity of 100 %RH, which is achieved by using the well-known effect that slowly cooling moist air over a liquid water surface yields saturated air. The advantage of using this fundamental thermodynamic principle is that no reference measurement is required to verify the humidity inside the SHC. This humidity level is at the upper end of the humidity sensor's operational range, which is a challenge to calibrate properly so that the quality of the manufacturer calibration at this humidity value is often reduced. However, proper quality of measurement data at high humidity levels is important to be able to reliably detect e.g. cloud passages or water/ice sensor contamination. The SHC provides a stable environment, both in terms of humidity and temperature, so that at the same time it is also possible to verify the performance of the radiosonde's temperature sensor by comparing to a reference sensor installed in the SHC.

It was recognised by GRUAN that the SHC provides an uncomplicated method to verify the performance and calibration of radiosondes at room temperature on an operational basis. This manufacturer-independent ground check using an SHC are routinely performed at the majority of GRUAN sites. In addition to revealing particular issues with individual radiosondes prior to launch, statistical analysis of the ground check results also revealed various radiosonde-specific systematic effects.

The SHC can be used to generate environments with other humidity levels as well. This can be realised by using a desiccant for 0%RH, or by using saturated aqueous solutions of certain inorganic salts for intermediate relative humidity values, examples of which are presented in Table 5.1. This has been used at Lindenberg observatory in the past to investigate the performance of humidity sensors over their full operational ranges.

Currently, 6 SHCs are in use for regular checks of the humidity calibration of radiosondes. These devices have been employed during the LABH part of the UAI laboratory campaign.

The radiosondes are labelled arbitrarily but anonymously using capital letters A to L throughout the descriptions of the humidity test results (LABH experiment) in this Chapter 5. For the sake of anonymity, the assignment of the letters to radiosondes is randomised in the presentation of the results of each of the other three laboratory tests described in Chapter 6 (sensor performance at low temperatures, TLAG and LOWT) and Chapter 7 (sensitivity of the temperature measurement to solar radiation, RADT).

5.2 EXPERIMENTAL SETUP

The SHC is a cylindrical chamber with an inner volume of 17 L. The water vapour content of the air inside the SHC is in thermodynamic equilibrium with the substance on the bottom (desiccant, distilled water or a saturated salt solution), generating a fixed and stable humidity value at discrete levels between 0%RH and 100%RH, with an uncertainty of less than 0.5%RH. The reference salt solutions and corresponding relative humidity employed during the campaign are listed in Table 5.1. The air inside the SHC is circulated by a fan to ensure homogeneous mixing of the air volume and proper exchange of water vapour between both media. The thickness of the medium on the bottom of the SHC is approximately 0.5 cm.

The large chamber volume in comparison to the radiosonde's sensor boom together with the thermal inertia of the metal walls that shield the air inside, ensure an environment with stable temperature and humidity conditions during the tests. The air circulates at 5 m s^{-1} , mimicking the ventilation during ascent. Air temperature is recorded with a Pt100 reference temperature sensor at the same sampling frequency as the radiosonde (1 Hz).

Figure 5.1 shows a SHC with the fan motor on top of the centre of the lid, a radiosonde sensor boom inserted at the front, and various orifices of different size and shape (closed or covered) for inserting the reference temperature sensors and for inserting the sensor booms of radiosondes with other dimensions. Custom-made adaptors were prepared for each radiosonde type to ensure proper fitting and to reduce exchange with ambient air as much as possible.



Figure 5.1: SHC with a candidate radiosonde measuring during the UAI campaign. The power supply for the fan motor is on the rack in the background.

The radiosondes were sequentially tested in the SHCs at the relative humidity levels listed in Table 5.1 and at room temperature conditions, while the measurement data were recorded continuously. Section 5.3.1 discusses the details about the measurement cycles. The radiosonde was inserted in the SHC such that the sensor boom pointed downwards, and the orientation relative to the airflow inside the SHC was similar to the situation encountered in flight.

Figure 5.2 shows a picture of the laboratory setup used during the UAI LABH measurements. It includes the six SHCs, the power supplies for the fan's motors, and a data acquisition system to record the reference temperature sensors. The photograph was taken while two radiosondes were tested in the 97%RH and 100%RH SHC.

During the tests in the SHCs, radiosonde data transmission was either by radio or by cable. Radio transmission was preferred because it allows for easier handling of the radiosondes during the

Table 5.1: Nominal relative humidity levels inside the 6 SHCs. The relative humidity over a saturated salt solution slightly depends on temperature. The calculated minimum and maximum values that occurred during the UAI campaign are given as well as uncertainty estimates.

Relative humidity / %	0	11	33	75	97	100
Minimum (actual)		11.297	32.734	74.509	95.479	
Maximum (actual)		11.309	33.046	74.823	96.274	
Uncertainty ($k = 1$)	0.20	≈0.10	≈0.09	≈0.21	≈0.31	0.50
Substance	desiccant	LiCl	MgCl ₂	NaCl	K ₂ SO ₄	H ₂ O



Figure 5.2: Laboratory setup for UAI relative humidity calibration checks. The data acquisition system for the reference sensors is mounted on the rack above the power supplies. The SHCs are lined up with increasing humidity from right to left.

tests. The radiosondes and the receiving systems were operated by the manufacturers since the laboratory tests constitute non-standard operation which requires expert knowledge.

5.2.1 Calibration of the reference temperature sensors

All SHCs were equipped with temperature sensors whose sensitive elements were exposed to the mixed air in the volume above the salt solution. In two of the chambers an additional sensor was used to independently measure the temperature of the salt solution (see further below).

For the campaign, care was taken to ensure that the used temperature sensors were SI¹ traceable. For this purpose, they were compared before and after each laboratory phase in a water bath to 2 platinum resistance temperature sensors. These two sensors are used as laboratory standard throughout the campaign and are calibrated in a certified calibration laboratory.

From the comparisons of the “working” sensors with the two references, mean differences were calculated and then used for offset corrections. The measurement uncertainties of the working sensor’s at laboratory temperatures around 20 °C are essentially given by the uncertainty of the

¹International System of Units (SI)

reference sensors, which is 0.03 K ($k = 1$) according to the calibration certificate. Statistical components were significantly smaller. Thus the combined uncertainty for all working temperature sensors used within the SHCs – and valid for the room temperature – was estimated to be 0.032 K ($k = 1$).

5.2.2 Establishing reference levels for relative humidity with SHC

The additional temperature measurements accounted for the effect that the relative humidity that sets up in equilibrium over a saturated salt solution depends not only on the type of salt but also on the temperature. It can be expected that in presence of temperature fluctuations in the air volume, slight differences between the temperature of the saturated solution and the air exist. Since the actual humidity in the air is determined by the temperature of the solution, such fluctuations may lead to calculations of humidities significantly deviating from true equilibrium values if only air temperature is used. This takes effect in particular for the 75 %RH and 97 %RH SHCs, which is why these two were equipped with additional sensors measuring the temperature of the salt solution.

The humidity in the air above the saturated salt solutions is calculated according to the data presented in Table 2 in [Greenspan \(1977\)](#). The uncertainties that are given in this table as well are at a confidence level of 3σ ($k = 3$), and have therefore been converted to $k = 1$ for use in this analysis.

The temperature data in the Greenspan paper are given in relation to the IPTS-68² temperature scale. The temperatures measured during the campaign, however, are traceable to the ITS-90³ scale. Although the differences are small, the temperatures were converted to the IPTS-68 scale before using Greenspan's polynomials for calculation of humidities. Thus, for the laboratory temperature of about 20 °C at which the radiosondes have been tested, a conversion factor according to ITS-90-IPTS-68 differences given in [Preston-Thomas \(1990\)](#) was applied for simple use and with sufficient accuracy: $T_{68} = 1.00024 \cdot T_{90}$, with T in °C.

The final uncertainty of the relative humidity in the SHCs is computed using Gaussian error propagation taking into account components from the analyses in [Greenspan \(1977\)](#) and from the measurements of the air temperature and salt solution temperature (if applicable) within the SHC during the UAII campaign tests. Conservative assumptions were made for the 0 %RH and 100 %RH chambers. The estimated uncertainties are listed in Table 5.1 and apply to the laboratory temperature range of 20 °C to 25 °C.

The SHCs were prepared prior to each two-week laboratory test-phase (see Section 4.2.2). This included refreshing the salt solutions (11 to 97 %RH), replacing the desiccant (0 %RH), and refreshing the distilled water (100 %RH). After preparation, test measurements with a well-characterised radiosonde were performed to verify proper functioning and consistency of the setup, including ventilation and relative humidity values inside the SHCs, and the data acquisition system.

5.3 MEASUREMENTS AND RESULTS

5.3.1 Measurement plan

The following measurement sequence was planned for each participating radiosonde in blocks of two to three days each:

- Preparatory tests:
 - Check for potential electromagnetic issues, such as disturbance or interference due to interaction with the metallic bodies of the SHCs,
 - Test of sensitivity of the relative humidity measurement to orientation of the sensor boom in the SHC,

²International Practical Temperature Scale of 1968 (IPTS-68)

³International Temperature Scale of 1990 (ITS-90)

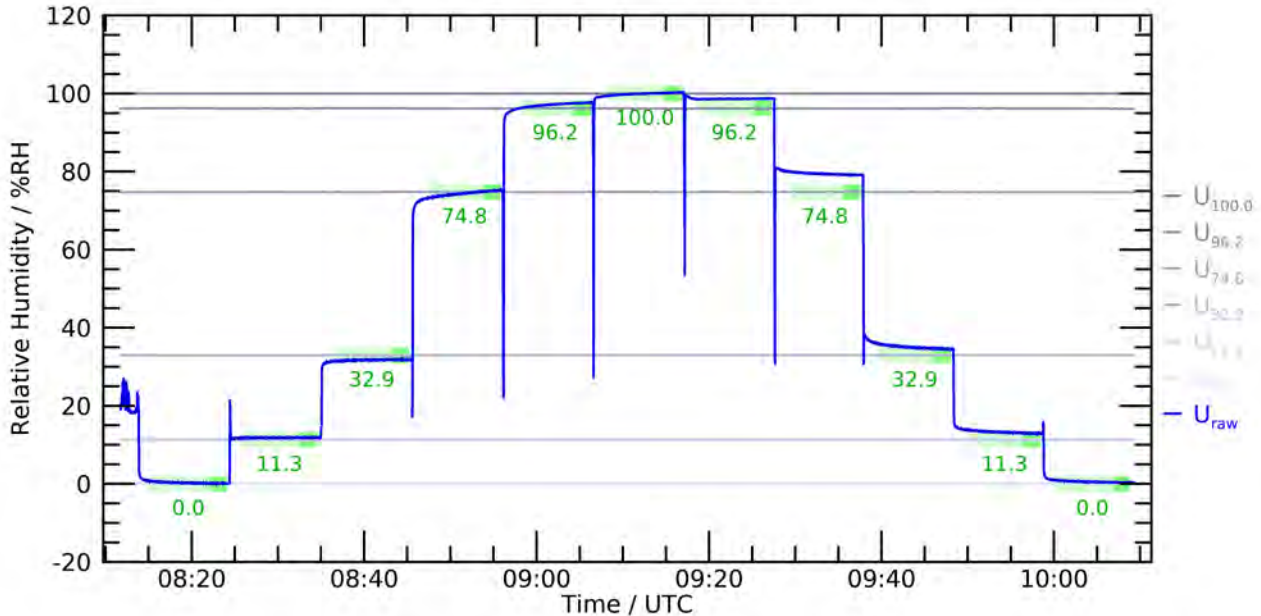


Figure 5.3: Complete cycle of measured relative humidity raw data (blue trace) of a candidate radiosonde over the full set of SHCs. The temperature-dependent reference humidity levels in the 6 chambers are drawn as grey traces. Green marks indicate the time periods (not the values) within each plateau, which were used for averaging the exact value for the actual reference humidity. The value measured by the radiosonde is averaged over the more intense green section of the green marks towards the end of the plateaus.

- Check for potential truncation of the raw data delivered by the radiosonde; the system should be able to record values below 0 %RH and above 100 %RH,
- Definition of residence time in each SHC.
- Measurement of one full cycle each (see Figure 5.3) with 10 copies of the same radiosonde model (statistical evaluation, batch reproducibility) – duration approx. one working day.
- Measurement of 5 full cycles in succession with 2 copies of the same radiosonde model (repeatability) – duration approx. one working day.
- Operation of 2 radiosondes in parallel (in adjacent SHCs) to save time (2 ground systems required).
- Sequence of a complete measuring cycle ('up' and 'down', in %RH): 0, 11, 33, 75, 97, 100, 97, 75, 33, 11, 0 – duration 1.5 h to 2.5 h.
- At each humidity level: waiting for stabilisation of the measured relative humidity value (entering plateau); stabilisation time 3 min to 10 min depending on sensor response; transfer of radiosondes (quickly) by hand to the next SHC.

Figure 5.3 shows the result of a full measurement cycle where the radiosonde has been tested in all SHCs in the above described order. Upon activation and preparation of the radiosonde, the temperature and relative humidity of the laboratory environment were recorded (approx. 20 °C to 25 °C and 20 %RH to 50 %RH). Then the sensor boom of the radiosonde was inserted into the first chamber and exposed to dry air (0.0 %RH). After a residence time of 3 to 10 minutes, the radiosonde was transferred to the next SHC. This was repeated up to the 100 %RH SHC, and then continued the way back to the 0 %RH SHC. The transfer between SHCs caused more or less sharp humidity peaks in the continuous data records because of the exposure to ambient air during the (short) times of transfer. With exception of the 100 %RH measurement, each relative humidity level was measured two times, however with a different short-term history of humidity conditions, depending on whether the measurement was performed on the upward or downward branch. This helped to test for hysteresis, or long-term sensor response.

The following effects or properties that can be considered characteristic for polymer sensors were

detected for the tested radiosonde types at varying degrees.

- Relatively quick initial change of the measured values towards the actual humidity level.
- Comparatively slow further convergence towards a constant equilibrium value (plateau).
- Constant deviations to the reference upon reaching the plateau (calibration bias).
- Systematically different deviations of plateau values connected to the upward and downward branches of the cycle (hysteresis).
- Tendency of increased deviations at the dry and humid ends of the humidity scale (e.g. below 10 %RH and above 90 %RH).

The measurement times per humidity level in an SHC were defined for each radiosonde type individually to between 3 min and 10 min, in cooperation with the manufacturers. The measurement time was limited to at most 10 min, so that the LABH measurement program could be completed for each manufacturer within the allocated 2 to 3 days.

As shown in the example plots in Figures 5.3 and 5.4, the humidity readings in many cases do not fully stabilise during the measurement intervals in the SHC. The sensors of some radiosonde models even seem to transition to a slow drifting after 5 min to 10 min.

The time limitations did not allow for further investigations of this behaviour. Also, as a result of the applied scheme of averaging the humidities measured by the radiosondes, this effect may have led in slight under- or over-estimations of the deviations from the reference humidities. However, uncertainties connected to such 'mis-estimations' were in general considerably smaller than the actually measured humidity deviations. The results of the repeatability tests disclose hysteresis-type and other memory effects for some of the radiosonde models. Such effects are known to occur with polymer sensors and were already detected in the preceding single-cycle tests.

It is noted here that the observed systematic effects can only be identified under the stable controlled experimental conditions the prevail inside the SHC, but hardly under the constantly changing humidity conditions during a real sounding, where they can be expected to have a corresponding effect on the quality of the measurement data.

The measurement repeatability was investigated by completing the whole measurement cycle five times in a row with the same radiosonde. This was repeated with two radiosondes. These tests disclosed the existence of memory effects at longer time scales (hysteresis) for several radiosonde models. which were already detected in the single-cycle tests.

5.3.2 Analysis

The analysis steps will be explained in detail below, based in the example plot in Figure 5.3.

The first step was to define those sections of the continuous data record of a full measurement cycle (up-down) that represent times when the radiosonde was installed in an SHC and was exposed to stable humidity and temperature conditions (pale green marks in Figure 5.3). The data points of the last 120 s of these sections immediately before transferring the radiosonde to the next SHC were selected in a second step for further analysis (shorter dark green marks in Figure 5.3). These selected sections were then analysed statistically for each plateau by calculation of the following parameters: the mean of the reference humidity, the mean of the humidity measured by the radiosonde, the difference between these two, and the standard deviation of the difference. In the next step, the evaluated values of the two associated plateaus from the 'up' and 'down' paths are set in relation, i.e. mean differences between values measured with the same radiosonde were calculated, which are interpreted as hysteresis: $\Delta U_{\text{hys}} = U_{\text{down}} - U_{\text{up}}$. The same analysis steps were applied to the temperature measurements.

Figure 5.4 summarises the results for the example cycle for relative humidity and temperature (left and right column, respectively). The six panels on each side correspond to the six evaluated humidity levels from 0 %RH to 100 %RH. The data are presented in green (upward branch), blue (downward branch) and red (difference between upward and downward, i.e. hysteresis). The highlighted parts of the traces (0 s to 120 s) mark the data taken during the last 120 s in the SHC, which is used for the subsequent analysis.

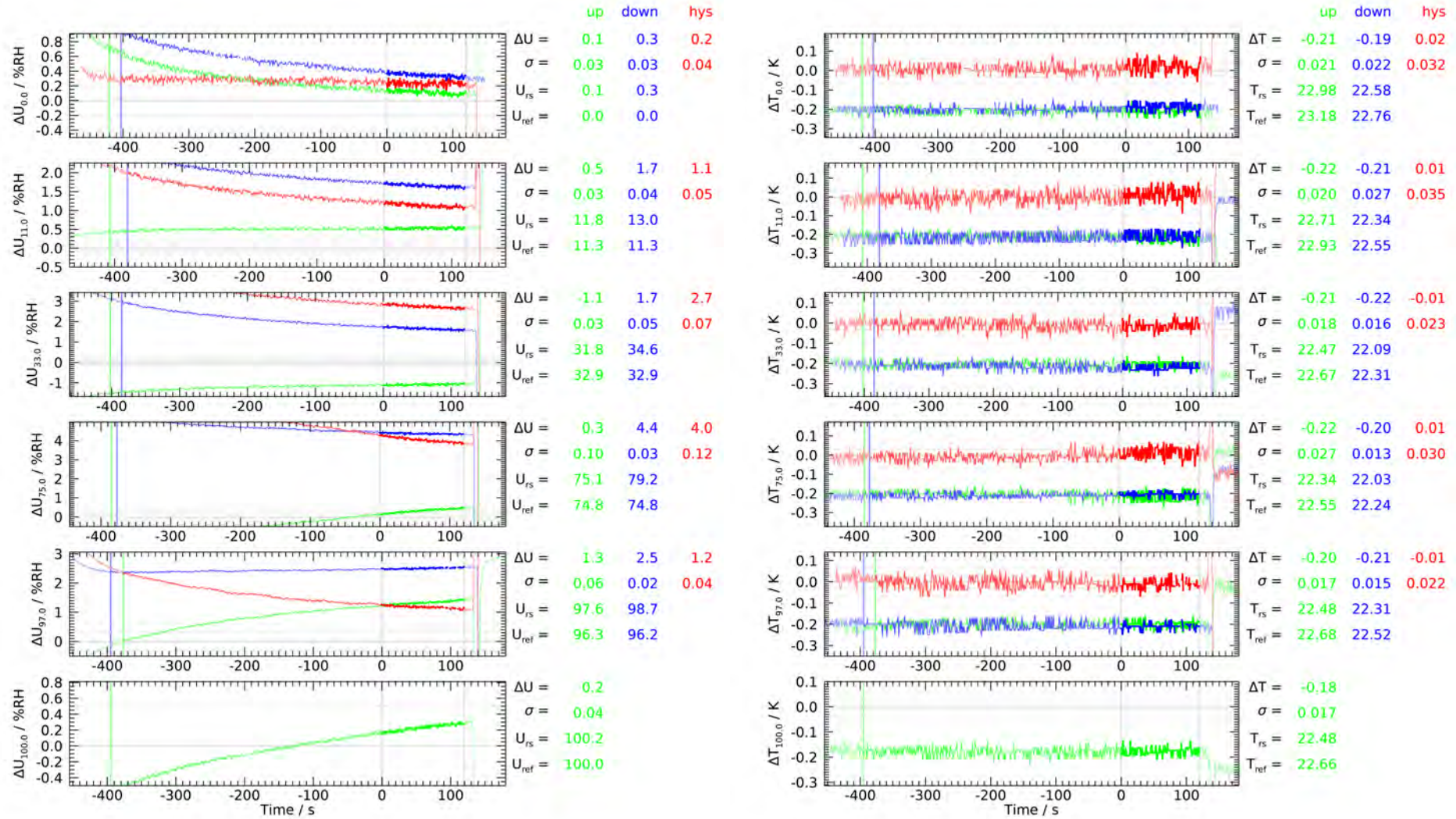


Figure 5.4: Analysis example of one measurement cycle: left column – relative humidity, right column – temperature. The humidity increases from 0%RH (top row) to 100%RH (bottom row). See Section 5.3.2 for a detailed description of this plot. The derived parameters are listed to the right of each panel.

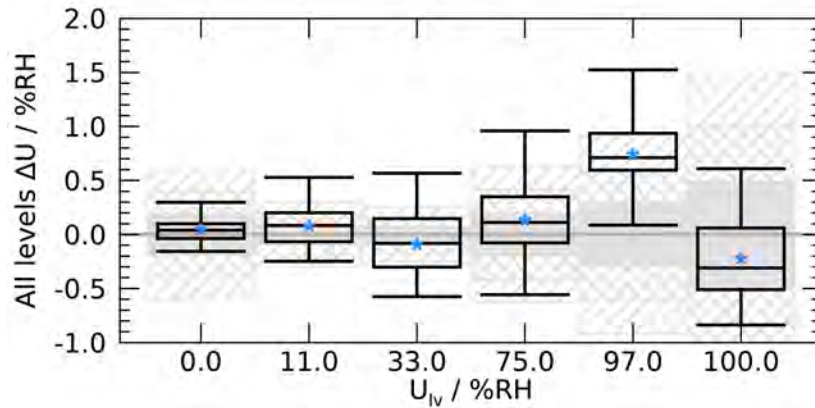


Figure 5.5: Example of the analysis showing mean deviations of relative humidity from the SHC reference ($\Delta U = U_{rs} - U_{ref}$) and statistical parameters at the six reference levels (U_{lv}) for the participant radiosonde B. See Section 5.3.3 for a detailed description.

The analysis in the following sections relies on the sets of mean values for each of the plateaus.

5.3.3 Relative Humidity

Figure 5.5 shows a statistical analysis of the results (relative humidity differences $\Delta U = U_{rs} - U_{ref}$) from the 10 tested radiosondes of the same type which all have passed the full 6-SHC measurement cycle. This scheme of presenting the results will be used throughout the rest of this chapter, and plots of this type and further evaluations will also be provided to the manufacturers.

In Figure 5.5, all plateaus measured during the entire cycle are included, i.e. a total of 20 values for each of the humidity levels (10 sondes with ‘up’ and ‘down’ measurements per cycle). An exception is the measurement at the 100%RH level where only 10 values are determined (1 measurement per cycle). This first summarised analysis including the data of both the ‘up’ and ‘down’ branches of the cycles without differentiation is motivated by the conditions during real flights where the sensor is exposed to a mixed sequence of relative humidity changes in both directions. Systematic differences between ‘up’ and ‘down’ are discussed later in the context of hysteresis effects.

The grey shaded areas in Figure 5.5 denote the estimated standard uncertainties of the reference humidities for $k = 1$ (filled), $k = 2$ (crosshatched) and $k = 3$ (hatched). The $k = 1$ uncertainty extends from about 0.1 %RH to 0.5 %RH in this example (see Table 5.1). The black boxes and horizontal bars indicate various statistical parameters: minimum value, lower quartile (Q1), median, upper quartile (Q3), and maximum value. A box thus encloses the distance Q1 to Q3 (the Inner Quartile Range: $IQR = Q3 - Q1$). Outliers were detected as values less than $Q1 - 3 \cdot IQR$ or greater than $Q3 + 3 \cdot IQR$. If present (not in this example), outliers are plotted as separate black dots. Blue stars denote the arithmetic mean.

In this particular example, the radiosonde measurements agree well with the reference values, which indicates a good calibration of the humidity sensor. With exception of the 97%RH level, the mean values (both arithmetic mean and median) are within the $k = 1$ uncertainty of the reference humidities. The mean values deviate less than 1.0%RH from the reference. There is no regular pattern for the deviations, both in magnitude and sign, which indicates the absence of significant systematic biases or trends. Such irregular fluctuations are observed for various candidate radiosondes at variable magnitude, however, some show regular trend-like pattern (see following discussion). At higher relative humidities, minimum to maximum deviations of about 1.5%RH were found in the example. This may be attributed to the enhanced uncertainty and variability connected with calibration.

Figure 5.6 presents the results of the statistical analysis for all 10 participant radiosondes. All plots use the same scaling of the axes, which allows for easier comparison.

With regard to relative humidity, most of the radiosonde types show on average deviations to the reference within ± 5 %RH. One exception is radiosonde G with deviations over the whole humidity

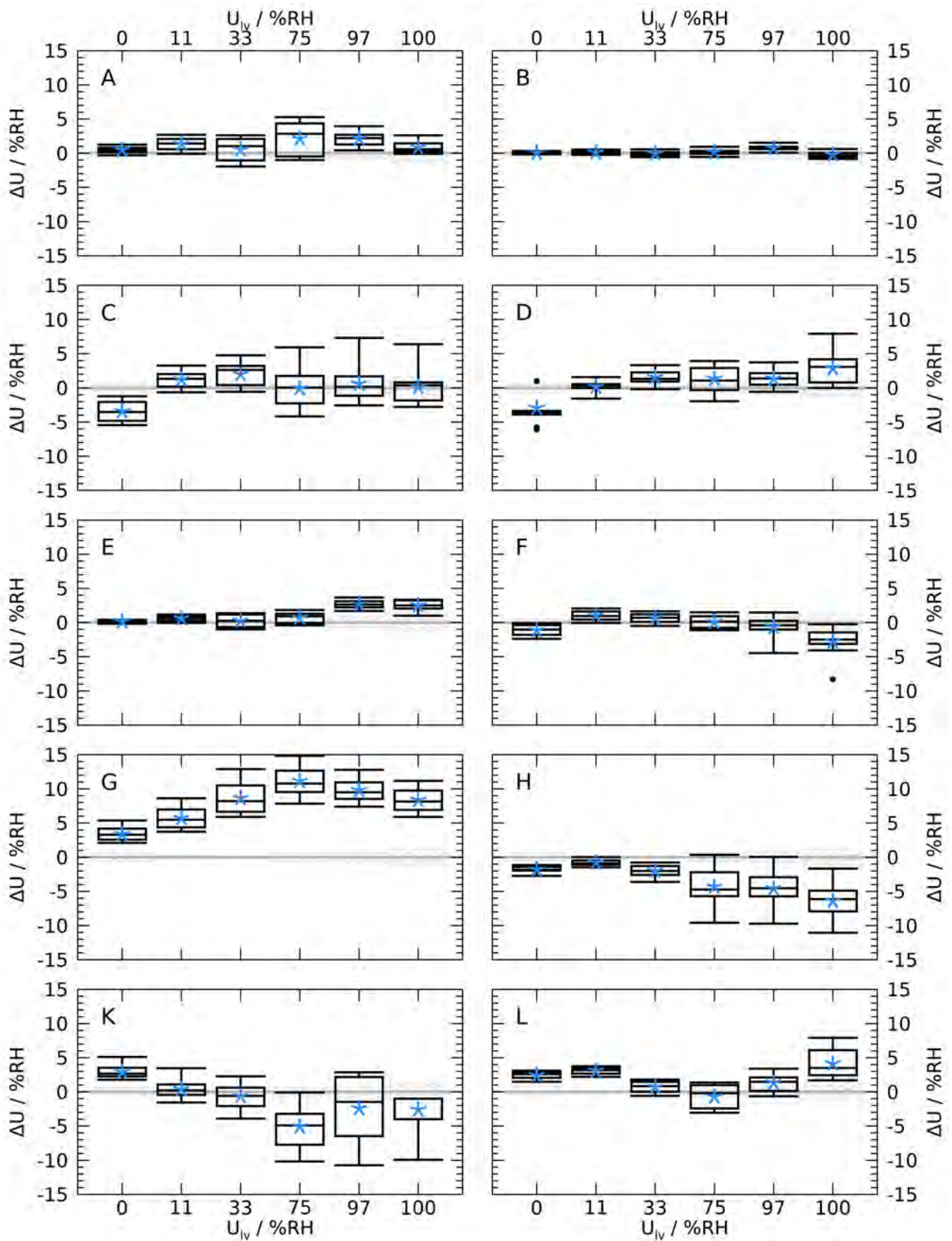


Figure 5.6: Results of the statistical analysis of difference measurements for relative humidity ($\Delta U = U_{rs} - U_{ref}$) in SHCs including approx. 10 sondes of each of the 10 participant radiosondes.

range between 5 %RH to 10 %RH systematically in the same direction. Also, the minimum-to-maximum amplitudes for some radiosondes are between 5 %RH to 10 %RH. The overall number of 10 sondes of the same type included in the tests is at the lower end of being a statistically representative sample, therefore general conclusions should be drawn with care. Nevertheless, the occurrence of systematic differences of such a magnitude may indicate significant issues connected with the calibration or stability of the humidity sensors of these radiosondes, which in parts would call compatibility of measurement results in soundings with the uncertainty requirements into question.

Discussions with manufacturers during the laboratory campaign revealed that the calibration points mostly do not fully cover the entire operational range (0 to 100 %RH). It appears to be common practice that the calibration range is limited to the range between approx. 10 %RH and 90 %RH, which is illustrated by the calibration information shown in Table 3.3. This may explain increased deviations at the 0, 97 and 100 %RH levels identified for some radiosondes, because extrapolation beyond the calibration range generally involves increased uncertainties. On the other hand it can be expected that deviations tend to be smaller at humidity values which are close to sensor calibrations points. This may in particular apply to the 11 %RH SHC.

Polymer-based humidity sensors can show hysteresis effects. The UAII LABH experiment was designed to identify and – if present – quantify this effect by measuring humidity with the above described ‘up-down’ cycle. Again, note that during the transfer between SHCs the sensors were exposed to laboratory air with different humidity and temperature for a short period of a few seconds.

The results for the candidate radiosondes are summarised in Figure 5.7. Differences between measured values in the same SHC on the ‘up’ and ‘down’ path of the cycle are evaluated (except of the measurements at 100 %RH): $\Delta U_{\text{hys}} = U_{\text{down}} - U_{\text{up}}$. No uncertainties are estimated because differences of measurements with the same sensor are analysed. The results are interpreted as a hysteresis effect. It can be observed that up to the 75 %RH level the effect increases (reaching 5 %RH) with increasing ambient humidity. In contrast, it goes back to smaller values at the 97 %RH level. This pattern is observed for all radiosonde models, however there is a considerable spread in the magnitude of the effect for the various models; the maximum values range from less than 0.4 %RH to more than 5 %RH.

It is worth considering that clipping of the raw data at 100 %RH may artificially reduce the hysteresis observed at 97 %RH for radiosondes that overestimate the humidity at high humidity levels and that perform clipping as well.

The repeatability of the humidity measurement was tested for each radiosonde type by repeating the entire SHC cycle five times with two radiosondes. It is noted here that the radiosondes were re-initialised according to the manufacturer-prescribed routine ground preparation procedures between each of these five cycles. Some of the radiosonde models (A and H) showed increased numbers of erroneous measurements or data failure in the fourth or fifth run so that no analysis at the 100 %RH level could be carried out. This may be due to the extended operation time of the radiosondes or the repeated handling while transferring the radiosonde between the SHCs. With a single measurement cycle taking 1 to 2 hours, the radiosondes were continuously operated for up to 10 hours at a time, which is much longer than the standard use during an operational sounding, and thus is likely to exceed the capacity of the battery.

Figure 5.8 shows an overview of the repeated measurements of a (randomly selected) radiosonde of each candidate. The repeatability is expressed in the representations of the statistical parameters in the figure (e.g. vertical size of the boxes), not in the deviation from the respective reference humidity. For the latter, compare also to Figure 5.6.

A few candidates (e.g. B, E, F) show very good repeatability within 2 %RH. Others cover, depending on relative humidity, a span of up to 5 %RH, in some cases up to 7 %RH.

Figure 5.9 illustrates with four examples how the results evolve with repeated runs of the experiment and how these vary among the different radiosonde types. Note the different y-axis scales. Panel (a) shows pattern that might indicate a long-term “training” or “saturation” effect of the sensor, i.e. the deviations of the measurement values change with the number of expositions of the sensors to the reference conditions, with a similar rate at all humidity levels. Panel (b): A similar “training” effect as in (a) might take effect, however evolving in the other direction, at least at lower humidity levels. Panel (c) . reflects what is most likely to be expected: no sig-

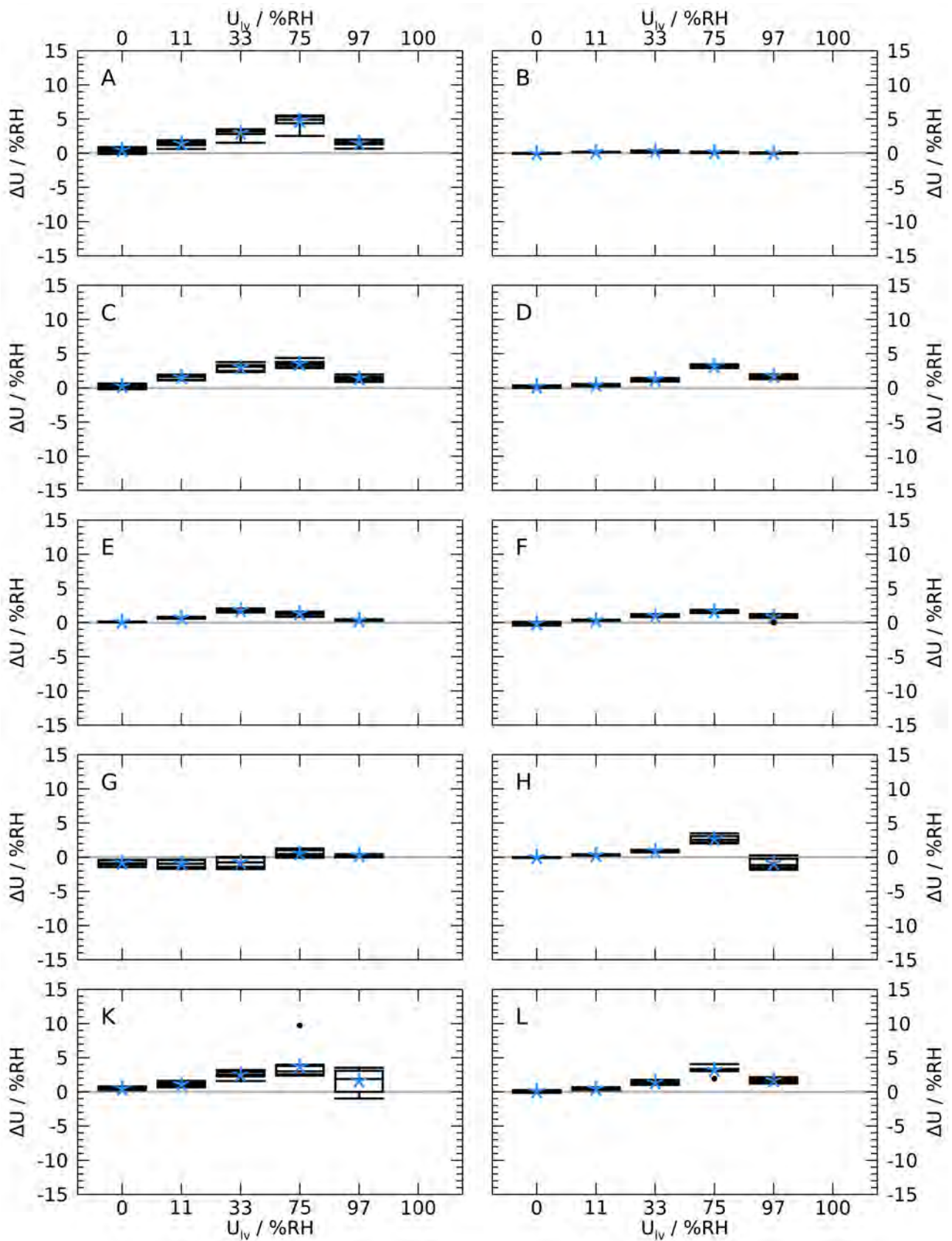


Figure 5.7: Averaged hysteresis effect (approx. 10 sondes) for relative humidity ($\Delta U_{\text{hys}} = U_{\text{rs,up}} - U_{\text{rs,down}}$) for the 10 UAI participant radiosondes.

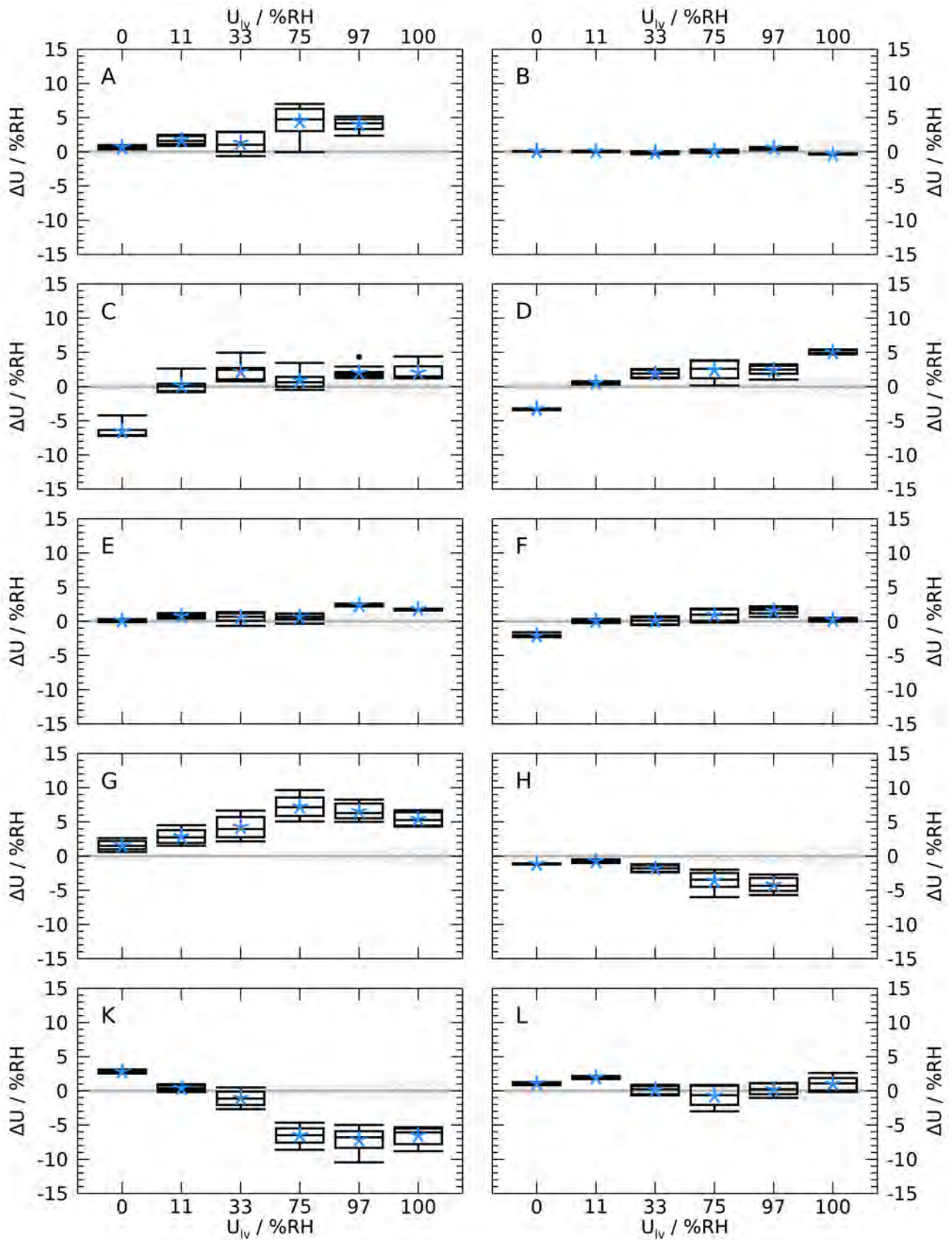


Figure 5.8: Repeatability of relative humidity measurement $\Delta U = U_{rs} - U_{ref}$ after running the SHC series five times. Each panel is for a single radiosonde unit of one of the 10 participants.

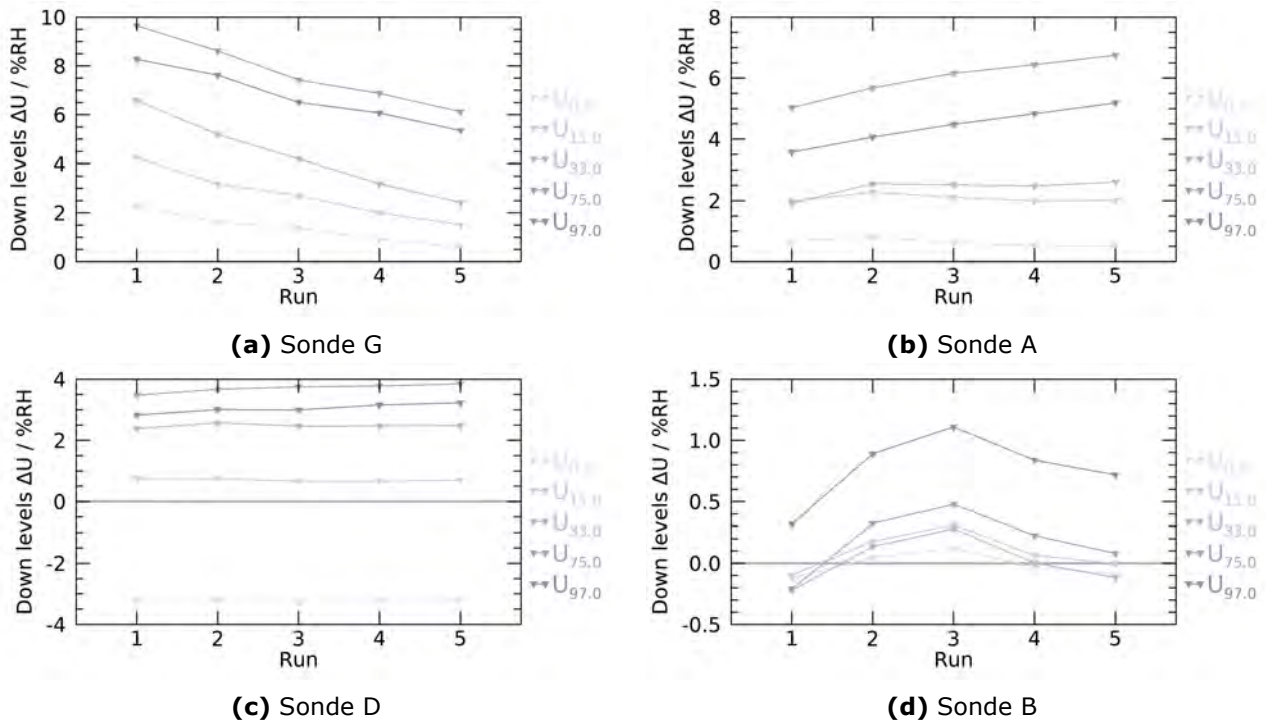


Figure 5.9: Results of the repeatability tests, showing the variability of the humidity deviations to the reference values over the five measurement runs for four of the tested radiosondes. Note the different y-axis scales.

nificant changes over all cycles. Panel (d): similar to (c), i.e. low variation over the runs (good reproducibility), no clear trend.

5.3.4 Temperature

In parallel to the performance tests of the relative humidity sensors also the radiosonde's temperature sensor data were used for comparison with the reference sensors installed in the SHCs. Although limited to ambient laboratory conditions between 20 °C and 24 °C, the results provide some insight into the temperature measurement under these conditions.

The plots used to present the results for temperature resemble those for relative humidity discussed in the previous sections. No systematic effects were expected over the six SHCs with regard to the differences to the references sensors, especially because the temperature measurement under the stable conditions in the SHCs should not be sensitive to actual humidity level.

An example of the results for a selected radiosonde is shown in Figure 5.10, in that case showing very small mean deviations of less than 0.01 K from the references and a scattering of the data within ± 0.03 K. Note that the calibration uncertainty of the reference sensors used in the comparisons is 0.03 K ($k = 1$).

The results in the example fit in with the expectation that the air temperature measurement is insensitive to the (humidity) conditions in the actual SHC. Therefore, the results from all SHCs are averaged, statistically analysed, and visualised in the following diagrams.

The overview plot in Figure 5.11 shows good results for about half of the participant radiosondes with the mean temperatures deviating less than ± 0.1 K from the reference, and with a data spread (maximum minus minimum) of a similar range. The other half shows larger mean deviations between ± 0.1 K and ± 0.2 K, with the minimum-maximum span reaching almost 1.0 K. Some units of the D and L radiosondes produced results that were categorised as outliers (black dots), consistently in all SHCs, which may indicate sensor instability, or more likely systematic offsets related to calibration.

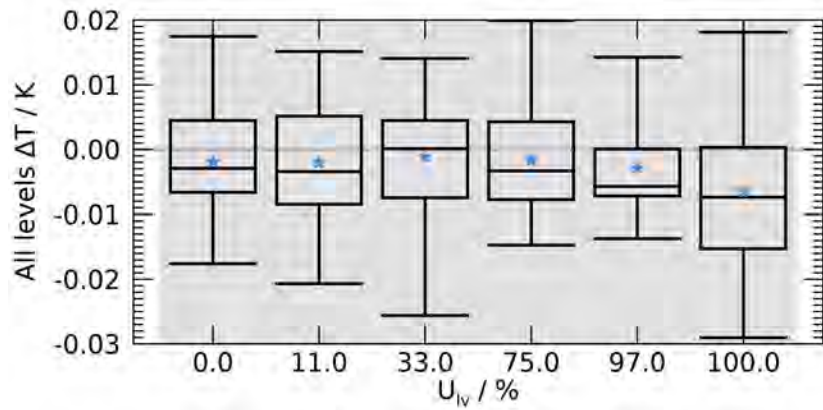


Figure 5.10: Statistical evaluation of the comparison measurements ($\Delta T = T_{rs} - T_{ref}$) at room temperature in the series of six SHCs with 10 sondes of the same type (C).

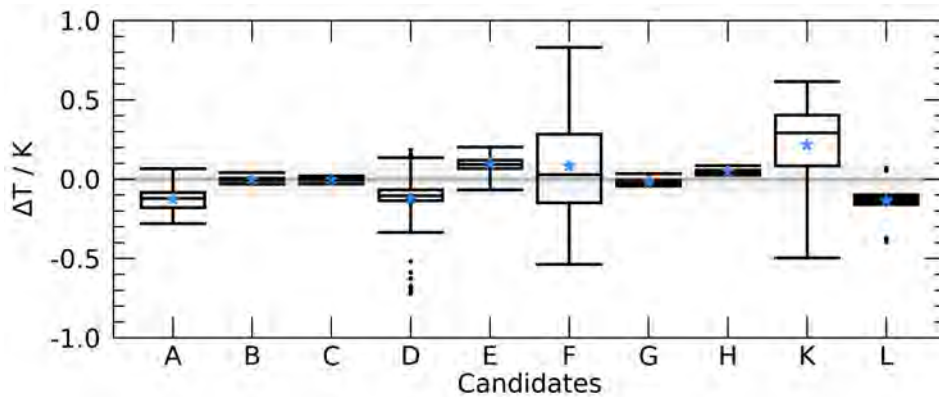


Figure 5.11: Statistical evaluation of the comparison results ($\Delta T = T_{rs} - T_{ref}$) at room temperature using 10 copies of each of the tested radiosonde models.

In analogy to the relative humidity measurement programme, the repeatability was investigated in the separate test series where two units of each candidate radiosonde were temperature-compared five times in a row in all SHCs. In contrast to humidity, no systematic drift or saturation effects are expected during the temperature measurements over the course of these tests, since radiosonde temperature sensors are generally assumed to be insensitive to the water vapour content in air (as long as there is no net evaporation or condensation at the sensor surfaces). Figure 5.12 summarises the results for a single unit of each of the radiosonde models. Apart from certain – probably calibration related – deviations of the means from the references, the repeatability is generally good, indicating good sensor stability and confirming the above expectation. An exception are the radiosondes F and K with comparatively large spread. Figures 5.13 and 5.14 provide a closer look to these two radiosonde types, showing the statistics of the reproducibility tests using 10 sondes (upper row in Figure 5.13) and the repeatability test for a single radiosonde running five times over the humidity cycle (lower row), all resolved for the six SHCs. Apparently systematically deviating values at the highest humidity levels (at least in (a), (b), and (c)) might suggest certain influence of the humidity on the temperature measurement.

Figure 5.14 shows the deviation to the reference temperature for the two single radiosondes F and K varies with the run number at all humidity levels rather than with humidity. This might indicate that certain (random) persisting offsets are added to the originally calibrated temperatures, which might be related to the radiosonde re-initialisation procedures before each of the measurement runs over the SHCs.

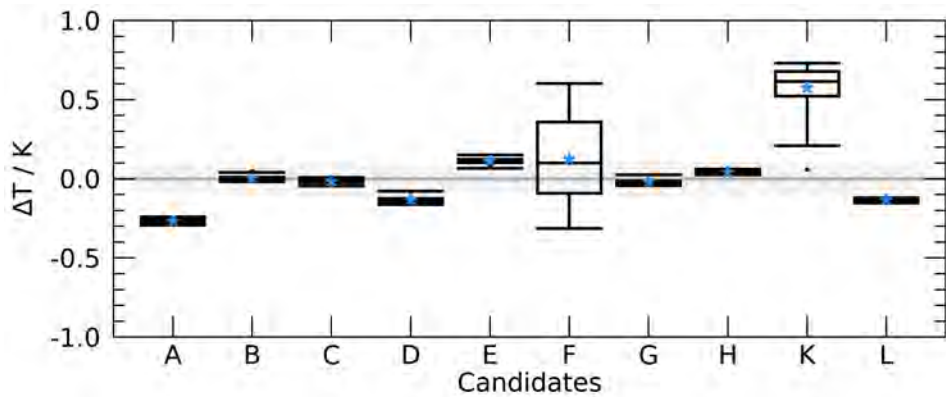


Figure 5.12: Statistical evaluation of repeatability of temperature differences ($\Delta T = T_{rs} - T_{ref}$), based on measurements using a single radiosonde of each candidate five times in a row over all SHCs.

5.4 CONCLUSIONS

The LABH tests that were performed in the SHC at room temperature between 0%RH and 100%RH, provide useful insights into the performance and the quality of the calibration for the humidity sensor. For the majority of the radiosonde models, the mean bias is less than 5%RH over the whole humidity range, which is in agreement with the uncertainty specification provided by the manufacturers. However, the models systematically show larger deviations of up to 10%RH. Hysteresis-like effects are observed for all radiosondes, with an average value of 5%RH, although considerable differences in magnitude among the individual candidates are found.

The repeatability test results, namely the measurement precision achieved with the same radiosonde in five consecutive measurement cycles under the same conditions, show that some of the radiosondes were stable within $<2\%$ RH, while others were less stable showing in parts trend-like variations, which might be connected to conditioning or saturation effects. Some of the measured deviations from the SHC reference humidities exceed 7%RH, which is substantial with regard to current quality requirements.

Regarding the temperature sensor tests at room temperature, mean deviations relative to the used references of virtually zero to about 0.3 K are identified, with about half of the 10 sondes showing deviations of less than 0.1 K. However, the distributions of the individual measurement points for a radiosonde as well as the occurrence of outliers varied considerably among the 10 candidates.

The investigation of some of the sensor properties of the temperature and humidity sensors at temperatures between 25 °C and as low as -75 °C is presented in Chapter 6.

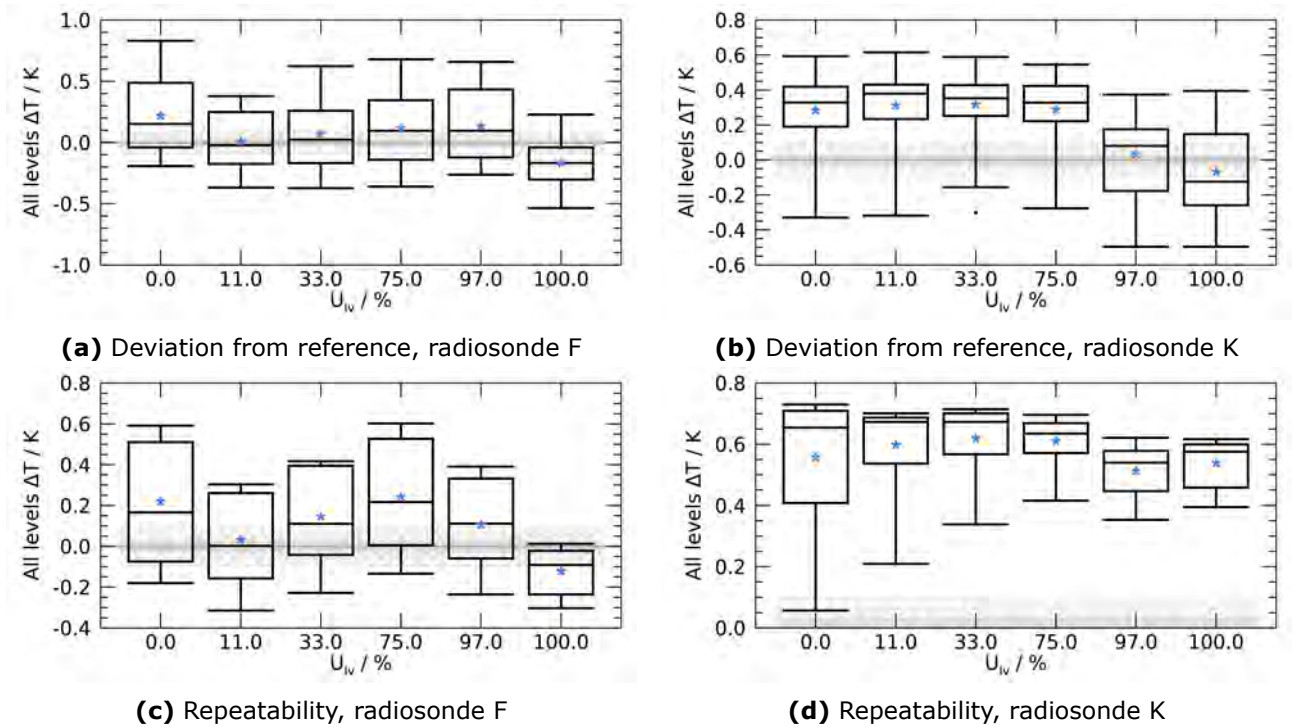


Figure 5.13: Detailed view on the results of the temperature comparison with reference for the two candidate radiosondes F and K. Upper row: statistics over 10 radiosondes of the same type. Lower row: statistics for repeatability tests with a selected single radiosonde.

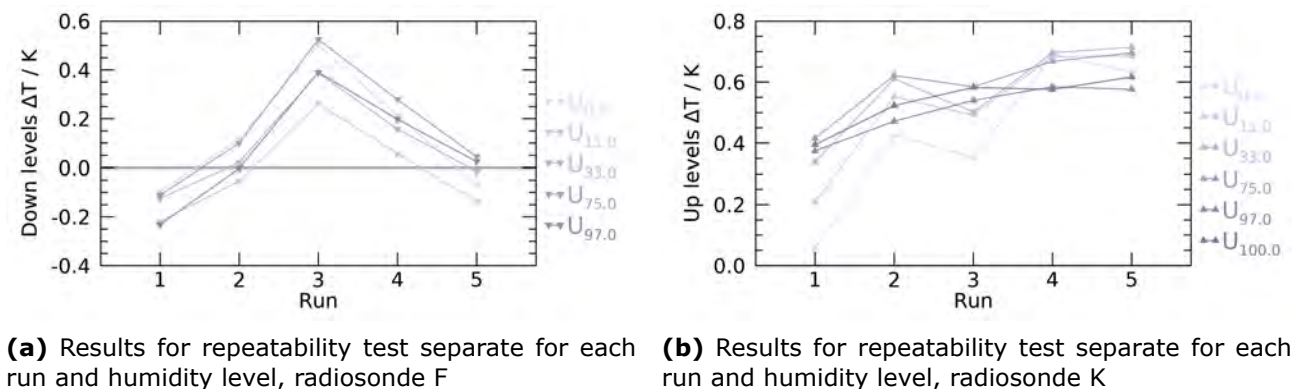


Figure 5.14: Time-dependent change of results of repeatability during 5 runs of temperature of two candidate radiosondes F and K.

6 HUMIDITY AND TEMPERATURE SENSOR PERFORMANCE AT LOW TEMPERATURE (TLAG, LOWT)

6.1 INTRODUCTION

The large range covered by atmospheric temperatures and water vapour content between the surface and the middle stratosphere is a challenge for the radiosonde's temperature sensor and especially its humidity sensor in view of the steadily growing demands on data quality. In Chapter 5 the measurements are described to test the performance of the radiosonde humidity sensors at room temperature. The purpose of the tests presented in this chapter is to investigate the performance of the humidity and temperature sensors at low temperatures. To do so, the sensors are exposed to an air flow at well-defined low temperatures under controlled conditions in a climatic chamber. The focus is on the ability of the humidity sensor to record rapid changes in relative humidity. Contemporary radiosondes employ capacitive polymer-type sensors, that are known to show a considerable delay in their response to humidity changes under cold conditions. In a second test, the temperature recorded by the radiosondes is compared to reference sensors, with the purpose of assessing the calibration of the temperature sensor at low temperatures.

All radiosondes participating in UAI 2022 employ hydrophilic polymer sensors. The polymer material is arranged as a thin film between two porous electrodes forming a plate capacitor. Water vapour molecules from the surrounding air diffuse into the pores of the polymer matrix and adsorb or desorb on the material surfaces. Adsorbed water vapour molecules change the relative permittivity (dielectric constant) of the polymer material and consequently the capacitance of the sensor element. This capacity is measured in an electronic circuit yielding the relative humidity of the ambient air after proper calibration of the capacitive sensor.

Under equilibrium conditions, the adsorption and desorption rates of water molecules in the polymer material are in a dynamic equilibrium. The response of the sensor to changes in humidity is determined by the time it takes to re-establish this equilibrium. The rates, and hence the response times, considerably slow down with decreasing temperature. As a consequence, the sensor is not able to follow the rapid humidity changes that usually occur in a radiosounding when ascending through layers with changing water vapour content. That is, vertical structures of humidity in the atmosphere that occur 'faster' than the sensor's response time will be smoothed, and the measured humidity follows the true profile with a delay; this effect is commonly referred to as 'time lag'. As a result, the values measured by the humidity sensor (raw data) may deviate considerably from the true humidity in certain parts of the profile, in particular in the upper troposphere and tropopause where ambient temperatures are low and where large humidity gradients often occur. Typical values for the time constant range from about 1 s at 20 °C to more than 100 s for temperatures below -60 °C, and is determined by properties such as its design, the employed materials for polymer and electrodes, and its shape and thickness. Consequently there is a considerable variation of the time lag among the different sensor versions from various manufacturers, and the differences at low temperatures can be one or two orders of magnitude.

Most manufacturers apply a time lag correction in their data processing, where the correction aims to reconstruct the true atmospheric humidity profile from the measured time-lagged raw data (see [Dirksen et al., 2014](#); [Miloshevich et al., 2004](#)). Therefore, a proper characterisation of the time-lag, specific for the actual sensor type and resolved for the temperatures covered in radiosonde soundings, is essential for the quality of the final relative humidity in the data product.

In the framework of GRUAN activities, a dedicated setup has been developed at the Lindenberg Meteorological Observatory to characterise the response time of humidity sensors at well-defined low temperatures. This test facility was used during the UAI 2022 laboratory campaign to assess the time lag behaviour of the humidity sensors (TLAG) as well as to check the performance of the air temperature sensor (LOWT) between 20 °C and low temperatures representative for the tropopause region. The TLAG and the LOWT tests were performed using the same setup but in separate measurement runs.

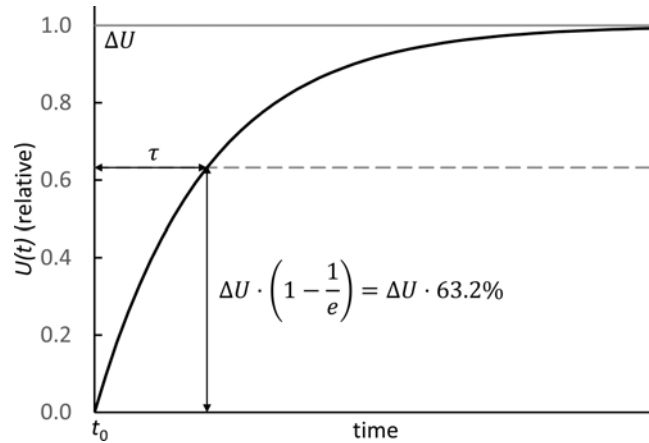


Figure 6.1: Illustration of the model sensor response time τ for an 'upward' step in relative humidity. ΔU denotes a (relative) step-wise change of relative humidity at $t = t_0$, and the black curve indicates the sensor's response.

6.1.1 Time lag measurement

The investigation of the humidity sensors (TLAG) aims at the identification of the response behaviour and the quantification of characteristic response times (the time lag) at various temperature levels. The underlying assumption is that the response of the sensor to a step-wise change in humidity can be modelled by a simple exponential equation, so that the sensor's time lag performance can be described with a single parameter, the response time τ . It can be determined directly from the response curve by sampling the measured values with time after exposing the sensor to a step-wise change of the relative humidity in the surrounding air stream. The response curve is then given by

$$U(t \geq t_0) = U_\infty - (U_\infty - U_0) \cdot e^{-\frac{t-t_0}{\tau}}. \quad (6.1)$$

Here, τ (in seconds) is the characteristic response time (inverse of the time constant), i.e. the time the sensor takes to reach 63.2% (or $1 - 1/e$) of the ambient humidity after the step-wise change, and t_0 is the moment the change is applied. U_∞ denotes the relative humidity to which the sensor converges (corresponding to the ambient humidity after the step-wise change) at a rate according to its characteristic response time. Figure 6.1 illustrates the shape of the sensor's response curve and how to determine the response time τ .

Despite the large variability of the time lag behaviour among different sensor types, the response behaviour in the temporal range is similar in its basic form, which allows to evaluate the measured time lag using the same approach (Section 6.3.1). The measurements were conducted at surface pressure. Since relative humidity is defined in terms of partial and saturation pressure of water vapour, it is assumed that the sensor response time is independent of air pressure.

The purpose of the tests within the TLAG experiments is to get an overview of the response of the sensors to rapid changes in humidity. Using the model in Equation (6.1), the response time is determined at various temperature levels, and the relation of the response time to temperature is evaluated. For these tests it is essential that the raw data is used with the manufacturer's calibration applied, but no further processing. The experiments do not assess the quality of relative humidity product data which are generally processed raw data and subject to various corrections.

The results relate to the particular experimental configuration as realised in the setup (see Sections 6.2 and 6.3.1), e.g. the particular air circulation pattern around the sensor boom, flow velocity, radiative environment, etc. The representativity for real ascents is not evaluated. The primary objective is to demonstrate the basic systematics for all involved radiosonde models at comparable conditions. A comprehensive characterisation of the time lag requires a more elaborate measurement program.

Provided that the sensor is well characterised (and that an appropriate time lag correction model is applied), corrected relative humidities of somewhat slower sensors can in principle still reasonably represent the actual atmospheric profile. However, the correction brings its own uncertainty, and

the uncertainties of the corrected humidity increase with the correction amount (i.e. with the amount of time lag). This is on the one hand due to the increasing uncertainties of the measured or estimated response times, and on the other hand because slower sensors smooth the natural atmospheric structures more, which leads to a deteriorated signal to noise ratio in the corrected profile. This means that faster sensors will generally provide relative humidity profiles of higher quality after correction, so that it is advantageous to employ fast humidity sensors.

6.1.2 Low temperature calibration assessment

Manufacturers use different methods to calibrate the temperature sensor of their radiosondes. They either rely on factory calibration from the supplier of the sensor, or perform a calibration themselves by immersing the sensor boom with integrated temperature sensor in a liquid bath at selected temperatures.

A relevant factor for the quality of the temperature profile measured by the radiosonde is the temperature range for which the sensor is calibrated. This range should cover the temperatures encountered in flight, otherwise extrapolation errors may occur. The number of temperatures at which the calibration is performed (support points) together with the applied fitting function contribute to the uncertainty of the calibration as well, especially if the calibration function deviates from linear. The supplier-calibration of the isolated sensor can differ from that of the fully integrated sensor due to influence of the electronic circuitry of the radiosonde. Therefore, relying solely on the supplier calibration without additional calibration checks carries the potential risk of inaccurate temperature measurements.

For the temperature comparison part of the experiments (LOWT), the readings of the radiosonde's temperature sensors are compared at selected temperatures to those of nearby-installed reference sensors. The aim of this test is to assess the calibration of the temperature sensor and to investigate the stability of the radiosonde at low temperatures. The time lag setup was not designed to perform precise calibration measurements, so that the uncertainties for the LOWT measurements are expected to be larger than these performed in dedicated calibration setups. However, the temperature comparisons could be performed 'for free' during night time as a spin-off of the time lag measurements, i.e. without requiring additional resources, making it worth the effort. The LOWT experiments are described in detail in Section 6.3.2.

6.2 EXPERIMENTAL SETUP

The setup creates a constant flow of either dry or humid air, that flows around the sensor booms of the radiosondes. The setup allows to switch quickly between the dry and moist flows, so that the sensors are exposed to a step-wise change in relative humidity. The setup is mounted inside a climatic chamber (Feutron KPK 400), allowing to control the temperature of the air flow between room temperature and approximately -75°C . Figure 6.2 shows a schematic sketch and a picture of the setup.

The main components of the setup are:

- Stainless steel and copper tubes with 6 mm inner diameter to guide the airflow. The incoming, dry air flows through a 25 m long coil for the purpose of heat exchange, so that the airflow is in thermal equilibrium with the climatic chamber.
- a home-made humidifier, consisting of a twisted 2 m long copper tube of 25 mm diameter. Inside the horizontally mounted humidifier the dry air flows over a water/ice layer, that moistens the air flow by evaporation/sublimation. The water vapour content of the air flow that exits the humidifier is close to saturation at room temperature and decreases somewhat with decreasing temperature.
- At the end of the cooling coil, the air flow is split into two branches, one of which is connected to the humidifier
- A system of two motor-driven 2-way-valves feed either dry or moist air into both measurement cells.
- Two quartz glass tubes (22 mm inner diameter) are the measurement cells in which the

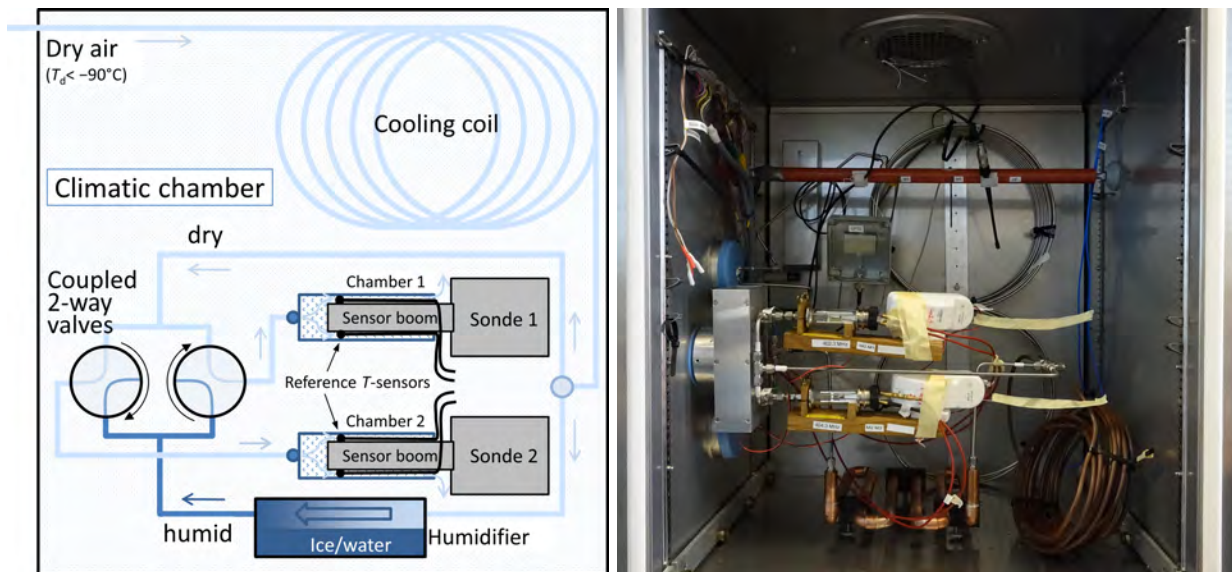


Figure 6.2: Sketch and photo of the experimental setup for the investigations of humidity and temperature sensor at low temperatures.

sensor boom of either radiosonde was mounted. Inside the cell, the boom is exposed to a constant air flow.

With this setup, two radiosondes can be operated and tested simultaneously. Both radiosondes are exposed to an airflow of the same origin (i.e. either dry or moist), and switching between dry and moist air and vice versa can be performed at will.

The switching time of the valve is well below 1 s, which enables the required step-wise change of humidity in the measurement cells. The water vapour content of the air exiting the humidifier is neither actively controlled nor measured, but previous tests have shown it to be close to saturation, especially in the upper half of the temperature range employed during the TLAG and LOWT measurements. In other words, the water vapour content in the moist air flow is always sufficient to produce humidity changes of the size needed to investigate humidity sensor time lag.

The air flow is controlled by the inlet pressure of the dry air, and is measured by a digital flow meter. During the tests a fixed flow of $\sim 6 \text{ L min}^{-1}$ was employed for each of the two measurement cells, which corresponds to an effective flow speed of $\sim 0.4 \text{ m s}^{-1}$. At this flow speed, the calculated exchange time of air in the cells is approximately 0.25 s. The air flow is produced from ambient air, which was dried in a high-performance desiccant unit before being fed into the setup. The dew point of the dry air is below -90°C (water vapour content $< 0.15 \text{ ppm}$).

Figure 6.3 shows a radiosonde sensor boom mounted in a measurement cell. The flat sensor boom is clamped in a small slit of the black end cap at the right-hand end of the cell. The cap also holds two PT100 sensors which are positioned inside the cell, close to the temperature sensor of the radiosonde, for independent measurement of the temperature inside the cell. Additional ventilation holes in the cap prevent the build-up of pressure inside the cell. It is assumed that the air inside the cell is well-mixed at all times.

Seven of the ten participating radiosonde models use a cover or a similar construction to shield the humidity sensor from direct solar radiation or from contamination by water or ice during the sounding. Since it cannot be excluded that the cover affects the airflow around the humidity sensor and thereby influences the result of the measurement in a specific way during the experiments, it was decided in mutual agreement with the manufacturers to remove the cover of one of the two simultaneously tested radiosondes for the TLAG and LOWT measurements. The comparison of the two enables proving the existence and general systematics of a possible cover effect.

The radiosondes were connected to an external power supply provided by the observatory to ensure continuous operation of the radiosonde during the prolonged measurement runs at low temperatures. The manufacturer receiving systems and computers were placed in the laboratory

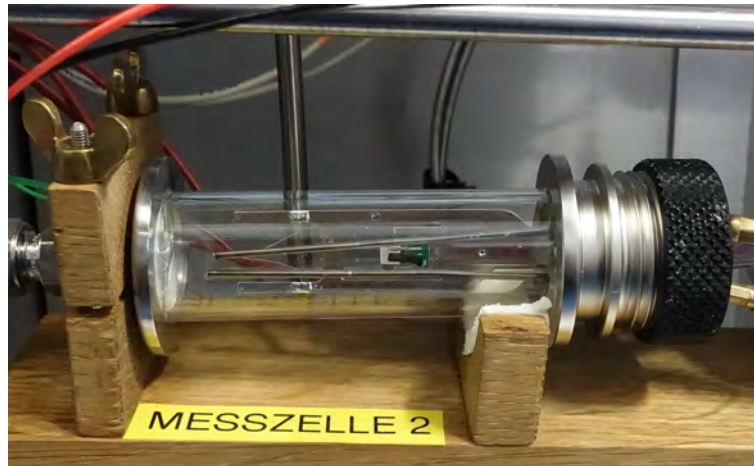


Figure 6.3: Installation of a radiosonde sensor boom within the glass cell together with two Pt100 sensors used as temperature reference.

room close to the climatic chamber. Transmitting frequencies of the radiosondes were set according to the specifications of the Lindenberg staff. In addition to the use of their sounding systems for data recording, the manufacturers provided tools for visualising incoming data in real-time. These visualisation tools enabled monitoring and on-the-fly evaluation of the measurement data, which is essential for defining the times of switching between dry/moist air flow during the TLAG experiments. All readings of the sondes under test as well as those of the setup sensors were recorded at a rate of 1 s^{-1} . The clocks of the radiosonde systems were synchronised manually with those of the setup's data acquisition system before the start of each measurement run.

The traceability of the Pt100 sensors used in the LOWT measurements (Section 6.3.2) is ensured by regular comparisons with two reference Pt100 sensors over the temperature range -90 °C to 20 °C . During the comparison procedures the sensors are immersed in a well-mixed temperature-stabilised bath of silicon oil. The two reference Pt100 sensors are calibrated at regular two-year intervals by the company Ahlborn against references that are traceable to the national standard that resides at the Physikalisch Technische Bundesanstalt (PTB), the national metrology institute in Germany. The resulting calibration uncertainty of the references Pt100 sensors is 0.06 K ($k = 2$).

6.3 MEASUREMENTS AND RESULTS

6.3.1 Quantification of humidity sensor response time (TLAG)

6.3.1.1 Measuring program

Three working days of laboratory activities were scheduled during the UAII 2022 TLAG experiments for each manufacturer, with a measurement program according to the following guideline:

- Day 1 - preparation: adaption and installation of the radiosondes into the measurement cells; test of proper functioning of the radiosonde systems and the setup; test runs at room temperature and determination of the lowest temperature at which the measurements produce meaningful results; initial assessment of the behaviour of the humidity sensor and the range of response times.
- Day 2 - execution of the 'mandatory' measurement program, which consists of at least two complete cycles (dry to humid and humid to dry) at -70 °C , -50 °C , -30 °C , and -10 °C . This mandatory program is performed in the same manner for each participating manufacturer. The time needed to perform the mandatory program varied among the participants because of different sensor response behaviour.
- Day 3 - continuation of the mandatory measurement program, if needed. Otherwise, there was the option for repeating measurements, or for performing tests at additional temperature levels, or for other tests defined cooperatively by the manufacturer and Lindenberg

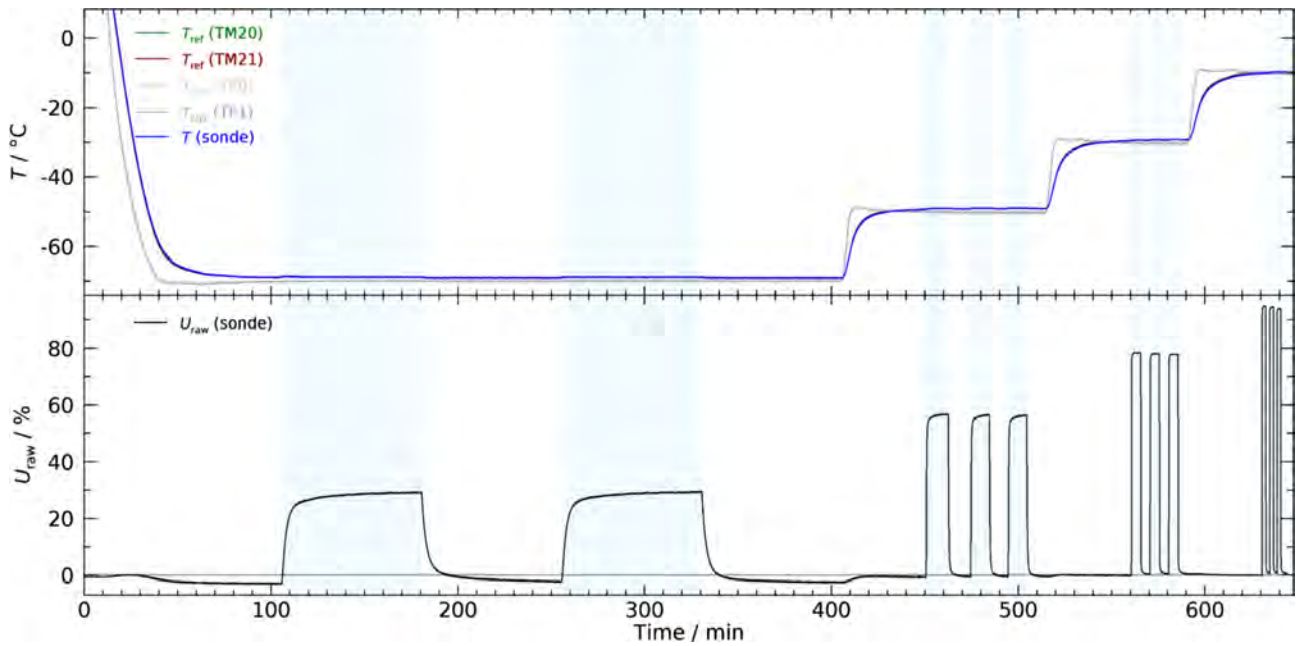


Figure 6.4: Example of a typical TLAG measurement run at four temperature levels of $-70\text{ }^{\circ}\text{C}$, $-50\text{ }^{\circ}\text{C}$, $-30\text{ }^{\circ}\text{C}$, and $-10\text{ }^{\circ}\text{C}$ in one of the two test cells. Upper panel: T of radiosonde sensor (blue), the two reference sensors (TM20 and TM21), and T of air circulating within the climatic chamber. Lower panel: Readings of uncorrected calibrated raw data of relative humidity. The blue shaded areas indicate the time intervals when the sensor boom was exposed to humid air. Several shifts between the dry and humid state are realised at each T .

staff.

Beyond the mandatory measurement program at $-70\text{ }^{\circ}\text{C}$, $-50\text{ }^{\circ}\text{C}$, $-30\text{ }^{\circ}\text{C}$, and $-10\text{ }^{\circ}\text{C}$, temperature levels for additional measurements were set individually. The decision on which measurements to perform depended on the actual progress, the occurrence of technical issue, and the actual sensor response behaviour.

6.3.1.2 Measurements

A typical measurement run consists of a series of humidity cycles at constant temperature levels. The measurement program starts at the lowest temperature level, and ends at the highest via the intermediate temperature levels. The rationale for this scheme is to avoid that the inner surfaces of tubing or valves are colder than the air flow and trap moisture. This minimises the risk of contamination of the dry air flow. At each stabilised T -level, several low-high-low humidity cycles are run to estimate measurement repeatability. The switching of the valve was triggered manually or automatically according to a predefined programme, depending on the situation.

Figure 6.4 shows an overview plot of a typical one-day measurement run in one of the two test cells. The upper panel shows temperature data from the radiosonde air temperature sensor (blue), the two Pt100 reference sensors in the actual cell where the radiosonde sensor boom is installed (green and dark red), and the air temperature inside the climatic chamber, measured by two other Pt100 sensors (grey) located near the glass cells. It can be seen in the upper panel that after setting a new level, the temperature in the test cell follows the climatic chamber temperature with some delay. Therefore, the actual measurements are started after the temperature inside the cell has sufficiently stabilised.

The lower panel shows uncorrected raw relative humidity data measured by the radiosonde. The blue shaded areas indicate phases when the sensor boom is exposed to humid air. Switching of the airflow can be identified in the data by the rising and falling flanks, and a slower response of the humidity sensor at low temperatures can be identified. The plot shows that the size of the humidity steps increases with temperature. This is connected to the fact that radiosondes report relative humidity over liquid water, which is lower than the relative humidity over ice for the same

water vapour content. Furthermore, the humidifier is less efficient at low temperature. However, for the TLAG measurements it is less important to have the same relative humidity at all temperature levels than to create sufficiently large humidity differences between the dry and moist airflow in order to have a good signal, and more importantly, to have temporal stability of the humidity value in the dry and humid airflow. The quality of the manufacturer's sensor calibration plays a subordinate role because the analysis of the response time is based on measurements of changes of humidity. It is also noted here that for fitting Equation (6.1) for evaluation of the response times (Section 6.3.1.3) it is advantageous but not essential to select data sections that fully extend from the beginning of the step into the new equilibrium state. That means, if the valve in the actual humidity state is switched back to the previous state some time before the equilibrium is fully established, the sampled data may still be sufficient for meaningful results if a sufficiently large portion of the full step is covered. This is applied in particular in cases where the sensor response time is in the order of several tens of minutes and waiting for the equilibrium to establish would take extraordinary long time.

6.3.1.3 Data evaluation

Temperature The temperature T_{ref} of the air stream is determined based on data of the two reference temperature sensors installed next to the radiosonde sensor boom in the test cells. For both sensors, temporal averages are calculated over time intervals starting with the valve switch until the values measured with the humidity sensors approach the new equilibrium value, and the mean of these two averages is then taken as the final temperature. The evaluated response times (see next Section 6.3.1.3) are related to these temperatures. An exception is sonde D, where for technical reasons the sonde's own temperature measurement was used.

The overall uncertainty $u(\overline{T_{\text{ref}}})$ representative for the ensemble of the N data points following the humidity steps is determined with the following scheme (all uncertainties given for $k = 1$).

- A possible underlying temporal trend is approximated with the help of a linear fit; a corresponding uncertainty is assigned with:

$$u_{\text{trend}}(T_{1,2}) = (T_{\text{max}} - T_{\text{min}})/(2\sqrt{3}).$$

- Noise in terms of the residual as of the above trend is accounted for with:

$$u_{\sigma}(T_{1,2}) = \sigma(T - T_{\text{trend}})/\sqrt{N}.$$

- These are combined to the uncertainty of the mean for each of the two reference T -sensors:

$$u(\overline{T_{1,2}}) = \sqrt{u_{\text{trend}}^2 + u_{\sigma}^2}.$$

- Calibration uncertainty ($k = 1$):

$$u_{\text{cal}} = 0.05 \text{ K}.$$

- All components are combined for the mean of sensors 1 and 2:

$$u(\overline{T_{\text{ref}}}) = \frac{1}{2} \sqrt{u^2(\overline{T_1}) + u^2(\overline{T_2}) + 2u_{\text{cal}}^2}. \quad (6.2)$$

The calibration component u_{cal} dominates. Values for $u(\overline{T_{\text{ref}}})$ typically range between 0.04 K and 0.06 K. The uncertainty of the radiosonde's temperature measurement is determined with a similar approach. However, information on uncertainties of the calibrated raw temperature data is not fully available for every radiosonde model.

Determination of response times For each humidity step change, the data are least-squares fitted using the model in Equation (6.1), separately for the increasing and decreasing step directions. The interval limits for the data points included into the fits are defined by hand for each upward and downward step, see examples in Figure 6.5. The fit procedure is repeated three times for

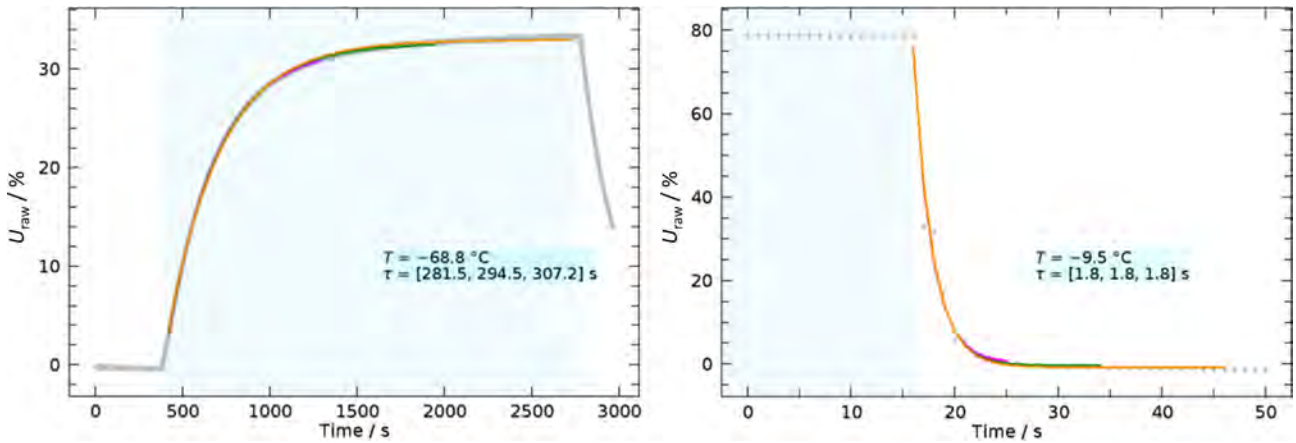


Figure 6.5: Examples of the sensor response to a step change in relative humidity and determination of the 63.2%-time τ . Left: step from dry to humid, $T \approx -68.9 \text{ }^\circ\text{C}$, mean $\tau \approx 294 \text{ s}$; Right: step from humid to dry, $T \approx -9.5 \text{ }^\circ\text{C}$, mean $\tau \approx 1.8 \text{ s}$. Grey dots are measured humidity raw data. The sampling rate is 1 s^{-1} for all sondes. Blue shaded areas denote times of humid air flow. The coloured lines are three equivalent model fit lines according to Equation (6.1) (see also Figure 6.1), but include data intervals of different lengths. Accordingly, three values for τ (fit parameter in Equation 6.1) are evaluated for each step, and averaged for use as the final value.

each step, with identical starting points at or short in time after the valve switch, but extending over different numbers of subsequent data points and therefore enclosing different portions of the step response. The parameter of interest, the 63.2% response time τ , is then taken as the arithmetic mean of the three individual fitted values. The uncertainty of that mean is estimated in two ways: a) using the $1\text{-}\sigma$ uncertainties of the fit parameter τ given by the fit procedure, and b) by calculation of the standard deviation of the three resulting τ . Finally, the larger of the two, which in most cases is the latter, is kept as overall estimate. This approach is motivated by the idea that the quality (or uncertainty) of the evaluated τ is generally determined by systematic deviations of the true sensor response behaviour (in combination with the ‘imperfections’ of the experimental setup) from the idealised model rather than by random noise of the data points. A robust goodness-of-fit analysis as a basis for estimating the uncertainties of the fit parameters and taking such effects into account appears to be complex and is not carried out within this analysis. It seems therefore evident that the uncertainty from that approach does not account for all effective components, so it shall be deemed to be a lower boundary.

The data sections or intervals for fitting are individually defined such that the size of the actual step has been substantially captured. Plots as shown in Figure 6.5 are created for each evaluated humidity step throughout the UAI 2022 laboratory measurements and used for visual checks before including the results in further analyses.

6.3.1.4 Results

The estimated 63.2% response times, based on humidity and temperature time series such as shown in the example in Figure 6.4, are related to the temperature of the air flow to which the sensors was exposed. The results are summarised in Figure 6.6. Each panel depicts one of the participant radiosondes, all with the same axis ranges. Note that, to preserve anonymity, the letters A to L (panel labels in Figure 6.6) are randomly assigned to the radiosonde models and different from assignments used to present the results of other experiments of the laboratory campaign. The plots are semi-logarithmic to account for the quasi-exponential increase of the sensor response times with decreasing temperature. Blue symbols stand for measurement runs with a protective cover installed over the humidity sensor as in routine sounding operation. Black symbols show results from tests where the sensor cover was removed beforehand, or for sonde models that do not use a cover. Upward and downward oriented triangles denote the direction of the steps from low to high humidity and vice versa, respectively.

The estimated τ generally cover two to three orders of magnitude over the temperature range of $0 \text{ }^\circ\text{C}$ to $-75 \text{ }^\circ\text{C}$. The absolute values at comparable temperatures differ among the sonde types

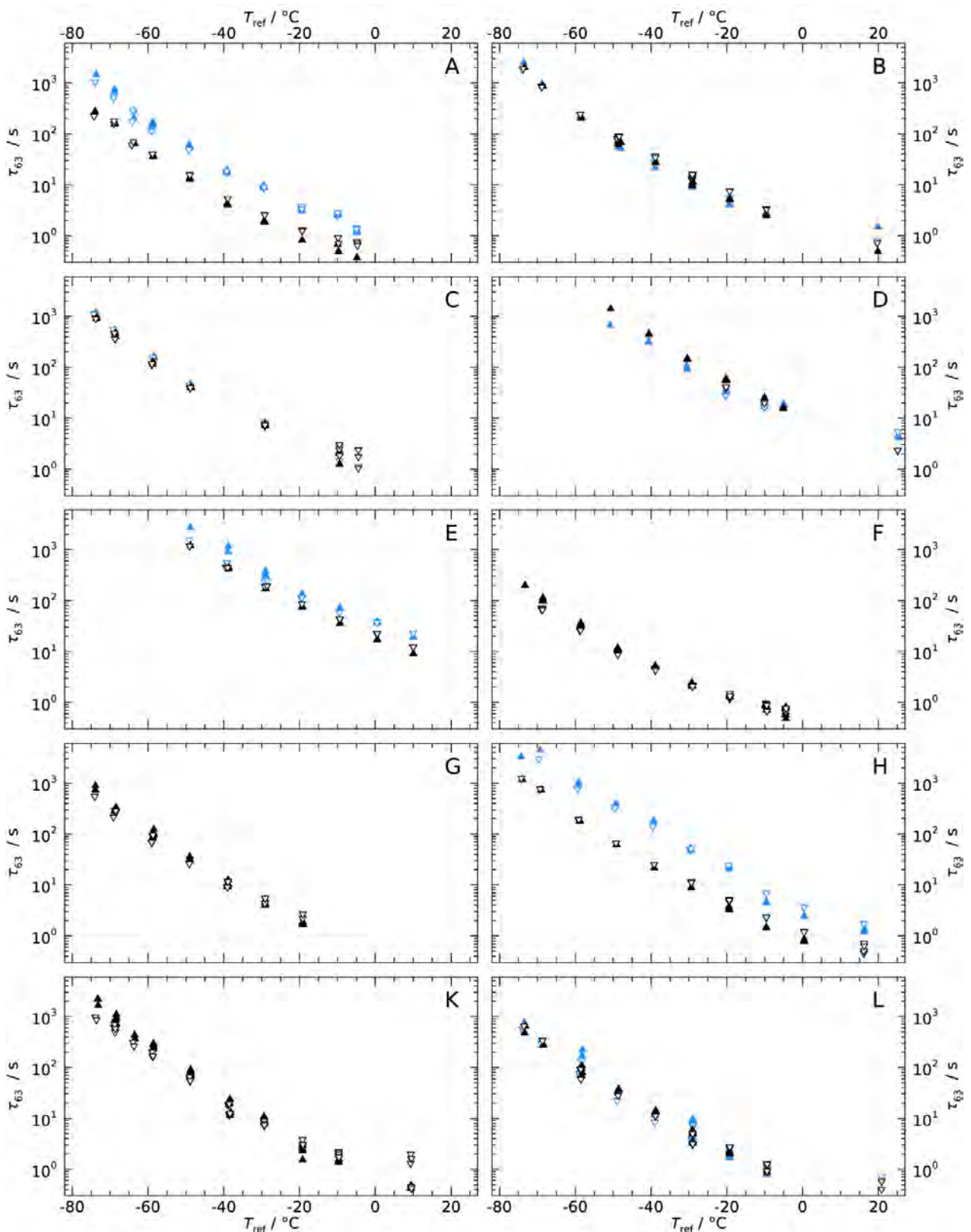


Figure 6.6: Response times (63.2% times) of humidity sensors versus air temperature. Each panel represents one of the ten radiosonde models. Blue symbols: cover installed on humidity sensor as in flight. Black symbols: cover removed during the tests, or sonde model does not own a cover. Upward (downward) triangles: steps from low to high (high to low) humidity.

by up to about one order of magnitude, sometimes more. At the lowest adjusted temperatures of about $-75\text{ }^{\circ}\text{C}$, the τ of some sondes reach several 1000 s. At the highest temperature level of the obligatory measurement program ($-10\text{ }^{\circ}\text{C}$), τ was determined between $<1\text{ s}$ and $\approx 80\text{ s}$.

It is important to note that the humidity sensors of some of the tested sondes are equipped with an active heating element in addition to their own temperature sensor. If the sensor is heated during operational soundings in a controlled manner so that its temperature is a few kelvin above the air temperature, the risk of contamination is minimised, and in particular the response time is reduced (e.g. 5 K heating reduces τ by a roughly factor of 1.5). In the UAI laboratory tests, the heating functionality of some of the models with heatable sensors was switched off for reasons of stability or integrity of the recorded data. This must be taken into account when evaluating the results in Figure 6.6.

As expected, all sondes follow an inverse relation with temperature, and the more or less linear courses of the data points in the semi-logarithmic plot suggest an exponential relationship. It is noted here that, when looking to the plots at a glance, the logarithmic scale for τ in Figure 6.6 bears a certain risk of underestimating differences or scatter of the data points: the size of the symbols alone corresponds to almost a factor of about 1.4 in τ .

Sensor covers The experimental tests reveal that the presence of a protective cover systematically and in parts considerably influence the results for three of the radiosondes (panels A, E, and H), while other models show smaller or less systematic effects (B, D, C, L). It is reasonable to assume that such a cover, which is primarily installed to protect the humidity sensor from direct solar radiation or contamination by water or ice, has the potential to reduce the exchange of air above the sensor surface with the 'free' overflowing air, and thus to introduce some kind of additional time lag, which may take effect when ambient humidity changes rapidly. The strength of this effect will be related to the cover design. Although one should be cautious with a quantitative evaluation because flow conditions and ventilation speed in the test cells are not the same as in real ascents, the results nevertheless reveal the presence of such an effect for some of the sondes, which may inspire the concerned manufacturers to further investigations in this regard. Sonde D shows the opposite effect of slightly lower response times with the cover installed for most of the temperature levels. This is somewhat unexpected, however, it cannot be excluded that there is a sensor-to-sensor variability of the response time which in this case may outweigh the effect from the cover (if present at all).

Direction of humidity steps Response times evaluated from upward or downward humidity step changes are distinguished in Figure 6.6 with the upward and downward orientation of the triangle symbols. A closer look reveals systematic factorial offsets over the whole temperature range or at least over coherent parts of it for some of the radiosondes (A, B, E, F, H, K). It is interesting that the temperature range at which this effect is visible varies among the radiosondes concerned, and that for some models the 'upward' response times exceed the downward (F, K), while others show the reverse (A, B, E, H). Without attempting a conclusive explanation, it can be assumed that this is a real effect that lies with the sensor technology of the radiosondes rather than being (solely) generated by the experimental setup. However, further investigations are required, which are beyond the scope of the UAI 2022 laboratory tests.

Uncertainty considerations The uncertainties discussed in Section 6.3.1.3 are not included in the plots in Figure 6.6 because they are generally smaller than the symbol size in that representation. It can be stated that the spread of τ from multiple measurements at the same temperature level generally exceeds the uncertainty which is estimated for single points (Section 6.3.1.3). This indicates the existence of other components that are not identified or quantified and therefore not taken into account. For example, different sonde units, especially when sampled from different production batches, may lead to enhanced scatter (as part of the reproducibility). Due to the limited number of measurements and tested radiosondes, such uncertainty components cannot be fully quantified. Also, undetected deviations of the sensor behaviour (or more precisely the combined effects of sensor and setup) from the model used to quantify the response times may add to more realistic overall uncertainties. Therefore, the uncertainties $u(\tau)$ analysed in the

context of the UAI 2022 measurements, which are also provided to the manufacturers, should be considered as lower boundaries or minimum estimates.

According to the actual sensitivities of the response times to temperature changes, $|\partial\tau/\partial T|$, the evaluated temperature uncertainties do not significantly contribute to the combined uncertainties in τ .

For low values of τ in the range of less than about 1 s at higher temperatures, the influence by the glass cells' own time-lag takes effect. Given the air speed of about 0.4 m s^{-1} and the geometry of the cylindrical glass cells, an effective time constant of the air exchange within the cell of $>2 \text{ s}^{-1}$ (according to a 'response' time of 0.5 s or less) can be assumed. The measured response time is the combination of both the sensor time lag and the cell exchange time. At values for τ of a few seconds or higher, the effect quickly becomes insignificant. An assumed true response of the sensor of 1 s would be exceeded by the measured τ by about 30%. That means, in the range of response times lower than about 1 s, the measurement results essentially reflect a peculiarity of the experimental setup. This also might account for the slight bending-in at the high-temperature end of the data sets in Figure 6.6 for some radiosondes. However, response times of 1 s or less do not introduce significant errors in humidity profiles of real soundings.

6.3.2 Assessment of temperature sensor calibration at low temperature (LOWT)

The LOWT measurements are performed at predefined temperature plateaus between $-75 \text{ }^\circ\text{C}$ and $20 \text{ }^\circ\text{C}$, with the same configuration of the measurement setup that is used for the TLAG measurements. The temperature controller of the climatic chamber is programmed to keep a constant temperature for 60 minutes before switching to the next temperature set point. Temperature intervals are 5 K below $-60 \text{ }^\circ\text{C}$ and 10 K above $-60 \text{ }^\circ\text{C}$. Figure 6.7 shows the evolution of the temperature inside the measurement cell during a typical LOWT measurement run. The 1 hour residence time at each temperature level is assumed to be long enough to stabilise the chamber and to minimise temperature gradients inside the measurement cell, while reaching a sufficient number of temperature levels in the time available. The readings of the radiosondes in both measurement cells, of the reference Pt100 temperature sensors inside the measurement cell, and of the chamber's monitor sensors, were recorded continuously at 1 s intervals. The LOWT measurements are performed after work hours, typically from 18:00 in the afternoon till 7:00 in the morning (local time), and does not require human intervention while the temperature program of the climatic chamber is executed.

As shown in Figure 6.7, the temperature program of the climatic chamber starts by cooling down to $-75 \text{ }^\circ\text{C}$ to return to $20 \text{ }^\circ\text{C}$ via the intermediate plateaus. The advantage of this approach is that the next morning the climatic chamber is at room temperature so that the set up is accessible for inspection or for the preparation of subsequent tests.

Inside the measurement cell, the Pt100 sensors are positioned as close as possible to the temperature sensor of the radiosonde in order to minimise the temperature difference between them (see Figure 6.3). However, as the time lag setup was not designed for precise temperature calibration, it can not be excluded that residual temperature gradients occur inside the cell, that will limit the accuracy of LOWT measurements. To illustrate this, Figure 6.8 shows the differences between both Pt100s for two different measurement runs. The clearly visible spike-like differences of approximately 0.2 K size are the result of temperature gradients inside the measurement cell when the climatic chamber is transitioning to another temperature level. In the course of several minutes, these temperature excursions flatten when the climatic chamber stabilises and the gradients disappear. However, from the dissimilarity between both plots in Figure 6.3 it is clear that the temperature gradient inside the cell evolves differently for different radiosonde models, presumably as a consequence of the exact placing of the Pt100s inside the cell and the way the sensor boom affects the airflow. It is observed that for about half of the participating radiosondes, the temperature difference between the Pt100s behaves similar to the upper plot in Figure 6.8, indicating small temperature gradients, whereas for other participants larger gradients, occur, resulting in temperature differences as in the lower panel of Figure 6.8, or larger.

Based on this, it is estimated that the LOWT measurements will provide information on the calibration of the temperature sensor with an uncertainty of 0.2 K.

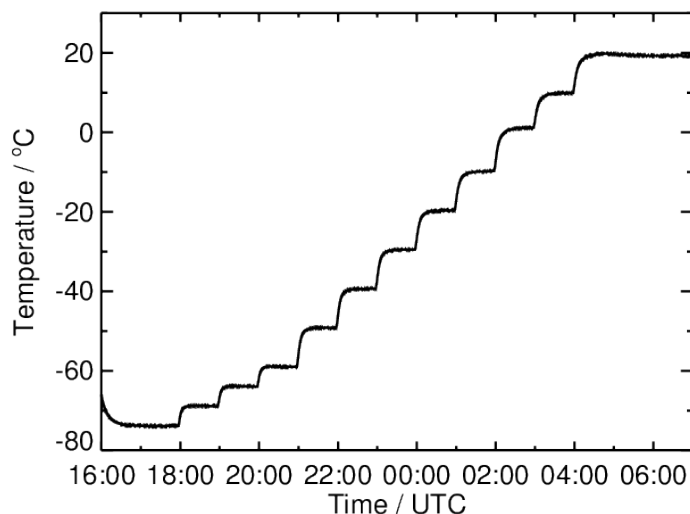


Figure 6.7: Example of the temperature inside the measurement cell during a typical LOWT measurement run. The measurement program starts in the evening at -75°C and ends at 20°C next morning.

Analysis of LOWT data For each temperature plateau the difference between the temperature readings of the radiosonde (calibrated raw data) and the Pt100 sensors is evaluated, using the last 1500 data points, or 30 minutes, of the plateau. This yields the statistical mean and standard deviation of the temperature differences of a sufficiently large sample. For this comparison, the data of the radiosonde and of the Pt100 sensors is synchronised using their respective UTC timestamps. The radiosonde temperature is compared to the average of both Pt100s in the cell.

The observed temperature differences $dT = T_s - T_{\text{ref}}$ for all participants are summarised in the plots in Figure 6.9, showing that for several participants (A, E, H, and L) the difference is less than 0.2 K, with a weak dependence on temperature. Note that, to preserve anonymity, the letters A to L (panel labels in Figure 6.9) are randomly assigned to the radiosonde models and different from assignments used to present the results of other experiments of the laboratory campaign. Although 0.2 K represents the earlier-discussed uncertainty limit of the LOWT measurement setup, it is noteworthy that basically all participants exhibit a predominantly negative bias. For participants C, D and K the difference is partly within 0.2 K, but increases steadily to exceed this 0.2 K near the extremes of the temperature range. In case of participant D this increasing bias with temperature is particularly profound for $T > 0^{\circ}\text{C}$ growing to 0.8 K at 20°C . For participant F the bias is within 0.2 K at 20°C , but increases steadily with decreasing temperature, to reach -1 K at -75°C . The results for participant B could not be evaluated. Due to technical reasons the Pt100 sensors could not be inserted into the measurement cell together with the radiosonde's sensor boom so that the measurements were performed with the Pt100 sensors outside the cell. However, this spatial separation between the radiosonde temperature sensor and the reference sensors introduced an additional, unknown, temperature bias which impeded a reliable assessment of the calibration of that radiosonde's temperature sensor.

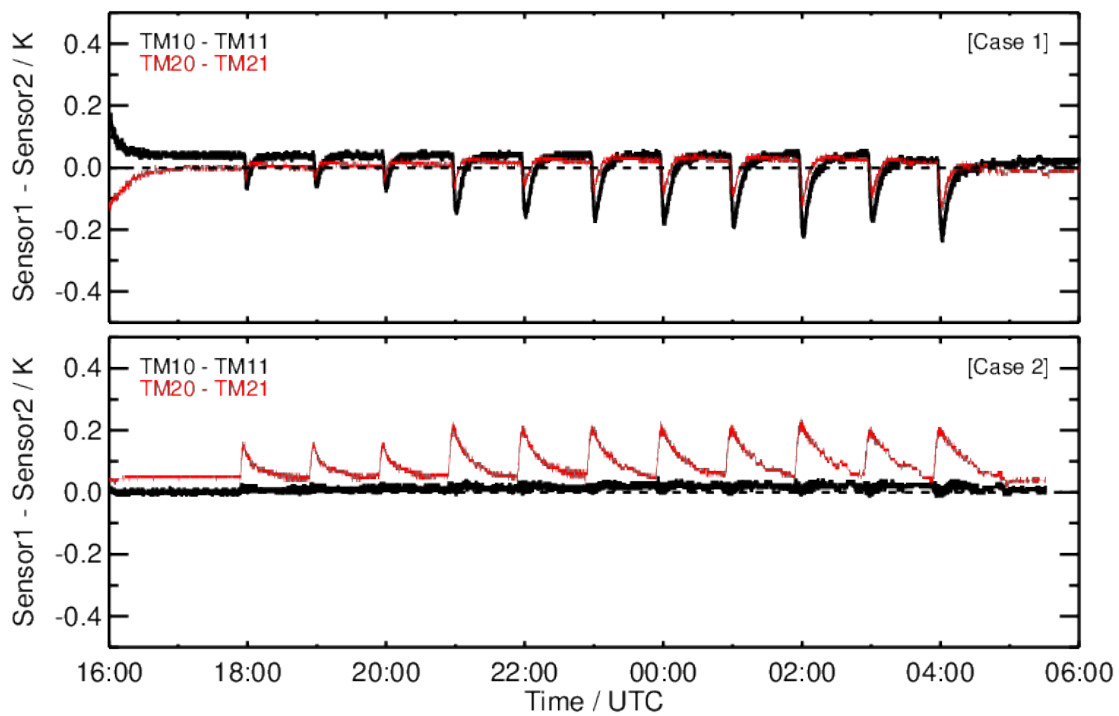


Figure 6.8: Evolution of the difference between the readings of both Pt100 temperature sensors inside a measurement cell during a LOWT measurement. The black trace represents the difference for cell 1 (TM10–TM11) and the red trace represents the difference for cell 2 (TM20–TM21). The upper panel shows a good-case scenario, i.e. a measurement run with small temperature differences, whereas the lower panel shows a measurement run with larger temperature differences. The time axis for the plot in the upper panel is the same as in Figure 6.7, the plots in the lower panel is from a different measurement run with other radiosondes than in the upper panel.

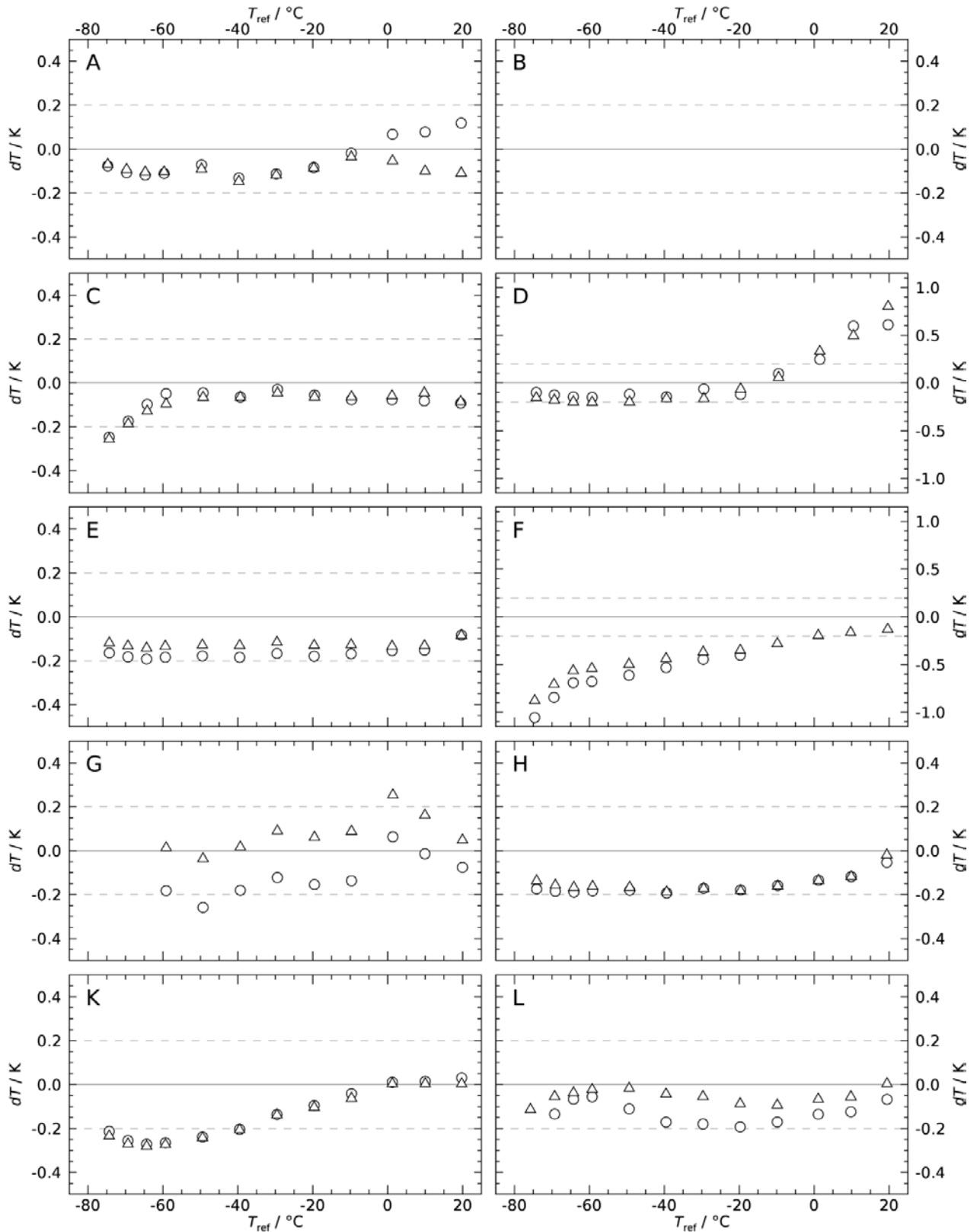


Figure 6.9: Differences between the temperature readings of the radiosonde and the reference temperature in the range -75°C to 20°C observed the last 30 min of the temperature plateaus shown in Figure 6.7. The reference temperature is given by the average of both Pt100 temperature sensors inside a measurement cell, and the triangles and squares represent the results from either measurement cell. The dashed lines represent the 0.2 K uncertainty of the setup. Results for one of the participants (panel B) are not shown because reference temperature measurements are not available for technical reasons. The y-axis ranges are the same for all plots, except for participants D and F.

7 RADIATION SENSITIVITY OF AIR TEMPERATURE MEASUREMENT (RADI)

7.1 INTRODUCTION

Sunlight influences daytime air temperature measurements by radiosondes due to warming of the sensor by absorption of radiant energy. The amount of heating varies with altitude and may exceed 1 K in the final part of the sounding. Accurate knowledge about the strength and characteristic of the solar heating is indispensable for developing and applying corrections. Since there is no way to determine the heating of the sensor in flight, one has to base the correction model on measurements in a laboratory environment.

At atmospheric conditions, the magnitude of the heating depends on the design of the radiosonde and on the employed sensor technology. This includes for example size, shape, and surface coating of the sensor boom and the sensing element, and on the orientation of sensor and the boom with respect to the Sun. However, the heating of the sensor also depends on the air flow over the sensor during ascent, because the flow induces convective cooling that counteracts the warming. As the cooling efficiency decreases with pressure, this leads to a steady increase of the sensor heating with altitude. The orientation of the sensor relative to the flow direction (i.e. the angle of the sensor boom) is another parameter that determines the resulting amount of heating because it defines the flow cross section and therefore the cooling rate.

The GRUAN Lead Centre at the Lindenberg Observatory developed a laboratory setup (Simulator for Investigation of Solar Temperature Error of Radiosondes, SISTER) to simulate conditions similar to those encountered during a radiosonde ascent, that allows to investigate the influence of a number of key parameters on the solar heating of the temperature sensor. These experimental parameters are the flux and incidence angle of the radiation, air pressure, and the speed of the air flow. SISTER is constructed as a rectangular-shaped ~ 2 m long closed-circuit wind tunnel (see Figure 7.1). The radiosonde is mounted inside a glass tube to allow for illumination by an external light source. The glass tube is wide enough to enable rotation of the radiosonde with unfolded sensor boom around the longitudinal axis (see Section 7.2). This design allows mimicking ascent conditions to a wide extent, including continuous changes of the illumination as a result of the spinning of the radiosonde. The exposure of a sizeable part of the sensor boom to the impinging light beam recreates the heat exchange between sensor and boom that occurs in flight. The aim of the setup is to measure the temperature increase that the irradiated sensor measures with respect to the constant background temperature of the circulating air, and to investigate how this warming depends on changes in the described parameters. A comprehensive description of the setup and the underlying concept can be found in [von Rohden et al. \(2022\)](#).

The goal of the experiment is to assess the sensitivity of the radiosonde's sensor and sensor boom to solar radiation, rather than the quality of the manufacturer's data product which is optimised for conditions in real soundings. Therefore, only raw data were recorded during the tests which are normally not accessible to the user (see Appendix C). Raw data are calibrated measurement data of temperature that were not subject to any further processing. This means that no corrections of measurement errors and other systematic effects were applied, and especially no correction for the solar radiation temperature error.

During the laboratory phase of the UAII 2022 campaign, all participating radiosondes were tested in the SISTER setup. The tests comprise a well-defined set of measurements at selected settings for pressure and ventilation speed at specific irradiances and incidence angles (see Section 7.3.1). These parameters are varied such that they essentially covered the atmospheric conditions encountered during an ascent so that a rough overview of the solar effect could be obtained.

One or at most two specimen of each radiosonde model were tested for each manufacturer. Certain variability of the radiation sensitivity may exist when testing several specimens of the same model under the same conditions (same set of parameters), for example due to production variability in sensor shape and size. This was not quantified within the UAII. No definite statement is therefore given about the representativity of the results in that regard.

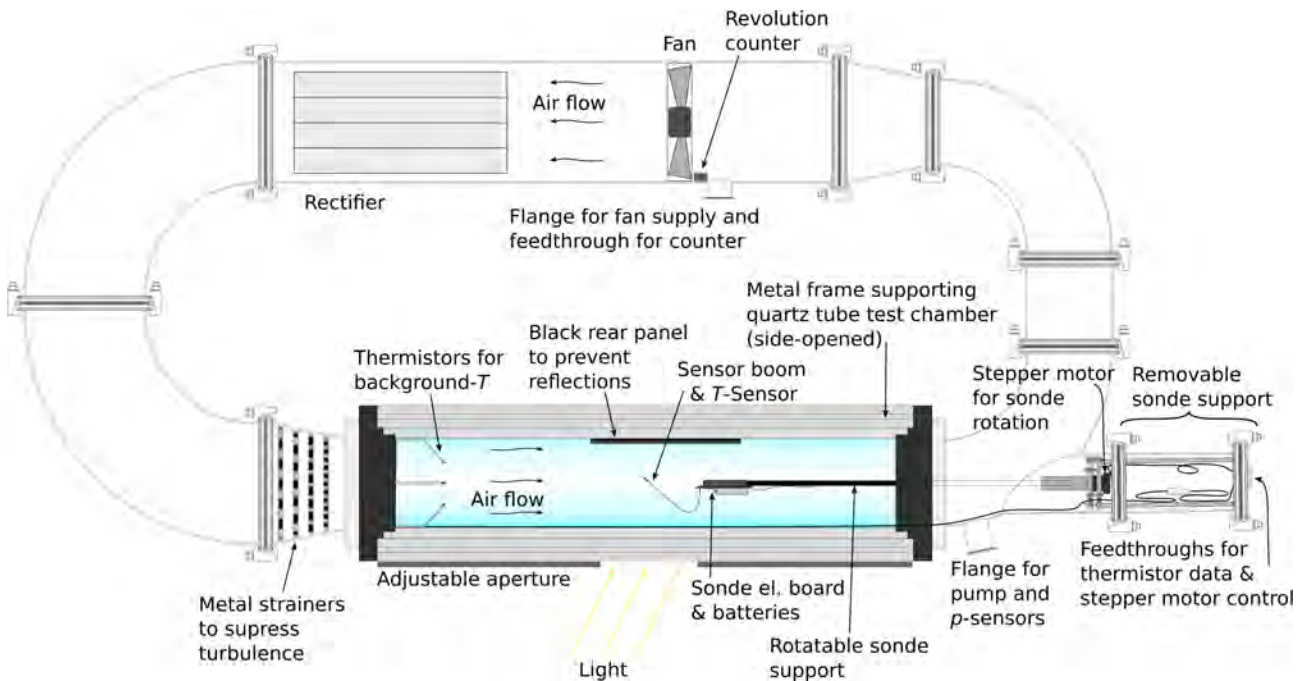


Figure 7.1: Sketch of the Simulator for Investigation of Solar Temperature Error of Radiosondes (SISTER), used to test the short wave radiation sensitivity of the temperature measurement with radiosondes participating in UAII 2022.

For a complete quantitative characterisation, more comprehensive measurements are required. The results from the laboratory tests may help the manufacturers in assessing the quality of their algorithms and underlying assumptions for the solar radiation correction.

7.2 EXPERIMENTAL SETUP

A schematic drawing of the setup is shown in Figure 7.1. The main parameters are controlled as explained in the following (detailed descriptions in [von Rohden et al. \(2022\)](#)).

- Light source: a 2500 W Xe-plasma lamp to simulate sunlight; a collimated beam with ≈ 25 cm diameter; the irradiance is controlled by changing the distance SISTER and the light source using a calibrated distance relationship; irradiance on sensor around 1000 W m^{-2} . It is assumed that the warming caused by the light source is the same as that by the Sun at the same irradiance level (i.e. the spectrum of the light source is similar to that of the Sun).
- Angle of incidence α (simulating solar elevation) controlled by turning the setup relative to the light source; adjustable range 0° to 60° .
- Pressure p controlled with a membrane pump, measured using two p -gauges (1000 hPa to 0 hPa and 13.652 hPa to 0 hPa); experimental p -range between ambient and ~ 3 hPa.
- Flow speed v controlled by fan voltage (U_{fan}); v at the position of the radiosonde determined from a look-up table $v(U_{\text{fan}}, p)$ which is based on extensive Laser Doppler Anemometry (LDA) calibration measurements; the fan's rotation speed is measured with an optical counter inside setup; v is continuously adjustable up to $\sim 6.5 \text{ m s}^{-1}$ (depending on p).
- Axial rotation of the radiosonde (to simulate the spinning during ascent); driven by a computer-controlled stepper motor; fixed positions can be selected,
- Exposure intervals controlled with a motor-driven shutter blocking the light beam; interval lengths chosen 'by hand' (half a minute to several minutes).
- Temperature of air stream: no active control (background temperature in the laboratory); measured at 1 s^{-1} using four thermistors mounted at various positions in the air flow upstream of the radiosonde.

- Water vapour content (relative humidity): neither controlled nor measured.

The radiosonde is mounted at the end of a rotatable support rod. The sonde's casing is removed before to reduce drag, and the sensor boom is fixed at an angle relative to the air flow that is similar to that in soundings. The radiosonde mount is then inserted into the glass tube, such that the sensor boom is positioned on the central axis in the middle of the chamber (see Figure 7.1). Continuous data recording of the radiosonde and the SISTER sensors is started. After setting pressure, air flow, incident angle and irradiance, light is directed from the external source through the glass wall of the chamber to the rotating sonde. With an adjustable aperture in front of the chamber, the beam diameter is adjusted so that essentially the entire sensor boom is illuminated. The length of the exposure is chosen so that the temperature measurement converged sufficiently towards the new 'heated' equilibrium state. After closing the shutter, an equally long time or more is used to let the sensor cool down to its original unilluminated state. During the measurements the radiosondes are battery-powered and data is transmitted by radio.

The solar heating is proportional to the irradiance with other parameters being constant. Thus, it is sufficient to conduct the measurements at a fixed setting of the radiative flux.

Data are collected by the SISTER data acquisition system and by the manufacturer receiving system, and both systems are time-synchronised before the start of the measurement.

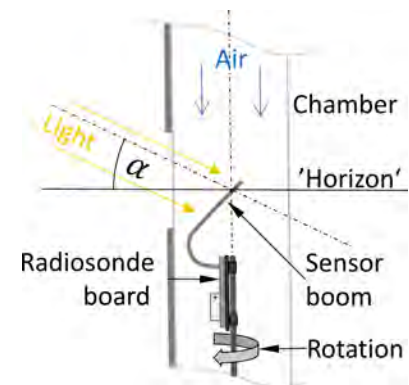
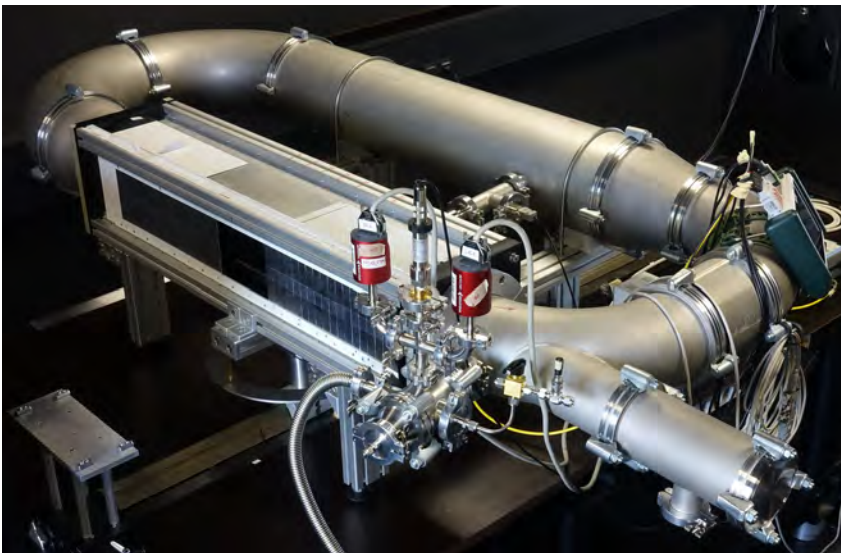


Figure 7.2: Photography of the wind tunnel setup for radiation experiments. Scheme on the right: Illustration (top view) of the illumination scheme. The incident angle α can be varied to mimic solar elevation.

7.3 MEASUREMENTS AND RESULTS

7.3.1 Measuring programme

The measurement programme is prepared with three parts as given in the following list. This schedule is considered a guideline, with deviations allowed depending on the actual progress of activities.

- A preparation phase (first day), intended for setting up the radiosonde systems and SISTER, preparation and mounting the radiosonde on the holder and installation in the chamber. First test runs are performed to check the data flow, the functionality of both the radiosonde system and the experimental setup, and to check out the behaviour and extent of temperature response of the radiosonde.
- Implementation of a 'mandatory' measurement program to go through with each participating manufacturer and for one radiosonde unit (scheduled for the second day). At a constant sonde rotation with a period of 15 s, a fixed angle of incidence of 30° , and an irradiance of

approximately 1000 W m^{-2} , the radiation induced warming of the temperature sensor (ΔT with Δ denoting a difference) is to be measured at 5 different pressure levels (950, 100, 50, 10 and 5) hPa, and at ventilation speeds of maximum and (5, 3 and 1) m s^{-1} at each pressure level. The exposure intervals range from 45 s to a few minutes depending on the sensor's response behaviour under the current conditions.

- A 'free' experimental phase (third day) for continuation of the mandatory program, or, if successfully completed, for repetitions or additional tests with other parameter combinations, or further tests after discussion with the manufacturer.

Beyond the obligatory programme with the above described settings, further measurements at other parameter settings are conducted after discussion and by mutual agreement with the manufacturer, based on the progress of the measurements, any technical incidents, and the appearance of the radiosonde data. For some sonde types, more than one copy is tested.

7.3.2 Measurements

Data from both SISTER and the radiosonde are continuously sampled in parallel, but independently, at 1 Hz. With SISTER, data for air temperature (four thermistors), pressure, and fan rotation are recorded using an integrated data acquisition system. Information on actual radiation, rotation or position of the radiosonde, and angle of irradiation are recorded as metadata. The manufacturer receiving systems and computers are placed close to the experimental setup. Radiosonde transmitting frequencies are adjusted according to the specifications of DWD. The manufacturers operated their systems in research mode or used special software to record calibrated raw data, and delivered the raw data to the campaign team in the UAI 2022 ASCII format (Section D in Appendix). Real-time visualisation of the data was provided by the manufacturers, which enabled adapting e.g. exposure times to the actual response of the radiosonde's temperature sensor. The radiosonde systems are manually synchronised with those of the setup before each measurement run.

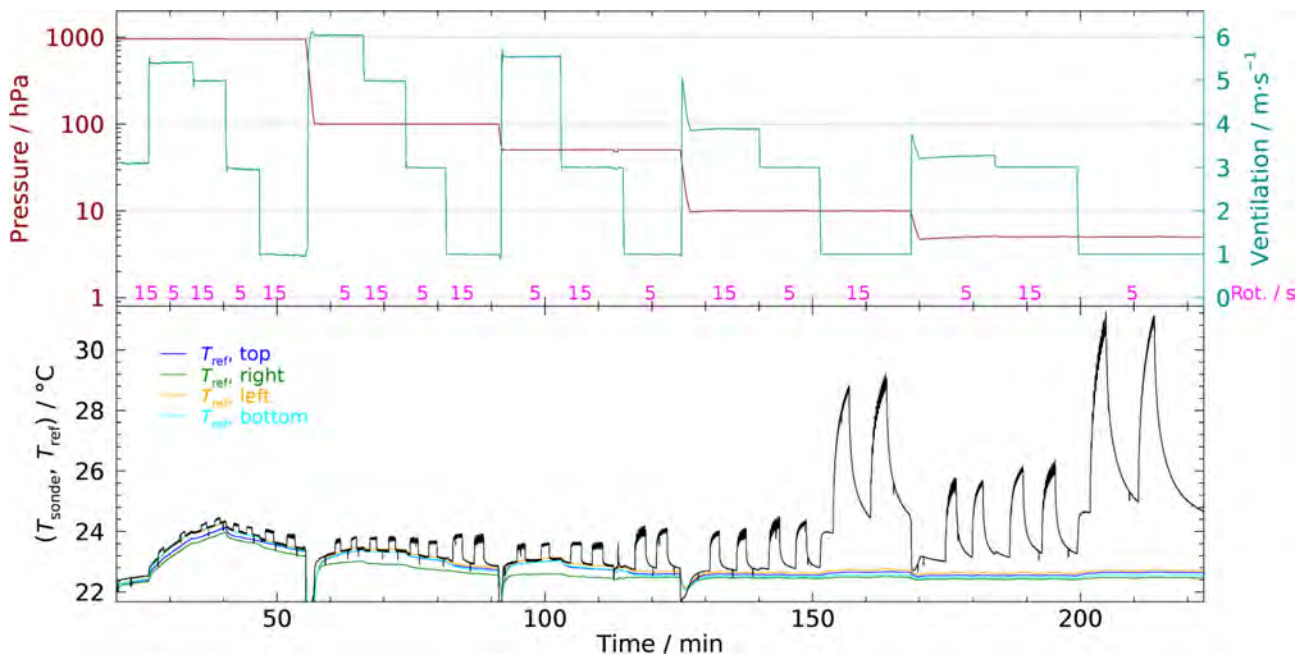


Figure 7.3: Example run of measurements of radiative sensor warming (irradiation $I = 1003 \text{ W m}^{-2}$ at an angle of $\alpha = 30^\circ$ (representing Sun elevation), extending over various combinations of pressure and flow speed according to the baseline measurement plan. Upper panel: pressure and flow speed adjustments. Lower panel: radiosonde temperature data (black) with the left flanks of the peaks indicating the response to radiant exposure; reference shaded temperature data (coloured). Numbers in magenta (upper panel) denote values, and their positions (roughly) the times of changes of the rotation speed.

Figure 7.3 shows an overview of measured data from both the radiosonde and SISTER during a typical run at a fixed value and angle of incidence and extending over various settings for pressure and ventilation speed. In that example, also the axial rotation of the radiosonde is alternately changed between 15 s and 5 s. The radiosonde temperature record (black trace in the lower panel) shows the expected increase of the radiation sensitivity with decreasing pressure and air flow. The background temperatures (coloured lines in the lower panel) disclose the occurrence of small temperature inhomogeneities in the air stream (e.g. between 60 min and 120 min). This is probably caused by local heat sources inside the wind tunnel (fan, stepper motor). Since the experiment aims at measuring temperature differences, such deviations play a minor role for the quality of the results with the applied evaluation procedure (Section 7.3.3.1) and only provide a small contribution to the uncertainty.

7.3.3 Data evaluation

7.3.3.1 Quantification of radiation sensitivity

The temperature sensor of the radiosonde generally responds with a quick rise after beginning of the exposure, followed by a slower convergence to a quasi-stationary value. The radiative sensor warming is the difference between this new thermal equilibrium value and the temperature of the air circulating in the wind tunnel. The air temperature is represented by the mean of the measurements taken with the four shaded reference sensors near the sonde in the test chamber. Examples of the temporal development of the relative temperature change during and after exposure are shown in Figure 7.4. The two vertical dashed lines delimit the exposure phase.

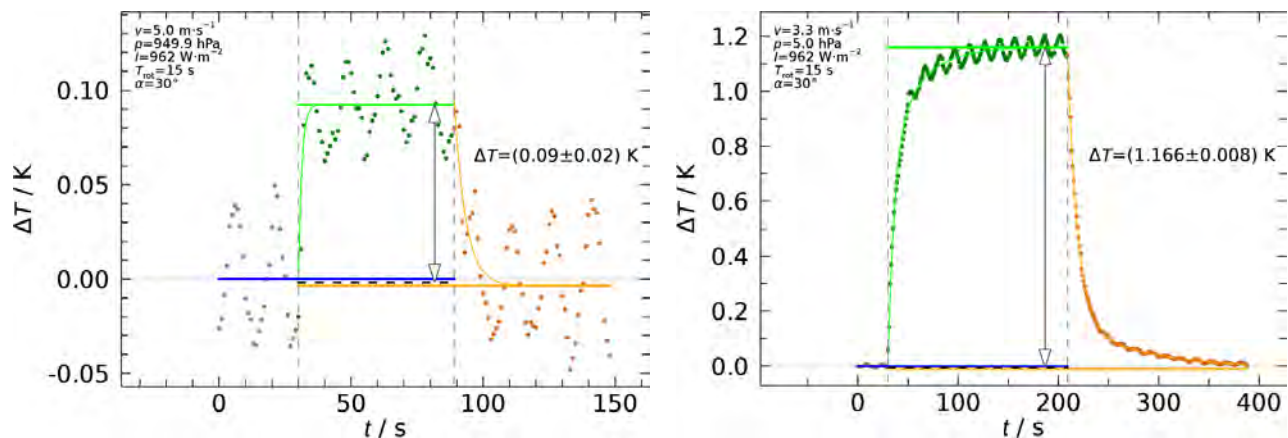


Figure 7.4: Examples of the temperature sensor response to irradiation (two different sondes). $\Delta T(t)$ is the measured difference of the radiosonde sensor temperature and the mean of the temperatures measured by the four unexposed reference sensors. The two vertical dashed lines delimit the exposure phase. Both measurements are taken at an irradiance of 962 W m^{-2} at an angle (solar elevation) of 30° , and with a sonde rotation of 15 s. Left: High pressure conditions ($v = 5 \text{ m s}^{-1}$, $p = 945 \text{ hPa}$). Right: low pressure conditions ($v = 3.3 \text{ m s}^{-1}$, $p = 5 \text{ hPa}$). The oscillating pattern are caused by the rotation of the sonde.

Before determination of the temperature difference, the mean of the thermistor temperatures in the period before opening the shutter (blue lines in Figure 7.4) is added an offset so that it matches the average temperature of the radiosonde in the same period. That is, the blue line is always at a ΔT of virtually zero value. This accounts for calibration-related systematic offsets between thermistor and radiosonde sensor readings.

The rotation of the radiosonde causes oscillating pattern on top of the mean signal. These oscillations result from variations of the heat uptake from radiation due to changes of the exposed surface of the sensor and the sensor boom, and also from small inhomogeneities of the air temperature in the wind tunnel over the cross-sectional area covered by the rotating sensor boom (up to a few tens of a kelvin).

To estimate the temperature elevation which the sensor readings approach in equilibrium after starting the illumination, the difference data covering the exposure period are fitted using the

model function

$$\Delta T'(t) = c_0 - (c_0 - c_1) [c_4 e^{-c_2 t} + (1 - c_4) e^{-c_3 t}]. \quad (7.1)$$

This procedure is equivalently applied to the temperature differences of the post-exposure period when the sensor temperature recover back to the shaded background level. Thus, t in the model is the elapsed time since the beginning or end of the exposure, respectively, and c_i are fit parameters. Examples of fit results are presented in Figure 7.4 with the green and orange curves. The parameter c_0 represents the predicted (relative) equilibrium temperatures (green and orange horizontal lines in Figure 7.4). The use of a fit model that combines the effect of two time constants (fit parameters c_2 and c_3) improves the results for conditions with low ventilation speed and low pressure because it accounts for both the quick initial temperature change and the much slower subsequent approach to the new equilibrium (see example in the right panel in Figure 7.4). For conditions where the sensor response is faster (left panel), a simpler fit with a single time constant is sufficient:

$$\Delta T'(t) = c_0 - (c_0 - c_1) e^{-c_2 t}. \quad (7.2)$$

The data intervals included in the fits are always selected such that they extend over integer multiples of the sonde rotation to avoid biases of the fit parameters.

The final temperature change ΔT is determined as the distance between the fitted equilibrium temperature difference under illumination (green horizontal line), and the mean of the two background temperature differences before and after exposure (dashed black horizontal line). It is indicated as double arrows in Figure 7.4. The fitting procedure allowed to determine ΔT even if the thermal equilibrium has not fully established within the time span covered by the included data points. This is useful in cases of low pressure and low ventilation speed, where the time to reach the equilibrium is long.

7.3.3.2 Uncertainties

The uncertainties of ΔT from the above described evaluation procedure are comparatively small and are of random nature. Contributing components are the reproducibility of the measured shaded temperature before and after exposure, noise produced by the setup, the rotation-related oscillations, and to a smaller extent the sensor intrinsic noise and resolution. Since the evaluation relies to changes of temperature rather than absolute values, uncertainties connected with the calibration or other systematic components of the radiosonde and the reference thermistors do not take effect.

Further components to be taken into account are the assigned (constant) uncertainties for pressure and ventilation (0.5 hPa and 0.5 ms^{-1} , respectively). They are systematic in nature. 'Converted' to uncertainty components in ΔT using the actual sensitivities ($|\partial \Delta T / \partial p|$, $|\partial \Delta T / \partial v|$; see Figures 7.5 and 7.6 in Section 7.3.4), their shares of the combined uncertainty of the final ΔT vary with the actual values for pressure and ventilation speed. The uncertainties of both become significant with decreasing p and v , with the uncertainty of the ventilation speed overall dominating.

The models in Equation (7.1) and Equation (7.2) used to predict the equilibrium temperatures may involve further uncertainties because of the imperfections in representing the true temporal behaviour of the temperature sensor signal. However, such uncertainty components are difficult to quantify and are therefore not accounted for within this analysis.

7.3.4 Results

In practice, the measurements for the various radiosonde types are performed at slightly varying irradiances I close to but not exactly at 1000 W m^{-2} , depending on the actual adjustments of the incidence angle or the distance to the light source. Taking this value as a reference I_{ref} , the originally determined $\Delta T(p, v)$ are corrected by applying a factor I/I_{ref} to enable comparison of the results.

Figures 7.5 and 7.6 summarise the results for the 10 participating radiosondes, separate as function of pressure and ventilation speed. Again, it is pointed out that, to preserve anonymity,

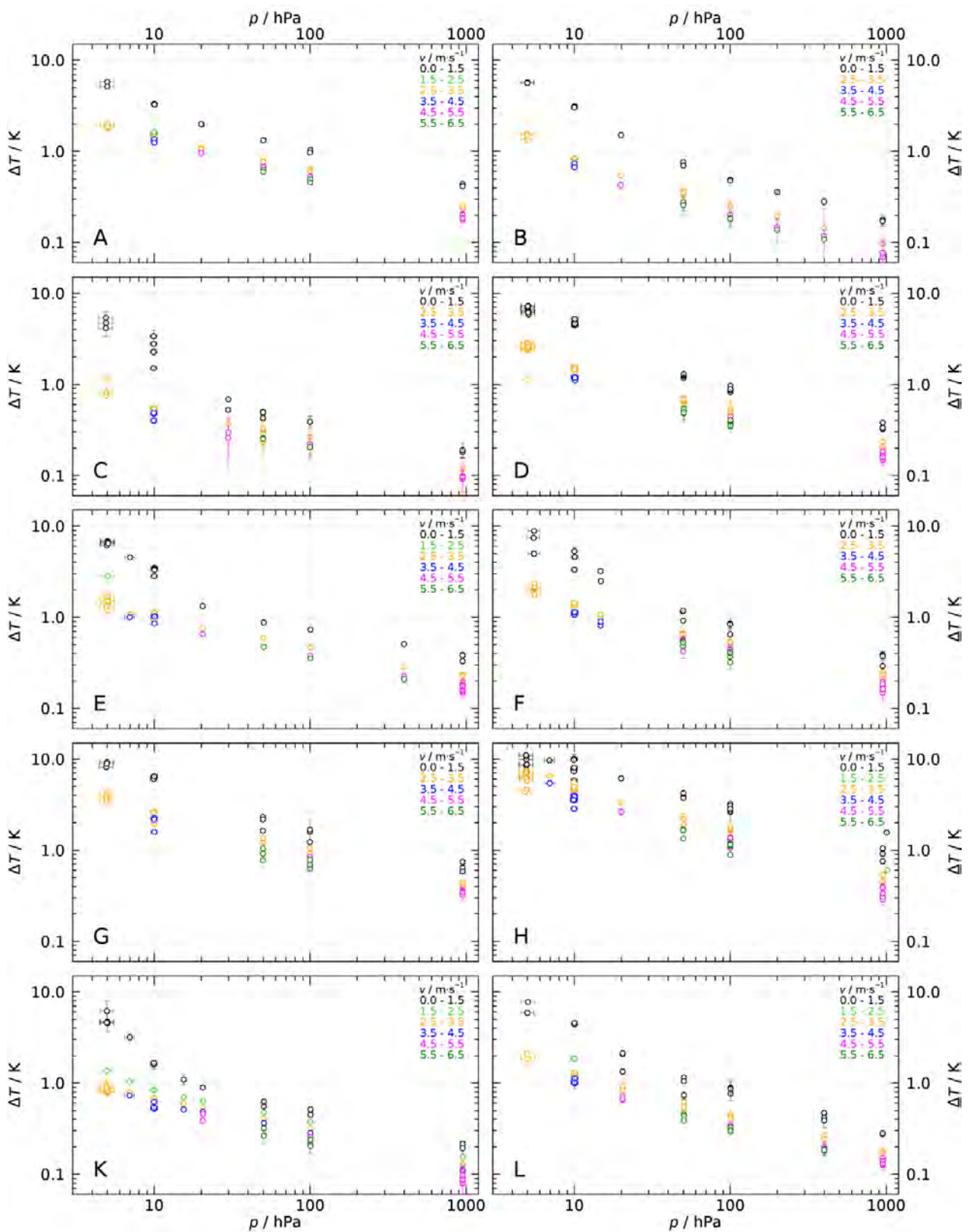


Figure 7.5: Radiation sensitivity ΔT of air temperature measurement as function of pressure for each participant radiosonde. Measurement values and uncertainties are linearly corrected to an irradiance of $1000 W m^{-2}$. Data sets in each panel are distinguished by colour according to specified ventilation speed intervals. Axes are logarithmic for better distinctiveness of data points.

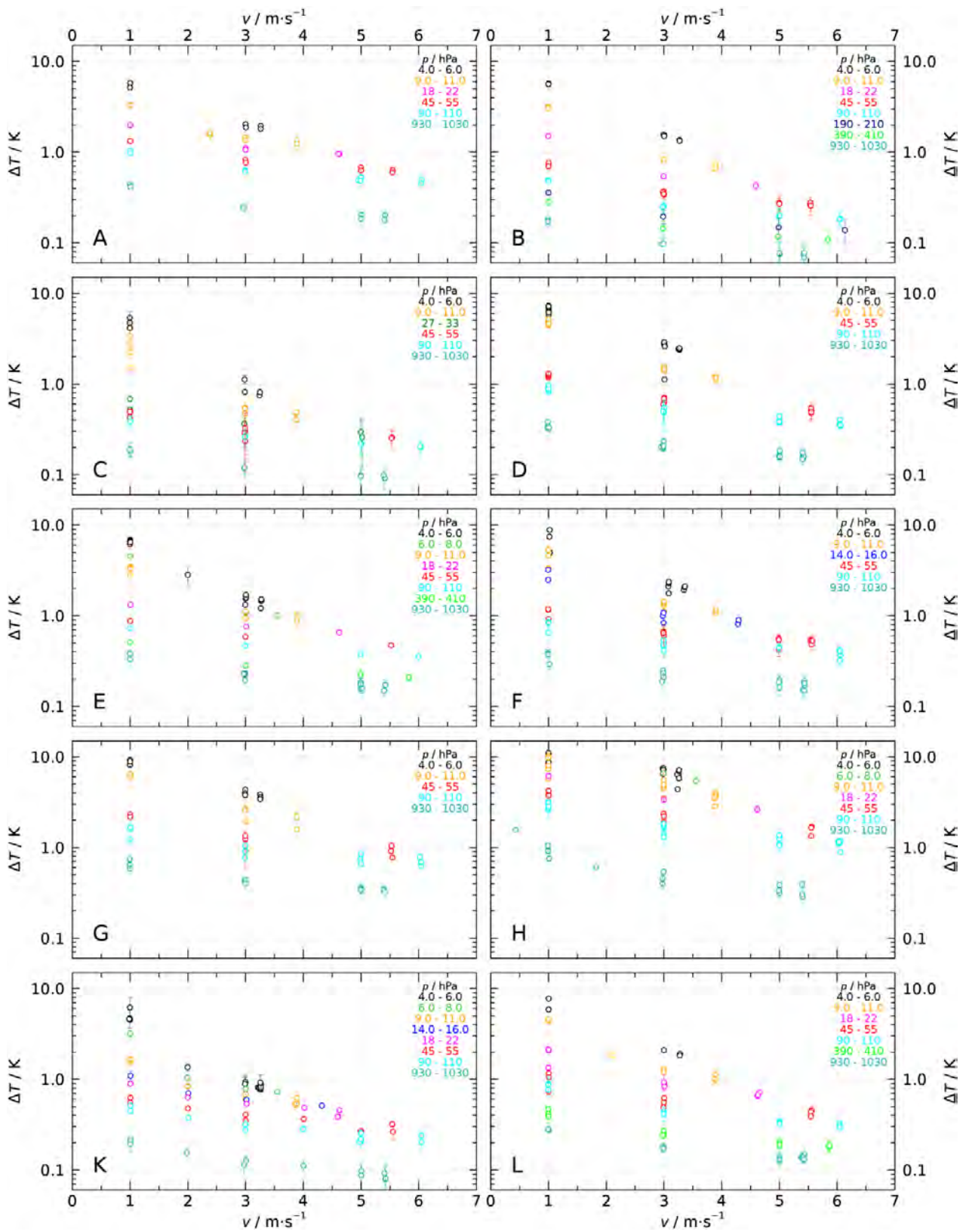


Figure 7.6: Radiation sensitivities of temperature measurement as function of ventilation speed (same data as in Figure 7.5); pressure is parameter. Uncertainties for ventilation speed (constant $0.5 m s^{-1}$) are not displayed.

the panel labels A to L in Figures 7.5 and 7.6 are consistent in both figures, but different from those used in result figures for the other experiments of the laboratory campaign.

The figures include the results from the mandatory measurement programme listed in Section 7.3.1, but also results from additional tests at various other settings of the experimental parameters. Therefore, the number of data points and their distribution with the parameters p and v are different for the individual sondes. The presented measurements are for an incidence of 30° , and the rotation period of the sondes was set to 15 s for most of the measurements. A few points at other rotation frequencies are present as well. The UAII campaign confirms the finding from previous tests that the solar warming – evaluated as a temporal average (Section 7.3.3) over the measured response of a rotating sonde – is insensitive to the rotation frequency.

Note that the axis scaling is the same for the 10 panels in both Figure 7.5 and Figure 7.6. A logarithmic scale was chosen for ΔT to make the dynamics visible also at high p and v . For the same reason, also the p -axis in Figure 7.5 is logarithmic.

Vertical bars indicate the uncertainty component for ΔT associated with the procedure to determine the temperature differences. It is usually smaller than the symbol size. In Figure 7.5, horizontal bars denote the pressure uncertainty. The constant uncertainty of the ventilation speed is not included in Figure 7.6 in favour of readability.

The measured radiation sensitivities at 1000 W m^{-2} are less than one tenth up to a few tenths of a kelvin at surface pressure, depending on the sonde model and strength of ventilation, and may reach several kelvin (up to $\sim 10 \text{ K}$ for some sonde types) at the lowest settings for pressure and ventilation. At 10 hPa and 4 m s^{-1} , ΔT ranges between 0.5 K and 3.8 K, with a value of about 1 K for most of the sondes. The results show the expected increase of the radiation sensitivity with decreasing pressure for all sondes in consistence with the observation that solar warming in real soundings increases continuously with altitude. This is due to the fact that the convective cooling, which limits the warming of the sensor construction, becomes less effective with decreasing pressure (or density) of the surrounding air. The results also show the strong increase of the radiation sensitivity with decreasing ventilation speed. Although the ascent speed in soundings is essentially uniform (around 5 m s^{-1} on average), variations of the ascent rate at shorter scales may cause variations in effective air speed which may induce fluctuations of the sensor cooling and therefore impress fluctuations to the measured air temperature profile. Such air speed variations occur due to changing dynamics of the air flow around the balloon, and in particular in conjunction with the pendulum motion of the radiosonde.

For some repeated measurements at constant settings of the main parameters irradiance, pressure, or ventilation speed, certain scatter can be identified, for example for sonde E at 5 hPa and 3 m s^{-1} in Figure 7.5 or sonde H at 5 hPa in the same figure. Such scatter does generally not depict the repeatability of the measurement, but reflects varying results in connection with different modes of sonde operation, e.g. in tests with both the heating functionality of the sonde's humidity sensor switched on and off, or special experimental settings, e.g. varied openings of the aperture in front of the measuring chamber to partially irradiate the sensor boom. The experimental repeatability is generally smaller than the symbol size.

For some of the radiosondes, a few more data points exist that have been measured at other particular experimental settings, for example other incidences than 30° , at vanishing ventilation speed or at fixed axial angular positions without continuous rotation. Such points are not included in Figures 7.5 and 7.6.

The UAII radiation experiments are designed to give an overview of the participant sonde's sensitivities of daytime temperature measurements to incoming solar radiation, and to map the variation of the sensitivities with the most important parameters. The results may help to assess the effect in particular at conditions that resemble the upper part of a sounding profile where the warming is strongest. However, the effect is significant also in the troposphere (even at the surface), and a reliable correction is essential also in that altitude range to ensure the increasing demands to the data quality of operational radiosonde observations.

Part III

Field Campaign

8 FLIGHT STATISTICS

8.1 OVERVIEW

The UAI 2022 field campaign took place from 2022-08-08 to 2022-09-16 at the Lindenberg Meteorological Observatory – Richard Assmann Observatory (MOL-RAO) in Northeastern Germany (see Section 4.1 for details on this location). It consisted of the following three successive phases:

Phase 1 – Setup of systems (2022-08-08 to 2022-08-15):

During six days, the representatives from radiosonde manufacturers that participated in the UAI 2022 each installed two ground receiving stations, to allow parallel soundings on a given rig. They also trained the independent operators assigned to their respective systems (see Section 4.3.1). A series of 5 test flights were launched during this phase, to verify that all systems were operational, and for training purposes. The data from these test flights were not archived and are not discussed in this report.

Phase 2 – Blind field campaign (2022-08-16 to 2022-09-14):

All the balloon flights used to assess the performance of the radiosondes involved in the UAI 2022 took place during this phase, after all the manufacturers’ representatives had left the MOL-RAO. This was a “blind” field campaign, in the sense that all radiosonde manufacturers were given access only to their own measurements (within 24 h of each flight). The manufacturers did not receive any other information regarding the campaign flights, and in particular did not have access to the GDP data files.

Phase 3 – Packing of systems (2022-09-15 to 2022-09-16):

During these two days, the operators and the UAI project team disassembled and packed the ground stations according to the manufacturers’ instructions.

A total of 83 soundings were performed during phase 2 of the UAI 2022 field campaign, including weekly scientific reference flights (4 in total) with a CFH as described in Section 4.3.11. The 79 “core” UAI 2022 flights (41 day flights; 38 night or evening twilight flights; labelled F1 to F79) were launched according to the principles outlined in Section 4.3. The basic characteristics for each of these flights are presented in Table 8.1. The geopotential height of the balloon burst and the tropopause, together with the ascent speed, are shown as a function of the flight number in Figure 8.1. A visual impression of the conditions at launch time is provided in Figure 8.2 for each flight.

Two reference radiosondes, one of each of the selected models discussed in Section 4.3.9, were flown on every rig. These two reference radiosondes were prepared and processed in accordance with the general GRUAN principles, and all applicable operational procedures described in the respective GRUAN Technical Documents (*Kizu et al., 2018b; Sommer et al., 2022, 2023*). These reference sondes were used only to generate GRUAN Data Products (GDPs). Their preparation and data post-processing was distinct from that of participating systems, including the IMS-100 and RS41 radiosondes, which were operated (solely, precisely, and exactly) according to their respective manufacturer guidelines and instructions.

For clarity, we will refer to datasets generated by participating radiosonde systems as “Manufacturer Data Products” (MDPs, see Section 9.5.2). On each of the 79 UAI 2022 flights, six to eight participating radiosondes were flown alongside the two reference sondes. The complete flight log, for each participating system, is presented in Table 8.2.

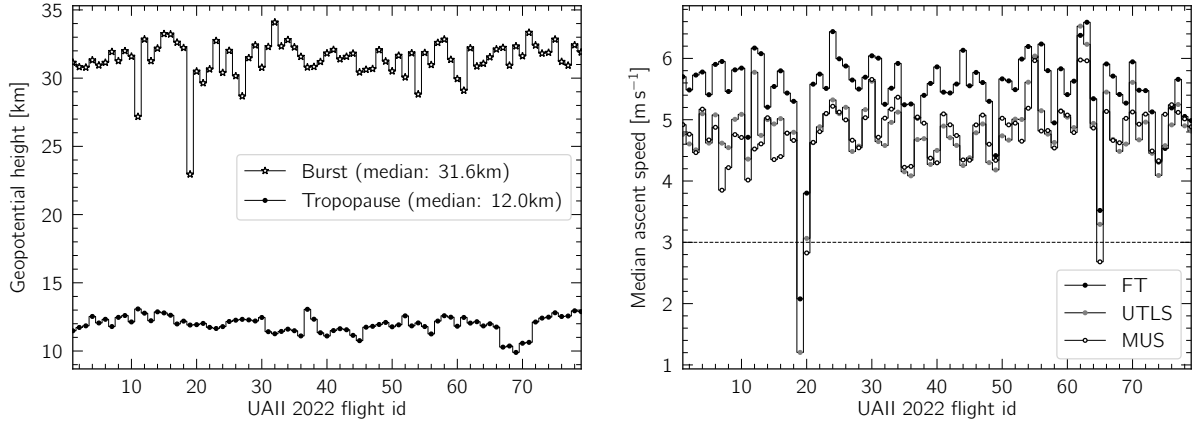


Figure 8.1: Left: Geopotential height of the burst point and tropopause for each of the UAII 2022 field campaign flights. Right: Median ascent speed in the Free Troposphere (FT), Upper Troposphere / Lower Stratosphere (UTLS) and Mid-Upper Stratosphere (MUS) for each UAII 2022 flight.

Table 8.1: Basic characteristics of the UAII 2022 flights performed during the blind campaign phase. Twilight flights are treated as night flights in our analysis (see Sections 4.3.3 and 9.1.2). The GRUAN flight Id and standard launch time are provided for legacy purposes, to enable the un-ambiguous identification of GDPs in the GRUAN archive. The synop cloud codes are based on manual observations made at launch times in accordance with the relevant WMO guidelines.

UAII flight Id	Time of day	Synop cloud code at launch time [$NC_LhC_M C_H$]	Geopotential height at burst [km]	Median ascent rate			GRUAN flight Id	GRUAN standard launch time [UTC]
				FT [$m s^{-1}$]	UTLS [$m s^{-1}$]	MUS [$m s^{-1}$]		
F01	day	00901	31.2	5.7	4.8	4.9	158362	2022-08-16T08:00:00
F02	day	32700	30.8	5.5	4.6	4.8	158647	2022-08-16T13:00:00
F03	night	15900	30.8	5.7	4.5	4.5	158363	2022-08-16T19:15:00
F04	day	40944	31.3	5.8	5.1	5.2	158705	2022-08-17T08:00:00
F05	day	32746	30.9	5.4	4.6	4.7	158373	2022-08-17T11:30:00
F06	day	32746	31.1	5.9	5.1	4.9	158543	2022-08-17T14:30:00
F07	night	20948	31.9	5.9	4.6	3.9	158561	2022-08-17T19:30:00
F08	night	00908	31.3	5.5	4.5	4.2	158375	2022-08-17T23:15:00
F09	day	00908	32.0	5.8	5.0	4.8	158449	2022-08-18T08:00:00
F10	day	53841	31.6	5.8	5.1	4.7	158562	2022-08-18T12:30:00
F11	night	737//	27.2	4.7	4.4	4.0	158563	2022-08-18T19:00:00
F12	night	20931	32.8	6.2	5.8	4.5	158450	2022-08-18T22:15:00
F13	day	3637//	31.3	6.1	4.7	4.6	158564	2022-08-19T08:00:00
F14	day	785//	32.2	5.2	5.0	5.0	158490	2022-08-19T12:30:00
F15	night	754//	33.2	5.5	4.9	4.3	158491	2022-08-19T19:00:00
F16	night	754//	33.2	5.8	5.0	4.4	158566	2022-08-19T22:45:00
F17	day	7097//	32.6	5.4	4.8	4.8	158568	2022-08-22T08:00:00
F18	day	2167//	32.2	5.3	4.8	4.7	158528	2022-08-22T12:45:00
F19	night	2582//	23.0	2.1	1.2	nan	158569	2022-08-22T19:00:00
F20	night	757//	30.5	3.8	3.1	2.8	158529	2022-08-22T22:30:00
F21	day	6137//	29.6	5.6	4.6	4.6	158531	2022-08-23T08:00:00
F22	day	5254//	30.7	5.7	4.9	4.8	158571	2022-08-23T13:00:00
F23	night	65700	32.7	5.5	5.1	5.1	158534	2022-08-23T19:00:00
F24	night	15800	30.4	6.4	5.3	5.2	158572	2022-08-23T22:00:00
F25	night	00900	32.0	6.0	5.1	5.1	158535	2022-08-24T01:00:00
F26	day	762//	30.2	5.9	5.2	5.0	158574	2022-08-24T07:30:00
F27	day	52500	28.7	5.6	4.5	4.7	158576	2022-08-24T10:30:00
F28	day	42600	31.5	5.5	4.6	4.5	158671	2022-08-24T13:45:00

Table 8.1: continued.

UAI flight Id	Time of day	Synop	Geopotential height at burst	Median ascent rate			GRUAN Flight ID	GRUAN standard launch time
		cloud code at launch time		FT	UTLS	MUS		
		[$N_C L_h C_M C_H$]	[km]	[$m s^{-1}$]	[$m s^{-1}$]	[$m s^{-1}$]		[UTC]
F29	night	00901	32.4	5.7	5.2	5.0	158676	2022-08-24T19:00:00
F30	night	00900	30.8	6.0	5.6	5.7	158673	2022-08-24T22:00:00
F31	night	10931	32.3	6.0	4.6	4.7	158678	2022-08-28T18:45:00
F32	night	10930	34.1	5.3	4.6	5.0	158674	2022-08-28T22:00:00
F33	day	65401	32.3	5.5	5.0	5.2	158706	2022-08-29T08:00:00
F34	day	58401	32.8	5.9	5.1	5.4	158675	2022-08-29T13:00:00
F35	night	10931	32.3	5.2	4.2	4.2	158712	2022-08-29T18:45:00
F36	night	15701	31.6	5.3	4.1	4.2	158740	2022-08-29T22:00:00
F37	day	723//	30.8	5.0	4.7	5.0	158739	2022-08-30T08:00:00
F38	day	68700	30.8	5.4	4.7	4.9	158741	2022-08-30T13:00:00
F39	night	30941	31.2	5.6	4.3	4.4	158767	2022-08-30T18:45:00
F40	night	00900	31.8	5.9	4.5	4.3	158772	2022-08-30T22:00:00
F41	day	11702	32.1	5.4	4.9	5.1	158769	2022-08-31T08:00:00
F42	day	32601	31.4	5.4	4.7	4.9	159218	2022-08-31T11:00:00
F43	day	32701	31.6	5.6	4.6	4.7	158770	2022-08-31T14:00:00
F44	night	14802	31.8	6.1	4.3	4.3	159221	2022-08-31T18:45:00
F45	night	55801	30.4	5.6	4.4	4.3	158771	2022-08-31T22:00:00
F46	day	11601	30.6	5.8	4.8	4.9	159223	2022-09-01T08:00:00
F47	day	42600	30.7	5.6	4.9	5.1	159234	2022-09-01T11:00:00
F48	night	12730	32.1	5.3	4.3	4.6	159257	2022-09-01T18:30:00
F49	night	00901	31.2	4.4	4.2	4.3	159224	2022-09-01T22:00:00
F50	day	10940	30.5	5.7	4.7	5.0	159259	2022-09-02T08:00:00
F51	day	52700	31.7	5.6	4.7	4.9	159230	2022-09-02T12:00:00
F52	day	00906	30.1	5.5	5.0	4.9	159232	2022-09-05T08:00:00
F53	day	22608	31.8	6.0	5.0	4.6	159263	2022-09-05T13:00:00
F54	night	28701	28.8	6.2	5.6	5.2	159264	2022-09-05T19:00:00
F55	night	00908	31.9	6.0	6.0	6.0	159233	2022-09-05T22:00:00
F56	day	00906	31.0	6.2	5.1	4.8	159222	2022-09-06T08:00:00
F57	day	4577//	32.6	5.8	4.8	4.8	159265	2022-09-06T13:00:00
F58	night	60950	32.8	4.9	4.6	4.5	159364	2022-09-06T18:30:00
F59	night	30944	31.4	5.8	5.1	5.1	159369	2022-09-06T21:20:00
F60	day	00908	29.9	5.4	5.0	5.1	159365	2022-09-07T08:00:00
F61	day	60941	29.1	5.6	4.9	4.8	159370	2022-09-07T12:30:00
F62	night	10967	32.2	6.4	6.5	6.0	159371	2022-09-07T20:00:00
F63	night	20941	30.9	6.6	6.2	6.0	159368	2022-09-07T22:45:00
F64	day	30987	31.1	5.3	4.9	4.9	159456	2022-09-08T07:45:00
F65	day	3147//	31.5	3.5	3.3	2.7	159515	2022-09-08T12:00:00
F66	night	48508	32.1	5.9	5.5	5.1	159516	2022-09-08T19:00:00
F67	night	15701	32.2	5.7	4.7	4.7	159457	2022-09-08T22:15:00
F68	day	20976	30.9	5.4	4.5	4.6	159366	2022-09-09T08:00:00
F69	day	52642	32.3	5.3	4.6	5.0	159517	2022-09-09T12:30:00
F70	night	29761	31.6	5.9	5.6	5.1	159458	2022-09-09T19:00:00
F71	night	32648	33.3	5.5	4.7	4.9	159603	2022-09-09T22:00:00
F72	day	61200	32.4	5.5	5.0	5.1	159604	2022-09-12T08:00:00
F73	day	22504	31.8	5.1	4.5	4.5	159460	2022-09-12T12:00:00
F74	night	00907	31.9	4.3	4.1	4.3	159461	2022-09-12T18:00:00
F75	night	00904	32.8	4.5	4.6	5.1	159605	2022-09-12T21:15:00
F76	day	8////	31.2	5.2	4.9	5.2	159606	2022-09-13T08:00:00
F77	day	5567//	30.9	5.7	5.2	5.1	159463	2022-09-13T12:00:00
F78	night	10931	32.4	5.1	4.9	5.0	159608	2022-09-13T18:00:00
F79	night	00901	31.9	5.0	4.8	4.9	159609	2022-09-13T21:00:00
R01	night	7093//	33.3	5.2	4.9	5.3	158544	2022-08-16T22:23:00
R02	day	785//	33.3	5.1	4.7	5.3	159634	2022-08-24T17:00:00
R03	day	58740	33.3	5.4	4.9	5.3	159626	2022-09-01T15:00:00

Table 8.1: continued.

UAI flight Id	Time of day	Synop	Geopotential height at burst	Median ascent rate			GRUAN Flight ID	GRUAN standard launch time
		cloud code at launch time		FT	UTLS	MUS		
		[$N_C L_h C_M C_H$]	[km]	[$m s^{-1}$]	[$m s^{-1}$]	[$m s^{-1}$]		[UTC]
R04	night	50950	33.5	5.2	4.5	4.6	159631	2022-09-07T01:00:00

Table 8.2: UAI 2022 flight data log. Systems that were prepared for a given flight are tagged with *. Systems physically present on a given rig and whose data contribute to the final assessment of a given sonde model are tagged with ⊗. Footnotes indicate the reason for dropping specific flights/profiles from the analysis (see Section 8.2).

RS Model	(gdp)iMS-100		(gdp)RS41		ATMS-3710		CF-06-AH		DFM-17		GTH3		iMet-54		iMS-100		M20		PS-B3		RS41		WXR-301D			
	Ground system Id	-	-	1	2	1	2	1	2	1	2	1	2	1	2	1	2	1	2	1	2	1	2	1	2	
Day																										
F01			⊗	⊗			⊗							⊗		⊗									⊗	
F02			⊗	⊗	⊗					⊗	⊗									⊗			⊗			
F04			⊗	⊗	⊗					⊗		*1	*1							⊗			⊗			
F05			⊗	⊗			⊗							⊗		⊗				⊗				⊗	*1	
F06			⊗	⊗	⊗	⊗				⊗		⊗								⊗			⊗			
F09			⊗	⊗			⊗							*1	⊗		⊗			⊗				⊗		
F10			⊗	⊗		*1				⊗		⊗								⊗			⊗			
F13			⊗	⊗	⊗					⊗		⊗								⊗	⊗		⊗			
F14			⊗	⊗			⊗	⊗						⊗		⊗				⊗				⊗		
F17			⊗	⊗	⊗					⊗		⊗								⊗			⊗			
F18			⊗	⊗			⊗							⊗		⊗	*1			⊗				⊗		
F21			⊗	⊗			⊗							⊗		⊗	⊗			⊗				*1	*1	
F22			⊗	⊗	⊗					⊗		⊗	⊗							⊗			⊗			
F26			⊗	⊗			⊗							⊗		⊗				⊗				⊗	⊗	
F27			⊗	⊗	⊗					⊗		⊗								⊗	⊗		⊗			
F28			⊗	⊗			⊗	⊗						⊗		⊗				⊗				⊗		
F33			⊗	⊗	⊗	⊗				⊗	⊗	*3								⊗			⊗			
F34			⊗	⊗			⊗							⊗	⊗		⊗			⊗				⊗		
F37			⊗	⊗			⊗							⊗		⊗	⊗			⊗				⊗		
F38			⊗	⊗	⊗					⊗		⊗	⊗							⊗			⊗			
F41			⊗	⊗	⊗	⊗				⊗		*3								⊗	⊗		⊗			
F42			⊗	⊗			⊗	⊗						⊗		⊗				⊗				⊗		
F43			⊗	⊗	⊗					⊗	⊗		⊗							⊗			⊗			
F46			⊗	⊗			⊗							⊗		⊗	⊗			⊗				⊗		
F47			⊗	⊗	⊗					⊗		⊗	⊗							⊗			⊗	⊗		
F50			⊗	⊗	⊗					⊗	⊗									⊗	⊗		⊗			
F51			⊗	⊗			⊗	⊗						⊗	⊗		⊗			⊗				⊗		

¹ No data (see Section 8.2.1). ⁵ Ascent speed below the valid operational range.
² Insufficient data (see Section 8.2.2). ⁶ Operational mishap (see Section 8.2.4).
³ Invalid data (see Section 8.2.3).
⁴ Rejected due to lack of CWS.

Table 8.2: continued.

RS Model	(gdp)IMS-100		ATMS-3710		CF-06-AH		DFM-17		GTH3		iMet-54		IMS-100		M20		PS-B3		RS41		WXR-301D	
	(gdp)RS41		1	2	1	2	1	2	1	2	1	2	1	2	1	2	1	2	1	2	1	2
F52	⊗	⊗			⊗						⊗		⊗		⊗	⊗						⊗
F53	⊗	⊗	⊗	⊗			⊗		⊗								⊗			⊗		
F56	⊗	⊗			⊗						⊗	⊗	⊗		⊗							⊗
F57	⊗	⊗	⊗				⊗		⊗								⊗	⊗	⊗			⊗
F60	⊗	⊗			⊗						⊗		⊗	⊗	⊗							⊗
F61	⊗	⊗	⊗				⊗		⊗	⊗ ^{*1}							⊗		⊗			⊗
F64	⊗	⊗	⊗	⊗			⊗	⊗	⊗								⊗		⊗			⊗
F65	* ⁵	* ⁵	* ⁵		* ⁵	* ⁵					* ⁵		* ⁵		* ⁵							* ⁵
F68	⊗	⊗	⊗				⊗		⊗								⊗		⊗	⊗		⊗
F69	⊗	⊗	⊗				⊗				⊗		⊗	⊗	⊗							⊗
F72	⊗	⊗			⊗						⊗			⊗	⊗							⊗
F73	⊗	⊗	⊗	⊗			⊗		* ³	⊗							⊗		⊗			
F76	⊗	⊗			⊗						⊗	⊗		⊗								⊗
F77	⊗	⊗	⊗				⊗		⊗	* ³				⊗			⊗		⊗			⊗

Night

F03	⊗	⊗			⊗						⊗		⊗		⊗	⊗						⊗
F07	⊗	⊗	⊗	⊗			⊗	⊗	* ³								⊗		⊗			
F08	⊗	⊗			⊗						⊗		⊗	* ¹	⊗					⊗		⊗
F11	⊗	⊗	⊗				⊗		⊗								⊗		⊗	⊗		
F12	⊗	⊗			⊗						* ³	⊗	⊗		⊗							⊗
F15	⊗	⊗			⊗	⊗					⊗		⊗		⊗							⊗
F16	⊗	⊗	⊗				⊗		* ¹								⊗	⊗	⊗			
F19	* ⁵	* ⁵	* ⁵				* ⁵		* ⁵								* ⁵		* ⁵	* ⁵		
F20	* ⁵	* ⁵			* ⁵						* ⁵		* ⁵	* ¹	* ⁵							* ⁵
F23	⊗	⊗			⊗						⊗		⊗	⊗	⊗							⊗
F24	⊗	⊗	⊗				⊗		⊗	⊗							⊗		⊗	⊗		
F25	⊗	⊗			⊗	⊗					⊗		* ¹		⊗	⊗						⊗
F29	⊗	⊗	⊗				⊗	⊗	⊗								⊗		⊗			
F30	⊗	⊗			⊗	⊗					⊗	⊗		⊗								⊗
F31	⊗	⊗	⊗				⊗		⊗	* ³							⊗		⊗			
F32	⊗	⊗			⊗						⊗		⊗		⊗							⊗
F35	⊗	⊗			⊗						⊗		⊗		⊗	⊗						⊗
F36	⊗	⊗	⊗				⊗		⊗								⊗		⊗	⊗		
F39	⊗	⊗	⊗	⊗			⊗		⊗								⊗		⊗			
F40	⊗	⊗			⊗						⊗	⊗		⊗								* ²
F44	⊗	⊗			⊗	⊗					⊗		⊗	⊗	⊗							⊗
F45	⊗	⊗	⊗				⊗		* ²	* ¹							⊗	⊗	⊗			
F48	* ^{1,4}	* ⁴	* ⁴		* ⁴	* ⁴	* ⁴	* ⁴	* ⁴								* ⁴		* ⁴			
F49	⊗	⊗			⊗				⊗		⊗	⊗		⊗		* ⁶						* ⁶
F54	⊗	⊗	⊗				⊗		⊗	⊗							⊗	⊗	⊗			

¹ No data (see Section 8.2.1).

² Insufficient data (see Section 8.2.2).

³ Invalid data (see Section 8.2.3).

⁴ Rejected due to lack of CWS.

⁵ Ascent speed below the valid operational range.

⁶ Operational mishap (see Section 8.2.4).

Table 8.2: continued.

RS Model	(gdp)IMS-100		ATMS-3710		CF-06-AH		DFM-17		GTH3		iMet-54		IMS-100		M20		PS-B3		RS41		WXR-301D	
	(gdp)RS41		1	2	1	2	1	2	1	2	1	2	1	2	1	2	1	2	1	2	1	2
F55	*	*			*	*					*		*	*								*
F58	*	*	*				*		*	*					*			*			*	*
F59	*	*	*				*	*	*	*					*			*	*		*	*
F62	*	*	*	*			*		*	*					*			*	*	*		
F63	*	*			*				*	*	*	*	*	*	*							*
F66	*	*			*	*			*	*	*	*	*	*	*	*						*
F67	*	*	*				*		*	*	*	*	*	*	*	*	*	*	*	*	*	*
F70	*	*	*				*		*	*				*	*	*	*	*	*	*	*	*
F71	*	*			*				*	*	*	*	*	*	*	*						*
F74	*	*	*				*		*	*	*	*	*	*	*	*	*	*	*	*	*	*
F75	*	*			*				*	*	*	*	*	*	*	*						*
F78	*	*			*				*	*	*	*	*	*	*	*						*
F79	*	*	*	*			*	*			*	*	*	*	*	*	*	*	*	*	*	*

¹ No data (see Section 8.2.1). ⁵ Ascent speed below the valid operational range.
² Insufficient data (see Section 8.2.2). ⁶ Operational mishap (see Section 8.2.4).
³ Invalid data (see Section 8.2.3).
⁴ Rejected due to lack of CWS.

8.2 SELECTION OF VALID FLIGHTS AND PROFILES

Assessing the performance of a given radiosonde model with respect to the WMO’s OSCAR requirement uncertainty criteria (see Section 9.3) relies on the combination of all valid profiles acquired during the UAI 2022 field campaign. In this section we discuss the handful of flights and profiles that were found to not be valid, and therefore excluded from this analysis.

We exclude 4 flights entirely from our analysis:

- F19, F20, F65: with a median ascent speed $< 3 \text{ m s}^{-1}$ in the troposphere and/or stratosphere (see Figure 8.1), these flights fall outside of the nominal operating range of many radiosonde systems. All three ascents were likely slowed because of additional mass on the balloon as a result of rain.
- F48: a communication interference resulted in the total data corruption of one of the reference sonde on this flight, preventing the assembly of the associated GDP, and thus of the Combined Working measurement Standard (CWS) for this flight (see Chapter 9.2 for details).

A number of profiles from individual systems are also excluded in their entirety (for all the variables) from the analysis. They are all marked accordingly in Table 8.2, and fall in four distinct categories:

1. attempted ascents for which no data were collected,
2. ascents for which insufficient data were collected,
3. profiles with invalid data, and
4. operational mishaps.

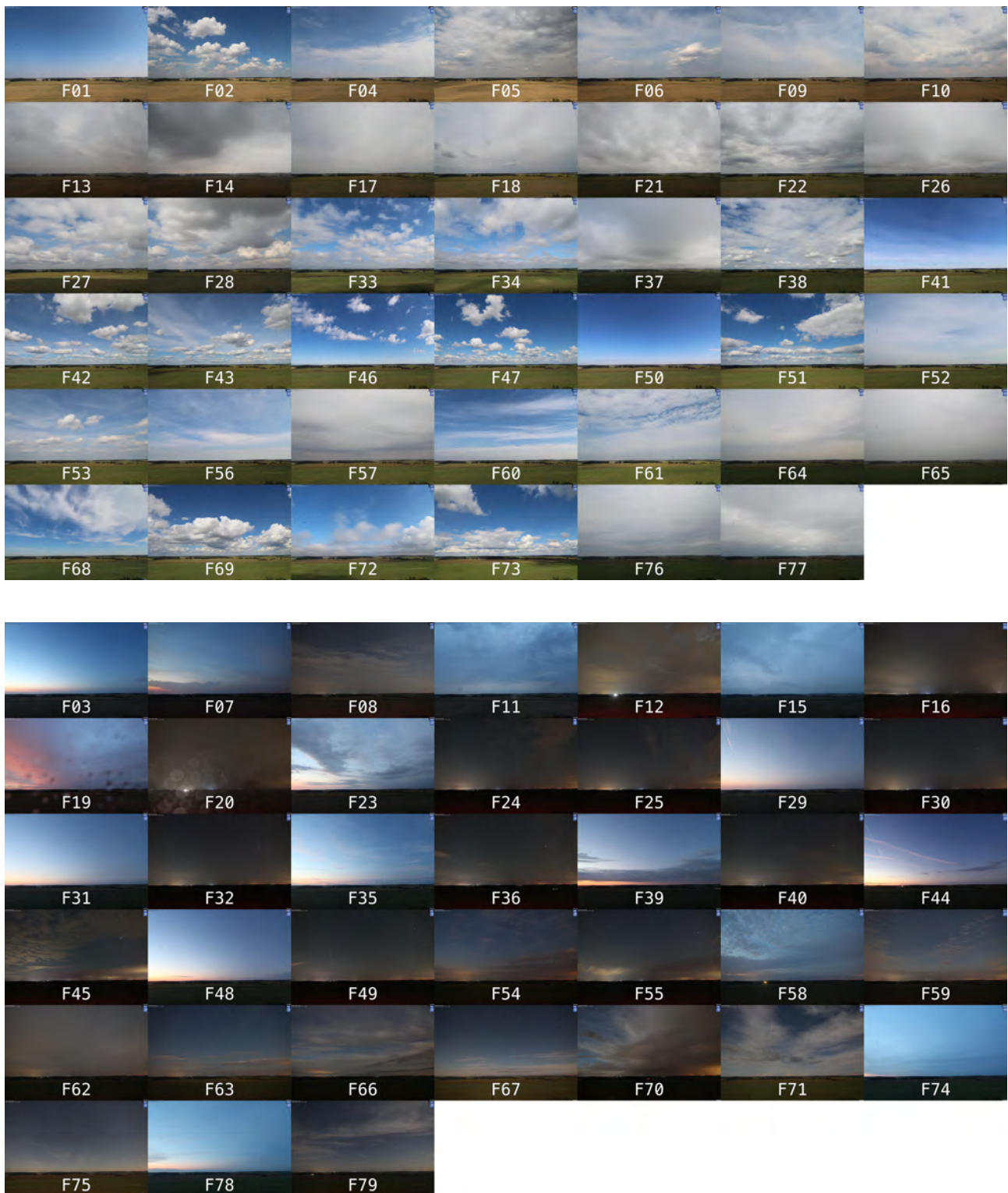


Figure 8.2: Top: View of the sky taken from the 99 m weather mast in Falkenberg ($52^{\circ}10'$ North, $14^{\circ}7'$ East), looking North-North-East. The mast is located ~ 5 km South from the site of the UAII 2022 field campaign. Each image shows the sky conditions within a maximum of 5 minutes from the launch of each day flight. The colour of the grass field at the bottom of each image illustrates the transition from dry and warm summer-like conditions to wetter and colder autumn-like conditions over the course of the UAII 2022 field campaign. Bottom: as for Top, but for the evening-twilight and night flights.

8.2.1 Attempted ascents with no data

Technical malfunctions of the sonde and/or the ground system before or after the balloon launch have resulted in a complete loss of data in the following cases:

- ATMS-3710: F10 (system 1), F79 (system 2)
- CF-06-AH: F71 (system 1)
- GTH3: F04 (system 1 & 2), F16 (system 1), F45 (system 2), F61 (system 2), F74 (system 2)
- iMet-54: F09 (system 1)
- IMS-100: F08 (system 2), F18 (system 2), F20 (system 2), F25 (system 1)
- WxR-301D: F05 (system 2), F21 (system 1 & 2)

8.2.2 Ascents with insufficient data

A profile is considered to have insufficient data if it does not contain valid geopotential height measurements up to at least 5000 m. This is a necessary condition to allow a robust synchronisation of the profile with the GDPs (see Section 9.5.3). Two profiles fall into this category: GTH3 for F45 (system 1), and WxR-301D for F40 (system 2).

8.2.3 Profiles with invalid data

We define and identify invalid profiles as follows:

Definition 1 *A sounding profile is deemed invalid if an independent operator, trained and certified in the use of the sounding system in accordance with the system's standard operating procedure, is able to unambiguously flag the profile measurements as being non-physical and/or subject to obvious technical malfunctions, and to do so without any external reference measurements.*

A direct consequence of this definition is that no comparison with GDPs is made in order to decide whether a given Manufacturer Data Product (MDP) should be included (or not) in the performance assessment of the associated radiosonde.

A total of 7 profiles from the GTH3 radiosonde are found to contain invalid data: F07 (system 1), F31 (system 2), F33 (system 1), F41 (system 1), F67 (system 1), F73 (system 1), and F77 (system 2). All of them are identifiable by an instantaneous drop in temperature of 60 K to 80 K within the first 15 min of the flight, which were all caused by a faulty temperature sensor.

A single profile from the iMet-54 radiosonde was found to contain invalid data: F12 (system 1). The corruption was noted by the independent operator. It took the form of a sudden 360 m jump in the geopotential height measurements as the sonde was being attached to the rig, with values that remained erroneous up to 3 km, well into the FT.

The special case of the WxR-301D (system 2) profile for flight F59 is discussed in Section 9.5.2.1.

8.2.4 Operational mishaps

Three profiles are excluded in their entirety following operational errors:

- The dataset of the GTH3 sonde for F58 (system 1) contains an incorrect pressure profile caused by a human error when typing the ground pressure at launch time.
- The unwinder string was torn at the time of the (first) launch of flight F49, which led to the rig falling on the ground. Communication with the M20 (system 1) and WxR-301D (system 2) was lost as a result of this landing. No noticeable impact on the data was detected for the other systems on the rig, which are therefore not excluded from our analysis.

In addition to the case of flight F58 (system 1) mentioned above, the manual input of ground values for the GTH3 radiosonde also led to a series of typos for the ground temperature (F29 system 1) and wind (horizontal) speed (F36 system 1, F54 system 1). Unlike for the pressure where a wrong ground value affects the entire profile, the ground temperature's influence only extends 2 s into the ascent, and 10 s for the ground wind (horizontal) speed. We thus do not drop these 3 profiles in their entirety from our analysis, but instead simply crop the first 2 s for the GTH3 profile of F29 (system 1), and the first 10 s for the GTH3 profiles of F36 (system 1) and F54 (system 1).

It is also worth mentioning that a technical issue with the unwinder for flight F53 resulted in the rig being stuck 15 m under the balloon for the entire flight, instead of the usual 60 m distance (see Appendix N.7). On flight F54, an operational mishap at launch time resulted in the reference iMS-100 radiosonde (used to generate one of the flight's GDPs) briefly touching the ground prior to launch. Since in both cases there is no noticeable impact on the data, these flights/profiles are not excluded from our analysis.

8.2.5 Early start detections and erroneous geopotential heights

A GNSS signal repeater was installed in the hangar hosting the radiosonde ground systems (see Section 4.1.5 for details). Unfortunately, it appears that the presence of this repeater (and possibly also the metallic nature of the hangar itself) is likely to have affected some of the measurements of geopotential height (as well as pressure and wind, as these are also derived from GNSS signals in most instances) from several radiosonde models, and this on several flights. The impact on the measurements is not systematic, nor is it uniform. It can take the form of an early start detection, and/or erroneous geopotential height, pressure and wind measurements at launch time and within the Planetary Boundary Layer (PBL). In a handful of cases, erroneous geopotential heights are observed to either last or first appear beyond the PBL, but it is much less evident that such behaviour could have resulted from the presence of a GNSS signal repeater in the hangar.

For any given case, the exact cause of erroneous geopotential height measurements remains impossible to formally ascertain. In essence, we are unable to distinguish the adverse impact of the GNSS repeater and/or metallic hangar from genuine sonde behaviours. The continuous distribution of error amplitudes also makes it impossible to set a threshold beyond which the origin of the problem can be identified with certainty.

In the spirit of transparency, the decision is therefore made not to drop any profile plausibly (negatively) affected by the presence of the GNSS repeater and/or the metallic hangar from the analysis¹. However, in the spirit of fairness, we also will not provide any performance assessment of the participating radiosondes for the geopotential height, pressure and wind (horizontal) speed/direction/vector variables within the PBL in Sections 10.1 and 11.1.

8.3 DATA AVAILABILITY STATISTICS

8.3.1 Radiosondes

The resulting, global flight statistics for each participating system are summarised in Table 8.3. For each system:

- at least 23 valid, individual profiles could be acquired over at least 19 distinct daytime flights, and
- at least 20 valid, individual profiles could be acquired over at least 17 distinct nighttime flights,

which is compliant with the statistical targets set for the field campaign (see Section 4.3.2). With the exception of the WxR-301D sonde, for which a technical issue with the ground system 1 prevented the acquisition of twin soundings after 29 August 2022:

- up to 5 but no less than 4 valid daytime twin soundings, and

¹The only exception is that of the clear-cut-case of the iMet-54 profile for flight F12 (system 1) mentioned in Section 8.2.3.

- up to 6 but no less than 3 valid nighttime twin soundings were secured for all the participating radiosondes.

Table 8.3: UAI 2022 field campaign global flight statistics, for all participating radiosonde systems. The flights F19, F20, F48, and F65 do not contribute to these statistics, as they are excluded in their entirety from the analysis.

	ATMS-3710	CF-06-AH	DFM-17	GTH3	iMet-54	iMS-100	M20	PS-B3	RS41	WXR-301D
Daytime										
Ascents with no data	1	0	0	3	1	1	0	0	0	3
Profiles with insufficient data	0	0	0	0	0	0	0	0	0	0
Profiles with unequivocally-invalid data	0	0	0	4	0	0	0	0	0	0
Operational mishap	0	0	0	0	0	0	0	0	0	0
Valid profiles	26	23	26	24	23	24	24	26	26	24
Valid flights (all)	21	19	21	20	19	19	19	21	21	23
Valid flights (twin)	5	4	5	4	4	5	5	5	5	1
Valid flights (mono)	16	15	16	16	15	14	14	16	16	22
Nighttime										
Ascents with no data	1	1	0	3	0	3	0	0	0	0
Profiles with insufficient data	0	0	0	1	0	0	0	0	0	1
Profiles with unequivocally-invalid data	0	0	0	3	1	0	0	0	0	1
Operational mishap	0	0	0	1	0	0	1	0	0	1
Valid profiles	20	23	21	21	23	21	23	22	22	20
Valid flights (all)	17	17	17	17	18	17	17	17	17	18
Valid flights (twin)	3	6	4	4	5	4	6	5	5	2
Valid flights (mono)	14	11	13	13	13	13	11	12	12	16

It must be stressed that the field campaign flight statistics presented in Table 8.3 are distinct from the actual success/failure rate of the different radiosonde models. Specifically, the numbers in Table 8.3 do not account for the fact that operators had to select (occasionally) multiple sondes before a functioning one passing all the manufacturer ground checks could be prepared for flight².

The GTH3 sonde showed the largest failure rate. In total, 28³ of these sondes failed to pass their manufacturer-designed ground-checks over the duration of the field campaign, and were rejected as a result. Tianjin Huayuntianyi Special Meteorological Sounding Tech. Co., Ltd. identified that a manufacturing problem was responsible for these failures (see Appendix G for details).

A total of 5 CF-06-AH sondes encountered problems during the ground check procedures (in all cases reporting an abnormally low measure of relative humidity) and were rejected as a result.

A total of 3 sondes were rejected following the ground-check and/or preparation procedures for each of the following systems: ATMS-3710, iMS-100, M20, and PS-B3.

Finally, 1 WXR-301D sonde was rejected following its ground-check. No sonde from the remaining systems (DFM-17, iMet-54, RS41) were found to fail their respective ground checks and/or preparation procedures over the course of the UAI 2022 field campaign.

²If no functioning radiosonde could be prepared in time, the flight was deemed "lost" for this specific sonde model, and is tagged accordingly in Table 8.2.

³An additional 2 sondes initially failed the manufacturer-designed ground check, but were eventually found to pass it.

8.3.2 Global Navigation Satellite System (GNSS) Integrated Water Vapour (IWV)

The UAI 2022 field campaign site of MOL-RAO hosts two GNSS receivers: LIN0, operated by GeoForschungsZentrum Potsdam (the German Research Centre for Geosciences) (GFZ) and LDB2, operated by Bundesamt für Kartographie und Geodäsie (the German Federal Agency for Cartography and Geodesy) (BKG). Both receivers are used to derive continuous IWV estimates ([Bevis et al., 1992](#); [Ning et al., 2016](#)). The GNSS IWV observations are required for the certification of any GRUAN site.

The development of a GNSS GDP is in its final stages of completion, but the products are still under development to fulfil the envisioned GRUAN requirements ([Wang et al., 2019](#)). Therefore, no reference is made to GNSS-derived IWV measurements in this report. The radiosonde flights acquired as part of the UAI 2022 field campaign represent only a very small fraction of all radiosonde GDP profiles available with simultaneous GNSS-GDP measurements in Lindenberg and other GRUAN sites worldwide. A detailed, exhaustive study of the statistical compatibility between radiosonde and GNSS GDPs is currently under discussion between the GRUAN Lead Centre and GRUAN task teams on GNSS and radiosondes, to which the interested reader is referred for further information.

8.3.3 Satellite overpasses

We provide in Appendix H the list of relevant satellite overpasses above MOL-RAO that most closely coincide with the different UAI 2022 field campaign flights. A small offset (both time- and distance-wise) between a given overpass and the associated UAI 2022 field campaign flight is only observed in a limited number of cases for any given satellite, as other factors primarily determined the launch schedule (see Section 4.3). This prevented us from performing a statistically robust and representative assessment of relevant satellite measurements for this report. We refer the readers interested to study this further to the radiosonde datasets provided in the UAI 2022 Supplementary Material (see Section 1.6).

9 DATA ANALYSIS METHODOLOGY

9.1 SCOPE

9.1.1 Geophysical variables

The following geophysical variables are being considered in our analysis (see Section 1.1):

- Geopotential height above mean sea level, in m
- Atmospheric temperature, in K
- Relative humidity, in %RH
- Atmospheric pressure, in hPa
- Wind (horizontal) direction, in ° clockwise from geographic North
- Wind (horizontal) speed, in m s^{-1}

All these (scalar) variables are directly reported in the official NetCDF files of GDPs. They are also reported by all the radiosondes participating in the UAII 2022, in their respective UAII-formatted MDP datafiles (see Section 9.5.2 and Appendix D for details).

The Lindenberg Remote Sensing Suite (LRSS) discussed in this report includes five remote sensing instruments¹, three based on active emission (wind profilers) and two on passive reception (Micro-Wave Radiometers - MWRs). Table 9.1 lists the geophysical variables retrieved from these instruments, alongside their geographical location in MOL-RAO (see Section 4.1.3).

Table 9.1: List of LRSS instruments, retrieved geophysical variables, and location

Instrument	Geophysical variable	Location (see Figure 4.4)
Microwave radiometer (MWR SMZ)	Atm. Temp. & Rel. Hum.	Roof of radiation measurement facility, at ⑥
Microwave radiometer (MWR MF)	Atm. Temp. & Rel. Hum.	Measurement field close to ⑨
Doppler wind lidar (WindLidar1)	Wind Dir. & Wind Speed	close to ⑨
Doppler wind lidar (WindLidar2)	Wind Dir. & Wind Speed	close to ⑨
Radar Wind Profiler (RWP) (High-mode, Low-mode)	Wind Dir. & Wind Speed	at ⑨

As will be discussed in Section 9.3, the OSCAR requirement uncertainty criterion (ORUC) used to assess the performance of radiosondes and remote sensing instruments in terms of wind (horizontal) measurements relies on the “wind (horizontal) vector”: an additional variable in our analysis, which can be easily assembled from a given pair of wind (horizontal) direction and speed measurements (see Appendix J.2.2). This variable implies the assessment of vector (instead of scalar) differences between a given upper-air instrument and the reference measurements.

9.1.2 Flight categories

The UAII 2022 field campaign flights are grouped in two categories \mathcal{C} : **day**, and **night** (see also Section 4.3.3). The decisive criterion, when assigning a given flight to one of these two categories, is as follows:

¹There are other remote sensing instruments being operated at MOL-RAO that are not being considered in this report, for different reasons: because they are not being operated a 24/7 basis (e.g. the Raman Lidar RAMSES), because they are prototypes in development (e.g. the broadband water vapour DIAL), or because they are providing data that is not relevant for a direct comparison with radiosondes (e.g. ceilometers and cloud radars).

A night flight has the Sun located below the horizon, from the perspective of the rig, at all times during the ascent.

This criterion implies that flights for which the RS41 GDP "g.Measurement.TimeofDay" attribute has the value "twilight" are treated as night flights in this analysis.

The day and night flights of the UAI 2022 field campaign are analysed and evaluated separately. In particular, radiosonde performance is reported individually for these two categories. This approach is motivated by the critical role that radiation corrections play for day flights (and radiative cooling corrections for night flights, respectively).

9.1.3 Atmospheric layers

The ORUCs used to assess the performance (see Section 9.3) of upper-air instruments are applicable to distinct atmospheric layers \mathcal{L} , including: the Planetary Boundary Layer (PBL), the Free Troposphere (FT), the Upper Troposphere / Lower Stratosphere (UTLS), and the Mid-Upper Stratosphere (MUS). Here, we formally define the vertical extent of these layers for the case of the UAI 2022 field campaign.

The Planetary Boundary Layer (PBL)

The PBL corresponds to the lowest part of the troposphere that is directly influenced by the presence of the Earth's surface, and in particular responds to forcing from the surface on a time scale of hours ([Stull, 1988](#)). Its upper-limit is known as the Planetary Boundary Layer Height (PBLH).

The Planetary Boundary Layer Height (PBLH)

The mean daytime and nighttime values of the PBLH over the course of the UAI 2022 field campaign are obtained from the high-resolution vertical profiles of temperature, relative humidity and wind from the operational radiosoundings performed on-site (in parallel with the UAI 2022 field campaign flights). These operational flights take place daily at 00, 06, 12 and 18 UTC.

Aggregated data from the 00/06 UTC and 12/18 UTC operational radiosoundings have been used to calculate the mean nighttime and daytime PBLH values of 350 m and 1270 m, respectively. The calculation is based on the Richardson Number (Ri) (see [Beyrich and Leps, 2012](#), for details).

We use the symbol z_1 to refer to the PBLH.

The Free Troposphere (FT)

Measurement points located above the PBLH and below the tropopause belong to the Free Troposphere (FT).

The tropopause

The original WMO definition of the (first) tropopause based on the temperature lapse-rate² ([WMO Bulletin, vol. IV, no. 4, 1957](#)) is as follows:

The first tropopause is defined as the lowest level at which the lapse rate decreases to 2 K km^{-1} or less, provided also the average lapse rate between this level and all higher levels within 2 km does not exceed 2 K km^{-1} .

Unfortunately, this definition is ambiguous with regards to the notion of *level*. In the case of modern radiosondes that provide individual temperature measurements at a frequency of 1 Hz

²The lapse-rate is the decrease of an atmospheric variable with height, the variable being temperature unless otherwise specified. Typically, the lapse-rate is the negative of the rate of temperature change with altitude change.

(equivalent to a vertical resolution of ~ 5 m), a strict application of this definition tends to underestimate the tropopause by ~ 1 km. This is due to the small vertical separation between the “levels” (\equiv the individual measurement points), which increases the noise associated with the lapse-rate measurements. The lapse-rate “trigger” criterion of 2 K km^{-1} is thus met significantly more often. The averaging of all subsequent lapse-rates then allows for a significant number of them to exceed the 2 K km^{-1} limit if enough others do not. In our experience, this leads to the systematic detection of the tropopause several hundred meters below its actual position, when using radiosounding temperature profiles at full vertical resolution.

The problems associated with the original WMO definition, when applied to modern datasets, are well known (see e.g. [Tinney et al., 2022](#), and references therein). As a result, the original WMO definition is typically adjusted to alleviate (some of) its limitations with respect to modern datasets. However, these adjustments are not always explicitly described.

For consistency with the GDPs, we adopt the following definition of the tropopause, used by the GRUAN Lead Centre:

Definition 2 *The first tropopause is the lowest level at which the lapse-rate decreases to 2 K km^{-1} or less, provided also **all the mean lapse rates between this level and all higher levels (computed from all sequential level pairs located within a given level interval) within 2 km do not exceed 2 K km^{-1} .***

The bold font highlights the deviations from the original WMO definition. We stress that in our analysis, we apply this algorithm to the temperature profiles of GDPs and CWSs at full vertical resolution, without smoothing. Doing so for all flights of the UAII 2022 field campaign, we find a median tropopause geopotential height of 12.0 km (see Figure 8.1).

We use the symbol γ to refer to the tropopause, and $\bar{\gamma}=12 \text{ km}$ to refer to the median tropopause during the UAII 2022 field campaign.

The Upper Troposphere / Lower Stratosphere (UTLS)

The UTLS region corresponds to the complex transition layer between the troposphere and the stratosphere, where a number of dynamical, chemical and micro-physical processes take place. The extent of this layer is not strictly defined: it roughly corresponds to the altitudes located within ± 5 km of the tropopause (see e.g. [Gettelman et al., 2011](#)). For the UAII 2022 field campaign, this corresponds to the geopotential height range of 7 km to 17 km.

We use the symbols \vdash and \dashv to refer to the UTLS lower- and upper-limit, respectively.

The Mid-Upper Stratosphere (MUS)

The MUS starts immediately above the UTLS and extends up to ~ 50 km. Given the maximum geopotential burst height of ~ 34 km reached during the UAII 2022 field campaign, all radiosonde measurements located above the UTLS belong to the MUS.

9.2 THE COMBINED WORKING MEASUREMENT STANDARDS

The fact that radiosonde GRUAN Data Products (GDPs) are fully characterised in their uncertainties (see Section 1.2) implies that:

- the statistical compatibility of their measurements can be unambiguously assessed, and
- where deemed compatible with one another, they can be combined in a way that accounts for their respective uncertainties.

We refer to the Combined Working measurement Standard (CWS) as the profile resulting from the combination of multiple GDPs that have flown together on a given rig. The full mathematical description of our CWS assembly strategy can be found in Appendix I, of which we provide a high-level summary here.

A unique CWS is assembled for each of the (valid) UAI 2022 field campaign flights. For each time step, the CWS is built from the weighted arithmetic³ average of the two GDP profiles of the flight. Each GDP measurement point is weighted by the inverse of its GRUAN-derived, total variance. Because the measurement uncertainties of the iMS-100 GDPs and RS41 GDPs differ from one another, one GDP will usually contribute more than the other to a given CWS profile. Specifically, the iMS-100 GDP tends to contribute most to the wind (horizontal) speed and direction CWS profiles; the RS41 GDP tends to contribute most to the temperature, relative humidity, geopotential height, and pressure CWS profiles. There are however several exceptions, in particular for the relative humidity, where some CWS profiles⁴ are most influenced by the iMS-100 GDP in the stratosphere. This is largely a consequence of the pre-flight SHC tests that can affect the GDP measurement uncertainty budget ([Sommer et al., 2022](#)).

Three distinct types of measurement uncertainties are associated to each CWS data point $\Omega_{e,i}$, for the time step i of the flight e : an uncorrelated (random) component, a spatially correlated (systematic) component, and a temporally correlated (systematic) component. These result from the full propagation of the corresponding iMS-100 and RS41 GDP measurement uncertainties through the equations used for the CWS assembly.

Not all these components are defined for all the variables. Only the daytime temperature measurements have a spatially correlated uncertainty. Wind speed and wind direction measurements have only an uncorrelated uncertainty. We refer the reader interested in the origin of these uncertainties to the iMS-100 GDP and RS41 GDP Technical Documents ([Sommer et al., 2023, 2022](#); [Kizu et al., 2018b](#); [Hoshino et al., 2022](#)) for further details.

A key feature of the UAI CWSs is that they are only assembled for the time steps where the underlying GDP measurements are *in agreement* with one another, according to the GRUAN principles ([Immler et al., 2010](#)). This corresponds to a statistical compatibility at the 2σ -level, which we assess using a Kolmogorov-Smirnov (KS) test (with a significance level $\alpha = 0.0455$) on the normalised difference between the GDP measurements at each time step. We refer the interested reader to Figures I.1 and I.2 in the Appendix I for an illustration of this GDP compatibility assessment scheme. Similar diagnostic plots are generated for all the UAI 2022 field campaign flights: they are made available to the interested reader as part of the UAI 2022 Supplementary Material.

We present in Figure 9.1 a view of the statistical agreement ratio between GDP measurements during the UAI 2022 field campaign, which is excellent overall. The (comparatively) lower minimal ratios visible in the PBL are a direct consequence of the smaller thickness of this layer, typically comprised of only 50 measurement points during the night. In a handful of profiles, cloud-induced sensor contamination leads to lower agreement ratios in the FT, UTLS and MUS for the relative humidity measurements, with up to 100% disagreement in the MUS for the (worst-case) flight F11. Inconsistencies in the GDP temperature measurements are driven by cloud-induced sensor contamination in the FT and the UTLS, whereas in the MUS they appear to be driven by nighttime infrared-cooling-correction mismatches above 27 km (prominently visible⁵ in F16 and F45, for example).

The resulting CWS profiles, assembled for all the valid UAI 2022 field campaign flights where

³For the wind (horizontal) direction, a weighted circular average is used instead.

⁴for example: F49

⁵in the dedicated CWS diagnostic diagrams included in the supplementary material

the GDPs are in statistical agreement, are shown in Figure 9.2. These reveal that the lowest tropopause temperature sampled during the UAII 2022 field campaign is $\sim -60^\circ\text{C}$. A wide-range of relative humidity values were observed below the tropopause, ranging from $\sim 5\% \text{RH}$ to $100\% \text{RH}$.

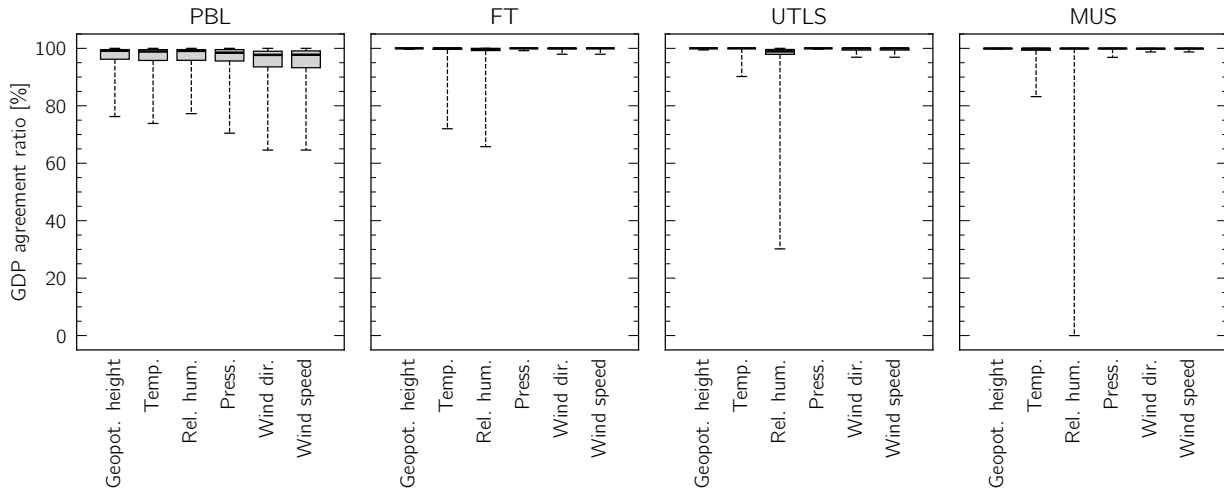


Figure 9.1: Distribution of the statistical agreement ratio of individual GDP measurements for all the valid UAII 2022 field campaign flights, for the different geophysical variables and atmospheric layers considered in this analysis. The black bars indicate the median value, the grey areas extend from the 25 percentile to the 75 percentile of each distribution, and the whiskers extend up to the minimum and maximum values. The agreement between GDP measurements is excellent for the vast majority of profiles.

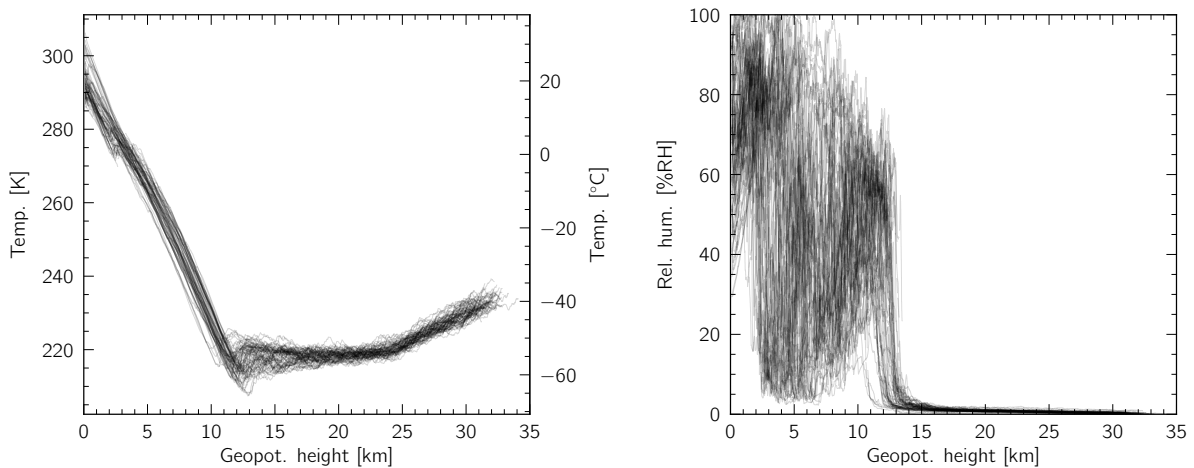


Figure 9.2: Left: CWS temperature profiles for all the valid flights of the UAII 2022 field campaign. Right: as for Left, but for the relative humidity.

9.3 ASSESSING UPPER-AIR INSTRUMENT PERFORMANCES WITH RESPECT TO OSCAR REQUIREMENTS

9.3.1 OSCAR requirement uncertainty criteria (ORUCs): definition and selection

The primary goal of the UAI 2022 field campaign is to assess the performance of upper-air instruments with respect to specific OSCAR requirements for the observation of physical variables in the atmosphere, in support of WMO Programmes and Co-sponsored Programmes.

OSCAR requirements, as defined in the dedicated online WMO documentation⁶, are:

expressed for geophysical variables in terms of 6 criteria: uncertainty, horizontal resolution, vertical resolution, observing cycle, timeliness, and stability.

These criteria are associated with a set of values for different levels, determined by experts:

- The “Threshold” level corresponds to “*the minimum requirement to be met to ensure that data are useful*”.
- The “Breakthrough” level corresponds to “*an intermediate level between “threshold” and “goal” which, if achieved, would result in a significant improvement for the targeted application. The breakthrough level may be considered as an optimum, from a cost-benefit point of view, when planning or designing observing systems*”.
- The “Goal” level corresponds to “*an ideal requirement above which further improvements are not necessary*”.

In this analysis, we focus on the OSCAR requirement uncertainty criterion (ORUC) to assess the performance of upper-air instruments. The duration of the UAI 2022 field campaign obviously prevents us from discussing the stability criterion. We also do not discuss the criteria related to the temporal and spatial sampling of the atmosphere, which are related to the implementation of operational soundings by NMHSs. It is clear, however, that these criteria can be very relevant in assessing the benefits of remote sensing instruments over radiosondes for specific application areas (see Section 11.2.3).

Terminology 1 We refer to the Threshold (T), Breakthrough (B), and Goal (G) levels of a specific ORUC for a given geophysical variable x over a given atmospheric layer \mathcal{L} as $\Theta_{x,\mathcal{L}}^T$, $\Theta_{x,\mathcal{L}}^B$, and $\Theta_{x,\mathcal{L}}^G$, respectively.

According to the OSCAR documentation:

The “uncertainty” criterion characterises the estimated range of observation errors on a given variable, with a 68 % confidence interval (1σ).

In a private communication on 2021-07-09, Erik Andersson (chair of the WMO Joint Expert Team on Earth Observing System Design and Evolution [JET-EOSDE] at the time) made the following clarification:

[One] should interpret the [OSCAR] uncertainty [criterion] as bias and random error, combined in the root-mean square sense.

The list of ORUCs used to assess the performance of upper-air instruments participating to the UAI 2022 is given in Table 9.2. They were extracted from the corresponding WMO website on 2023-05-31. They are associated to three geophysical variables of interest for the UAI 2022: atmospheric temperature, relative humidity, and wind (horizontal) vector. They stem from the following application areas within the Earth System Application Category “*Atmospheric Applications*”:

- 2.1 – Global Numerical Weather Prediction and Real-time Monitoring
- 2.2 – High-Resolution Numerical Weather Prediction
- 2.3 – Nowcasting / Very Short-Range Forecasting
- 2.5 – Atmospheric Climate Forecasting and Monitoring
- 2.8 – Aeronautical Meteorology

⁶Source: <https://space.oscar.wmo.int/observingrequirements>, accessed on 2023-02-10.

As of May 2023, no ORUCs exist for the other variables of interest in this analysis (geopotential height, atmospheric pressure, wind (horizontal) speed and direction).

Table 9.2: ORUC Threshold (T), Breakthrough (B) and Goal (G) values $\Theta_{x,\mathcal{L}}$ used to assess the performances of the upper-air instruments participating in the UAI 2022, grouped by application area, as a function of the associated geophysical variable x and atmospheric layer \mathcal{L} . The “High-Resolution Numerical Weather Prediction” and “Global Numerical Weather Prediction and Real-time Monitoring” application areas are shown together, on the basis that their ORUC values are almost always identical (with differences tagged accordingly). Extracted from the WMO OSCAR webpages on 2023-05-31.

Geophysical variable x	Atmospheric layer \mathcal{L}	Unit	$\Theta_{x,\mathcal{L}}^T$	$\Theta_{x,\mathcal{L}}^B$	$\Theta_{x,\mathcal{L}}^G$	OSCAR Id
2.8 - Aeronautical Meteorology						
Atmospheric temperature	PBL FT UTLS	K	5.0	3.0	2.0	15
Relative humidity	PBL	%RH ¹	10.0	7.0	5.0	21
Wind (horizontal) vector	PBL UTLS	m s ⁻¹	5.0	3.0	2.0	23
Wind (horizontal) vector	FT	m s ⁻¹	5.0	2.7	2.0	22
2.3 - Nowcasting / Very Short-Range Forecasting						
Atmospheric temperature	PBL	K	3.0	1.0	0.5	427
Atmospheric temperature	FT	K	2.0	1.0	0.5	428
Relative humidity	PBL	%RH ¹	10.0	5.0	2.0	704
Relative humidity	FT	%RH ¹	20.0	8.0	5.0	448
Wind (horizontal) vector	PBL UTLS	m s ⁻¹	5.0	2.0	1.0	452, 453
Wind (horizontal) vector	FT	m s ⁻¹	8.0	2.0	1.0	451
2.1 - Global Numerical Weather Prediction and Real-time Monitoring 2.2 - High-Resolution Numerical Weather Prediction						
Atmospheric temperature	PBL FT UTLS	K	3.0	1.0	0.5	255-257, 339-341
Atmospheric temperature	MUS	K	5.0 ²	3.0 ²	0.5 ²	254
Relative humidity	PBL FT	%RH ¹	10.0	5.0	2.0	302, 303, 378, 379
Wind (horizontal) vector	PBL UTLS	m s ⁻¹	5.0	3.0 ³	1.0	312, 313, 384, 385
Wind (horizontal) vector	FT	m s ⁻¹	8.0	3.0	1.0	311, 383
Wind (horizontal) vector	MUS	m s ⁻¹	10.0 ²	5.0 ²	1.0 ²	310
2.5 - Atmospheric Climate Forecasting and Monitoring						
Atmospheric temperature	PBL FT UTLS MUS	K	0.5 ⁴	0.25 ⁴	0.05 ⁴	778, 779, 780, 1016
Relative humidity	PBL FT	%RH	0.5 ⁴	0.25 ⁴	0.05 ⁴	789, 997
Relative humidity	UTLS	%RH	1.0 ⁴	0.5 ⁴	0.25 ⁴	790
Wind (horizontal) vector	PBL FT UTLS	m s ⁻¹	2.5 ⁴	1.5 ⁴	0.5 ^{4,5}	781, 988, 989
Wind (horizontal) vector	MUS	m s ⁻¹	5.0 ⁴	2.5 ⁴	0.5 ⁴	1017

¹ Converted from % g kg⁻¹ to %RH (see Appendix K)

² High-Resolution Numerical Weather Prediction: not applicable

³ High-Resolution Numerical Weather Prediction, for the PBL: 2.0

⁴ Converted from 2 σ to 1 σ level (see Sec. 9.3.1.2).

⁵ For the PBL: 0.25

9.3.1.1 *Relative versus specific humidity criteria*

ORUCs for relative humidity (in units of %RH) are defined only for the “Atmospheric Climate Forecasting and Monitoring” application area. The other application areas listed previously contain ORUCs for specific humidity instead. Furthermore, unlike all the other geophysical variables considered in this analysis, the ORUC values for specific humidity are expressed in relative terms rather than absolute ones by the WMO. This implies that the corresponding absolute requirements are (comparatively) more stringent for lower humidity measurements.

The UAI 2022 field campaign does not provide us with sufficient flights to sub-divide profiles in distinct humidity classes with sufficient individual sampling. Hence, we are not able to evaluate the performance of a given upper-air instrument against a relative ORUC value. Instead, we convert the original relative ORUC values for specific humidity into absolute ones for relative humidity. Although the digits are identical, the ORUC values specified in Table 9.2 are provided in units of %RH and differ fundamentally from the original WMO ones, which were provided in units of % g kg⁻¹. The conversion methodology is discussed in detail in Appendix K, to which we refer the interested reader for details.

We note that this conversion of ORUC values for specific humidity is conservative. An upper-air instrument that is not-fit-for-purpose (see Section 9.3.2) with respect to converted ORUC values for humidity listed in Table 9.2 is also not-fit-for-purpose with respect to the original ORUC values from the WMO.

9.3.1.2 *The “Atmospheric Climate Forecasting and Monitoring” application area*

The ORUC values associated to the “Atmospheric Climate Forecasting and Monitoring” application area were updated by the WMO in April 2023 to match the 2022 Global Climate Observing System (GCOS) Essential Climate Variables (ECVs) requirements ([GCOS-245, 2022](#)).

Unlike all other application areas, the ORUC values for this specific category are quoted at a 2σ level in the OSCAR webpages, and characterise “[...] *the dispersion of the values that could reasonably be attributed to the measurand*”. For the sake of consistency, we convert these to a 1σ level in Table 9.2 (and our analysis) by dividing them by 2, and treat them using the same root-mean-square-error-like approach (to be discussed in Section 9.3.2) applicable to all other application areas. This decision is motivated by the following argument.

Assessing climate-driven, long term variations in geophysical variables using a single system is not affected by its bias (provided this bias is stable over time, which is described by a separate 2022 GCOS criterion, see [GCOS-245, 2022](#)). However, if one is to combine multiple distinct systems into a global trend analysis, understanding and accounting for the relative bias of each system becomes paramount.

The duration of the UAI 2022 field campaign is evidently too short to assess the stability of the participating upper-air instruments over months or years. It does however enable us to assess their capacity of being part of global climate trend analysis alongside other systems. Doing so requires to account for both the dispersion and the absolute bias of their measurements, thereby motivating the root-mean-square-error-like approach of our analysis also for the ORUC values of the “Atmospheric Climate Forecasting and Monitoring” application area.

Essentially, the present analysis uses the UAI field campaign measurements and the ORUC values associated to the “Atmospheric Climate Forecasting and Monitoring” to assess the capacity of participating systems to make useful contributions to the study of climate-driven trends (for the geophysical variables of interest) when used in combination with other upper-air instruments.

9.3.2 The OSCAR requirement uncertainty criterion (ORUC) assessment function

The performance of radiosonde measurements are assessed against ORUC values by comparing a radiosonde's individual measured quantity values with the equivalent reference quantity values provided by the CWS, to determine the individual measurement errors. The resulting set of measurement errors provides the basis for a general characterisation of the systematic and random components of these errors, alongside an assessment of the uncertainty contributions associated with the measurements, and the propagation of these uncertainties to determine key properties of the overall distributions of measurement errors. In what follows, we describe this approach mathematically.

Terminology 2 We introduce $\Lambda_{\mathcal{C},\mathcal{L}}$, the ORUC assessment function of an upper-air instrument \mathcal{R} for a given scalar⁷ geophysical variable x assembled from a series of N field campaign flights in a given category \mathcal{C} (either day, or night), as:

$$\Lambda_{\mathcal{C},\mathcal{L}} = \sqrt{\frac{1}{J} \sum_{\substack{x_{e,i} \in \mathcal{L} \\ e \in \mathcal{C}}} (x_{e,i} - \Omega_{e,i})^2}, \quad (9.2)$$

where J is the total number of individual measurement points $x_{e,i}$ belonging to the atmospheric layer \mathcal{L} over the N flights in the category \mathcal{C} , and $\Omega_{e,i}$ the corresponding individual CWS measurement point for the profile e at the time step i .

Essentially, $\Lambda_{\mathcal{C},\mathcal{L}}$ is the root-mean-square of the individual measurement errors of a given upper-air instrument observed during the UAI 2022 field campaign, with the CWSs measurements acting as reference quantity values. The demonstration that $\Lambda_{\mathcal{C},\mathcal{L}}$ can be directly compared with ORUC values $\Theta_{x,\mathcal{L}}$ is given in Appendix J, to which we refer the interested reader for details.

One should note that the case for remote sensing instruments is slightly more complicated than outlined in Equation 9.2, on the basis that their synchronisation with the CWS is less straightforward than for radiosondes located on the same rig. These specificities will be discussed in Section 9.6.2.

A measurement uncertainty $\epsilon_{\mathcal{C},\mathcal{L}}$ is associated to $\Lambda_{\mathcal{C},\mathcal{L}}$. It stems from the individual CWS measurement uncertainties, and we refer the interested reader to Equation (J.10) for a detailed discussion of its derivation. In essence, $\epsilon_{\mathcal{C},\mathcal{L}}$ limits the resolution with which upper-air instrument performances can be evaluated using the UAI 2022 field campaign flight dataset. The following three scenarios are possible for any given upper-air instrument \mathcal{R} , flight category \mathcal{C} , and ORUC value $\Theta_{x,\mathcal{L}}$:

- Case 1: if

$$\Lambda_{\mathcal{C},\mathcal{L}} + k\epsilon_{\mathcal{C},\mathcal{L}} < \Theta_{x,\mathcal{L}}, \quad (9.3)$$

one can conclude, with a level of confidence k -sigma, that the upper-air instrument \mathcal{R} is **fit-for-purpose** with respect to the ORUC value $\Theta_{x,\mathcal{L}}$, for flights in the category \mathcal{C} .

- Case 2: if

$$\Lambda_{\mathcal{C},\mathcal{L}} - k\epsilon_{\mathcal{C},\mathcal{L}} > \Theta_{x,\mathcal{L}}, \quad (9.4)$$

one can conclude, with a confidence level of k -sigma, that the upper-air instrument \mathcal{R} is **not fit-for-purpose** with respect to the ORUC value $\Theta_{x,\mathcal{L}}$, for flights in the category \mathcal{C} .

- Case 3: if

$$\Theta_{x,\mathcal{L}} - k\epsilon_{\mathcal{C},\mathcal{L}} \leq \Lambda_{\mathcal{C},\mathcal{L}} \leq \Theta_{x,\mathcal{L}} + k\epsilon_{\mathcal{C},\mathcal{L}}, \quad (9.5)$$

one cannot conclude, with a confidence level of k -sigma, whether the upper-air instrument

⁷The expression of $\Lambda_{\mathcal{C},\mathcal{L}}^{\text{wvec}}$ for the wind (horizontal) vector variable is somewhat more complicated, in that it combines two distinct scalar variables – Wind (horizontal) speed and direction – to compute the modulus of the observed wind vector difference:

$$\Lambda_{\mathcal{C},\mathcal{L}}^{\text{wvec}} = \sqrt{\frac{1}{J} \sum_{\substack{x_{e,i} \in \mathcal{L} \\ e \in \mathcal{C}}} \left((x_{e,i}^{\text{wspeed}})^2 + (\Omega_{e,i}^{\text{wspeed}})^2 - 2x_{e,i}^{\text{wspeed}} \Omega_{e,i}^{\text{wspeed}} \cos(x_{e,i}^{\text{wdir}} - \Omega_{e,i}^{\text{wdir}}) \right)} \quad (9.1)$$

\mathcal{R} is fit-for-purpose or not, with respect to the ORUC value $\Theta_{x,\mathcal{L}}$, for flights in the category \mathcal{C} .

These different cases can also be described as a function of the *effective* confidence level k_{eff} :

$$k_{\text{eff}} = \frac{\Theta_{x,\mathcal{L}} - \Lambda_{\mathcal{C},\mathcal{L}}}{\epsilon_{\mathcal{C},\mathcal{L}}} \quad (9.6)$$

which leads to the following, formal interpretation:

Terminology 3 *The upper-air instrument \mathcal{R} is (not) fit-for-purpose with respect to the ORUC value $\Theta_{x,\mathcal{L}}$, for the flight category \mathcal{C} , with a statistical confidence level of $|k_{\text{eff}}|$ -sigma, if $k_{\text{eff}} > 0$ ($k_{\text{eff}} < 0$, respectively).*

The case 3 outlined in Equation (9.5) occurs when the absolute value of k_{eff} is less than a chosen significance level (typically 2).

9.4 DVAS: THE ANALYSIS SOFTWARE FOR THE UAI 2022

The `dvas` software (DOI: [10.5281/zenodo.8177527](https://doi.org/10.5281/zenodo.8177527)) was written by the UAI 2022 Project Team to handle the core data processing and analysis tasks associated with the UAI 2022 field campaign in an automated and reproducible manner. It takes the form of an open-source Python 3.11 package, developed on Github⁸ and released on the Python Package Index (PyPI). Specifically, `dvas` has been designed to:

1. ingest the MDP and GDP datafiles generated by radiosondes during the UAI 2022 field campaign (see Appendix D),
2. clean and synchronise the atmospheric profiles on a flight-by-flight basis (see Sections 9.5.1, 9.5.2 and 9.5.3),
3. assemble CWS profiles (see Section 9.2), and finally
4. compute the $\Lambda_{c,\ell}$ profiles for the participating radiosonde systems (see Section 9.3).

We shall not discuss the technical implementation of `dvas` here, nor provide explicit usage instructions, but instead refer the interested reader to the dedicated online documentation:

<https://meteoswiss.github.io/dvas>

Suffice it to say that the `dvas` package consists of two distinct modules⁹, which rely on an SQLite database to store and access the data as it is being processed.

As an open-source code, the algorithmic content of `dvas` can be freely inspected by the interested user. It is also possible to re-execute the exact processing steps of the UAI 2022 field campaign dataset presented in this document using `dvas` v1.1.0, with specific instructions available in the online documentation. The readers interested to do so should be aware of the processing time involved. On a 2021 MacBook Pro (16-inch) with 64 GB RAM and an Apple M1 Max CPU with 10 cores, processing of all the UAI 2022 field campaign daytime flights takes 62.5 hours (51.7 hours for the nighttime flights).

9.4.1 The `dvas` diagrams

Specific figures and diagrams are generated by several `dvas` processing steps. Altogether, the processing of the entire UAI 2022 field campaign dataset generates over 6000 individual figure files. These fall into 4 distinct categories:

- high-level flight overview diagrams,
- individual CWS diagnostic diagrams (which include Figures I.1, I.2 and I.3),
- δ “delta” diagnostic diagrams (which include Figure J.1), and
- Λ “big lambda” diagnostic diagrams (which include Figures 10.13 and 11.1).

Most of these figures are intended to inspect the details of specific profiles on a flight-by-flight basis. They are all made available to the interested reader as part of the UAI 2022 Supplementary Material. To facilitate their perusal, a dedicated web-based exploration platform¹⁰ is made available alongside the individual `.pdf` and `.png` files.

It should be noted that not all of the field campaign analysis figures included in this report were generated directly by `dvas`. For those that were not, custom scripts ingesting the `dvas`-generated NetCDF datafiles were (typically) used instead.

9.4.2 The `dvas` NetCDF datafiles

In addition to diagrams, the `dvas` code also creates NetCDF files:

⁸<https://github.com/MeteoSwiss/dvas>

⁹`dvas`, the core module which defines dedicated routines and classes; `dvas_recipes`, which assembles these into logical processing steps.

¹⁰We refer the interested reader to the usage instructions included in the UAI 2022 Supplementary Material.

- for each flight, one NetCDF file per sonde on the rig (including the reference ones), containing the cleaned and synchronised profiles,
- for each flight, one NetCDF file containing the CWS profile, and
- for each sonde model and flight category, one NetCDF file containing the $\Lambda_{c,c}$ profiles for each geophysical variable considered in this analysis.

These datafiles represent a unified and coherent dataset, that should facilitate reprocessing of the UAI 2022 field campaign data by individual users, without having to deal with the necessary metadata extraction or data homogenisation aspects detailed in Sections 9.5.2 and 9.5.3. As such, these datafiles should also facilitate any future reprocessing of the UAI 2022 field campaign dataset by users who cannot/do not wish to use the `dvas` Python package to do so.

9.5 RADIOSONDES

9.5.1 The GRUAN Data Product (GDP) datafiles

The creation process of GDPs is described in Section 4.3.10.1. The software designed to process the UAI 2022 field campaign data (*dvas*, see Section 9.4) is able to extract the GDP data directly from the original GRUAN NetCDF files. In particular, a number of small bugs and unexpected features in these GDP datafiles, discovered during the analysis of the UAI 2022 field campaign data, are automatically handled by *dvas* in the following manner:

- **IMS-100 GDP:**

- Valid horizontal wind speed and wind direction measurements with assigned Not a Number (NaN) or (exactly) zero values for the uncorrelated uncertainties are flagged as invalid and dropped from the analysis. On average, this affects (0.1 ± 0.1) % of the data points in a profile.
- Relative humidity measurements with NaN values but valid assigned uncertainties are flagged as invalid and dropped from the analysis. This affects on average (1.9 ± 6.9) % of the data points in a profile.

- **RS41 GDP:**

- measurement uncertainties are divided by 2, to convert the original coverage factor of $k = 2$ to $k = 1$, and
- temporal-uncertainty values of geopotential height set to NaN are replaced by the largest temporal-uncertainty value of the profile, in accordance with the official GRUAN guidelines for this GDP ([Sommer et al., 2022](#)). The mean occurrence rate of this correction is (0.06 ± 0.33) % of measurement points per profile.

The corrections applied to the IMS-100 GDP data are warranted by the following features that were identified in the version 2 of the data product:

- The first and last points in measured wind speed and wind direction profiles have an uncertainty with a value of exactly 0.
- A wind (horizontal) speed of exactly 0 m s^{-1} has an undetermined uncertainty (i.e. NaN).
- Wind (horizontal) direction uncorrelated uncertainties greater than 180° ($k = 1$) are masked with NaNs.
- Relative humidity measurements with a value $rh + \sigma(rh) < 0$ are masked with NaN, with $\sigma(rh)$ the associated total measurement uncertainty at $k = 1$.

9.5.2 The Manufacturer Data Product (MDP) datafiles

Manufacturers participating in the UAI 2022 were requested to have their respective radiosounding systems export sounding profiles as American Standard Code for Information Interchange (ASCII) text files with a specific format (see Appendix D for details). We refer to these files as Manufacturer Data Products (MDPs).

The data in these MDPs form the basis of the performance assessments of the different radiosonde systems. The *dvas* code has been specifically designed to read these files directly and ingest their content. Doing so automatically, however, requires dealing with a number of non-uniformities between the different MDPs.

A core requirement of the UAI 2022 ASCII data format is to provide vertical profile measurements with a time sampling of exactly 1 Hz: the sampling frequency of GDPs. This allows synchronising all the profiles of a given flight (see Section 9.5.3) without the need for any interpolation.

Two systems did not provide data files with a vertical profile sampling of exactly 1 Hz: the RS41 sonde, and the WxR-301D sonde. The RS41 system, that specifies measurement times with millisecond resolution, has irregular time steps that fluctuate around the value of 1 s. After discussion with representatives of Vaisala Oyj during the setup phase of the UAI 2022 field campaign, it was decided that time steps for the RS41 systems should be rounded to the nearest

second. The resulting rounding error is typically less than 0.1 s (and never larger than 0.15 s), which is equivalent to ~ 0.5 m given a nominal ascent rate of 5 m s^{-1} (typical for UAI 2022 field campaign flights, see Figure 8.1). This is less than the uncertainty of 0.5 s resulting from the assumption that profile measurements are synchronised between sondes on a given rig (see Section 9.5.3).

The WxR-301D system also specifies measurement times with millisecond resolution, but with an average time step smaller than 1 s (typically of the order of 0.97 s). After discussion with the representatives from Weathex during the setup phase of the UAI 2022 field campaign, it was decided that measurements from the WxR-301D system should be linearly interpolated onto a regular grid with fixed 1 s time steps, and this for all the geophysical variables of interest.

Other inconsistencies present in some of the MDPs include:

- missing time steps, that are automatically filled with NaN values by `dvas`,
- duplicate time steps, that are removed entirely from the analysis,
- decreasing time steps, that are removed entirely from the analysis,
- geometric altitudes instead of geopotential heights, that are converted to geopotential heights using the so-called “Mahoney proposition” (see Equation 12.10, Section 12.3.6 in [WMO-No.8-Vol.I, 2021](#)), assuming a fixed geodetic latitude of 52.21° North for the entire profiles, and
- wind speeds in knots, that are converted to m s^{-1} by `dvas`.

The MDPs subject to these inconsistencies are listed in Table 9.3.

Table 9.3: List of inconsistencies identified in MDPs and their associated corrective actions.

Inconsistency	Affected MDPs	Corrective action
Measurement sampling $\neq 1$ Hz	RS41	Time step rounding
	WxR-301D	Linear interpolation of profiles
Missing time steps	ATMS-3710, M20, PS-B3, RS41, WxR-301D	Filled with NaNs
Duplicate time steps	ATMS-3710	Removed from analysis
Decreasing time steps	PS-B3	Removed from analysis
Geometric altitudes	ATMS-3710	Converted to geopotential height
Wind speed in knots	DFM-17	Converted to m s^{-1}

We note that the atmospheric temperature measurements are converted from $^\circ\text{C}$ to K, for all MDPs, by adding +273.15 to the individual measurements. We extract the atmospheric pressure values measured *indirectly* (from the GNSS position, surface pressure, temperature, and relative humidity; see e.g. [Nash, 2015](#)) for all systems but one. The manufacturer of the ATMS-3710 system requested during the UAI 2022 field campaign that the pressure values derived *directly* from the in-built pressure sensor of the sonde be used and assessed instead.

The manufacturers were also asked to provide in the header of their MDP datafiles the absolute times of 1) the initial data point in the profile, 2) the balloon launch, and 3) the balloon burst. For all systems, the timestamp of the first datapoint is extracted directly from the first data row, with the following exceptions:

- for the DFM-17 and GTH3 sondes, the first timestamp is taken to be the same as the `Launch.TimeStamp` header keyword, and
- for the iMet-54 sonde, it is taken from the `Initial.TimeStamp` header keyword.

In addition:

- for the ATMS-3710 and M20 MDPs: the value of `Launch.TimeStamp` is incorrect. We used the timestamp of the first profile point (which is specified explicitly for these system) as the launch timestamp.
- for the WxR-301D MDPs: the `Burst.TimeStamp` value is not reliable, and was ignored.

9.5.2.1 Reprocessing of the wind direction measurements for the WxR-301D sonde

In the data analysis phase after the conclusion of the field campaign, Weathex contacted the UAI Project Leads about errors in several parameters in the MDP data files as a result of bugs in their data processing. One of the affected parameters concerned the wind direction; a faulty implementation of an averaging (smoothing) filter resulted in a 180° wind direction for winds coming from the north. Weathex argued that this error was introduced as a result of modifying their software to support the export of MDP datafiles in the prescribed UAI-specific data format, and requested permission to submit reprocessed data where this error was corrected.

This matter was discussed by the UAI Project Team, and it was decided to allow the submission of reprocessed data with only the wind direction data field corrected, under the condition that documentation of changes to the source code is provided to the Project Team.

Correction/reprocessing of the other, undisclosed, parameters in question was not allowed. The rationale for allowing the reprocessing of the wind direction data is that this is the result of a very obvious programming bug, and that correcting this bug does not constitute an unfair advantage with respect to the other participating manufacturers, because it will not result in further improvements of the data product. It was also deemed in the interest of the campaign to evaluate the system that is available on the market, i.e. to do the analysis based on data that is equal to the normal operational data of the Weathex system.

When inspecting the reprocessed wind direction profiles provided by Weathex, it was identified that for various flights the reprocessed profiles were significantly time-shifted compared to the original measurements. The cause of these time-shifts is unclear, but it is evident that it is related to the reprocessing procedure. The project leads informed Weathex of this fact, and subsequently 8 flights were processed again, yielding “twice-reprocessed” MDP datafiles. For these twice-processed flights the time-shifts were resolved, except for flight F59 (system 2).

Consequently, the UAI Project Leads decided to remove the WxR-301D profile of flight F59 from the analysis (this applies to all parameters in the data file). Accordingly, this flight is flagged as “invalid” in Section 8.2.3.

9.5.3 Profile synchronisation

The performance assessment of MDPs using CWSs, presented in Section 11.1.1, is based on the following core premise of the UAI 2022 data analysis:

Premise 1 *The measurements of all the sondes flying together on a given rig are synchronised.*

Strictly speaking, this statement is incorrect. Each sounding system operates independently from the others, and is entirely oblivious to them. However, all GDPs and MDPs provide profile measurements at a frequency of 1 Hz (either exactly, or nearly, as discussed in Section 9.5.2). This implies that for a given time step, the measurement from any given system will always be performed no more than ± 0.5 s apart from the measurements of all the other systems on the rig. This is equivalent to a (maximum) vertical offset of ~ 2.5 m in the spatial location of the sondes¹¹.

Adopting the Premise 1 is equivalent to ignoring this vertical offset between sondes. This can be scientifically justified on the basis that:

1. the relative offsets between sondes are random across the different campaign flights, and
2. the interpolation of profiles to sub-second time resolution would lead to undesirable (and unnecessary) loss of data quality.

Under the Premise 1, synchronising M MDPs and GDPs of a given flight only requires to identify a series of integer shifts $s_p \forall p \in [1; \dots; M]$.

All radiosonde systems that participated in the UAI 2022, MDPs and GDPs alike, are equipped with a GNSS receiver. Ideally, one would use the GNSS-derived timestamps of each measurement to derive *absolute* synchronisation shifts. In the case of the UAI 2022 field campaign flights, however, this is not possible because the measurement time stamps reported by several radiosonde models are inconsistent (see Section 10.1.1).

¹¹assuming a nominal ascent rate of 5 m s^{-1} , which is typical for the UAI 2022 field campaign flights (see Figure 8.1).

Therefore, for all radiosonde models but one, we rely on the geopotential heights measurements to identify the best *relative* synchronisation shifts between each profile of a given flight. We do this in a two step process. For a given flight, we first derive a robust initial guess s_p^0 for each profile, by syncing the measurement points closest to the geopotential height of 5000 m with each others. The RS41 GDP is used as the synchronisation reference profile, on the basis that it systematically contributes the most to the CWS profile of geopotential height (see Section 9.2).

To alleviate the impact of measurement noise on these initial synchronisation shifts, we refine them using the geopotential height measurements between 4000 m and 6000 m, as follows. We define the synchronisation function $S_p(i)$ for the sonde p at the time step i as:

$$S_p(i) = \left| 1 - \frac{h_{(\text{gdp})\text{RS41}}(i)}{h_p(i + s_p^0 + s_p^1)} \right| \quad \forall h_p(i), h_{(\text{gdp})\text{RS41}}(i) \in [4000 \text{ m}; 6000 \text{ m}] \quad (9.7)$$

where s_p^1 is the (integer) correction to the initial (integer) synchronisation shift s_p^0 for the profile p , and $h_p(i)$ the geopotential height measured by the system p at the time step i . The value of s_p^1 is chosen to minimise the score $\overline{S_p(i)}$, with $s_p^1 \in [-20; 20]$. We find that the uncertainty of this synchronisation scheme is $\pm 1 \text{ s}$ (1σ). It is limited by the fact that we restrict ourselves to integer shifts according to the Premise 1.

This synchronisation approach evidently requires the geopotential height measurements of the different sondes to be sufficiently accurate in the range of 4000 m to 6000 m (as any systematic error would translate in an erroneous synchronisation shift). We find this to be almost always the case, with the following exceptions¹²:

- DFM-17 sonde on flight F64 (system 1): this profile required the addition of a manual shift of -12 s to the value of $s_p^0 + s_p^1$, which was derived manually from an inspection of the temperature and relative humidity profiles with respect to those of the iMS-100 and RS41 GDPs. The use of UTC measurement times for synchronisation purposes is not possible for this system (see Section 10.1.1 for details).
- iMet-54 sonde on flights F51 (system 2) and F76 (system 2): as this system was found to display reliable measurement times systematically, these were used to synchronise all its profiles (for consistency's sake) against the measurement times of the iMS-100 GDP.

¹²whose origin is very plausibly found in the campaign-related geopotential height problems discussed in Section 8.2.5

9.6 REMOTE SENSING OBSERVATIONS

9.6.1 Lindenberg Remote Sensing Suite (LRSS): principles and limitations

The geophysical variables listed in Section 9.1 are retrieved from the LRSS's measurements along the troposphere and partially along the UTLS (e.g. for the high-mode RWP). The manufacturers provide recommendations to the users based on the technical specifications of the different remote sensing instrumentation composing the LRSS listed in Table 9.1 and the applications for which the instruments are best performing. Hereafter, we give an overview of the technical strengths and limitations of each LRSS system through different periods of the day, meteorological conditions and atmospheric layers \mathcal{L} . It shall be noted that, even though the solar radiation causes the background level to increase in the LRSS acquisition system, this increase has an almost flat response with respect to the flight category \mathcal{C} . In contrast to the CWS, the LRSS instrument do not suffer a significant increase of noise in the measured signal due to solar radiation. However, for the sake of keeping the same data analysis structure, the statistics of the REMI will also be separated into the flight categories \mathcal{C} .

Micro-Wave Radiometer (MWR):

For our statistical analysis we assess the level-2 products (operational retrieval), i.e. temperature and humidity retrievals from the Brightness Temperature (BT) measurements from the troposphere above the MWR during day and night. The deployed MWRs measure in scan- and zenith-mode through the PBL, FT and the first 3 km of the UTLS. The operational retrieval uses seven channels in the frequency bands around the water vapour absorption line at 22.235 GHz for water vapour profiling and seven channels within the 51.26 GHz to 58.00 GHz oxygen band for temperature profiling. The temporal resolution of the humidity and temperature profile retrieved from both MWR is 1 min using neural network inversion ([Cimini et al., 2006](#)). The temperature profile used for our analysis is a combination of two profiles, the "high" vertical resolution boundary layer profile and the "low" vertical resolution full tropospheric profile. The two profiles are glued together at 1200 m by applying a cubic spline fit. The vertical resolution is constrained by a weighted average over the atmospheric portion that contributes to the brightness temperature observed by the MWR. Across the layer 0 m to 2000 m, the vertical resolution varies from 25 m to 100 m and down to 300 m toward the top of the troposphere. The humidity profile spans the range 0 m to 10 000 m, likewise the temperature, the highest vertical resolution is within the PBL with 25 m and it decreases to 100 m and 300 m reaching the top of the troposphere. The operational retrieval rejects data with the rain flag activated according to the manufacturer's guidelines and makes no distinction between cloudy and clear sky.

Doppler Wind Lidar (DWL):

For our statistical analysis we assess the Lindenberg's operational retrieval of the profiles of mean horizontal wind speed and wind direction, as a variant of the Velocity Azimuth Display (VAD) retrieval method first described by [Browning and Wexler \(1968\)](#). All the information about the variant used in Lindenberg can be found in the articles by [Päschke et al. \(2015\)](#) and [Teschke and Lehmann \(2017\)](#). The fundamental variable "wind vector" is derived from the wind speed and wind direction using the VAD method outlined in Figure 9.3. The retrieval uses the Doppler signal from the scattering medium that, for a DWL, is represented by aerosols and cloud particles. Optically thick (liquid) clouds or fog significantly limit data availability as they strongly extinct the emitted laser radiation by the DWL. However, ice clouds are usually excellent lidar targets. Data from rainy skies can also be used provided that the signal is not fully extinct. In the period from August the 8th to September the 16th, 2022, both DWL measured continuously in a VAD setup at 75° elevation angle. The WindLidar1 performed measurements in the "50 m-TP" measurement mode, i.e. 50 m Line Of Sight (LOS) at 10 kHz Pulse-Repetition Frequency (PRF). The two DWL systems are based on the same measuring principle, but the pulse duration of the older WindLidar2 is almost twice as long as the WindLidar1. The LOS-resolution can be adjusted by the user for both instruments, but a fixed setup has been kept for the duration of the field campaign. For the WindLidar1, the sampled timeseries is binned into fixed intervals. A Fast Fourier Transform (FFT) within each interval is performed and the power spectral density are calculated as the absolute square of these individual FFTs. This restricts the available LOS-resolutions, but the operator can choose amongst 25 m, 50 m, 75 m or 100 m. Each resolution corresponds to a

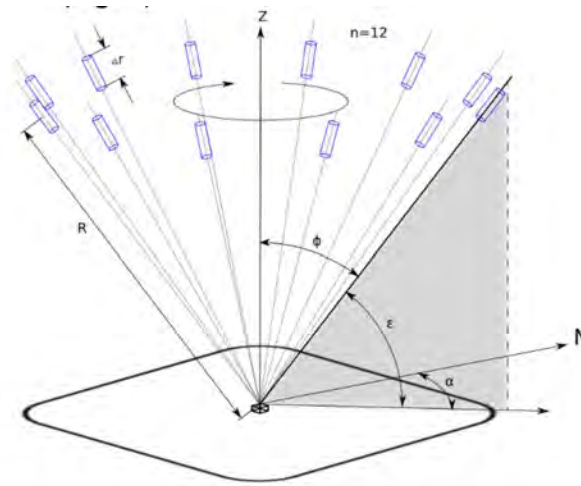


Figure 9.3: Scan geometry of a VAD with 12 directions. The coordinates α , ϵ , ϕ and r describe the position of the measurement volume. Adapted after Päsche et al. (2015).

different pulse length and a different PRF. The PRF parameter is different when “TP-mode” is used, even though the range resolution is the same.

Radar Wind Profiler (RWP):

The Lindenberg 482 MHz-RWP is a fully coherent pulsed Doppler Radar system with an Radio Acoustic Sounding System (RASS) component, it is operated using two measuring modes spanning the vertical ranges 500–9300 m in low mode and 5500–16 000 m in high mode (Lehmann, 2012). Both modes have been considered for our analysis to maximise the overlap with the UTLS region (High-mode) and to complement/compare the information brought by the DWL across the PBL and FT (Low-mode). The routine wind measurement is performed using a four-beam “Doppler Beam Swinging” configuration. For the retrieval of the mean wind vector, the (mean) wind field is assumed to be stationary and horizontally homogeneous over the sampled volume; therefore averaging is performed for about 15 min for each mode as detailed in Section 4.4. The vertical resolution and pulse width in low-mode and high-mode are, respectively, 150 m at 1 μ s and 330 m at 2.2 μ s.

The retrieved geophysical variables from the five remote sensing instruments of the LRSS are compared to the variables measured by the reference CWS (see Section 9.2). Based on the instruments’ technical specifications and the related literature, Table 9.4 shows, for each instrument of the LRSS, the Instrument Optimal Vertical Range (IOVR) along which each geophysical variable χ can be reliably retrieved. The variable χ is compared with the CWS over the integration time $\Delta time$, i.e. the time needed for the CWS to go through the range of altitudes R_χ Above Ground Level (AGL) at the ascent speed ν_{CWS} .

Table 9.4: For each instrument of the LRSS, for each retrieved variable χ , for each flight category C , the Instrument Optimal Vertical Range (IOVR) R_χ Above Ground Level (AGL) is shown along with the corresponding integration time $\Delta time$ at the ascent speed ν_{CWS}

Instrument	day/night	R_{temp}	R_{RH}	R_{WVECT}	R_{WS}	ν_{CWS}	$\Delta time$
MWR	day	0 – 2 km	0 – 2 km			5 ms^{-1}	400 s
	night	0 – 3 km	0 – 3 km			5 ms^{-1}	600 s
DWL	day			0 – 3 km	0 – 3 km	5 ms^{-1}	600 s
	night			0 – 3 km	0 – 5 km	5 ms^{-1}	1000 s
High-mode RWP	day			5.5 – 16.3 km	5.5 – 16.3 km	5 ms^{-1}	2100 s
	night			9 – 16.3 km	9 – 16.3 km	5 ms^{-1}	2100 s
Low-mode RWP	day			0.5 – 9.3 km	0.5 – 9.3 km	5 ms^{-1}	1740 s
	night			9 – 16.3 km	9 – 16.3 km	5 ms^{-1}	1740 s

In order to homogenise the comparison of the five remote sensing instruments with the CWS, the range has been set to 0–9000 m for both flight categories \mathcal{C} , with the exception of the High-mode RWP, which is compared to the CWS along the range of altitudes 5500–16 000 m. The integration time is then $\Delta time = 30$ min based on the balloon's ascent rate $\nu_{CWS} = 5 \text{ m s}^{-1}$ (rounded to 30 min). The atmospheric region spanning 0–9000 m embeds the PBL topped by the PBLH (z_l), part or the entire FT (depending on the height of the tropopause) and the first 2 km of the UTLS (z_{\pm}). For the High-mode RWP, the embedded atmospheric layers \mathcal{L} are the upper part of the FT and the UTLS.

9.6.2 Profile synchronisation

All the LRSS instruments provide Level-2 products (the operational products for each geophysical variable) with vertical grids, which are fixed over time and differ from the one of the CWS. The CWS has a constant 1 s temporal resolution that, based on the the ascent speed ν_{CWS} , translates into 5 m-resolution. Each Level-2 profile retrieved from the MWR, DWL and RWP have either a constant or variable vertical resolution, coarser than the CWS's. Table 9.5 shows the range of vertical resolutions of each instrument of the LRSS and the one selected for the field campaign over the range 0–16 000 m ASL.

Table 9.5: Vertical grid of the LRSS instruments

Instrument	vert. grid type	vertical res. [m AGL]
MWR	variable	25–300 m
DWL "WindLidar1"	constant	48 m
DWL "WindLidar2"	constant	48 m
RWP low-mode	constant	93 m
RWP high-mode	constant	314 m

When comparing the geophysical variable χ_{lrss} retrieved from the LRSS with the same geophysical variable χ_{cws} measured by the CWS at the height z , the value $\chi_{cws}(z)$ is measured instantaneously and represents the layer $\Delta z = 5$ m, while $\chi_{lrss}(z)$ represents a much wider spatial interval being the result of a longer average in time and space. In order to reduce the effect of the different temporal and space averaging, the CWS variables have been averaged in space over the layers $[z - \Delta Z_{lrss}/2, z + \Delta Z_{lrss}/2]$, where ΔZ_{lrss} is the vertical resolution shown in Table 9.5 and z is the grid point along the LRSS grid vector. Compared to a simple interpolation of the CWS geopotential height grid onto the geometric vertical grid at the exact level z , averaging over $[z - \Delta Z_{lrss}/2, z + \Delta Z_{lrss}/2]$ reduces the uncertainty of the comparison. In the approximation of a constant gravitational acceleration through the atmospheric layers \mathcal{L} , a 1 : 1 conversion has been applied between geopotential and geometric altitude.

9.6.3 The Remote Sensing Data Product (RSDP) datafiles

The data format of the LRSS products is NetCDF, and the data are integrated into daily files containing profiles with different integration time $\Delta time$. The DWL and the RWP daily NetCDF files count 48 profiles with $\Delta time = 30$ min (for the RWP 13 min low mode, 14 min high mode). The MWR daily NetCDF files count a maximum of 1440 profiles with $\Delta time = 1$ min. The LRSS data are generated continuously, 24h/7d and characterised by different quality levels depending on the occurring weather conditions. The LRSS data are filtered based on flags for rain and cloud presence and stored into daily RSDP files. The data used for the comparison with the CWS were selected from the RSDP over the time interval starting at the CWS official launch time, t_s , till $t_s + 30$ min. This means, 1 profile for DWL, 1 profile for the high-mode RWP, 1 profile for the low-mode RWP and 30 profiles for the MWR.

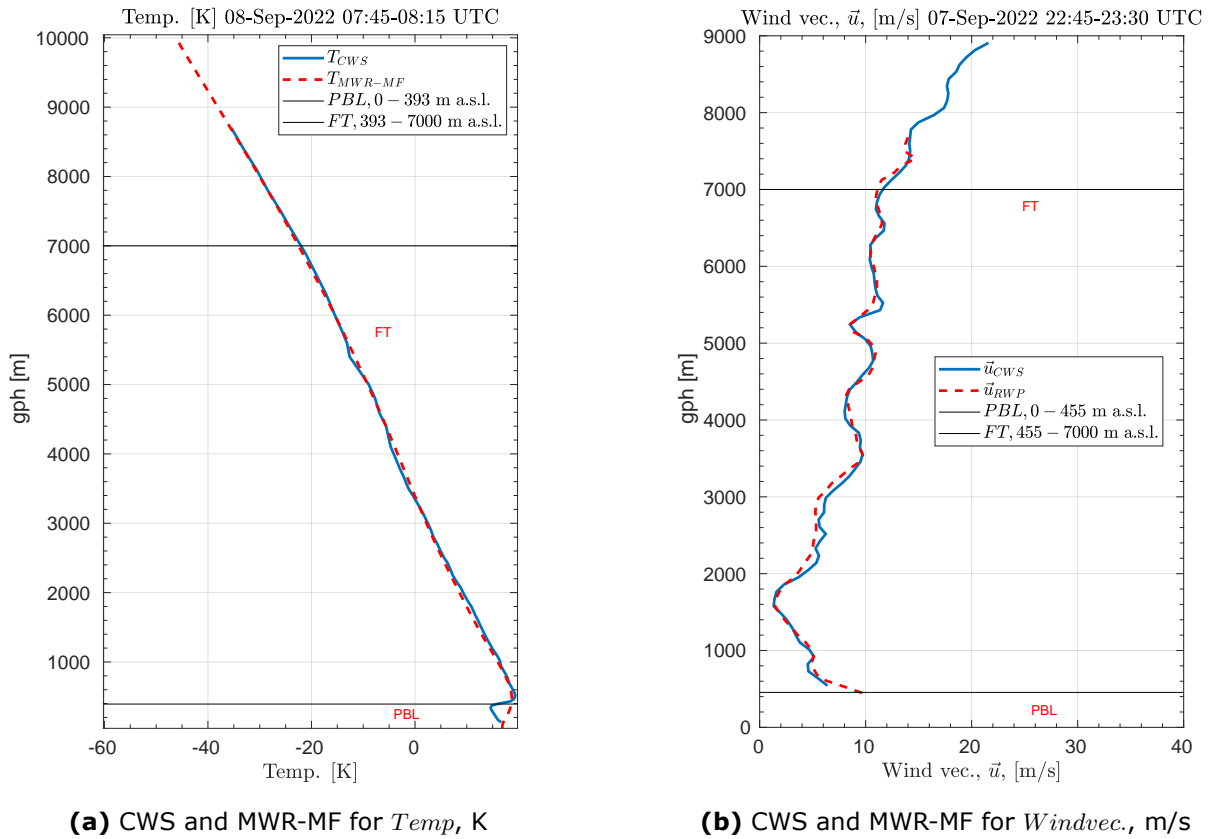


Figure 9.4: Synchronisation of the CWS and LRSS profiles for specific flight and geophysical variable

9.6.4 Software analysis for the REMote sensing Intercomparison (REMI)

The Data Visualization and Analysis Software (*dvas*) (see Section 9.4) is used to synchronise the radiosondes profiles with the GDPs, to construct the CWS and ultimately to compute the $\Lambda_{c,\mathcal{L}}$ profiles. The analysis software used for the UAII REMote sensing Intercomparison (REMI) is based on the same principles and logic of *dvas*. The Remote Sensing Software Analysis (RSSA) is MATLAB-based, it is built to read the Combined Working measurement Standard (CWS) NetCDF datafiles output from *dvas*, to synchronise them with the profiles of each geophysical variable retrieved from the LRSS (Section 9.6.2) and to calculate the $\Lambda_{c,\mathcal{L}}$ profiles for all valid flights of the UAII 2022. Figure 9.5 shows an example of synchronisation of the CWS with respect to the vertical grid of the MWR-MF, Figure 9.4a, and the low-mode RWP, Figure 9.4b, on the 8th and 7th of September.

The RSSA can be summarised in four main processing blocks, as outlined in Figure 9.5. The first block is the ingestion of the NetCDF data files from *dvas* and from LRSS. The second block is the synchronisation of all daytime and nighttime *dvas* profiles onto the LRSS vertical grid (for %RH in Figure 9.5). The third block generates the mean measurement error $\bar{\delta}_{c,\mathcal{L}}$ (night flight category in Figure 9.5) and the fourth block calculates the assessment function $\Lambda_{c,\mathcal{L}}$.

9.6.5 Limitations of the REMote sensing Intercomparison (REMI)

An important remark shall be done to allow a correct interpretation of the assessment results of the LRSS with respect to the OSCAR requirement uncertainty criterion (ORUC) presented in Section 10.2 and 11.2.2. The geophysical variables retrieved by the LRSS in the framework of the REMI undergo the same data analysis as for the Radio Sounding Intercomparison (RSI), i.e. they are compared directly to the CWS by means of the Remote Sensing Software Analysis (RSSA) (Section 9.6.4), which is based on the same statistical principles as *dvas*. However, there are two fundamental differences when the remote sensing or a radiosonde is compared to the CWS:

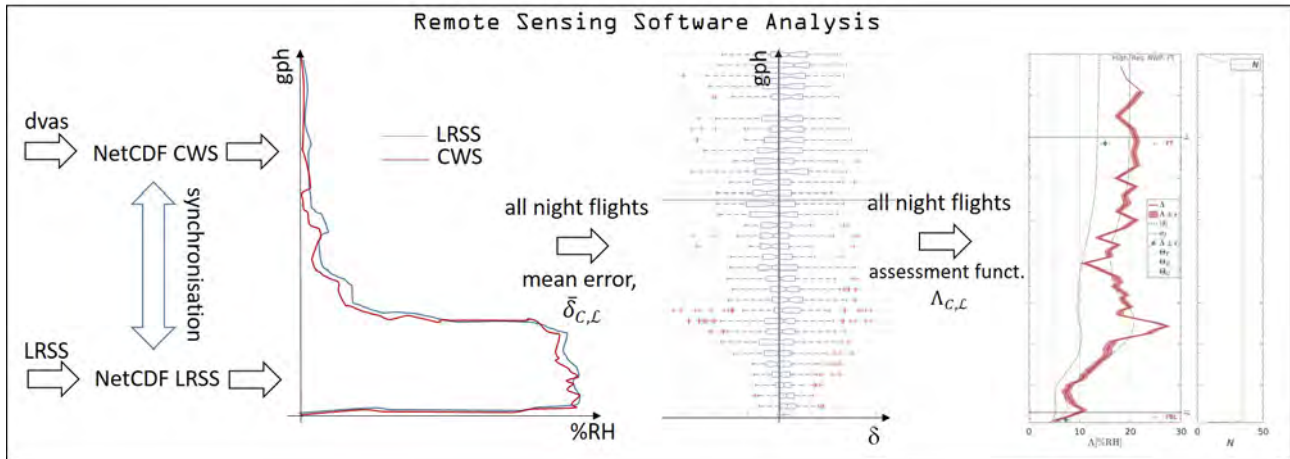


Figure 9.5: outline of the four main processing blocks of the RSSA for flight category $\mathcal{C} = \text{night}$

1. **spatial:** the geophysical variables measured by the CWS and retrieved from the LRSS measurements do not coincide in space because the CWS attached to the balloon drifts away from the LRSS.
2. **temporal:** the instantaneous profile values measured by the CWS are compared with the values retrieved from the LRSS instruments over a longer average in time and space (Section 9.6.2).

The radiosondes are compared against the CWS in a (drifting) Lagrangian reference framework, whereas the remote sensing systems provide data in a (static) Eulerian reference framework, namely in a strictly vertical column above the site. As a consequence, in addition to the instrumental correlated and uncorrelated uncertainty, for the LRSS, a further source of uncertainty adds to the retrievals due to the lack of temporal and spatial co-localisation of the drifting CWS. The total uncertainty of a LRSS instrument ($\Lambda_{\mathcal{C},\mathcal{L}}$) is then increased by the variance of the atmospheric humidity, temperature and horizontal wind in time and space. This additional uncertainty contribution cannot be quantified precisely for the retrieved geophysical variable. As a result, when the calculated value of $\Lambda_{\mathcal{C},\mathcal{L}}$ is too large to assess a LRSS instrument fit-for purpose with respect to a specific ORUC requirement, the two limitations above do not allow to retain the negative assessment with absolute certitude. On the contrary, when the assessment of a LRSS instrument is “fit-for-purpose” with respect to a specific ORUC requirement, the assessment is provided with absolute certitude. For this reason, and to ensure a fair interpretation of the assessment of the LRSS instruments, in Tables 11.5-11.7 only the “fit-for-purpose” assessment is provided. Consequently, Tables 10.7 and 10.8 provide the “lower-bound assessment”, i.e. the minimum-level of performance that the LRSS can ensure given the **spatial** and **temporal** limitations of the REMI.

10 RESULTS

10.1 RADIOSONDES

10.1.1 UTC measurement times

In our analysis, the radiosonde profiles from any given flight are synchronised with each other using their respective geopotential height measurements (see Section 9.5.3). A visual inspection of the synchronised profiles reveals that the uncertainty of this approach is typically of the order of 1 s (1σ). Each radiosonde also reports UTC times for their measurements. For each profile, it is thus possible to measure Δt , the UTC time offset of a given sonde, by comparing its UTC times to those of a (synchronised) reference profile. The `dvas`-processed NetCDF profile data files (included in the UAI 2022 Supplementary Material, see Section 9.4.2) contain an attribute named `"d.Metadata.first_timestamp"`. It reports the UTC time of the first profile point. It allows to compute the value of $\Delta t_{\mathcal{R}}$ for the radiosonde model \mathcal{R} , for any given UAI 2022 field campaign flight:

$$\Delta t_{\mathcal{R}} = \text{d.Metadata.first_timestamp}_{\mathcal{R}} - \text{d.Metadata.first_timestamp}_{\text{ref}}. \quad (10.1)$$

We present in Figure 10.1 the distribution of $\Delta t_{\mathcal{R}}$ for all the radiosondes that participated in the UAI 2022, computed with respect to the UTC times reported by the iMS-100 GDP.

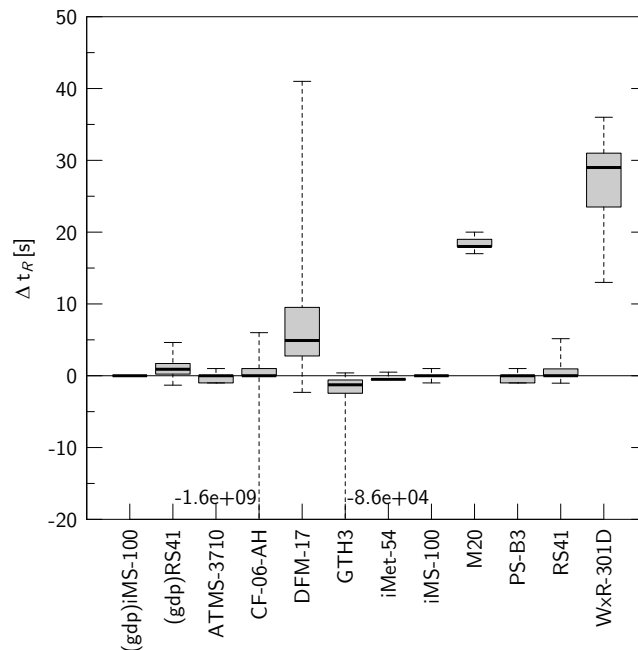


Figure 10.1: Distribution of $\Delta t_{\mathcal{R}}$ for each radiosonde model \mathcal{R} that participated in the UAI 2022, computed with respect to the iMS-100 GDP. For each sonde, the black bar indicates the median value, the grey area extends from the 25 percentile to the 75 percentile of the distribution, and the whiskers extend up to the minimum and maximum values. When those extend beyond the range of the diagram, the value of the extremum is indicated.

Five sonde models (ATMS-3710, iMet-54, iMS-100, PS-B3, and RS41) have a median $\Delta t_{\mathcal{R}}$ value of approximately 0 s, with a maximum error of ~ 5 s. Within the uncertainty of the adopted profile-synchronisation scheme, the UTC times reported by these sondes appear to be consistent with those of the iMS-100 GDP, used as reference.

The relative agreement of the reported UTC times is less good for the other systems. In particular:

- the CF-06-AH and GTH3 models have $\Delta t_{\mathcal{R}} \ll -20$ s for several profiles,

- the UTC times reported by the M20 model appear to be a systematic 18 s early, and
- the DFM-17 and WxR-301D models both show large errors and a non-zero median value for $\Delta t_{\mathcal{R}}$, of the order of 5 s and 27 s, respectively.

We also note that the UTC times of the RS41 GDP profiles appear to lie systematically ahead from those of the iMS-100 GDP by a few seconds.

The existence of these errors is surprising, given that all radiosondes are equipped with a GNSS receiver. Their exact cause remains uncertain to us¹, but we do note that, for the specific case of the M20 sonde, a lag of 18 s is strongly reminiscent of the number of leap seconds that have been added to UTC since the year 1980.

Irrespective of their origin, it is all these errors that lead us to rely on the geopotential height measurements of the different sondes to synchronise profiles that have flown together on a given rig (see Section 9.5.3). The resulting uncertainty of this approach, of the order of 1 s (1σ) for all the sondes, is better than the relative consistency of the UTC times reported from the different systems. Using the reported UTC measurement times to synchronise profiles would result in errors of several tens of meters for some systems. This would, in turn, unduly worsen the statistical assessment of the sonde performances for at least 5 models.

10.1.2 Launch detection

With the exception of the ATMS-3710² and GTH3³ models, all the radiosondes that participated in the UAI 2022 field campaign report in their MDP data files the time of the balloon launch, as detected (automatically) by them. We here briefly quantify Δt_{launch} , the error of these automated detections, with respect to that of the iMS-100 GDP⁴. In order to disentangle the error of the launch detection from that of the absolute times (discussed in Section 10.1.1), we compute Δt_{launch} in relative seconds from the first measurement point of the synchronised profiles, using the appropriate attributes provided in the dvas-processed NetCDF profile datafiles (accessible in the UAI 2022 Supplementary Material):

$$\Delta t_{\text{launch},\mathcal{R}} = (\text{d.Metadata.launch_timestamp}_{\mathcal{R}} - \text{d.Metadata.first_timestamp}_{\mathcal{R}}) - (\text{d.Metadata.launch_timestamp}_{\text{ref}} - \text{d.Metadata.first_timestamp}_{\text{ref}}). \quad (10.2)$$

A value of $\Delta t_{\text{launch},\mathcal{R}} > 0$ implies that the launch was detected by the sonde \mathcal{R} later than the iMS-100 GDP.

The distributions of $\Delta t_{\text{launch},\mathcal{R}}$ for all the radiosondes, including the reference ones, are shown in Figure 10.2. For all the systems that automatically measure a launch time, the start detections are typically within 2 s to 4 s from one another. On average, the WxR-301D is the system that last detects the launch, with a mean delay of 10 s. In a handful of cases, some systems detected launch some tens/hundreds of seconds too early. It is highly plausible that several of these “early starts” are a consequence of the campaign setup (see Section 8.2.5): they thus should not be considered representative of normal behaviour.

¹After reviewing this report ahead of its publication, two manufacturers made the following comments regarding Figure 10.1 to the UAI Project Team:

- Meteomodem confirmed that the observed behaviour of the M20 sonde is indeed related to the difference between GNSS and UTC time.
- Graw Radiosondes GmbH & Co. KG indicated that their “software uses the ground station computer as an absolute time reference [for the DFM-17 sonde]. [The time of the ground station computer] is normally synced to less than 1 ms by Network Time Protocol (NTP) [...]. [However,] no syncing via NTP was possible during the campaign [as a result of the ground station being disconnected from the world wide web (see Section 4.1.5)].”.

²The launch times provided by the ATMS-3710 sonde in the UAI-formatted MDP data files are incorrect, in that they appear to correspond to the burst times instead.

³The GTH3 sonde relied on a manual (operator-driven) launch detection.

⁴The iMS-100 GDP is taken as reference for consistency with Section 10.1.1. Using the RS41 GDP instead would lead to similar results.

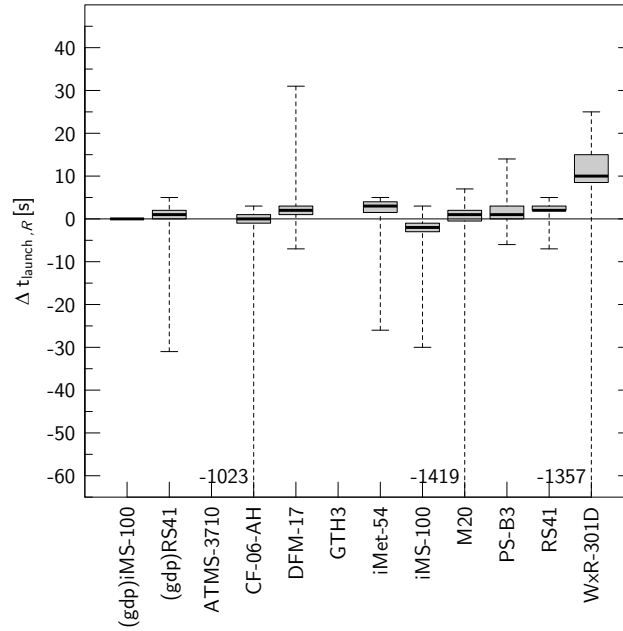


Figure 10.2: Distribution of $\Delta t_{\text{launch},\mathcal{R}}$ for each radiosonde model that participated in the UAI 2022, including references, computed with respect to the iMS-100 GDP launch detection. For each sonde, the black bar indicates the median value, the grey area extends from the 25 percentile to the 75 percentile of the distribution, and the whiskers extend up to the minimum and maximum values. No automatically-detected launch times are available for the ATMS-3710 and GTH3 sondes. Individual distributions ought to be compared to that of the RS41 GDP, which essentially represents the range of agreement between the two GDPs.

10.1.3 Missing data

Here, we briefly quantify the typical amount of missing data for the different radiosonde models that participated in the UAI 2022. We do so using the average number of missing (i.e. NaN) measurements between launch and balloon burst, assembled from all the valid field campaign flights. The averages, alongside the associated standard deviations, are presented in Table 10.1 for all sondes and geophysical variables.

Table 10.1: Average number of missing measurement points, and associated standard deviation, in %, reported by the different radiosonde models participating in the UAI 2022, measured over the valid profiles acquired during the field campaign by each system between balloon launch and burst.

	Temp.	Rel. humidity	Press.	Geopot. height	Wind dir.	Wind speed
ATMS-3710	03.6 ± 14.4	03.6 ± 14.4	03.6 ± 14.4	03.6 ± 14.4	03.6 ± 14.4	03.6 ± 14.4
CF-06-AH	02.4 ± 06.7	02.4 ± 06.7	01.2 ± 04.6	01.2 ± 04.6	01.2 ± 04.6	01.2 ± 04.6
DFM-17	00.2 ± 00.3	00.3 ± 00.5	00.2 ± 00.3	00.2 ± 00.3	00.2 ± 00.3	00.2 ± 00.3
GTH3	00.1 ± 00.1	00.1 ± 00.1	00.1 ± 00.1	00.1 ± 00.1	00.1 ± 00.1	00.1 ± 00.1
iMet-54	01.7 ± 10.0	01.7 ± 10.0	01.7 ± 10.0	01.7 ± 10.0	01.7 ± 10.0	01.7 ± 10.0
iMS-100	00.4 ± 01.6	00.4 ± 01.6	00.4 ± 01.6	00.4 ± 01.6	00.4 ± 01.6	00.4 ± 01.6
M20	00.4 ± 01.4	00.4 ± 01.4	00.4 ± 01.4	00.4 ± 01.4	00.4 ± 01.4	00.4 ± 01.4
PS-B3	01.6 ± 03.6	72.5 ± 02.6	01.6 ± 03.6	01.6 ± 03.6	01.9 ± 03.7	01.9 ± 03.7
RS41	00.1 ± 00.1	00.1 ± 00.1	00.1 ± 00.1	00.1 ± 00.1	00.1 ± 00.1	00.1 ± 00.1
WxR-301D	15.0 ± 25.8	15.0 ± 25.8	15.0 ± 25.8	15.0 ± 25.8	15.0 ± 25.8	15.0 ± 25.8

The number of missing measurements for the majority of the sondes and variables is small. For a typical profile of 6000 points, a loss rate of 0.1 % corresponds to 6 missing points. The majority of these are related to mismatches in the launch and/or burst detection.

Some sonde models have a larger amount of missing data on average. The data losses for all these models are comprised of both temporary gaps and definitive connectivity interruptions prior to burst. The (comparatively) larger standard deviations associated to these measurements indicate that the loss of data is however not systematic: some flights are subject to data losses, while others are not. For example, if a sonde stops recording data half-way through the ascent for a single profile out of forty, the resulting mean data loss will be (1.3 ± 7.8) %.

One must note that the PS-B3 radiosonde intentionally masks relative humidity measurements when the ambient atmospheric temperature falls below -40 °C, as the relative humidity sensor has not been characterised below this value as of yet. Under the atmospheric conditions of the UAI 2022 field campaign, measurements were typically reported up to a geopotential height of 10 km by this sonde model, resulting in 72 % of missing measurements of relative humidity per flight, on average. Interestingly, the temperature inversion in the stratosphere implies that for certain flights, the PS-B3 radiosonde does report a handful of relative humidity measurements shortly before balloon burst, above 30 km. This behaviour is clearly visible in the corresponding $\Lambda_{c,L}$ diagnostic diagrams (see Section 10.1.5 and Figures L.101 & L.102 in Appendix L).

10.1.4 BUFR files

In addition to the MDP datafiles in ASCII format, all manufacturers were required to provide their ascending profiles in Binary Universal Form for the Representation of meteorological data (BUFR) format. Some manufacturers provided both ascending and descending BUFR files, and all are encouraged to do so operationally. However, only the required ascending BUFR data are analysed here. The WMO has defined two templates for reporting radiosonde profiles in BUFR format: 3 09 052 and 3 09 057. The latter is capable of reporting pressure and geopotential height with higher precision, and stations are encouraged to make use of it if it is available at their site. For the analysis here, no distinction was made between these two templates. When files using both templates were provided, we only used the more recent template 3 09 057.

The BUFR format is a table-driven format, for which the underlying tables are updated regularly. The structure of BUFR files is defined in the WMO Manual on Codes ([WMO-No.306, 2022](#)). Manufacturers used different master table versions ranging from version 14 from March 2010 to version 34 from May 2020.

We analyse the BUFR data for correct information and consistent representation of the data contained in the corresponding MDP datafiles. We analyse all profile parameters, but restrict the analysis of metadata parameters to those which are essential to describe the instrument mode that has been launched as well as the location and time of the launch. These fields are the minimum of metadata required to properly assimilate the data profile in a numerical model. We do not validate the proper coding of the extended vertical sounding significance flags even though we did notice some differences between the manufacturers.

The ATMS-3710, DFM-17, GTH3, iMet-54, iMS-100, PS-B3, and RS41 systems report data with a resolution of 1 s in BUFR. The M20 system reports data with a resolution of 2 s. The WxR-301D system used an incorrect time stamp, and the CF-06-AH system generated unusable BUFR files.

Relative humidity and dewpoint temperature showed disagreements between BUFR and MDP datafiles for several manufacturers. These inconsistencies are also present in the MDP datafiles that provide both these variables. Relative humidity is measured directly by the current radiosonde technology, whereas dewpoint temperature is calculated from it using a formulation of the saturation vapour pressure over liquid water. All manufacturers specified the vapour pressure equation they used. The inconsistency is negligible near the surface and increases in magnitude with altitude. In the upper troposphere, this inconsistency exceeds typical measurement uncertainties and can reach more than 10 %.

Although it is difficult to know the source of the problem, it is possibly related to the inverse of the vapour pressure equation that is required to calculate the dewpoint temperature. To convert between the two, the vapour pressure equation and its inverse need to be known. By definition of the WMO, dewpoint temperature, not relative humidity, is coded in BUFR files and, therefore,

remains an error-prone quantity. Manufacturers whose systems show this inconsistency should review their calculations.

Table 10.2 presents an overview of the coding and processing issues that were identified, which are described in detail below.

Using BUFR files in the data assimilation of numerical weather centres requires correct metadata and profile data. Incorrect data may at best be rejected and in worse cases may cause undesirable biases in forecast products.

Operators of sounding systems generating BUFR files are strongly encouraged to verify proper coding of all data and metadata to minimise potential problems that users of these data may encounter.

ATMS-3710 - Azista Industries Pvt. Ltd.

The BUFR files generated by the ATMS-3710 system contain numerous issues and would not be useful for data assimilation:

- The date and time of launch is the same in all files and months off the true launch date.
- The station ID is incorrectly listed as 42369 (instead of 10393).
- The coordinates of the launch site places the sounding in India.
- The elevation of the launch site was set to 274 m.
- The radiosonde model was incorrectly identified as that from a different manufacturer.
- The radiosonde serial number is missing.
- The timestamp of the profile data is not relative to launch and both BUFR and MDP datafiles include substantial amounts of pre-launch data.
- There is a small difference ($<1\%$ RH) between the humidity in the BUFR file and the MDP file.
- The wind speed in the BUFR file is in knots instead of the expected m/s.
- The profile contains only static position data, not a trajectory.

CF-06-AH - Aerospace Newsky Technology Co., Ltd.

The BUFR files generated by the CF-06-AH system during the campaign contain only section 1 and neither metadata nor profile data relating to the radiosounding. This is due to a misconfiguration of the sounding system, which was not noticed during the campaign.

The manufacturer provided reprocessed BUFR files for several soundings during the review of this report, which were properly coded. These files indicate the radiosonde model as "Beijing Changfeng CF-06".

In these files the radiosonde serial number is missing and the relative humidity in the stratosphere is clipped at 1% RH. Furthermore, the time stamp is encoded 50 s later than that in the MDP data file.

DFM-17 - Graw Radiosondes GmbH & Co. KG

The BUFR files generated by the DFM-17 system contain a few issues:

- The seconds of the launch time are truncated.
- The station ID is coded incompletely. The WMO Block Number is missing; however, the WIGOS local identifier contains the complete station ID.
- The humidity data in the BUFR file is smoothed more than those in the MDP file and are inconsistent with the MDP files (see comment above).

Table 10.2: Overview over the quality of BUFR files generated by all manufacturers that participated in the UAI 2022. The × symbol indicates a serious problem that makes this parameter (and potentially the entire sounding) useless. The ~ symbol indicates a missing parameter or a minor issue, which is unlikely to cause problems in the data assimilation. The symbol ✓ indicates that no issue was identified.

Parameter	ATMS-3710	CF-06-AH	DFM-17	GTH3	iMet-54	iMS-100	M20	PS-B3	RS41	WXR-301D
Metadata										
Date and time	×	×	~	✓	✓	✓	✓	✓	✓	×
Station ID	×	×	~	×	✓	✓	✓	×	✓	×
Station coordinates	×	×	✓	✓	✓	✓	~	✓	✓	✓
Elevation	×	×	✓	×	✓	✓	✓	✓	✓	~
Radiosonde model	×	×	✓	~	✓	✓	✓	~	✓	×
Serial number	~	×	✓	~	~	✓	✓	✓	✓	~
BUFR table version	14	14	33	14	34	32	18	21	31	21
Profile data										
Time stamp	×	×	✓	✓	✓	✓	✓	~	✓	×
Pressure	✓	×	✓	✓	✓	✓	✓	✓	✓	✓
Temperature	✓	×	✓	✓	✓	✓	✓	✓	✓	×
Humidity	~	×	~	~	~	~	~	~	✓	×
Wind speed	×	×	✓	~	✓	✓	✓	✓	✓	×
Wind direction	✓	×	✓	~	✓	✓	✓	✓	✓	✓
Latitude, longitude	×	×	✓	✓	✓	✓	✓	✓	✓	×

GTH3 - Tianjin Huayuntianyi Special Meteorological Sounding Tech. Co., Ltd.

The BUFR files generated by the GTH3 system contain several issues:

- The station is coded as mobile station without WMO block and station number. It uses the identifier `Lindenber` in the primary system and `SUDAN` in the secondary.
- The elevation of the launch site is set to 0 m.
- The radiosonde model coded in the files is slightly different than the model used.
- The radiosonde serial number is missing.
- Relative humidity uses a lower resolution than in the MDP data files. BUFR files encode dewpoint temperature, which was most likely calculated from integer values of relative humidity.
- In several soundings, the launch time is correct, but the launch date is off by one day.

iMet-54 - Diel Met Systems (Pty) Ltd. trading as InterMet

The BUFR files generated by the iMet-54 system contains only two minor issues:

- The radiosonde serial number is missing.
- The relative humidity in the stratosphere is clipped at 1 %RH.

iMS-100 - Meisei Electric Co., Ltd.

The BUFR files generated by the iMS-100 system only exhibit an inconsistency in relative humidity (see comment above). In the upper troposphere, the difference is up to 9 %RH.

M20 - Meteomodem

The BUFR files generated by the M20 system contain only two minor issues:

- The launch location shows a large scatter around the true launch point.
- The relative humidity in the BUFR file is less smoothed than that in the MDP datafile and is inconsistent (see comment above). In the upper troposphere, the difference is up to 6 %RH.

RS41 - Vaisala Oyj

The BUFR files generated by the RS41 system do not show any inconsistencies.

PS-B3- Vikram Sarabhai Space Center, Indian Space Research Organisation

The BUFR files generated by the PS-B3 system contain four issues:

- The station ID is incorrectly coded as 43373 (instead of 10393).
- The radiosonde model is missing.
- The time stamp of the profile data is about 2 s off from the time stamp in the MDP datafiles.
- The relative humidity is set to missing starting well below the tropopause. This is consistently done in the MDP datafile.

WxR-301D - Weather

The BUFR files generated by the WxR-301D system contain numerous issues and would not be useful for data assimilation:

- The launch date and time are months earlier than the true launch date.
- The station ID is incorrectly coded as 47257 (instead of 10393).
- The elevation of the launch site is set to 112 m.
- The radiosonde model is incorrectly coded as Jin Yang RSG-20A.
- The radiosonde serial number is missing.
- The time stamp of the profile is in integer minutes, not seconds.
- The temperature data appear to contain uncorrected and unfiltered raw data.
- The humidity data appear to contain uncorrected and unfiltered raw data.
- The wind speed is inconsistent with the MDP datafiles and too low by about a factor of 2.
- The latitude and longitude displacements in the profile data have sign errors, which have the trajectory going into the opposite direction.

10.1.5 OSCAR requirement uncertainty criterion (ORUC) assessment profiles Λ

We present in Tables 10.3, 10.4 and 10.5 the values of the ORUC assessment function $\Lambda_{c,\mathcal{L}} \pm \epsilon_{c,\mathcal{L}}$ (see Section 9.3.2) together with those of the mean measurement error $\bar{\delta}_{c,\mathcal{L}}$ and standard deviation of the individual measurement errors $\sigma(\delta)_{c,\mathcal{L}}$ (see Section 10.1.5.2) for all the atmospheric layers \mathcal{L} and flight categories \mathcal{C} considered in this analysis, and for all the radiosondes that participated in the UAI 2022. These measurements form the basis of our assessment of the different systems with respect to specific ORUC values, that will be discussed in Section 11.1.1. The Figures 10.3 to 10.12 provide a visual counterpart to these Tables, to aid in their perusal.

There are other sources of performance criteria for upper-air geophysical variables beside OSCAR (for example: [WMO-No.8-Vol.I, 2021](#)). Some readers of this report may also have their own sets of criteria. The Tables 10.3 to 10.5 are thus also meant to enable the assessment, by interested readers, of the performance of the systems that participated in the UAI 2022 according to other criteria than those discussed in Section 11.1.1: provided, of course, that those alternative criteria are based on a metric comparable to that of the ORUCs (see Section 9.3).

The Table 10.5 reveals that the amplitude of the ORUC assessment function measurement uncertainty $\epsilon_{c,\mathcal{L}}$ for the wind (horizontal) speed, direction and vector variables is systematically (very) small. This is a direct consequence of the fact that no correlated uncertainties are associated with the GDP measurements of the wind (horizontal) speed and direction. The value of $\epsilon_{c,\mathcal{L}}$ for all the other geophysical variables is affected by both correlated and uncorrelated uncertainties.

This document does not provide values of $\Lambda_{c,\mathcal{L}}$ for the geopotential height, pressure and wind (horizontal) speed, direction & vector variables in the PBL. As discussed in Section 8.2.5, several profiles were likely affected by the specific campaign setup in this atmospheric layer, such that the observed performances for these geophysical variables are very plausibly not representative of normal sonde behaviour.

The performances of the different sondes is being assessed separately for the daytime and nighttime categories, and this for every geophysical variable, including those that one may not expect to be affected by the diurnal cycle. It is paramount to remember here that *correlation does not necessarily imply causation*. In the present case, a difference between the daytime and nighttime performances of a given sonde does not necessarily imply that it was caused by the presence (or not) of the Sun in the sky. It merely indicates that a different behaviour was observed between the two sets of profiles. Understanding the actual origin of any daytime/nighttime differences visible in Tables 10.3 to 10.5 requires a dedicated inspection of the underlying data, for example by means of the so-called $\Lambda_{c,\mathcal{L}}$ diagrams that we shall introduce in the next Section.

Table 10.3: Values of the ORUC assessment function $\Lambda_{C,\mathcal{L}}$, its measurement uncertainty $\epsilon_{C,\mathcal{L}}$, the mean measurement error $\bar{\delta}_{C,\mathcal{L}}$ and the standard deviation of the individual measurement errors $\sigma(\delta)_{C,\mathcal{L}}$ (organised spatially as follows: $\Lambda_{\sigma(\delta)}^{\bar{\delta}} \pm \epsilon$) measured from the valid flights of the UAI 2022 field campaign, for the atmospheric temperature and relative humidity measurements, for all participating radiosondes, as a function of the flight category C (day, or night) and atmospheric layer \mathcal{L} (PBL, FT, UTLS, or MUS). Fitness-for-purpose, given a certain ORUC value $\Theta_{x,\mathcal{L}}$, can be assessed directly using these values following Equations 9.3 to 9.5. These values also indicate whether a given performance is driven by systematic or random errors (see Section 10.1.5.3).

		Atmospheric temperature [K]				Relative humidity [%RH]			
		PBL	FT	UTLS	MUS	PBL	FT	UTLS	MUS
ATMS-3710	Day	0.67 ^{+0.57} _{0.35} ± 0.09	0.64 ^{+0.09} _{0.63} ± 0.01	0.89 ^{-0.12} _{0.88} ± 0.02	2.55 ^{+2.00} _{1.59} ± 0.10	11.63 ^{-10.26} _{5.48} ± 0.82	26.01 ^{-21.43} _{14.75} ± 0.89	23.40 ^{-13.76} _{18.92} ± 0.71	0.74 ^{+0.06} _{0.74} ± 0.07
	Night	0.34 ^{+0.07} _{0.33} ± 0.02	1.40 ^{-1.01} _{0.98} ± 0.07	2.67 ^{-2.41} _{1.14} ± 0.09	4.65 ^{-4.39} _{1.54} ± 0.09	5.50 ^{-2.49} _{4.90} ± 0.36	21.66 ^{-16.03} _{14.56} ± 0.84	21.02 ^{-9.38} _{18.81} ± 0.64	3.62 ^{+1.99} _{3.02} ± 0.16
CF-06-AH	Day	0.14 ^{-0.09} _{0.12} ± 0.06	0.14 ^{+0.03} _{0.13} ± 0.02	0.17 ^{+0.06} _{0.16} ± 0.03	0.28 ^{-0.02} _{0.28} ± 0.01	3.10 ^{+2.63} _{1.63} ± 0.80	5.09 ^{+3.65} _{3.55} ± 0.63	5.19 ^{+3.55} _{3.80} ± 0.55	5.13 ^{+3.03} _{4.14} ± 0.32
	Night	0.07 ^{-0.02} _{0.07} ± 0.03	0.04 ^{-0.01} _{0.04} ± 0.01	0.04 ^{+0.00} _{0.04} ± 0.00	0.06 ^{-0.01} _{0.05} ± 0.01	3.49 ^{+3.16} _{1.47} ± 0.80	3.85 ^{+3.16} _{2.20} ± 0.70	3.77 ^{+2.70} _{2.62} ± 0.52	1.81 ^{+1.20} _{1.35} ± 0.21
DFM-17	Day	0.24 ^{-0.21} _{0.12} ± 0.09	0.26 ^{-0.24} _{0.11} ± 0.10	0.26 ^{-0.20} _{0.16} ± 0.09	0.52 ^{-0.40} _{0.33} ± 0.10	5.06 ^{+4.61} _{2.09} ± 0.81	3.63 ^{+1.00} _{3.49} ± 0.17	2.74 ^{+0.43} _{2.71} ± 0.00	0.55 ^{+0.40} _{0.37} ± 0.39
	Night	0.12 ^{-0.02} _{0.12} ± 0.02	0.17 ^{-0.12} _{0.13} ± 0.07	0.20 ^{+0.03} _{0.20} ± 0.01	0.21 ^{+0.06} _{0.20} ± 0.03	5.99 ^{+5.08} _{3.17} ± 0.75	4.13 ^{-0.08} _{4.13} ± 0.18	3.47 ^{-0.81} _{3.38} ± 0.45	0.59 ^{+0.52} _{0.28} ± 0.26
GTH3	Day	0.18 ^{-0.05} _{0.17} ± 0.03	0.12 ^{+0.05} _{0.11} ± 0.04	0.09 ^{+0.01} _{0.08} ± 0.02	0.27 ^{-0.22} _{0.16} ± 0.10	7.00 ^{-5.43} _{4.41} ± 0.74	8.75 ^{-3.50} _{8.02} ± 0.60	7.73 ^{-1.55} _{7.58} ± 0.40	1.69 ^{+1.48} _{0.82} ± 0.46
	Night	0.38 ^{-0.18} _{0.34} ± 0.05	0.15 ^{+0.02} _{0.15} ± 0.02	0.12 ^{+0.06} _{0.10} ± 0.05	0.10 ^{-0.03} _{0.10} ± 0.02	4.72 ^{+0.74} _{4.66} ± 0.15	6.41 ^{+2.16} _{6.03} ± 0.11	6.82 ^{+3.70} _{5.74} ± 0.26	1.71 ^{+1.54} _{0.74} ± 0.28
iMet-54	Day	0.22 ^{+0.02} _{0.22} ± 0.01	0.14 ^{-0.07} _{0.12} ± 0.05	0.20 ^{-0.18} _{0.13} ± 0.10	0.29 ^{-0.26} _{0.13} ± 0.11	3.12 ^{-1.55} _{2.70} ± 0.48	4.37 ^{-1.39} _{4.14} ± 0.34	3.15 ^{-1.08} _{2.96} ± 0.39	1.03 ^{-0.35} _{0.97} ± 0.18
	Night	0.14 ^{+0.04} _{0.13} ± 0.03	0.09 ^{-0.02} _{0.09} ± 0.02	0.12 ^{-0.11} _{0.05} ± 0.09	0.13 ^{-0.12} _{0.05} ± 0.09	2.38 ^{-0.87} _{2.21} ± 0.36	3.50 ^{-2.23} _{2.70} ± 0.66	3.13 ^{-1.71} _{2.63} ± 0.57	0.50 ^{-0.38} _{0.32} ± 0.26
iMS-100	Day	0.12 ^{+0.04} _{0.11} ± 0.04	0.12 ^{-0.00} _{0.12} ± 0.01	0.14 ^{-0.06} _{0.13} ± 0.05	0.22 ^{-0.05} _{0.22} ± 0.03	1.89 ^{+1.24} _{1.43} ± 0.61	2.32 ^{+0.89} _{2.15} ± 0.37	2.38 ^{+0.33} _{2.36} ± 0.31	2.08 ^{-0.43} _{2.03} ± 0.11
	Night	0.09 ^{+0.05} _{0.07} ± 0.06	0.07 ^{+0.06} _{0.04} ± 0.08	0.08 ^{+0.06} _{0.05} ± 0.08	0.11 ^{-0.02} _{0.10} ± 0.02	2.57 ^{+2.31} _{1.15} ± 0.77	1.93 ^{+0.67} _{1.82} ± 0.31	2.07 ^{+0.48} _{2.02} ± 0.39	0.48 ^{-0.35} _{0.32} ± 0.25
M20	Day	0.22 ^{+0.04} _{0.21} ± 0.02	0.22 ^{+0.12} _{0.19} ± 0.06	0.15 ^{+0.01} _{0.15} ± 0.01	0.30 ^{+0.06} _{0.29} ± 0.03	3.13 ^{+2.22} _{2.21} ± 0.67	6.37 ^{+5.39} _{3.39} ± 0.74	6.38 ^{+4.77} _{4.23} ± 0.69	0.75 ^{-0.65} _{0.36} ± 0.45
	Night	0.12 ^{-0.06} _{0.11} ± 0.05	0.15 ^{+0.10} _{0.11} ± 0.07	0.11 ^{+0.06} _{0.09} ± 0.06	0.12 ^{+0.08} _{0.10} ± 0.07	5.78 ^{+5.14} _{2.65} ± 0.76	8.02 ^{+7.32} _{3.27} ± 0.78	7.44 ^{+5.79} _{4.68} ± 0.65	0.52 ^{-0.43} _{0.29} ± 0.28
PS-B3	Day	0.20 ^{-0.06} _{0.19} ± 0.03	0.40 ^{+0.31} _{0.26} ± 0.08	0.65 ^{+0.59} _{0.28} ± 0.10	1.02 ^{+0.88} _{0.52} ± 0.11	10.82 ^{-9.44} _{5.30} ± 0.80	14.59 ^{-10.21} _{10.43} ± 0.74	17.78 ^{-13.24} _{11.86} ± 0.79	0.45 ^{+0.13} _{0.43} ± 0.11
	Night	0.35 ^{-0.27} _{0.21} ± 0.08	0.26 ^{-0.23} _{0.12} ± 0.09	0.15 ^{-0.12} _{0.09} ± 0.08	0.31 ^{-0.22} _{0.21} ± 0.07	6.12 ^{+3.39} _{5.10} ± 0.49	10.44 ^{-0.53} _{10.43} ± 0.21	14.38 ^{+0.53} _{14.37} ± 0.12	4.89 ^{+4.72} _{1.28} ± 0.20
RS41	Day	0.08 ^{-0.04} _{0.07} ± 0.05	0.07 ^{-0.01} _{0.07} ± 0.01	0.08 ^{-0.03} _{0.07} ± 0.04	0.22 ^{-0.17} _{0.14} ± 0.10	0.98 ^{+0.47} _{0.86} ± 0.44	1.31 ^{+0.60} _{1.16} ± 0.47	1.04 ^{+0.53} _{0.90} ± 0.48	0.40 ^{+0.24} _{0.32} ± 0.33
	Night	0.08 ^{-0.03} _{0.07} ± 0.04	0.05 ^{-0.03} _{0.04} ± 0.05	0.05 ^{-0.03} _{0.03} ± 0.07	0.05 ^{-0.01} _{0.05} ± 0.01	0.91 ^{+0.34} _{0.84} ± 0.33	1.20 ^{+0.33} _{1.16} ± 0.29	0.93 ^{+0.30} _{0.88} ± 0.26	0.46 ^{+0.38} _{0.24} ± 0.26
WxR-301D	Day	0.45 ^{-0.15} _{0.42} ± 0.03	0.32 ^{-0.03} _{0.32} ± 0.01	0.38 ^{+0.01} _{0.38} ± 0.01	0.59 ^{-0.06} _{0.58} ± 0.02	5.26 ^{-3.54} _{3.88} ± 0.68	7.67 ^{-5.37} _{5.47} ± 0.75	6.76 ^{-3.28} _{5.91} ± 0.53	0.45 ^{+0.21} _{0.40} ± 0.26
	Night	0.17 ^{-0.16} _{0.06} ± 0.10	0.12 ^{-0.11} _{0.06} ± 0.09	0.12 ^{-0.11} _{0.06} ± 0.09	0.35 ^{-0.28} _{0.22} ± 0.08	4.57 ^{-2.80} _{3.62} ± 0.60	7.74 ^{-5.79} _{5.12} ± 0.65	6.07 ^{-2.31} _{5.61} ± 0.33	0.55 ^{+0.44} _{0.32} ± 0.24

Table 10.4: Same as Table 10.3, but for the geopotential height and atmospheric pressure. No performance assessment is made in the PBL (tagged with ×), as several profiles were likely affected by the UAI campaign setup in this atmospheric layer (see Section 8.2.5 for details).

		Geopotential height [m]				Pressure [hPa]			
		PBL	FT	UTLS	MUS	PBL	FT	UTLS	MUS
ATMS-3710	Day	×	$3.5_{3.5}^{-0.7} \pm 1.1$	$3.7_{3.7}^{+0.1} \pm 0.0$	$3.8_{3.7}^{+1.1} \pm 1.5$	×	$11.0_{4.7}^{-9.9} \pm 0.3$	$9.5_{4.6}^{-8.3} \pm 0.2$	$2.9_{1.0}^{-2.7} \pm 0.0$
	Night	×	$3.7_{3.7}^{+0.1} \pm 0.0$	$4.0_{3.9}^{+1.0} \pm 1.0$	$4.5_{4.2}^{+1.7} \pm 2.0$	×	$10.8_{5.3}^{-9.5} \pm 0.3$	$9.7_{4.7}^{-8.5} \pm 0.2$	$2.8_{1.0}^{-2.6} \pm 0.0$
CF-06-AH	Day	×	$4.8_{4.8}^{+0.3} \pm 0.5$	$7.9_{7.9}^{-0.3} \pm 0.1$	$9.6_{9.5}^{+0.9} \pm 0.3$	×	$0.3_{0.3}^{-0.0} \pm 0.0$	$0.2_{0.2}^{-0.1} \pm 0.1$	$0.1_{0.1}^{-0.1} \pm 0.0$
	Night	×	$3.9_{3.8}^{+1.2} \pm 1.6$	$4.0_{3.8}^{+1.4} \pm 1.9$	$6.5_{5.8}^{+3.0} \pm 2.4$	×	$0.3_{0.3}^{+0.1} \pm 0.2$	$0.1_{0.1}^{+0.1} \pm 0.1$	$0.0_{0.0}^{+0.0} \pm 0.0$
DFM-17	Day	×	$12.6_{12.5}^{+1.7} \pm 0.8$	$12.9_{12.6}^{+3.0} \pm 1.2$	$6.4_{5.8}^{+2.6} \pm 2.1$	×	$0.9_{0.8}^{-0.4} \pm 0.2$	$0.6_{0.4}^{-0.5} \pm 0.2$	$0.3_{0.1}^{-0.3} \pm 0.0$
	Night	×	$4.1_{3.9}^{+1.1} \pm 1.3$	$4.4_{3.9}^{+2.2} \pm 2.4$	$5.5_{4.3}^{+3.4} \pm 3.4$	×	$0.4_{0.4}^{-0.0} \pm 0.1$	$0.2_{0.2}^{-0.1} \pm 0.1$	$0.1_{0.0}^{-0.0} \pm 0.0$
GTH3	Day	×	$5.9_{5.5}^{+2.0} \pm 1.8$	$13.2_{8.6}^{+10.0} \pm 3.8$	$29.5_{17.9}^{+23.4} \pm 4.2$	×	$0.4_{0.4}^{-0.0} \pm 0.1$	$0.4_{0.2}^{-0.3} \pm 0.1$	$0.3_{0.1}^{-0.2} \pm 0.0$
	Night	×	$5.8_{5.8}^{+0.4} \pm 0.4$	$11.5_{8.6}^{+7.7} \pm 3.4$	$26.7_{16.8}^{+20.7} \pm 4.2$	×	$0.5_{0.5}^{+0.1} \pm 0.2$	$0.3_{0.2}^{-0.1} \pm 0.1$	$0.1_{0.1}^{-0.1} \pm 0.0$
iMet-54	Day	×	$12.9_{12.9}^{-0.1} \pm 0.1$	$10.8_{10.8}^{-0.7} \pm 0.3$	$6.7_{6.6}^{-1.3} \pm 1.0$	×	$0.7_{0.7}^{-0.1} \pm 0.0$	$0.4_{0.4}^{-0.2} \pm 0.1$	$0.2_{0.1}^{-0.2} \pm 0.0$
	Night	×	$5.1_{4.7}^{+2.0} \pm 2.1$	$8.0_{7.1}^{+3.7} \pm 2.3$	$10.2_{9.1}^{+4.6} \pm 2.4$	×	$0.3_{0.3}^{+0.0} \pm 0.1$	$0.2_{0.2}^{-0.1} \pm 0.1$	$0.1_{0.1}^{-0.1} \pm 0.0$
iMS-100	Day	×	$4.7_{4.7}^{-0.1} \pm 0.1$	$5.5_{4.7}^{-2.7} \pm 2.6$	$5.3_{3.6}^{-3.9} \pm 3.8$	×	$1.1_{1.1}^{+0.3} \pm 0.1$	$0.6_{0.6}^{+0.1} \pm 0.0$	$0.2_{0.1}^{-0.1} \pm 0.0$
	Night	×	$4.8_{4.8}^{+0.4} \pm 0.4$	$5.5_{5.0}^{-2.1} \pm 1.9$	$4.6_{4.0}^{-2.3} \pm 2.7$	×	$0.4_{0.4}^{+0.1} \pm 0.1$	$0.3_{0.3}^{+0.2} \pm 0.1$	$0.1_{0.1}^{+0.1} \pm 0.0$
M20	Day	×	$4.7_{4.6}^{+0.5} \pm 0.6$	$5.5_{5.4}^{+0.9} \pm 0.9$	$5.5_{5.1}^{+2.0} \pm 1.9$	×	$0.4_{0.4}^{+0.1} \pm 0.2$	$0.2_{0.2}^{-0.0} \pm 0.0$	$0.1_{0.1}^{-0.1} \pm 0.0$
	Night	×	$5.1_{4.7}^{+2.0} \pm 2.1$	$6.1_{5.2}^{+3.2} \pm 2.8$	$7.3_{6.2}^{+3.8} \pm 2.7$	×	$1.1_{1.0}^{+0.4} \pm 0.1$	$0.5_{0.5}^{+0.2} \pm 0.1$	$0.1_{0.1}^{+0.0} \pm 0.0$
PS-B3	Day	×	$5.4_{5.4}^{-0.7} \pm 0.6$	$4.4_{4.4}^{+0.7} \pm 0.9$	$4.1_{4.0}^{+1.1} \pm 1.3$	×	$1.0_{0.7}^{-0.7} \pm 0.3$	$0.6_{0.4}^{-0.4} \pm 0.2$	$0.1_{0.1}^{+0.0} \pm 0.0$
	Night	×	$4.6_{4.5}^{+0.7} \pm 0.6$	$5.1_{4.2}^{+2.9} \pm 2.9$	$5.3_{3.9}^{+3.6} \pm 3.7$	×	$1.2_{0.6}^{-1.0} \pm 0.3$	$0.9_{0.4}^{-0.8} \pm 0.2$	$0.2_{0.1}^{-0.2} \pm 0.0$
RS41	Day	×	$3.6_{3.5}^{-0.8} \pm 1.2$	$3.6_{3.5}^{+0.8} \pm 1.1$	$3.7_{3.1}^{+2.1} \pm 3.0$	×	$0.3_{0.3}^{+0.0} \pm 0.1$	$0.2_{0.1}^{-0.2} \pm 0.1$	$0.2_{0.1}^{-0.1} \pm 0.0$
	Night	×	$3.7_{3.7}^{+0.2} \pm 0.2$	$4.1_{3.8}^{+1.5} \pm 1.9$	$4.7_{3.9}^{+2.6} \pm 3.1$	×	$0.3_{0.3}^{+0.1} \pm 0.2$	$0.1_{0.1}^{+0.0} \pm 0.0$	$0.0_{0.0}^{-0.0} \pm 0.0$
WxR-301D	Day	×	$5.0_{5.0}^{+0.3} \pm 0.3$	$4.9_{4.9}^{+0.8} \pm 0.9$	$241.8_{241.1}^{-18.3} \pm 0.4$	×	$9.8_{4.3}^{+8.8} \pm 0.4$	$5.4_{2.7}^{+4.7} \pm 0.2$	$2.3_{2.0}^{+1.1} \pm 0.0$
	Night	×	$4.7_{4.7}^{+0.3} \pm 0.4$	$6.1_{6.0}^{+1.0} \pm 0.8$	$112.7_{110.6}^{+21.6} \pm 1.0$	×	$10.2_{4.9}^{+9.0} \pm 0.4$	$5.6_{2.9}^{+4.8} \pm 0.2$	$1.1_{0.8}^{+0.7} \pm 0.0$

Table 10.5: Same as Table 10.3, but for the wind (horizontal) direction, wind (horizontal) speed, and wind (horizontal) vector. No performance assessment is made in the PBL (tagged with ×), as several profiles were likely affected by the UAI campaign setup in this atmospheric layer (see Section 8.2.5 for details).

		Wind (horizontal) direction [°]				Wind (horizontal) speed [m s ⁻¹]				Wind (horizontal) vector [m s ⁻¹]			
		PBL	FT	UTLS	MUS	PBL	FT	UTLS	MUS	PBL	FT	UTLS	MUS
ATMS-3710	Day	×	12.8 ^{-0.2} _{12.8} ± 0.1	8.2 ^{-0.3} _{8.2} ± 0.0	22.9 ^{-3.5} _{22.7} ± 0.1	×	0.9 ^{-0.3} _{0.9} ± 0.0	1.0 ^{-0.2} _{1.0} ± 0.0	1.0 ^{-0.2} _{1.0} ± 0.0	×	1.4 ^{+1.1} _{0.8} ± 0.0	1.5 ^{+1.2} _{0.8} ± 0.0	1.5 ^{+1.4} _{0.7} ± 0.0
	Night	×	12.3 ^{-0.2} _{12.3} ± 0.1	8.3 ^{-0.3} _{8.3} ± 0.1	23.1 ^{-2.7} _{23.0} ± 0.1	×	0.9 ^{-0.3} _{0.9} ± 0.0	1.0 ^{-0.2} _{1.0} ± 0.0	1.0 ^{-0.2} _{1.0} ± 0.0	×	1.4 ^{+1.1} _{0.9} ± 0.0	1.5 ^{+1.3} _{0.9} ± 0.0	1.5 ^{+1.3} _{0.7} ± 0.0
CF-06-AH	Day	×	5.3 ^{-0.3} _{5.3} ± 0.3	3.0 ^{+0.0} _{3.0} ± 0.4	8.9 ^{+0.6} _{8.9} ± 0.2	×	0.2 ^{-0.0} _{0.2} ± 0.0	0.2 ^{-0.0} _{0.2} ± 0.0	0.3 ^{-0.1} _{0.3} ± 0.0	×	0.3 ^{+0.3} _{0.2} ± 0.0	0.3 ^{+0.2} _{0.2} ± 0.0	0.5 ^{+0.3} _{0.4} ± 0.0
	Night	×	6.2 ^{-0.1} _{6.2} ± 0.2	3.7 ^{+0.1} _{3.7} ± 0.1	12.5 ^{+0.6} _{12.5} ± 0.1	×	0.2 ^{-0.0} _{0.2} ± 0.0	0.2 ^{-0.0} _{0.2} ± 0.0	0.5 ^{-0.1} _{0.5} ± 0.0	×	0.3 ^{+0.2} _{0.2} ± 0.0	0.3 ^{+0.2} _{0.2} ± 0.0	0.9 ^{+0.5} _{0.8} ± 0.0
DFM-17	Day	×	9.1 ^{-0.2} _{9.1} ± 0.1	6.3 ^{-0.3} _{6.3} ± 0.1	17.0 ^{-3.1} _{16.7} ± 0.1	×	0.6 ^{-0.1} _{0.6} ± 0.0	0.7 ^{+0.0} _{0.7} ± 0.0	0.7 ^{+0.0} _{0.7} ± 0.0	×	0.9 ^{+0.8} _{0.5} ± 0.0	1.1 ^{+0.9} _{0.6} ± 0.0	1.1 ^{+1.0} _{0.5} ± 0.0
	Night	×	9.1 ^{-0.1} _{9.1} ± 0.2	6.5 ^{-0.4} _{6.5} ± 0.1	15.8 ^{-2.0} _{15.7} ± 0.1	×	0.6 ^{-0.1} _{0.6} ± 0.0	0.7 ^{+0.0} _{0.7} ± 0.0	0.7 ^{+0.0} _{0.7} ± 0.0	×	0.9 ^{+0.8} _{0.5} ± 0.0	1.0 ^{+0.9} _{0.5} ± 0.0	1.0 ^{+0.9} _{0.5} ± 0.0
GTH3	Day	×	3.6 ^{-0.4} _{3.6} ± 0.2	2.5 ^{-0.2} _{2.5} ± 0.3	6.1 ^{-0.4} _{6.1} ± 0.2	×	0.2 ^{-0.0} _{0.2} ± 0.0	0.2 ^{-0.0} _{0.2} ± 0.0	1.3 ^{-0.0} _{1.3} ± 0.0	×	0.3 ^{+0.2} _{0.1} ± 0.0	0.3 ^{+0.2} _{0.2} ± 0.0	1.5 ^{+0.3} _{1.5} ± 0.0
	Night	×	2.6 ^{-0.2} _{2.6} ± 0.2	2.4 ^{-0.1} _{2.4} ± 0.1	4.5 ^{-0.6} _{4.4} ± 0.2	×	0.2 ^{-0.0} _{0.2} ± 0.0	0.2 ^{+0.0} _{0.2} ± 0.0	0.2 ^{-0.0} _{0.2} ± 0.0	×	0.2 ^{+0.2} _{0.1} ± 0.0	0.2 ^{+0.2} _{0.1} ± 0.0	0.4 ^{+0.3} _{0.3} ± 0.0
iMet-54	Day	×	4.1 ^{-0.2} _{4.1} ± 0.4	2.7 ^{+0.1} _{2.7} ± 0.4	6.5 ^{+0.5} _{6.5} ± 0.2	×	0.2 ^{-0.1} _{0.1} ± 0.0	0.2 ^{-0.1} _{0.2} ± 0.0	0.3 ^{-0.1} _{0.2} ± 0.0	×	0.2 ^{+0.2} _{0.1} ± 0.0	0.2 ^{+0.2} _{0.2} ± 0.0	0.4 ^{+0.3} _{0.3} ± 0.0
	Night	×	2.9 ^{+0.1} _{2.9} ± 0.1	2.3 ^{+0.1} _{2.3} ± 0.1	6.1 ^{+0.3} _{6.1} ± 0.1	×	0.2 ^{-0.0} _{0.1} ± 0.0	0.2 ^{-0.1} _{0.2} ± 0.0	0.3 ^{-0.1} _{0.2} ± 0.0	×	0.2 ^{+0.2} _{0.1} ± 0.0	0.2 ^{+0.2} _{0.1} ± 0.0	0.4 ^{+0.3} _{0.3} ± 0.0
iMS-100	Day	×	3.0 ^{-0.1} _{3.0} ± 0.3	1.9 ^{-0.0} _{1.9} ± 0.2	4.2 ^{-0.3} _{4.1} ± 0.2	×	0.1 ^{+0.0} _{0.1} ± 0.0	0.2 ^{+0.0} _{0.2} ± 0.0	0.2 ^{+0.1} _{0.2} ± 0.0	×	0.2 ^{+0.1} _{0.1} ± 0.0	0.2 ^{+0.1} _{0.1} ± 0.0	0.3 ^{+0.2} _{0.2} ± 0.0
	Night	×	2.7 ^{+0.1} _{2.7} ± 0.1	1.7 ^{-0.0} _{1.7} ± 0.1	6.2 ^{-0.5} _{6.2} ± 0.2	×	0.2 ^{+0.0} _{0.2} ± 0.0	0.2 ^{+0.0} _{0.2} ± 0.0	0.3 ^{+0.1} _{0.3} ± 0.0	×	0.2 ^{+0.2} _{0.1} ± 0.0	0.2 ^{+0.2} _{0.2} ± 0.0	0.4 ^{+0.3} _{0.3} ± 0.0
M20	Day	×	6.8 ^{-0.2} _{6.8} ± 0.3	3.3 ^{+0.1} _{3.3} ± 0.2	8.2 ^{+0.5} _{8.2} ± 0.2	×	0.3 ^{-0.0} _{0.3} ± 0.0	0.3 ^{-0.0} _{0.3} ± 0.0	0.3 ^{-0.1} _{0.3} ± 0.0	×	0.4 ^{+0.4} _{0.2} ± 0.0	0.4 ^{+0.4} _{0.2} ± 0.0	0.5 ^{+0.4} _{0.3} ± 0.0
	Night	×	5.0 ^{+0.1} _{5.0} ± 0.2	3.6 ^{-0.0} _{3.6} ± 0.1	7.3 ^{+0.2} _{7.3} ± 0.1	×	0.3 ^{-0.0} _{0.3} ± 0.0	0.3 ^{-0.0} _{0.3} ± 0.0	0.3 ^{-0.1} _{0.3} ± 0.0	×	0.4 ^{+0.3} _{0.2} ± 0.0	0.4 ^{+0.3} _{0.2} ± 0.0	0.5 ^{+0.4} _{0.3} ± 0.0
PS-B3	Day	×	7.2 ^{-0.5} _{7.2} ± 0.1	4.4 ^{-0.2} _{4.4} ± 0.1	9.1 ^{+0.1} _{9.1} ± 0.2	×	0.5 ^{-0.0} _{0.5} ± 0.0	0.5 ^{-0.0} _{0.5} ± 0.0	0.4 ^{-0.1} _{0.4} ± 0.0	×	0.7 ^{+0.6} _{0.4} ± 0.0	0.7 ^{+0.6} _{0.4} ± 0.0	0.6 ^{+0.5} _{0.3} ± 0.0
	Night	×	5.7 ^{-0.2} _{5.7} ± 0.2	3.5 ^{-0.1} _{3.5} ± 0.1	10.7 ^{+0.4} _{10.7} ± 0.2	×	0.5 ^{-0.0} _{0.5} ± 0.0	0.5 ^{-0.0} _{0.5} ± 0.0	0.4 ^{-0.1} _{0.4} ± 0.0	×	0.7 ^{+0.6} _{0.4} ± 0.0	0.7 ^{+0.6} _{0.4} ± 0.0	0.6 ^{+0.5} _{0.3} ± 0.0
RS41	Day	×	2.5 ^{-0.3} _{2.4} ± 0.1	1.6 ^{-0.1} _{1.6} ± 0.1	5.2 ^{-0.4} _{5.2} ± 0.3	×	0.1 ^{-0.0} _{0.1} ± 0.0	0.1 ^{-0.0} _{0.1} ± 0.0	0.2 ^{-0.0} _{0.2} ± 0.0	×	0.2 ^{+0.2} _{0.1} ± 0.0	0.2 ^{+0.2} _{0.1} ± 0.0	0.3 ^{+0.2} _{0.3} ± 0.0
	Night	×	1.9 ^{-0.1} _{1.9} ± 0.2	1.7 ^{+0.0} _{1.7} ± 0.1	5.6 ^{+0.1} _{5.6} ± 0.1	×	0.1 ^{-0.0} _{0.1} ± 0.0	0.1 ^{-0.0} _{0.1} ± 0.0	0.3 ^{-0.0} _{0.3} ± 0.0	×	0.2 ^{+0.1} _{0.1} ± 0.0	0.2 ^{+0.2} _{0.1} ± 0.0	0.4 ^{+0.3} _{0.3} ± 0.0
WxR-301D	Day	×	16.1 ^{-0.3} _{16.1} ± 0.2	8.2 ^{-0.0} _{8.2} ± 0.1	23.6 ^{-2.1} _{23.5} ± 0.1	×	0.9 ^{+0.2} _{0.9} ± 0.0	1.0 ^{+0.2} _{1.0} ± 0.0	1.3 ^{+0.6} _{1.1} ± 0.0	×	1.5 ^{+1.3} _{0.8} ± 0.0	1.6 ^{+1.3} _{0.9} ± 0.0	2.0 ^{+1.7} _{1.1} ± 0.0
	Night	×	24.6 ^{-0.2} _{24.6} ± 0.1	18.0 ^{+0.0} _{18.0} ± 0.0	32.4 ^{-3.9} _{32.2} ± 0.1	×	1.0 ^{+0.3} _{1.0} ± 0.0	1.1 ^{+0.3} _{1.0} ± 0.0	1.3 ^{+0.7} _{1.1} ± 0.0	×	2.1 ^{+1.5} _{1.5} ± 0.0	2.1 ^{+1.5} _{1.5} ± 0.0	2.6 ^{+2.0} _{1.6} ± 0.0

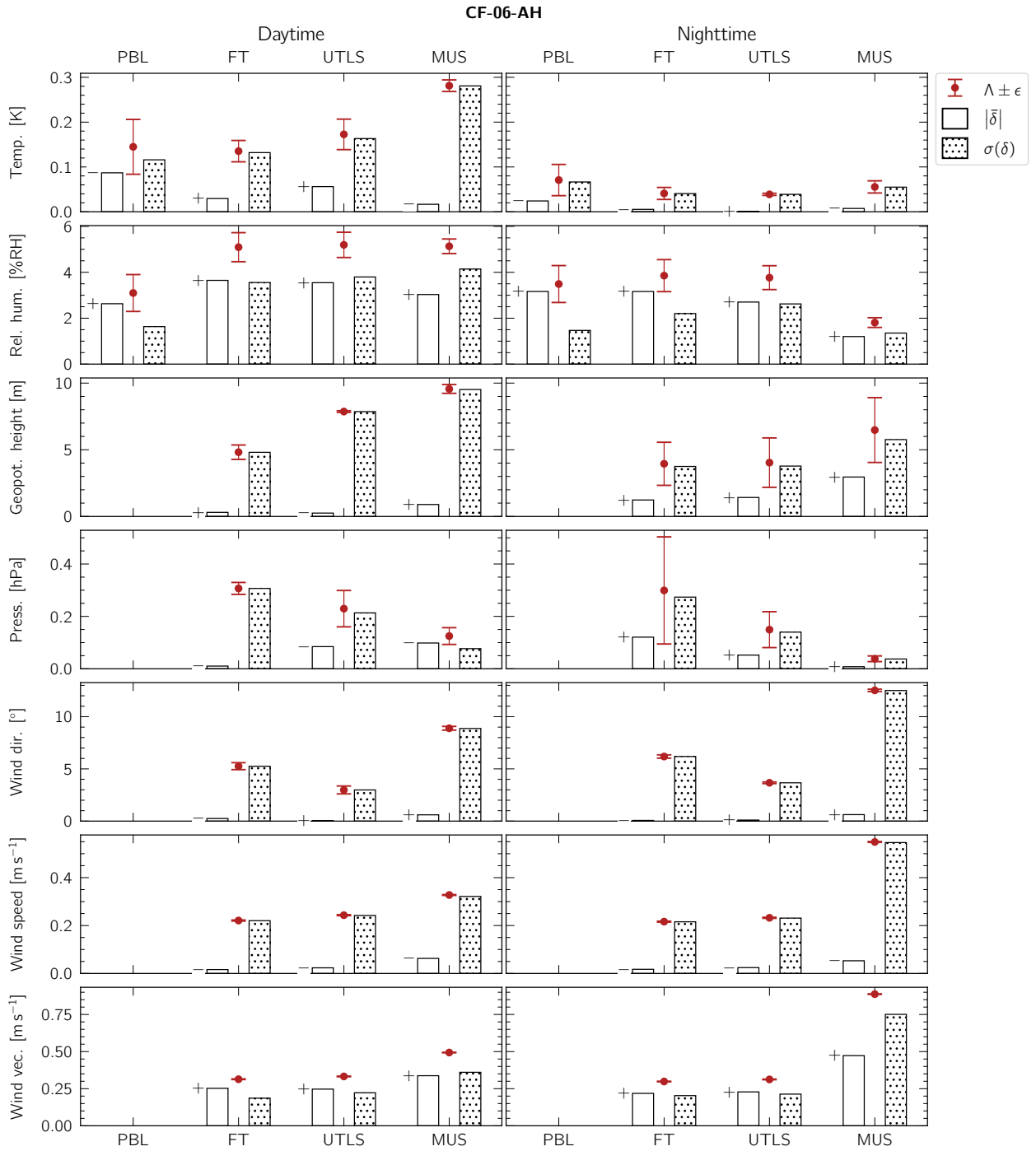


Figure 10.4: Same as Figure 10.3, but for the CF-06-AH radiosonde.

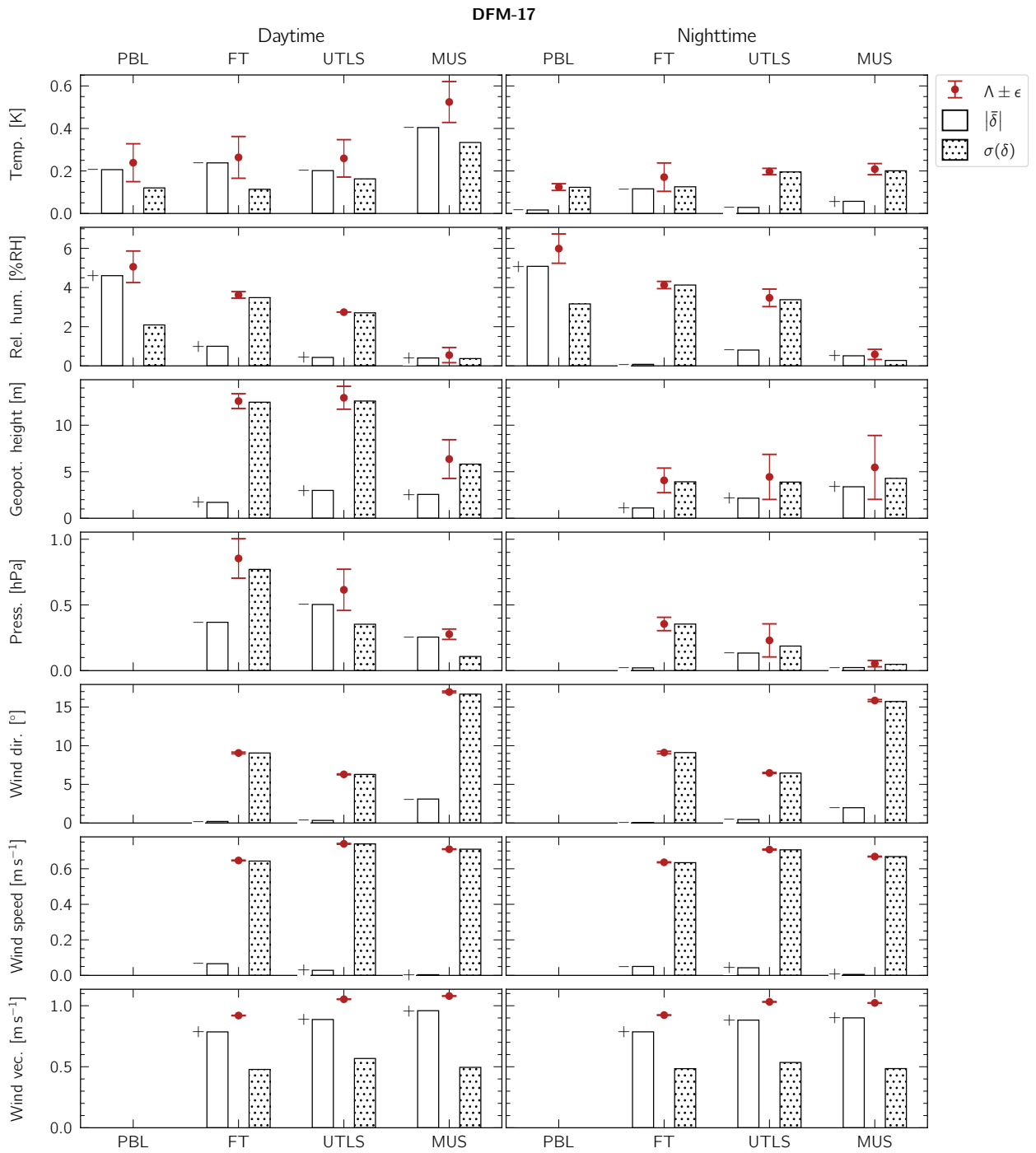


Figure 10.5: Same as Figure 10.3, but for the DFM-17 radiosonde.

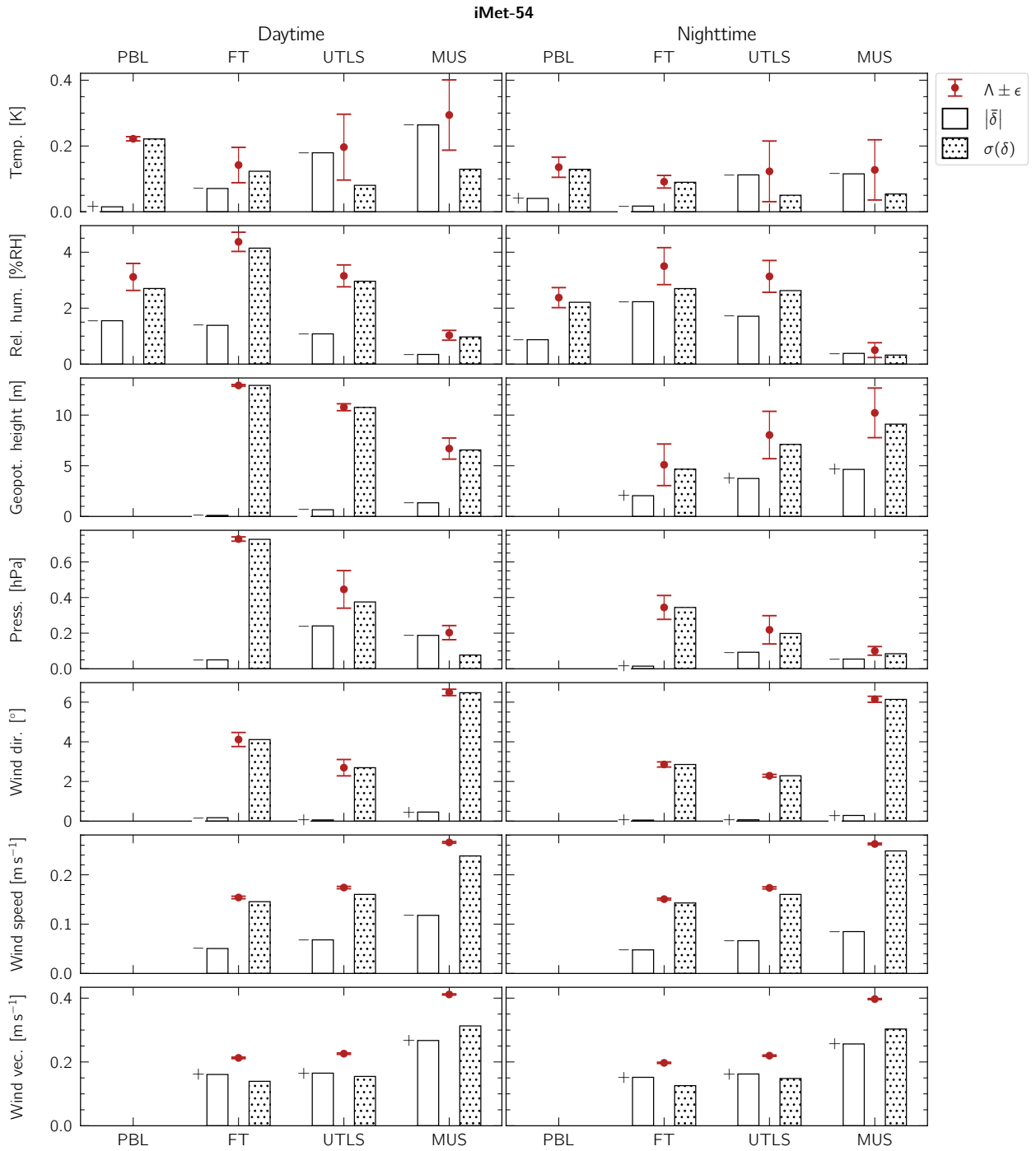


Figure 10.7: Same as Figure 10.3, but for the iMet-54 radiosonde.

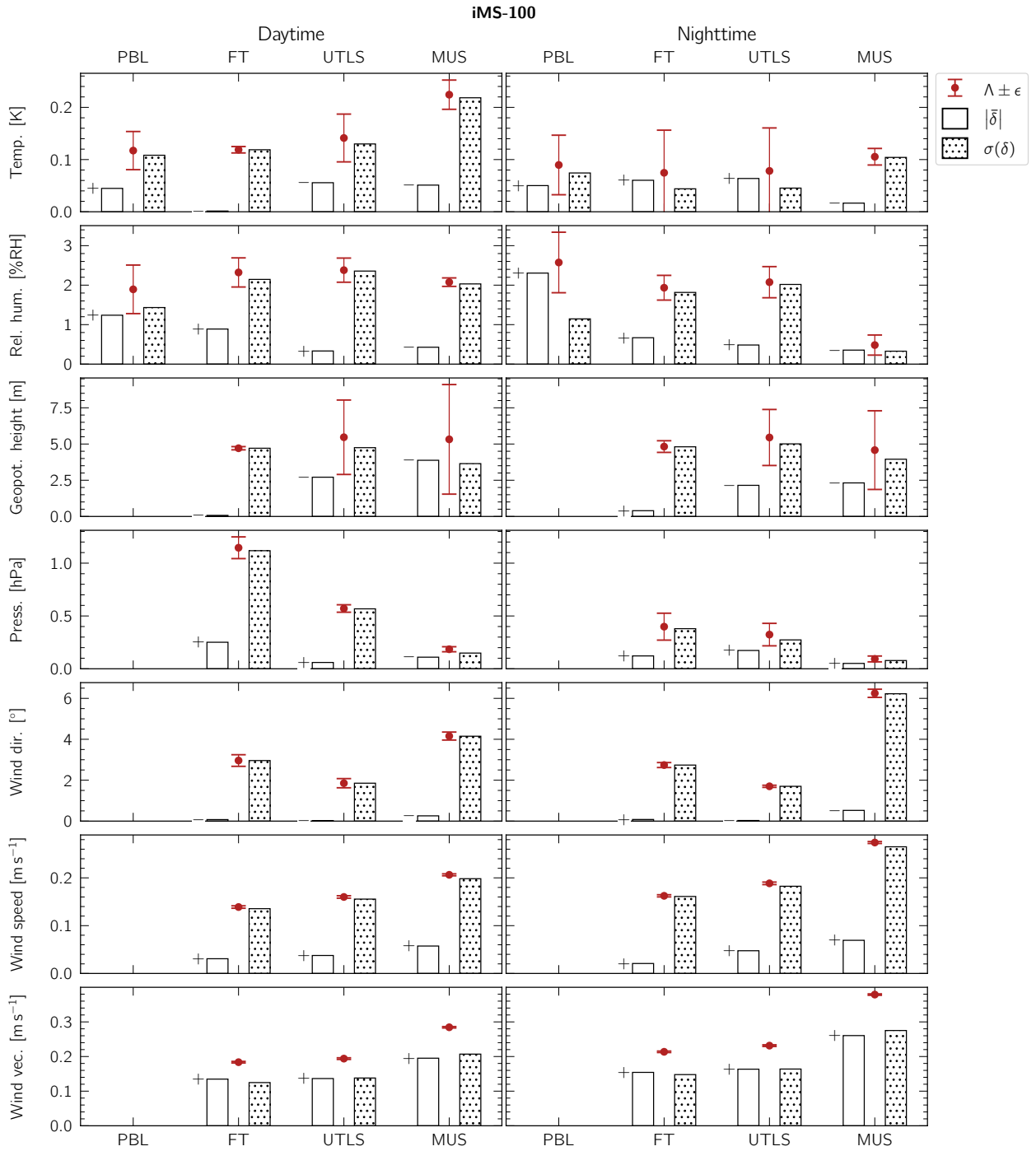


Figure 10.8: Same as Figure 10.3, but for the iMS-100 radiosonde.

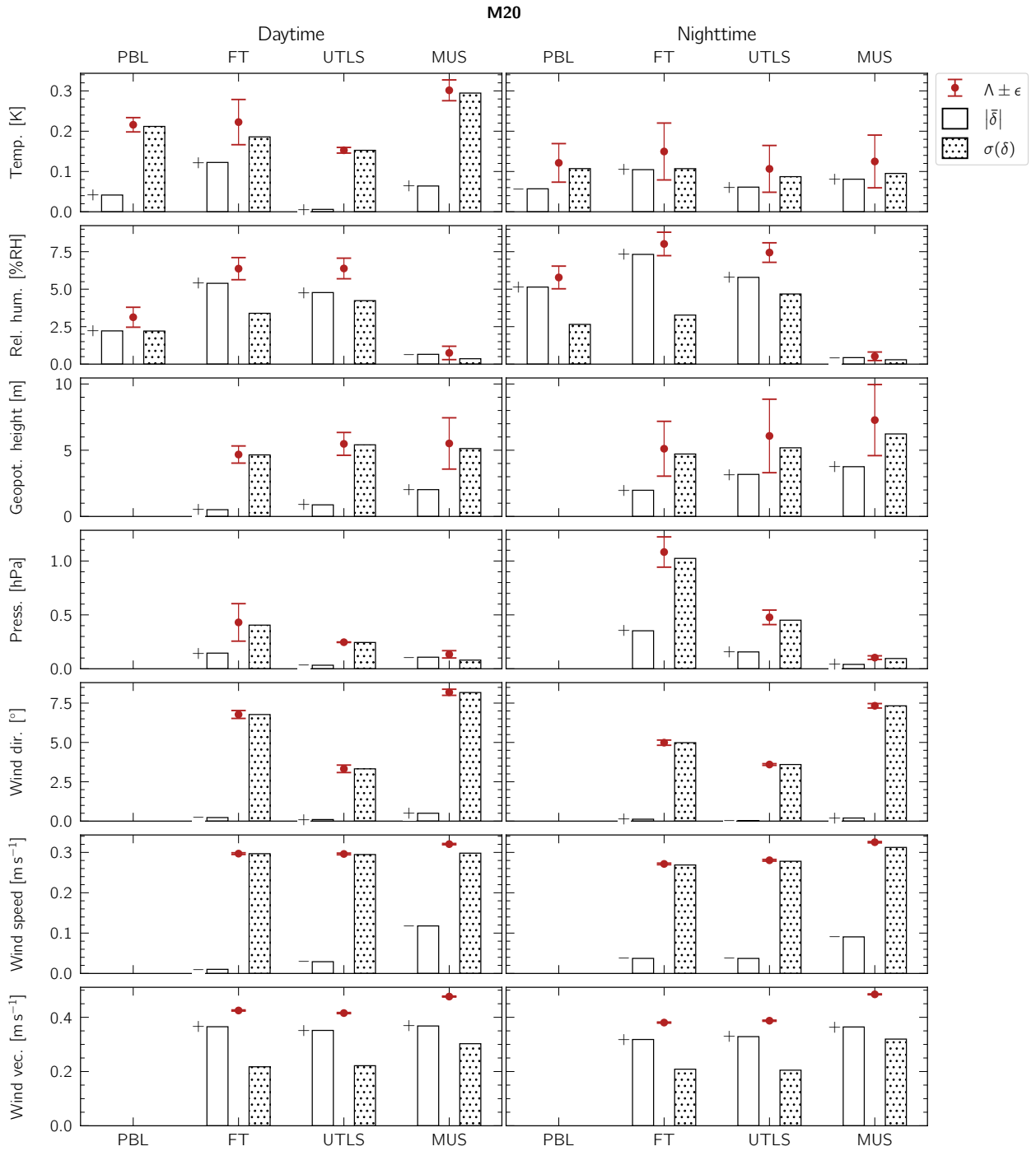


Figure 10.9: Same as Figure 10.3, but for the M20 radiosonde.

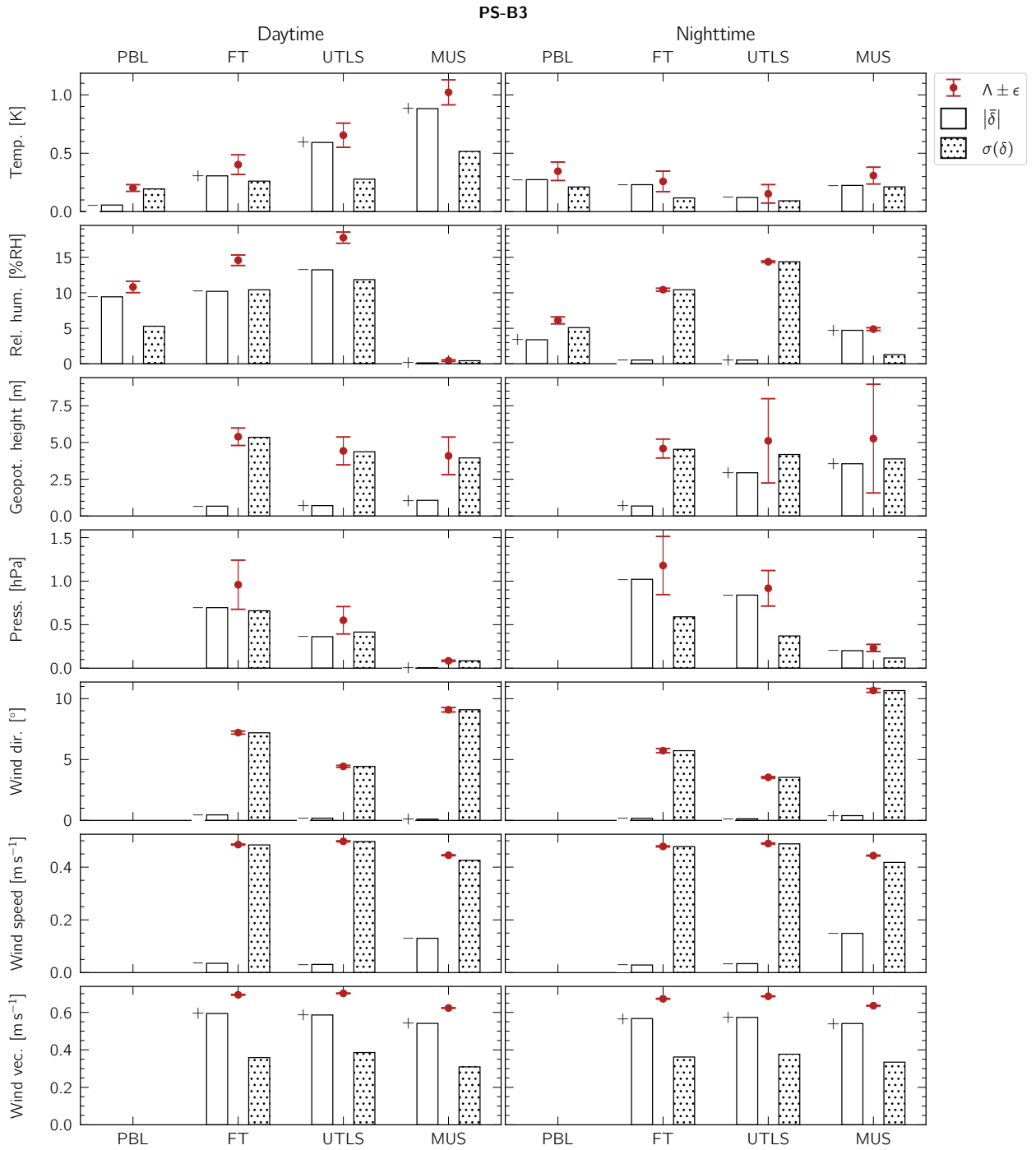


Figure 10.10: Same as Figure 10.3, but for the PS-B3 radiosonde.

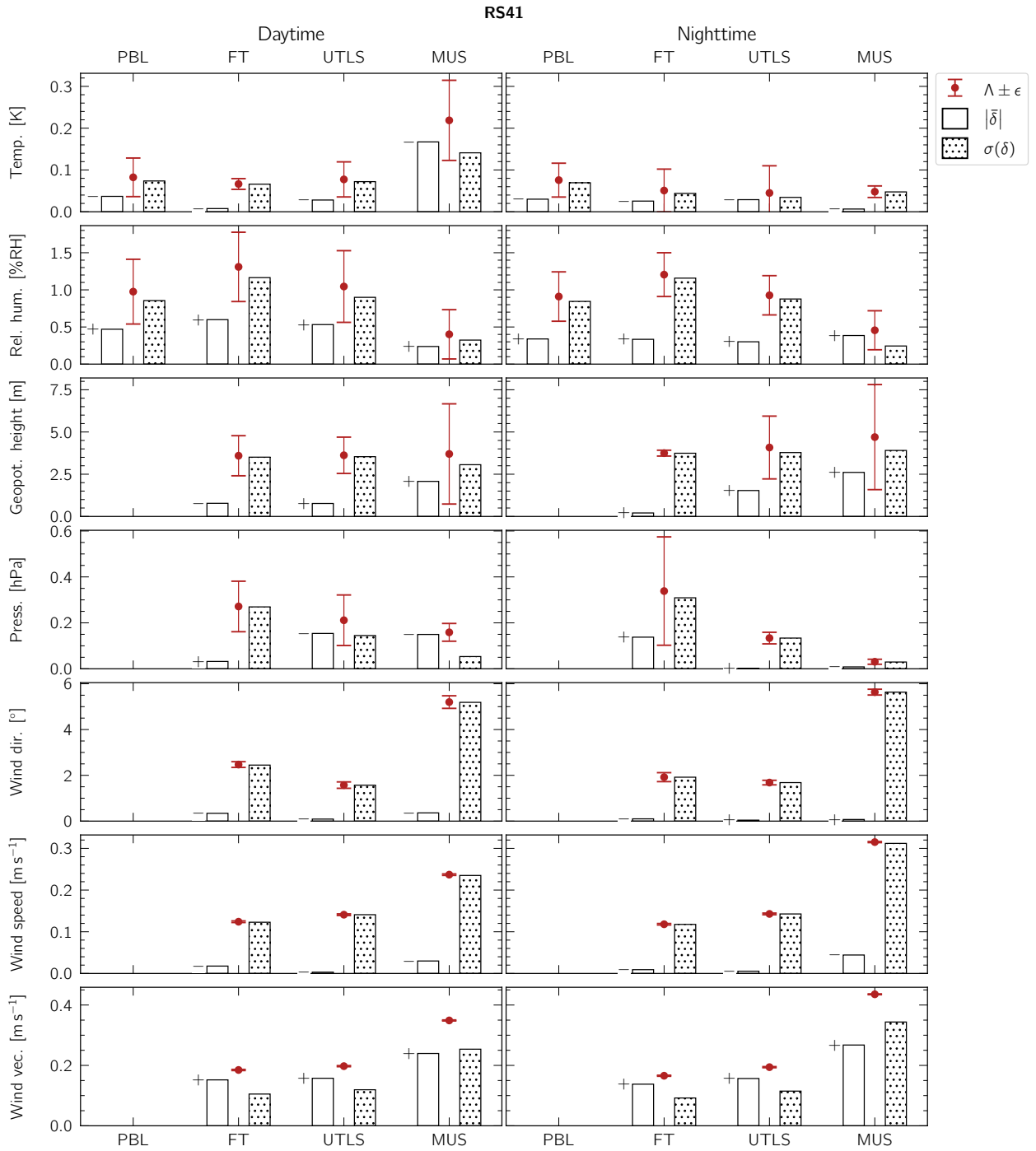


Figure 10.11: Same as Figure 10.3, but for the RS41 radiosonde.

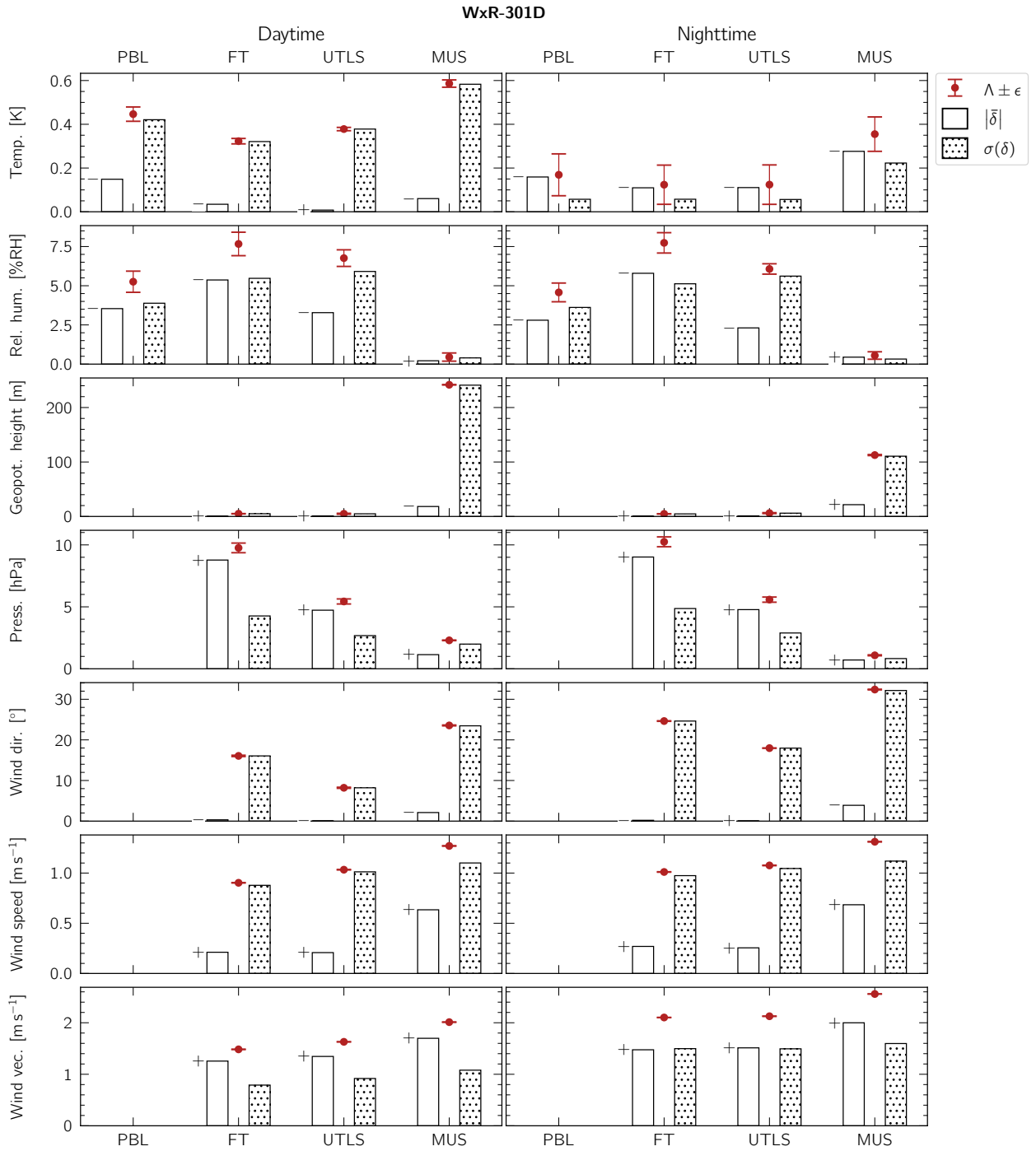


Figure 10.12: Same as Figure 10.3, but for the WxR-301D radiosonde.

10.1.5.1 The ORUC assessment function ($\Lambda_{C,\mathcal{L}}$) diagnostic diagrams

The ORUC assessment function $\Lambda_{C,\mathcal{L}}$ can also be computed over thinner atmospheric layers \mathcal{L} , in addition to the PBL, FT, UTLS, and MUS. For all radiosondes and flight categories C , we compute the ORUC assessment function profile $\Lambda_{C,100m}$ with a vertical resolution of 100 m. These profiles are provided as NetCDF files in the UAI 2022 Supplementary Material, along with dedicated diagnostic diagrams.

An example of these diagrams is shown in Figure 10.13, for the atmospheric temperature measured by the ATMS-3710 radiosonde during daytime. These diagrams essentially provide a high-resolution view of $\Lambda_{C,\mathcal{L}}$ against which the values (integrated over larger atmospheric layers) presented in Tables 10.3 to 10.5 and Figures 10.3 to 10.12 can be compared. For completeness, similar diagrams for all the geophysical variables considered in this analysis are included in Appendix L, for all the radiosondes that participated in the UAI 2022.

The distribution of the individual measurement errors $\delta_{e,i}$ (computed with respect to the CWSs), together with the profiles of 1) the absolute mean measurement error $|\bar{\delta}|$ and 2) the standard deviation of the individual measurement errors $\sigma(\delta)$, show the geopotential height ranges where $\Lambda_{C,100m}$ is dominated by the measurement bias of the sonde. In the specific case of Figure 10.13, this occurs above ~ 20 km where $|\bar{\delta}| > \sigma(\delta)$. The interested reader can thus use these detailed diagrams to understand if/where the $\Lambda_{C,\mathcal{L}}$ scores of a given sonde are primarily driven by the presence of systematic measurement errors, random measurement errors, or both (see Section 10.1.5.3).

10.1.5.2 On the behaviour of $\Lambda_{C,\mathcal{L}}$ with respect to correlated uncertainties

The mathematical form of Equation 9.2 leads to the following behaviour of $\Lambda_{C,\mathcal{L}}$ with respect to the propagation of uncertainties (to derive $\epsilon_{C,\mathcal{L}}$, the total uncertainty of $\Lambda_{C,\mathcal{L}}$, via Equation J.10 in Appendix J.2):

The influence of correlated uncertainties on $\epsilon_{C,\mathcal{L}}$ tends to vanish for atmospheric layers \mathcal{L} where the measurement bias $\bar{\delta}_{C,\mathcal{L}}$ of the sonde approaches zero. Only the uncorrelated uncertainty sources remain in those regions, but their influence decreases as the number of pooled measurements J increases, with $J \gg 1$ for the case of the UAI 2022 field campaign (in particular: $J \gtrsim 400$ for $\Lambda_{C,100m}$).

At first glance, this may appear counter-intuitive given that CWS measurements represent the only source of uncertainties that contribute to $\epsilon_{C,\mathcal{L}}$; and these are evidently common to all the sonde measurements on any given rig. However, their impact on $\epsilon_{C,\mathcal{L}}$ also depends on the measurement bias of each sonde, which is specific to each radiosonde model and can vary as a function of geopotential height.

We present in Figure 10.14 an example of this behaviour, by means of the $\Lambda_{C,\mathcal{L}}$ diagnostic diagram (introduced in Section 10.1.5.1) for the nighttime temperature measurements of the iMS-100 radiosonde. The uncertainty envelope of the high-resolution $\Lambda_{\text{night},100m}$ profile (grey area) is smallest in the vicinity of 26 500 m, where the measurement bias $\bar{\delta}$ of the sonde approaches 0.

Intuitively, this behaviour of $\Lambda_{C,\mathcal{L}}$ with respect to correlated uncertainties can be understood if one remembers that:

$$\Lambda_{C,\mathcal{L}} = (A^2 + B^2)^{\frac{1}{2}} \quad (10.3)$$

with:

$$A = (\bar{\delta}_{C,\mathcal{L}})^2 \quad \text{and} \quad B = (\sigma(\delta)_{C,\mathcal{L}})^2 \quad (10.4)$$

In other words, $\Lambda_{C,\mathcal{L}}$ can be seen as resulting from the combination of A) the measurement bias of a given sonde, together with B) the standard deviation of its individual measurement errors.

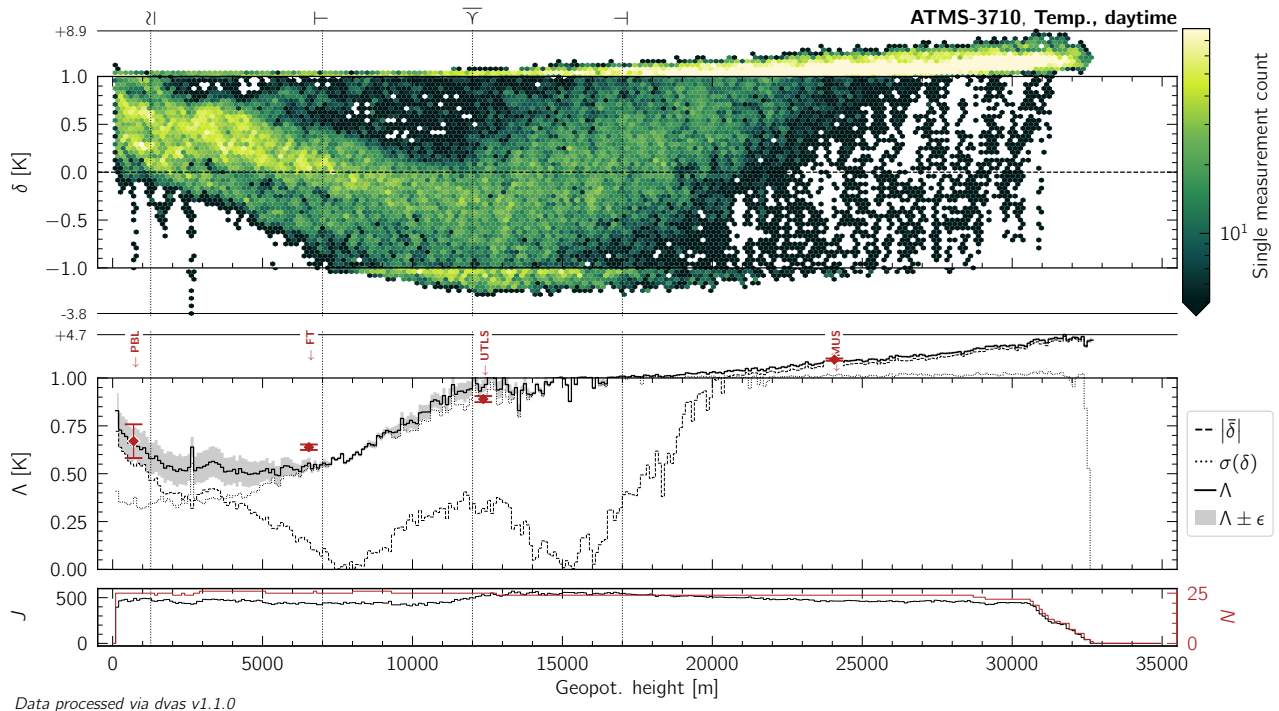


Figure 10.13: Example of an ORUC assessment function ($\Lambda_{C,\mathcal{L}}$) diagnostic diagram. Top: distribution of the individual measurement errors $\delta_{e,i} = x_{e,i} - \Omega_{e,i}$, the difference between the atmospheric temperature measured by the ATMS-3710 sonde ($x_{e,i}$) and the corresponding CWS value ($\Omega_{e,i}$) for the time step i of flight e , for all daytime flights. A positive value of $\delta_{e,i}$ is synonymous with a warm offset. Middle: profiles of $|\delta|$ (the absolute mean measurement error; dashed line), $\sigma(\delta)$ (the standard deviation of the individual measurement errors; dotted line), and $\Lambda_{\text{day},100\text{m}}$ (the root-mean-square of the individual measurement errors, see Equation (9.2); full line) as a function of geopotential height, computed over height bins of 100 m. The grey-shaded area extends $\pm\epsilon_{\text{day},100\text{m}}$ around $\Lambda_{\text{day},100\text{m}}$ (see Section 9.3). The values of $\Lambda_{\text{day},\mathcal{L}}$ for the PBL, the FT, the UTLS and the MUS atmospheric layers \mathcal{L} are marked using red diamonds (tagged accordingly), each with error bars extending $\pm\epsilon_{\text{day},\mathcal{L}}$ above and below each marker (see Table 10.3). Bottom: Histogram of the number of individual measurement points (J) and profiles (N) that contribute to each 100 m-bin. Bins with $J < 300$ are subject to larger statistical errors (see Appendix J), and should not be over-interpreted. The geopotential heights of the PBLH and the median tropopause are tagged with λ and $\bar{\gamma}$, respectively. The lower- and upper-bounds of the UTLS are marked with \vdash and \dashv .

As the measurement bias $\bar{\delta}_{\mathcal{C},\mathcal{L}}$ of a sonde approaches 0, the measurement uncertainties associated to $\sigma(\delta)_{\mathcal{C},\mathcal{L}}$ start to dominate the value of $\Lambda_{\mathcal{C},\mathcal{L}}$ ⁵.

The behaviour of $\epsilon_{\mathcal{C},\mathcal{L}}$ illustrated in Figure 10.14 is then driven by the fact that a standard deviation is not sensitive to correlated uncertainties but only to uncorrelated ones, whose importance diminish as the sample size becomes larger.

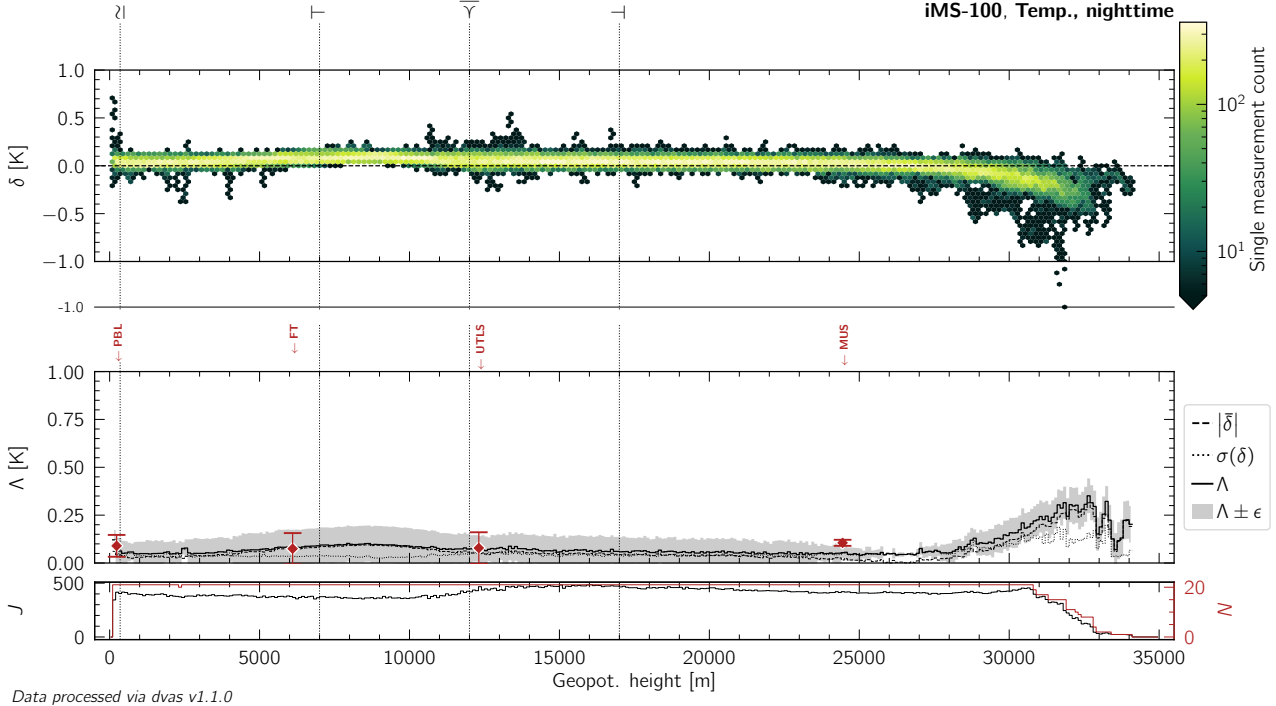


Figure 10.14: ORUC assessment function ($\Lambda_{\mathcal{C},\mathcal{L}}$) diagnostic diagram –as introduced in Figure 10.13– for the nighttime temperature measurements by the iMS-100 radiosonde. The amplitude of $\epsilon_{\text{night},100\text{ m}}$ (light grey area), the uncertainty envelope of $\Lambda_{\text{night},100\text{ m}}$, decreases significantly around the geopotential height of 26.5 km where the measurement bias $\bar{\delta}_{\text{night},100\text{ m}}$ approaches zero (dashed curve). The measure of $\Lambda_{\text{night},\text{MUS}}$ also has a very small uncertainty, as the measurement bias computed over the entire MUS region is ≈ 0 .

⁵To demonstrate this, let us introduce ϵ_A and ϵ_B the uncertainties of A and B , respectively. We have:

$$\frac{\partial \Lambda}{\partial A} = \frac{A}{\Lambda} \quad (10.5)$$

$$\frac{\partial \Lambda}{\partial B} = \frac{B}{\Lambda} \quad (10.6)$$

Such that:

$$\begin{aligned} V(\Lambda) &= \mathbf{G} \cdot \mathbf{U} \cdot \mathbf{G}^T \\ &= \begin{pmatrix} \frac{A}{\Lambda} & \frac{B}{\Lambda} \end{pmatrix} \cdot \begin{pmatrix} \epsilon_A^2 & \epsilon_A \epsilon_B \\ \epsilon_A \epsilon_B & \epsilon_B^2 \end{pmatrix} \cdot \begin{pmatrix} \frac{A}{\Lambda} \\ \frac{B}{\Lambda} \end{pmatrix} \\ &= \frac{A^2}{\Lambda^2} \epsilon_A^2 + \frac{B^2}{\Lambda^2} \epsilon_B^2 + 2\epsilon_A \epsilon_B \frac{AB}{\Lambda^2} \\ \bar{\delta}_{\mathcal{C},\mathcal{L}} \rightarrow 0 &\xrightarrow{J \gg 1} \frac{B^2}{\Lambda^2} \epsilon_B^2 \gg 0 \end{aligned} \quad (10.7)$$

10.1.5.3 The ORUC assessment function ($\Lambda_{c,\mathcal{L}}$) as a combined score of random and systematic measurement errors

Equation 10.3 has a profound implication: $\Lambda_{c,\mathcal{L}}$ is influenced both by the systematic measurement errors (via $\bar{\delta}_{c,\mathcal{L}}$) and the random measurement errors (via $\sigma(\delta)_{c,\mathcal{L}}$) of the system being evaluated. The assessment of a system's fitness-for-purpose with respect to a given ORUC is thus influenced by both its systematic and random measurement errors assessed with respect to the CWSs.

Understanding whether the performance of a given system is dominated by systematic or random measurement errors (or both) can be crucial, depending on its intended use. Two radiosondes may have similar $\Lambda_{c,\mathcal{L}}$ scores, but one may be driven systematic measurement errors, whereas the other could be driven random ones. Depending on the use case, a user may favour one over the other. For example, if working at lower temporal (i.e. vertical) resolution is acceptable, one may prefer a system with (comparatively) larger random errors, the influence of which can be mitigated through vertical data binning.

The Figures 10.3 to 10.12 and the $\Lambda_{c,\mathcal{L}}$ diagnostic plots provided in Appendix L can be used to clarify whether the $\Lambda_{c,\mathcal{L}}$ score of a given system is primarily driven by:

1. random measurement errors, if $|\bar{\delta}|_{c,\mathcal{L}} < \sigma(\delta)_{c,\mathcal{L}}$,
2. systematic measurement errors, if $|\bar{\delta}|_{c,\mathcal{L}} > \sigma(\delta)_{c,\mathcal{L}}$, or
3. both, if $|\bar{\delta}|_{c,\mathcal{L}} \approx \sigma(\delta)_{c,\mathcal{L}}$.

The behaviour of $\Lambda_{c,\mathcal{L}}$ with respect to correlated uncertainties discussed in Section 10.1.5.2 also provides an interesting means to distinguish the relative influence of systematic and random measurements errors in Tables 10.3 to 10.5 and Figures 11.1 to 11.3. For a given $\Lambda_{c,\mathcal{L}}$ values, a profile with a larger $\epsilon_{c,\mathcal{L}}$ uncertainty will be comparatively more affected by systematic measurement errors than a profile with a smaller $\epsilon_{c,\mathcal{L}}$ uncertainty.

It must be noted that random errors can have different sources, on which the value of $\Lambda_{c,\mathcal{L}}$ itself cannot say much. For example, large random errors could be the result of either intrinsic measurement noise, or heavy profile smoothing with respect to the variability seen in the CWSs. Differentiating between these two cases cannot be done directly from the $\Lambda_{c,\mathcal{L}}$ diagrams in Appendix L. This is unlike (for example) radiation correction errors, that give rise to systematic measurement errors with a (typically) recognisable trend, and a clear difference between daytime and nighttime behaviours. Discussing the exact source of random measurement errors for the different systems falls outside the scope of this report. Nonetheless, the different datasets provided in the UAI 2022 Supplementary Material can be used by the interested reader to study this question further.

10.1.6 Twin soundings

A series of twin soundings were performed for all radiosonde systems participating in the UAII 2022 field campaign (see Section 4.3.5). The detailed twin sounding statistics is specified for each system in Tables 8.2 and 8.3. The differences between these (synchronised) profile pairs are shown in Figures 10.15 to 10.21 at a resolution of 1 s for each system, for all the geophysical variables considered in this analysis. These figures give some insight into the repeatability of the different sondes, and are provided here for the benefit of the interested reader.

The number of twin soundings remains limited for all systems, with at most 5 (6) successful twin daytime (nighttime) soundings per system acquired over the course of the UAII 2022 field campaign. This obviously limits the *statistical exploitability* of these twin measurements. However, Figures 10.15 to 10.21 reveal a number of specific, noteworthy behaviours for some of the radiosondes. These sonde-specific points will be discussed in Section 10.1.9. Here we shall briefly mention some global behaviours shared by all/most sondes.

In Figure 10.15, the daytime temperature difference profiles are systematically noisier than nighttime ones. This is a direct consequence of the response of the temperature sensor/sonde to solar radiation. A (comparatively) higher noise level in the twin difference profiles suggests⁶ a higher sensitivity of the measurements from a given sonde to the instantaneous ventilation speed, and/or a stronger angular dependence of its temperature sensor on the incoming solar radiation (see Section 7.3.3.1). Such an angular dependence may be caused either by the geometry of the sensor/sensor-boom/sonde itself, and/or by some variability in the manufacturing process. Identifying the exact cause for each radiosonde would require dedicated laboratory measurements akin to those described in Chapter 7. In any case, an a posteriori correction of such rapid, solar-driven temperature fluctuations would remain very challenging, given 1) the (typically) unknown orientation of the sonde at any given moment in time, and 2) the (usually) “rotation-averaged” nature of corrections related to solar radiation. Careful sensor/sonde design is key to reducing the solar-driven noise in diurnal temperature measurements, and thus reducing random measurement errors.

Such a strong daytime-nighttime difference is not seen for the relative humidity measurements in Figure 10.16. For this variable, the presence of large offsets appears to be more directly related to the conditions of the flight itself (or, possibly, to the underlying calibration of the sensors), rather than to the mere visibility (or not) of the Sun in the sky.

Finally, large offsets in the wind (horizontal) speed, direction and vector measurements are visible for most systems shortly after launch (see Figures 10.19 to 10.21). Although some of this behaviour is very plausibly related to the campaign setup (see Section 8.2.5), these offsets nonetheless suggest a general difficulty in performing wind (horizontal) measurements within the few tens of seconds after launch.

⁶since the sondes were hanging freely under the rig, see Appendix F.3.2.

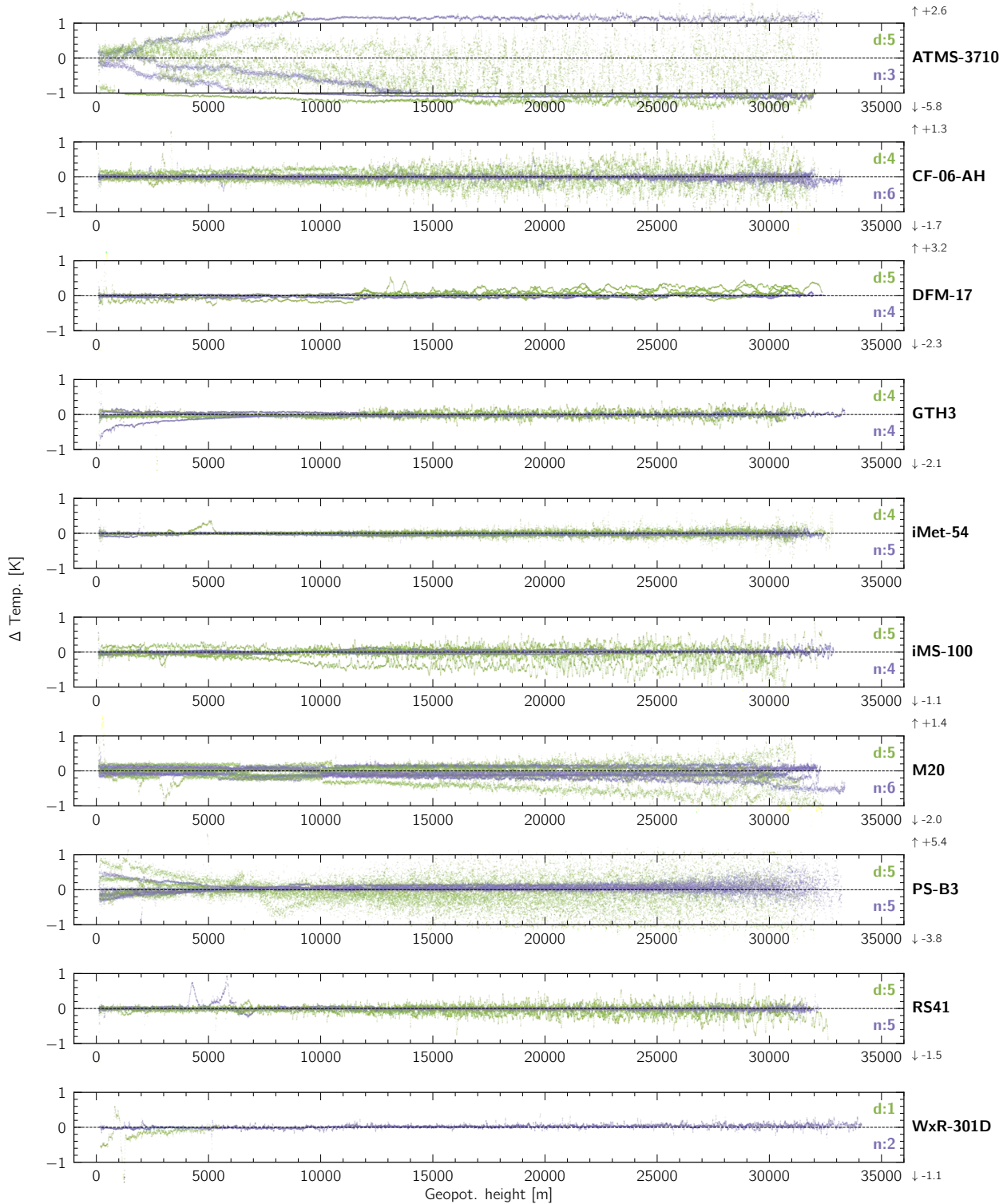


Figure 10.15: Twin sounding profile differences for daytime (green dots) and nighttime (purple dots) flights, for atmospheric temperature. Each dot shows the difference between two measurement points acquired by two sondes of the same model during a twin sounding. Each profile is shown in its entirety, including beyond the nominal vertical range of each diagram, where the y-location of each dot is scaled linearly between the diagram's edge and the extremum value. The minimum and maximum difference values of all the curves are shown to the right of each panel, when these are located beyond the range of the diagram. The number of curves in each diagram is given to the right of each panel for both the daytime (top) and nighttime (bottom) flights. Fewer twin flights were acquired for the WxR-301D sonde due to the critical failure of one of its ground systems (see Section 8.3).

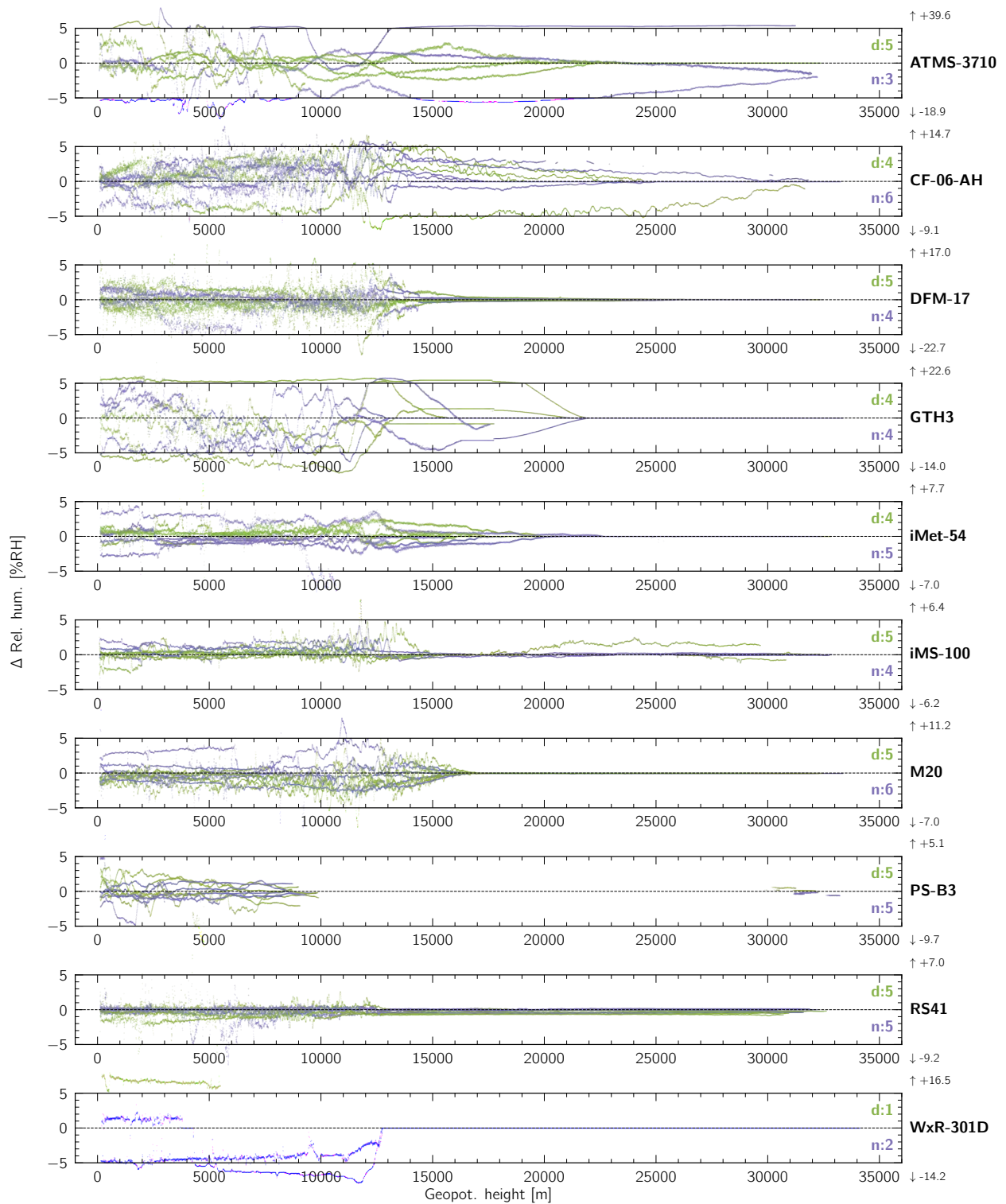


Figure 10.16: Same as Figure 10.15, but for the relative humidity.

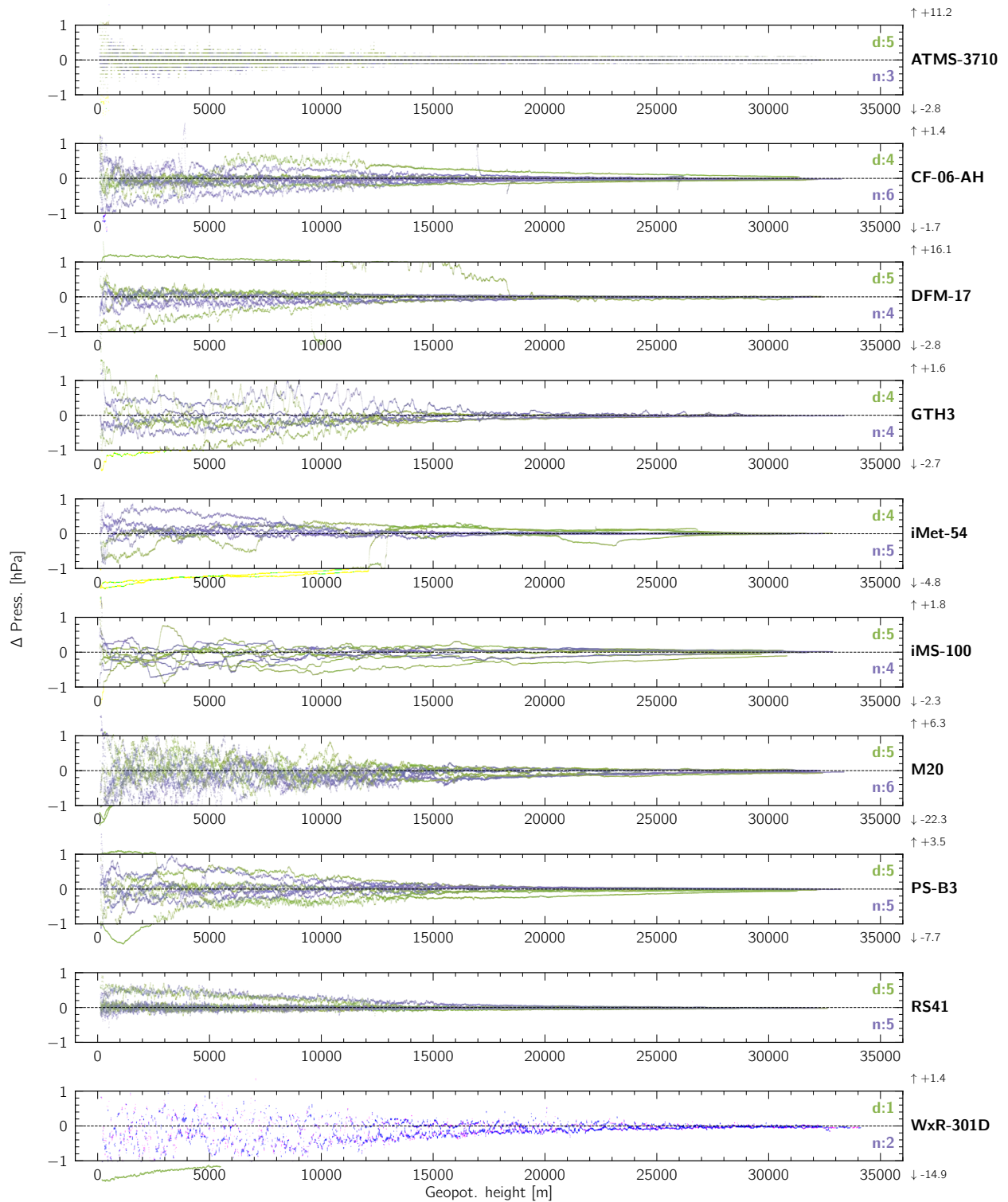


Figure 10.17: Same as Figure 10.15, but for the atmospheric pressure.

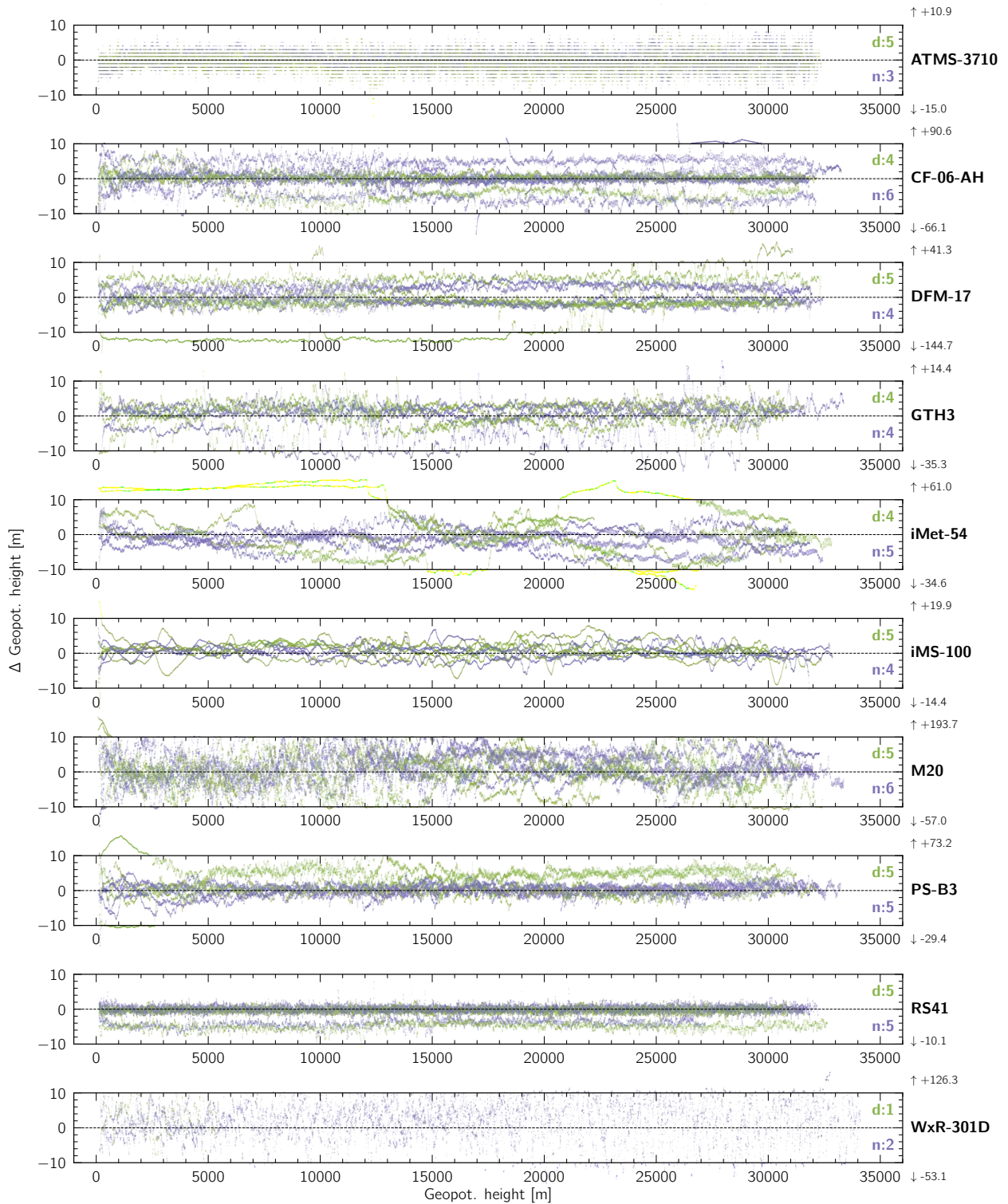


Figure 10.18: Same as Figure 10.15, but for the geopotential height.

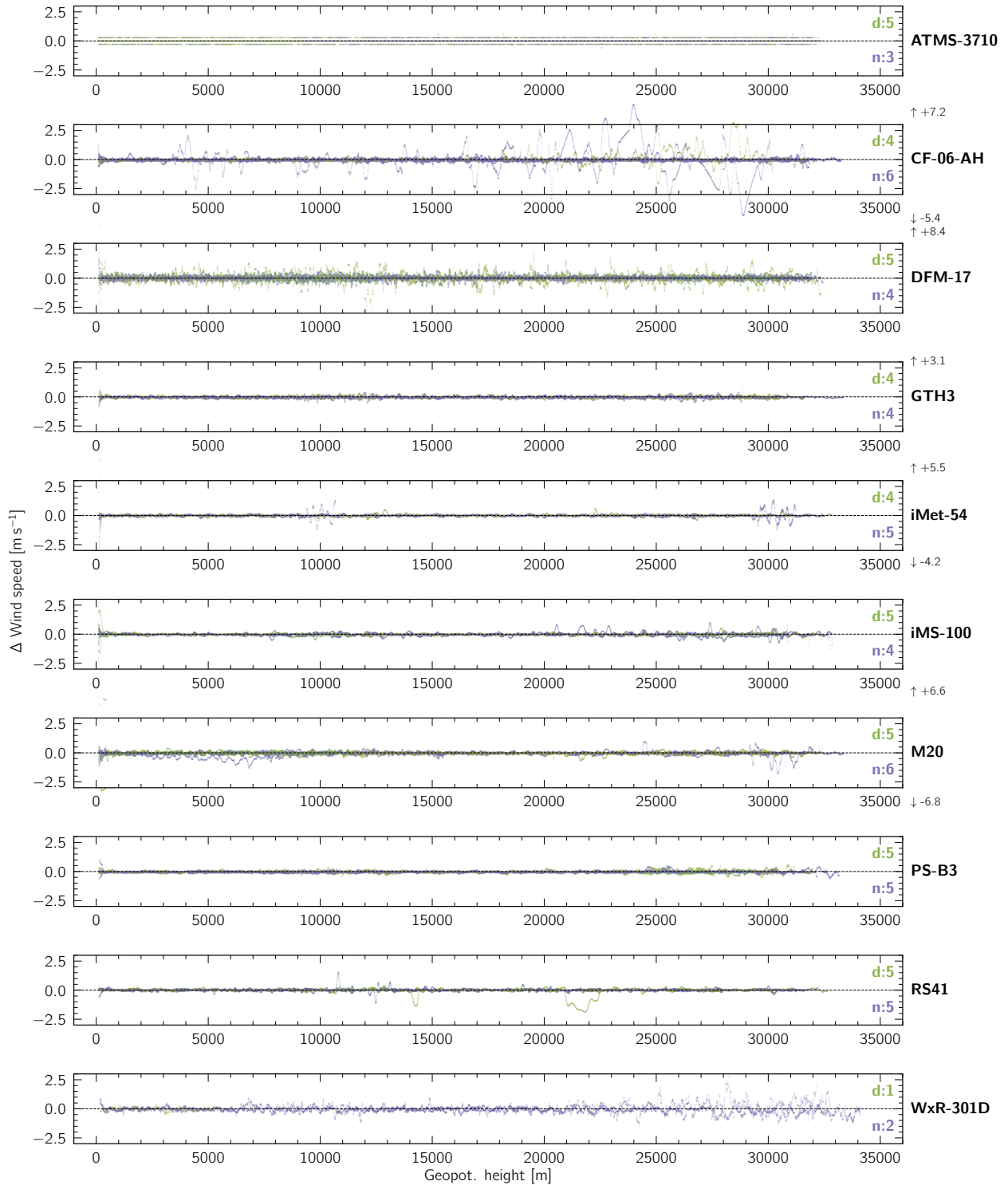


Figure 10.19: Same as Figure 10.15, but for the wind (horizontal) speed.

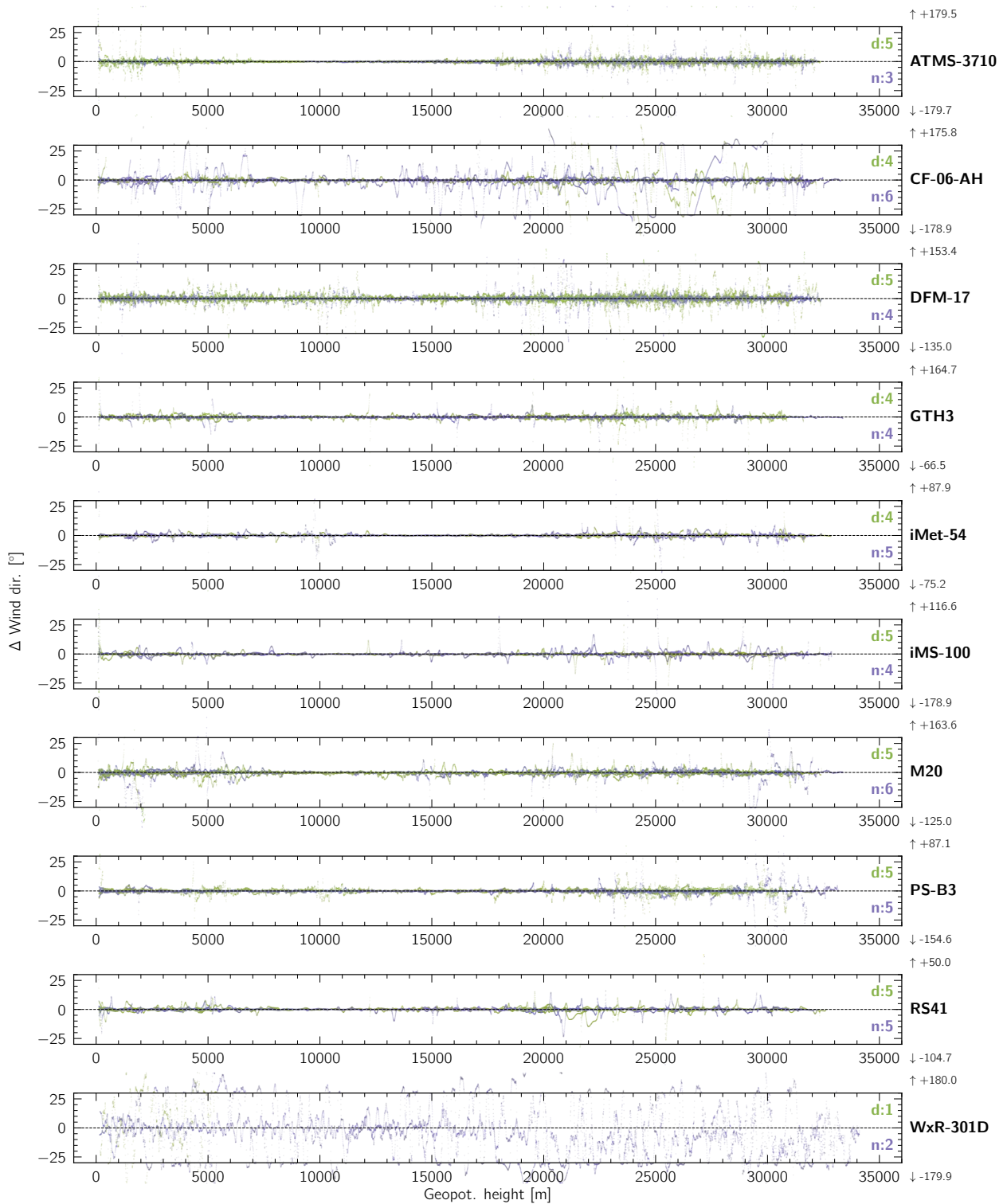


Figure 10.20: Same as Figure 10.15, but for the wind (horizontal) direction.

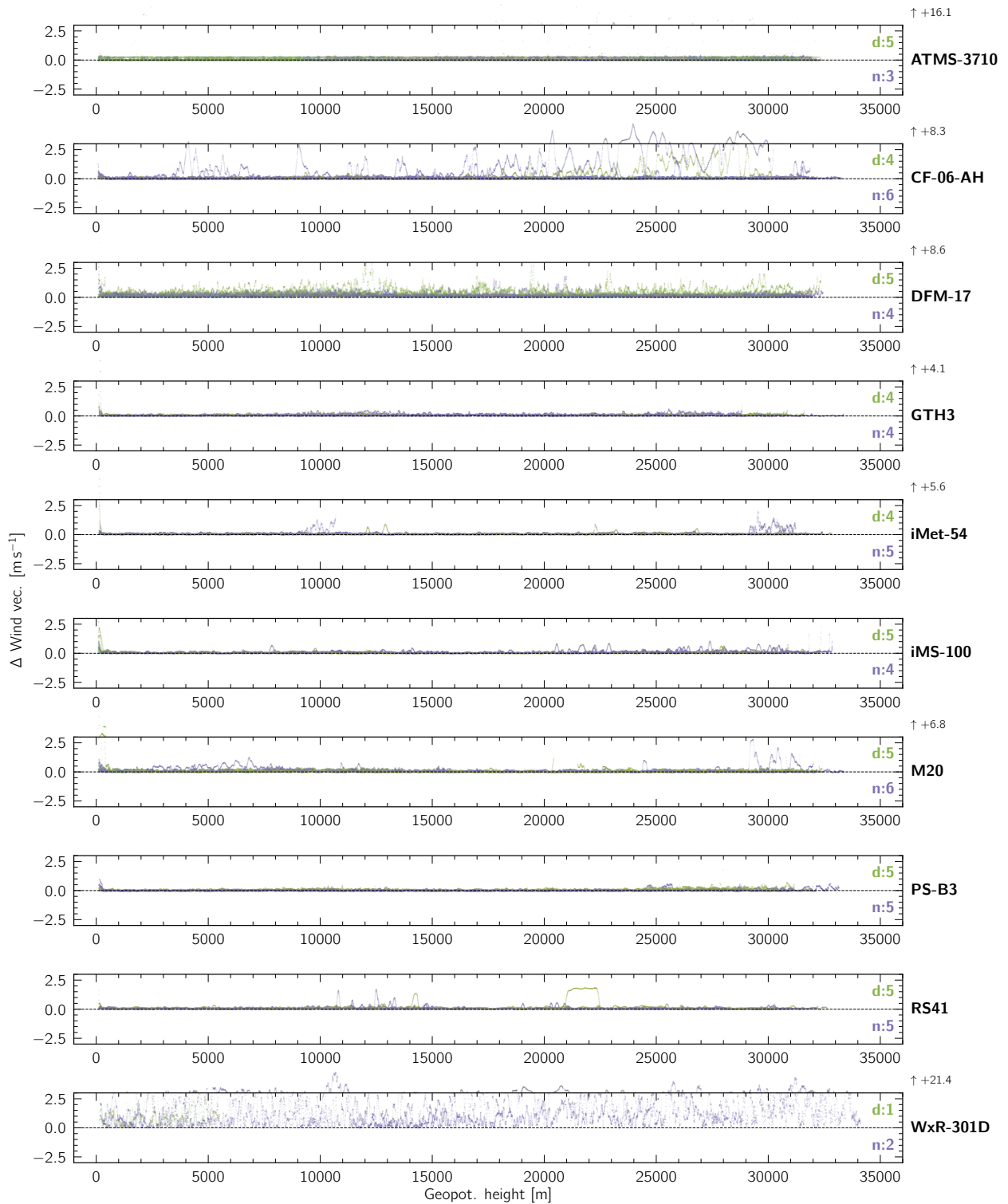


Figure 10.21: Same as Figure 10.15, but for the wind (horizontal) vector.

10.1.7 Cloud exits

10.1.7.1 Atmospheric temperature

The so-called “wet-bulb” effect refers to cooler-than-ambient-air temperature measurements resulting from the evaporation of water that has accumulated on the temperature sensor of a radiosonde after passing through a cloud or rain. This behaviour is most noticeable after exiting clouds when dry air leads to rapid evaporation, and thus rapid cooling of the temperature sensor that can result in super-adiabatic lapse rates. To prevent or inhibit this effect and the resulting measurement errors, some radiosonde manufacturers apply a hydrophobic coating to the temperature sensor and/or use dedicated algorithms to detect and correct regions of super-adiabatic cooling.

All radiosondes participating in the UAI 2022 field campaign were subject to the wet-bulb effect, with varying degrees of intensity. In order to characterise the associated temperature measurement error for each system, we consider cases where no atmospheric temperature CWS can be assembled for at least 20 s (consecutive; according to the statistical compatibility criterion discussed in Section 9.2) as a result of the wet-bulb effect. With no CWS available, we compute the difference between the temperature measurements of each sonde on the rig and the warmest GDP⁷ over a window of 600 s starting at the lowest level where no CWS could be assembled. We restrict ourselves to the atmospheric region above the PBL and below the UTLS in order to remain within the regime of liquid or mixed phase clouds.

As shown in Figure 10.22, we find that wet-bulb-induced temperature measurement errors reach up to almost 4 K for some systems. We cannot exclude the possibility that the warmest GDP may itself be subject to the wet-bulb effect, so that the values visible in Figure 10.22 should be considered as lower limits. On the other hand, it is evidently not because (at least) one of the GDPs is subject to the wet-bulb effects that all the sondes on the rig will be too: this is reflected in the fact that not all profiles in Figure 10.22 indicate large temperature errors.

For all sondes, the temperature error profiles are highly variable – a direct consequence of the variability in the atmospheric conditions and the amount of sensor contamination on each individual flight. With a maximum measurement error of ~ 1 K, the RS41 sonde shows the lowest wet-bulb-induced errors for the atmospheric conditions sampled during the UAI 2022 field campaign.

From the cases that show clear wet-bulb-driven temperature errors, we find that all sondes typically recover from the wet-bulb effect within 500 s ($\cong 2500$ m at a typical ascent speed of 5 m s^{-1}) except the DFM-17 sonde, where recovery exceeds 600 s in at least two cases. The ATMS-3710 sonde shows long lasting errors, but these are related to the general behaviour of this sonde (see Section 10.1.9.1), and not just the wet-bulb effect.

10.1.7.2 Relative humidity

In some circumstances, the passage of a radiosonde through dense, mixed-phase clouds can lead to long-lasting erroneous measurements of relative humidity. This is due to the deposition of water on the humidity sensor, which can lead to an overestimation of the ambient relative humidity after exiting the cloud. While any sonde can be affected by this problem, the extent and duration of the elevated measurements will typically depend on the design of the humidity sensor and sensor-boom (including the presence/absence of a protective cap, the sensor coating, and the presence/absence of sensor heating).

In Figure 10.23, we show the difference between the relative humidity measured by a given sonde and the driest GDP before and after exiting from dense clouds above the PBL and below the UTLS. Dense-cloud regions are identified as cases where the CWS reports at least 20 consecutive relative humidity measurements equal to or larger than 99.9 %RH. The profile differences are then computed over a window extending 600 s beyond the “in-cloud” region, to assess the behaviour of the relative humidity sensor after the cloud exit.

In this visualisation, the contamination of a relative humidity sensor takes the form of a dis-

⁷which is the RS41 GDP in 61 % of cases, and the IMS-100 GDP in 39 % of cases.

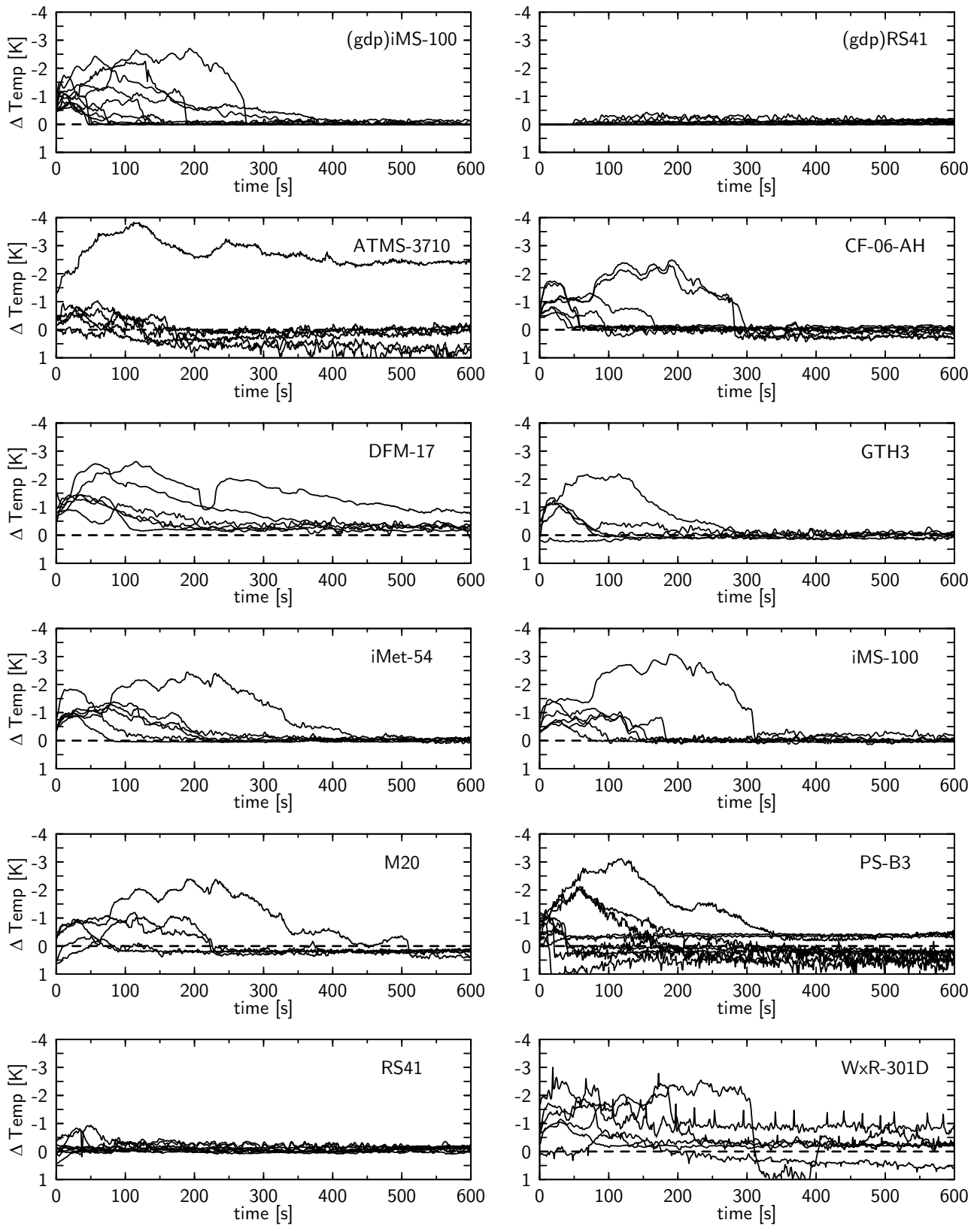


Figure 10.22: Temperature differences between a given sonde and the warmest GDP profile of the rig, for cases where temperature GDP profiles are statistically incompatible due to wet-bulb effects above the PBL and below the UTLS.

continuity at the cloud exit. The majority of radiosondes show such discontinuities in some of their profiles, with errors growing up to 30 %RH or so. In several instances, the error is seen to decrease over a duration of 300 s. However, this is not always the case, the contamination of the relative humidity measurements can remain in place up to and beyond 600 s. For an illustration of this behaviour, we refer the interested reader to the CWS diagnostic diagrams of flight F20 in the UAI 2022 Supplementary Material, where the persistent contamination of the iMS-100 GDP results in the impossibility of assembling a relative humidity CWS in the stratosphere.

Some systems (M20, RS41, and WxR-301D) do not appear to have experienced severe contamination of their humidity sensor in the cases evaluated in Figure 10.23. However, it is important to remember that the contamination of a particular humidity sensor on a particular flight will always be affected by random factors. Therefore, it cannot be concluded that these systems are completely immune to the problem. The small number of profiles considered here certainly prevents us from drawing firm conclusions, statistically speaking. On the basis of data available, we see no obvious correlation between the behaviour of a given sensor and its characteristics, as outlined in Table 3.2.

10.1.8 In-clouds behaviours

The ability of radiosondes to measure 100 %RH is essential for several applications, such as cloud thickness analysis. In Figure 10.24, we show the distribution of $\Delta\text{Rel. hum.}|_{\text{cloud}}$, the difference between the relative humidity measured by a given sonde and the CWS, for cases where 100 %RH (or more) is measured by the latter. Most sonde models perform an active clipping of relative humidity measurements above 100 %RH. Bearing this fact in mind, we find that six sondes are able to measure relative humidity values of 100 %RH in agreement with the CWS (within the associated CWS measurement uncertainties): CF-06-AH, DFM-17, iMet-54, iMS-100, M20, and RS41. The median measurement error of the WxR-301D sonde is close to 0 %RH, but the range of measurement errors extends significantly to negative offsets (indicating a dry bias) up to and beyond -5 %RH. Three sonde models stand out with median measurement errors outside of the CWS measurement uncertainty range: ATMS-3710 (-17.5 %RH), GTH3 (-8.1 %RH), and PS-B3 (-13.8 %RH).

The ability of radiosondes to reach 100 %RH has also been tested, independently of the CWS, by means of pre-flight SHC tests (see Section 4.3.8). The SHC provides a controlled environment at 100 %RH and ambient temperature. The distributions of $\Delta\text{Rel. hum.}|_{\text{SHC}}$, the relative humidity measurement errors in the SHCs, are shown in Figure 10.25. The overall distributions appear to be broadly consistent with the in-flight behaviour, bearing in mind that the SHC observations may not have been processed in exactly the same way as the in-flight measurements by the various systems. Both the ATMS-3710 sonde and the PS-B3 display a dry bias in the SHC as they do in-flight, albeit with different amplitudes most certainly due to the temperature differences between the SHC and the atmosphere. However, the behaviour of two sondes in the SHC appears to be different from their in-flight behaviour: the iMS-100 sonde shows a median overestimation of 2.6 %RH in the SHC, while the iMet-54 shows a median underestimation of -6.8 %RH which is not seen in-flight. The exact reason for these different behaviours, and in particular that of the iMet-54 sonde, is unknown.

So far, we have only discussed the global behaviour of sondes in the pre-flight SHC tests. An immediate follow-up question is whether the correlation between SHC and in-flight behaviour also exists on a flight-by-flight basis: that is, whether measurements in the SHC do correlate strictly (or not) with the in-flight behaviour of a given sonde. We explore this aspect in Figure 10.26, which shows the distribution of $\Delta\text{Rel. hum.}|_{\text{cloud}} - \Delta\text{Rel. hum.}|_{\text{SHC}}$ computed on a flight-by-flight basis. A narrow distribution would indicate that the SHC test is predictive of the in-cloud behaviour (modulo a possible temperature-related offset in the error amplitude). On the other hand, a broad distribution (i.e. broader than the individual distribution of the in-flight relative humidity measurement errors) would indicate that the sonde behaviour in the SHC is decoupled from its behaviour in-flight. We find that the latter scenario does not apply. Sonde behaviour during the SHC tests is found to be well correlated with the in-flight behaviour overall, including for the iMet-54 sonde which consistently shows a drier bias in the SHC.

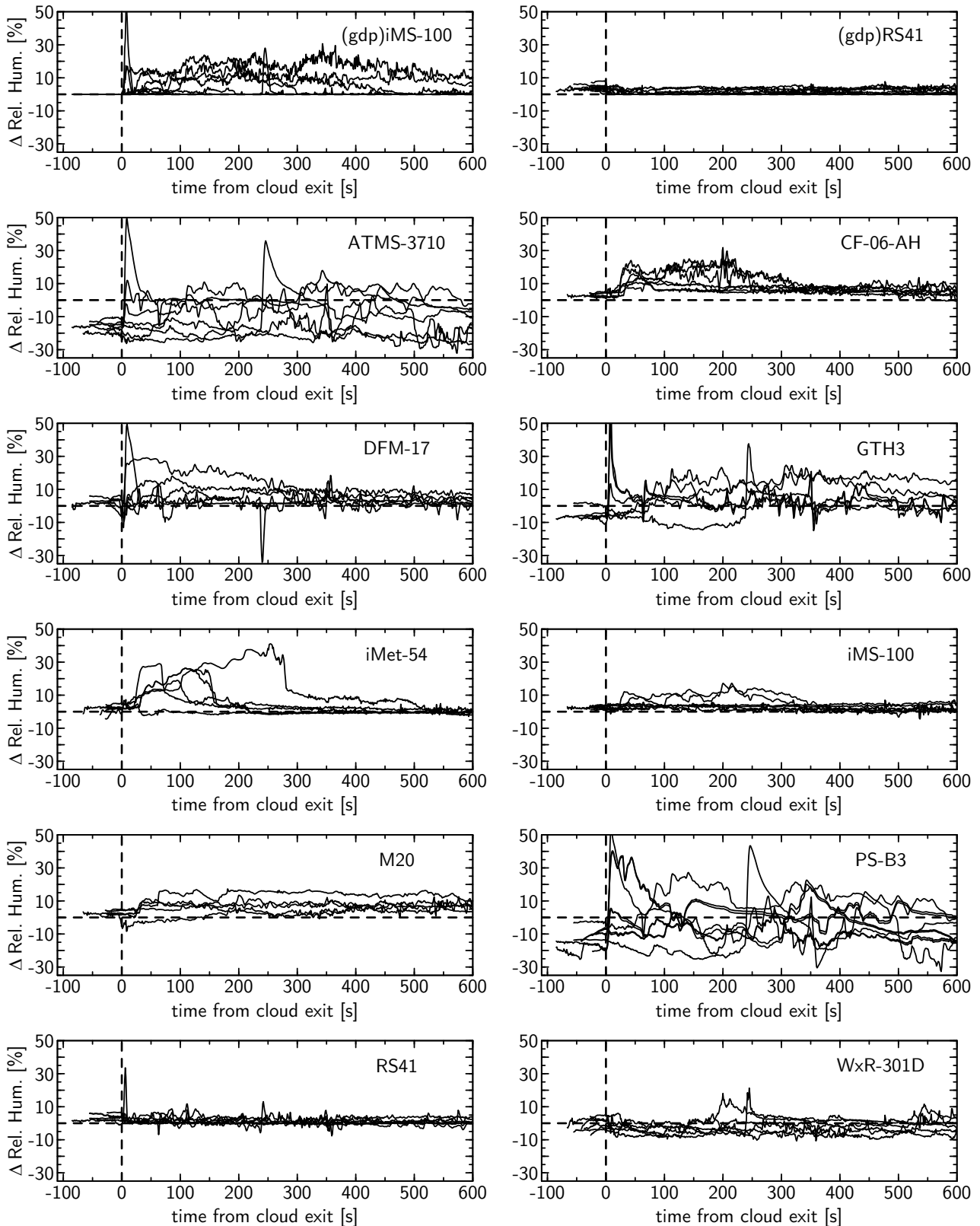


Figure 10.23: Relative humidity measurement error observed after passing through dense, mixed-phase clouds. Each curve corresponds to the difference between the relative humidity measured by a given sonde and the driest GDP on the rig. Cases are identified as regions where the CWS reports at least 20 consecutive relative humidity measurements equal to or larger than 99.9%RH between the PBLH and the UTLS. The profile differences are then computed over a window extending 600s beyond the “in-cloud” region, with the moment of cloud exit centred at 0s. Contamination of a humidity sensor takes the form of a discontinuity (with respect to the in-cloud behaviour) that appears at the cloud exit.

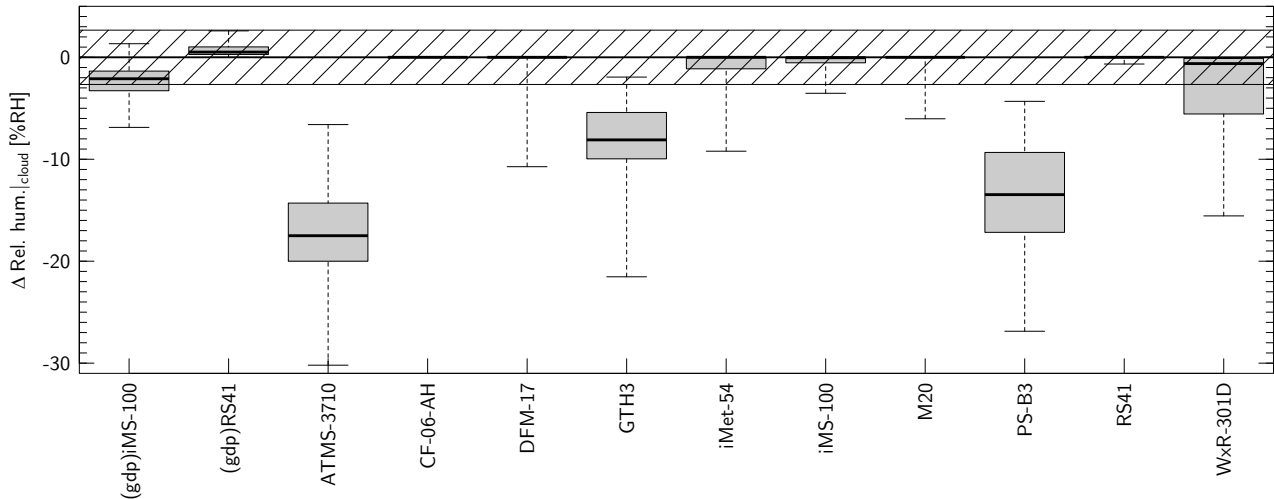


Figure 10.24: Distribution of the relative humidity measurement errors ($\Delta\text{Rel. hum.}|_{\text{cloud}}$, computed with respect to the CWSs) for each radiosonde model that participated in the UAI 2022 field campaign, for cases where exactly 100 %RH is measured by the CWS. For each sonde, the black bar indicates the median value, the grey area extends from the 25 percentile to the 75 percentile of the distribution, and the whiskers extend up to the minimum and maximum values. The maximum, total measurement uncertainty of the (individual) CWS measurements is shown by the hatched region ($k = 1$). The average number of data point per sonde is 744 ± 202 .

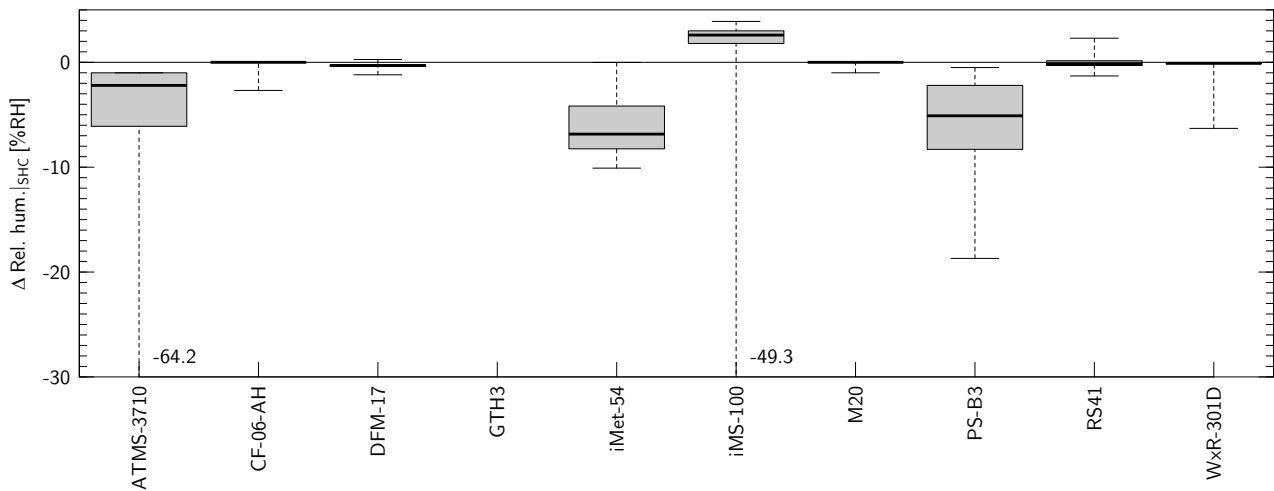


Figure 10.25: Distribution of the relative humidity measurement errors in the pre-flight SHC tests ($\Delta\text{Rel. hum.}|_{\text{SHC}}$) for each radiosonde model that participated in the UAI 2022 field campaign, with the exception of GTH3 for which no pre-flight SHC tests could be performed*. For each sonde, the black bar indicates the median value, the grey area extends from the 25 percentile to the 75 percentile of the distribution, and the whiskers extend up to the minimum and maximum values.

* In view of the high failure rate of the GTH3 radiosonde model during the campaign (see Section 8.2.3), it was decided (after a few flights) to not put this sonde through the pre-flight SHC to minimise the “stress” experienced by the system pre-flight.

10.1.9 Model-specific observations

In the following Sections, we discuss systematic behaviours specific to each radiosonde participating in the UAI 2022 field campaign that have not been discussed elsewhere. These Sections are absolutely not meant to serve as executive summaries of each systems. Rather, they are

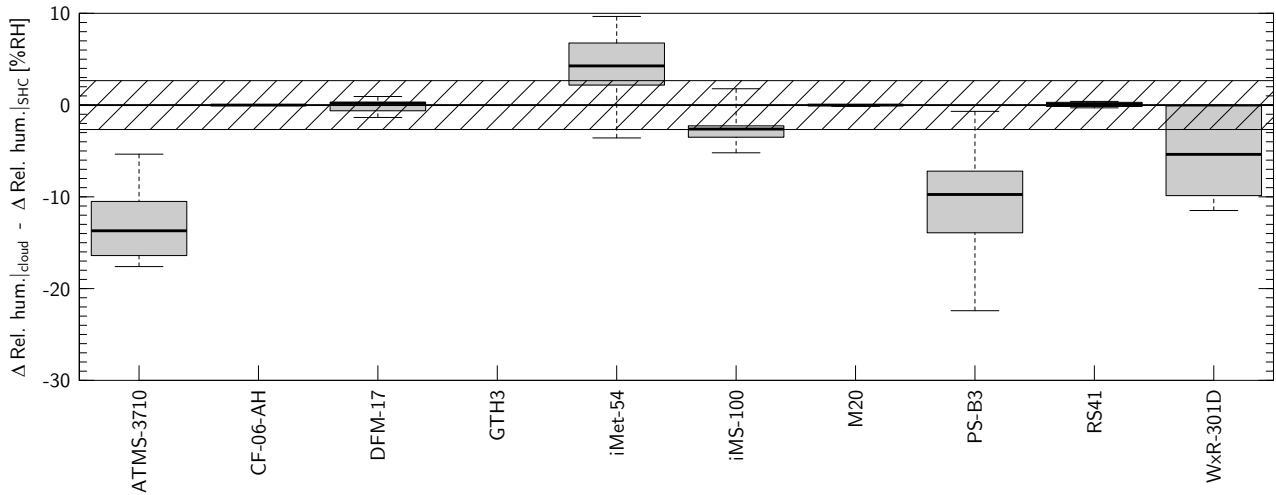


Figure 10.26: Distribution of $\Delta \text{Rel. hum.}|_{\text{cloud}} - \Delta \text{Rel. hum.}|_{\text{SHC}}$ (computed on a flight-by-flight basis) for each radiosonde model that participated in the UAI 2022 field campaign (except the GTH3 sonde for which no pre-flight SHC checks could be made). For each sonde, the black bar indicates the median value, the grey area extends from the 25 percentile to the 75 percentile of the distribution, and the whiskers extend up to the minimum and maximum values. The maximum uncertainty of the (individual) CWS measurements of relative humidity ($k = 1$) is shown by the hatched region.

intended to complement the other observations reported elsewhere in this report.

10.1.9.1 ATMS-3710

The ATMS-3710 sonde shows a strong, warm measurement bias for daytime flights ($\bar{\delta} \approx +4$ K at 30 km, see Figure L.1) and cold measurement bias for nighttime flights ($\bar{\delta} \approx -7.5$ K at 30 km, see Figure L.2). In particular, the nighttime flights show a large and uniform spread of the temperature measurement errors above the tropopause. The twin sounding flights of this sonde also show large, systematic temperature differences up to 2 K (see Figure 10.15).

The ATMS-3710 sonde shows a dry measurement bias for relative humidity that increases with altitude up to $\bar{\delta} \approx -35$ %RH at the tropopause, for both daytime and nighttime flights. This sonde is the only system relying on direct pressure measurements. Its pressure measurement errors also show a characteristic trend, with a mean measurement error of $\bar{\delta} \approx -14$ hPa at 8 km.

10.1.9.2 CF-06-AH

The CF-06-AH sonde has one of the smallest temperature measurement biases of all the sondes involved in the UAI 2022, with a mean measurement error of $|\bar{\delta}| < 0.05$ K, particularly for nighttime flights (see Figures 11.1 and L.16). It is this characteristic that lets it be the only sonde found to be “fit-for-purpose” with respect to the (most challenging) ORUC Goal value associated with the application area “Atmospheric Climate Forecasting and Monitoring”, albeit still only in the UTLS for nighttime flights (see Table 11.4).

The CF-06-AH sonde shows a wet measurement bias of $\bar{\delta} \approx +3$ %RH up to the tropopause. For several flights where the sonde passed through a 100 %RH layer (e.g. F26, F69, F76), this sonde reports elevated relative humidity readings throughout the stratosphere (up to 15 %RH for certain flights, see Figure L.17).

10.1.9.3 DFM-17

The DFM-17 sonde displays a cold temperature bias during the day of the order of $\bar{\delta} \approx 0.2$ K up to the top of the UTLS, gradually increasing in the MUS up to $\bar{\delta} \approx 0.5$ K at 30 km (see Figure L.29). The nighttime measurement bias for atmospheric temperature is less than 0.2 K at all altitudes (see Figure L.30).

10.1.9.4 GTH3

The GTH3 sonde shows a small temperature measurement bias at all altitudes ($|\bar{\delta}| \lesssim 0.15$ K), except for the MUS for daytime flights where it displays a cold measurement bias that increases with altitude, up to $\bar{\delta} \approx -0.4$ K at 30 km (see Figure L.43). For relative humidity, the measurement errors of this sonde show a wide spread up to the tropopause with $\sigma(\delta) \approx 7.5$ %RH for daytime flights (see Figure L.45) and $\sigma(\delta) \approx 5$ %RH for nighttime flights (see Figure L.46). The relative humidity differences observed during the twin-sounding flights reached up to 10 %RH (throughout the FT) on at least two occasions (see Figure 10.16).

The GTH3 sonde shows a bimodal behaviour with respect to its geopotential height measurements. Although a number of profiles report geopotential heights within 10 m of the CWSs throughout the entire ascent, the majority of profiles show a geopotential height measurement error that increases linearly with altitude, with individual measurement errors up to 50 m at 30 km, resulting in a geopotential height measurement bias of $\bar{\delta} \approx 30$ m at 30 km (see Figures L.47 and L.48).

10.1.9.5 iMet-54

The temperature measurement errors for the iMet-54 sonde show a small spread at all altitudes with $\sigma(\delta) \lesssim 0.1$ K (see Figures L.57 and L.58). However, this sonde also shows a very systematic trend in its temperature measurement bias $\bar{\delta}$: from $\bar{\delta} \approx 0$ K in the lower troposphere for daytime flights, a cold measurement bias develops in the UTLS to reach up to $\bar{\delta} \approx -0.2$ K at the tropopause and beyond. A similar behaviour is observed with nighttime flights, although with a somewhat smaller amplitude with the cold measurement bias reaching up to $\bar{\delta} \approx -0.12$ K in the MUS.

10.1.9.6 iMS-100

The iMS-100 sonde shows a small temperature measurement bias for both daytime and nighttime flights, with $|\bar{\delta}| \lesssim 0.1$ K (see Figure L.71), with one exception: a cold bias is seen to develop above 27 km for nighttime flights, reaching up to $\bar{\delta} \approx -0.25$ K at 32 km (see Figure L.72).

10.1.9.7 M20

For nighttime flights, the small scatter of the temperature measurement errors ($\sigma(\delta) < 0.1$ K up to 25 km, see Figure L.86) displayed by the M20 sonde is associated with a clear trend in the sonde's mean temperature measurement bias $\bar{\delta}$. It is seen to increase up to $\bar{\delta} \approx +0.2$ K in the first 2 km after launch, before gradually decreasing towards the tropopause. A similar behaviour is observed for daytime flights (see Figure L.85), with the addition of a linear increase of the standard deviation of the individual temperature measurement errors in the MUS up to $\sigma(\delta) \approx 0.35$ K at 30 km.

Several twin sounding flights of the M20 sonde reveal the presence of discontinuities of the order of ~ 0.1 K in the temperature difference between two sondes, which appear to be systematically located around 7 km and 10 km. Similar discontinuities are also observed with respect to the CWS (for example: F03 (system 1), F08, F09, F15, F26 (system 1), ...).

Regarding relative humidity, the M20 shows a wet measurement bias in the FT, which increases up to $\bar{\delta} \approx +10$ %RH at 10 km for nighttime flights (see Figure L.88).

10.1.9.8 PS-B3

The PS-B3 sonde has a warm temperature measurement bias that increases linearly up to $\bar{\delta} \approx +1.5$ K at 30 km for daytime flights, alongside a dispersion of individual temperature measurement errors that increases linearly up to $\sigma(\delta) \approx 0.7$ K at 30 km (see Figure L.99).

For nighttime flights, the sonde displays a cold measurement bias of $\bar{\delta} \approx -0.3$ K in the PBL that decreases to $\bar{\delta} \approx -0.15$ K in the UTLS, before increasing to $\bar{\delta} \approx -0.5$ K at 30 km (see Figure L.100).

For daytime flights, the PS-B3 sonde displays a dry measurement bias of $\bar{\delta} \approx -15$ %RH in the FT, which is not seen for nighttime flights (see Figure L.101 and L.102). No assessment of relative humidity measurements is possible for this sonde above ~ 9 km where the ambient air temperature falls below -40 °C. The relative humidity sensor of the PS-B3 sonde has not been characterised in this regime by Vikram Sarabhai Space Center, Indian Space Research Organisation as of yet, and its measurements are not reported. We note, however, that there are some relative humidity readings from this sonde above 30 km. These result from the atmospheric temperature increasing above the cropping threshold of -40 °C at these altitudes, for certain flights of the UAI 2022 field campaign.

The geopotential height measurements from the PS-B3 sonde are found to be systematically within ± 10 m of the CWS (see Figure L.104). However, its pressure measurements have well-structured measurement errors with a characteristic trend that is maximum at 5 km with a measurement bias of $\bar{\delta} \approx -1.3$ hPa (see Figure L.106).

10.1.9.9 RS41

The RS41 sonde shows both a small temperature measurement bias and dispersion, with $|\bar{\delta}| < 0.1$ K and $\sigma(\delta) < 0.1$ K in all cases except for daytime flights in the stratosphere (see Figure L.113). There, a cold temperature measurement bias develops gradually from the tropopause and reaches $\bar{\delta} \approx -0.3$ K at 30 km. The standard deviation of the temperature measurement errors also increases in this region, reaching $\sigma(\delta) \approx 0.15$ K at 30 km.

10.1.9.10 WxR-301D

The WxR-301D sonde displays a cold measurement bias for nighttime flights, with $\bar{\delta} \approx -0.15$ K up to the MUS, where the temperature cold bias starts to increase to $\bar{\delta} \approx -0.6$ K at 31 km (see Figure L.128). This cold measurement bias is not seen during daytime flights (see Figure L.127), where the distribution of individual temperature measurement errors of this sonde instead shows a wide spread with $\sigma(\delta) \approx 0.6$ K in the MUS.

The WxR-301D sonde shows a dry measurement bias of $\bar{\delta} \approx -5$ %RH up to the tropopause for both daytime and nighttime flights (see Figure L.129 and L.130). The WxR-301D sonde also shows a measurement bias in the reported pressure, of which the individual measurement errors display a specific trend as a function of altitude with a maximum measurement bias of $\bar{\delta} \approx +12$ hPa at 3 km (see Figures L.133 and L.134).

10.2 REMOTE SENSING

The assessment of the performance of the LRSS instruments is obtained by evaluating the values of the ORUC assessment function $\Lambda_{\mathcal{C},\mathcal{L}}$ and its associated measurement uncertainty $\epsilon_{\mathcal{C},\mathcal{L}}$ (see Section 9.3.2) for the atmospheric layers $\mathcal{L}=[\text{PBL}, \text{FT}, \text{UTLS}]$ and flight categories \mathcal{C} considered in this analysis.

In this Section we provide the results of the comparison of the remote sensing against the reference Combined Working measurement Standard (CWS), these results will be used in Section 11.2 to assess the performances of the LRSS instruments with respect to specific ORUC requirements.

10.2.1 Missing data

As outlined in Section 9.6.1, based on their measuring principles, the Signal-to-Noise Ratio (SNR) of the Doppler Wind Lidar (DWL) and Radar Wind Profiler (RWP) cannot be the same through all atmospheric layers \mathcal{L} . The signal intensity depends on the strength of the particular scattering process along the line of sight of the DWL and RWP and must be large enough in order for the signal to be above the overall measurement's noise. The amount of data (i.e. data availability) is determined by both the propagation characteristics of the used radiation through the atmosphere as well as by the scattering properties of the sampled volume. Data points below the SNR threshold are filtered out by the quality control and are not available for the comparison with the CWS. Similar to the RWP, the Micro-Wave Radiometer (MWR) can measure in almost all weather conditions except during rain. Thus, also for the MWR, the data availability is depleted due to filtering by the software during rain periods (active rain flag). Table 10.6 shows the average number of missing measurement points (data missing rate), and associated standard deviation, in %, reported for each LRSS instrument participating in UAI field campaign. For the two DWL, we split the statistics in two atmospheric regions, 0 km to 1.5 km and 1.5 km to 9 km, as the data availability within and above the PBL is significantly different for the DWL (see Section 9.6.1).

Table 10.6: Average number of missing measurement points, and associated standard deviation, in %, measured by the different LRSS instruments, during the UAI 2022.

	Temp.	Rel. humidity	Wind dir.	Wind speed
MWR-SMZ	06.64 ± 01.36	06.33 ± 01.45		
MWR-MF	07.91 ± 01.37	07.59 ± 01.45		
WindLidar1 (0–1.5 km)			30.80 ± 14.22	29.41 ± 14.21
WindLidar1 (1.5–9 km)			91.42 ± 13.51	91.31 ± 13.87
WindLidar2 (0–1.5 km)			30.38 ± 24.49	28.14 ± 25.03
WindLidar2 (1.5–9 km)			93.05 ± 11.52	92.72 ± 12.50
WindProfiler-HighMode			47.64 ± 28.67	49.91 ± 28.63
WindProfiler-LowMode			32.81 ± 25.73	29.90 ± 27.59

The data in Table 10.6 should be interpreted differently from those shown for the radiosondes in Table 10.1. A typical radiosonde profile contains 6000 points on average, while each instrument of the LRSS has a different and coarser vertical resolution leading to a much lower number of points and to higher values of missing data in percentage. The typical MWR profile contains 94 points, such that a missing rate of 7.5 % corresponds to about 7 missing points. For the DWL, the 0 km to 1.5 km region is comprised of 30 points, such that an average missing rate of 30% in the PBL corresponds to about 10 points. Above the PBL the average missing rate is much higher for the DWL, i.e. the 92% corresponding to about 240 points. The RWP profiles count 35 vertical points in high mode and 96 in low mode. The missing rate correspond then to about 15 and 30 missing points for the high and low mode, respectively.

Important note: the missing data rate for remote sensing systems must be carefully interpreted in comparison to the radiosondes because it strongly depends on the sampling configuration of

the instruments. For example, the sampling of the DWL is typically configured in such a way that signals can be obtained from cirrus clouds near the Tropopause. As such, measurements are of course not always possible due to propagation limitations of the infrared laser radiation (e.g. in case of low level liquid cloud layers) the number of missing measurement points will necessarily be high under such circumstances. This parameter thus reflects not only the performance of the particular instrument, but also the atmospheric conditions.

10.2.2 ORUC assessment functions (Λ)

For all the geophysical variables, instruments of the LRSS, flight categories \mathcal{C} , and atmospheric layers \mathcal{L} , the profiles of $\Lambda_{\mathcal{C},\mathcal{L}} \pm \epsilon_{\mathcal{C},\mathcal{L}}$, of the mean measurement error $\bar{\delta}_{\mathcal{C},\mathcal{L}}$ and of the standard deviation $\sigma(\delta)_{\mathcal{C},\mathcal{L}}$ are calculated with the vertical resolutions listed in Table 9.5. For the MWR-SMZ and the %RH variable, Figure 10.27 shows an example of $\Lambda_{\mathcal{C},\mathcal{L}} \pm \epsilon_{\mathcal{C},\mathcal{L}}$. The width of the atmospheric layers \mathcal{L} is not constant through the atmospheric column and corresponds to the vertical resolution of the MWR-SMZ. The absolute mean measurement error $|\bar{\delta}_{\mathcal{C},\mathcal{L}}|$ (dashed line) and the standard deviation of the individual measurement errors $\sigma(\delta)_{\mathcal{C},\mathcal{L}}$ (solid black), represent the two terms contributing to the total value of $\Lambda_{\mathcal{C},\mathcal{L}}$ in Equation (J.3). The values of $\bar{\delta}_{\mathcal{C},\mathcal{L}}$ and $\sigma(\delta)_{\mathcal{C},\mathcal{L}}$ change significantly for different instruments, flight category and atmospheric layer \mathcal{L} . The value of $\bar{\delta}_{\mathcal{C},\mathcal{L}}$ can be interpreted as the measurement bias. When it approaches zero, only the standard deviation contributes to the total value of $\Lambda_{\mathcal{C},\mathcal{L}}$ and vice versa when the term $\sigma(\delta)_{\mathcal{C},\mathcal{L}}$ becomes negligible. In Figure 10.27, in the FT, the mean error $\bar{\delta}_{\mathcal{C},\mathcal{L}}$ is constantly smaller than the standard deviation $\sigma(\delta)_{\mathcal{C},\mathcal{L}}$, which almost overlies the profile $\Lambda_{\mathcal{C},\mathcal{L}}$.

The values $\Lambda_{\mathcal{C},\mathcal{L}} \pm \epsilon_{\mathcal{C},\mathcal{L}}$ over the atmospheric layers $\mathcal{L} = [\text{PBL}, \text{FT}, \text{UTLS}]$ are calculated for each instrument of the LRSS along with the values $\bar{\delta}_{\mathcal{C},\mathcal{L}}$ and $\sigma(\delta)_{\mathcal{C},\mathcal{L}}$. Especially the type of instrument and the atmospheric layer \mathcal{L} are sensitive parameters that determine the ratio $\bar{\delta}_{\mathcal{C},\mathcal{L}}/\sigma(\delta)_{\mathcal{C},\mathcal{L}}$. Figures 10.28-10.33 show, for each LRSS instrument, the contributions of $\bar{\delta}_{\mathcal{C},\mathcal{L}}$ and $\sigma(\delta)_{\mathcal{C},\mathcal{L}}$ separately as a function of \mathcal{C} and \mathcal{L} .

In Section 10.2.3, we provide an interpretation of Figures 10.28-10.33 for each instrument of the LRSS.

10.2.3 Instrument-specific observations

Sections 10.1.5.1-10.1.5.3 provide a detailed description of the contributions of the mean measurement error $\bar{\delta}_{\mathcal{C},\mathcal{L}}$ and standard deviation $\sigma(\delta)_{\mathcal{C},\mathcal{L}}$ to the value of the ORUC assessment function ($\Lambda_{\mathcal{C},\mathcal{L}}$) for the radiosounding comparison. Likewise, here we present the values of $\bar{\delta}_{\mathcal{C},\mathcal{L}}$ and $\sigma(\delta)_{\mathcal{C},\mathcal{L}}$ for each LRSS instrument, geophysical variable, flight category \mathcal{C} and atmospheric layer \mathcal{L} . Tables 10.7-10.8 list the values $\bar{\Lambda}_{\mathcal{C},\mathcal{L}} \pm \bar{\epsilon}_{\mathcal{C},\mathcal{L}}$ as well as the values $\bar{\delta}_{\mathcal{C},\mathcal{L}}$ and $\sigma(\delta)_{\mathcal{C},\mathcal{L}}$ for the geophysical variables "atmospheric temperature" and "relative humidity" and for the "horizontal wind direction", "speed" and "vector". The values in the tables can be used by the interested readers and applied to any application areas for evaluation of the fitness-for-purpose of a specific variable.

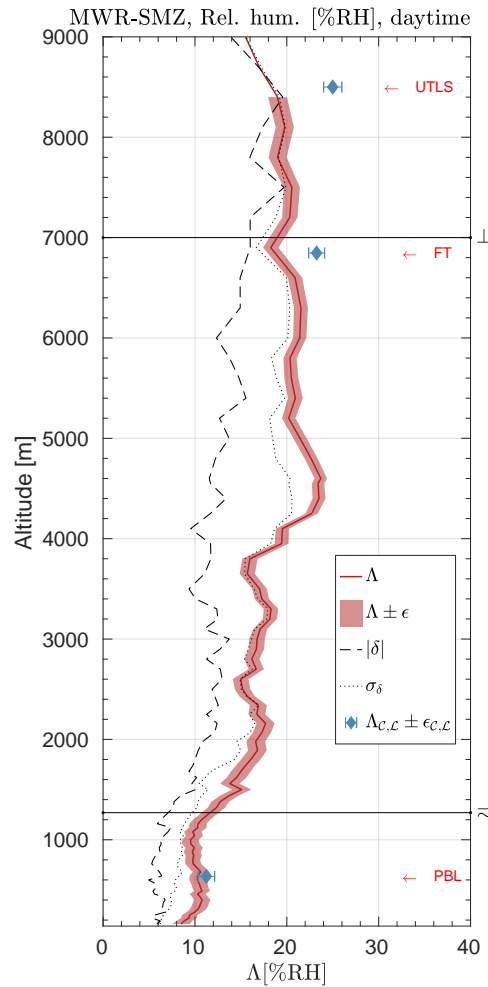


Figure 10.27: Example of profiles of $\Delta_{c,L} \pm \epsilon_{c,L}$, $\bar{\delta}_{c,L}$ and $\sigma(\delta)_{c,L}$ for the %RH measured by the MWR-SMZ during the flight category $\mathcal{C} = \text{day}$. The vertical resolution of the profiles corresponds to the resolutions of the MWR-SMZ as shown in Table 9.5. The cyan diamonds are the values $\Delta_{c,L}$ calculated over the atmospheric layers PBL, FT and UTLS and the error bars are their uncertainty $\pm \epsilon_{c,L}$.

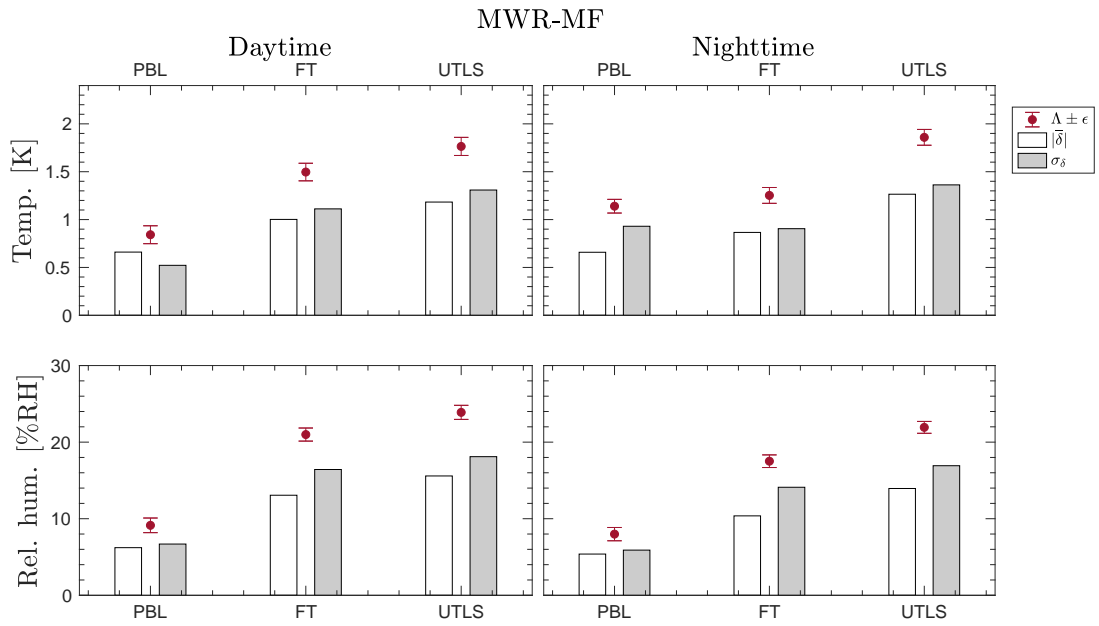


Figure 10.28: Measured values of $\Lambda_{c,\mathcal{L}}$ (red dots, with error bars extending $\pm\epsilon_{c,\mathcal{L}}$) for all geophysical variables and atmospheric layers considered in this analysis, for the MWR-MF. For each case, columns indicate the values of $|\bar{\delta}|_{c,\mathcal{L}}$ and $\sigma(\delta)_{c,\mathcal{L}}$, of which $\Lambda_{c,\mathcal{L}}$ is being comprised of (see Section 10.1.5.2 for details).

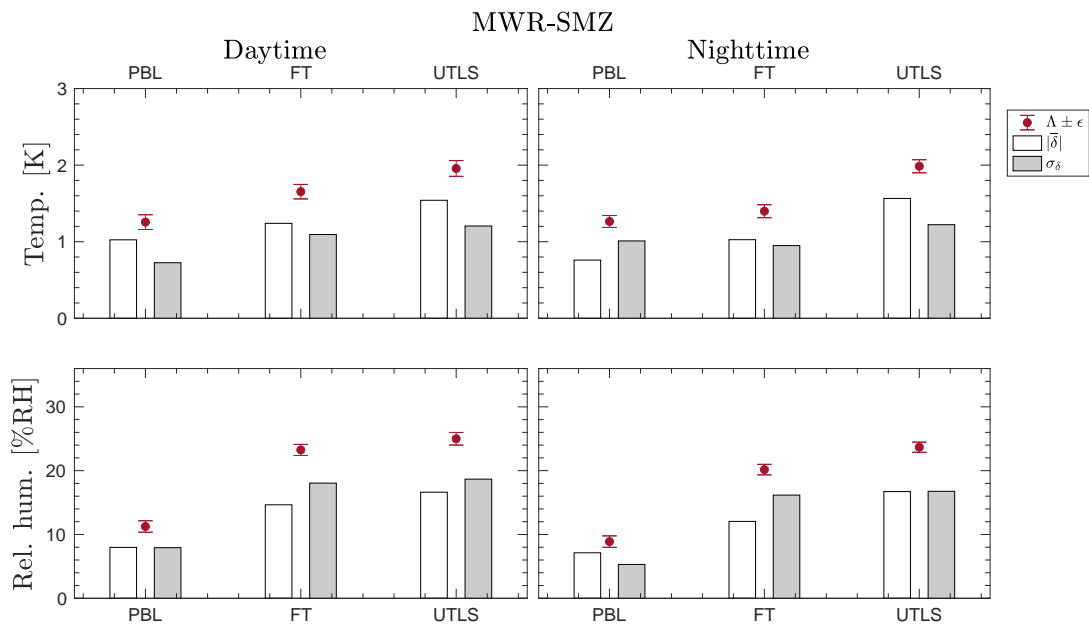


Figure 10.29: Same as Figure 10.28, but for the MWR-SMZ.

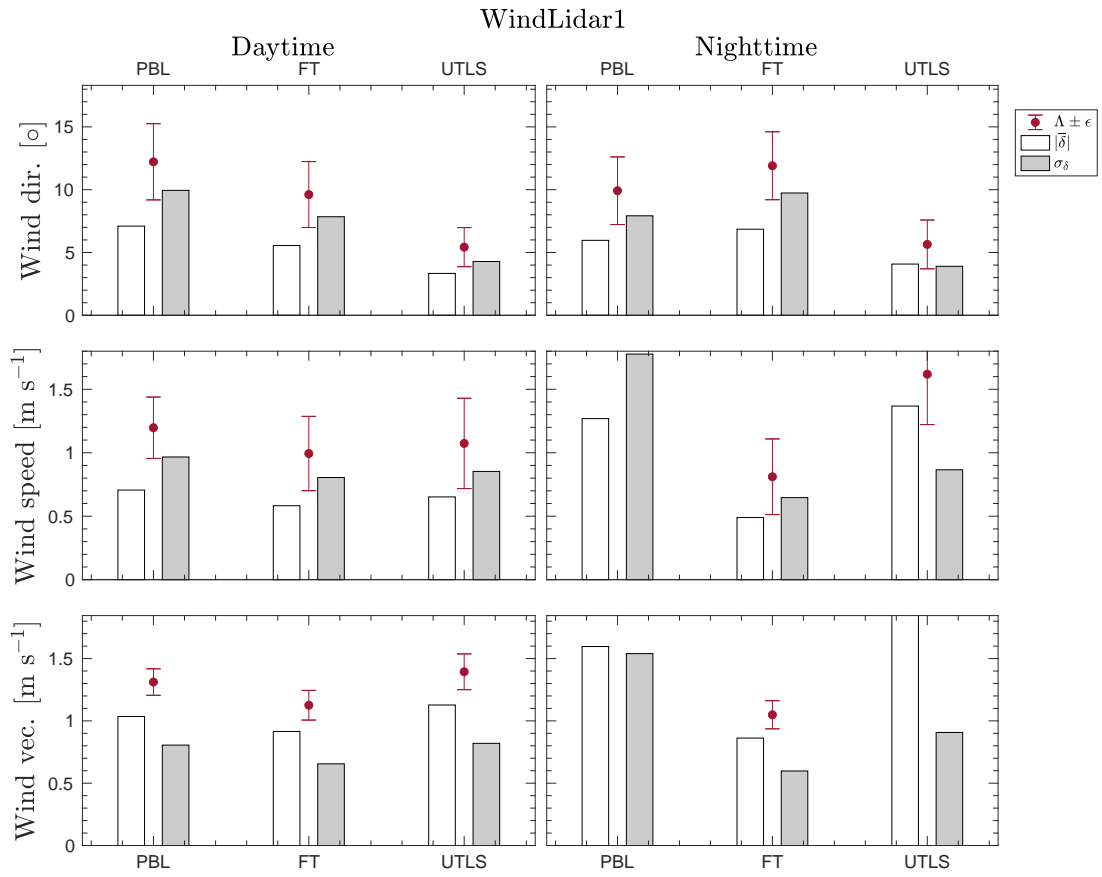


Figure 10.30: Same as Figure 10.28, but for the DWL “WindLidar1”.

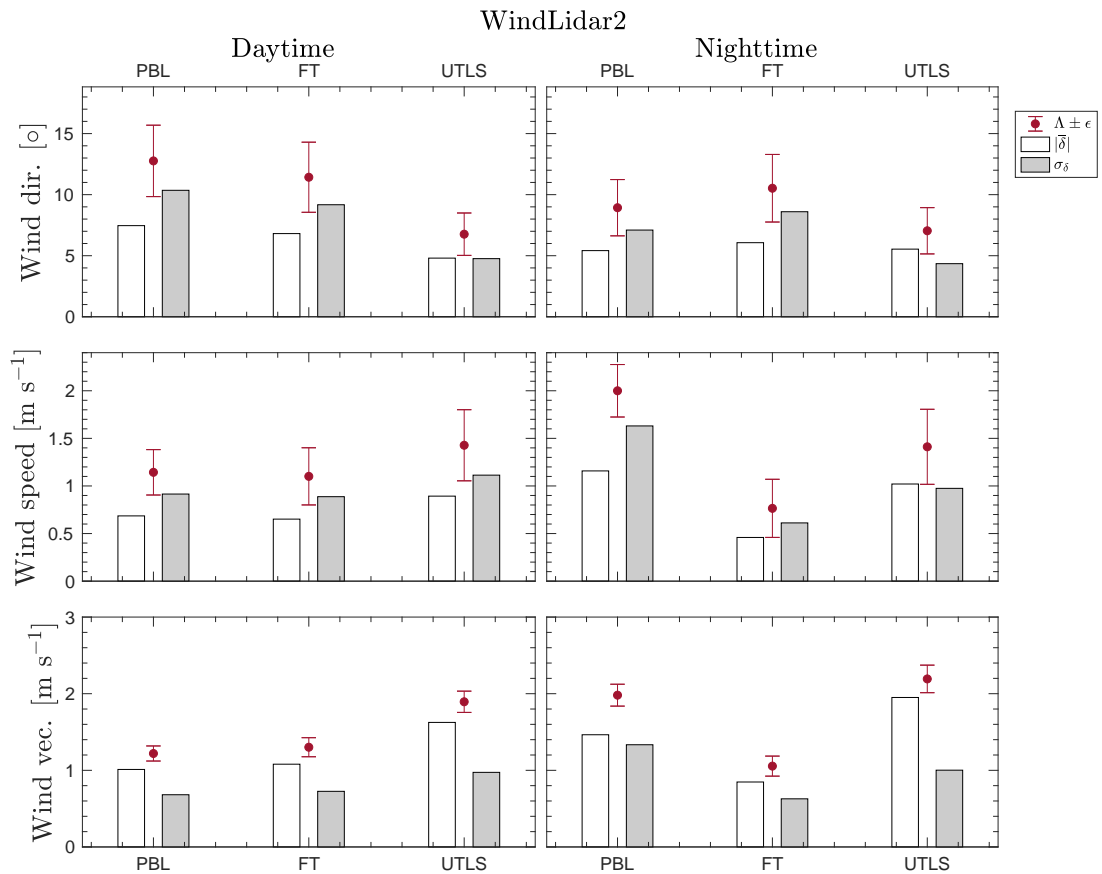


Figure 10.31: Same as Figure 10.28, but for the DWL “WindLidar2”.

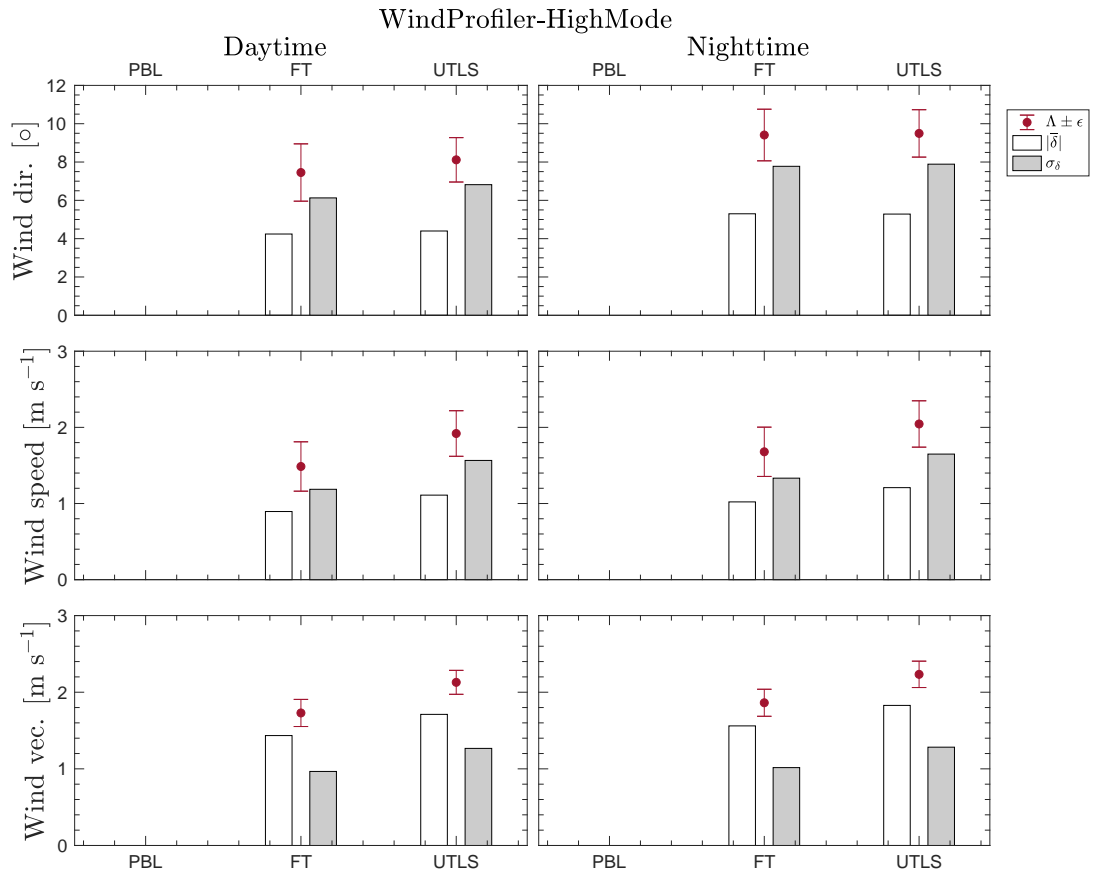


Figure 10.32: Same as Figure 10.28, but for the High-mode RWP

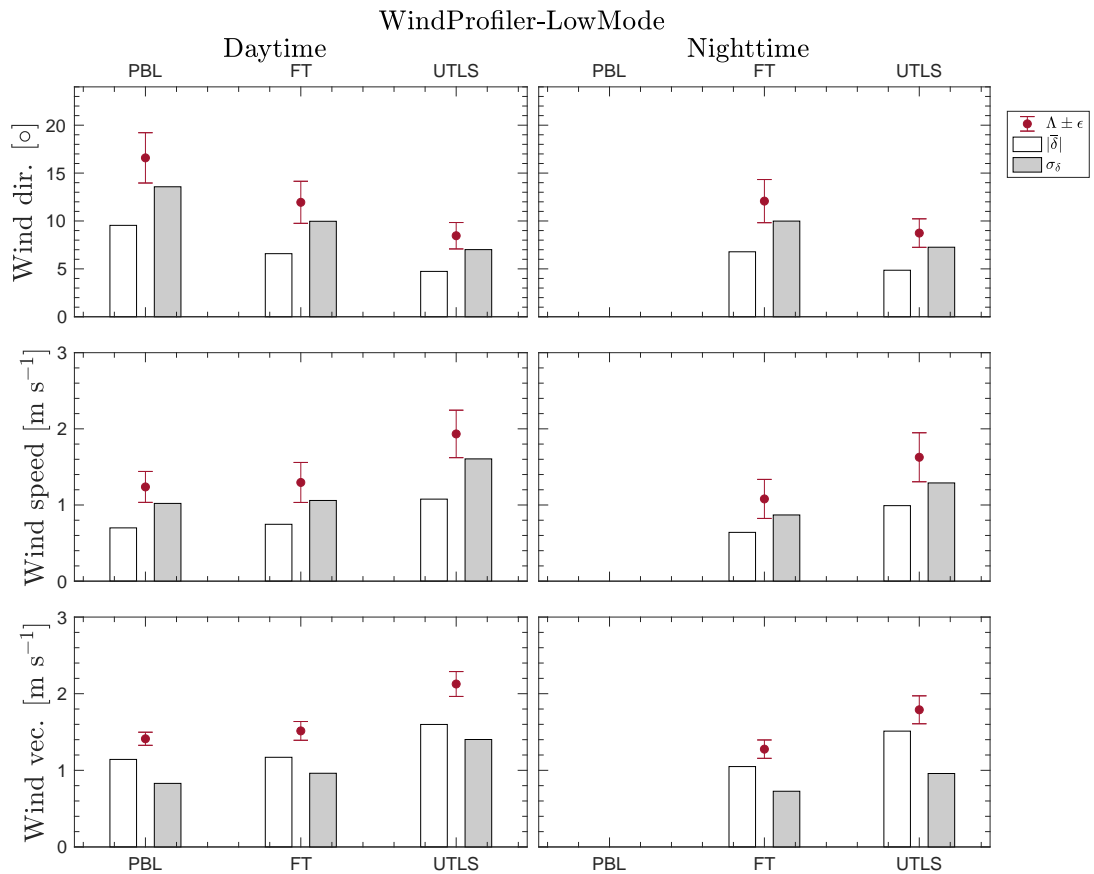


Figure 10.33: Same as Figure 10.3, but for the Low-mode RWP.

Table 10.7: The Table shows for all the LRSS instruments, the values of $\Lambda_{C,\mathcal{L}} \pm \epsilon_{C,\mathcal{L}}$ along with the values of $\bar{\delta}_{C,\mathcal{L}}$ (Λ 's superscript) and $\sigma(\delta)_{C,\mathcal{L}}$ (Λ 's subscript) for the geophysical variables temperature and relative humidity, all flight categories C and atmospheric layers \mathcal{L} .

		Atmospheric temperature [K]				Relative humidity [%RH]			
		PBL	FT	UTLS	MUS	PBL	FT	UTLS	MUS
MWR-MF	Day	0.84 ^{+0.66} _{0.52} ± 0.09	1.50 ^{+1.00} _{1.11} ± 0.09	1.76 ^{+1.18} _{1.31} ± 0.09	NaN	9.14 ^{+6.22} _{6.69} ± 0.95	20.99 ^{+13.07} _{16.43} ± 0.85	23.89 ^{+15.58} _{18.10} ± 0.92	NaN
	Night	1.14 ^{+0.66} _{0.93} ± 0.07	1.25 ^{+0.87} _{0.90} ± 0.08	1.86 ^{+1.26} _{1.36} ± 0.08	NaN	7.99 ^{+5.38} _{5.90} ± 0.87	17.51 ^{+10.37} _{14.11} ± 0.82	21.93 ^{+13.95} _{16.92} ± 0.77	NaN
MWR-SMZ	Day	1.26 ^{+1.02} _{0.73} ± 0.10	1.65 ^{+1.24} _{1.09} ± 0.09	1.96 ^{+1.54} _{1.21} ± 0.10	NaN	11.25 ^{+7.98} _{7.93} ± 0.90	23.24 ^{+14.65} _{18.05} ± 0.87	25.00 ^{+16.62} _{18.67} ± 0.99	NaN
	Night	1.26 ^{+0.76} _{1.01} ± 0.08	1.40 ^{+1.03} _{0.95} ± 0.08	1.99 ^{+1.56} _{1.22} ± 0.09	NaN	8.88 ^{+7.13} _{5.30} ± 0.90	20.16 ^{+12.05} _{16.17} ± 0.82	23.67 ^{+16.72} _{16.76} ± 0.80	NaN

Table 10.8: Same as Table 10.7, but for the wind (horizontal) direction, speed and vector.

		Wind (horizontal) direction [°]				Wind (horizontal) speed [m s ⁻¹]				Wind (horizontal) vector [m s ⁻¹]			
		PBL	FT	UTLS	MUS	PBL	FT	UTLS	MUS	PBL	FT	UTLS	MUS
Wind lidar (1)	Day	12.2 ^{+7.1} _{9.9} ± 3.0	9.6 ^{+5.6} _{7.8} ± 2.6	5.4 ^{+3.3} _{4.3} ± 1.6	NaN	1.2 ^{+0.7} _{1.0} ± 0.2	1.0 ^{+0.6} _{0.8} ± 0.3	1.1 ^{+0.7} _{0.9} ± 0.4	NaN	1.3 ^{+1.0} _{0.8} ± 0.1	1.1 ^{+0.9} _{0.7} ± 0.1	1.4 ^{+1.1} _{0.8} ± 0.1	NaN
	Night	9.9 ^{+6.0} _{7.9} ± 2.7	11.9 ^{+6.9} _{9.7} ± 2.7	5.6 ^{+4.1} _{3.9} ± 1.9	NaN	2.2 ^{+1.3} _{1.8} ± 0.3	0.8 ^{+0.5} _{0.6} ± 0.3	1.6 ^{+1.4} _{0.9} ± 0.4	NaN	2.2 ^{+1.6} _{1.5} ± 0.2	1.0 ^{+0.9} _{0.6} ± 0.1	2.1 ^{+1.9} _{0.9} ± 0.1	NaN
Wind lidar (2)	Day	12.8 ^{+7.5} _{10.4} ± 2.9	11.4 ^{+6.8} _{9.2} ± 2.9	6.8 ^{+4.8} _{4.8} ± 1.7	NaN	1.1 ^{+0.7} _{0.9} ± 0.2	1.1 ^{+0.7} _{0.9} ± 0.3	1.4 ^{+0.9} _{1.1} ± 0.4	NaN	1.2 ^{+1.0} _{0.7} ± 0.1	1.3 ^{+1.1} _{0.7} ± 0.1	1.9 ^{+1.6} _{1.0} ± 0.1	NaN
	Night	8.9 ^{+5.4} _{7.1} ± 2.3	10.5 ^{+6.1} _{8.6} ± 2.8	7.0 ^{+5.5} _{4.3} ± 1.9	NaN	2.0 ^{+1.2} _{1.6} ± 0.3	0.8 ^{+0.5} _{0.6} ± 0.3	1.4 ^{+1.0} _{1.0} ± 0.4	NaN	2.0 ^{+1.5} _{1.3} ± 0.1	1.1 ^{+0.8} _{0.6} ± 0.1	2.2 ^{+2.0} _{1.0} ± 0.2	NaN
Wind profiler (High Mode)	Day	NaN	7.5 ^{+4.2} _{6.1} ± 1.5	8.1 ^{+4.4} _{6.8} ± 1.2	NaN	NaN	1.5 ^{+0.9} _{1.2} ± 0.3	1.9 ^{+1.1} _{1.6} ± 0.3	NaN	NaN	1.7 ^{+1.4} _{1.0} ± 0.2	2.1 ^{+1.7} _{1.3} ± 0.2	NaN
	Night	NaN	9.4 ^{+5.3} _{7.8} ± 1.3	9.5 ^{+5.3} _{7.9} ± 1.2	NaN	NaN	1.7 ^{+1.0} _{1.3} ± 0.3	2.0 ^{+1.2} _{1.6} ± 0.3	NaN	NaN	1.9 ^{+1.6} _{1.0} ± 0.2	2.2 ^{+1.8} _{1.3} ± 0.2	NaN
Wind profiler (Low Mode)	Day	16.6 ^{+9.5} _{13.6} ± 2.6	11.9 ^{+6.6} _{10.0} ± 2.2	8.5 ^{+4.7} _{7.0} ± 1.4	NaN	1.2 ^{+0.7} _{1.0} ± 0.2	1.3 ^{+0.7} _{1.1} ± 0.3	1.9 ^{+1.1} _{1.6} ± 0.3	NaN	1.4 ^{+1.1} _{0.8} ± 0.1	1.5 ^{+1.2} _{1.0} ± 0.1	2.1 ^{+1.6} _{1.4} ± 0.2	NaN
	Night	NaN	12.1 ^{+6.8} _{10.0} ± 2.3	8.7 ^{+4.9} _{7.3} ± 1.5	NaN	NaN	1.1 ^{+0.6} _{0.9} ± 0.3	1.6 ^{+1.0} _{1.3} ± 0.3	NaN	NaN	1.3 ^{+1.0} _{0.7} ± 0.1	1.8 ^{+1.5} _{1.0} ± 0.2	NaN

Figures 10.28-10.33 provide the visual counterpart to Tables 10.7 and 10.8, to aid understanding and interpreting correctly the results shown therein and represent the basis for the discussion in Chapter 11.

10.2.3.1 $\Lambda_{c,\mathcal{L}}, \bar{\delta}_{c,\mathcal{L}}, \sigma(\delta)_{c,\mathcal{L}}$ diagrams: Micro-Wave Radiometer (MWR)

The operational retrieval of temperature and humidity profiles from the measurements of the MWR uses the manufacturer's neural network inversion algorithm. For atmospheric layers above 2000 m AGL, the retrieval is derived from a training dataset known a priori. The a priori dataset is obtained by a climatology of thermodynamic profiles taken near the MWR deployment's site and the corresponding brightness temperature observations, i.e. the retrieval is based on the local climatology of radiosoundings (see e.g. [Löhnert et al., 2009](#), and references therein). The retrievals through the FT and UTLS represent more the local climatology of temperature and humidity profiles than the real-time measurements. The fact of being strongly driven by the local climatology may induce a bias at these atmospheric levels. Based on the statistical analysis by [Massaro et al. \(2015\)](#), the Root-Mean Square Error (RMSE) of the daytime MWR retrievals are slightly better during nighttime than during daytime. The vertical range that can be used is then slightly larger during night than during day. Although in general the microwave radiometer has a constant performance in conditions with clear or cloudy skies, the quality of the measurements in heavy rain conditions ($> 2000 \text{ g m}^{-2}$) is poor, as described also by [Löhnert et al. \(2009\)](#). Cloud cover (overcast) can represent an offset in the brightness temperature, due to the emission by the liquid water in the clouds, but this can be corrected in the retrieval.

MWR-MF:

Figure 10.28 shows that the overall ratio $\bar{\delta}_{c,\mathcal{L}}/\sigma(\delta)_{c,\mathcal{L}}$ does not vary much amongst temperature, relative Humidity, FT and UTLS, day and night. Most of the variability occurs within the PBL between day and night. The behaviour is however different for temperature and relative humidity. For the temperature, the ratio $\bar{\delta}_{c,\mathcal{L}}/\sigma(\delta)_{c,\mathcal{L}}$ is > 1 during daytime and < 1 during nighttime. The temperature measurements are dominated by the bias during day and by the standard deviation during night. This behaviour is less pronounced for the relative humidity, for which the ratio $\bar{\delta}_{c,\mathcal{L}}/\sigma(\delta)_{c,\mathcal{L}}$ is close to 1 in the PBL between day and night.

MWR-SMZ:

Figure 10.29 shows that the daytime temperature retrievals are dominated by the bias through the PBL, FT and UTLS. The ratio becomes $\bar{\delta}_{c,\mathcal{L}}/\sigma(\delta)_{c,\mathcal{L}} < 1$ only in the nighttime-PBL. The relative humidity has almost the same behaviour of the MWR-MF for the daytime retrievals, i.e. characterised by a larger standard deviation compared with the bias. The nighttime relative humidity retrievals in the PBL have more bias than the daytime.

10.2.3.2 $\Lambda_{c,\mathcal{L}}, \bar{\delta}_{c,\mathcal{L}}, \sigma(\delta)_{c,\mathcal{L}}$ diagrams: Doppler Wind Lidar (DWL)

The functioning principle of the DWL is based on the scattering of the infrared radiation by aerosols and liquid and ice cloud particles. The Doppler signal from aerosols comes mainly from the PBL and to some extent from the FT. The quality and availability of the data thus depend on the presence, concentration, type and size distribution of these aerosol and cloud particles. The PBL is the layer with the highest concentration of aerosols and is often topped by the cloud base, thus the DWL provides reliable wind speed and wind direction measurements through the PBL. When cirrus clouds are present or when aerosol layers are advected above the PBL, the DWL can measure at altitudes well above the PBLH, e.g. the FT and the UTLS. Its performance and data quality do not depend on the time of the day. The main atmospheric parameters affecting the quality and availability of wind speed and wind direction measurements are the targets' concentrations and the relative humidities within the backscatter volume.

WindLidar1:

Figure 10.30 shows that for the wind speed and the wind direction the standard deviation dominates the ratio $\bar{\delta}_{c,\mathcal{L}}/\sigma(\delta)_{c,\mathcal{L}}$ at the exception of the nighttime UTLS. However, as it is shown in Table 10.6, the data availability of the DWL decreases abruptly above 1.5 km, so the FT and UTLS statistics are based on a much smaller data sample than in the PBL. On the contrary, the wind vector is characterised by the ratio $\bar{\delta}_{c,\mathcal{L}}/\sigma(\delta)_{c,\mathcal{L}} > 1$ for all the atmospheric

layers and time categories.

WindLidar2: Figure 10.31 shows an almost identical pattern as in Figure 10.30 at the exception of the nighttime wind speed in the UTLS where the bias dominates the ratio.

10.2.3.3 $\bar{\Lambda}_{c,\mathcal{L}}, \bar{\delta}_{c,\mathcal{L}}, \sigma(\delta)_{c,\mathcal{L}}$ diagrams: Radar Wind Profiler (RWP)

The RWP has very stable performances through all types of weather and different time of the day. Thus, the Instrument Optimal Vertical Range (IOVR) of the RWP does not change for different flight categories \mathcal{C} and different weather conditions. When comparing the high-mode RWP with the CWS, no data can be used in the PBL, as the lowest range point is at 5500 m. In low-mode, the daytime data of the RWP can be used for comparison with the CWS in the PBL layer 500–1270 m (lowest range point = 500 m, $PBLH_{day} = 1270$ m AMSL). On the contrary, no nighttime data from the low-mode RWP can be used for comparison with the CWS in the PBL as $PBLH_{night} = 350$ m AMSL.

WindProfiler High-mode:

Figure 10.32 shows a very similar pattern as for the DWL with the standard deviation that dominates the ratio $\bar{\delta}_{c,\mathcal{L}}/\sigma(\delta)_{c,\mathcal{L}}$ for the wind speed and direction at all \mathcal{L} and for all \mathcal{C} . The situation is reversed for the wind vector, where the ratio is dominated by the bias. The $\Lambda_{c,\mathcal{L}}$ values show very close values for the wind speed, direction and vector over day and night.

WindProfiler Low-Mode: The low-mode daytime values of the ratio $\bar{\delta}_{c,\mathcal{L}}/\sigma(\delta)_{c,\mathcal{L}}$ in the PBL are comparable with the daytime values of the DWL. The $\Lambda_{c,\mathcal{L}}$ values for the wind vector in the UTLS are slightly smaller than those of the high-mode RWP.

Part IV

Outcomes

11 DISCUSSION

11.1 RADIOSONDES

11.1.1 Fitness-for-purpose with respect to OSCAR

Assessing the performance of radiosondes with respect to the OSCAR requirement uncertainty criterion (ORUC) values listed in Table 9.2 implies the computation of the effective confidence level k_{eff} , following Equation (9.6) and Terminology 3, using the measured values of ORUC assessment function $\Lambda_{\mathcal{C},\mathcal{L}}$ reported in Section 10.1.5. The results are presented in Tables 11.1 to 11.4, where each Table corresponds to one OSCAR application area. Values that are statistically significant are shown in peach or blue; those that are not (at the 2σ level, following Equation (9.5)) are in grey. For cases in the latter category, the radiosonde performance is sufficiently close to a given ORUC value –or the associated uncertainty resulting from the UAI 2022 field campaign flights is sufficiently large– that one cannot state (with sufficient statistical confidence) whether or not the radiosonde is actually fit-for-purpose.

Although we rely on the OSCAR criteria from the WMO to assess the fitness-for-purpose of radiosondes in this analysis, we stress that readers interested in using their own set of performance criteria –different from those given in Table 9.2– can do so easily using Equation (9.6) and the measured $\Lambda_{\mathcal{C},\mathcal{L}}$ values reported in Table 10.3 to 10.5 to perform their own fitness-for-purpose assessment.

It is paramount to remember that the values quoted in Tables 11.1 to 11.4 indicate the statistical confidence of the sonde performances observed during the UAI 2022 field campaign: they do not describe how close a given sonde stands from being (un-)fit-for-purpose in terms of its actual performance. Answering this latter question requires A) a direct comparison of the $\Lambda_{\mathcal{C},\mathcal{L}}$ values quoted in Tables 10.3 to 10.5 against the ORUC values in Table 9.2, and B) an analysis of the underlying systematic and random measurement errors ($\bar{\delta}_{\mathcal{C},\mathcal{L}}$ and $\sigma(\delta)_{\mathcal{C},\mathcal{L}}$; see Section 10.1.5.2 and Appendix J.2 for details). On a sonde-by-sonde and variable-by-variable basis, this is best performed by means of the results presented in Section 10.1 and in particular:

1. the Figures 10.3 to 10.12, as well as,
2. the $\Lambda_{\mathcal{C},\mathcal{L}}$ diagrams presented in Appendix L, and
3. the Figures 11.1 to 11.3 which provide a combined view of the high-resolution $\Lambda_{\mathcal{C},100\text{m}}$ profiles for the day and night categories \mathcal{C} , for all the participating radiosondes, for the atmospheric temperature, relative humidity, and wind (horizontal) vector variables.

Similar diagrams for the other geophysical variables considered in this analysis are provided in Appendix M for completeness.

Table 11.1: Performance assessment of the radiosondes that participated in the UAII 2022 field campaign, with respect to the WMO’s ORUC Threshold (Θ^T), Breakthrough (Θ^B) and Goal (Θ^G) values for the **Aeronautical Meteorology** application area (extracted on 2023-05-31; see Section 9.3.1). The value of k_{eff} , defined in Equation (9.6), is shown where an ORUC value exists (see Table 9.2) and $-6 \leq k_{\text{eff}} \leq +6$. The symbols \uparrow and \downarrow indicate that $k_{\text{eff}} > +6$ and $k_{\text{eff}} < -6$, respectively. The colour of each cell provides a visual cue regarding the performance of a given sonde with respect to a given criterion: peach \equiv fit-for-purpose $\equiv k_{\text{eff}} > +2$; blue \equiv not fit-for-purpose $\equiv k_{\text{eff}} < -2$; grey \equiv uncertain $\equiv -2 \leq k_{\text{eff}} \leq +2$ (see Section 9.3.2). No performance assessment is made in the PBL for the wind (horizontal) vector (tagged with \times), as several profiles were likely affected by the UAII campaign setup in this atmospheric layer (see Section 8.2.5).

		Atmospheric temperature												Relative humidity									Wind (horizontal) vector												
		Θ^T				Θ^B				Θ^G				Θ^T			Θ^B			Θ^G			Θ^T			Θ^B			Θ^G						
		PBL	FT	UTLS	MUS	PBL	FT	UTLS	MUS	PBL	FT	UTLS	MUS	PBL	FT	UTLS	MUS	PBL	FT	UTLS	MUS	PBL	FT	UTLS	MUS	PBL	FT	UTLS	MUS	PBL	FT	UTLS	MUS	PBL	FT
ATMS-3710	Day	\uparrow	\uparrow	\uparrow	\uparrow	\uparrow	\uparrow	\uparrow	\uparrow	\uparrow	\uparrow	\uparrow	\uparrow	grey	blue	blue	\times	\uparrow	\uparrow	\times	\uparrow	\uparrow	\times	\uparrow	\uparrow	\times	\uparrow	\uparrow	\times	\uparrow	\uparrow	\times	\uparrow	\uparrow	
	Night	\uparrow	\uparrow	\uparrow	\uparrow	\uparrow	+3.7	\uparrow	\uparrow	\downarrow	\uparrow	peach	grey	\times	\uparrow	\uparrow	\times	\uparrow	\uparrow	\times	\uparrow	\uparrow	\times	\uparrow	\uparrow	\times	\uparrow	\uparrow	\times	\uparrow	\uparrow	\times	\uparrow	\uparrow	
CF-06-AH	Day	\uparrow	\uparrow	\uparrow	\uparrow	\uparrow	\uparrow	\uparrow	\uparrow	\uparrow	\uparrow	peach	peach	\times	\uparrow	\uparrow	\times	\uparrow	\uparrow	\times	\uparrow	\uparrow	\times	\uparrow	\uparrow	\times	\uparrow	\uparrow	\times	\uparrow	\uparrow	\times	\uparrow	\uparrow	
	Night	\uparrow	\uparrow	\uparrow	\uparrow	\uparrow	\uparrow	\uparrow	\uparrow	\uparrow	\uparrow	peach	grey	\times	\uparrow	\uparrow	\times	\uparrow	\uparrow	\times	\uparrow	\uparrow	\times	\uparrow	\uparrow	\times	\uparrow	\uparrow	\times	\uparrow	\uparrow	\times	\uparrow	\uparrow	
DFM-17	Day	\uparrow	\uparrow	\uparrow	\uparrow	\uparrow	\uparrow	\uparrow	\uparrow	\uparrow	\uparrow	peach	grey	\times	\uparrow	\uparrow	\times	\uparrow	\uparrow	\times	\uparrow	\uparrow	\times	\uparrow	\uparrow	\times	\uparrow	\uparrow	\times	\uparrow	\uparrow	\times	\uparrow	\uparrow	
	Night	\uparrow	\uparrow	\uparrow	\uparrow	\uparrow	\uparrow	\uparrow	\uparrow	\uparrow	+5.4	grey	grey	\times	\uparrow	\uparrow	\times	\uparrow	\uparrow	\times	\uparrow	\uparrow	\times	\uparrow	\uparrow	\times	\uparrow	\uparrow	\times	\uparrow	\uparrow	\times	\uparrow	\uparrow	
GTH3	Day	\uparrow	\uparrow	\uparrow	\uparrow	\uparrow	\uparrow	\uparrow	\uparrow	\uparrow	+4.0	grey	blue	\times	\uparrow	\uparrow	\times	\uparrow	\uparrow	\times	\uparrow	\uparrow	\times	\uparrow	\uparrow	\times	\uparrow	\uparrow	\times	\uparrow	\uparrow	\times	\uparrow	\uparrow	
	Night	\uparrow	\uparrow	\uparrow	\uparrow	\uparrow	\uparrow	\uparrow	\uparrow	\uparrow	\uparrow	peach	grey	\times	\uparrow	\uparrow	\times	\uparrow	\uparrow	\times	\uparrow	\uparrow	\times	\uparrow	\uparrow	\times	\uparrow	\uparrow	\times	\uparrow	\uparrow	\times	\uparrow	\uparrow	
iMet-54	Day	\uparrow	\uparrow	\uparrow	\uparrow	\uparrow	\uparrow	\uparrow	\uparrow	\uparrow	\uparrow	peach	peach	\times	\uparrow	\uparrow	\times	\uparrow	\uparrow	\times	\uparrow	\uparrow	\times	\uparrow	\uparrow	\times	\uparrow	\uparrow	\times	\uparrow	\uparrow	\times	\uparrow	\uparrow	
	Night	\uparrow	\uparrow	\uparrow	\uparrow	\uparrow	\uparrow	\uparrow	\uparrow	\uparrow	\uparrow	peach	peach	\times	\uparrow	\uparrow	\times	\uparrow	\uparrow	\times	\uparrow	\uparrow	\times	\uparrow	\uparrow	\times	\uparrow	\uparrow	\times	\uparrow	\uparrow	\times	\uparrow	\uparrow	
iMS-100	Day	\uparrow	\uparrow	\uparrow	\uparrow	\uparrow	\uparrow	\uparrow	\uparrow	\uparrow	\uparrow	peach	peach	\times	\uparrow	\uparrow	\times	\uparrow	\uparrow	\times	\uparrow	\uparrow	\times	\uparrow	\uparrow	\times	\uparrow	\uparrow	\times	\uparrow	\uparrow	\times	\uparrow	\uparrow	
	Night	\uparrow	\uparrow	\uparrow	\uparrow	\uparrow	\uparrow	\uparrow	\uparrow	\uparrow	\uparrow	peach	peach	\times	\uparrow	\uparrow	\times	\uparrow	\uparrow	\times	\uparrow	\uparrow	\times	\uparrow	\uparrow	\times	\uparrow	\uparrow	\times	\uparrow	\uparrow	\times	\uparrow	\uparrow	
M20	Day	\uparrow	\uparrow	\uparrow	\uparrow	\uparrow	\uparrow	\uparrow	\uparrow	\uparrow	\uparrow	peach	peach	\times	\uparrow	\uparrow	\times	\uparrow	\uparrow	\times	\uparrow	\uparrow	\times	\uparrow	\uparrow	\times	\uparrow	\uparrow	\times	\uparrow	\uparrow	\times	\uparrow	\uparrow	
	Night	\uparrow	\uparrow	\uparrow	\uparrow	\uparrow	\uparrow	\uparrow	\uparrow	\uparrow	+5.6	grey	grey	\times	\uparrow	\uparrow	\times	\uparrow	\uparrow	\times	\uparrow	\uparrow	\times	\uparrow	\uparrow	\times	\uparrow	\uparrow	\times	\uparrow	\uparrow	\times	\uparrow	\uparrow	
PS-B3	Day	\uparrow	\uparrow	\uparrow	\uparrow	\uparrow	\uparrow	\uparrow	\uparrow	\uparrow	grey	blue	blue	\times	\uparrow	\uparrow	\times	\uparrow	\uparrow	\times	\uparrow	\uparrow	\times	\uparrow	\uparrow	\times	\uparrow	\uparrow	\times	\uparrow	\uparrow	\times	\uparrow	\uparrow	
	Night	\uparrow	\uparrow	\uparrow	\uparrow	\uparrow	\uparrow	\uparrow	\uparrow	\uparrow	\uparrow	grey	grey	\times	\uparrow	\uparrow	\times	\uparrow	\uparrow	\times	\uparrow	\uparrow	\times	\uparrow	\uparrow	\times	\uparrow	\uparrow	\times	\uparrow	\uparrow	\times	\uparrow	\uparrow	
RS41	Day	\uparrow	\uparrow	\uparrow	\uparrow	\uparrow	\uparrow	\uparrow	\uparrow	\uparrow	\uparrow	peach	peach	\times	\uparrow	\uparrow	\times	\uparrow	\uparrow	\times	\uparrow	\uparrow	\times	\uparrow	\uparrow	\times	\uparrow	\uparrow	\times	\uparrow	\uparrow	\times	\uparrow	\uparrow	
	Night	\uparrow	\uparrow	\uparrow	\uparrow	\uparrow	\uparrow	\uparrow	\uparrow	\uparrow	\uparrow	peach	peach	\times	\uparrow	\uparrow	\times	\uparrow	\uparrow	\times	\uparrow	\uparrow	\times	\uparrow	\uparrow	\times	\uparrow	\uparrow	\times	\uparrow	\uparrow	\times	\uparrow	\uparrow	
WxR-301D	Day	\uparrow	\uparrow	\uparrow	\uparrow	\uparrow	\uparrow	\uparrow	\uparrow	\uparrow	\uparrow	peach	grey	\times	\uparrow	\uparrow	\times	\uparrow	\uparrow	\times	\uparrow	\uparrow	\times	\uparrow	\uparrow	\times	\uparrow	\uparrow	\times	\uparrow	\uparrow	\times	\uparrow	\uparrow	
	Night	\uparrow	\uparrow	\uparrow	\uparrow	\uparrow	\uparrow	\uparrow	\uparrow	\uparrow	\uparrow	peach	peach	\times	\uparrow	\uparrow	\times	\uparrow	\uparrow	\times	\uparrow	\uparrow	\times	\uparrow	\uparrow	\times	blue	blue	\times	blue	blue	\times	blue	blue	

Table 11.2: Same as table 11.1, but for the **Nowcasting / Very Short-Range Forecasting** application area.

		Atmospheric temperature									Relative humidity									Wind (horizontal) vector																
		Θ^T			Θ^B			Θ^G			Θ^T			Θ^B			Θ^G			Θ^T			Θ^B			Θ^G										
		PBL	FT	UTLS	MUS	PBL	FT	UTLS	MUS	PBL	FT	UTLS	MUS	PBL	FT	UTLS	MUS	PBL	FT	UTLS	MUS	PBL	FT	UTLS	MUS	PBL	FT	UTLS	MUS	PBL	FT	UTLS	MUS			
ATMS-3710	Day	↑	↑			+3.7	↑			-1.9	↓			-2.0	↓			↓	↓			↓	↓			×	↑	↑		×	↑	↑		×	↓	↓
	Night	↑	↑			↑	-5.7			↑	↓			↑	-2.0			-1.4	↓			↓	↓			×	↑	↑		×	↑	↑		×	↓	↓
CF-06-AH	Day	↑	↑			↑	↑			+5.8	↑			↑	↑			+2.4	+4.6			-1.4	-0.1			×	↑	↑		×	↑	↑		×	↑	↑
	Night	↑	↑			↑	↑			↑	↑			↑	↑			+1.9	+6.0			-1.9	+1.6			×	↑	↑		×	↑	↑		×	↑	↑
DFM-17	Day	↑	↑			↑	↑			+2.9	+2.4			↑	↑			-0.1	↑			-3.8	↑			×	↑	↑		×	↑	↑		×	↑	↓
	Night	↑	↑			↑	↑			↑	+4.9			+5.4	↑			-1.3	↑			-5.3	+4.7			×	↑	↑		×	↑	↑		×	↑	↓
GTH3	Day	↑	↑			↑	↑			↑	↑			+4.0	↑			-2.7	-1.2			↓	↓			×	↑	↑		×	↑	↑		×	↑	↑
	Night	↑	↑			↑	↑			+2.5	↑			↑	↑			+1.9	↑			↓	↓			×	↑	↑		×	↑	↑		×	↑	↑
iMet-54	Day	↑	↑			↑	↑			↑	↑			↑	↑			+3.9	↑			-2.3	+1.8			×	↑	↑		×	↑	↑		×	↑	↑
	Night	↑	↑			↑	↑			↑	↑			↑	↑			↑	↑			-1.0	+2.3			×	↑	↑		×	↑	↑		×	↑	↑
iMS-100	Day	↑	↑			↑	↑			↑	↑			↑	↑			+5.1	↑			+0.2	↑			×	↑	↑		×	↑	↑		×	↑	↑
	Night	↑	↑			↑	↑			↑	+5.2			↑	↑			+3.2	↑			-0.7	↑			×	↑	↑		×	↑	↑		×	↑	↑
M20	Day	↑	↑			↑	↑			↑	+4.9			↑	↑			+2.8	+2.2			-1.7	-1.9			×	↑	↑		×	↑	↑		×	↑	↑
	Night	↑	↑			↑	↑			↑	+5.0			+5.6	↑			-1.0	-0.0			-5.0	-3.9			×	↑	↑		×	↑	↑		×	↑	↑
PS-B3	Day	↑	↑			↑	↑			↑	+1.2			-1.0	↑			↓	↓			↓	↓			×	↑	↑		×	↑	↑		×	↑	↑
	Night	↑	↑			↑	↑			+2.0	+2.7			↑	↑			-2.3	↓			↓	↓			×	↑	↑		×	↑	↑		×	↑	↑
RS41	Day	↑	↑			↑	↑			↑	↑			↑	↑			↑	↑			+2.3	↑			×	↑	↑		×	↑	↑		×	↑	↑
	Night	↑	↑			↑	↑			↑	↑			↑	↑			↑	↑			+3.3	↑			×	↑	↑		×	↑	↑		×	↑	↑
WxR-301D	Day	↑	↑			↑	↑			+1.6	↑			↑	↑			-0.4	+0.4			-4.8	-3.6			×	↑	↑		×	↑	↑		×	↓	↓
	Night	↑	↑			↑	↑			+3.5	+4.2			↑	↑			+0.7	+0.4			-4.3	-4.2			×	↑	↑		×	↓	↓		×	↓	↓

Table 11.3: Same as table 11.1, but for the **Global Numerical Weather Prediction and Real-time Monitoring** application area.

		Atmospheric temperature												Relative humidity						Wind (horizontal) vector																	
		Θ^T				Θ^B				Θ^G				Θ^T		Θ^B		Θ^G		Θ^T				Θ^B				Θ^G									
		PBL	FT	UTLS	MUS	PBL	FT	UTLS	MUS	PBL	FT	UTLS	MUS	PBL	FT	UTLS	MUS	PBL	FT	UTLS	MUS	PBL	FT	UTLS	MUS	PBL	FT	UTLS	MUS	PBL	FT	UTLS	MUS	PBL	FT	UTLS	MUS
ATMS-3710	Day	↑	↑	↑	↑	+3.7	↑	↑	+4.5	-1.9	↓	↓	↓	-2.0	↓			↓	↓							×	↑	↑	↑	×	↑	↑	↑	×	↓	↓	↓
	Night	↑	↑	+3.7	+3.7	↑	-5.7	↓	↓	↑	↓	↓	↓	↑	↓			-1.4	↓			↓	↓			×	↑	↑	↑	×	↑	↑	↑	×	↓	↓	↓
CF-06-AH	Day	↑	↑	↑	↑	↑	↑	↑	↑	+5.8	↑	↑	↑	↑	↑			+2.4	-0.1			-1.4	-4.9			×	↑	↑	↑	×	↑	↑	↑	×	↑	↑	↑
	Night	↑	↑	↑	↑	↑	↑	↑	↑	↑	↑	↑	↑	↑	↑			+1.9	+1.6			-1.9	-2.7			×	↑	↑	↑	×	↑	↑	↑	×	↑	↑	↑
DFM-17	Day	↑	↑	↑	↑	↑	↑	↑	↑	+2.9	+2.4	+2.7	-0.3	↑	↑			-0.1	↑			-3.8	↓			×	↑	↑	↑	×	↑	↑	↑	×	↑	↓	↓
	Night	↑	↑	↑	↑	↑	↑	↑	↑	↑	+4.9	↑	↑	+5.4	↑			-1.3	+4.7			-5.3	↓			×	↑	↑	↑	×	↑	↑	↑	×	↑	↓	↓
GTH3	Day	↑	↑	↑	↑	↑	↑	↑	↑	↑	↑	↑	+2.3	+4.0	+2.1			-2.7	↓			↓	↓			×	↑	↑	↑	×	↑	↑	↑	×	↑	↑	↓
	Night	↑	↑	↑	↑	↑	↑	↑	↑	+2.5	↑	↑	↑	↑	↑			+1.9	↓			↓	↓			×	↑	↑	↑	×	↑	↑	↑	×	↑	↑	↑
iMet-54	Day	↑	↑	↑	↑	↑	↑	↑	↑	↑	↑	+3.0	+1.9	↑	↑			+3.9	+1.8			-2.3	↓			×	↑	↑	↑	×	↑	↑	↑	×	↑	↑	↑
	Night	↑	↑	↑	↑	↑	↑	↑	↑	↑	↑	+4.1	+4.1	↑	↑			↑	+2.3			-1.0	-2.3			×	↑	↑	↑	×	↑	↑	↑	×	↑	↑	↑
iMS-100	Day	↑	↑	↑	↑	↑	↑	↑	↑	↑	↑	↑	↑	↑	↑			+5.1	↑			+0.2	-0.9			×	↑	↑	↑	×	↑	↑	↑	×	↑	↑	↑
	Night	↑	↑	↑	↑	↑	↑	↑	↑	↑	+5.2	+5.1	↑	↑	↑			+3.2	↑			-0.7	+0.2			×	↑	↑	↑	×	↑	↑	↑	×	↑	↑	↑
M20	Day	↑	↑	↑	↑	↑	↑	↑	↑	↑	+4.9	↑	↑	↑	+4.9			+2.8	-1.9			-1.7	-5.9			×	↑	↑	↑	×	↑	↑	↑	×	↑	↑	↑
	Night	↑	↑	↑	↑	↑	↑	↑	↑	↑	+5.0	↑	+5.7	+5.6	+2.5			-1.0	-3.9			-5.0	↓			×	↑	↑	↑	×	↑	↑	↑	×	↑	↑	↑
PS-B3	Day	↑	↑	↑	↑	↑	↑	+3.3	↑	↑	+1.2	-1.5	-4.9	-1.0	↓			↓	↓			↓	↓			×	↑	↑	↑	×	↑	↑	↑	×	↑	↑	↑
	Night	↑	↑	↑	↑	↑	↑	↑	↑	+2.0	+2.7	+4.4	+2.7	↑	-2.2			-2.3	↓			↓	↓			×	↑	↑	↑	×	↑	↑	↑	×	↑	↑	↑
RS41	Day	↑	↑	↑	↑	↑	↑	↑	↑	↑	↑	↑	+2.9	↑	↑			↑	↑			+2.3	+1.5			×	↑	↑	↑	×	↑	↑	↑	×	↑	↑	↑
	Night	↑	↑	↑	↑	↑	↑	↑	↑	↑	↑	↑	↑	↑	↑			↑	↑			+3.3	+2.7			×	↑	↑	↑	×	↑	↑	↑	×	↑	↑	↑
WxR-301D	Day	↑	↑	↑	↑	↑	↑	↑	↑	+1.6	↑	↑	-5.1	↑	+3.1			-0.4	-3.6			-4.8	↓			×	↑	↑	↑	×	↑	↑	↑	×	↓	↓	↓
	Night	↑	↑	↑	↑	↑	↑	↑	↑	+3.5	+4.2	+4.2	+1.8	↑	+3.5			+0.7	-4.2			-4.3	↓			×	↑	↑	↑	×	↑	↑	↑	×	↓	↓	↓

Table 11.4: Same as table 11.1, but for the **Atmospheric Climate Forecasting and Monitoring** application area.

		Atmospheric temperature												Relative humidity												Wind (horizontal) vector															
		Θ^T				Θ^B				Θ^G				Θ^T				Θ^B				Θ^G				Θ^T				Θ^B				Θ^G							
		PBL	FT	UTLS	MUS	PBL	FT	UTLS	MUS	PBL	FT	UTLS	MUS	PBL	FT	UTLS	MUS	PBL	FT	UTLS	MUS	PBL	FT	UTLS	MUS	PBL	FT	UTLS	MUS	PBL	FT	UTLS	MUS	PBL	FT	UTLS	MUS	PBL	FT	UTLS	MUS
ATMS-3710	Day	-1.9	↓	↓	↓	-4.8	↓	↓	↓	↓	↓	↓	↓	↓	↓	↓	↓	↓	↓	↓	↓	↓	↓	↓	↓	×	↑	↑	↑	×	↑	-1.5	↑	×	↓	↓	↓				
	Night	↑	↓	↓	↓	-4.8	↓	↓	↓	↓	↓	↓	↓	↓	↓	↓	↓	↓	↓	↓	↓	↓	↓	↓	↓	×	↑	↑	↑	×	↑	↓	↑	×	↓	↓	↓				
CF-06-AH	Day	+5.8	↑	↑	↑	+1.7	+4.8	+2.3	-2.4	-1.6	-3.6	-3.6	↓	-3.2	↓	↓	↓	-3.5	↓	↓	↓	-3.8	↓	↓	↓	×	↑	↑	↑	×	↑	↑	↑	×	↑	↑	+3.8				
	Night	↑	↑	↑	↑	+5.1	↑	↑	↑	-0.6	+0.7	+4.7	-0.4	-3.7	-4.8	-5.3	↓	-4.0	-5.2	↓	↓	-4.3	-5.5	↓	↓	×	↑	↑	↑	×	↑	↑	↑	×	↑	↑	↓				
DFM-17	Day	+2.9	+2.4	+2.7	-0.3	+0.1	-0.1	-0.1	-2.9	-2.1	-2.2	-2.4	-4.9	-5.7	↓	↓	↓	-6.0	↓	↓	↓	↓	↓	↓	↓	×	↑	↑	↑	×	↑	↑	↑	×	↓	↓	↓				
	Night	↑	+4.9	↑	↑	↑	+1.2	+3.5	+1.6	-4.7	-1.8	↓	↓	↓	↓	-5.5	↓	↓	↓	↓	↓	↓	↓	↓	↓	×	↑	↑	↑	×	↑	↑	↑	×	↓	↓	↓				
GTH3	Day	↑	↑	↑	+2.3	+2.8	+3.1	↑	-0.2	-5.0	-1.8	-1.7	-2.2	↓	↓	↓	↓	↓	↓	↓	↓	↓	↓	↓	↓	×	↑	↑	↑	×	↑	↑	↓								
	Night	+2.5	↑	↑	↑	-2.9	+5.9	+2.5	↑	↓	-5.6	-1.2	-2.4	↓	↓	↓	↓	↓	↓	↓	↓	↓	↓	↓	↓	×	↑	↑	↑	×	↑	↑	↑	×	↑	↑	↑				
iMet-54	Day	↑	↑	+3.0	+1.9	+4.4	+2.0	+0.5	-0.4	↓	-1.7	-1.5	-2.3	-5.4	↓	-5.5	↓	-5.9	↓	↓	↓	↓	↓	↓	↓	×	↑	↑	↑	×	↑	↑	↑	×	↑	↑	↑				
	Night	↑	↑	+4.1	+4.1	+3.7	↑	+1.4	+1.3	-2.8	-2.2	-0.8	-0.8	-5.2	-4.5	-3.8	↓	-5.9	-4.9	-4.6	↓	↓	-5.2	-5.1	↓	×	↑	↑	↑	×	↑	↑	↑	×	↑	↑	↑				
IMS-100	Day	↑	↑	↑	↑	+3.6	↑	+2.4	+0.9	-1.8	↓	-2.0	↓	-2.3	-4.9	-4.5	↓	-2.7	-5.6	↓	↓	-3.0	↓	↓	↓	×	↑	↑	↑	×	↑	↑	↑	×	↑	↑	↑				
	Night	↑	+5.2	+5.1	↑	+2.8	+2.1	+2.1	↑	-0.7	-0.3	-0.3	-3.5	-2.7	-4.6	-2.7	↓	-3.0	-5.4	-4.0	↓	-3.3	↓	-4.6	↓	×	↑	↑	↑	×	↑	↑	↑	×	↑	↑	↑				
M20	Day	↑	+4.9	↑	↑	+1.9	+0.5	↑	-2.0	↓	-3.1	↓	↓	-3.9	↓	↓	↓	-4.3	↓	↓	↓	-4.6	↓	↓	↓	×	↑	↑	↑	×	↑	↑	↑	×	↑	↑	↑				
	Night	↑	+5.0	↑	+5.7	+2.7	+1.4	+2.5	+1.9	-1.5	-1.4	-1.0	-1.1	↓	↓	↓	↓	↓	↓	↓	↓	↓	↓	↓	↓	×	↑	↑	↑	×	↑	↑	↑	×	↑	↑	↑				
PS-B3	Day	↑	+1.2	-1.5	-4.9	+1.7	-1.8	-3.9	↓	-5.3	-4.2	-5.8	↓	↓	↓	↓	↓	↓	↓	↓	↓	↓	↓	↓	↓	×	↑	↑	↑	×	↑	↑	↑	×	↓	↓	↓				
	Night	+2.0	+2.7	+4.4	+2.7	-1.2	-0.1	+1.2	-0.8	-3.7	-2.4	-1.3	-3.6	↓	↓	↓	↓	↓	↓	↓	↓	↓	↓	↓	↓	×	↑	↑	↑	×	↑	↑	↑	×	↓	↓	↓				
RS41	Day	↑	↑	↑	+2.9	+3.6	↑	+4.1	+0.3	-0.7	-1.3	-0.7	-1.8	-1.1	-1.7	-0.1	↓	-1.7	-2.3	-1.1	↓	-2.1	-2.7	-1.6	↓	×	↑	↑	↑	×	↑	↑	↑	×	↑	↑	↑				
	Night	↑	↑	↑	↑	+4.3	+3.9	+3.2	↑	-0.6	-0.0	+0.1	+0.1	-1.2	-2.4	+0.3	↓	-2.0	-3.2	-1.6	↓	-2.6	-3.9	-2.6	↓	×	↑	↑	↑	×	↑	↑	↑	×	↑	↑	↑				
WxR-301D	Day	+1.6	↑	↑	-5.1	↓	-5.9	↓	↓	↓	↓	↓	↓	↓	↓	↓	↓	↓	↓	↓	↓	↓	↓	↓	↓	×	↑	↑	↑	×	↑	↓	↑	×	↓	↓	↓				
	Night	+3.5	+4.2	+4.2	+1.8	+0.8	+1.4	+1.4	-1.3	-1.2	-0.8	-0.8	-3.9	↓	↓	↓	↓	↓	↓	↓	↓	↓	↓	↓	↓	×	↑	↑	↑	×	↓	↓	↓	×	↓	↓	↓				

11.1.1.1 Atmospheric temperature

With one exception (the ATMS-3710 sonde, for nighttime measurements), all the systems meet all the Breakthrough OSCAR requirements for atmospheric temperature measurements in the application areas of “Aeronautical Meteorology”, “Nowcasting/Very Short-Range Forecasting”, and “Global Numerical Weather Prediction and Real-time Monitoring”.

The situation is less clear for the demanding application area “Atmospheric Climate Forecasting and Monitoring”, for which not all systems meet the Breakthrough level requirements (either fully, or partially). Performance is systematically worse for daytime measurements: a direct consequence of the impact of solar radiation –and its required correction– on temperature measurements. The influence of solar radiation was already observed in the twin sounding flight analysis in Section 10.1.6. This daytime-nighttime difference in the radiosondes performance (for the temperature) is clearly visible at the Goal level of this application area, where the vast majority of radiosondes fail to meet the requirements for daytime measurements. The daytime performance of radiosondes, for atmospheric temperature measurements, is also (comparatively) worse at higher altitudes (see Figure 11.1), where the importance of radiation correction is stronger.

The CF-06-AH sonde is the only model found to meet a (single) Goal performance criterion, for nighttime atmospheric temperature measurements in the “Atmospheric Climate Forecasting and Monitoring” application area (specifically, in the UTLS). The other systems either do not meet the requirements in this category, or have a performance located within 2σ of the corresponding ORUC value, which prevents a sufficiently confident statistical assessment. It is worth noting that the CF-06-AH sonde is found to be fit-for-purpose with respect to the OSCAR Goal value in the UTLS thanks to the absence of a measurement bias in its nighttime measurements of atmospheric temperature (in this layer; see Figure L.16 and Section 10.1.5.2).

We also note that four radiosondes (GTH3, iMS-100, PS-B3, and WxR-301D) are found to have their nighttime temperature (cold) measurement bias $\bar{\delta}$ increase noticeably above 25 km to 27 km (see Figure 11.1). Measuring colder-than-ambient temperatures at these altitudes is suggestive of an imperfect correction of the radiative (infrared) cooling of the sonde, the importance of which grows with decreasing atmospheric pressure.

11.1.1.2 Relative humidity

Meeting the ORUC criteria for relative humidity measurements is clearly a challenge for all radiosonde systems. Only 5 sondes meet the Breakthrough ORUC values (for both the daytime and nighttime categories) for the “Aeronautical Meteorology” application area, with a statistical certainty of at least 2σ . This number decreases to 3 and 2 (respectively) for the application areas “Nowcasting / Very Short-Range Forecasting” and “Global Numerical Weather Prediction and Real-time Monitoring”. The situation is only marginally better if one considers the FT alone: 5 sondes meet the ORUC values at the 2σ level for this layer in the “Nowcasting / Very Short-range Forecasting” application area, while 3 do so for the “Global Numerical Weather Prediction and Real-time Monitoring” application area.

The ORUC values associated with the “Atmospheric Climate Forecasting and Monitoring” application area (see Section 9.3.1.2) appear particularly challenging, with all but one system failing to meet even the Threshold level with a statistical confidence level of 2σ .

It is well known that measuring relative humidity with radiosondes can be challenging when flying in and out of clouds (see Section 10.1.8). However, it is important to remember that the most “intense” cloud exits experienced by radiosondes during the UAI 2022 field campaign, for which the reference GDP profiles are no longer in statistical agreement with one another, are not included in the statistical analysis leading to the Tables 11.1 to 11.4 (see Section 9.2). The fact that (nearly) all radiosondes still fail to meet the Threshold level for the relative humidity ORUC values of the “Atmospheric Climate Forecasting and Monitoring” application area (0.5 %RH in the PBL and FT at the 1σ level, 1.0 %RH in the UTLS) with this selection is thus a clear indication that these are genuinely challenging levels to reach in terms of measurement errors.

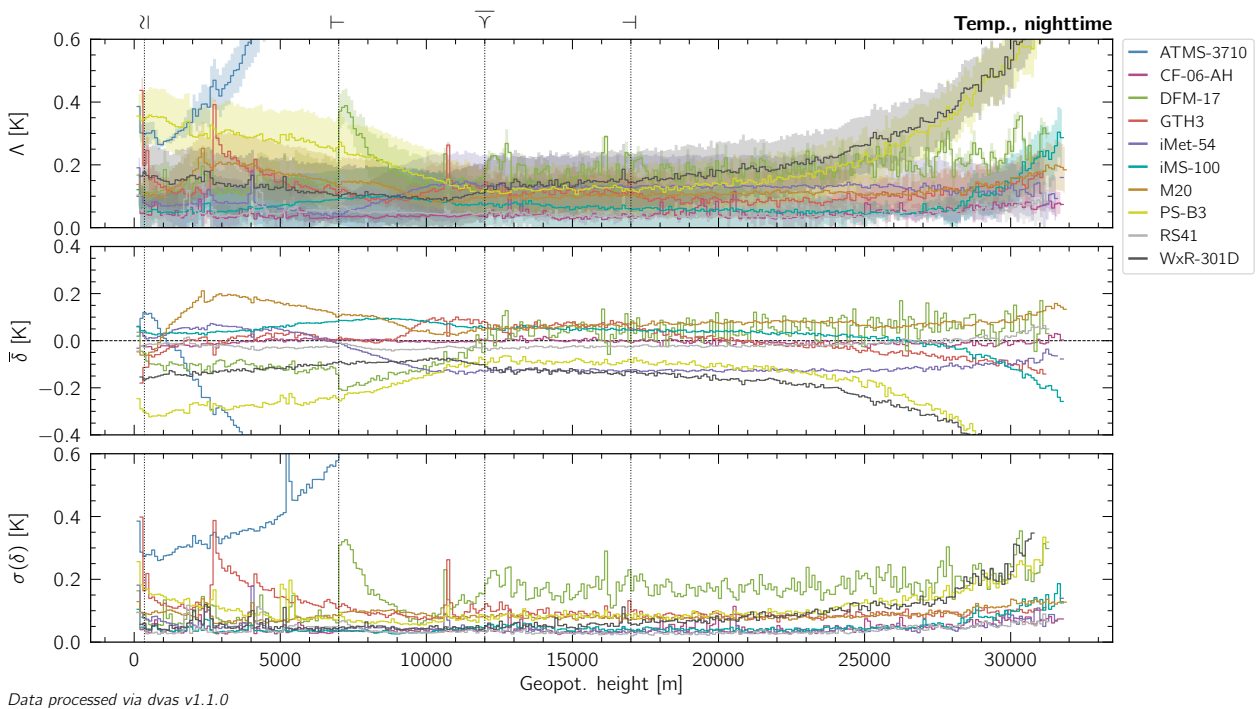
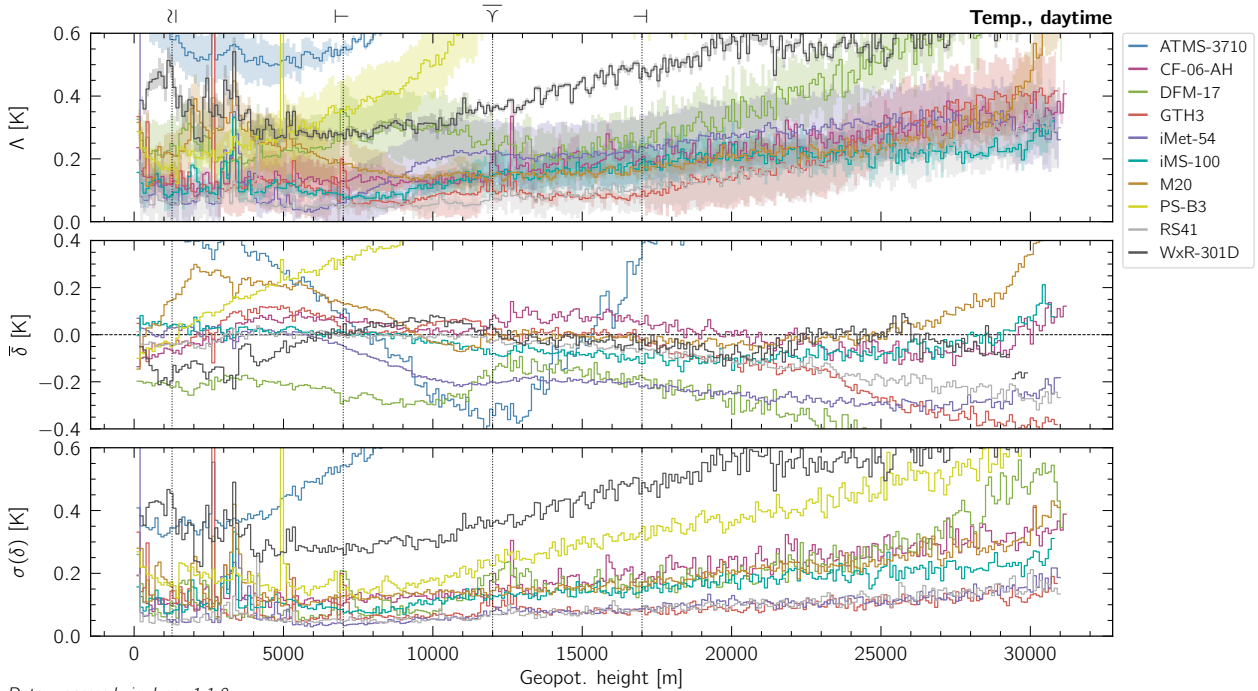


Figure 11.1: Top: The first panel shows the $\Delta_{\text{day},100,\text{m}}$ profiles for temperature (see Section 10.1.5) assembled from valid daytime flights, for all the radiosondes that participated in the UAI 2022 field campaign. These profiles can be directly compared to the ORUC values listed in Table 9.2, and the sonde-specific diagrams in Appendix L. The shaded area surrounding each curve extends $\pm \epsilon_{\text{day},100,\text{m}}$. The geopotential height of the PBLH (λ), median tropopause ($\bar{\gamma}$), and lower-/upper-limits of the UTLS (\pm) are indicated using vertical lines. Only layers to which at least $J \geq 300$ individual measurement points contribute are shown. The other panels show the resolved systematic and random measurement error profiles $\bar{\delta}_{c,100,\text{m}}$ and $\sigma(\delta)_{c,100,\text{m}}$ that make up $\Delta_{\text{day},100,\text{m}}$ (see Section 10.1.5.3 for details). Bottom: as for Top, but for the nighttime flights.

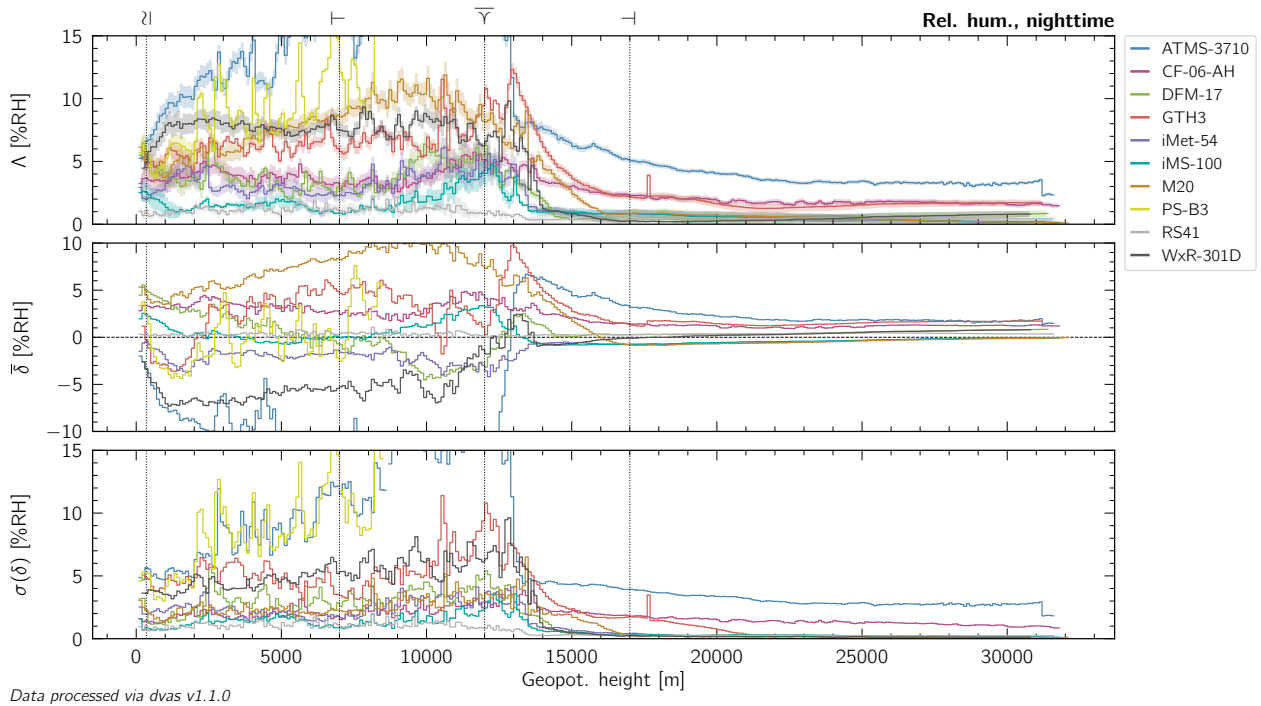
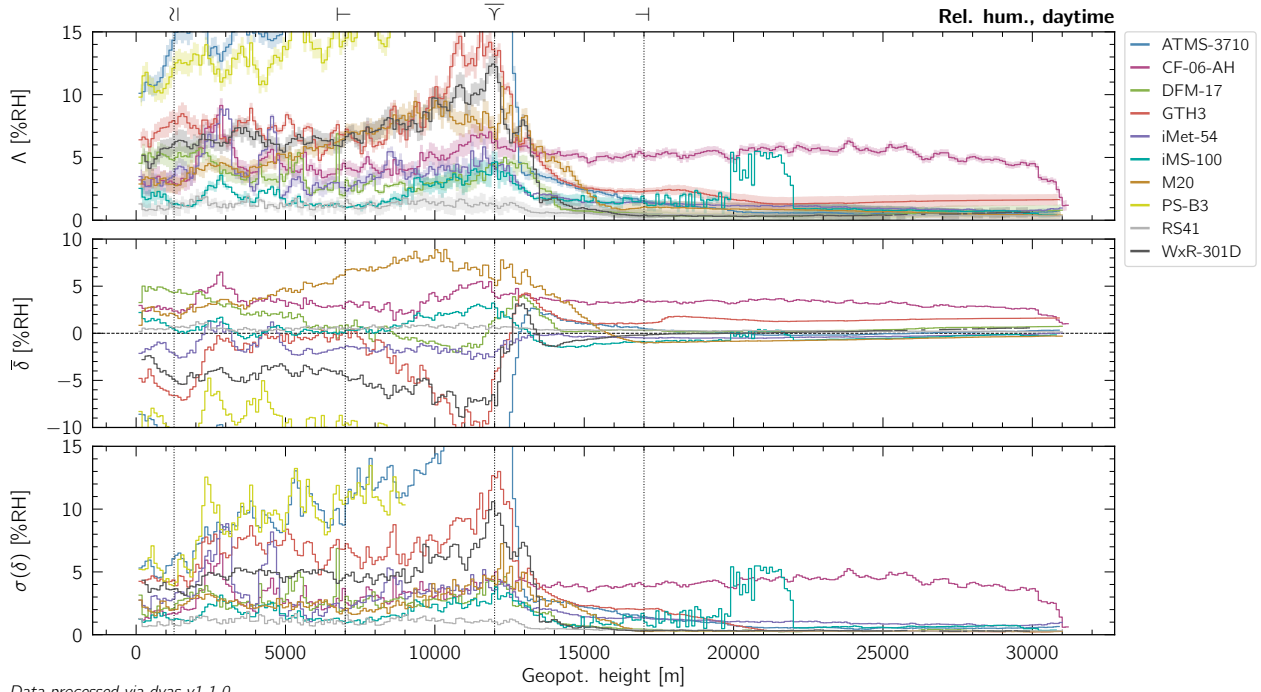


Figure 11.2: Same as Figure 11.1, but for the relative humidity.

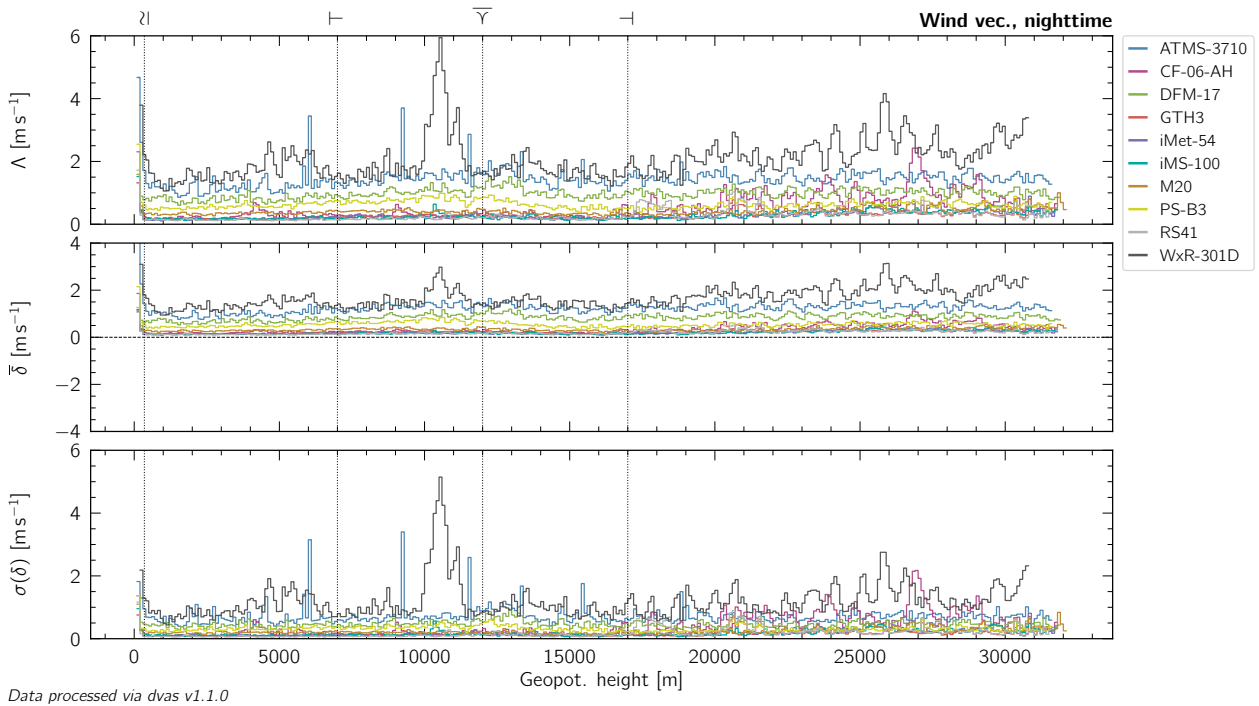
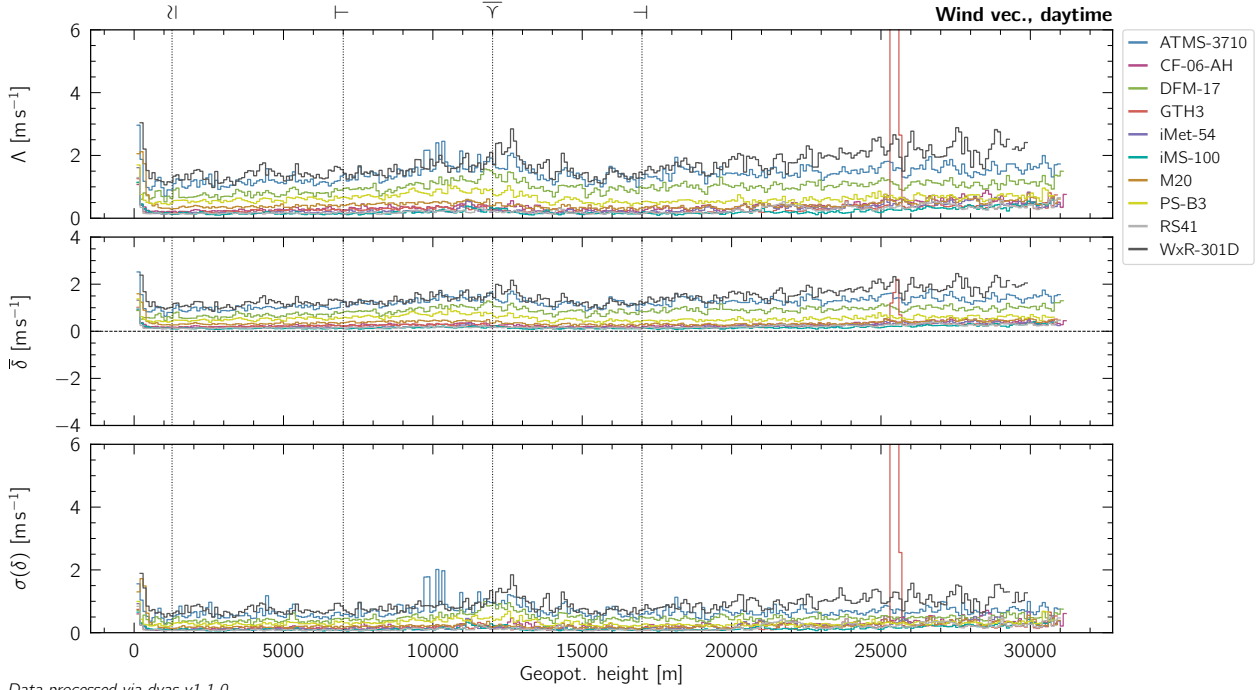


Figure 11.3: Same as Figure 11.1, but for the wind (horizontal) vector.

11.1.1.3 Wind (horizontal) vector

The uncertainties on the measurements of $\Lambda_{c,\mathcal{L}}$ for the wind (horizontal) vector variable are vanishingly small, since they are influenced only by uncorrelated sources (see Section 9.2). As a result, Equation (9.6) essentially becomes a “pass-or-fail” criterion which is reflected in the small number of statistically uncertain (grey) cases in Tables 11.1 to 11.4. Altogether, a majority of radiosondes appear to be fit-for-purpose at the Breakthrough level for all the application areas considered in this analysis.

11.1.2 User friendliness

To help WMO Members evaluate the user friendliness of the participating sounding systems, the project team relied on independent operators, which were selected by WMO (see Section 4.3.1). Since the sounding technology is rapidly developing, this report can only provide a snapshot of the state of soundings systems at the time of the intercomparison. The information provided here may help WMO Members inquiring about the capabilities, features, and reliability of sounding systems they may be interested in.

All operators had previous experience with at least one radiosonde system; however, none of the operators worked with systems they had used previously in their professional career. This allows for qualified evaluations of the user friendliness of the radiosonde sounding systems, that are not influenced by previous work experience.

During the UAI 2022 field campaign, all operators had to complete a survey, were interviewed by a member of the project team, and had to complete a written summary of their experience at the completion of the campaign. This included backup operators, who had been trained to take over sounding duties should it be necessary to substitute any of the primary operators and who occasionally assisted in sonde preparations. In addition, we made use of observations of the project team during the campaign.

The survey was developed prior to the campaign based on the experience of students, who had participated in the Sundowner Winds Experiment (SWEX) in spring of 2022 and operated different sounding systems during that campaign. This survey was refined by the project team to clarify the questions and to help operators provide unbiased and objective feedback.

The interviews were conducted towards the end of the campaign. Each operator was interviewed individually by a different member of the project team, who observed the operation of all radiosonde systems.

Lastly, all operators were asked to provide a written summary of their experiences after the completion of the campaign. This summary allowed operators to describe any experience not covered in the previous efforts to collect feedback.

Operators commented on the ease of operating a system, on the reliability of the sondes during preparation, on required preparation procedures, and on sonde design. We do not evaluate features of sounding systems that were not necessary to collect and process data, such as additional features to display, re-analyse, or transmit data. Only sounding system features, which were essential in generating high quality observations, are considered.

Overall, experiences on any sounding system were shared by all primary and backup operators commenting on their respective performance with little indication of bias in any of the statements. Comments were regarding the sounding system ground equipment as well as the radiosonde.

Below we summarise key findings for the user friendliness of the participating sounding systems. Where required, we explicitly highlight experiences which may help radiosonde manufacturers improve their sounding systems.

11.1.2.1 System ease of use

The DFM-17, iMet-54, iMS-100, M20, and RS41 systems were found to be very easy to use. These systems worked reliably and allowed for a smooth sonde preparation.

The WxR-301D system was found to be easy to use, but exhibited some quirks. For example the system did not allow updating surface reference data after the radiosonde had been prepared.

The ATMS-3710, CF-06-AH, GTH3, and PS-B3 systems were found to be inefficient, which impeded the preparation of the sondes. Without specifying here which system exhibited which inefficiency, operators noted for some systems:

- complicated or archaic Graphical User Interfaces (GUIs), and/or
- error-prone communication between the software and the ground check unit, and/or
- difficulties in placing the radiosonde in the ground check unit, and/or
- the need for confirming launch detection manually.

The GUI for the GTH3 system had not been completely translated into English at the time of the UAI 2022 field campaign; however, the interface elements in the original language caused no additional problems for the operators.

11.1.2.2 Ground check

To achieve the highest possible data quality, the calibration of all sensors should be checked or verified prior to launch. The CF-06-AH, GTH3, iMet-54, iMS-100, M20, RS41, PS-B3, WxR-301D and DFM-17 systems use a ground check to validate or recalibrate the radiosonde sensors during sonde preparation.

The RS41 and DFM-17 systems use an internal check of their sensors during their ground check, while other manufacturers use external sensors to verify the proper function and calibration.

The ATMS-3710 system does not use a ground check for their sondes.

The ground check added a small amount of time to the overall sonde preparation, which was not felt to be significant. In some systems more than one sonde were rejected in the ground check unit (see Section 8.3). This is considered an essential feature of a sounding system to be able to identify radiosondes, which do not meet manufacturer expectations.

The ground check sets of the CF-06-AH and GTH3 systems caused some problems and delays. The placement of the sonde in the unit proved to be difficult in both of these units and sometimes required restarting the ground check. The unit of the CF-06-AH system had no power switch and had to run for the entire duration of the campaign.

11.1.2.3 Time required for preparing a sonde

Sondes in systems without a ground check could be prepared slightly faster compared to those requiring it. In all systems, sondes could generally be prepared within 5 min to 10 min. However, sonde rejections by the ground check unit, the inability to connect to the receiver or ground check unit, or the inability to properly set the telemetry frequency occasionally led to increased preparation times for the CF-06-AH, GTH3, and PS-B3 systems.

11.1.2.4 Radiosonde handling

Despite some differences to regular balloon operations, all sonde handlings were nearly identical to regular balloon launches. One difference is that operators were required to connect the radiosonde to a string that was already attached to the payload rig instead of connecting an unwinder to the inflated balloon.

Some systems required external parts to be clipped or screwed into the radiosondes. For most systems, connecting this part was obvious and easy.

Some operators found it difficult to screw the string connector into the CF-06-AH sonde. The small size of the connector screw provided potential for it to get lost. The radiation shield for the humidity sensor of this sonde also had to be removed before and replaced after successful reconditioning. This gave rise to the risk of the cap being forgotten or lost (even though this did not happen during the UAI 2022 field campaign).

The PS-B3 radiosonde was provided with a string that was connected to the radiosonde internally. In some cases, this string came loose during normal handling and had to be retied. In addition, it was possible to accidentally drop the PS-B3 radiosonde, if it was held only from one of the two half shells making-up the radiosonde body.

Finally, it was found that the clip of the ATMS-3710 radiosonde, which properly positioned the sensor boom, was difficult to install, and thus is considered to be a risk factor for damaging the sensors.

11.1.2.5 Frequency selection

The transmission frequency of all systems were carefully coordinated to minimise radio frequency interference between the different sondes. Operators had to change frequencies only infrequently. All systems were able to use frequencies over the entire 403MHz band; however, some systems allowed only a coarse frequency selections with increments between 0.02 and 1.0 MHz.

There were substantial differences in the ease of setting the telemetry frequency, with operators noting the complexity for some.

11.1.2.6 Launch detection and surface reference

Operational systems are expected to detect the balloon launch automatically. All systems but one did so. The GTH3 system required the operator to observe and confirm the balloon launch manually in the software. The errors in the launch detection of the different systems is analysed in detail in Section 10.1.2.

Surface reference observations had to be entered manually into all systems due to the specifics of the intercomparison operations. Inherently, this made all systems susceptible to operator error entering reference values incorrectly.

The ATMS-3710 system recorded numerous errors in the surface reference pressure. The WxR-301D system swapped wind direction and wind speed in storing the surface reference observations. Furthermore, this system required surface reference observations at the time of the ground check, and could not be updated at launch. For both systems, these reference values were not used in the calculations and did not affect the profile data and analyses.

The GTH3 system did encounter several incorrectly entered surface reference observations, that are listed in Section 8.2.4 alongside the affected profile data (that were subsequently cropped from the analysis).

11.1.2.7 File generation

All systems detected balloon burst automatically and some continued recording descending data after burst. Files were generated either at the end of the ascending phase of the sounding or after telemetry transmission was lost during the descending phase.

All manufacturers were required to provide data for the ascending phase of the sounding in a format defined by the project team (see Appendix D) and, in addition, in (high vertical resolution) BUFR format defined by WMO.

In a few cases, the telemetry transmission of the PS-B3 radiosonde stopped before balloon burst and the required files had to be generated manually. The CF-06-AH and GTH3 systems required manual generation of the files after the termination of the sounding.

Generation of data files for the descending portion of the sounding was not a requirement of the UAI 2022 field campaign and these data were not analysed. Nevertheless, station managers installing new systems should inquire about the system's ability to generate descending data files in an appropriate WMO BUFR sequence, which can be shared through the WMO GTS.

11.1.3 Forcing of relative humidity measurements in the stratosphere

The performance assessment of radiosonde measurements against the WMO's ORUCs has already shown that relative humidity is a particularly challenging variable to measure correctly (see Section 11.1.1.2). This is particularly true above the tropopause where the number density of water drops to very small values, which are difficult to measure with capacitive sensor technology.

The UAI 2022 Project Team realised, over the course of the UAI 2022 field campaign, that a small number of manufacturers may be artificially forcing¹ the relative humidity measurements from their sonde to a very low value in the stratosphere. If true, such practice would violate some of the most elementary principles of metrology. It would also pose a profound ethical problem if, in addition, this decision is not visibly and explicitly described in the system's documentation. From this perspective, the masking of specific measurements, known by the manufacturer to be unreliable or that are yet to be formally characterised², would appear more transparent.

Some may argue that the forcing of relative humidity measurements to very low values in the stratosphere is not artificial, but merely driven by elementary physics and the typical state of the atmosphere at high altitudes. Such an argument is obviously fallacious, as illustrated by the polar stratospheric dehydration ([Vömel et al., 1995](#)) or the eruption of the Hunga Tonga-Hunga Ha'apai submarine volcano in January 2022³.

The UAI 2022 dataset does not allow us to state with absolute certainty which radiosonde, if any, is forcing measurements of relative humidity (be it to systematically reach low values in the stratosphere, or 100%RH in clouds). The project team of the UAI 2022 would however never condone the artificial forcing of measurements for any geophysical variable, irrespective of any resulting performances reported in Section 11.1.1 and elsewhere in this analysis.

Therefore, we strongly recommend that users of any radiosonde system seek explicit clarification from the manufacturer regarding any artificial forcing of measurements, and particularly for relative humidity in the stratosphere. In turn, we also strongly recommend that manufacturers systematically describe exactly how they handle measurements of relative humidity in the stratosphere and in high-humidity environments in the troposphere: and do so very visibly if they decide to artificially alter any of their measurements⁴.

¹By "artificial data forcing", we mean the use of corrective factors, functions, or any other post-processing means that have no scientific justification, with the sole aim to render measurements more "pleasing". It is different from data clipping or data masking.

²as is for example the case for the PS-B3 radiosonde, see Section 10.1.3.

³This volcanic eruption in the South Pacific sent an unprecedented 100 Tg to 146 Tg of water into the stratosphere ([Khaykin et al., 2022](#); [Carr et al., 2022](#); [Millán et al., 2022](#); [Vömel et al., 2022](#)). This represents a sudden increase of ~10% in the stratospheric water content of the Earth's atmosphere. Within weeks, these newly injected water molecules circulated throughout the Southern Hemisphere ([Schoeberl et al., 2022](#); [Taha et al., 2022](#)). They were responsible for the development of several temperature and circulation anomalies in the lower stratosphere over the months following the eruption ([Coy et al., 2022](#); [Vömel et al., 2022](#)). The consequences of this record-breaking volcanic eruption remain under active scrutiny by the atmospheric physics community, given its potential to alter climate on a global scale. If radiosonde systems artificially force their measurements of relative humidity in the stratosphere, this would evidently prove devastating to studies of the atmospheric consequences of such an event (see e.g. the Supplementary Materials for [Vömel et al., 2022](#)).

⁴that users would otherwise very likely assume to have been conducted in strict accordance with standard metrological principles.

11.2 REMOTE SENSING OBSERVATIONS

11.2.1 Limitations of the REMote sensing Intercomparison (REMI)

In this Section we provide the necessary information to interpret correctly the assessment results of the LRSS with respect to the OSCAR requirement uncertainty criterion (ORUC) presented in Section 10.2 and 11.2.2. The geophysical variables retrieved from the LRSS have been analysed by the Remote Sensing Software Analysis (RSSA) (Section 9.6.4) in the same way as the radiosounding data have been analysed by *dvas* against the reference Combined Working measurement Standard (CWS), i.e. the RSSA is based on the same statistical principles as *dvas*. However, there are two fundamental differences that must be accounted for when comparing the remote sensing with the CWS:

1. **spatial**: the geophysical variables measured by the CWS and retrieved from the LRSS measurements do not coincide in space because the CWS attached to the balloon drifts away from the LRSS.
2. **temporal**: the instantaneous values measured by the CWS are compared with the values retrieved from the LRSS instruments over a longer average in time and space (Section 9.6.2).

Essentially, the radiosondes are compared against the CWS in a (drifting) Lagrangian reference framework, whereas the remote sensing systems provide data in a (static) Eulerian reference framework, namely in a strictly vertical column above the site. As a consequence, in addition to the instrumental correlated and uncorrelated uncertainty, for the LRSS, a further source of uncertainty stems from the lack of temporal and spatial co-localisation of the drifting CWS. This additional uncertainty contribution cannot be quantified precisely for the retrieved geophysical variables, with the consequence that the $\Lambda_{C,L}$ values reported in Section 10.2 are overestimates of the actual systems' performance. This has the following consequences for the results of the present analysis. When the assessment of a LRSS instrument indicates that it is "fit-for-purpose" with respect to a specific ORUC requirement, the assessment is provided with absolute certitude. But if the assessment leads to an uncertain or negative outcome, one cannot guarantee that the actual performances are not, in fact, fit-for-purpose.

For this reason, and to ensure a fair interpretation of the assessment of the LRSS instruments, in Tables 11.5-11.7 only the "fit-for-purpose" assessment is provided in color, to indicate that this outcome is certain. The performance scores provided in Tables 10.7 and 10.8 must be read as "lower-bound assessment", i.e. the assessed performances could only be better, given the (uncorrected) impacts driven by the **spatial** and **temporal** limitations.

11.2.2 Fitness-for-purpose with respect to OSCAR

The effective confidence level k_{eff} , defined in equation (9.6) is used in Tables 11.5-11.7 to assess the fitness-for-purpose of an instrument of the LRSS. The values for all cases are provided for completeness, but only those where the system is found to be fit-for-purpose (with $k_{\text{eff}} \geq 2$) are coloured. Cases with $k_{\text{eff}} < 2$ are not coloured, because we cannot be certain of the level at which the performances are underestimated by the **spatial** and **temporal** limitations inherent to our analytical approach. The cases assessed "fit-for-purpose" are shown in peach.

Table 11.5: Fitness-for-purpose assessment of the MWR-MF and MWR-SMZ remote sensing instruments for the **atmospheric temperature**, with respect to the WMO’s ORUC Threshold (Θ^T), Breakthrough (Θ^B) and Goal (Θ^G) values (extracted on 2023-05-31; see Section 9.3.1). The value of k_{eff} , defined in Equation (9.6), is shown where an ORUC value exists (see Table 9.2) and $-6 \leq k_{\text{eff}} \leq +6$. The symbols \uparrow and \downarrow indicate that $k_{\text{eff}} > +6$ and $k_{\text{eff}} < -6$, respectively. The symbol $-$ indicates that a fitness-for-purpose assessment cannot be made due to the lack of observations. Cells coloured in peach indicate that the instrument is fit-for-purpose ($\equiv k_{\text{eff}} > +2$) with respect to the associated ORUC.

		Aeronautical Meteorology									Nowcasting / Very Short-Range Forecasting									Global NWP and Real-time Monitoring									Atmospheric Climate Forecasting and Monitoring									
		Θ^T			Θ^B			Θ^G			Θ^T			Θ^B			Θ^G			Θ^T			Θ^B			Θ^G												
		PBL	FT	UTLS	PBL	FT	UTLS	PBL	FT	UTLS	PBL	FT	UTLS	PBL	FT	UTLS	PBL	FT	UTLS	PBL	FT	UTLS	PBL	FT	UTLS	PBL	FT	UTLS										
MWR-MF	Day	\uparrow	\uparrow	\uparrow	\uparrow	\uparrow	\uparrow	\uparrow	+5.5	+2.5	\uparrow	+5.5	+1.7	-5.4	-3.7	\downarrow	\uparrow	\uparrow	\uparrow	-	+1.7	-5.4	\downarrow	-	-3.7	\downarrow	\downarrow	-	-3.7	\downarrow	\downarrow	-	\downarrow	\downarrow	-	\downarrow	\downarrow	-
	Night	\uparrow	\uparrow	\uparrow	\uparrow	\uparrow	\uparrow	\uparrow	\uparrow	+1.7	\uparrow	\uparrow	-2.0	-3.1	\downarrow	\downarrow	\uparrow	\uparrow	\uparrow	-	-2.0	-3.1	\downarrow	-	\downarrow	\downarrow	\downarrow	-	\downarrow	\downarrow	\downarrow	-	\downarrow	\downarrow	-	\downarrow	\downarrow	-
MWR-SMZ	Day	\uparrow	\uparrow	\uparrow	\uparrow	\uparrow	\uparrow	\uparrow	+3.7	+0.4	\uparrow	+3.7	-2.6	\downarrow	\downarrow	\downarrow	\uparrow	\uparrow	\uparrow	-	-2.6	\downarrow	\downarrow	-	\downarrow	\downarrow	-	\downarrow	\downarrow	\downarrow	-	\downarrow	\downarrow	-	\downarrow	\downarrow	-	
	Night	\uparrow	\uparrow	\uparrow	\uparrow	\uparrow	\uparrow	\uparrow	\uparrow	+0.2	\uparrow	\uparrow	-3.4	-4.7	\downarrow	\downarrow	\uparrow	\uparrow	\uparrow	-	-3.4	-4.7	\downarrow	-	\downarrow	\downarrow	-	\downarrow	\downarrow	\downarrow	-	\downarrow	\downarrow	-	\downarrow	\downarrow	-	

Table 11.6: Same as Table 11.5, but for **relative humidity**.

		Aeronautical Meteorology									Nowcasting / Very Short-Range Forecasting									Global NWP and Real-time Monitoring									Atmospheric Climate Forecasting and Monitoring								
		Θ^T			Θ^B			Θ^G			Θ^T			Θ^B			Θ^G			Θ^T			Θ^B			Θ^G											
		PBL	FT	UTLS	PBL	FT	UTLS	PBL	FT	UTLS	PBL	FT	UTLS	PBL	FT	UTLS	PBL	FT	UTLS	PBL	FT	UTLS	PBL	FT	UTLS	PBL	FT	UTLS									
MWR-MF	Day	+0.9			-2.2			-4.3			+0.9	-1.2	-4.3	\downarrow	\downarrow	\downarrow	+0.9	\downarrow	-4.3	\downarrow	\downarrow	\downarrow	-	-4.3	\downarrow	\downarrow	\downarrow	\downarrow	\downarrow	\downarrow	-	\downarrow	\downarrow	-	\downarrow	\downarrow	-
	Night	+2.3			-1.1			-3.4			+2.3	+3.0	-3.4	\downarrow	\downarrow	\downarrow	+2.3	\downarrow	-3.4	\downarrow	\downarrow	\downarrow	-	-3.4	\downarrow	\downarrow	\downarrow	\downarrow	\downarrow	\downarrow	-	\downarrow	\downarrow	-	\downarrow	\downarrow	-
MWR-SMZ	Day	-1.4			-4.7			\downarrow			-1.4	-3.7	\downarrow	\downarrow	\downarrow	\downarrow	-1.4	\downarrow	\downarrow	\downarrow	\downarrow	\downarrow	-	\downarrow	\downarrow	\downarrow	\downarrow	\downarrow	\downarrow	\downarrow	-	\downarrow	\downarrow	-	\downarrow	\downarrow	-
	Night	+1.2			-2.1			-4.3			+1.2	-0.2	-4.3	\downarrow	\downarrow	\downarrow	+1.2	\downarrow	-4.3	\downarrow	\downarrow	\downarrow	-	-4.3	\downarrow	\downarrow	\downarrow	\downarrow	\downarrow	\downarrow	-	\downarrow	\downarrow	-	\downarrow	\downarrow	-

Table 11.7: Same as Table 11.5, but for **wind (horizontal) vector** measurements by the DWL WindLidar1 and WindLidar2 and of the low- and high-mode RWP remote sensing instruments.

	Aeronautical Meteorology												Nowcasting / Very Short-Range Forecasting												Global NWP and Real-time Monitoring												Atmospheric Climate Forecasting and Monitoring											
	Θ^T				Θ^B				Θ^G				Θ^T				Θ^B				Θ^G				Θ^T				Θ^B				Θ^G															
	PBL	FT	UTLS	MUS	PBL	FT	UTLS	MUS	PBL	FT	UTLS	MUS	PBL	FT	UTLS	MUS	PBL	FT	UTLS	MUS	PBL	FT	UTLS	MUS	PBL	FT	UTLS	MUS	PBL	FT	UTLS	MUS	PBL	FT	UTLS	MUS	PBL	FT	UTLS	MUS								
Wind lidar (1)	Day	↑	↑	↑	↑	↑	↑	↑	↑	+4.2	↑	↑	↑	↑	↑	+4.2	-2.9	-1.1	-2.7	↑	↑	↑	-	-2.9	-1.1	-2.7	-	↑	↑	↑	-	+1.8	+3.1	+0.7	-	↓	-5.3	↓	-									
	Night	↑	↑	↑	+4.6	↑	↑	-1.3	↑	-0.7	↑	↑	↑	-1.3	↑	-0.7	↓	-0.4	↓	↑	↑	↑	-	+4.6	↑	↑	-	↓	-0.4	↓	-	+1.7	↑	+2.9	-	-4.2	+4.0	-4.3	-	↓	-4.9	↓	-					
Wind lidar (2)	Day	↑	↑	↑	↑	↑	↑	↑	+5.6	+0.8	↑	↑	↑	↑	+5.6	+0.8	-2.2	-2.4	↓	↑	↑	↑	-	↑	↑	↑	-	-2.2	-2.4	↓	-	↑	↑	+4.4	-	+2.8	+1.6	-2.8	-	↓	↓	↓	-					
	Night	↑	↑	↑	↑	↑	+4.5	+0.1	↑	-1.1	↑	↑	↑	+0.1	↑	-1.1	↓	-0.4	↓	↑	↑	↑	-	↑	↑	+4.5	-	↓	-0.4	↓	-	+3.6	↑	+1.7	-	-3.4	+3.4	-3.9	-	↓	-4.2	↓	-					
Wind profiler (High Mode)	Day	-	↑	↑	-	+5.5	+5.6	-	+1.5	-0.8	-	↑	↑	-	+1.5	-0.8	-	-4.1	↓	-	↑	↑	-	↑	+5.6	-	-	-4.1	↓	-	-	+4.4	+2.4	-	-	-1.3	-4.0	-	-	↓	↓	-						
	Night	-	↑	↑	-	+4.8	+4.5	-	+0.8	-1.4	-	↑	↑	-	+0.8	-1.4	-	-4.9	↓	-	↑	↑	-	↑	+4.5	-	-	-4.9	↓	-	-	+3.6	+1.6	-	-	-2.1	-4.3	-	-	↓	↓	-						
Wind profiler (Low Mode)	Day	↑	↑	↑	↑	↑	+5.4	↑	+4.0	-0.8	↑	↑	↑	↑	+4.0	-0.8	-4.8	-4.2	↓	↑	↑	↑	-	↑	↑	+5.4	-	-4.8	-4.2	↓	-	↑	↑	+2.3	-	+1.0	-0.1	-3.9	-	↓	↓	↓	-					
	Night	-	↑	↑	-	↑	↑	-	↑	+1.2	-	↑	↑	-	↑	+1.2	-	-2.3	-4.3	-	↑	↑	-	↑	↑	-	-	-2.3	-4.3	-	-	↑	+3.9	-	-	+1.9	-1.6	-	-	↓	↓	-						

11.2.2.1 Micro-Wave Radiometers (MWRs)

In order to help understanding the contribution of the mean error (mean bias δ) to the overall Λ -value, we show in Figures 11.4-11.5 the δ -values in box-plots for the atmospheric temperature (Figure 11.4) and the relative humidity (Figure 11.5).

From the values shown in the four box-subplots in Figure 11.4, we can observe that:

1. all four temperature δ profiles suffer a cold bias at almost all atmospheric levels \mathcal{L} and for both MWR,
2. there is essentially no difference between the day and night flight categories;
3. the MWR-SMZ has a cold bias almost twice as large as the MWR-MF, and
4. the width of the whiskers at each height gives an idea of the vertical profile of $\sigma(\delta)_{\mathcal{C},\mathcal{L}}$.

From the relative humidity δ diagrams, we can observe that:

1. for both flight categories and over the atmospheric column up to 9000 m, the median δ RH is close to zero especially for the MWR-MF,
2. the MWR-MF have comparable median dry bias in the lower 0–5000 m during day or night, and
3. the MWR-SMZ have comparable median wet bias in the lower 0–5000 m during day or night.

As visual support for Tables 11.5-11.6, we show in Figure 11.6 the profiles of $\Lambda_{\mathcal{C},\mathcal{L}} \pm \epsilon_{\mathcal{C},\mathcal{L}}$, $\bar{\delta}_{\mathcal{C},\mathcal{L}}$ and $\sigma(\delta)_{\mathcal{C},\mathcal{L}}$ for the atmospheric temperature and relative humidity. For the two variables retrieved from the MWR-MF and the MWR-SMZ measurements, the four sub-figures also show the values $\Lambda_{\mathcal{C},\mathcal{L}} \pm \epsilon_{\mathcal{C},\mathcal{L}}$ (\diamond) calculated over the atmospheric layers $\mathcal{L} = [\text{PBL}, \text{FT}, \text{UTLS}]$ for both flight categories and with respect to the Θ_T , Θ_B and Θ_G ORUC levels. The case shown in Figure 11.6a corresponds to the assessment values k_{eff} in Table 11.5 for the MWR-MF, for the atmospheric temperature, the flight category $\mathcal{C} = \text{Day}$ with respect to the ORUC of the Nowcasting / Very Short-Range Forecasting application areas over the atmospheric layer $\mathcal{L} = \text{PBL}$.

As it is shown by both Table 11.5 and Figure 11.6a, the MWR-MF is fit-for purpose ($k_{\text{eff}} > 6$) in terms of atmospheric temperature measurements with respect to the *threshold* ORUC for the PBL. The MWR-MF cannot be assessed ($k_{\text{eff}} = +1.7$) with respect to the *breakthrough* ORUC for the PBL. Graphically, this translates into the $\Lambda_{\text{day},\text{PBL}} \pm \epsilon_{\text{day},\text{PBL}}$ overlapping the *breakthrough* value (Θ_B) in Figure 11.6a. The MWR-MF cannot be assessed ($k_{\text{eff}} = -3.7$) with respect to the Goal requirement, Θ_G , this is also shown in Figure 11.6a by the value of $\Lambda_{\text{day},\text{PBL}} \pm \epsilon_{\text{day},\text{PBL}}$ with respect to Θ_G .

As a direct comparison with the MWR-MF, Figure 11.6c displays the profiles of $\Lambda_{\mathcal{C},\mathcal{L}} \pm \epsilon_{\mathcal{C},\mathcal{L}}$, $\bar{\delta}_{\mathcal{C},\mathcal{L}}$ and $\sigma(\delta)_{\mathcal{C},\mathcal{L}}$ for the same variable (temperature), flight category (day), atmospheric layer (PBL), application area and ORUC requirements, but for the MWR-SMZ. Correspondingly, Table 11.5 shows the k_{eff} values based on the value $\Lambda_{\text{day},\text{PBL}} \pm \epsilon_{\text{day},\text{PBL}}$ with respect to Θ_B , Θ_B and Θ_G for the PBL. Both Figure 11.6c and Table 11.5 show a slightly worse performance of the MWR-SMZ with the values of k_{eff} smaller than for the MWR-MF.

Figures 11.6b and 11.6d show, for relative humidity, for flight category $\mathcal{C} = \text{night}$, for the ORUC's levels Θ_T , Θ_B and Θ_G of the Aeronautical Meteorology application area, the profiles of $\Lambda_{\text{night},\mathcal{L}} \pm \epsilon_{\text{night},\mathcal{L}}$, $\bar{\delta}_{\text{night},\mathcal{L}}$ and $\sigma(\delta)_{\text{night},\mathcal{L}}$ as well as the values $\Lambda_{\text{night},\text{PBL}} \pm \epsilon_{\text{night},\text{PBL}}$ calculated over $\mathcal{L} = \text{PBL}$. Correspondingly, Table 11.5 shows, for the relative humidity, the assessment values k_{eff} for the MWR-MF and MWR-SMZ for $\mathcal{C} = \text{night}$ and $\mathcal{L} = \text{PBL}$. For the relative humidity, the MWR-MF is assessed fit-for-purpose with $k_{\text{eff}} = +2.3$, in contrast, the MWR-SMZ cannot be assessed for any of the ORUC's levels, application areas, flight categories and atmospheric layers. The MWR-MF is assessed fit-for-purpose also for the application area "Nowcasting / Very Short-Range Forecasting", $\mathcal{C} = \text{night}$, where $k_{\text{eff}} = +2.3$ and $+3.0$, respectively for $\mathcal{L} = \text{PBL}$ and FT.

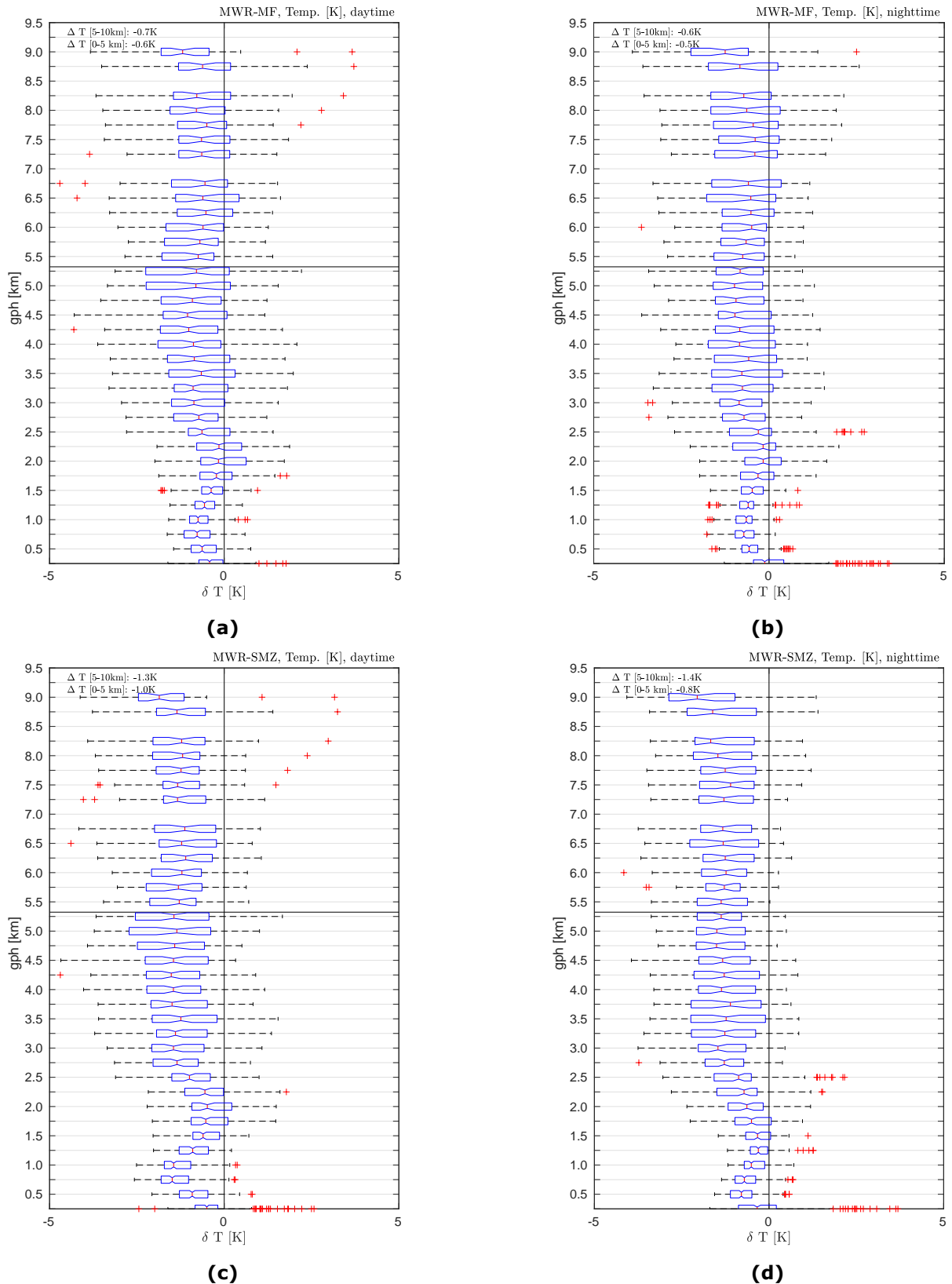


Figure 11.4: Box-plots of δ -values for the atmospheric temperature retrieved from the two MWRs. The biases $\delta = \text{LRSS} - \text{CWS}$ are integrated into 250 m bins. The vertical red segment inside each box is the median δ -value, the box's limits are the 25th-75th percentile. The whiskers extend to the most extreme data points not considered outliers, and the outliers are plotted individually using the + symbol. (a): Daytime δ atm. temp. by MWR-MF, in K (b): Nighttime δ atm. temp. by MWR-MF, in K (c): Daytime δ atm. temp. by MWR-SMZ, in K (d): Nighttime δ atm. temp. by MWR-MF, in K

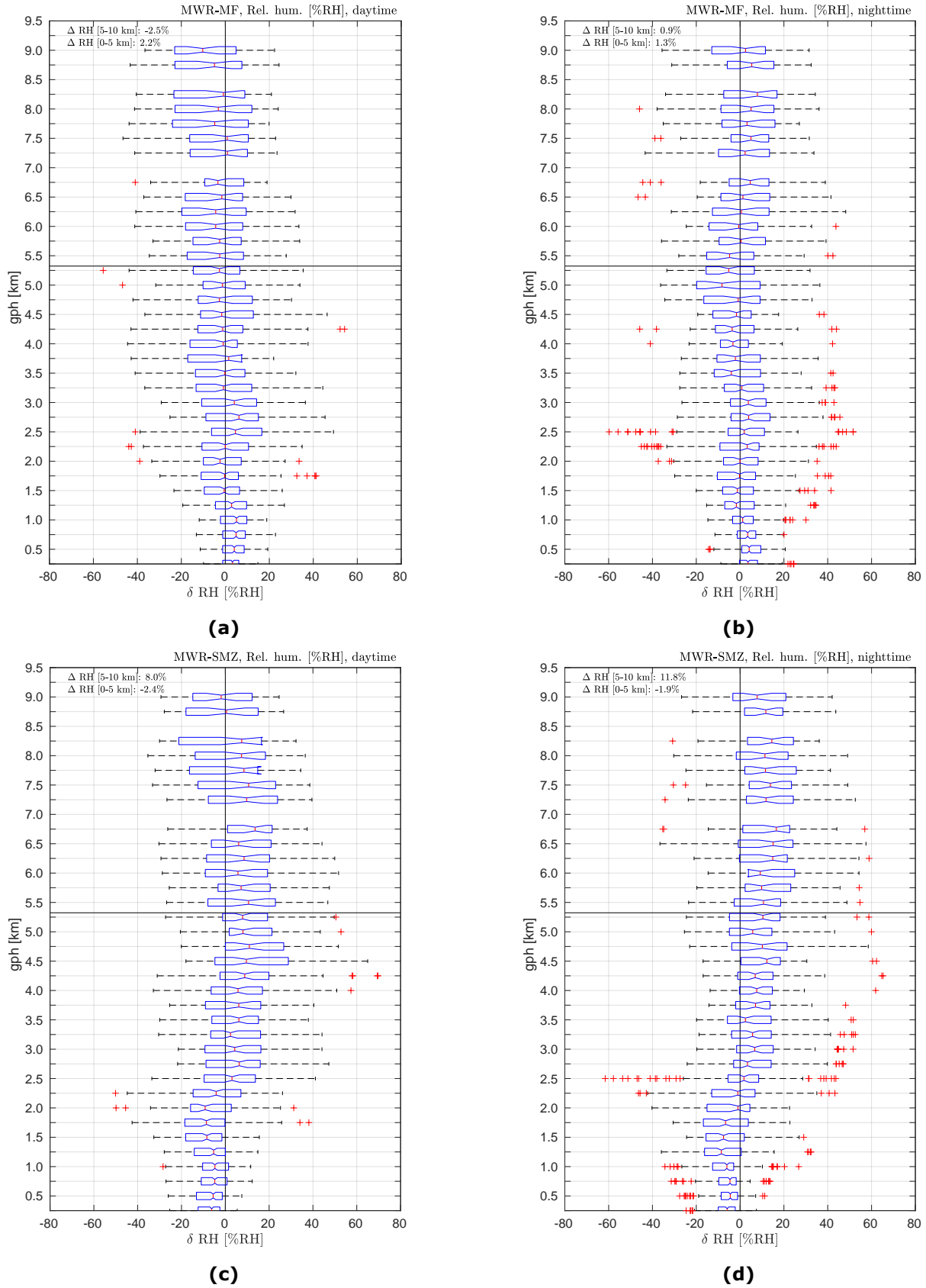


Figure 11.5: Box-plot of δ values for the relative humidity retrieved by the two MWRs. Symbols, lines and colours are as in Figure 11.4. (a): Daytime δ rel. hum. by MWR-MF, in %RH (b): Nighttime δ rel. hum. by MWR-MF, in %RH. (c): Daytime δ rel. hum. by MWR-SMZ, in %RH. (d): Nighttime δ rel. hum. by MWR-MF, in %RH.

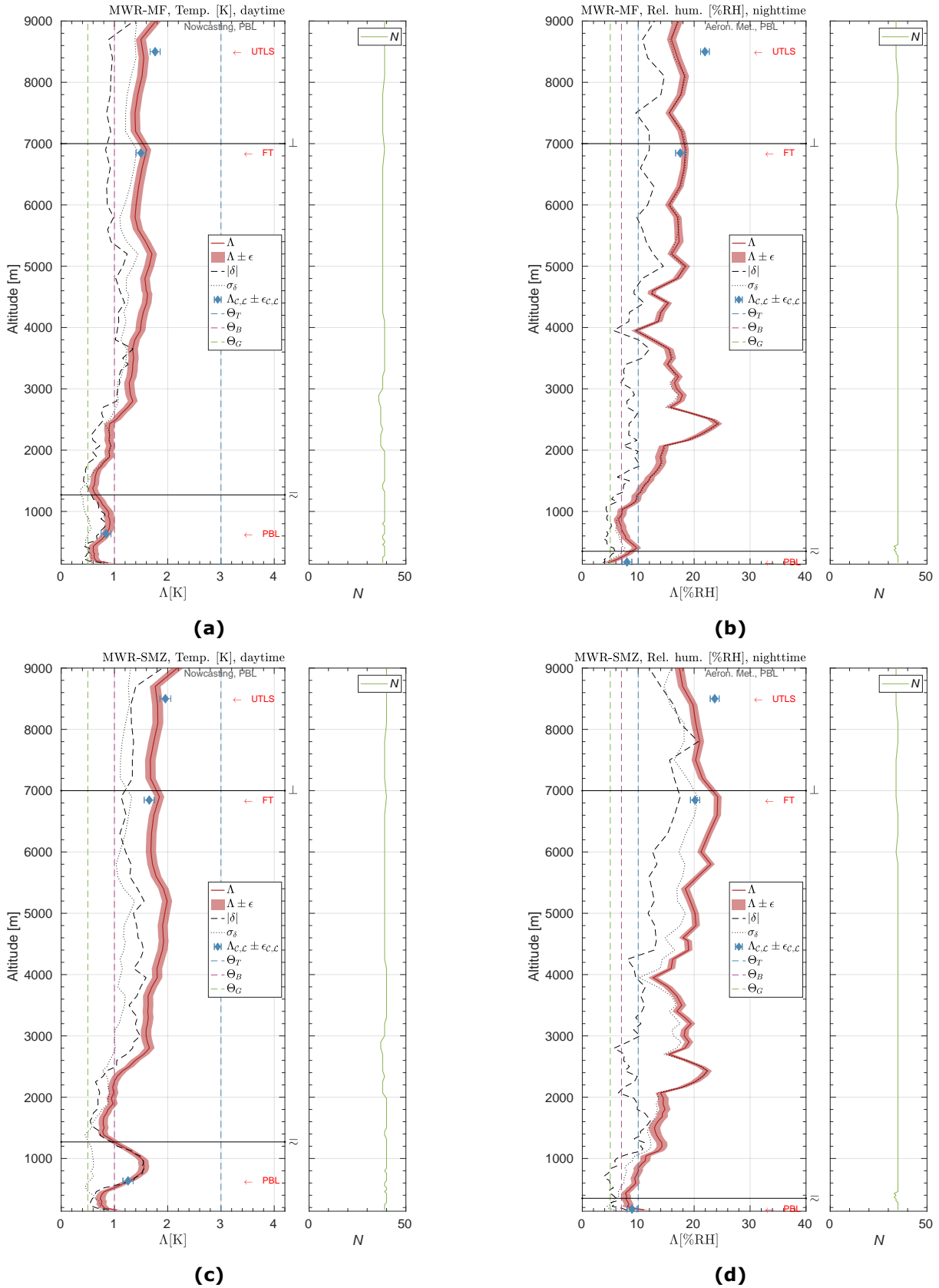


Figure 11.6: Left panels in the four sub-figures: profiles of $\Lambda_{c,\mathcal{L}} \pm \epsilon_{c,\mathcal{L}}$, $\bar{\delta}_{c,\mathcal{L}}$ and $\sigma(\delta)_{c,\mathcal{L}}$ for the MWR-MF in (a) and (b) and for the MWR-SMZ in (c) and (d). The left column (a, c) displays the atmosph. temp. for the flight category $\mathcal{C} = \text{day}$, while the right column displays the %RH for the flight category $\mathcal{C} = \text{night}$. All symbols and line styles as described in Figure 10.27. The right panels of the four sub-figures show the data availability of the MWR-MF and MWR-SMZ over all valid flights for each flight category during the UAII field campaign.

11.2.2.2 Doppler Wind Lidars (DWLs) and Radar Wind Profiler (RWP)

Like for Figure 11.4 and Figure 11.5, also Figure 11.7 shows the δ -values, but for the geophysical variable “wind speed” retrieved from the four wind profilers of the LRSS and for the flight category $C = \text{day}$. The daytime cases are shown as the DWL have higher data availability in the PBL, which is deeper in daytime than in nighttime. All δ -subplots show the mean measurement error in boxes of 250-m except for the high-mode RWP for which the box size is twice the mean vertical resolution, i.e. 628-m along the range 5500–16 000 m. From the values shown in the four box-subplots (a)-(d) we can observe that

1. None of the four wind profilers exceeds the value $|\delta| = 0.5 \text{ m s}^{-1}$;
2. Figure 11.7b shows a broader deviation from the median value in the region 3500–10 000 m, this is also related to the lower data availability above the PBLH of the WindLidar2 compared to the other profilers;
3. the relatively large spread of the δ -values around the median value in Figure 11.7c translates into a larger $\sigma(\delta)_{\text{Day,FT}}$ contribution to $\Lambda_{\text{Day,FT}}$.

For the horizontal wind vector, we proceed in the same way as for the temperature and the relative humidity retrieved from the two MWR. Figure 11.8 helps understanding the assessment values k_{eff} in Table 11.7. The profiles of $\Lambda_{\text{day},\mathcal{L}} \pm \epsilon_{\text{day},\mathcal{L}}$, $\bar{\delta}_{\text{day},\mathcal{L}}$ and $\sigma(\delta)_{\text{day},\mathcal{L}}$ as well as the values $\Lambda_{\text{day,FT}} \pm \epsilon_{\text{day,FT}}$ shown in Figure 11.8 are calculated for the variable “wind vector”, the flight category $C = \text{day}$, the atmospheric layer $\mathcal{L} = \text{FT}$, the ORUC’s requirements Θ_T , Θ_B and Θ_G of the application area Atmospheric Climate Forecasting and Monitoring (“Climate”), for the four wind profilers of the LRSS. In Table 11.7 and in Figure 11.8a the values of, respectively, $\Lambda_{\text{day,FT}} \pm \epsilon_{\text{day,FT}}$ and k_{eff} show that the WindLidar1 is fit-for-purpose with respect to Θ_T and Θ_B but cannot be assessed with respect to Θ_G ($k_{\text{eff}} = -5.3$). Figure 11.8b, shows that the WindLidar2 is fit-for-purpose with respect to Θ_T , but cannot be assessed with respect to Θ_B (the error bars $\epsilon_{\text{day,FT}}$ overlap with Θ_B) no assessment is possible with respect to Θ_G either. Figure 11.8c and Figure 11.8d show slightly different performances of the high- and low-mode RWP for the wind vector: both RWP modes are fit-for purpose with respect to the Θ_T requirement (the low mode has larger k_{eff} value than the high mode). Neither the low-mode RWP ($k_{\text{eff}} = -0.1$) nor the high-mode RWP ($k_{\text{eff}} = -1.3$) can be assessed with respect to the Θ_B requirement. The same is true for the high-mode and the low-mode RWP with respect to the Θ_G requirement with $k_{\text{eff}} < -6$.

11.2.3 Added value of remote sensing measurements

For the RSI we do not discuss the OSCAR criteria related to the temporal and spatial sampling of the atmosphere. A radiosounding can be performed realistically with no better temporal frequency than 6 h for operational, long-term measurement programs. High costs of staff and material and need of authorisation to launch sondes limit the frequency to more realistic 12 h temporal resolution in most of the radiosounding stations across the world. In terms of the OSCAR “Observing Cycle” criterion, being fit-for-purpose appears to be very challenging for radiosounding technology in most application areas; much less so for remote sensing observations.

With raw-data temporal resolutions spanning 30 min for the RWP and up to 1 min of the MWR, the remote sensing meets the OSCAR requirements for the “Observing Cycle” criterion for almost all geophysical variables and application areas. Table 11.8 shows that the most stringent “Goal” requirement amongst the three geophysical variables and the five application areas corresponds to 5 min for the horizontal wind vector in the PBL, FT and UTLS for the application area “Aeronautical Meteorology” and to 5 min for the specific humidity and the horizontal wind vector for the “Nowcasting / Very Short-Range Forecasting” in the PBL. For the UAII, the remote sensing data have been processed and made available at 30 min temporal resolution (see Section 9.6.2). Two reasons determine the value $\delta_{\text{time}} = 30 \text{ minute}$:

- to cover the atmospheric region 0–9000 m at the sonde’s ascent speed $\nu_{\text{CWS}} = 5 \text{ m s}^{-1}$ (temperature and humidity by the MWR), and
- to match the temporal resolution of the RWP measurements (wind speed and direction by DWL and RWP).

But in principle, the instruments temporal sampling would allow the MWR and DWL to be fit-for-

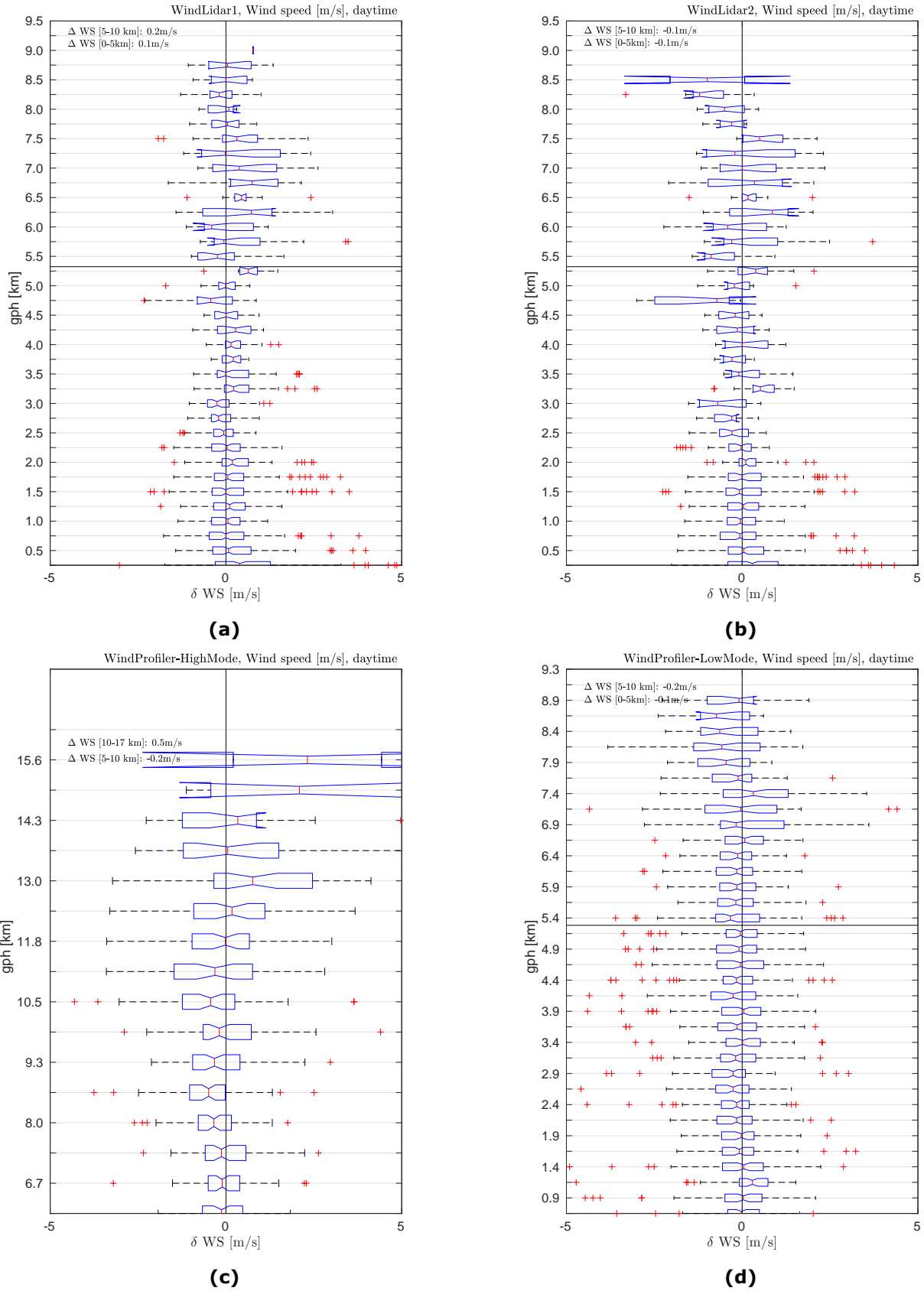


Figure 11.7: Box-plot of δ values for the variable “wind speed” in $m s^{-1}$ retrieved by the two DWL and the high- and low-mode RWP. Symbols, lines and colours as in Figure 11.4. (a): daytime δ wind speed by WindLidar1, (b): Nighttime δ wind speed by WindLidar2. (c): daytime δ wind speed by high-mode RWP (d): daytime δ wind speed by low-mode RWP.

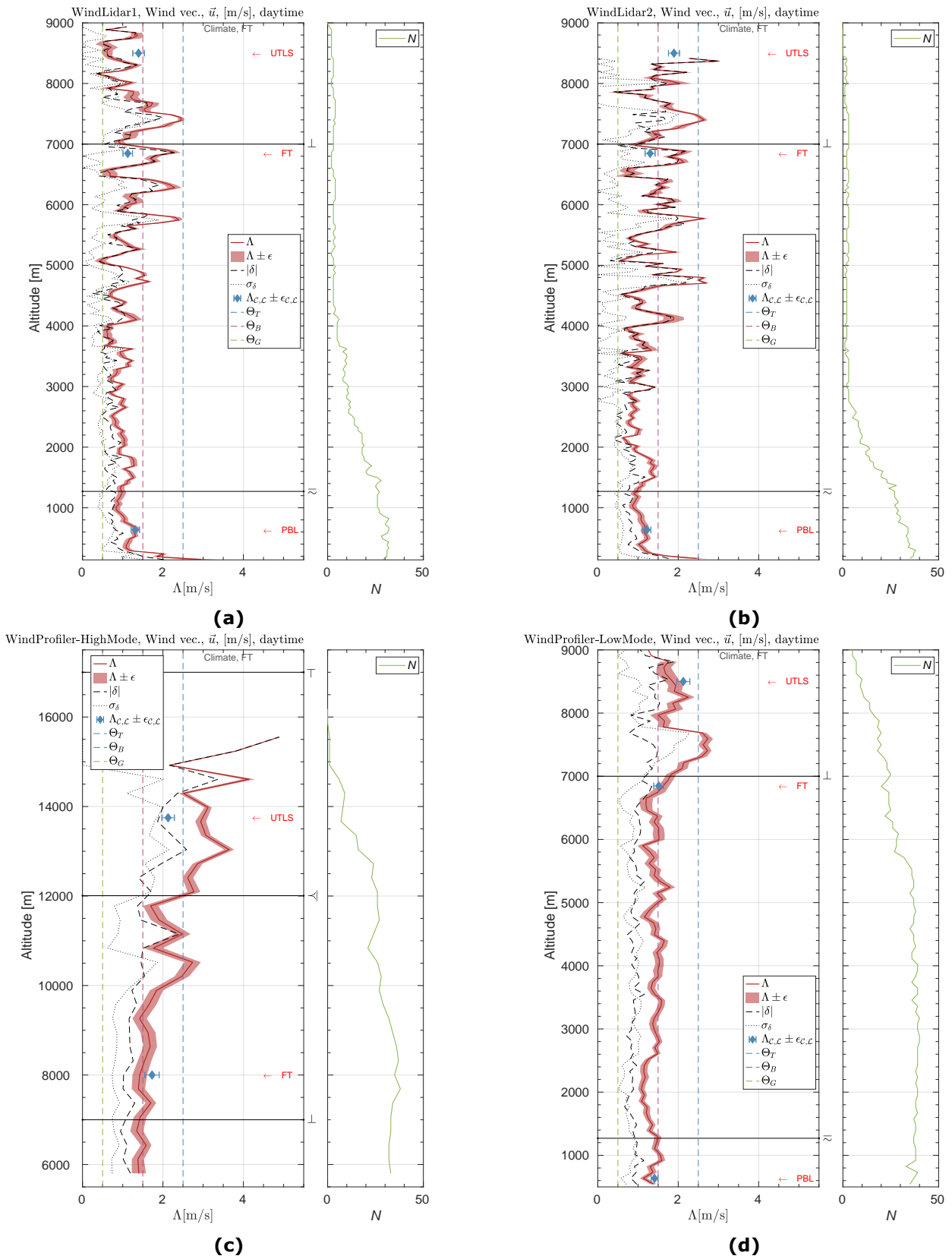


Figure 11.8: Profiles $\Lambda_{C,\mathcal{L}} \pm \epsilon_{C,\mathcal{L}}$, $\bar{\delta}_{C,\mathcal{L}}$ and $\sigma(\delta)_{C,\mathcal{L}}$ of the wind horiz. vector (in m s^{-1}) for the “Atmospheric Climate Forecasting and Monitoring” application area, and $\mathcal{L} = \text{FT}$, $\mathcal{C} = \text{day}$. All symbols and line styles as in Figure 10.27. (a) horizontal wind vector from the WindLidar1; (b) horizontal wind vector from the WindLidar2; (c) horizontal wind vector from the high-mode RWP; (d) horizontal wind vector from the low-mode RWP. The right panels of the four sub-figures show the data availability of the four wind profilers over all valid flights for each flight category during the UAII field campaign.

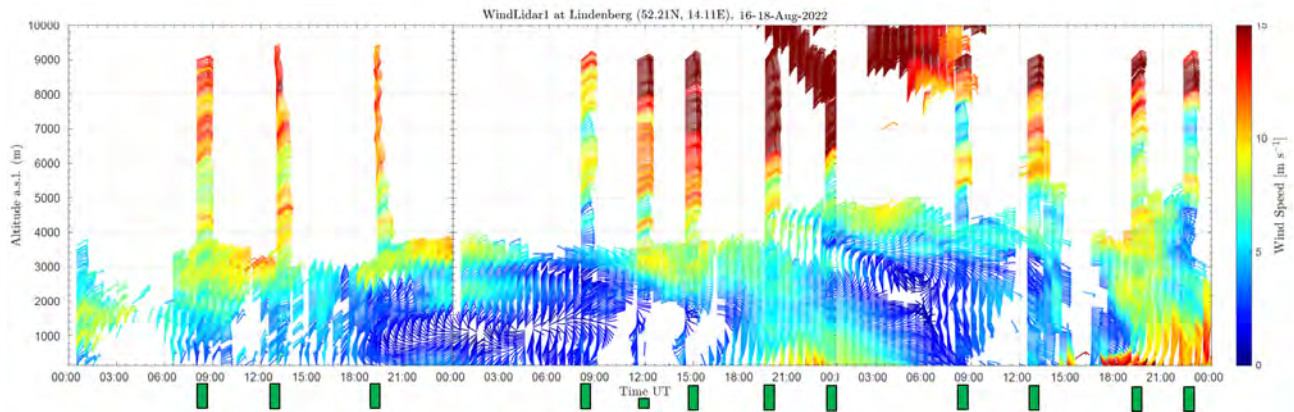


Figure 11.9: Timeseries of horizontal wind vector retrieved from the WindLidar1 during the period from 2022-08-16 to 2022-08-18. The green rectangles below the time axis show the timestamp of the CWS flights from F01 to F12. Superimposed to the CWS wind profiles are the 30-minute DWL profiles over the entire 72-hour series

purpose against all the requirements in Table 11.8

As a visual example of the performance with respect to the “Observing Cycle” criterion, Figure 11.9 shows the higher temporal sampling of a DWL with respect to radiosounding during the period 2022-08-16 to 2022-08-18. The example shows the time-series of the horizontal wind vector retrieved from the WindLidar1 at 30-minute temporal resolution and the superimposed CWS F01-F12 flights. The CWS are synchronised onto the WindLidar1 vertical grid (see Section 9.6.2) and cut at 9000 m. Beyond the added value of continuous measurements versus spot measurements, especially for data assimilation purposes or nowcasting, one can appreciate the dynamics of the retrieved wind field between flight F03 and F04 and between F08 and F09 that would be entirely lost if only the radiosounding were available.

Table 11.8: OSCAR requirement “Observing Cycle” criteria Threshold (T), Break-through (B) and Goal (G) values, grouped by application area, as a function of the associated geophysical variable x and atmospheric layer \mathcal{L} . Extracted from the WMO OSCAR webpages on 2023-11-24.

Geophysical variable x	Atmospheric layer \mathcal{L}	T	B	G	OSCAR Id
2.8 Aeronautical Meteorology					
Atmospheric temperature	FT PBL UTLS	3 h	90 min	60 min	15
Specific humidity	PBL	3 h	90 min	60 min	21
Wind (horizontal)	PBL UTLS	10 min	7 min	5 min	23
Wind (horizontal)	FT	10 min	6 min	5 min	22
2.3 Nowcasting / Very Short-Range Forecasting					
Atmospheric temperature	PBL	60 min	10 min	5 min	427
Atmospheric temperature	FT	60 min	30 min	15 min	428
Specific humidity	PBL	60 min	10 min	5 min	704
Specific humidity	FT	60 min	30 min	15 min	448
Wind (horizontal)	PBL	3 h	30 min	5 min	453
Wind (horizontal)	FT	3 h	60 min	15 min	451
Wind (horizontal)	UTLS	6 h	60 min	15 min	452
2.1 Global Numerical Weather Prediction and Real-time Monitoring					
Atmospheric temperature	PBL FT UTLS MUS	24 h	6 h	60 min	254, 255, 256, 257
Specific humidity	PBL FT	12 h	6 h	60 min	302, 303
Wind (horizontal) vector	PBL FT UTLS MUS	12 h	6 h	60 min	310, 311, 312, 313
2.2 High-Resolution Numerical Weather Prediction					
Atmospheric temperature	PBL	3 h	60 min	15 min	341
Atmospheric temperature	FT UTLS	6 h	60 min	15 min	339, 340
Specific humidity	PBL FT	6 h	60 min	15 min	378, 379
Wind (horizontal)	PBL FT	12 h	60 min	15 min	383, 385
Wind (horizontal)	UTLS	12 h	60 min	30 min	384
2.5 Atmospheric Climate Monitoring					
Atmospheric temperature	PBL	12 h	6 h	60 min	778
Atmospheric temperature	FT UTLS MUS	24 h	12 h	60 min	779, 780, 1016
Relative humidity	PBL FT	12 h	6 h	30 min	789, 997
Relative humidity	UTLS	24 h	6 h	3 h	790
Wind (horizontal) vector	PBL	12 h	60 min	30 min	781
Wind (horizontal) vector	FT UTLS	12 h	6 h	60 min	988, 989
Wind (horizontal) vector	MUS	24 h	6 h	60 min	1017

12 CONCLUSIONS

12.1 SUMMARY OF THE RESULTS AND RECOMMENDATIONS

12.1.1 Radiosondes

- Precise measurement times can be important to unambiguously synchronise radiosonde observations against references and/or other remote-sensing systems. Yet, half of the participating radiosonde systems failed to deliver the absolute time of their individual measurements with an uncertainty below 1 s, even though they were all equipped with a GNSS receiver.

Recommendation: *Manufacturers should strive to provide (UTC) measurement times with an error of 1 s or less, to allow for the unambiguous synchronisation of their profile with other datasets.*

- Under laboratory conditions, raw humidity measurements at room temperature are within 5 %RH from the reference for all but three radiosonde models, for which we found differences between 5 %RH and 10 %RH. This is mostly within the uncertainty specified by the manufacturer and consistent with the humidity statistics in the Planetary Boundary Layer (PBL) from the field campaign.

Recommendation: *Given the stringent relative humidity requirements for various application areas, the laboratory tests show that the calibration of the humidity sensors should be improved. Users of radiosondes should check with the vendors whether the humidity calibration covers the operational range of the intended application.*

- The performances of the humidity sensors vary strongly both with temperature for a specific sensor and among the different sensor types. Response times under the specific conditions of the laboratory tests range from 4 s to 450 s at $-40\text{ }^{\circ}\text{C}$.

Recommendation: *These results highlight the importance of both minimising sensor time lag and implementing accurate time-lag corrections, as demonstrated already at moderately cold temperatures. There is a lot of room for improvement in terms of response time, which would be particularly beneficial for measurements in the troposphere where temperature can get as low as $-85\text{ }^{\circ}\text{C}$.*

- Under laboratory conditions at room temperature, half of the radiosondes show mean deviations from the reference of less than $\pm 0.1\text{ K}$ at room temperature, which is a good result. The others are on average mostly within less than $\pm 0.2\text{ K}$, however with larger individual deviations reaching almost 1.0 K. At lower temperatures (climate chamber tests, Chapter 6), measurements lie mostly within the uncertainty of the reference of $\pm 0.2\text{ K}$. We identify potential for improvement for some sondes at low temperatures, particularly below $-60\text{ }^{\circ}\text{C}$.

Recommendation: *Radiosonde manufacturers should make sure that the temperature sensors are calibrated for the full operational measurement range.*

- Solar radiation is the most important error source for daytime temperature measurements using radiosondes. The sensitivity of the temperature measurements to solar radiation under laboratory conditions varies strongly among the investigated models. At a representative flux of 1000 W m^{-2} the uncorrected radiation errors range from 0.2 K to 1.4 K at 100 hPa and 5 m s^{-1} ventilation speed, and from 0.5 K to 3.8 K at 10 hPa and 4 m s^{-1} .

Recommendation: *Manufacturers should strive to provide good solar radiation corrections, but also to reduce the intrinsic sensitivity of their system to solar radiation in the first place. Furthermore, the radiosonde manufacturers should provide the contribution of the radiation correction to the estimated uncertainty of the temperature measurement in their documentation. Additional information on the derivation and implementation of the radiation correction (including related to nighttime infrared cooling) would be very useful to the users.*

- We found that half of the radiosondes that participated in the UAI 2022 display an increasingly-colder-than-ambient-air-temperature measurement bias above 25 km to 27 km during nighttime. This suggests an imperfect correction for infrared radiative cooling.

Recommendation: *Manufacturers should carefully evaluate the need and importance of accurate infrared radiative cooling corrections for temperature measurements in the stratosphere for their system.*

- Liquid clouds are still a challenge for many radiosondes. Our analysis reveals that all radiosondes can suffer from the wet-bulb effect after exiting a liquid cloud, although the magnitude varies from a few tenths of a kelvin up to 4 K. The effect can last up to 600 s or longer. Saturation within clouds is mostly properly detected, however three radiosonde models exhibit a significant dry bias. These results are consistent with the independent pre-flight ground checks in the SHC.

Recommendation: *Manufacturers should continue their efforts in improving the hydrophobic coating of the temperature sensor(s).*

- For pressure observations, we see good agreement with the CWS for the nine radiosonde systems that derive pressure from GNSS altitude and temperature, with only one of these systems showing deviations of more than 2 hPa from the reference.
- Radiosonde performances are assessed against OSCAR requirements. This provides a differentiated and objective picture of the fitness-for-purpose of each system for different application areas. For temperature, we found that all but one radiosonde model meet the breakthrough requirements of Aeronautical Meteorology, Nowcasting / Very Short-Range Forecasting and Global Numerical Weather Prediction (NWP) and Real-time Monitoring in all atmospheric layers. This good performance is also reflected in the laboratory results.
- While most radiosondes also meet the threshold requirements for the Atmospheric Climate Forecasting and Monitoring application area for temperature, there is a clear gap between the goal requirements and the current capabilities. We consider radiosonde design and solar radiation correction to be important areas for improvement. To a lesser extent, infrared cooling affects temperature measurements during nighttime and also needs to be addressed.
- All but two radiosonde models meet the threshold requirements for relative humidity for the Nowcasting / Very Short-Range Forecasting and Global NWP and Real-time Monitoring application areas.
- We note that the requirements for relative humidity for the Atmospheric Climate Forecasting and Monitoring application area are very stringent and reveal a significant gap between the capabilities of radiosondes and the threshold requirement in all atmospheric layers, as none of the radiosondes meets the threshold requirement.
- In general, we found good performances for wind. All radiosondes meet the breakthrough requirements for wind for the Aeronautical Meteorology, Nowcasting / Very Short-Range Forecasting and Global NWP and Real-time Monitoring application areas, in all atmospheric layers except for the PBL during nighttime. There, only three radiosondes meet the threshold requirement.
- Seven out of ten radiosonde systems produce a useful BUFR file, fit for data dissemination on the GTS. However, improvements should be made for most systems. Most importantly, we found issues with the reporting of dew point in the BUFR files resulting most likely from the conversion of relative humidity to dew point.

Recommendation: *Users and manufacturers alike should verify the correctness of the BUFR data generated by their radiosonde system, including the consistency between humidity and dew point. Crucially, manufacturers should ensure that they are using the correct sonde model identification code in their BUFR.*

- Most of the radiosonde systems that participated in the UAI 2022 are fit for routine operation. Two days of training are generally sufficient to enable an experienced radiosonde operator to carry out operational soundings and basic troubleshooting on any of the radiosonde systems participating in the UAI 2022, without having prior knowledge or experience on that particular system.
- In terms of user friendliness and based on the experience of the independent operators of

the UAII 2022 field campaign, we consider six out of the ten radiosonde systems to be very user friendly, while the remaining four systems show inefficiencies that could affect data quality and/or data availability.

12.1.2 Remote sensing

- The spatial and temporal averaging of remote sensing measurements is significantly different from that of the CWS. In the scope of this campaign, it was only possible to account for the differences in vertical resolutions and the resulting statistics are still affected by the differences in temporal sampling and horizontal displacement. Therefore, our results give only a lower bound of the expected performance.
- We found good performance for microwave radiometer temperature retrievals, that meet at least threshold requirements for the Aeronautical Meteorology, Nowcasting and Very Short-Range Forecasting and Global NWP and Real-time Monitoring application areas, for all atmospheric layers except the MUS.
- Humidity retrievals from microwave radiometers meet only a few requirements, and only in the nighttime planetary boundary layer. This result is not surprising, and driven by the low information content of such humidity retrievals. The retrieved water vapour column, for which significantly better performance can be expected based on the scientific literature, has not been evaluated as part of the UAII 2022.

Recommendation: *The users should make themselves familiar with the particularities of humidity profile retrievals from microwave radiometers before integrating such data into their applications. Users should also consider using retrieved integrated water vapour or brightness temperatures instead.*

- For wind, we found very good performance for Doppler Lidars and radar wind profilers with wind profile retrievals meeting at least breakthrough requirements for the Aeronautical Meteorology, Nowcasting and Very Short-Range Forecasting and Global NWP and Real-time Monitoring application areas. For the Atmospheric Climate Forecasting and Monitoring application area, wind profile retrievals meet at least threshold requirements in all atmospheric layers except for the MUS.
- In terms of the OSCAR Observation Cycle criterion, remote sensing technology as a whole is able to meet goal requirements of all applications areas, which is an important added value.

12.1.3 Other results

- As of 2022, the GTS could not be used to build reliable statistics on the use of specific radiosondes worldwide, because the sonde codes were not used correctly or clearly documented.

Recommendation: *The WMO should ensure that all current and expired radiosonde codes are clearly documented and easily accessible. Furthermore, the WMO should periodically confirm the validity of data submitted to the GTS and facilitate the means by which radiosonde manufacturers can request new identification codes for newly-developed systems.*

- The use of GRUAN Data Products (GDPs) worked well and enabled the assembly of combined working measurement standards with a high statistical success rate. Nonetheless, there is still room for improvement with respect to the issues listed in Section 9.5.1 and, more generally, in terms of sharing common syntax and terminology, error budgets, and attributes. Having 3 GDPs from distinct manufacturers would also be very useful for the next campaign.

Recommendation: *GRUAN and GDP creators should strive to maximise the statistical and syntactic compatibility of existing and future GDPs.*

- Understanding the exact origin of the OSCAR requirements uncertainty values is not always possible with the information currently provided by the WMO. Being able to trace how the different criteria are defined would be of great interest to put the outcome of this report in perspective.

Recommendation: *In addition to the periodic review of the OSCAR requirement values, the WMO should strive to provide full, exhaustive and explicit traceability of their derivation.*

- At the time of writing, OSCAR requirements for relative humidity exist only for the Atmospheric Climate Forecasting and Monitoring application area. This is a clear limitation of OSCAR, given the fact that commercial radiosondes measure relative humidity directly. In this report, we have converted the specific humidity requirements for the other application areas to relative humidity.

Recommendation: *The WMO should consider extending OSCAR to include uncertainty requirements for relative humidity for a wider range of application areas.*

- Results from the UAI 2022 laboratory campaign highlight the importance of assessing the performances of upper-air instruments over the full range of conditions that can be experienced in regular operation.

Recommendation: *When planning the next UAI, the WMO should take into account the limitations of the UAI 2022 field campaign in terms of the sampled atmospheric conditions.*

- The focus of UAI 2022 was set on mature radiosonde systems, ideally already in operational use. This choice may have excluded new and innovative radiosondes with potentially good performance.

Recommendation: *The WMO should review the scope of future UAIs, to consider how new systems from new manufacturers could be assessed.*

- Having UAIs organised at regular intervals is key to encourage upper-air system manufacturers to continually improve their systems, and support a diversity of products and techniques. A total of 12 years separate the UAI 2022 from the previous WMO's UAI. This gap was increased somewhat by an extraordinary event (see Section 1.4) beyond the control of the WMO and UAI 2022's Project Team. Nonetheless, it remains too long in comparison to the timescale of radiosonde evolution (be it in the form of improvement of existing systems, or emergence of new models and/or manufacturers).

Recommendation: *The WMO should strive at having UAIs organised at (more) regular intervals, possibly with different scales (e.g. field or laboratory campaign only) to facilitate their implementation.*

12.2 LESSONS LEARNED FOR FUTURE UAIs

From an organisers' perspective we can phrase the following conclusions and recommendations for improvements concerning the organisation, implementation and logistical aspects of the campaign:

- The availability of two ground systems per manufacturer is useful not only for performing twin soundings, but also for resilience, i.e. the ability to continue the campaign in case of malfunction or mishap. Hence, we strongly recommend to use two ground systems in future campaigns, even if twin soundings are not planned.
- For the UAI 2022, a special ASCII file format was introduced for data collection. This required the radiosonde manufacturers to modify their software. This choice by the project team was inconsistent with the idea to mimic an operational environment during the field campaign. It resulted in last-minute changes to the operational software and additional processing steps for the operators, which are specific to the UAI 2022. We suggest that future UAIs consider using high-resolution BUFR messages for the field campaign instead, and sample BUFR data files (from each manufacturer) should be pre-screened to ensure correct encoding before participation. However, for a laboratory campaign a well-defined ASCII file with unprocessed calibrated sensor data should be used.
- GNSS signal interference can lead to faulty measurements for geopotential height, and (by chain reaction) pressure and wind. The use of a GNSS repeater should be carefully considered in the next UAIs, and if it is employed, it is recommended to look for telltale signs of GNSS interference during radiosonde preparation, and steps should be taken to reduce the potential for it to act as a contamination source. Careful consideration should also be

given to the location where the ground systems are being setup, with the aim to ease direct GNSS signal reception from the sky. One should be aware that metallic structures such as hangars have the potential to act as Faraday cages or to reflect GNSS signals.

- Rainy conditions can prove challenging for radiosondes, and thus interesting from an inter-comparison perspective. To avoid the rejection of flights as a result of low ascent speeds, care should be taken to account for the additional weight of water accumulating on the balloon, and increase the amount of balloon gas accordingly. As a rule of thumb a wet TX1500 balloon is approximately 500 g heavier than a dry one.
- The concept of independent operators was implemented successfully in the UAI 2022 field campaign. It was possible to train an experienced radiosonde operator within two days to perform operational soundings and basic trouble shooting on a radiosonde system with which he or she had no prior knowledge or experience. This concept ensured the independent and transparent acquisition of data during the campaign, and it proved very helpful in assessing the actual usability and reliability of the systems.
- The laboratory campaign was highly appreciated by both the manufacturers and the campaign organisers. For a future campaign with a laboratory and field campaign hosted at the same site, it is recommended to plan the laboratory phase after the field campaign. This guarantees that all systems arrive at the field campaign site at roughly the same time, and thus significantly reduces the risk of unfair advantage due to different shipping times. Furthermore, the laboratory activities would conclude a manufacturer's campaign involvement, so that they can take care of packing and shipping before leaving the campaign site.
- We believe that putting the results in the context of OSCAR is of added value for the user, and in particular because it allows to assess the systems' fitness-for-purposes for different application areas in a transparent manner, using criteria defined by a well-recognised authority.
- Twin soundings were very useful to investigate repeatability and to unveil particular issues not seen otherwise in regular intercomparisons configurations. We recommend to implement twin flights in upcoming UAIs.
- It was the project's ambition to evaluate also environmental aspects. However, formally assessing the sustainability of radiosondes is difficult, and could not be made during the UAI 2022. It requires dedicated, concerted efforts that include experts in sustainability, materials, production chains - together with clear willingness from manufacturers to produce and share this information.
- Descent data was not analysed during the UAI 2022, but given the increasing use of descent data in operational meteorology, it should be included in the next UAI.
- In addition to the manufacturer-prescribed ground check, we performed an additional manufacturer independent ground check at 100%RH using an SHC for each radiosonde and before each launch. These data were useful to complement the assessment from both the laboratory and the field campaign. We therefore recommend to use a similar procedure for the next UAI.
- In the framework of the field campaign, we performed a relatively simple and straightforward analysis which make our results robust and transparent. The NetCDF data files with synchronised and cleaned radiosonde data, provided as Supplementary Material to this report, are a valuable output that should facilitate further studies.
- Overall, the novelties of the UAI 2022 (CWS, independent operators, performance assessment against OSCAR, open-source analysis, laboratory campaign) worked out well and yielded useful results for WMO Members. This principle can be adopted for future inter-comparison campaigns. It can also allow to perform small-scale UAIs-like campaigns at any desired location and link their results to the UAI 2022, provided there is the possibility to perform atmospheric soundings following the GRUAN principles using at least two distinct GRUAN-certified reference systems.
- The integration of surface based remote sensing in the UAI 2022 was successful and the obtained results are of added value for the WMO Members. We recommend to consider including surface based remote sensing in the next UAI. Doing so, the scope of the remote sensing part has to be defined carefully in advance and the implications in terms of logistics

and work load have to be considered.

Appendix

A SELECTION RULES FOR PARTICIPANTS

This document describes the selection criteria that are applied when the number of registered radiosonde models exceeds the capacity of the test site and selection of participants is necessary.

General rules for participation in the campaign are

- The campaign will not be used to test prototypes.
- The radiosounding system must be compatible with the infrastructural limitations of the Lindenberg site.

Prototype in this respect means a radiosonde type that is not commercially available.

In case the number of registered radiosonde models exceeds the capacity of Lindenberg observatory, an assessment will be made to select the participants. The selection is based on a scoring table, taking into account the following factors:

1. The radiosounding system is ready to be employed in an operational network.
2. The system is able to submit data to the GTS (BUFR).
3. Is the system currently used to provide data to a national data centre/GTS?
4. The world-wide market share of the model.
5. The number of years the model has been in operation.

The selection does not apply to radiosonde models that are used as working reference.

We intend to give radiosondes from emerging markets the opportunity to participate in the campaign.

A.1 QUESTIONNAIRE FOR MANUFACTURERS

Table A.1: Questionnaire for manufacturers

S. No.	Question
<i>Section 0</i>	
0-1	Name of Radiosonde Model
0-2	Name of Upper air sounding system
<i>Section 1</i>	
1-1	Can your system be operated by 1 person?
1-2	Does your system comply with the local frequency requirements at Lindenberg Observatory (402 MHz to 406 MHz and maximum bandwidth of 100 kHz)?
1-3	Does your radiosonde have a radio signal output power of less than 200 mW?
1-4	Does your radiosonde weigh less than 400 g?
1-5	Does your system use a radar system?
1-6	Do you have certified evidence of electrical safety testing?
1-7	Can you provide software, documentation and output files in English?

This table is continued on the next page.

Table A.1 – Continued from previous page

S. No.	Question
1-8	Does your System has ground Check Device?
1-9	Can your system generate high resolution BUFR?
<i>Section 2</i>	
2-1	Please provide documentation detailing the system operation, setup and specifications, and photographs of the radiosonde and system.
2-2	Please provide sample dataset of 5 high resolution BUFR files for analysis from within the last 12 months.
2-3	Please provide any customer references and links to relevant academic publications.
2-4	Please provide evidence of ISO certification, or equivalent.
2-5	Please provide evidence of product CE marking, or equivalent.
2-6	Please provide an assessment of product environmental impact.
<i>Section 3</i>	
3-1	Weight of the radiosonde?
3-2	Material of the radiosonde's housing.
3-3	Frequency range (discrete or continuous).
3-4	How is the transmission frequency set?
3-5	What is the transmission bandwidth?
3-6	What are the characteristics of the transmission side bands (power spectrum)?
3-7	What is the transmission power?
3-8	What is the data downlink rate?
3-9	What is the battery life (how long can the sonde be operated on battery power)?
3-10	List the radiosonde's sensors providing the Measured parameter the sensor type (e.g. thermistor, polymer sensor etc.) the sensor's operating range.
3-11	Describe the receiving equipment (e.g. antenna, receiver etc).
3-12	Operational requirements for the antenna (e.g. mounting location, separation from other equipment)?
3-13	Procedure for pre-flight preparation of the radiosonde?
3-14	Describe the properties of the ground check unit.
3-15	Can the sonde be switched off after ground check and be turned on again prior to the launch?
3-16	Annual capacity of manufacturing for the model listed above?
3-17	Indicate the market share of your radiosondes on GTS.

B UAI 2022 CONFIDENTIALITY AND CODE OF CONDUCT

All participants to the UAI 2022 were asked to sign and certify that they would abide by the following rules.

B.1 CONFIDENTIALITY AGREEMENT

This campaign is conducted blind for manufacturers. All manufacturers will have access only to data from their own systems during the campaign and until the final report has been published. No other data will be shared with the manufacturers. After the training period at the beginning of the campaign, each manufacturer will receive the data for their own system from the data manager of the campaign following each sounding, or once a day. No data (plots, graphs, pictures, or photographs, etc. of data) produced in the context of the WMO 2022 Upper-Air Instrument Intercomparison shall be shared outside of the campaign team¹ prior to the publication of the final report.

No data, images, pictures, graphs, or documents generated during the campaign, during the preparation of the final report, or after publication of the final report may be used as marketing material, for commercial advertising, or for gaining an advantage over any of the other participating manufacturers. Manufacturers shall not use any statement, figure, data, graph, or image published in the final report in promoting their products.

The project team maintains an official website² and the members of the campaign team and the manufacturers shall refer to the official website on their public websites and social channels and not publish material themselves.

The project team will promote the UAI 2022 at conferences and show selected contents illustrating the activity.

Manufacturers may contact the campaign lead via a hotline (hotline@uai2022.info or by phone) if they notice a malfunction or previously unidentified misconfiguration of their system or if they recognize an operator error. In these cases, the campaign lead will establish a direct communication with the operators. Manufacturers shall not contact operators directly.

Operators may contact the manufacturers directly in case of a problem with the system. The operators shall document any exchange with the manufacturers and inform the project lead.

Operators will transfer the data of the systems, for which they are responsible, only to the campaign Data Manager. Data for each sounding system will be sent to the respective manufacturer by the Data Manager. Operators shall not share data outside the campaign team; in particular, operators shall not share data with the manufacturer directly.

Training material received from one manufacturer shall not be shared with another manufacturer, nor outside of the project team.

The data policy of the campaign, provided in a separate document, is an inherent part of this agreement and must be signed separately by each participant.

¹The campaign team consists of the TT-UAI members, the operators, WMO Secretariat staff supporting the UAI-2022, and other support staff members designated by Lindenberg Observatory to support the campaign. All campaign team members will have to sign the code of conduct and data policy.

²<https://www.gruan.org/community/campaigns/uai2022>

B.2 CODE OF CONDUCT

The Project Team is committed to providing a safe, productive, and welcoming environment for all participants of the Upper Air Instrument Intercomparison, no matter what role they play or their background. This includes respectful treatment of everyone regardless of gender, sexual orientation, disability, physical appearance, age, body size, race, religion, national origin, ethnicity, or level of experience. All participants (Project Team, Operators, Manufacturers, and WMO Secretariat and staff at Lindenberg) involved in the Upper Air Instrument Intercomparison are required to abide by this Code of Conduct.

Expected Behavior:

- All participants agree to professional and respectful behavior during the campaign.
- All participants are treated with respect and consideration, valuing a diversity of views and opinions.
- Be considerate, respectful, and collaborative.
- Communicate openly with respect for others, critiquing ideas rather than individuals.
- Avoid personal attacks directed toward other participants.
- Be mindful of your surroundings and of your fellow participants.
- Alert the Project Team if you notice a dangerous situation or someone in distress.
- Respect the rules and policies of the Upper Air Instrument Intercomparison.
- To comply with the house rules of the Lindenberg observatory.

Unacceptable Behavior includes, but is not limited to:

- Harassment, intimidation, or discrimination in any form.
- Physical or verbal abuse by anyone to anyone, including but not limited to a participant, member of the public, guest, member of any institution or sponsor.
- Unwelcome sexual attention or advances.
- Personal attacks directed at other participants, staff, etc.
- Alarming, intimidating, threatening, or hostile comments or conduct.
- Inappropriate use of nudity and/or sexual images in public spaces or in presentations.
- Threatening or stalking anyone.
- Other conduct which could reasonably be considered inappropriate in a professional setting.

Anyone requested to stop unacceptable behavior is expected to comply immediately. Project Co-Leads or their designee may take any action deemed appropriate, including immediate removal from the campaign without warning. The home institution may be notified of an infraction, if there has been a potentially serious confidentiality or code of conduct violation.

C UAI 2022 DATA POLICY

C.1 DEFINITIONS

Laboratory data	Calibrated radiosonde data (p , T , RH) at a native resolution of the sounding system where no corrections (time lag, radiation, etc.) have been applied.
Raw sounding data	Same as laboratory data (including but not limited to time, lat, long, p , T , RH, u , v) from atmospheric soundings.
Processed sounding data	Manufacturer's processed data including corrections, aggregations, and QC ¹ (final product) from the atmospheric soundings.
Standard dataset	Includes the processed sounding data from all participating radiosonde systems (including the GRUAN data products) and BUFR messages.
Complete dataset	Includes the Standard dataset, the raw sounding data, and laboratory data from all participating sounding systems.
Data provider	Manufacturer of radiosounding systems that participate in the campaign.

C.2 PRINCIPLES

The following are the principles for data policy of the intercomparison agreed by the UAI-2022 Project Team:

- The intercomparison standard dataset is kept by the WMO Secretariat, and the project co-leads (DWD and MCH). WMO may, if requested, export whole or part of the standard dataset on the WMO website, or another website, as soon as the Final Report is published.
- The standard dataset will be assigned a DOI² after the publication of the Final Report.
- The WMO authorizes the Project Co-Leads (following Project Team members' consensus), with the agreement of the relevant INFCOM³ supervisory body, to publish full results in a Final Report of the intercomparison on behalf of the Project Team.
- The results of the laboratory tests will be published anonymously.
- The Project Team members may use preliminary results, and material (photos, etc.) of the intercomparison for communication matters, and may publish their partial scientific results before the end of the intercomparison, provided the material/publication was authorized by the Project Co-Leads and that the participating instruments remain anonymous in that material/publication.
- Prior to the publication of the Final Report, the standard dataset may be provided to other parties for scientific studies on the subject. This requires the approval of the Project Co-Leads. Third parties may publish their studies after the publication of the Final Report with the agreement of the data providers (if the studies are published within 5 years of the publication of the Final Report).
- Publications on the intercomparison dataset and/or results, that include the names of other manufacturers, shall not be used for commercial or promotional purposes in any way. Manufacturers shall avoid qualitative assessment of their instrument in comparison with any other participant's instrument(s).

¹Quality Control (QC)

²Digital Object Identifier (DOI)

³Commission for Observation, Infrastructure and Information Systems (INFCOM)

- Any publication based on the intercomparison data and/or results must acknowledge the source of the information and comply with the WMO copyright provisions.
- Raw data of the radiosounding systems obtained during the field campaign may be made available after the publication of the report, only upon expressed consent of the manufacturer.

D UAI 2022 DATA FORMATS

D.1 OVERVIEW

This appendix describes the formats of the data files created from the radiosonde measurements during the UAI 2022 campaign. Different formats are required for the laboratory and sounding parts of the campaign. Result files from the laboratory tests should be ASCII single text files for each of the test measurements, including columns with timestamps and data columns containing the raw measurements of the relevant variables. The output files of the soundings should be single ASCII text files as well for each sounding, including the profile data table and a header section containing meta-data. In addition, the BUFR message is mandatory. Original sounding archive files are mandatory if such files are available.

Table D.1: Requirement of generated data file

Data format	Requirement	Purpose
WMO HR BUFR	mandatory	GTS, archiving, further analyses
ASCII Text Sounding	mandatory	Input to dvas (Data Visualization and Analysis Software)
ASCII Text Laboratory	mandatory	Input to laboratory data analysis software
Original Sounding Archive Files (often proprietary)	mandatory (if available)	Archiving of complete set of sounding-related data (raw data, data product, meta data, configuration, ...) used by sounding software of participant; often a proprietary format

D.2 SPECIAL UAI 2022 ASCII TEXT FILE FORMATS

D.2.1 Base format of UAI 2022 ASCII text files

The UAI 2022 ASCII Text file consists of a header section and a data section (measured profile). A regular grid with integer time steps in seconds (ideally 1 s is mandatory).

- Meta-data can be stored as header lines using the following syntax:
 - # <key> = <value>
 - key ... unique without any whitespace or "special characters"
 - * keys can be defined as a "tree", separated with dots, e.g. <key-p1>.<key-p2> or <key-p1>.<key-p2>.<key-p3>
 - * the full key must be unique (and well defined)
 - value ... formatting depends on data type, e.g.
 - * <number> (point as decimal separator, e.g. "1234.5678901")
 - * <number> <unit> (e.g. "182.943 K", with a single space " " separating number and unit)
 - * <string> (e.g. "a comment of arbitrary length")
 - * <dateTime> (ISO timestamp (UTC), e.g. "2019-12-13T12:22:05.571Z")

- The profile section consists of a CSV table using the following rules:
 - Semicolon “;” as separator between columns
 - (optional) additional white space is allowed, e.g. to format the table for better manual reading
 - Single-line table header:
 - * <name> [<unit>]
 - * Unique column name (e.g. “temp”)
 - * (optional) a unit can be added, enclosed in brackets, separated by a single space “ ” (e.g. “temp [°C]”)
- Missing Value:
 - Missing value must be marked as “NaN”

D.2.2 Data variables and meta data of UAII 2022 ASCII text files

Table D.2 lists the potential parameters for which data can be included in the ASCII Text Sounding and Laboratory files. Table D.3 shows a list of meta-data that can be added to the header section. Beyond what is listed in tables it is allowed to add further information in the metadata section or data columns of measured parameters to the files. A definition (parameter, description, unit, uncertainties) of additional parameters should be provided to the UAII 2022 team.

Table D.2: List and details of allowed parameters

Parameter	Description	Unit	Precision
<i>Time variables</i>			
time	Passed time relative to timestamp of launch detected by sounding system (sounding campaign); or passed time relative to a documented timestamp (laboratory campaign)	s – second [0...n]	1 digit
time_stamp	Time (UTC) derived by synchronised computer time or GNSS Time, e.g. “2019-12-13T08:43:15.349Z”	UTC timestamp (full with date & time)	3 digits
<i>Data product variables</i>			
gph_gnss	Geopotential height derived from GNSS	gpm – geopotential meters	1 digit
gph_press	Geopotential height derived from pressure sensor	gpm – geopotential meters	1 digit
press_gnss	Atmospheric pressure derived from the GNSS	hPa – hectopascal	3 digits
press_sens	Atmospheric pressure measured by pressure sensor (if a pressure sensor is available)	hPa – hectopascal	3 digits
temp	Air temperature	°C – degC – degree Celsius	2 digits

This table is continued on the next page.

Table D.2 – Continued from previous page

Parameter	Description	Unit	Precision
dew_point	Dew point	°C – degC – degree Celsius	2 digits
rh	Relative humidity	%RH – percent relative humidity	2 digits
wind_speed	GNSS-derived wind speed	m/s – meters per second	2 digits
wind_dir	GNSS-derived wind direction	° – deg – degree	1 digit
lat	Latitude from GNSS	°N – degN – degree North	6 digits
lon	Longitude from GNSS	°E – degE – degree East	6 digits
alt	Altitude from GNSS (WGS84 ^a geodetic datum)	m – meters	1 digit
height_amsl	Geometric height above mean sea level	m – meters	1 digits
ascent_speed	Ascent speed of radiosonde derived from GNSS	m/s – meters per second	2 digits
<i>Raw data variables</i>			
temp_air_raw	Air temperature without corrections, e.g. radiation, time-lag, smoothing.	°C – degC – degree Celsius	3 digits
rh_air_raw	Air humidity with respect to the water without corrections, e.g. radiation, time-lag, smoothing.	%RH – percent relative humidity	3 digits
rh_heat_raw	Original measurement of heated humidity sensor	%RH – percent relative humidity	3 digits
temp_rh_heat_raw	Temperature of heated humidity sensor	°C – degC – degree Celsius	3 digits
press_sens_raw	Atmospheric pressure measured by pressure sensor (if available)	hPa – hectopascal	4 digits

^a World Geodetic System 1984 (WGS84)

Table D.3: List of possible metadata

Parameter	Description	Unit
File.CreatedAt	Timestamp of file creation, e.g. "2021-10-01T07:13:31.742Z"	UTC timestamp
File.CreatedBy	Name and version of used software to create the file	string
File.Format	Name of specific file format: "UAI2022 ASCII Text Sounding" or "UAI2022 ASCII Text Laboratory"	string

This table is continued on the next page.

Table D.3 – Continued from previous page

Parameter	Description	Unit
General.WVFormula	Water vapour formula which is related to the measurements of the RH sensor	string
Launch.TimeStamp	Detected launch time (UTC) of sounding derived by synchronized computer time or GNSS Time, e.g. "2019-12-13T09:18:45.023Z"	UTC timestamp
Burst.TimeStamp	Detected Burst time (UTC) of sounding derived by synchronized computer time or GNSS Time, e.g. "2019-12-13T09:18:45.023Z"	UTC timestamp
Sonde.Manufacturer	Name of manufacturer	string
Sonde.Model	Key of the radiosonde model	string
Sonde.SerialNumber	Unique serial number of radiosonde	string/number
Initial.TimeStamp	Detected start time (UTC) of measurement or data recording (incl. pre-flight period) derived by synchronized computer time or GNSS Time, e.g. "2019-12-13TZ08:43:15.349Z"	UTC timestamp
Station.Latitude	Station Latitude	°N – degN – degree North
Station.Longitude	Station Longitude	°E – degE – degree East
Station.Altitude	Station Altitude	m – meters
SurfaceData.Pressure	Surface Pressure (from surface station)	hPa – hectopascal
SurfaceData.RH	Surface Relative Humidity (from surface station)	%RH – percent relative humidity
SurfaceData.Temperature	Surface Temperature (from surface station)	°C – degC – degree Celsius
SurfaceData.WindDir	Wind Direction (from surface station)	° – deg – degree
SurfaceData.WindSpeed	Wind Speed (from surface station)	m/s – meters per second
Station.LaunchAltitude	Altitude of launch site (or sonde at launch?)	m – meters
Station.PressureAltitude	Altitude of the surface pressure sensor; should be related to the value of "SurfaceData.Pressure"	m – meters
Station.GnssAntennaAltitude	Altitude of GNSS antenna (if such an antenna is used)	m – meters
Station.TypeOfAltitude	Altitude reference e.g. AMSL, WGS84, ...	key/string

D.2.3 UAII 2022 ASCII Text Sounding file

Tables D.4 and D.5 list the parameters that can or must be added into the ASCII Text Sounding file.

Table D.4: List of metadata parameters (header section) of a ASCII Text Sounding file

Parameter	Level of requirement
File.CreatedAt	mandatory
File.CreatedBy	mandatory (constant value)
File.Format	mandatory (constant value)
General.WVFormula	mandatory (constant value)
Launch.TimeStamp	mandatory
Burst.TimeStamp	recommended
Sonde.Manufacturer	recommended (constant value)
Sonde.Model	mandatory (constant value)
Sonde.SerialNumber	mandatory
Initial.TimeStamp	recommended
Station.Latitude	mandatory
Station.Longitude	mandatory
Station.Altitude	mandatory
SurfaceData.Pressure	mandatory
SurfaceData.Temperature	mandatory
SurfaceData.RH	mandatory
SurfaceData.WindSpeed	mandatory
SurfaceData.WindDir	mandatory

It is allowed to add further metadata parameters to the file. A definition (parameter, description, unit) of these additional parameters should be provided to the UAII 2022 team.

Table D.5: List of parameter columns (data section) of a ASCII Text Sounding file

Parameter	Level of requirement
time	mandatory (if "time_stamp" is not present); Preferred over "time_stamp"
time_stamp	mandatory (if "time" is not present)
gph_gnss	mandatory
gph_press	recommended (if sensor is present)
press_gnss	mandatory
press_sens	mandatory (if sensor is present)
temp	mandatory

This table is continued on the next page.

Table D.5 – Continued from previous page

Parameter	Level of requirement
rh	mandatory
dew_point	recommended
wind_speed	mandatory
wind_dir	mandatory
lat	mandatory
lon	mandatory
alt	recommended
height_amsl	recommended
ascent_speed	recommended

Any other defined parameter columns (e.g. raw data) are optional. It is allowed to add further parameter columns to the file. A definition (parameter, description, unit, precision) of these additional parameters should be provided to the UAII 2022 team.

Example one of a UAII 2022 ASCII Text Sounding file:

```

1 # File.CreatedAt           = 2021-08-25T11:34:51.004Z
2 # File.CreatedBy          = Special export function of XXX (v1.234)
3 # File.Format              = UAII2022 ASCII Text Sounding
4 # General.WVFormula        = HylandWexler
5 # Launch.TimeStamp         = 2019-12-13T13:15:45.072Z
6 # Sonde.Manufacturer       = Example LTD
7 # Sonde.Model              = RSxx
8 # Sonde.SerialNumber       = Z01234567
9 # Initial.TimeStamp        = 2019-12-13T12:22:06.571Z
10 # Station.Latitude         = 46.834190 degN
11 # Station.Longitude        = 6.928969 degE
12 # Station.Altitude         = 491 m
13 # SurfaceData.Pressure     = 961.25 hPa
14 # SurfaceData.Temperature = 23.25 degC
15 # SurfaceData.RH           = 74.25 %RH
16 # SurfaceData.WindSpeed    = 4.20 m/s
17 # SurfaceData.WindDirection = 281.0 deg
18 #
19 time_stamp;gph_gnss;gph_press;press_gnss;press_sens;temp;rh;dew_point;wind_speed;wind_dir;lat;lon;alt
20 2019-12-13T13:15:45.072Z;491.2;NaN;961.085;NaN;21.11;81.55;12.55;4.21;330.1;46.834191;6.928968;510.8
21 2019-12-13T13:15:46.072Z;496.2;NaN;960.150;NaN;20.21;80.15;13.12;3.87;342.9;46.834236;6.929120;515.7
22 ...

```

Example two of a UAII 2022 ASCII Text Sounding file:

```

1 # <meta data see example one>
2 time; gph_gnss; press_gnss; temp; rh; dew_point; wind_speed; wind_dir; lat; lon; alt
3 0.0; 491.2; 961.085; 21.11; 81.55; 12.55; 4.21; 330.1; 46.834191; 6.928968; 510.8
4 1.0; 496.2; 960.150; 20.21; 80.15; 13.12; 3.87; 342.9; 46.834236; 6.929120; 515.7
5 ...

```

D.2.4 UAII 2022 ASCII Text Laboratory file

Tables D.6 and D.7 list the parameters that can or must be added into the ASCII Text Laboratory file.

Table D.6: List of metadata parameters (header section) of a ASCII Text Laboratory file

Parameter	Level of requirement
File.CreatedAt	recommended
File.CreatedBy	recommended (constant value)
File.Format	mandatory (constant value)
General.WVFormula	mandatory (constant value)
Sonde.Manufacturer	mandatory (constant value)
Sonde.Model	mandatory (constant value)
Sonde.SerialNumber	mandatory
Initial.TimeStamp	mandatory

It is allowed to add further metadata parameters to the file. A definition (parameter, description, unit) of these additional parameters should be provided to the UAI 2022 team.

Table D.7: List of parameter columns (data section) of a ASCII Text Laboratory file

Parameter	Level of requirement
time	mandatory (if "time_stamp" is not present); Preferred over time_stamp
time_stamp	mandatory (if "time" is not present)
temp_air_raw	mandatory
rh_raw	mandatory
rh_heat_raw	mandatory (if humidity sensor is heated)
temp_rh_heat_raw	mandatory (if humidity sensor is heated)
press_sens_raw	mandatory (if pressure sensor is present)

It is allowed to add further parameter columns to the file. A definition (parameter, description, unit, precision) of these additional parameters should be provided to the UAI 2022 team.

Example one a UAI 2022 ASCII Text Laboratory file:

```

1 # File.CreatedAt           = 2021-08-25T11:34:51.004Z
2 # File.CreatedBy          = Special export function of XXX (v1.234)
3 # File.Format              = UAI2022 ASCII Text Laboratory
4 # General.WVFormula        = HylandWexler
5 # Sonde.Manufacturer       = Example LTD
6 # Sonde.Model              = RSxx
7 # Sonde.SerialNumber       = Z01234567
8 # Initial.TimeStamp        = 2019-12-13T12:22:05.571Z
9 #
10 time_stamp;temp_air_raw;rh_raw;rh_heat_raw;temp_rh_heat_raw;press_sens_raw
11 2019-12-13T12:22:05.571Z;23.255;67.22;57.21;30.21;960.21
12 2019-12-13T12:22:06.571Z;23.264;67.11;57.18;30.22;NaN
13 ...

```

Example two a UAI 2022 ASCII Text Laboratory file:

```

1 # <meta data see example one>
2 time; temp_air_raw; rh_raw; rh_heat_raw; temp_rh_heat_raw; press_sens_raw

```

```
3 0.0; 23.255; 67.22; 57.21; 30.21; 960.21
4 1.0; 23.264; 67.11; 57.18; 30.22; NaN
5 ...
```

Example three a UAI 2022 ASCII Text Laboratory file:

```
1 # <meta data see example one>
2 time [s]; temp_air_raw [°C]; rh_raw [%]; rh_heat_raw [%]; temp_rh_heat_raw [°C]; press_sens_raw [hPa]
3 0.0; 23.255; 67.22; 57.21; 30.21; 960.21
4 1.0; 23.264; 67.11; 57.18; 30.22; NaN
5 ...
```

D.3 WMO BUFR FILES

The minimum requirement for BUFR (FM 94 BUFR using template 3 09 052 or 3 09 057) file is regulated by the WMO B/25: https://library.wmo.int/doc_num.php?explnum_id=10722.

The minimal temporal resolution of high-resolution profile data is five seconds. Recommended is one second or two seconds.

Additionally, if the manufacturer is able to produce descent data BUFR with template 3 09 056, this message should be provided for future investigations.

D.4 ORIGINAL SOUNDING ARCHIVE FILES (OFTEN PROPRIETARY)

Archiving of complete set of sounding-related data (raw data, data product, meta data, configuration, ...) produced by sounding software of participant is mandatory. Depending on the manufacturer, these files can have very different formats, which are often proprietary.

E TEMPLATES OF PROTOCOLS USED IN THE UAI 2022

Radiosounding protocol UAI2022 (operator)

General information

Flight number: <small>(F##)</small>	<input style="width: 90%;" type="text"/>	Time of day:	<input style="width: 90%;" type="text" value="day / night"/>
Scheduled day: <small>(yyyy-MM-dd)</small>	<input style="width: 90%;" type="text"/>	Scheduled time: <small>(HH:mm)</small>	<input style="width: 90%;" type="text" value="UTC"/>
Radiosonde model: <small>(type)</small>	<input style="width: 90%;" type="text"/>	Ground system:	<input style="width: 90%;" type="text" value="1 / 2"/>
Serial number:	<input style="width: 90%;" type="text"/>	Frequency: <small>(###.##)</small>	<input style="width: 90%;" type="text" value="MHz"/>
Position on rig: <small>(slot A to L)</small>	<input style="width: 90%;" type="text"/>	Detected launch time: <small>(HH:mm:ss)</small>	<input style="width: 90%;" type="text" value="UTC"/>
Type of usage:	<input style="width: 90%;" type="text" value="candidate/reference"/>	Operator: <small>(name or initials)</small>	<input style="width: 90%;" type="text"/>

Preparation

Start time of preparation: <small>(HH:mm:ss)</small>	<input style="width: 90%;" type="text" value="UTC"/>	Computer time checked:	<input style="width: 90%;" type="text" value="yes / no"/>
---	--	------------------------	---

Manufacturer ground check

<input style="width: 90%;" type="text" value="yes / no"/>	Time: <small>(HH:mm)</small>	<input style="width: 90%;" type="text" value="UTC"/>	
Reference temperature: <small>(##.##)</small>	<input style="width: 90%;" type="text" value="°C"/>	Radiosonde temperature: <small>(##.##)</small>	<input style="width: 90%;" type="text" value="°C"/>
Reference humidity: <small>(###.##)</small>	<input style="width: 90%;" type="text" value="%RH"/>	Radiosonde humidity: <small>(###.##)</small>	<input style="width: 90%;" type="text" value="%RH"/>
Reference pressure: <small>(###.##)</small>	<input style="width: 90%;" type="text" value="hPa"/>	Radiosonde pressure: <small>(###.##)</small>	<input style="width: 90%;" type="text" value="hPa"/>

Ground check using SHC
(check done, SHC number #)

<input style="width: 90%;" type="text" value="yes / no"/>	Time & duration: <small>(HH:mm, #)</small>	<input style="width: 90%;" type="text" value="UTC"/>	<input style="width: 90%;" type="text" value="min"/>
Reference temperature: <small>(##.##)</small>	<input style="width: 90%;" type="text" value="°C"/>	Radiosonde temperature: <small>(##.##)</small>	<input style="width: 90%;" type="text" value="°C"/>
Reference humidity: <small>(###.##)</small>	<input style="width: 90%;" type="text" value="100.0 %RH"/>	Radiosonde humidity: <small>(###.##)</small>	<input style="width: 90%;" type="text" value="%RH"/>

Comments (about anything what could maybe relevant)

Verification after data upload (please sign)

Operator: Assistant: Supervisor:

Figure E.1: Template of operator protocol related to one radiosonde of a launch during field campaign

Radiosounding protocol UAI2022 (supervisor)

General information

Flight number: <small>(F##)</small>		Supervisor: <small>(name or initials)</small>	
Scheduled day: <small>(yyyy-MM-dd)</small>		Scheduled time: <small>(HH:mm)</small>	UTC
Time of day:	day / night	Launch time: <small>(HH:mm:ss)</small>	UTC

Assembly of train incl. radiosondes

Balloon: <small>(type)</small>		Filling weight / Buoyancy force: <small>(####.#)</small>	g
Parachute: <small>(type)</small>		Unwinder & mode of launch: <small>(type, string length, mode)</small>	m M / U
Rig: <small>(type, weight ####.#)</small>		Load weight: <small>(####.#)</small>	g
Position A: <small>(type, freq. ###.##)</small>	c r	Position B: <small>(type, frequency ###.##)</small>	MHz
Position C: <small>(type, freq. ###.##)</small>	c r	Position D: <small>(type, frequency ###.##)</small>	MHz
Position E: <small>(type, freq. ###.##)</small>	c r	Position F: <small>(type, frequency ###.##)</small>	MHz
Position G: <small>(type, freq. ###.##)</small>	c r	Position H: <small>(type, frequency ###.##)</small>	MHz
Position K: <small>(type, freq. ###.##)</small>	c r	Position L: <small>(type, frequency ###.##)</small>	MHz

Surface conditions, weather, and clouds at launch

Pressure (at launch height): <small>(####.#)</small>	hPa	Pressure (at balloon hall height): <small>(####.#)</small>	hPa
Temperature: <small>(##.#)</small>	°C	Humidity: <small>(###.#)</small>	%RH
Wind speed: <small>(##.#)</small>	m/s	Wind direction: <small>(###.#)</small>	°
Weather (N VV ww WW):		Weather remarks:	
Clouds (Nh CL h CM CH):		Clouds in plain text:	

Details of flight and burst

Burst: <small>(time UTC, height ##.#)</small>		km		Ascent speed: <small>(trop., strat., mean: #.#)</small>	tropo. strato. mean		m/s
--	--	----	--	--	---------------------	--	-----

Remarks and verification

	Supervisor (sign):

Figure E.2: Template of supervisor protocol of a launch during field campaign

F SUPPLEMENT TO IMPLEMENTATION OF THE CAMPAIGN

F.1 SUPPLEMENT TO DESCRIPTION OF OBSERVATORY

F.1.1 Aerological observation and testing site

Balloon-borne radiosondes are still the worldwide standard technique for measuring vertical profiles of air pressure, temperature, humidity and wind in the troposphere and the lower stratosphere, up to approximately 35 km altitude.

Regular daily radiosoundings at Lindenberg commenced in 1947. Currently, four operational soundings are routinely performed each day (at 00, 06, 12 and 18 UTC) together with weekly in-situ measurements of the ozone profile. Every month, one or more research soundings are performed with a dedicated instrument for accurate measurements of the water vapour content in the stratosphere.

MOL-RAO is also the DWD's aerological testing site. The activities aim at testing and characterising contemporary radiosondes and, in particular, at examining the calibration, response behaviour and radiation sensitivity of the sensors. Dedicated laboratory facilities, including a climate chamber, are available for this purpose. In addition, special research instruments are used to validate operational radiosonde measurements during comparison flights. Procedures for correcting and testing radiosonde sensors are developed and shared with the international scientific community in the framework of the GCOS Reference Upper-Air Network (GRUAN). Testing of equipment for radiosounding, such as the balloons and parachutes, is performed as well.

F.1.2 GRUAN Lead Centre

To date, climate research can make only limited use of the measurement data taken in the upper troposphere and lower stratosphere within the well-developed global radiosounding network. Although there has been great and steady progress in the development of radiosondes and sensor design in recent years, and despite a large number of radiosonde models currently available on the market, many systems do not yet satisfactorily meet the high quality standards, especially for humidity measurements, required for climate monitoring and research. The biggest problems lie in the corrections of systematic measurement errors that arise under sounding conditions, and in systematic deviations of the measurement data between different sonde models. The latter can lead to discontinuities in the data series when the model for operational observations is changed. This is also due to the fact that correction algorithms and technical changes on the part of the manufacturers are usually not disclosed or sufficiently documented. This requires elaborate comparative measurement programmes with sufficient statistics within the framework of change management so that the discontinuities can be quantified to enable the subsequent homogenisation of the data sets in climate analyses.

The WMO responded to this deficit by establishing GCOS Reference Upper-Air Network (GRUAN) as an international observing network of aerological reference stations in 2008. GRUAN¹ is designed to meet the specific requirements of climate monitoring and fill an important gap in the current global observing system. GRUAN is envisaged as a global network which will comprise 30 to 40 sites with dedicated equipment to obtain high-quality data from the free atmosphere on a long-term basis. The network currently consists of 31 stations, with Lindenberg taking the role of GRUAN's Lead Centre and thus being responsible for monitoring and developing the entire network. This includes coordinating the network itself as well as organising the coordination among the stations, defining, testing and introducing quality assurance procedures, training launch staff, archiving and disseminating GRUAN data and reporting to the WMO. Within the GRUAN framework, the results of MOL-RAO's activities as an aerological test and launch site are shared with the international scientific community. In this capacity, MOL-RAO contributes to the scientific

¹<https://www.gruan.org>

understanding of the performance of radiosonde sensors, to the development of standardised test procedures and to operational correction algorithms for measurement errors.

F.1.3 Ground-based remote sensing

Over the last three decades, several new and powerful observing methods have become available to quantitatively characterise the state of the atmosphere. In addition to the satellite-based technologies, a number of ground-based remote sensing techniques have been developed and improved. These include radar systems operating at decimetre and millimetre wavelengths, laser-based measuring systems (lidar) that operate in the spectral range from ultraviolet through to near infrared, and passive instruments measuring the atmosphere's natural radiation, particularly at centimetre wavelengths.

These remote sensing methods enable the continuous observation of the vertical profiles of atmospheric parameters, such as wind, temperature and air humidity, at high temporal and vertical resolution. In this way, it is possible to record small-scale and short-lived structures in the atmosphere – that are usually not accessible to radiosondes launched every six or twelve hours. It is also possible to obtain indirect information about small liquid and solid particles that are suspended in the atmosphere (clouds, aerosols). These particles are of considerable relevance to the physical processes in the atmosphere and thus for weather and climate (e.g. clouds and precipitation formation, radiation balance). These measurement methods are being tested and developed further at MOL-RAO with the aim of using them operationally in the DWD measurement network or as part of the Lindenberg Column research measurement programme.

See section 4.4 for a further description of the remote sensing instruments relevant for UAI 2022.

F.1.4 Boundary layer measurements

The atmospheric boundary layer is the part of the lower atmosphere which is directly influenced by the surface of the Earth. Important processes include radiation, surface friction and the effects of obstacles on the wind, as well as, the exchange of energy and trace substances between the soil/vegetation system and the air. The atmospheric boundary layer is that part of the atmosphere where humans predominantly live and act. This is also where the temporal and spatial variability of temperature, air humidity or wind is most pronounced. Dew, hoar-frost, fog, turbulence and convection are typical examples of boundary layer phenomena.

Understanding boundary layer processes is crucial for a reliable weather forecast and consequently for many of DWD's advisory services. Therefore, a comprehensive boundary layer measurement programme has been in place at the MOL-RAO since 1998. A dedicated measurement site was established in Falkenberg, a few kilometres south of Lindenberg. Another measurement site was established in a pine forest near Kehrigk (approximately ten kilometres to the west of Falkenberg). The profiles of wind, temperature and atmospheric water vapour are measured at both sites on high masts (99 m at Falkenberg and 30 m at Kehrigk). The turbulent fluxes of momentum, energy and water vapour between the ground and the atmosphere are also recorded at high temporal resolution.

Measurements above mast height are carried out using ground-based remote sensing systems, namely Sodar/RASS and lidar. Short and long-wave upward and downward radiation fluxes as well as the temperature and the water content of the soil are also measured. Scintillometry is used between the two locations at Falkenberg and Lindenberg to determine the integral influence of meadows, fields and populated areas on the transfer of energy. These systems measure fluctuations in the intensity of infrared or microwave radiation along the approximately five kilometre long propagation path.

F.1.5 Radiation processes – national and regional radiation measurement centre

The short- and long-wave radiant fluxes from the Sun, the sky and the surface of the Earth are the most important factors supporting life on Earth and make the biggest contribution to the global energy balance. Temporal and spatial differences in the radiation balance drive dynamical

processes in the atmosphere and thus have a crucial impact on weather and climate. Solar radiation changes as it passes through the atmosphere, so that analysis of its spectral composition, in particular, provides information about atmospheric trace gases (e.g. ozone, water vapour) or particles (aerosols).

The MOL-RAO's tasks include acquiring and analysing high-time-resolution data of both the direct and diffuse (i.e. scattered by molecules in the atmosphere and/or reflected by the clouds) short-wave solar (ir)radiance as well as the global radiation (i.e. the sum of direct and diffuse solar (ir)radiance). This is done using pyrheliometers and pyranometers. Pyrgeometers measure the atmospheric thermal radiance which results from the thermal emission by the different constituents of the atmosphere (gases, aerosols and clouds). For more than 20 years, the resulting data sets are submitted to the Baseline Surface Radiation Network (BSRN), one of WMO's global climate observing activities.

Sun and star photometers can be used under clear-sky conditions to determine the atmosphere's integral aerosol and water vapour content, which are important parameters for climate change studies. Other measurements of spectral radiation provide information on the total ozone column and about UV² radiation. Furthermore, spectral radiance measurements yield information on clouds, that have a large and highly variable effect on the Earth's radiation budget.

In its capacity as Germany's national and WMO's regional (RA VI Europe) radiation measurement centre, MOL-RAO participates in international campaigns to calibrate its instruments against the world radiation standards, and takes care of the calibration and maintenance of the radiation measuring instruments employed in the DWD network.

F.1.6 Historical milestones of Lindenberg observatory

April 1905	Beginning of captive balloon and kite ascents in Lindenberg
16 October 1905	Inauguration of the Royal Prussian Aeronautical Observatory in Lindenberg in the presence of Emperor Wilhelm II and Prince Albert of Monaco
1910	Warning service for aviation; observation network of 15 pilot balloon sounding sites across Germany with headquarters in Lindenberg
1 August 1919	Altitude world record for kite ascent (9750 m) using a train of eight kites
22 May 1930	First ascent of a radiosonde in Lindenberg (14.5 km)
15 July 1947	Start of regular aerological radiosonde ascents, ongoing without interruption until today
1950	Foundation of the Meteorological Service (MD) of the German Democratic Republic and integration of the Lindenberg Aerological Observatory in the MD
21 October 1964	Start of the first drifting balloon with a volume of up to 6400 m ³ for wind measurements in the stratosphere
1 December 1974	Start of weekly ozone soundings in Lindenberg
1975	First ozone soundings in the Antarctic by scientists from the Lindenberg Observatory
1983	Development of a ground-based atmosphere spectrometer to determine the spectral aerosol optical depth (since 1986 part of the routine measuring programme)
21 October 1988	Launch of the first meteorological rocket at Zingst research station
1 January 1991	Integration of the Lindenberg Meteorological Observatory in DWD following the unification of Germany
7 October 1993	Beginning of the operation of the radar/RASS wind profiler (1290 MHz)
1 October 1994	Beginning of routine radiation measurements at Lindenberg global BSRN station

²Ultra Violet (UV)

1998	Beginning of operational measurements at the Falkenberg boundary layer field site
2003	Inauguration of the radiation measurement centre at the observatory
2005	Renaming as Lindenberg Meteorological Observatory – Richard Assmann Observatory on the occasion of the observatory’s 100th anniversary
2008	Foundation of the Lead Centre for the newly established WMO’s GCOS Reference Upper-Air Network (GRUAN)
2022	Hosting of the WMO radiosonde intercomparison campaign UAI 2022

F.2 SUNRISE AND SUNSET

Twilight zones are defined by the sun elevation angle below the horizon ($<0^\circ$): civil twilight ($<-6^\circ$), nautical twilight ($<-12^\circ$), and astronomical twilight ($<-18^\circ$). It was decided to avoid civil twilight. That means night conditions are defined to be at times excluding civil but including nautical and astronomical twilight.

Table F.1: Times and duration of sunset, twilight phases after sunset and before sunrise, night-time (without civil twilight) and daylight (from sunrise to sunset) during field campaign (dates in the first column are Monday/Tuesday). Times are local time (Central European Summer Time (CEST)=UTC+02:00).

Date	Sun-set	Twilight after			Night (civ.)	Twilight before			Sun-rise	Daylight
		civ.	naut.	astr.		astr.	naut.	civ.		
01./02.8.	20:58	21:40	22:37	00:07	07h05m	02:23	03:48	04:45	05:27	15h31m
08./09.8.	20:45	21:26	22:19	23:29	07h32m	02:55	04:05	04:58	05:38	15h07m
15./16.8.	20:32	21:10	22:00	23:01	08h01m	03:21	04:22	05:11	05:50	14h42m
22./23.8.	20:17	20:54	21:41	22:36	08h30m	03:43	04:37	05:24	06:02	14h15m
29./30.8.	20:01	20:37	21:22	22:12	09h00m	04:02	04:52	05:37	06:13	13h48m
05./06.9.	19:45	20:20	21:03	21:50	09h30m	04:20	05:07	05:50	06:25	13h20m
12./13.9.	19:29	20:03	20:45	21:29	09h59m	04:36	05:20	06:02	06:37	12h52m
19./20.9.	19:12	19:46	20:27	21:09	10h28m	04:51	05:33	06:14	06:48	12h24m

F.3 STRING LENGTH

F.3.1 Experimental investigations

Some experimental investigations were carried out to determine the influence of the string length (i.e. the distance between the radiosonde and the rod above it) on the measurements. It is known that surfaces which are in the air stream in front of the sensor can lead to contamination (temperature and humidity). The further away a sensor is from such a surface, the less the contamination should be measurable, i.e. relevant. Concluding following potential effects seem possible:

- Temperature influence of radiosonde sensors by warmer (or colder) air generated by the warmer or colder surface of the rods;
- Humidity influence of the radiosonde sensors by the evaporation of water or ice, which is accumulated on the rods;
- Change of the rotation and swinging behaviour of the radiosondes;

- Influence of a changed radiation field on the sensors because additional surfaces around.

In Lindenberg, therefore, six flights were carried out in May and July 2019, where four or five identical radiosondes flew on a rig, differing only in their different suspension lengths: 80 cm, 60 cm, 40 cm, 20 cm, and taped (so that the sensor boom was unaffected by the rods). Four day flights and two night flights were carried out. One day flight and one night flight were contaminated by rain and thick mixed clouds respectively. The other flights took place in almost cloud-free situations.

The analysis shows temperature differences within ± 0.1 K (not water contaminated) and some single points above 25 km show sometimes ± 0.3 K (daytime). At night the differences are even smaller up to 25 km. The humidity differences are less than ± 1.3 %RH (not water contaminated). In the stratosphere the calibration accuracy is shown with small absolute relative humidity (near 1 %RH or less). The expected dependence between string length and difference – i.e. the closer to the rod, the greater the difference – cannot clearly be identified.

The two flights with partly heavy contamination show interesting effects. Icing of the balloons could not be identified with this experiment. Icing of the temperature sensors plays a role, because larger differences are recognisable. During the day, however, this problem is only relevant up to 1 or 2 km above the cloud, but not in the stratosphere. Icing of the rods plays a very important role, because the differences can be extremely large (ΔT_{raw} up to ± 1.4 K). This problem is only relevant in the stratosphere during the day, and it is extremely relevant in the stratosphere above about 25 km (55 hPa) altitude.

Some consequences can be derived from these observations. Contaminated flights of radiosonde comparisons with the use of rigs (rods, etc.) will be a challenge in the statistical analysis. That means, if a contaminated case occurs during a campaign, it will lead to larger differences between references (GDP sondes) and a larger spread in the final statistics of participating radiosondes. Basically, from the point of view of data quality, it does not matter significantly whether a radiosonde is taped or hanged 20 cm, 40 cm, 60 cm or 80 cm. The limit for significant differences is ± 0.1 K for temperature and ± 1.5 %RH for humidity at altitudes lower than 25 km. Above 25 km the limit of temperature differences is ± 0.2 K. Of course, these statements only applies if the rods are quite thin (here approx. 1 cm to 2 cm). It would look different if very large surfaces or bodies were located above or directly next to a radiosonde. In order to allow a normal rotation of the radiosondes, it is preferable to hang them rather than tape them on. As the radiosonde otherwise only rotates with the rotation of the entire rig, which is normally much slower (up to 40 s per turn). As no specification of the string length seems to be meaningful with regard to data quality, the practical (operational) boundary conditions should rather be decisive: not too long for the operator to be able to handle it easily, and not too short, because otherwise the radiosonde might strike the rod.

F.3.2 Practical considerations

Since the experiment could not provide a final specification for the optimal string length, some theoretical considerations were also carried out in order to optimise the string length and the distances between the attachment points.

First some rather practical considerations can be taken into account in such a theoretical reflection:

- Such a rig is started manually and therefore it is necessary that this is manageable. This leads to a limitation of the length of a radiosonde's hanging from the rod, because these radiosondes should not drag on the ground and should not touch anywhere. The typical size of the active persons should therefore also be taken into consideration.
- Radiosondes should be mounted sufficiently far apart from each other that no interference from the emitted radio waves is to be expected.
- Radiosondes should be mounted in such a way that a collision of the sondes during take-off and ascent is unlikely or even impossible.

Figure F.1 shows the relevant parameters that are needed for the theoretical considerations. First, a maximum excursion angle was defined, which reflects how far sondes are expected to swing, especially during the launch process. According to our experience, a maximum excursion angle

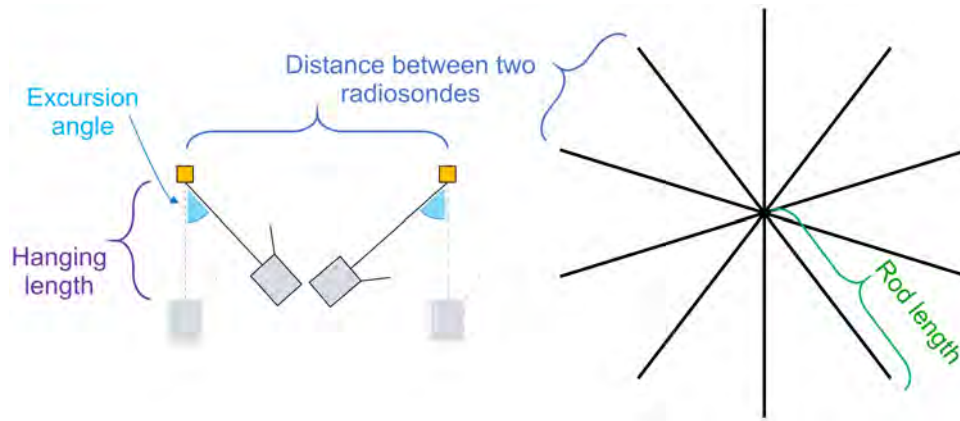


Figure F.1: Relevant parameters for the theoretical considerations of string length

of 40° was chosen as the limit. Therefore, all considered variants should allow at least this (or more) before 2 neighbouring sondes hit each other.

Table F.2 demonstrates, how the string length affects the size of the whole 10-star rig.

Table F.2: Considered variants of different string lengths. A mean length of radiosondes is assumed as 0.15 m. The limit of excursion angle was defined as 40°. Marked is the chosen string length of 0.7 m.

String length	Tip distance	Rod length	Rig size	Excursion angle
[m]	[m]	[m]	[m]	[°]
0.4	0.75	1.21	2.43	43.0
0.5	0.85	1.38	2.75	40.8
0.6	1.00	1.62	3.24	41.8
0.7	1.10	1.78	3.56	40.3
0.8	1.25	2.02	4.05	41.1
0.9	1.35	2.18	4.37	40.0
1.0	1.50	2.43	4.85	40.7

The string length was finally chosen as long as possible to keep any effects due to the rods as insignificant as possible (even though the experiment did not show a clear correlation). The maximum allowed size of the rig was 4.0 m, not larger. So, related to Table F.2, a total size of the rig of about 3.56 m was possible at most – which corresponds to the string length of 0.70 m. And this is in the range of the two longest experimentally tested string lengths.

Decision: A string length of 0.7 m was finally chosen for the campaign.

F.4 DAILY SCHEDULE

Table F.3: Information about daily schedule for the weeks of active soundings during the field campaign (August and September 2022). The times are local, that is time zone Central European Summer Time (CEST) with UTC+02:00.

Step	Dur.	15.-19.8.	22.-26.8.	29.8.-2.9.	5.-9.9.	12.-16.9.
<i>Day shift (9 to 10 hours in total)</i>						
Specific planning	1H00M	08:00	08:00	08:00	08:00	08:00
Briefing launch 1	15M	09:00	09:00	09:00	09:00	09:00
Preparation	45M	09:15	09:15	09:15	09:15	09:15
Launch 1 & ascent	1H30M	10:00	10:00	10:00	10:00	10:00
Burst & descent	1H00M	11:30	11:30	11:30	11:30	11:30
Follow-up	30M	12:30	12:30	12:30	12:30	12:30
<i>Lunch break</i>	<i>1H00M</i>	<i>13:00</i>	<i>13:00</i>	<i>13:00</i>	<i>13:00</i>	<i>13:00</i>
Briefing launch 2	15M	14:00	14:00	14:00	14:00	14:00
Preparation	45M	14:15	14:15	14:15	14:15	14:15
Launch 2 & ascent	1H30M	15:00	15:00	15:00	15:00	15:00
Burst & descent	1H00M	16:30	16:30	16:30	16:30	16:30
Follow-up	30M	17:30	17:30	17:30	17:30	17:30
End of day shift	-	18:00	18:00	18:00	18:00	18:00
<i>Night shift (8 to 9 hours in total)</i>						
Specific planning	1H00M	19:15	19:00	18:45	18:30	18:00
Briefing launch 1	15M	20:15	20:00	19:45	19:30	19:00
Preparation	45M	20:30	20:15	20:00	19:45	19:15
Launch 1 & ascent	1H30M	21:15	21:00	20:45	20:30	20:00
Burst & descent	1H00M	22:45	22:30	22:15	22:00	21:30
Follow-up	30M	23:45	23:30	23:15	23:00	22:30
Briefing launch 2	15M	00:15	00:00	23:45	23:30	23:00
Preparation	45M	00:30	00:15	00:00	23:45	23:15
Launch 2 & ascent	1H30M	01:15	01:00	00:45	00:30	00:00
Burst & descent	1H00M	02:45	02:30	02:15	02:00	01:30
Follow-up	30M	03:45	03:30	03:15	03:00	02:30
End of night shift	-	04:15	04:00	03:45	03:30	03:00

G MANUFACTURER INTERACTIONS

List of extraordinary interactions between Project Leads and manufacturers during the campaign:

Graw Radiosondes GmbH & Co. KG

The manufacturer found discrepancies in the launch time of the parallel sounding F07 and contacted the project lead on August 23, 2022. Upon instructions given by the manufacturer, regular checks of the computer time and the GNSS indicator were performed by the operators.

Azista Industries Pvt. Ltd.

The manufacturer updated the software during the preparation week to obtain a UAI-format-compliant MDP datafile.

Diel Met Systems (Pty) Ltd. trading as InterMet

On August 15, 2022, the manufacturer sent an update of their Quick Reference Guide to the project lead which was distributed to the operators.

A few days into the field campaign the sounding software on one of the systems froze during start up. After consulting the manufacturer the cause for this problem was identified and resolved. The reason for the problem was that the sounding software uses MS-Edge libraries, and scheduled MS-Edge updates could not be downloaded because the computer was, per campaign rules, not connected from the internet. The problem was resolved by temporarily connecting the computer to the internet to allow for the installation of the necessary MS-Edge updates.

The manufacturer noted issue with the reported GNSS altitude before start and informed the project leads. The project lead received some specific instructions for the operators which have been implemented to remedy the issue.

Meisei Electric Co., Ltd.

During the field campaign the cable connecting the antenna and the operator computer was damaged overnight by a rodent. The manufacturer was informed about this issue and a provisional repair was performed by Lindenberg staff

Radio signal interferences have been identified before and during some flights. Countermeasures were discussed with the manufacturer to improve the signal reception.

Generation of some UAI ASCII files on the acquisition computer was not possible. Assistance of the manufacturer was needed to recover some UAI ascii files from the internal database.

Aerospace Newsky Technology Co., Ltd.

The manufacturer informed the project leads that they observed increased data loss (50%) for F20 (2022-08-24) and suspected interference from other radiosondes. Request to the operators to check the spectrum for the presence of signals from other radiosondes before switching on the radiosonde.

Meteomodem

The Eoscans software was updated on Wednesday, August 10 2022, from version 1.9.220804 to 1.9.220810. This correction patch removes multiple interpolation lines into UAII data file.

On August 15, 2022, Meteomodem made a new software version of Eoscan available to the project team. This release fixed the altitude issues in the UAII data files.

Tianjin Huayuntianyi Special Meteorological Sounding Tech. Co., Ltd.

A substantial number of radiosondes exhibited a problem with the temperature sensor during preparation or shortly after start, causing it to report temperatures below -60°C . This problem is also described in Section 8.2.3. The manufacturer was contacted by the project leads, and they informed us that the malfunctioning of the temperature sensor is due a manufacturing error. This problem could not be resolved other than by attempting to identify and replacing malfunctioning radiosondes prior to launch. The manufacturer was granted permission by the project leads to ship replacement radiosondes for the laboratory tests in January 2023.

Weathex

The antenna cable for the second radiosounding system was missing, which caused premature termination of data recording for several soundings performed with this system. Following consultation with the manufacturer, both systems were connected to the same antenna using an antenna-splitter. In parallel, a second cable was sent to Lindenberg by courier and installed by the project team.

Failure of sounding system #1 on August 29, 2022. Despite manufacturer consultation, this could not be resolved so that twin soundings were not possible for the remainder of the campaign.

After the field campaign, on August 25, 2022, the manufacturer contacted the WMO secretariat with copy to the project leads informing about several issues with their data processing. The manufacturer found "incorrect calculations" and missing corrections in the MDP and formally requested the permission for reprocessing of the sounding files. The manufacturer has provided details of the encountered issues to the project team. On March 21, 2023, the project lead granted the reprocessing of the wind direction, but not of the other parameters. The filter to smooth the wind direction did not account for the discontinuity at 360° resulting in southerly winds while the individual data points represented northerly winds. See also Section 9.5.2.1.

H LIST OF SATELLITE OVERPASSES

In order to identify satellite overpasses that coincide in time and space with the UAI 2022 field campaign flights, a subset of approximately 20 uniformly-distributed profile points are extracted from each of the 79 ascents. These serve to represent the trajectory from the launch to the balloon burst. For each of these points, we identify all satellite overpasses that comply with the following selection criteria:

- ≤ 300 km horizontal distance to the radiosonde,
- $\leq \pm 1$ h temporal distance, and
- a maximum nadir angle between the satellite and the radiosonde's projected surface position of 30° .

From the set of "matching" points for a given flight-satellite pair, only the one with the lowest calculated value for the (normalised) product of time offset and horizontal distance is selected and listed in Table H.1. One should note that our overpass selection criteria do not include whether a given satellite was in the process of acquiring relevant data at the time of the overpass.

Table H.1: Overpasses of various satellites coinciding with the UAI 2022 field campaign flights. The list includes points in the radiosonde trajectories that best fulfil the following criteria: maximum viewing angle (satellite-sonde nadir) of 30°, overpass within ± 1 h and at a horizontal distance of less than 300 km.

Flight	Timestamp [UTC]	Latitude [°N]	Longitude [°E]	Altitude [m]	Name	Overpass time [UTC]	Distance [km]	Offset [min]	Latitude [°N]	Longitude [°E]	Nadir [°]	Sun elev. [°]
F01	2022-08-16T08:18:10	52.2091	14.1210	120	ICESAT-2	2022-08-16T07:45:53	111	32	52.15	15.74	12.83	34.54
F01	2022-08-16T09:59:47	52.4819	14.2478	31 151	ISS	2022-08-16T10:01:53	77	-2	51.79	14.22	10.38	49.22
F01	2022-08-16T09:34:10	52.4691	14.3437	23 290	METOP-B	2022-08-16T09:34:18	263	0	53.10	10.60	17.46	47.18
F01	2022-08-16T09:59:47	52.4819	14.2478	31 151	MICROMAS-2A	2022-08-16T10:46:52	210	-47	52.91	11.23	24.63	51.15
F01	2022-08-16T09:59:47	52.4819	14.2478	31 151	NOAA 18	2022-08-16T10:20:08	229	-20	53.04	10.99	14.99	50.23
F03	2022-08-16T20:46:01	52.2958	14.5260	25 565	LANDSAT 8	2022-08-16T20:44:08	206	2	51.89	11.60	16.07	-17.55
F03	2022-08-16T21:05:41	52.2660	14.4595	30 787	MICROMAS-2A	2022-08-16T21:23:12	112	-18	52.06	12.85	13.77	-20.70
F04	2022-08-17T09:30:19	52.4388	14.3847	21 417	GPM-CORE	2022-08-17T09:30:39	48	0	52.74	14.90	6.65	46.63
F04	2022-08-17T09:14:10	52.4022	14.3669	16 680	ISS	2022-08-17T09:13:20	79	1	51.70	14.44	10.61	45.02
F04	2022-08-17T10:01:02	52.4486	14.2796	31 323	LANDSAT 8	2022-08-17T10:15:26	274	-14	53.08	10.35	20.95	49.74
F04	2022-08-17T09:14:10	52.4022	14.3669	16 680	METOP-B	2022-08-17T09:13:34	74	1	52.22	15.41	5.08	45.05
F04	2022-08-17T10:01:02	52.4486	14.2796	31 323	NOAA 18	2022-08-17T10:08:04	34	-7	52.51	13.79	2.30	49.34
F05	2022-08-17T13:20:29	52.5662	14.4057	27 148	CALIPSO	2022-08-17T13:20:02	96	0	52.35	13.03	7.93	42.71
F05	2022-08-17T13:20:29	52.5662	14.4057	27 148	CLOUDSAT	2022-08-17T13:20:52	80	0	52.38	13.26	6.62	42.62
F05	2022-08-17T13:17:54	52.5685	14.4145	26 371	FENGYUN 3A	2022-08-17T13:16:47	67	1	52.41	13.46	4.56	43.07
F05	2022-08-17T12:44:10	52.5104	14.4154	16 938	GOSAT	2022-08-17T12:45:24	47	-1	52.40	15.08	3.95	46.26
F05	2022-08-17T11:47:53	52.2092	14.1209	121	ISS	2022-08-17T10:49:59	219	58	50.31	13.32	27.40	51.16
F05	2022-08-17T11:47:53	52.2092	14.1209	121	NOAA 20	2022-08-17T11:37:37	92	10	52.40	15.43	6.25	50.84
F06	2022-08-17T16:13:26	52.5508	14.4713	25 610	AEOLUS	2022-08-17T16:15:26	92	-2	52.71	15.80	16.31	18.20
F07	2022-08-17T21:02:23	52.5545	14.5745	25 695	CRYOSAT 2	2022-08-17T21:04:01	30	-2	52.52	14.14	2.33	-19.37
F07	2022-08-17T19:35:02	52.2104	14.1035	1019	ICESAT-2	2022-08-17T19:34:43	121	0	52.15	12.34	13.94	-10.27
F07	2022-08-17T19:32:14	52.2091	14.1206	125	LANDSAT 7	2022-08-17T18:55:11	75	37	52.35	15.19	6.08	-5.20
F07	2022-08-17T19:52:05	52.2674	14.1690	7052	METOP-C	2022-08-17T19:54:04	91	-2	52.05	12.88	6.27	-12.55
F07	2022-08-17T20:43:45	52.5453	14.6140	21 102	TERRA	2022-08-17T20:41:38	103	2	52.32	13.14	8.26	-17.46
F08	2022-08-18T01:15:17	52.5251	14.4939	31 262	FENGYUN 3D	2022-08-18T01:34:26	97	-19	52.30	15.86	6.59	-17.13
F08	2022-08-18T01:15:17	52.5251	14.4939	31 262	GPM-CORE	2022-08-18T02:13:41	67	-58	52.11	15.20	9.22	-13.09

This table is continued on the next page.

Table H.1 – Continued from previous page

Flight	Timestamp [UTC]	Latitude [°N]	Longitude [°E]	Altitude [m]	Name	Overpass time [UTC]	Distance [km]	Offset [min]	Latitude [°N]	Longitude [°E]	Nadir [°]	Sun elev. [°]
F08	2022-08-18T01:15:17	52.5251	14.4939	31 262	NOAA 20	2022-08-18T01:30:07	280	-15	53.21	10.49	18.41	-17.53
F09	2022-08-18T08:22:59	52.2183	14.1059	3560	ISS	2022-08-18T08:24:43	110	-2	51.24	14.34	14.63	39.23
F09	2022-08-18T08:26:51	52.2277	14.1124	4884	LANDSAT 7	2022-08-18T08:25:08	44	2	52.30	13.49	3.55	39.28
F09	2022-08-18T09:51:24	52.4911	14.2850	30 373	NOAA 18	2022-08-18T09:55:58	167	-5	52.12	16.66	11.11	48.24
F09	2022-08-18T09:51:24	52.4911	14.2850	30 373	TERRA	2022-08-18T10:12:52	176	-21	52.87	11.75	13.89	49.26
F10	2022-08-18T12:27:27	52.2092	14.1210	120	AQUA	2022-08-18T11:47:07	222	40	52.70	17.28	17.28	50.18
F10	2022-08-18T12:27:27	52.2092	14.1210	120	AURA	2022-08-18T12:21:19	268	6	51.70	10.31	20.52	48.24
F10	2022-08-18T12:59:52	52.3494	14.2456	11 780	FENGYUN 3A	2022-08-18T12:58:43	245	1	52.91	17.74	16.10	44.87
F10	2022-08-18T12:27:27	52.2092	14.1210	120	GCOM-W1	2022-08-18T12:11:08	290	16	51.66	9.99	22.06	48.93
F10	2022-08-18T12:27:27	52.2092	14.1210	120	OCO 2	2022-08-18T12:05:56	154	22	51.89	11.93	12.22	49.24
F11	2022-08-18T19:04:42	52.2092	14.1210	116	ICESAT-2	2022-08-18T19:09:07	266	-4	52.39	18.01	28.39	-7.34
F11	2022-08-18T20:32:22	52.4731	14.5659	23 073	LANDSAT 8	2022-08-18T20:31:56	10	0	52.44	14.44	0.76	-16.91
F11	2022-08-18T19:31:39	52.2804	14.1367	7926	METOP-C	2022-08-18T19:33:19	252	-2	52.88	17.72	16.78	-10.38
F11	2022-08-18T19:04:42	52.2092	14.1210	116	NOAA 19	2022-08-18T18:16:49	76	48	52.02	13.06	5.09	-0.16
F12	2022-08-18T23:13:35	52.4323	14.3147	20 976	GOSAT 2	2022-08-18T23:12:26	99	1	52.63	15.74	9.04	-24.89
F13	2022-08-19T08:24:26	52.2859	14.1387	9117	GPM-CORE	2022-08-19T09:20:23	240	-56	50.87	11.53	29.91	45.16
F13	2022-08-19T09:12:09	52.4775	14.2665	22 460	ISS	2022-08-19T09:12:52	96	-1	51.62	14.13	12.90	44.33
F13	2022-08-19T09:43:16	52.4874	14.1601	31 259	LANDSAT 8	2022-08-19T10:03:13	65	-20	52.61	13.22	5.25	48.38
F13	2022-08-19T09:26:13	52.4764	14.2153	26 387	METOP-C	2022-08-19T09:24:43	90	1	52.66	12.93	6.19	45.44
F13	2022-08-19T09:43:16	52.4874	14.1601	31 259	MICROMAS-2A	2022-08-19T10:34:49	1	-52	52.48	14.15	0.14	49.87
F13	2022-08-19T07:59:24	52.2092	14.1210	123	NOAA 15	2022-08-19T07:21:40	61	38	52.33	13.25	4.33	30.41
F14	2022-08-19T12:31:07	52.2065	14.1413	1512	GOSAT 2	2022-08-19T12:29:06	199	2	51.83	16.97	17.61	47.33
F14	2022-08-19T12:26:16	52.2092	14.1211	120	SUOMI NPP	2022-08-19T11:51:17	129	35	51.92	12.30	8.80	49.67
F15	2022-08-19T20:56:21	52.5454	14.0024	33 246	CRYOSAT 2	2022-08-19T21:02:07	59	-6	52.50	13.14	4.66	-19.69
F15	2022-08-19T20:02:21	52.5455	14.1426	19 141	METOP-B	2022-08-19T20:00:14	210	2	52.10	11.16	14.12	-13.68
F15	2022-08-19T20:56:21	52.5454	14.0024	33 246	MICROMAS-2A	2022-08-19T21:11:10	116	-15	52.77	15.68	14.21	-20.41
F15	2022-08-19T18:59:55	52.2091	14.1211	113	NOAA 19	2022-08-19T18:04:54	123	55	52.49	15.87	8.22	1.27
F15	2022-08-19T20:28:57	52.5595	14.0858	26 175	TERRA	2022-08-19T20:29:22	132	0	52.83	15.99	10.53	-16.72
F16	2022-08-19T23:20:12	52.3437	14.1447	9241	GOSAT	2022-08-19T23:19:52	74	0	52.48	15.20	6.21	-25.26

This table is continued on the next page.

Table H.1 – Continued from previous page

Flight	Timestamp [UTC]	Latitude [°N]	Longitude [°E]	Altitude [m]	Name	Overpass time [UTC]	Distance [km]	Offset [min]	Latitude [°N]	Longitude [°E]	Nadir [°]	Sun elev. [°]
F16	2022-08-19T23:26:52	52.4253	14.1342	11 578	GOSAT 2	2022-08-19T23:28:28	155	-2	52.12	11.93	13.88	-25.07
F17	2022-08-22T08:57:30	52.3995	14.1068	17 098	CRYOSAT 2	2022-08-22T08:55:41	276	2	52.31	18.15	20.60	41.71
F17	2022-08-22T08:01:53	52.2092	14.1210	116	FENGYUN 3C	2022-08-22T07:06:17	81	56	52.37	12.97	5.46	27.47
F17	2022-08-22T08:13:53	52.1782	14.0851	3806	GPM-CORE	2022-08-22T08:17:14	84	-3	51.66	13.19	11.53	37.29
F17	2022-08-22T08:13:53	52.1782	14.0851	3806	ISS	2022-08-22T08:23:41	107	-10	51.23	13.83	14.32	38.11
F17	2022-08-22T09:10:52	52.4220	14.0932	20 764	METOP-B	2022-08-22T09:10:04	150	1	52.09	16.22	10.25	43.19
F17	2022-08-22T09:51:12	52.4680	13.9397	32 617	MICROMAS-2A	2022-08-22T10:22:22	225	-31	52.09	17.18	26.23	48.43
F17	2022-08-22T08:01:53	52.2092	14.1210	116	NOAA 19	2022-08-22T07:37:43	172	24	51.82	16.54	11.23	31.99
F17	2022-08-22T09:46:16	52.4610	13.9491	31 277	TERRA	2022-08-22T09:48:18	250	-2	51.99	17.52	19.23	46.44
F18	2022-08-22T12:42:33	52.2092	14.1210	121	AURA	2022-08-22T11:56:48	141	46	52.50	16.13	11.20	48.40
F18	2022-08-22T13:08:36	52.2646	14.0764	8417	CALIPSO	2022-08-22T13:09:27	116	-1	52.51	15.74	9.52	42.61
F18	2022-08-22T13:08:36	52.2646	14.0764	8417	CLOUDSAT	2022-08-22T13:10:12	134	-2	52.55	15.98	10.94	42.53
F18	2022-08-22T14:31:47	52.5156	13.9741	32 224	DMSP 5D-3 F16	2022-08-22T15:05:48	171	-34	52.92	16.41	11.29	27.50
F18	2022-08-22T14:18:28	52.4854	14.0163	28 649	DMSP 5D-3 F18	2022-08-22T14:22:04	32	-4	52.54	14.48	2.13	33.66
F18	2022-08-22T13:27:48	52.4033	14.0751	14 344	FENGYUN 3A	2022-08-22T13:27:10	222	1	51.95	10.92	14.69	40.58
F18	2022-08-22T12:42:33	52.2092	14.1210	121	GCOM-W1	2022-08-22T11:46:34	119	56	52.45	15.82	9.52	48.86
F18	2022-08-22T12:42:33	52.2092	14.1210	121	NOAA 20	2022-08-22T11:43:56	14	59	52.16	13.94	0.93	48.96
F19	2022-08-22T23:22:01	53.1936	14.3415	21 414	GOSAT	2022-08-22T23:20:09	34	2	53.25	14.85	2.89	-25.39
F19	2022-08-22T19:03:13	52.2091	14.1210	111	ICESAT-2	2022-08-22T19:00:50	212	2	52.34	17.22	23.42	-7.49
F19	2022-08-22T19:03:13	52.2091	14.1210	111	LANDSAT 7	2022-08-22T19:00:29	21	3	52.15	13.83	1.73	-7.45
F19	2022-08-22T19:49:08	52.2983	14.0677	8029	METOP-C	2022-08-22T19:50:34	28	-1	52.22	13.68	1.94	-13.67
F19	2022-08-22T20:39:08	52.8054	14.1117	12 621	NOAA 18	2022-08-22T20:40:07	128	-1	52.51	12.29	8.45	-18.57
F19	2022-08-22T23:45:29	53.2091	14.2633	22 953	TROPICS PATHFINDER	2022-08-23T00:15:34	276	-30	53.81	18.29	27.06	-23.75
F20	2022-08-23T01:27:29	52.5977	14.0208	27 324	AURA	2022-08-23T01:28:06	59	-1	52.46	14.85	4.71	-19.25
F20	2022-08-23T01:51:36	52.6369	13.9566	30 498	CALIPSO	2022-08-23T02:37:29	114	-46	52.39	15.58	9.31	-11.81
F20	2022-08-23T01:51:36	52.6369	13.9566	30 498	CLOUDSAT	2022-08-23T02:38:13	132	-47	52.36	15.85	10.82	-11.72
F20	2022-08-23T01:41:55	52.6257	13.9842	29 547	FENGYUN 3D	2022-08-23T01:42:22	6	0	52.60	14.06	0.42	-17.89
F20	2022-08-23T01:17:55	52.5886	14.0556	25 599	GCOM-W1	2022-08-23T01:17:52	33	0	52.50	14.52	2.67	-20.15
F20	2022-08-22T23:17:52	52.1837	14.0831	2174	GOSAT	2022-08-22T23:19:54	83	-2	52.34	15.27	6.96	-26.41

This table is continued on the next page.

Table H.1 – Continued from previous page

Flight	Timestamp [UTC]	Latitude [°N]	Longitude [°E]	Altitude [m]	Name	Overpass time [UTC]	Distance [km]	Offset [min]	Latitude [°N]	Longitude [°E]	Nadir [°]	Sun elev. [°]
F20	2022-08-23T00:58:44	52.5855	14.1368	21 999	GPM-CORE	2022-08-23T01:00:07	74	-1	53.05	13.35	10.15	-21.57
F20	2022-08-23T01:13:08	52.5834	14.0860	24 706	OCO 2	2022-08-23T01:12:42	165	0	52.25	16.44	13.02	-20.58
F21	2022-08-23T08:09:50	52.2092	14.1211	123	ISS	2022-08-23T07:35:03	59	35	51.68	14.05	8.03	31.38
F21	2022-08-23T08:32:15	52.2272	14.0873	7345	LANDSAT 7	2022-08-23T08:30:25	138	2	52.51	12.12	11.06	38.65
F21	2022-08-23T08:09:50	52.2092	14.1211	123	NOAA 15	2022-08-23T07:20:15	37	50	52.28	13.59	2.65	29.27
F22	2022-08-23T12:59:26	52.2091	14.1211	117	AQUA	2022-08-23T12:04:15	60	55	52.07	13.28	4.83	47.66
F22	2022-08-23T14:08:45	52.2905	14.1523	21 206	DMSP 5D-3 F18	2022-08-23T14:09:10	240	0	52.86	17.56	15.45	35.09
F22	2022-08-23T13:06:36	52.1951	14.1070	2313	FENGYUN 3A	2022-08-23T13:09:04	80	-2	52.35	15.25	5.43	42.36
F22	2022-08-23T12:59:26	52.2091	14.1211	117	GOSAT	2022-08-23T12:45:37	57	14	52.08	14.93	4.85	44.62
F23	2022-08-23T20:29:59	52.1896	14.0512	30 028	CRYOSAT 2	2022-08-23T20:58:13	197	-28	52.10	11.18	15.14	-21.01
F23	2022-08-23T20:29:59	52.1896	14.0512	30 028	LANDSAT 8	2022-08-23T20:50:15	274	-20	51.67	10.16	20.92	-20.31
F23	2022-08-23T20:25:50	52.1822	14.0656	28 711	NOAA 18	2022-08-23T20:27:52	95	-2	52.39	15.42	6.33	-18.17
F24	2022-08-23T21:55:00	52.2092	14.1210	128	CRYOSAT 2	2022-08-23T20:58:13	202	57	52.12	11.18	15.50	-21.02
F25	2022-08-24T01:34:15	52.1102	14.1007	12 884	AQUA	2022-08-24T01:35:32	153	-1	52.43	11.92	12.13	-19.19
F25	2022-08-24T01:23:03	52.1822	14.1132	8971	FENGYUN 3D	2022-08-24T01:23:57	293	-1	51.59	18.25	19.15	-20.22
F25	2022-08-24T01:20:22	52.1931	14.1165	7941	NOAA 20	2022-08-24T01:17:45	65	3	52.32	13.20	4.41	-20.76
F26	2022-08-24T08:54:11	52.1696	13.9536	25 255	CRYOSAT 2	2022-08-24T08:53:51	216	0	52.08	17.10	16.45	41.06
F26	2022-08-24T07:34:37	52.2091	14.1211	118	ICESAT-2	2022-08-24T07:29:18	4	5	52.20	14.17	0.42	30.32
F26	2022-08-24T07:34:37	52.2091	14.1211	118	ISS	2022-08-24T06:46:24	46	48	51.80	14.12	6.22	24.06
F26	2022-08-24T09:09:56	52.1976	13.8988	30 160	METOP-C	2022-08-24T09:21:18	22	-11	52.23	13.58	1.50	43.80
F27	2022-08-24T10:44:26	52.2074	14.1180	1228	MICROMAS-2A	2022-08-24T10:44:56	166	-1	52.53	11.74	20.04	48.78
F27	2022-08-24T10:41:31	52.2091	14.1211	116	NOAA 18	2022-08-24T10:24:23	292	17	52.93	9.99	18.85	48.15
F27	2022-08-24T11:53:41	52.1948	13.9867	21 823	SUOMI NPP	2022-08-24T11:57:37	226	-4	51.72	10.79	15.06	47.70
F28	2022-08-24T15:20:23	52.2373	13.9354	28 875	AEOLUS	2022-08-24T16:15:32	132	-55	52.47	15.83	22.64	16.45
F29	2022-08-24T18:56:31	52.2092	14.1210	111	LANDSAT 7	2022-08-24T18:43:04	264	13	52.79	17.89	20.46	-5.71
F29	2022-08-24T19:54:51	52.1927	13.9922	18 683	METOP-B	2022-08-24T19:56:38	131	-2	51.90	12.14	9.00	-15.07
F29	2022-08-24T20:39:57	52.2098	13.8314	32 415	MICROMAS-2A	2022-08-24T21:21:04	23	-41	52.16	13.51	2.85	-23.10
F29	2022-08-24T20:11:57	52.2023	13.9547	23 720	NOAA 18	2022-08-24T20:15:48	300	-4	52.95	18.20	19.12	-17.19
F29	2022-08-24T20:39:57	52.2098	13.8314	32 415	TERRA	2022-08-24T20:47:31	146	-8	51.91	11.76	11.57	-20.31

This table is continued on the next page.

Table H.1 – Continued from previous page

Flight	Timestamp [UTC]	Latitude [°N]	Longitude [°E]	Altitude [m]	Name	Overpass time [UTC]	Distance [km]	Offset [min]	Latitude [°N]	Longitude [°E]	Nadir [°]	Sun elev. [°]
F30	2022-08-24T23:12:22	52.2061	13.9882	15 117	GOSAT 2	2022-08-24T23:12:22	128	0	52.46	15.81	11.54	-27.12
F31	2022-08-28T18:44:46	52.2091	14.1211	113	NOAA 19	2022-08-28T17:58:28	249	46	52.83	17.64	16.13	-0.61
F31	2022-08-28T20:23:47	52.2570	14.5810	30 171	TERRA	2022-08-28T20:22:54	209	1	52.71	17.57	16.34	-19.55
F32	2022-08-28T23:20:02	52.2556	14.6660	23 048	GOSAT	2022-08-28T23:20:02	42	0	52.32	15.27	3.56	-28.37
F32	2022-08-28T22:53:53	52.2264	14.5979	15 507	GPM-CORE	2022-08-28T22:53:12	164	1	51.24	16.36	21.61	-28.48
F32	2022-08-28T23:43:14	52.2403	14.6584	30 392	TROPICS PATHFINDER	2022-08-29T00:25:04	126	-42	52.48	16.46	13.28	-26.01
F33	2022-08-29T09:15:54	52.1620	14.6668	20 161	METOP-C	2022-08-29T09:17:46	16	-2	52.18	14.44	1.10	42.30
F33	2022-08-29T08:10:10	52.2091	14.1211	116	NOAA 19	2022-08-29T07:55:08	100	15	52.43	12.70	6.59	32.62
F33	2022-08-29T09:47:12	52.1623	14.6847	30 288	TERRA	2022-08-29T09:54:17	89	-7	51.97	15.95	7.15	45.12
F34	2022-08-29T12:59:18	52.2091	14.1211	118	AURA	2022-08-29T12:02:51	41	56	52.28	14.71	3.30	45.61
F34	2022-08-29T14:33:41	52.2326	14.7019	30 529	DMSP 5D-3 F16	2022-08-29T15:15:30	19	-42	52.17	14.45	1.24	23.49
F34	2022-08-29T14:33:41	52.2326	14.7019	30 529	DMSP 5D-3 F18	2022-08-29T14:32:48	189	1	51.82	12.02	12.33	29.63
F34	2022-08-29T12:59:18	52.2091	14.1211	118	FENGYUN 3A	2022-08-29T13:01:27	194	-2	52.64	16.88	12.95	41.04
F34	2022-08-29T12:59:18	52.2091	14.1211	118	GOSAT	2022-08-29T12:45:45	57	14	52.08	14.93	4.85	42.50
F35	2022-08-29T18:45:34	52.1965	14.1358	2057	ICESAT-2	2022-08-29T19:09:47	284	-24	52.11	9.99	29.99	-11.01
F35	2022-08-29T18:49:52	52.1937	14.1593	3387	LANDSAT 7	2022-08-29T18:48:20	167	2	52.54	16.55	13.37	-8.12
F35	2022-08-29T20:13:12	52.2846	14.8292	25 914	LANDSAT 8	2022-08-29T20:13:32	282	0	52.93	18.85	21.48	-18.99
F35	2022-08-29T19:51:54	52.2789	14.8232	20 101	METOP-B	2022-08-29T19:53:06	131	-1	51.99	12.98	8.93	-16.71
F35	2022-08-29T20:40:25	52.2383	14.8529	32 267	MICROMAS-2A	2022-08-29T21:30:25	242	-50	51.83	11.39	27.82	-25.79
F35	2022-08-29T18:39:38	52.2092	14.1211	120	NOAA 15	2022-08-29T17:53:59	98	46	51.98	12.74	6.91	-0.28
F36	2022-08-29T22:00:24	52.2092	14.1210	117	MICROMAS-2A	2022-08-29T21:30:25	192	30	51.87	11.37	22.83	-25.62
F37	2022-08-30T08:47:00	52.2036	14.6017	14 644	CRYOSAT 2	2022-08-30T08:48:08	35	-1	52.20	14.09	2.75	39.00
F37	2022-08-30T08:15:53	52.1912	14.1641	5443	LANDSAT 7	2022-08-30T08:18:16	47	-2	52.08	14.83	3.84	35.34
F37	2022-08-30T09:36:58	52.2237	14.7489	29 437	LANDSAT 8	2022-08-30T09:44:53	194	-8	51.84	17.51	15.24	44.13
F37	2022-08-30T09:36:58	52.2237	14.7489	29 437	MICROMAS-2A	2022-08-30T10:18:58	234	-42	51.82	18.10	27.10	46.01
F37	2022-08-30T07:58:41	52.2091	14.1211	123	NOAA 19	2022-08-30T07:43:13	99	15	51.97	15.51	6.51	30.76
F38	2022-08-30T13:09:33	52.2092	14.1211	119	CALIPSO	2022-08-30T13:12:04	84	-3	52.38	15.32	6.94	39.60
F38	2022-08-30T13:09:33	52.2092	14.1211	119	CLOUDSAT	2022-08-30T13:12:41	104	-3	52.42	15.61	8.57	39.53
F38	2022-08-30T14:49:26	52.2313	14.8498	30 225	DMSP 5D-3 F16	2022-08-30T15:02:30	187	-13	52.67	17.50	12.34	24.98

This table is continued on the next page.

Table H.1 – Continued from previous page

Flight	Timestamp [UTC]	Latitude [°N]	Longitude [°E]	Altitude [m]	Name	Overpass time [UTC]	Distance [km]	Offset [min]	Latitude [°N]	Longitude [°E]	Nadir [°]	Sun elev. [°]
F38	2022-08-30T14:21:25	52.2335	14.7827	21 628	DMSP 5D-3 F18	2022-08-30T14:19:56	19	1	52.25	15.06	1.25	31.02
F39	2022-08-30T18:45:49	52.2092	14.1211	118	ICESAT-2	2022-08-30T18:44:09	107	2	52.26	15.68	12.37	-7.85
F39	2022-08-30T19:30:28	52.1685	14.6274	14 097	METOP-B	2022-08-30T19:32:20	229	-2	52.70	17.87	15.35	-14.53
F39	2022-08-30T20:36:47	52.1477	14.8732	31 200	NOAA 18	2022-08-30T20:44:05	221	-7	51.67	11.76	14.44	-22.54
F40	2022-08-30T23:08:47	52.1485	14.7337	19 432	GOSAT 2	2022-08-30T23:12:18	81	-4	52.30	15.89	7.34	-29.26
F40	2022-08-30T22:41:09	52.1519	14.4806	12 642	GPM-CORE	2022-08-30T22:42:26	138	-1	53.02	13.03	18.47	-29.14
F41	2022-08-31T09:21:05	52.1641	14.5769	24 305	METOP-B	2022-08-31T09:23:51	118	-3	52.42	12.90	8.09	42.18
F41	2022-08-31T08:01:20	52.2092	14.1211	113	NOAA 15	2022-08-31T07:17:24	11	44	52.17	14.26	0.75	26.91
F41	2022-08-31T09:43:06	52.1738	14.6146	31 432	TERRA	2022-08-31T09:41:58	300	1	51.62	18.88	22.68	43.61
F42	2022-08-31T11:51:00	52.1966	14.4814	16 457	AURA	2022-08-31T11:50:35	220	0	52.69	17.62	17.13	45.43
F42	2022-08-31T12:25:23	52.1871	14.5784	26 468	FENGYUN 3D	2022-08-31T12:24:00	264	1	51.64	10.85	17.43	43.41
F42	2022-08-31T11:39:02	52.2056	14.3584	13 387	GCOM-W1	2022-08-31T11:40:17	207	-1	52.66	17.31	16.18	45.86
F42	2022-08-31T12:28:38	52.1832	14.5952	27 487	GOSAT 2	2022-08-31T12:29:03	168	0	51.86	16.98	15.01	43.03
F42	2022-08-31T11:26:15	52.1727	14.1672	9 521	SUOMI NPP	2022-08-31T11:26:17	281	0	52.85	18.16	18.49	46.32
F43	2022-08-31T15:39:22	52.1633	14.6183	29 830	AEOLUS	2022-08-31T16:15:46	82	-36	52.30	15.80	14.57	13.75
F43	2022-08-31T14:06:39	52.2058	14.1014	2 516	DMSP 5D-3 F18	2022-08-31T14:07:07	274	0	52.87	17.99	17.50	32.75
F43	2022-08-31T15:39:22	52.1633	14.6183	29 830	METEOR-M 2	2022-08-31T16:34:44	263	-55	52.77	18.35	17.47	10.83
F44	2022-08-31T20:04:44	52.1117	14.4650	21 815	METOP-C	2022-08-31T20:04:16	280	0	51.55	10.51	18.53	-18.64
F44	2022-08-31T20:31:33	52.0859	14.4856	29 223	NOAA 18	2022-08-31T20:31:59	9	0	52.09	14.62	0.63	-21.63
F44	2022-08-31T20:41:58	52.0876	14.5217	31 814	TERRA	2022-08-31T20:53:23	293	-11	51.54	10.37	22.21	-23.68
F45	2022-08-31T23:19:54	52.0851	14.3903	20 980	GOSAT	2022-08-31T23:20:04	66	0	52.20	15.33	5.54	-29.62
F45	2022-08-31T23:29:31	52.0771	14.4034	23 562	GOSAT 2	2022-08-31T23:28:19	164	1	51.75	12.08	14.68	-29.49
F46	2022-09-01T08:46:03	52.1236	14.0171	12 867	CRYOSAT 2	2022-09-01T08:46:15	65	0	52.14	13.07	5.09	38.02
F46	2022-09-01T08:08:32	52.2092	14.1210	117	ICESAT-2	2022-09-01T07:12:35	102	56	52.26	12.63	11.81	25.98
F46	2022-09-01T09:03:36	52.0933	14.1650	17 412	METOP-B	2022-09-01T09:03:06	253	1	51.58	17.74	16.90	39.86
F46	2022-09-01T09:42:35	52.0796	14.2423	29 050	MICROMAS-2A	2022-09-01T10:41:06	103	-59	52.27	12.76	12.81	46.07
F47	2022-09-01T11:56:32	52.1142	14.1607	16 349	AQUA	2022-09-01T11:55:53	82	1	52.28	15.33	6.61	44.95
F47	2022-09-01T12:04:14	52.1065	14.2209	18 455	FENGYUN 3D	2022-09-01T12:05:28	71	-1	52.25	15.24	4.88	44.43
F47	2022-09-01T12:39:25	52.1120	14.2976	29 360	GOSAT	2022-09-01T12:45:50	43	-6	52.01	14.90	3.64	41.42

This table is continued on the next page.

Table H.1 – Continued from previous page

Flight	Timestamp [UTC]	Latitude [°N]	Longitude [°E]	Altitude [m]	Name	Overpass time [UTC]	Distance [km]	Offset [min]	Latitude [°N]	Longitude [°E]	Nadir [°]	Sun elev. [°]
F47	2022-09-01T12:39:25	52.1120	14.2976	29360	GOSAT 2	2022-09-01T12:45:06	83	-6	52.27	13.12	7.54	41.49
F47	2022-09-01T11:05:05	52.2092	14.1210	120	MICROMAS-2A	2022-09-01T10:41:04	92	24	52.38	12.81	11.39	45.93
F47	2022-09-01T11:56:32	52.1142	14.1607	16349	NOAA 20	2022-09-01T11:56:34	225	0	51.64	10.98	15.02	44.91
F48	2022-09-01T18:30:00	52.2091	14.1210	122	FENGYUN 3C	2022-09-01T17:45:17	222	45	51.75	10.98	14.74	0.02
F48	2022-09-01T19:12:59	52.1401	14.1373	13439	LANDSAT 7	2022-09-01T19:11:02	214	2	51.73	11.10	16.85	-12.24
F48	2022-09-01T20:21:28	52.0860	14.4248	32061	LANDSAT 8	2022-09-01T20:44:04	192	-23	51.70	11.70	15.08	-23.15
F48	2022-09-01T19:45:16	52.0977	14.3502	21950	METOP-C	2022-09-01T19:43:29	75	2	52.25	15.41	5.14	-16.51
F48	2022-09-01T20:21:28	52.0860	14.4248	32061	MICROMAS-2A	2022-09-01T21:17:03	19	-56	52.11	14.70	2.40	-25.96
F48	2022-09-01T20:21:28	52.0860	14.4248	32061	NOAA 18	2022-09-01T20:19:54	213	2	52.59	17.44	13.96	-20.72
F49	2022-09-02T00:28:22	52.1126	14.4653	29625	AQUA	2022-09-02T01:27:11	35	-59	52.17	13.96	2.86	-22.52
F49	2022-09-02T00:28:22	52.1126	14.4653	29625	SUOMI NPP	2022-09-02T01:00:06	214	-32	51.67	17.49	14.32	-24.97
F50	2022-09-02T09:36:17	52.1914	14.3820	28032	LANDSAT 8	2022-09-02T10:15:30	290	-39	52.86	10.26	21.98	44.81
F50	2022-09-02T09:36:17	52.1914	14.3820	28032	METOP-C	2022-09-02T09:35:00	280	1	52.86	10.41	18.58	42.36
F50	2022-09-02T09:36:17	52.1914	14.3820	28032	NOAA 18	2022-09-02T10:16:27	173	-40	52.59	11.93	11.47	44.85
F51	2022-09-02T13:25:00	52.2423	14.4385	27387	CALIPSO	2022-09-02T13:25:13	152	0	51.93	12.28	12.36	36.93
F51	2022-09-02T13:25:00	52.2423	14.4385	27387	CLOUDSAT	2022-09-02T13:25:49	131	-1	51.96	12.58	10.75	36.87
F51	2022-09-02T12:52:41	52.2305	14.3185	17825	FENGYUN 3A	2022-09-02T13:29:53	299	-37	51.65	10.07	19.46	36.47
F51	2022-09-02T11:54:00	52.2092	14.1210	117	NOAA 20	2022-09-02T11:37:46	88	16	52.39	15.37	6.00	45.23
F51	2022-09-02T13:32:59	52.2610	14.4769	29855	TROPICS PATHFINDER	2022-09-02T14:03:04	184	-30	52.63	11.84	19.24	32.34
F52	2022-09-05T08:42:44	52.1003	14.5984	15816	CRYOSAT 2	2022-09-05T08:42:26	243	0	52.26	11.06	18.28	36.70
F52	2022-09-05T07:53:37	52.2092	14.1211	115	FENGYUN 3C	2022-09-05T06:54:14	86	59	52.01	15.33	5.78	22.32
F52	2022-09-05T07:53:37	52.2092	14.1211	115	ICESAT-2	2022-09-05T07:04:15	155	49	52.30	11.85	17.56	23.77
F52	2022-09-05T09:18:04	52.0497	14.8203	26107	METOP-B	2022-09-05T09:20:21	80	-2	52.21	13.68	5.52	40.48
F52	2022-09-05T09:31:04	52.0322	14.8706	30067	TERRA	2022-09-05T10:00:14	30	-29	52.08	14.44	2.43	43.28
F53	2022-09-05T12:53:57	52.2092	14.1210	116	AURA	2022-09-05T12:08:52	59	45	52.07	13.29	4.76	42.65
F53	2022-09-05T14:39:19	52.0548	14.9668	31837	DMSP 5D-3 F16	2022-09-05T15:25:16	185	-46	51.65	12.37	12.21	19.55
F53	2022-09-05T12:53:57	52.2092	14.1210	116	GCOM-W1	2022-09-05T11:58:32	80	55	52.03	12.99	6.42	43.23
F54	2022-09-05T19:54:49	52.0924	14.6752	17687	CRYOSAT 2	2022-09-05T19:56:18	162	-1	52.18	17.03	12.52	-19.65
F54	2022-09-05T20:30:19	52.0242	14.8702	28821	GPM-CORE	2022-09-05T20:38:29	83	-8	51.52	15.74	11.25	-24.32

This table is continued on the next page.

Table H.1 – Continued from previous page

Flight	Timestamp [UTC]	Latitude [°N]	Longitude [°E]	Altitude [m]	Name	Overpass time [UTC]	Distance [km]	Offset [min]	Latitude [°N]	Longitude [°E]	Nadir [°]	Sun elev. [°]
F54	2022-09-05T20:14:15	52.0526	14.7930	23 562	LANDSAT 8	2022-09-05T20:19:36	193	-5	52.47	17.53	15.10	-22.34
F54	2022-09-05T20:01:07	52.0772	14.7265	19 538	METOP-C	2022-09-05T20:00:43	238	0	51.59	11.36	15.94	-20.20
F55	2022-09-05T23:12:36	52.0824	14.7917	22 044	GOSAT 2	2022-09-05T23:12:14	79	0	52.23	15.92	7.21	-31.51
F56	2022-09-06T08:05:54	52.2204	14.1166	3 282	LANDSAT 7	2022-09-06T08:06:05	244	0	51.77	17.59	19.05	31.86
F56	2022-09-06T09:28:56	52.0864	14.9672	29 046	LANDSAT 8	2022-09-06T09:51:05	73	-22	51.93	16.00	5.88	42.39
F56	2022-09-06T08:58:06	52.1303	14.8247	20 000	METOP-B	2022-09-06T08:59:33	269	-1	51.59	18.63	17.88	38.22
F56	2022-09-06T07:56:52	52.2091	14.1210	121	NOAA 19	2022-09-06T08:00:37	172	-4	52.62	11.69	11.15	31.18
F57	2022-09-06T12:52:23	52.2091	14.1210	116	AQUA	2022-09-06T12:13:01	202	39	51.80	11.26	15.80	42.02
F57	2022-09-06T14:39:31	52.0899	15.1407	32 601	DMSP 5D-3 F16	2022-09-06T15:12:16	21	-33	52.12	15.44	1.42	21.02
F57	2022-09-06T14:35:46	52.0870	15.1112	31 561	DMSP 5D-3 F18	2022-09-06T14:30:41	183	5	51.69	12.53	11.95	26.98
F57	2022-09-06T12:52:23	52.2091	14.1210	116	FENGYUN 3D	2022-09-06T12:13:25	53	39	52.07	13.38	3.65	41.99
F57	2022-09-06T12:52:23	52.2091	14.1210	116	GOSAT 2	2022-09-06T12:29:00	200	23	51.83	16.97	17.73	40.91
F58	2022-09-06T19:42:44	52.0249	14.8707	18 344	METOP-C	2022-09-06T19:39:55	101	3	52.23	16.30	6.90	-18.18
F58	2022-09-06T20:34:47	51.9601	15.1777	32 844	MICROMAS-2A	2022-09-06T21:24:56	155	-50	51.68	12.98	18.85	-28.75
F58	2022-09-06T18:39:30	52.2092	14.1210	119	NOAA 15	2022-09-06T17:51:07	50	48	52.08	13.43	3.52	-2.57
F58	2022-09-06T20:17:33	51.9562	15.0906	28 360	TERRA	2022-09-06T20:16:25	286	1	52.61	19.15	21.78	-22.57
F59	2022-09-06T23:18:55	51.9755	14.9903	26 892	GOSAT	2022-09-06T23:20:08	30	-1	52.02	15.42	2.50	-31.86
F59	2022-09-06T23:28:41	51.9743	15.0415	29 954	GOSAT 2	2022-09-06T23:28:14	204	0	51.59	12.16	18.01	-31.70
F59	2022-09-06T23:31:40	51.9764	15.0650	30 853	ISS	2022-09-07T00:19:25	128	-48	50.85	15.43	16.74	-29.50
F59	2022-09-06T21:55:40	52.2092	14.1210	122	MICROMAS-2A	2022-09-06T21:25:01	90	31	52.04	12.83	11.30	-28.23
F60	2022-09-07T08:21:15	52.2377	14.4111	11 807	CRYOSAT 2	2022-09-07T08:40:30	296	-19	52.45	10.08	21.89	35.71
F60	2022-09-07T09:17:40	52.1577	14.9014	28 635	METOP-C	2022-09-07T09:31:28	259	-14	52.77	11.23	17.25	40.65
F60	2022-09-07T07:45:27	52.2091	14.1211	116	NOAA 19	2022-09-07T07:48:42	27	-3	52.13	14.49	1.76	29.37
F60	2022-09-07T09:17:40	52.1577	14.9014	28 635	TERRA	2022-09-07T09:47:53	176	-30	51.81	17.40	13.89	41.77
F61	2022-09-07T12:30:20	52.2092	14.1210	121	AURA	2022-09-07T11:56:36	145	34	52.51	16.18	11.48	42.56
F61	2022-09-07T13:57:35	52.2005	14.9617	26 891	CALIPSO	2022-09-07T13:14:35	2	43	52.18	14.96	0.17	36.05
F61	2022-09-07T13:24:08	52.2302	14.7166	17 305	CLOUDSAT	2022-09-07T13:15:09	36	9	52.29	15.24	3.02	36.07
F61	2022-09-07T14:01:47	52.2026	14.9976	28 133	DMSP 5D-3 F16	2022-09-07T14:59:19	241	-58	52.79	18.41	15.73	22.60
F61	2022-09-07T14:01:47	52.2026	14.9976	28 133	DMSP 5D-3 F18	2022-09-07T14:17:51	35	-16	52.26	15.50	2.30	28.37

This table is continued on the next page.

Table H.1 – Continued from previous page

Flight	Timestamp [UTC]	Latitude [°N]	Longitude [°E]	Altitude [m]	Name	Overpass time [UTC]	Distance [km]	Offset [min]	Latitude [°N]	Longitude [°E]	Nadir [°]	Sun elev. [°]
F61	2022-09-07T12:30:20	52.2092	14.1210	121	FENGYUN 3D	2022-09-07T11:54:55	252	35	52.82	17.69	16.68	42.64
F61	2022-09-07T12:30:20	52.2092	14.1210	121	GCOM-W1	2022-09-07T11:46:15	124	44	52.47	15.89	9.89	43.03
F61	2022-09-07T12:45:41	52.2249	14.2008	5468	GOSAT	2022-09-07T12:45:57	53	0	52.10	14.95	4.46	39.11
F61	2022-09-07T12:45:41	52.2249	14.2008	5468	GOSAT 2	2022-09-07T12:45:02	73	1	52.36	13.16	6.62	39.19
F61	2022-09-07T12:30:20	52.2092	14.1210	121	NOAA 20	2022-09-07T11:44:05	17	46	52.15	13.89	1.17	43.11
F61	2022-09-07T12:30:20	52.2092	14.1210	121	OCO 2	2022-09-07T11:41:09	256	49	52.79	17.76	19.66	43.22
F62	2022-09-07T19:52:52	52.2091	14.1214	120	CRYOSAT 2	2022-09-07T19:54:26	129	-2	52.27	16.01	10.04	-19.83
F62	2022-09-07T20:27:35	52.2552	14.4300	13 544	GPM-CORE	2022-09-07T20:29:14	193	-2	53.49	12.42	24.81	-23.80
F62	2022-09-07T20:47:01	52.2454	14.6395	20 440	NOAA 18	2022-09-07T20:48:16	271	-1	51.68	10.81	17.53	-25.74
F63	2022-09-08T00:13:17	52.2364	14.8632	28 146	ISS	2022-09-08T01:07:38	52	-54	51.77	14.83	7.02	-25.98
F63	2022-09-08T00:13:17	52.2364	14.8632	28 146	OCO 2	2022-09-08T01:12:30	108	-59	52.00	16.39	8.64	-25.53
F64	2022-09-08T09:15:44	52.4047	14.7835	28 605	LANDSAT 8	2022-09-08T09:38:45	299	-23	51.85	19.05	22.61	40.58
F64	2022-09-08T09:09:42	52.4003	14.7538	26 722	METOP-C	2022-09-08T09:10:39	101	-1	52.17	16.18	6.95	38.37
F64	2022-09-08T07:41:55	52.2092	14.1211	116	NOAA 15	2022-09-08T07:14:33	58	27	52.07	14.94	4.12	24.46
F64	2022-09-08T07:41:55	52.2092	14.1211	116	NOAA 19	2022-09-08T07:36:45	227	5	51.71	17.33	14.60	27.51
F65	2022-09-08T11:59:39	52.2217	14.1206	1103	AQUA	2022-09-08T12:00:15	12	-1	52.23	14.29	0.96	41.98
F65	2022-09-08T14:05:17	52.6967	14.8583	25 310	DMSP 5D-3 F18	2022-09-08T14:05:09	236	0	53.26	18.24	15.19	29.47
F65	2022-09-08T13:22:36	52.7331	14.5254	17 553	FENGYUN 3A	2022-09-08T13:22:21	208	0	52.30	11.54	13.92	34.65
F65	2022-09-08T11:55:18	52.2091	14.1210	115	NOAA 20	2022-09-08T11:25:17	292	30	52.92	18.27	19.12	43.31
F66	2022-09-08T18:58:11	52.2091	14.1211	119	LANDSAT 7	2022-09-08T18:58:52	21	-1	52.15	13.82	1.75	-13.05
F66	2022-09-08T19:54:05	52.4902	14.3332	18 450	LANDSAT 8	2022-09-08T20:50:23	300	-56	51.93	10.05	22.66	-26.01
F66	2022-09-08T19:46:50	52.4841	14.2660	16 392	METOP-B	2022-09-08T19:46:09	16	1	52.50	14.50	1.09	-19.10
F66	2022-09-08T20:35:28	52.4828	14.6091	31 428	NOAA 18	2022-09-08T20:36:13	73	-1	52.30	13.57	4.92	-24.78
F67	2022-09-09T00:07:24	52.5184	14.7071	32 237	ISS	2022-09-09T00:19:09	87	-12	51.74	14.76	11.52	-29.79
F68	2022-09-09T07:37:27	52.2091	14.1211	115	ICESAT-2	2022-09-09T06:55:53	208	42	52.34	11.09	22.87	21.55
F68	2022-09-09T08:27:08	52.4537	14.4889	15 008	LANDSAT 7	2022-09-09T08:28:43	157	-2	52.78	12.24	12.55	33.70
F69	2022-09-09T13:05:05	52.4488	14.4728	12 731	FENGYUN 3A	2022-09-09T13:04:15	99	1	52.65	15.90	6.75	36.37
F69	2022-09-09T12:23:38	52.2092	14.1210	126	SUOMI NPP	2022-09-09T11:57:45	237	26	51.72	10.77	15.74	41.73
F69	2022-09-09T13:58:15	52.5149	14.8948	28 056	TROPICS PATHFINDER	2022-09-09T13:57:56	115	0	52.74	13.23	12.46	30.10

This table is continued on the next page.

Table H.1 – Continued from previous page

Flight	Timestamp [UTC]	Latitude [°N]	Longitude [°E]	Altitude [m]	Name	Overpass time [UTC]	Distance [km]	Offset [min]	Latitude [°N]	Longitude [°E]	Nadir [°]	Sun elev. [°]
F70	2022-09-09T19:53:20	52.4394	14.5059	17 321	CRYOSAT 2	2022-09-09T19:52:35	31	1	52.43	14.97	2.47	-20.39
F70	2022-09-09T20:30:12	52.4161	14.7565	28 679	MICROMAS-2A	2022-09-09T21:10:37	107	-40	52.62	16.29	13.24	-28.32
F70	2022-09-09T20:27:38	52.4217	14.7388	27 872	NOAA 18	2022-09-09T20:24:07	120	4	52.69	16.45	8.01	-24.03
F70	2022-09-09T20:30:12	52.4161	14.7565	28 679	TERRA	2022-09-09T20:47:03	214	-17	52.00	11.70	16.69	-26.30
F71	2022-09-09T23:20:07	52.4670	14.5075	19 695	GOSAT	2022-09-09T23:20:21	46	0	52.54	15.17	3.89	-32.51
F71	2022-09-09T23:33:26	52.4587	14.6068	23 625	ISS	2022-09-09T23:30:40	122	3	51.37	14.84	16.02	-32.30
F71	2022-09-09T23:57:59	52.4628	14.7652	31 224	TROPICS PATHFINDER	2022-09-10T00:43:41	189	-46	52.12	12.05	19.60	-28.48
F72	2022-09-12T09:25:19	51.6805	14.5339	29 037	METOP-C	2022-09-12T09:28:05	195	-3	52.12	11.79	13.23	39.03
F72	2022-09-12T09:25:19	51.6805	14.5339	29 037	MICROMAS-2A	2022-09-12T10:20:01	240	-55	51.28	17.92	27.55	41.94
F72	2022-09-12T07:51:33	52.2091	14.1211	119	NOAA 15	2022-09-12T07:13:06	82	38	52.01	15.28	5.79	23.20
F72	2022-09-12T09:25:19	51.6805	14.5339	29 037	NOAA 18	2022-09-12T09:56:31	143	-31	51.36	16.52	9.51	40.89
F72	2022-09-12T09:25:19	51.6805	14.5339	29 037	TERRA	2022-09-12T10:06:13	122	-41	51.92	12.82	9.70	41.38
F73	2022-09-12T12:13:25	52.1518	14.1542	5 594	AURA	2022-09-12T12:15:00	162	-2	51.82	11.85	12.84	39.61
F73	2022-09-12T13:02:27	51.7563	14.5140	19 056	CALIPSO	2022-09-12T13:03:52	228	-1	52.27	17.73	18.16	35.77
F73	2022-09-12T13:02:27	51.7563	14.5140	19 056	CLOUDSAT	2022-09-12T13:04:23	250	-2	52.32	18.04	19.81	35.72
F73	2022-09-12T12:04:25	52.2013	14.1303	2 718	FENGYUN 3D	2022-09-12T12:02:49	125	2	52.47	15.91	8.51	40.30
F73	2022-09-12T12:04:25	52.2013	14.1303	2 718	GCOM-W1	2022-09-12T12:04:29	180	0	51.84	11.58	14.16	40.21
F73	2022-09-12T12:27:01	52.0086	14.2198	9 948	GOSAT 2	2022-09-12T12:29:02	189	-2	51.65	16.90	16.76	38.73
F73	2022-09-12T11:55:25	52.2091	14.1210	117	NOAA 20	2022-09-12T11:50:24	122	5	51.93	12.39	8.32	40.91
F73	2022-09-12T11:59:55	52.2078	14.1239	1 400	OCO 2	2022-09-12T11:59:23	46	1	52.10	13.48	3.70	40.48
F74	2022-09-12T19:54:55	51.7918	14.7534	29 537	LANDSAT 8	2022-09-12T20:25:43	102	-31	51.99	16.19	8.14	-25.81
F74	2022-09-12T19:54:55	51.7918	14.7534	29 537	METOP-B	2022-09-12T20:03:12	285	-8	51.22	10.75	18.86	-23.31
F74	2022-09-12T18:19:55	52.1825	14.1663	4 725	NOAA 19	2022-09-12T18:21:17	94	-1	51.95	12.85	6.23	-9.20
F75	2022-09-12T22:54:51	51.8515	14.7367	28 162	GOSAT	2022-09-12T23:20:15	50	-25	51.94	15.45	4.22	-34.23
F75	2022-09-12T22:54:51	51.8515	14.7367	28 162	GOSAT 2	2022-09-12T23:28:11	181	-33	51.50	12.19	16.07	-34.06
F75	2022-09-12T22:40:13	51.8671	14.6835	23 420	ISS	2022-09-12T22:41:50	18	-2	51.70	14.69	2.47	-34.32
F75	2022-09-12T21:16:15	52.2091	14.1210	112	LANDSAT 8	2022-09-12T20:25:51	130	50	52.48	15.97	10.32	-25.25
F76	2022-09-13T09:08:41	52.0101	15.0475	18 175	METOP-C	2022-09-13T09:07:13	128	1	51.72	16.85	8.79	36.87
F77	2022-09-13T12:15:15	52.1338	14.5382	8 605	AQUA	2022-09-13T12:17:17	298	-2	51.57	10.32	22.56	38.98

This table is continued on the next page.

Table H.1 – Continued from previous page

Flight	Timestamp [UTC]	Latitude [°N]	Longitude [°E]	Altitude [m]	Name	Overpass time [UTC]	Distance [km]	Offset [min]	Latitude [°N]	Longitude [°E]	Nadir [°]	Sun elev. [°]
F77	2022-09-13T12:44:25	51.9135	15.0740	17837	GOSAT	2022-09-13T12:46:08	14	-2	51.93	14.87	1.21	36.73
F77	2022-09-13T12:44:25	51.9135	15.0740	17837	GOSAT 2	2022-09-13T12:45:03	140	-1	52.19	13.09	12.59	36.82
F77	2022-09-13T11:49:44	52.2092	14.1211	122	NOAA 20	2022-09-13T11:31:35	189	18	52.64	16.80	12.69	41.21
F78	2022-09-13T19:42:08	51.9032	15.5492	32424	CRYOSAT 2	2022-09-13T19:48:37	173	-6	51.82	13.04	13.32	-22.26
F78	2022-09-13T18:26:00	52.0760	14.7049	9547	GPM-CORE	2022-09-13T18:25:47	18	0	51.96	14.88	2.51	-10.57
F78	2022-09-13T19:09:01	51.8803	15.3659	22159	LANDSAT 7	2022-09-13T19:03:59	192	5	51.51	12.66	15.21	-16.41
F78	2022-09-13T19:42:08	51.9032	15.5492	32424	METOP-B	2022-09-13T19:42:24	9	0	51.90	15.67	0.59	-21.50
F78	2022-09-13T18:09:14	52.1825	14.3216	4391	NOAA 19	2022-09-13T18:09:21	95	0	52.39	15.67	6.29	-7.90
F78	2022-09-13T19:42:08	51.9032	15.5492	32424	TERRA	2022-09-13T20:22:15	157	-40	52.23	17.77	12.42	-26.08
F79	2022-09-13T21:52:33	51.9492	15.1532	13623	ISS	2022-09-13T21:53:21	70	-1	51.33	15.29	9.39	-33.17
F79	2022-09-13T21:07:35	52.2091	14.1210	120	TERRA	2022-09-13T20:22:24	240	45	52.74	17.54	18.53	-25.27

I MATHEMATICAL DESCRIPTION OF THE CWSs ASSEMBLY

I.1 INTRODUCTION

In what follows, we refer to the different balloon flights of the UAI 2022 field campaign as measurement *events*. For each event $e \in [1; \dots; N]$, M radiosondes are flown together. Out of these, 2 reference sondes are used to generate GDPs (see Section 4.3.10). Each radiosonde provides measurements of geophysical variables at a frequency of 1 Hz (see Section 9.5.3), resulting in K_e distinct time steps from launch to balloon burst for the event e .

Terminology 4 We define $x_{e,p,i}$ the measured quantity value of a geophysical variable x (either pressure, temperature, relative humidity, geopotential height, wind (horizontal) speed, or wind (horizontal) direction) measured by a specific radiosonde \mathcal{R} with index $p \in [1; \dots; M]$ during the event e at the time step $i \in [0; 1; \dots; K_e - 1]$.

Terminology 5 Given a mathematical variable y , we define $V(y)$ its variance, $\sigma = \sqrt{V(y)}$ its standard deviation, and $\langle y \rangle$ its expectation value, such that $V(y) = \langle y^2 \rangle - \langle y \rangle^2$.

I.2 GDP UNCERTAINTIES

The RS41 GDP version 1 specifies up to three distinct types of measurement uncertainties (at a coverage factor of $k = 2$) for each $x_{e,p,i}$ measurement point: a so-called *uncorrelated* (i.e. random) component $\sigma_{e,p,i}^U$ (tagged `_uc_ucor` in the NetCDF file of the GDPs), and two *correlated* (i.e. systematic) components $\sigma_{e,p,i}^S$ and $\sigma_{e,p,i}^T$ (tagged `_uc_scor` and `_uc_tcor`, respectively).

$\sigma_{e,p,i}^S$ (where S refers to *spatial*) includes all the uncertainty contributions that are correlated between different time steps within a given event, but not across different ones. $\sigma_{e,p,i}^T$ (where T refers to *temporal*) includes all the uncertainty contributions that are correlated within a single event, and also over longer periods of time (and thus across different RS41 GDP profiles acquired over multiple events). We note that in version 1 of the RS41 GDP, $\sigma_{e,p,i}^S$ is exactly 0 for all variables except for the atmospheric temperature during daytime flights (Sommer et al., 2022, 2023). For the wind (horizontal) direction and wind (horizontal) speed, $\sigma_{e,p,i}^T$ is always exactly 0.

The IMS-100 GDP version 2 does not follow exactly the same scheme. It provides a *total correlated* component, that essentially incorporate both the spatial and temporal components specified separately by the RS41 GDP version 1.

Given this state-of-affair, we adopt a statistical treatment of uncertainties capable of correctly handling three distinct components (see e.g. Barlow, 1997, for a general description). We assume that:

$$x_{e,p,i} = x_{e,p,i}^S + x_{e,p,i}^T + x_{e,p,i}^U \quad (\text{I.1})$$

where $x_{e,p,i}^S$, $x_{e,p,i}^T$, and $x_{e,p,i}^U$ are three independent variables with errors $\sigma_{e,p,i}^S$, $\sigma_{e,p,i}^T$, and $\sigma_{e,p,i}^U$, respectively¹. Remembering that the covariance $\text{cov}(a; b) = \langle ab \rangle - \langle a \rangle \langle b \rangle$ of two independent variables is exactly 0, the variance of a specific measurement of the geophysical variable x by a

¹One does not actually need to define what $x_{e,p,i}^S$, $x_{e,p,i}^T$, and $x_{e,p,i}^U$ correspond to in reality: they are introduced here purely as a mathematical artifice. Intuitively, however, it may help to think of $x_{e,p,i}^U$ as the *raw* measurement from the radiosonde, $x_{e,p,i}^S$ as the flight-specific corrections, and $x_{e,p,i}^T$ as the flight-independent corrections.

radiosonde model R with index p during event e at the time step i is thus:

$$\begin{aligned}
 (\sigma_{e,p,i})^2 = V(x_{e,p,i}) &= \langle x_{e,p,i}^2 \rangle - \langle x_{e,p,i} \rangle^2 \\
 &= \langle [x_{e,p,i}^S + x_{e,p,i}^T + x_{e,p,i}^U]^2 \rangle - \langle x_{e,p,i}^S + x_{e,p,i}^T + x_{e,p,i}^U \rangle^2 \\
 &= \langle x_{e,p,i}^S{}^2 + x_{e,p,i}^T{}^2 + x_{e,p,i}^U{}^2 + 2x_{e,p,i}^S x_{e,p,i}^T + 2x_{e,p,i}^S x_{e,p,i}^U + 2x_{e,p,i}^T x_{e,p,i}^U \rangle \\
 &\quad - \langle x_{e,p,i}^S \rangle^2 - \langle x_{e,p,i}^T \rangle^2 - \langle x_{e,p,i}^U \rangle^2 \\
 &\quad - 2\langle x_{e,p,i}^S \rangle \langle x_{e,p,i}^T \rangle - 2\langle x_{e,p,i}^S \rangle \langle x_{e,p,i}^U \rangle - 2\langle x_{e,p,i}^T \rangle \langle x_{e,p,i}^U \rangle \\
 &= V(x_{e,p,i}^S) + V(x_{e,p,i}^T) + V(x_{e,p,i}^U) \\
 &\quad + 2[\text{COV}(x_{e,p,i}^S; x_{e,p,i}^T) + \text{COV}(x_{e,p,i}^S; x_{e,p,i}^U) + \text{COV}(x_{e,p,i}^T; x_{e,p,i}^U)] \\
 &= \sigma_{e,p,i}^S{}^2 + \sigma_{e,p,i}^T{}^2 + \sigma_{e,p,i}^U{}^2, \tag{I.2}
 \end{aligned}$$

which is exactly consistent with the definition of the total uncertainty of the RS41 GDP version 1.

Let us now examine $\text{cov}(x_{e,p,i}; x_{e,q,j})$, the covariance between two distinct GDP measurements of the variable x acquired by two radiosondes with index p and q during event e at time steps i and j (with $i, j \in [0; \dots; K_e - 1]$). We have:

$$\begin{aligned}
 \text{COV}(x_{e,p,i}; x_{e,q,j}) &= \langle x_{e,p,i} x_{e,q,j} \rangle - \langle x_{e,p,i} \rangle \langle x_{e,q,j} \rangle \\
 &= \langle (x_{e,p,i}^S + x_{e,p,i}^T + x_{e,p,i}^U) \cdot (x_{e,q,j}^S + x_{e,q,j}^T + x_{e,q,j}^U) \rangle \\
 &\quad - \langle x_{e,p,i}^S + x_{e,p,i}^T + x_{e,p,i}^U \rangle \cdot \langle x_{e,q,j}^S + x_{e,q,j}^T + x_{e,q,j}^U \rangle \\
 &= \text{COV}(x_{e,p,i}^S; x_{e,q,j}^S) + \text{COV}(x_{e,p,i}^S; x_{e,q,j}^T) + \text{COV}(x_{e,p,i}^S; x_{e,q,j}^U) \\
 &\quad + \text{COV}(x_{e,p,i}^T; x_{e,q,j}^S) + \text{COV}(x_{e,p,i}^T; x_{e,q,j}^T) + \text{COV}(x_{e,p,i}^T; x_{e,q,j}^U) \\
 &\quad + \text{COV}(x_{e,p,i}^U; x_{e,q,j}^S) + \text{COV}(x_{e,p,i}^U; x_{e,q,j}^T) + \text{COV}(x_{e,p,i}^U; x_{e,q,j}^U). \tag{I.3}
 \end{aligned}$$

Here, we have indirectly exploited a very important premise:

Premise 2 All GDP uncertainties, irrespective of the measurand or the radiosonde model, can be associated to a σ^S -, σ^T -, or σ^U -type of uncertainty in terms of its correlation coefficients with other measurements.

This is realised for all variables of the RS41 GDP version 1. For the iMS-100 GDP version 2, we treat the total uncertainty component as a temporal component. This choice is motivated by the following facts:

1. It is the most conservative approach in terms of uncertainty propagation, and
2. for the RS41 GDP version 1, the temporal uncertainty component is generally larger than the spatial component (if the latter exists at all).

Recalling the fact that $x_{e,p,i}^S$, $x_{e,p,i}^T$ and $x_{e,p,i}^U$ are independent variables with respect to each other (by definition), as is $x_{e,p,i}^U$ with respect to $x_{e,q,j}^U$ since these are characterised by uncorrelated uncertainties only, Equation (I.3) becomes:

$$\text{COV}(x_{e,p,i}; x_{e,q,j}) = \text{COV}(x_{e,p,i}^S; x_{e,q,j}^S) + \text{COV}(x_{e,p,i}^T; x_{e,q,j}^T). \tag{I.4}$$

Terminology 6 We introduce the correlation coefficients $\rho_{e,p,i}^{f,q,j}$ and $\eta_{e,p,i}^{f,q,j}$ as:

$$\rho_{e,p,i}^{f,q,j} = \frac{\text{COV}(x_{e,p,i}^S; x_{f,q,j}^S)}{\sigma_{e,p,i}^S \sigma_{f,q,j}^S} \quad \text{and} \quad \eta_{e,p,i}^{f,q,j} = \frac{\text{COV}(x_{e,p,i}^T; x_{f,q,j}^T)}{\sigma_{e,p,i}^T \sigma_{f,q,j}^T} \tag{I.5}$$

By definition, $\rho_{e,p,i}^{f,q,j} = \rho_{f,q,j}^{e,p,i}$ and $\eta_{e,p,i}^{f,q,j} = \eta_{f,q,j}^{e,p,i}$.

A correct propagation of (correlated) uncertainties evidently requires a precise understanding of the correlation coefficients between different variables and measurements. According to the

definition of the GRUAN Lead Centre ([Sommer et al., 2022, 2023](#)), we have:

$$\rho_{e,p,i}^{f,q,j} \Big|_{p=q,f=e} = 1 \quad \forall i, j, p, e, \quad (\text{I.6})$$

which is to say that the *spatial* systematic uncertainty component $\sigma_{e,p,i}^S$ should be considered fully correlated between any measurement within a given profile. For the *temporal* systematic uncertainty component, the correlation also extends across distinct flights for a given radiosonde model:

$$\eta_{e,p,i}^{f,q,j} = 1 \quad \forall i, j, p, q, e, f, \text{ and with the model of the sondes with index } p \text{ and } q \text{ identical} \quad (\text{I.7})$$

As of March 2023, no GRUAN guidelines exist regarding the combination of GDPs from distinct radiosonde models. In particular, the GRUAN technical document for the iMS-100 GDP and the RS41 GDP only discuss uncertainties and their correlations from their own perspective ([Sommer et al., 2022, 2023](#); [Hoshino et al., 2022](#); [Kizu et al., 2018b](#)).

In our analysis of the UAI 2022 field campaign, we assume that no correlation exist between any iMS-100 GDP and RS41 GDP measurements. In other words, we assume that:

$$\eta_{e,p,i}^{f,q,j} = \eta_{e,p,i}^{f,q,j} = 0 \quad \forall i, j, p, q, e, f, \text{ and with the model of the sondes with index } p \text{ and } q \text{ distinct} \quad (\text{I.8})$$

In absence of explicit, official GRUAN guidelines, this choice is motivated by the fact that the radiation correction applied to the iMS-100 and RS41 data products as part of the GRUAN data processing –which represents the primary source of temporal correlated uncertainties– differs significantly between the two GDPs, that are thus essentially uncorrelated to a first order approximation.

I.3 ASSESSING THE STATISTICAL COMPATIBILITY OF GDPs

GDPs provide atmospheric profiles of geophysical variables that are fully characterised in their uncertainties. This allows to assess, statistically, the level of agreement between any two GDP measurements ([Immler et al., 2010](#)). For the purpose of the UAI 2022 analysis, the GDPs from any given flight are combined (using a weighted-average scheme; see Appendix I.4) to form the flight's CWS, against which the performance of all radiosondes participating to the UAI 2022 can be assessed. Evidently, the use of a CWS only makes sense, from a physical perspective, if the underlying GDP measurements are in statistical agreement with one another.

Terminology 7 We introduce $\Delta_{e,i}^{p,q}$, the difference between two simultaneous GDP measurements of a given geophysical variable x , acquired with two sondes with index p and q at the time step i of the measurement event e , as:

$$\Delta_{e,i}^{p,q} = x_{e,p,i} - x_{e,q,i} \quad (\text{I.9})$$

One should note that we here indirectly rely on the UAI 2022 premise 1, in that we assume the individual measurements are simultaneous (see Section 9.5.3 for details).

To the first order, the variance $V(f(y_1, \dots, y_n))$ of a multi-variable function $f(y_1, \dots, y_n)$ can be expressed as:

$$V(f(y_1, \dots, y_n)) = \sum_{i=1}^n \left(\frac{\partial f}{\partial y_i} \right)^2 V(y_i) + \sum_{i=1}^n \sum_{j \neq i} \frac{\partial f}{\partial y_i} \frac{\partial f}{\partial y_j} \text{cov}(y_i; y_j) \quad (\text{I.10})$$

Transposing this to $\Delta_{e,i}^{p,q}$, we have:

$$\begin{aligned} V(\Delta_{e,i}^{p,q}) &= V(x_{e,p,i}) + V(x_{e,q,i}) - 2 \text{COV}(x_{e,p,i}; x_{e,q,i}) \\ \stackrel{\text{Eq. (I.2)}}{=} & \sigma_{e,p,i}^S{}^2 + \sigma_{e,p,i}^T{}^2 + \sigma_{e,p,i}^U{}^2 + \sigma_{e,q,i}^S{}^2 + \sigma_{e,q,i}^T{}^2 + \sigma_{e,q,i}^U{}^2 - 2 \text{COV}(x_{e,p,i}; x_{e,q,i}) \\ \stackrel{\text{Eq. (I.5)}}{=} & \sigma_{e,p,i}^U{}^2 + \sigma_{e,q,i}^U{}^2 \\ & + \left[\sigma_{e,p,i}^S{}^2 - 2\rho_{e,p,i}^{e,q,i} \sigma_{e,p,i}^S \sigma_{e,q,i}^S + \sigma_{e,q,i}^S{}^2 \right] + \left[\sigma_{e,p,i}^T{}^2 - 2\eta_{e,p,i}^{q,i} \sigma_{e,p,i}^T \sigma_{e,q,i}^T + \sigma_{e,q,i}^T{}^2 \right] \quad (\text{I.11}) \end{aligned}$$

Terminology 8 We define $k_{e,i}^{p,q}$, the statistical level of agreement between two GDP measurements acquired at the time step i of the event e by the sondes with index p and q , as:

$$k_{e,i}^{p,q} = \frac{\Delta_{e,i}^{p,q}}{\sqrt{V(\Delta_{e,i}^{p,q})}}. \quad (\text{I.12})$$

One should note that $k_{e,i}^{p,q}$ may be negative.

If a set of simultaneous GDP measurements are *consistent* with each other, the corresponding $k_{e,i}^{p,q}$ values will be normally distributed around zero with a standard deviation of unity: provided, of course, that the uncorrelated, correlated spatial, and correlated temporal uncertainties of the individual measurements have been correctly estimated.

The “normality” of $k_{e,i}^{p,q}$ can be assessed using a Kolmogorov-Smirnov (KS) test, where the significance level α of the test corresponds to the required level of statistical consistency. KS tests can be performed either for an individual time step i (i.e. for a specific pair of GDP measurements $x_{e,p,i}$ and $x_{e,q,i}$), or for a series of m time steps $[i, i+1, \dots, i+m-1]$. For the UAII 2022, the statistical compatibility of the GDP measurements is done at high-resolution, with $m = 1$.

We adopt a significance level $\alpha = 0.0455$ for the KS test. A p-value² of the KS test smaller than α (for a given time step i) would thus indicate the underlying two GDP measurements to be in statistical disagreement at a 2σ -level. For $m = 1$, this is equivalent to assessing whether:

$$k_{e,i}^{p,q} \stackrel{?}{\leq} 2. \quad (\text{I.13})$$

According to the GRUAN guidelines for GDPs, simultaneous measurement pairs that comply with this criteria can be deemed to be *in agreement*; those that do not are deemed *significantly different* (Immler et al., 2010). An example of a “KS diagnostic diagram” generated by dvas (see Section 9.4) is presented in Figure I.1. It illustrates the practical use of Equation (I.13) for the UAII 2022 field campaign flights. Similar diagrams, for all the UAII 2022 field campaign flights and geophysical variables, are included in the UAII 2022 supplementary material.

I.4 STATISTICAL COMBINATION OF GDPs INTO CWSs

Terminology 9 We define $\Omega_{e,i}$, the Combined Working measurement Standard (CWS) for a given geophysical variable during the event e at the time step i .

For the temperature, pressure, relative humidity, geopotential altitude, and wind (horizontal) speed, the CWS of a given event e is computed as the weighted *arithmetic* mean of the individual GDP measurements at each time step i :

$$\Omega_{e,i} = \frac{\sum_{p=1}^Q w_{e,p,i} x_{e,p,i}}{\sum_{p=1}^Q w_{e,p,i}} \quad (\text{I.14})$$

with Q the number of distinct GDPs to be combined, and:

$$w_{e,p,i} = \begin{cases} 0 & \text{if } x_{e,p,i} \text{ is invalid (i.e. NaN), and} \\ \frac{1}{(\sigma_{e,p,i})^2} & \text{otherwise,} \end{cases} \quad (\text{I.15})$$

with $\sigma_{e,p,i}$ the total uncertainty of the GDP measurement point $x_{e,p,i}$.

For the wind (horizontal) direction, where $x_{e,p,i}$ values are angles, the CWS is computed as the

²The p-value measures the probability that the observed deviations from a normal distribution are due to chance.

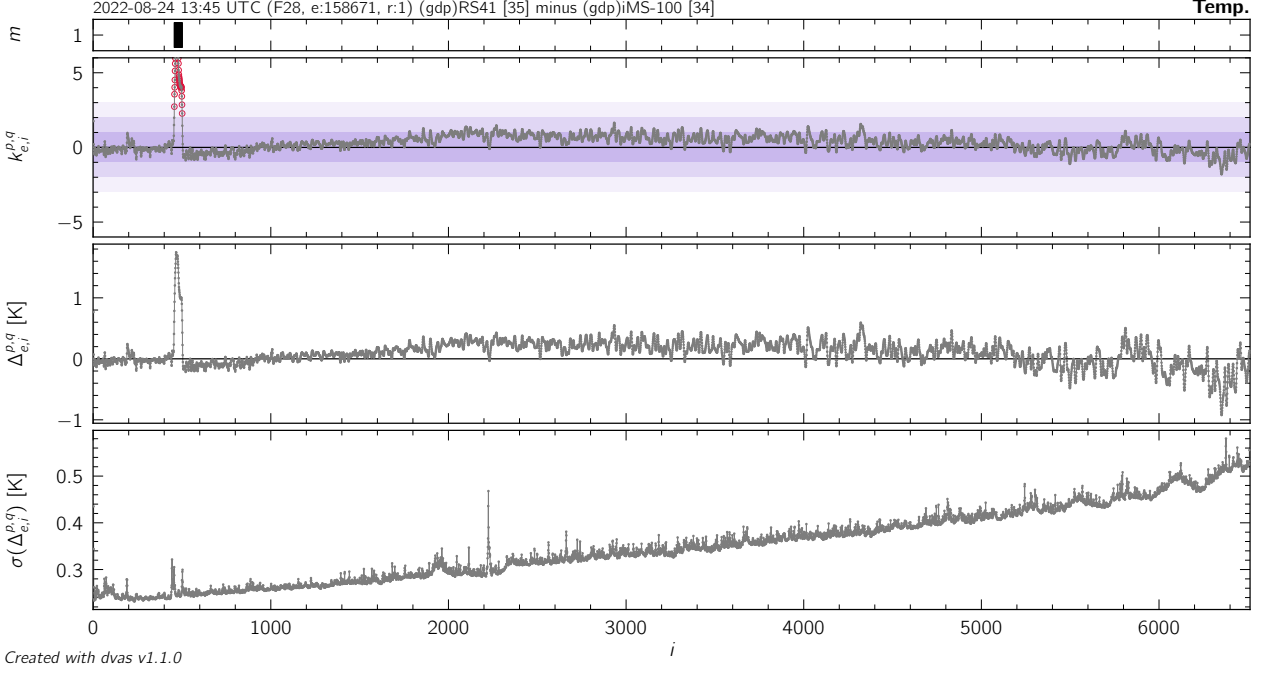


Figure I.1: Example of a so-called “KS diagnostic diagram” of the UAI 2022 field campaign, generated by *dvas* for the temperature GDP profiles of flight F28. The value of $k_{e,i}^{p,q}$, computed from the underlying IMS-100 GDP and RS41 GDP at all time steps i , is shown in the second panel from the top. The purple-shaded areas indicate the 1σ -, 2σ -, and 3σ -level agreement zones. Time steps where Equation (I.13) is not satisfied are flagged with red circles in this panel, and also using black bars in the top panel. The remaining two panels show the high-resolution profiles of $\Delta_{e,i}^{p,q}$ and $\sigma(\Delta_{e,i}^{p,q}) = (V(\Delta_{e,i}^{p,q}))^{0.5}$. The region where the GDPs are *significantly different* from one another, around $i = 500$, is the result of a large temperature difference between the sondes following a cloud exit.

weighted *circular* mean of the individual GDP measurements at each time step i :

$$\check{\Omega}_{e,i} = \arctan2 \left(\sum_{p=1}^Q w_{e,p,i} \sin(x_{e,p,i}); \sum_{p=1}^Q w_{e,p,i} \cos(x_{e,p,i}) \right) \quad (\text{I.16})$$

with the convention that:

$$\arctan2(y; x) = \begin{cases} \arctan\left(\frac{y}{x}\right) & \text{if } x > 0 \text{ and } y \geq 0 \\ \arctan\left(\frac{y}{x}\right) + 2\pi & \text{if } x > 0 \text{ and } y < 0 \\ \arctan\left(\frac{y}{x}\right) + \pi & \text{if } x < 0 \\ +\frac{\pi}{2} & \text{if } x = 0 \text{ and } y > 0 \\ +3\frac{\pi}{2} & \text{if } x = 0 \text{ and } y < 0 \\ 0 & \text{if } x = y = 0 \end{cases} \quad (\text{I.17})$$

which ensures that $\check{\Omega}_{e,i} \in [0; 2\pi[$.

For the UAI 2022 field campaign flights, CWSs are assembled only for the time steps where the underlying GDP measurements are *in agreement* with each others according the criterion specified in Section I.3 and Equation (I.13). We present in Figure I.2 the so-called “CWS diagnostic diagram” generated by *dvas* for the temperature profile of flight F28. No CWS is assembled for the time steps in the vicinity of $i = 500$, where the GDPs are *significantly different*, as illustrated in Figure I.1.

CWSs values are subject to measurement uncertainties stemming from the underlying GDP measurements. The variance V of a function $f(y_1, \dots, y_n)$ with variables y_1, \dots, y_n can be assembled

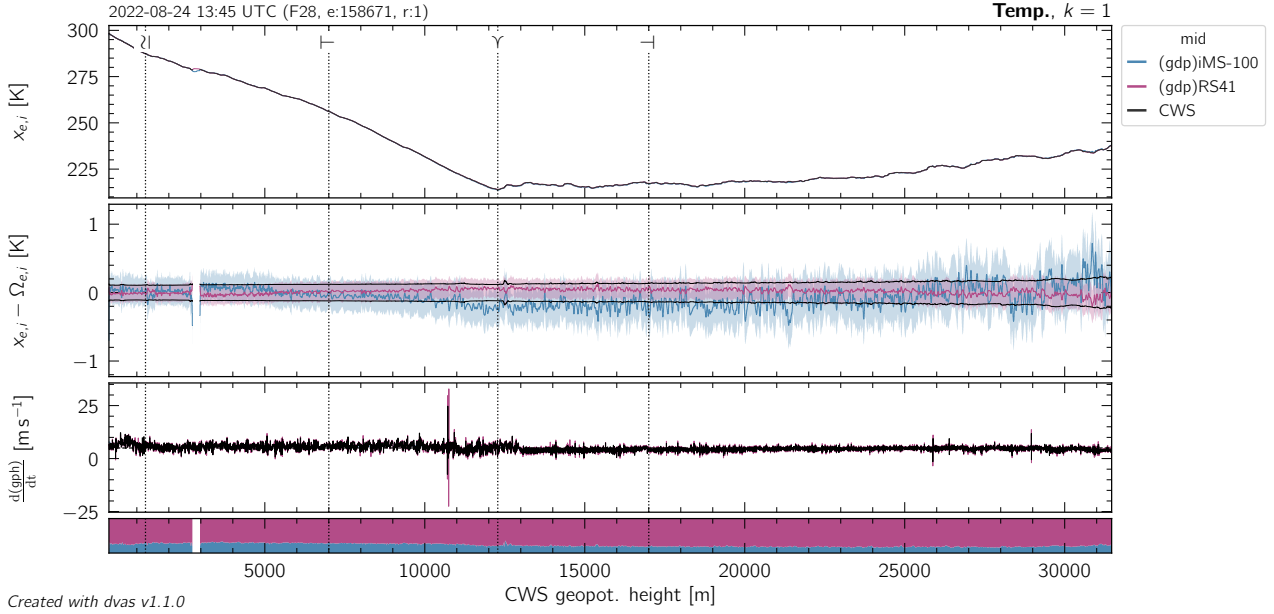


Figure I.2: Example of a so-called “CWS diagnostic diagram” of the UAI 2022 field campaign, generated by *dvas* from the temperature GDP profiles of flight F28. The GDP and CWS profiles are visible in the top panel, alongside the location of the PBL (λ), the tropopause (γ), and the lower- (\ominus) and upper-limit (\oplus) of the UTLS. The middle panel shows the values of $x_{e,p,i} - \Omega_{e,i}$, the difference between each of the GDP profiles and the CWS, including the associated (total) uncertainties of the GDPs ($k=1$) as shaded areas. The grey-shaded area corresponds to the total CWS uncertainty. The third panel from top shows the instantaneous ascent speed of the different profiles. The bottom panel indicates the relative contribution of the GDP measurements to the CWS following Equation (I.15), given their respective (total) uncertainties.

via Equation (I.10). It can also be expressed using the dot product of two matrices:

$$V(f) = \mathbf{G} \cdot \mathbf{U} \cdot \mathbf{G}^T \tag{I.18}$$

with \mathbf{U} the covariance matrix of size $n \times n$, and \mathbf{G} the Jacobian matrix of size $1 \times n$ with \mathbf{G}^T its transpose, such that:

$$\mathbf{U}_{ab} = \text{COV}(y_a; y_b) \quad \mathbf{G}_b = \frac{\partial f}{\partial y_b} \tag{I.19}$$

1.4.1 The Jacobian matrix

For both the cases of $f = \Omega_{e,i}$ and $f = \check{\Omega}_{e,i}$, there are two³ “variables” involved (one from each of the UAI 2022 GDPs): $x_{e,p,i}$ with $p \in [1; 2]$. From Equation (I.14), the Jacobian matrix elements associated to $\check{\Omega}_{e,p,i}$ are:

$$\bar{\mathbf{G}}_{e,P,i} = \frac{\partial \bar{\Omega}_{e,i}}{\partial x_{e,P,i}} = w_{e,P,i} \left(\sum_{p=1}^2 w_{e,p,i} \right)^{-1} \tag{I.20}$$

³Equation (I.18) can be extended to derive the variance of all CWS data points $\Omega_{e,i}$ at once. Doing so, for the case of the UAI 2022 flights, implies the assembly of covariance matrices with $(2K_e)^2 = \mathcal{O}(10^8)$ elements, which would be prohibitively large from a practical perspective. For efficiency purposes, *dvas* computes CWS uncertainties by *chunks* of 150 – 200 time steps: a value that can be adjusted based on the specific characteristics of the system running *dvas*.

The expression of $\check{\mathbf{G}}_{e,P,i}$ requires somewhat more efforts to be derived. Let us first define:

$$A = \sum_{p=1}^2 w_{e,p,i} \sin(x_{e,p,i}) \quad (\text{I.21})$$

$$B = \sum_{p=1}^2 w_{e,p,i} \cos(x_{e,p,i}) \quad (\text{I.22})$$

with:

$$\frac{\partial A}{\partial x_{e,P,i}} = w_{e,P,i} \cos(x_{e,P,i}) \quad \text{and} \quad \frac{\partial B}{\partial x_{e,P,i}} = -w_{e,P,i} \sin(x_{e,P,i}) \quad (\text{I.23})$$

Given that $\arctan 2(A; B)$ is essentially equal to $\arctan(A/B)$ modulo a constant, we have:

$$\begin{aligned} \check{\mathbf{G}}_{e,P,i} &= \frac{\partial \check{\Omega}_{e,i}}{\partial x_{e,P,i}} = \frac{\partial \arctan 2(A; B)}{\partial x_{e,P,i}} = \frac{\partial \arctan(AB^{-1})}{\partial x_{e,P,i}} \\ &= \frac{1}{1 + (AB^{-1})^2} \frac{\partial}{\partial x_{e,P,i}} (AB^{-1}) \end{aligned} \quad (\text{I.24})$$

$$= \frac{B^2}{A^2 + B^2} \left(B^{-1} \frac{\partial A}{\partial x_{e,P,i}} - AB^{-2} \frac{\partial B}{\partial x_{e,P,i}} \right) \quad (\text{I.25})$$

$$= \frac{B}{A^2 + B^2} \left(\frac{\partial A}{\partial x_{e,P,i}} - AB^{-1} \frac{\partial B}{\partial x_{e,P,i}} \right), \quad (\text{I.26})$$

such that:

$$\check{\mathbf{G}}_{e,P,i} = \frac{B}{A^2 + B^2} (w_{e,P,i} \cos(x_{e,P,i}) + AB^{-1} w_{e,P,i} \sin(x_{e,P,i})). \quad (\text{I.27})$$

I.4.2 The covariance matrix and CWS variance

Recalling Equation (I.3), the element of the covariance matrix \mathbf{U} for two measurements $x_{e,p,i}$ and $x_{e,q,j}$, which conveys all the information regarding the cross-correlation of these variables, is:

$$\mathbf{U}_{e,p,i}^{e,q,j} = \text{cov}(x_{e,p,i}^S; x_{e,q,j}^S) + \text{cov}(x_{e,p,i}^T; x_{e,q,j}^T) + \text{cov}(x_{e,p,i}^U; x_{e,q,j}^U). \quad (\text{I.28})$$

Recalling the fact that:

$$\text{cov}(x_{e,p,i}^U; x_{e,q,j}^U) = 0 \quad \forall (e,p,i) \neq (e,q,j), \quad (\text{I.29})$$

we have:

$$\mathbf{U} = \mathbf{I} \odot \sigma^U \sigma^{U\top} + \mathbf{P} \odot \sigma^S \sigma^{S\top} + \mathbf{H} \odot \sigma^T \sigma^{T\top} \quad (\text{I.30})$$

with \mathbf{I} the identity matrix, \odot the Hadamard product, $\sigma^U = (\sigma_{e,p,i}^U \quad \sigma_{e,q,j}^U)$, $\sigma^S = (\sigma_{e,p,i}^S \quad \sigma_{e,q,j}^S)$, $\sigma^T = (\sigma_{e,p,i}^T \quad \sigma_{e,q,j}^T)$ the one-dimensional (random, spatial and temporal) uncertainty arrays of length 2, and \mathbf{P} , \mathbf{H} the correlation (square) matrices of size 2×2 , with their elements:

$$\mathbf{P}_{e,p,i}^{e,q,j} = \rho_{e,p,i}^{e,q,j} \quad \text{and} \quad \mathbf{H}_{e,p,i}^{e,q,j} = \eta_{e,p,i}^{e,q,j}. \quad (\text{I.31})$$

Remembering that the matrix dot product is distributive with respect to matrix addition, Equation (I.30) implies that one can distinguish between the different types of uncertainty sources also at the level of the CWSs. Namely, combining Equation (I.18) and Equation (I.30), we can write:

$$V(\Omega_{e,i}) = V^S(\Omega_{e,i}) + V^T(\Omega_{e,i}) + V^U(\Omega_{e,i}), \quad (\text{I.32})$$

with:

$$\begin{aligned} V^S(\Omega_{e,i}) &= \mathbf{G} \cdot (\mathbf{P} \odot \sigma^S \sigma^{S\top}) \cdot \mathbf{G}^\top \\ V^T(\Omega_{e,i}) &= \mathbf{G} \cdot (\mathbf{H} \odot \sigma^T \sigma^{T\top}) \cdot \mathbf{G}^\top \\ V^U(\Omega_{e,i}) &= \mathbf{G} \cdot (\mathbf{I} \odot \sigma^U \sigma^{U\top}) \cdot \mathbf{G}^\top. \end{aligned} \quad (\text{I.33})$$

$V^U(\Omega_{e,i})$ is based upon all the uncorrelated (random) uncertainties, $V^S(\Omega_{e,i})$ is based upon all

the spatial correlated (systematic) uncertainties, and $V^T(\Omega_{e,i})$ is based upon all the temporal correlated (systematic) uncertainties.

A diagram illustrating the different GDP and CWS uncertainty profiles for flight F28 is presented in Figure I.3. Similar diagnostic diagrams for all the UAI 2022 field campaign flights are made available to the interested reader as part of the UAI 2022 Supplementary Material.

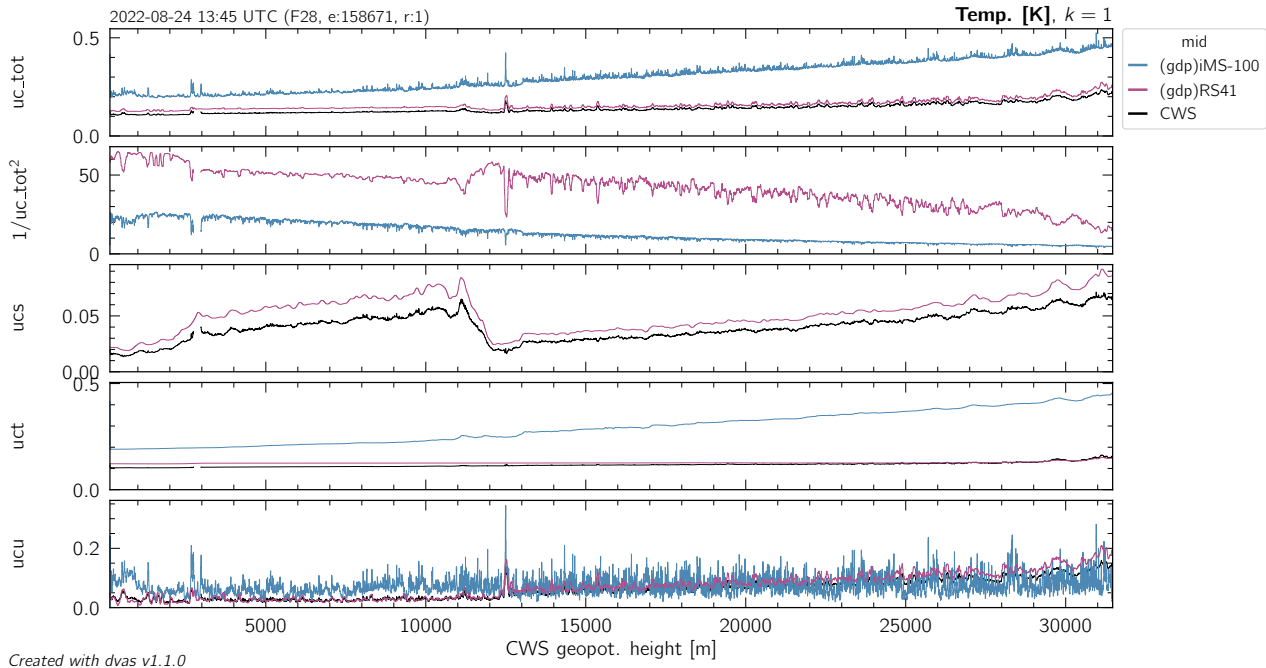


Figure I.3: Example of a dvas-generated diagram showing the temperature uncertainty profiles of GDPs and CWS for flight F28, as a function of altitude. First panel: total uncertainty. Second panel: profiles of $(\sigma_{e,p,i}^{-2})$ (see Equation I.15). Third panel: spatial component of the correlated uncertainty. Fourth panel: temporal component of the correlated uncertainty. Fifth panel: uncorrelated component of the uncertainty. All uncertainty components are shown at $k = 1$.

J MATHEMATICAL DESCRIPTION OF THE ASSESSMENT OF UPPER-AIR INSTRUMENTS WITH RESPECT TO ORUCS

J.1 INTRODUCTION

One of the primary goal of the UAI 2022 is to assess the performance of upper-air instruments with respect to a series of OSCAR requirement uncertainty criterion (ORUC) values $\Theta_{x,\mathcal{L}}$ (see Section 9.3). This requires combining measurements from different balloon flights. The mathematical assembly of CWSs described in Appendix I is done for each flight of the UAI 2022 field campaign, on a time step basis. In other words, the CWS is build at maximum vertical resolution determined by the 1 Hz sampling frequency of the GDPs. Evidently, the exact balloon ascent speed as a function of time is flight dependent. This implies that the specific vertical altitude sampling will be different between flights.

Terminology 10 We define $h_{e,p,i}$, the geopotential altitude of the measurement point $x_{e,p,i}$, acquired by the upper-air instrument \mathcal{R} with index p during the measurement event (flight) e at the time step $i \in [0; 1; \dots; K_e - 1]$. For the case of the M radiosondes, that are all physically attached to the same rig for a given event e , we have $h_{e,p,i} = h_{e,q,i} \forall p, q \in [1; \dots; M]$.

The value of $h_{e,p,i}$ is taken, for all radiosondes on a given rig, from $\Omega_{e,i}^{\text{gph}}$, the CWS profile of geopotential height for the event e . It is important to note here that $h_{e,p,i}$ is the *reference* height value used to group measurements across distinct flights. It is not to be confused with the sonde-specific measurements of geopotential height, that are analysed like any other variables.

Each radiosonde and remote-sensing instrument participating in the UAI 2022 is treated and analysed separately. To simplify the notations throughout this Appendix, we will focus on the case of one upper-instrument \mathcal{R} with index p , and make the following simplifications with respect to the notations employed throughout Appendix I: $x_{e,p,i} \equiv x_{e,i}$, and $h_{e,p,i} \equiv h_{e,i}$. That is, we no longer explicitly specify the instrument index, and will always (unless otherwise specified) implicitly refer to the upper-air instrument \mathcal{R} .

Terminology 11 We introduce \mathcal{L} a given atmospheric layer. For each UAI 2022 field campaign flight e , the layer \mathcal{L} corresponds to a specific range of geopotential heights $[\mathcal{L}_e^-; \mathcal{L}_e^+]$. A specific measurement $x_{e,i}$ "belongs" to the layer \mathcal{L} if $\mathcal{L}_e^- \leq h_{e,i} \leq \mathcal{L}_e^+$.

\mathcal{L} can be one of the layers defined in Section 9.1.3, or a smaller range of geopotential heights.

J.2 OSCAR REQUIREMENT UNCERTAINTY CRITERIA

J.2.1 Scalar variables

The official, worded definition of ORUCs (see Section 9.3) can be translated mathematically into the following, formal assessment criteria:

Terminology 12 Given a specific ORUC value $\Theta_{x,\mathcal{L}}$, an upper-air instrument \mathcal{R} with a **population** of P profiles in a given category \mathcal{C} (e.g. daytime, or nighttime) resulting in a total of T individual measurements $x_{e,i}$ within the atmospheric layer \mathcal{L} , for the (scalar) geophysical variable x , is fit-for-purpose with respect to $\Theta_{x,\mathcal{L}}$ if:

$$\Lambda_{\mathcal{C},\mathcal{L}}^* = \sqrt{\frac{1}{T} \sum_{\substack{x_{e,i} \in \mathcal{L} \\ e \in \mathcal{C}}} (x_{e,i} - x_{e,i}^*)^2} < \Theta_{x,\mathcal{L}}, \quad (\text{J.1})$$

where $x_{e,i}^*$ corresponds to the true value of the geophysical scalar variable x during the measurement event e at the time step i .

Terminology 13 We introduce $\delta_{e,i}^* = x_{e,i} - x_{e,i}^*$ the true measurement error of the upper-air instrument \mathcal{R} at the time step i of the measurement event e , for the scalar variable x .

Terminology 14 We introduce $\overline{\delta^*}_{\mathcal{C},\mathcal{L}}$, the arithmetic mean of the individual true measurement errors $\delta_{e,i}^*$ within the atmospheric layer \mathcal{L} for the entire population of P events, and $\sigma(\delta^*)_{\mathcal{C},\mathcal{L}}$ their standard deviation.

For a series of T measurements z_t with $t \in [1; \dots; T]$, with arithmetic mean \bar{z} and standard deviation $\sigma(z)$, their mean square z_{rms}^2 can be expressed as:

$$\begin{aligned} \frac{1}{T} \sum_t z_t^2 = z_{\text{rms}}^2 &= \bar{z}^2 + z_{\text{rms}}^2 - 2\bar{z}^2 + \bar{z}^2 \\ &= \bar{z}^2 + \frac{1}{T} \sum_t z_t^2 - \frac{2}{T} \bar{z} \sum_t z_t + \frac{1}{T} \sum_t \bar{z}^2 \\ &= \bar{z}^2 + \frac{1}{T} \sum_t (z_t - \bar{z})^2 \\ &= \bar{z}^2 + \sigma(z)^2. \end{aligned} \quad (\text{J.2})$$

We can thus express the left-hand term of Equation (J.1) as:

$$(\Lambda_{\mathcal{C},\mathcal{L}}^*)^2 = (\overline{\delta^*}_{\mathcal{C},\mathcal{L}})^2 + (\sigma(\delta^*)_{\mathcal{C},\mathcal{L}})^2. \quad (\text{J.3})$$

Obviously, one does not have access to the entire **population** of measurements of a given upper-air instrument (that includes all past and future measurements) to assess its compatibility with a given ORUC. The flights of the UAI 2022 field campaign represent a **sample** of $N \ll P$ measurement events of the entire population, from which we want to estimate the value of $\Lambda_{\mathcal{C},\mathcal{L}}^*$.

As discussed at length in Section 9.2 and Appendix I, two GDPs are combined, for each flight e of the UAI 2022 field campaign, into a CWS $\Omega_{e,i}$. This serves as our reference quantity value of $x_{e,i}^*$: the true (but unknowable) value of the geophysical variable x at the time step i during event e .

Terminology 15 We introduce the individual measurement error $\delta_{e,i} = x_{e,i} - \Omega_{e,i}$: the difference between the upper-air instrument \mathcal{R} and the CWS $\Omega_{e,i}$ of the event e at the time step i , for the scalar variable x . A real example of the $\delta_{e,i}$ profile is presented in Figure J.1.

Terminology 16 We introduce $\bar{\delta}_{\mathcal{C},\mathcal{L}}$, the arithmetic mean of the individual measurement errors $\delta_{e,i}$ that belong to the atmospheric layer \mathcal{L} for the entire sample of N events in the category \mathcal{C} , and $\sigma(\delta)_{\mathcal{C},\mathcal{L}}$ their standard deviation. Assuming that a total of J individual measurements are located within the atmospheric layer \mathcal{L} over these N events, we have:

$$\bar{\delta}_{\mathcal{C},\mathcal{L}} = \frac{1}{J} \sum_{\substack{x_{e,i} \in \mathcal{L} \\ e \in \mathcal{C}}} \delta_{e,i} \quad \text{and} \quad \sigma(\delta)_{\mathcal{C},\mathcal{L}} = \sqrt{\frac{1}{J} \sum_{\substack{x_{e,i} \in \mathcal{L} \\ e \in \mathcal{C}}} (\delta_{e,i} - \bar{\delta}_{\mathcal{C},\mathcal{L}})^2}. \quad (\text{J.4})$$

Essentially, with the flights of the UAI 2022 field campaign, one does not measure $\delta_{e,i}^*$ but $\delta_{e,i}$. However, the arithmetic mean of a sample is an unbiased estimator of the arithmetic mean of the parent population. As such, $\bar{\delta}_{\mathcal{C},\mathcal{L}}$ is a suitable estimate of $\overline{\delta^*}_{\mathcal{C},\mathcal{L}}$.

The variance of a sample, on the other hand, is a biased estimator of the population's variance. The bias can be alleviated using Bessel's correction $J(J-1)^{-1}$ to obtain the *sample variance* $(s(\delta)_{\mathcal{C},\mathcal{L}})^2$ which is an unbiased estimator of $(\sigma(\delta^*)_{\mathcal{C},\mathcal{L}})^2$:

$$(s(\delta)_{\mathcal{C},\mathcal{L}})^2 = \frac{J}{J-1} (\sigma(\delta)_{\mathcal{C},\mathcal{L}})^2 \quad (\text{J.5})$$

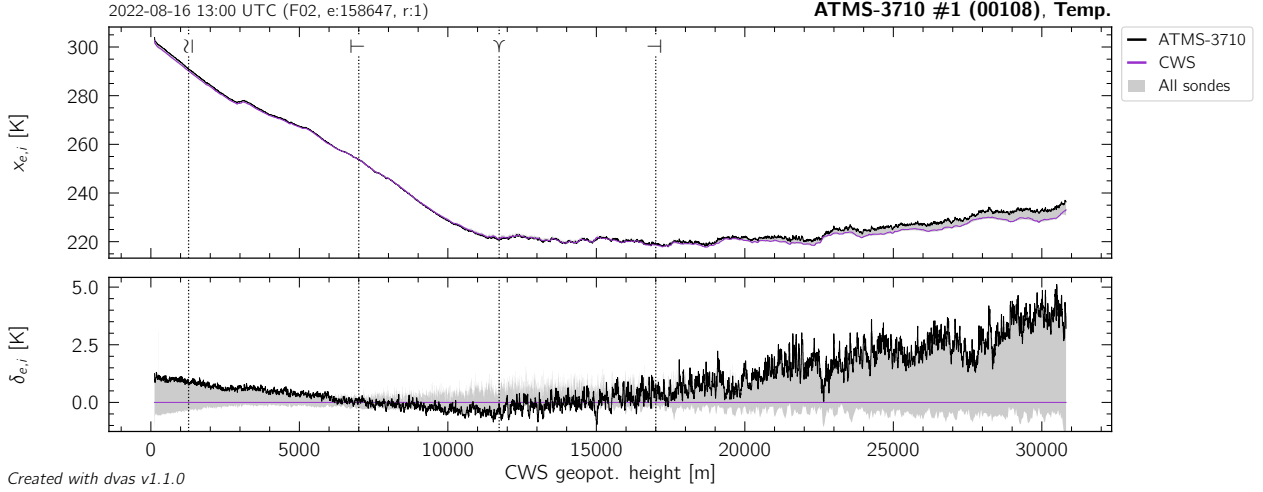


Figure J.1: Example of a $\delta_{e,i}$ profile (bottom, black curve) computed from the temperature measurements of a participating radiosonde (top panel, black curve) and the corresponding CWS (top panel, purple curve). The grey area indicates the span of profiles from all the sondes on this specific flight. Similar diagrams for all participating radiosondes, field campaign flights, and geophysical variables are included in the UAI 2022 Supplementary Material.

In the case of the UAI 2022, the fitness-for-purpose of radiosondes with respect to ORUCs is assessed over at least 20 profiles per category (nighttime or daytime, see Section 8.3), each with a vertical sampling of $1 \text{ Hz} \equiv 5 \text{ m}$. The smallest atmospheric layer width that is used is 100 m, in order to assemble a high-resolution Λ -profile. Even in this extreme case, the amplitude of the Bessel correction remains below 0.5 % with:

$$\frac{J}{J-1} = \frac{15 \cdot \frac{100 \text{ m}}{5 \text{ m}}}{15 \cdot \frac{100 \text{ m}}{5 \text{ m}} - 1} = 1.003, \quad (\text{J.6})$$

such that, for simplicity, we shall ignore it entirely and assume that:

$$(s(\delta)_{\mathcal{C},\mathcal{L}})^2 \approx (\sigma(\delta)_{\mathcal{C},\mathcal{L}})^2. \quad (\text{J.7})$$

The best estimate of $(\Lambda_{\mathcal{C},\mathcal{L}}^*)^2$, built from the sample of N flights in the category \mathcal{C} accessible through the UAI 2022 field campaign, is thus given by:

$$(\Lambda_{\mathcal{C},\mathcal{L}}^*)^2 \simeq (\bar{\delta}_{\mathcal{C},\mathcal{L}})^2 + (s(\delta)_{\mathcal{C},\mathcal{L}})^2 \approx (\bar{\delta}_{\mathcal{C},\mathcal{L}})^2 + (\sigma(\delta)_{\mathcal{C},\mathcal{L}})^2 = (\Lambda_{\mathcal{C},\mathcal{L}})^2 = \frac{1}{J} \sum_{\substack{x_{e,i} \in \mathcal{L} \\ e \in \mathcal{C}}} (\delta_{e,i})^2 \quad (\text{J.8})$$

such that:

$$\Lambda_{\mathcal{C},\mathcal{L}} = \sqrt{\frac{1}{J} \sum_{\substack{x_{e,i} \in \mathcal{L} \\ e \in \mathcal{C}}} (\delta_{e,i})^2} = \sqrt{\frac{1}{J} \sum_{\substack{x_{e,i} \in \mathcal{L} \\ e \in \mathcal{C}}} (x_{e,i} - \Omega_{e,i})^2}. \quad (\text{J.9})$$

The value of $\Lambda_{\mathcal{C},\mathcal{L}}$ is subject to measurement uncertainties $\epsilon_{\mathcal{C},\mathcal{L}}$, linked to the ability of GDPs to correctly report the true value of the geophysical variable x . $\epsilon_{\mathcal{C},\mathcal{L}}$ can be computed with a complete propagation of the CWS (and thus GDP) measurement uncertainties through Equation (J.9), using the same approach outlined in Section I and Equation (I.18):

$$(\epsilon_{\mathcal{C},\mathcal{L}})^2 = \mathbf{G} \cdot \mathbf{U} \cdot \mathbf{G}^T \quad (\text{J.10})$$

In the present case, we have $f = \Lambda_{\mathcal{C},\mathcal{L}}$ and $y_b = \delta_{e,i}$, such that the elements of the Jacobian matrix

G are:

$$\mathbf{G}_{e,i,\mathcal{C},\mathcal{L}} = \frac{\partial(\Lambda_{\mathcal{C},\mathcal{L}})}{\partial\delta_{e,i}} = \frac{\partial}{\partial\delta_{e,i}} \left(\frac{1}{J} \sum_{\substack{x_{e,i} \in \mathcal{L} \\ e \in \mathcal{C}}} \delta_{e,i}^2 \right)^{\frac{1}{2}} = \frac{J^{-1}\delta_{e,i}}{\Lambda_{\mathcal{C},\mathcal{L}}}. \quad (\text{J.11})$$

On the other hand, the elements of the covariance matrix **U** are:

$$\mathbf{U}_{e,i}^{f,j} = \text{cov}(\delta_{e,i}; \delta_{f,j}). \quad (\text{J.12})$$

Terminology 17 We introduce the uncorrelated (random), spatially correlated (systematic), and temporally correlated (systematic) uncertainties $\sigma_{\Omega_{e,i}}^U$, $\sigma_{\Omega_{e,i}}^S$, and $\sigma_{\Omega_{e,i}}^T$ of CWSs:

$$\sigma_{\Omega_{e,i}}^S = \sqrt{V^S(\Omega_{e,i})} \quad (\text{J.13})$$

$$\sigma_{\Omega_{e,i}}^T = \sqrt{V^T(\Omega_{e,i})} \quad (\text{J.14})$$

$$\sigma_{\Omega_{e,i}}^U = \sqrt{V^U(\Omega_{e,i})}. \quad (\text{J.15})$$

For the scalar variable x , the value of $\delta_{e,i} = x_{e,i} - \Omega_{e,i}$ also has uncertainties $\sigma_{\Omega_{e,i}}^S$, $\sigma_{\Omega_{e,i}}^T$, and $\sigma_{\Omega_{e,i}}^U$. This is a direct consequence of the fact that $x_{e,i}$ is being treated as the *reading of an instrument*. Hence, following the exact same methodology described in detail in Section I (see Equation (I.30)), we have:

$$\mathbf{U} = \mathbf{I} \odot \sigma_{\Omega}^U \sigma_{\Omega}^{U\top} + \mathbf{P} \odot \sigma_{\Omega}^S \sigma_{\Omega}^{S\top} + \mathbf{H} \odot \sigma_{\Omega}^T \sigma_{\Omega}^{T\top}, \quad (\text{J.16})$$

with σ_{Ω}^U , σ_{Ω}^S , and σ_{Ω}^T one-dimensional arrays of length J whose elements are comprised of $\sigma_{\Omega_{e,i}}^U$, $\sigma_{\Omega_{e,i}}^S$, and $\sigma_{\Omega_{e,i}}^T$ (respectively) such that $x_{e,i} \in \mathcal{L}$. For the purpose of the correlation coefficients, the CWS spatially and temporally correlated uncertainties are being treated in the same manner as for GDPs (see Section I.2).

J.2.2 Wind (horizontal) vector

The case of the wind (horizontal) vector variable is somewhat more complicated than that of scalar variables like temperature, relative humidity, pressure, and geopotential height. It essentially requires to combine two distinct scalar variables – wind (horizontal) speed and direction – to compute the modulus of vector differences.

The mathematical development presented in Section J.2.1 remains largely applicable to the wind (horizontal) vector variable, but with the following differences related to the vectorial nature of the variable. First, Equation (J.1) becomes:

$$\Lambda_{\mathcal{C},\mathcal{L}}^* = \sqrt{\frac{1}{T} \sum_{\substack{x_{e,i} \in \mathcal{L} \\ e \in \mathcal{C}}} \|\vec{x}_{e,i} - \vec{x}_{e,i}^*\|^2} < \Theta_{x,\mathcal{L}}, \quad (\text{J.17})$$

such that $\delta_{e,i}^* = \|\vec{x}_{e,i} - \vec{x}_{e,i}^*\|$, and:

$$\begin{aligned} \delta_{e,i} &= \|\vec{x}_{e,i} - \vec{\Omega}_{e,i}\| \\ &= \sqrt{\|\vec{x}_{e,i}\|^2 + \|\vec{\Omega}_{e,i}\|^2 - 2\vec{x}_{e,i} \cdot \vec{\Omega}_{e,i}} \\ &= \sqrt{\left(x_{e,i}^{\text{wspeed}}\right)^2 + \left(\Omega_{e,i}^{\text{wspeed}}\right)^2 - 2x_{e,i}^{\text{wspeed}}\Omega_{e,i}^{\text{wspeed}} \cos(x_{e,i}^{\text{wdir}} - \Omega_{e,i}^{\text{wdir}})}. \end{aligned} \quad (\text{J.18})$$

Equation (J.9) thus becomes, for the case of the wind (horizontal) vector variable:

$$\Lambda_{\mathcal{C},\mathcal{L}}^{\text{wvec}} = \sqrt{\frac{1}{J} \sum_{\substack{x_{e,i} \in \mathcal{L} \\ e \in \mathcal{C}}} \left((x_{e,i}^{\text{wspeed}})^2 + (\Omega_{e,i}^{\text{wspeed}})^2 - 2x_{e,i}^{\text{wspeed}}\Omega_{e,i}^{\text{wspeed}} \cos(x_{e,i}^{\text{wdir}} - \Omega_{e,i}^{\text{wdir}}) \right)}. \quad (\text{J.19})$$

The uncertainty of $\delta_{e,i} = \|\vec{x}_{e,i} - \vec{\Omega}_{e,i}\|$ is dependent upon both the CWSs for the wind (horizontal) direction and speed. Remembering that the GDP wind (horizontal) direction and speed measurements are not subject to any correlated uncertainties, we have:

$$\begin{aligned} \sigma(\delta_{e,i})^2 = V(\delta_{e,i}) &= \left(\frac{\partial \delta_{e,i}}{\partial \Omega_{e,i}^{\text{wspeed}}} \right)^2 \left(\sigma_{\Omega_{e,i}^{\text{wspeed}}}^U \right)^2 + \left(\frac{\partial \delta_{e,i}}{\partial \Omega_{e,i}^{\text{wdir}}} \right)^2 \left(\sigma_{\Omega_{e,i}^{\text{wdir}}}^U \right)^2 \\ &= \left(\frac{\sigma_{\Omega_{e,i}^{\text{wspeed}}}^U}{\delta_{e,i}} \right)^2 \left(\Omega_{e,i}^{\text{wspeed}} - x_{e,i}^{\text{wspeed}} \cos(x_{e,i}^{\text{wdir}} - \Omega_{e,i}^{\text{wdir}}) \right)^2 \\ &\quad + \left(\frac{\pi}{180} \frac{\sigma_{\Omega_{e,i}^{\text{wdir}}}^U}{\delta_{e,i}} \right)^2 \left(-x_{e,i}^{\text{wspeed}} \Omega_{e,i}^{\text{wspeed}} \sin(x_{e,i}^{\text{wdir}} - \Omega_{e,i}^{\text{wdir}}) \right)^2 \end{aligned} \quad (\text{J.20})$$

with the factor $\pi/180$ resulting from the conversion of wind directions from degrees to radians inside the trigonometric functions.

K DERIVATION OF THE ORUC VALUES FOR HUMIDITY

OSCAR requirement uncertainty criterion (ORUC) values are formally introduced in Section 9.3.1. They characterise the desirable measurement errors of a given variable, with distinct values specified for different atmospheric layers (e.g. PBL, FT, ...). The OSCAR application areas of "Aeronautical Meteorology", "Global Numerical Weather Prediction and Real-time Monitoring", "High-Resolution Numerical Weather Prediction" and "Nowcasting / Very Short-Range Forecasting" contain ORUC values for specific humidity, but not for relative humidity. These are expressed in relative terms of $\% \text{ g kg}^{-1} \equiv \% \text{ kg kg}^{-1}$. Here, we describe our conversion of these ORUC values into absolute levels of relative humidity (i.e. into %RH).

Let us formally define the relative humidity RH as the ratio of the water vapour partial pressure e and the water vapour saturation pressure $e_s(T)$, which is a function of the temperature T :

$$RH = 100 \cdot \frac{e}{e_s(T)} \quad (\text{K.1})$$

The specific humidity q is the ratio of the mass of water vapour m_{vapour} in a given volume V and the sum of the mass of water vapour and mass of dry air $m_{\text{dry air}}$ in the same volume:

$$q = \frac{m_{\text{vapour}}}{m_{\text{vapour}} + m_{\text{dry air}}}, \quad (\text{K.2})$$

whereas the mixing ratio r is defined as:

$$r = \frac{m_{\text{vapor}}}{m_{\text{dry air}}}. \quad (\text{K.3})$$

such that:

$$q = \frac{r}{r + 1}. \quad (\text{K.4})$$

From the ideal gas law, we have:

$$m_{\text{dry air}} \frac{R}{M_{\text{dry air}}} = \frac{(P - e)V}{T}, \quad (\text{K.5})$$

$$m_{\text{vapour}} \frac{R}{M_{\text{vapour}}} = \frac{eV}{T}, \quad (\text{K.6})$$

where P is the total pressure in the volume V , R is the universal gas constant, and $M_{\text{dry air}} = 28.9644 \text{ g mol}^{-1}$ and $M_{\text{vapour}} = 18.0153 \text{ g mol}^{-1}$ are the molar masses of dry air and water vapour, such that:

$$P = e (\alpha r^{-1} + 1), \quad (\text{K.7})$$

with $\alpha = M_{\text{vapour}} \cdot M_{\text{dry air}}^{-1} \approx 0.62198$. Hence, we can express relative humidity as a function of specific humidity:

$$\begin{aligned} RH &= 100 \cdot \frac{e}{e_s(T)} = 100 \cdot \frac{P}{e_s(T)} \cdot (\alpha r^{-1} + 1)^{-1} \\ &= 100 \cdot \frac{P}{e_s(T)} \cdot \left(\alpha \frac{1 - q}{q} + 1 \right)^{-1} \\ &= 100 \cdot \frac{P}{e_s(T)} \cdot \frac{q}{\alpha + q(1 - \alpha)} \end{aligned} \quad (\text{K.8})$$

Let us introduce $\Theta_{q[\%], \mathcal{L}}$, the ORUC value for specific humidity and a given atmospheric layer \mathcal{L} , defined in units of $\% \text{ kg kg}^{-1}$. For any given specific humidity measurement q , it can be converted

into $\Theta_{q,\mathcal{L}}$, the corresponding value in units of kg kg^{-1} :

$$\Theta_{q,\mathcal{L}} = q \cdot \frac{\Theta_{q[\%],\mathcal{L}}}{100} \quad (\text{K.9})$$

Using Equation (K.8), we can derive $\Theta_{RH,\mathcal{L}}$, the equivalent ORUC value in terms of relative humidity:

$$\Theta_{RH,\mathcal{L}} = 100 \cdot \frac{P}{e_s(T)} \cdot \frac{\Theta_{q,\mathcal{L}}}{\alpha + \Theta_{q,\mathcal{L}}(1 - \alpha)} \approx 100 \cdot \frac{P}{e_s(T)} \cdot \frac{q \cdot 0.01 \cdot \Theta_{q[\%],\mathcal{L}}}{\alpha} \approx RH \cdot \frac{\Theta_{q[\%],\mathcal{L}}}{100}, \quad (\text{K.10})$$

where we have taken advantage of the fact that $q \lesssim 0.01 \text{ kg kg}^{-1}$ for all the flights of the UAI 2022 field campaign, such that:

$$\alpha + q(1 - \alpha) \approx \alpha \quad \text{and} \quad \alpha + q \cdot 0.01 \cdot \Theta_{q[\%],\mathcal{L}} \cdot (1 - \alpha) \approx \alpha \quad (\text{K.11})$$

Equation (K.10) shows that, to a very good approximation, a *relative ORUC value for specific humidity* can be used directly as a *relative ORUC value for relative humidity*.

We present in Figure K.1 the individual Combined Working measurement Standard (CWS) profiles (assembled from GRUAN Data Product (GDP) profiles, see Section 9.2) of the UAI 2022 field campaign, and the associated values of $\Theta_{RH,\mathcal{L}}$ for each individual measurement. A wide range of relative humidity values have been sampled at all altitudes up to the tropopause. These result in a proportionally-equally large range of $\Theta_{RH,\mathcal{L}}$ values, given the relative nature of the OSCAR criteria for specific humidity.

The number of flights acquired during the UAI 2022 field campaign is not sufficient to sub-divide profiles into distinct relative humidity bins while maintaining sufficient number statistics in each bin. Therefore, we cannot strictly evaluate the radiosondes performance against a relative ORUC value. Instead, we take the conservative alternative approach of using a single, absolute ORUC value $\Theta_{RH,\mathcal{L}}$, chosen as the maximum (i.e. least stringent) value applicable to the UAI 2022 field campaign flights:

$$\Theta_{RH,\mathcal{L}} = RH_{\max} \cdot \frac{\Theta_{q[\%],\mathcal{L}}}{100} = \Theta_{q[\%],\mathcal{L}} \quad (\text{K.12})$$

which stems from the fact that the maximum relative humidity measurement encountered during the UAI 2022 field campaign for the PBL and FT is 100 %RH.

The admittedly-confusing implication of Equation (K.12) is that the ORUC values quoted in Table 9.2 for relative humidity in the application areas of "Aeronautical Meteorology", "Global Numerical Weather Prediction and Real-time Monitoring", "High-Resolution Numerical Weather Prediction" and "Nowcasting / Very Short-Range Forecasting" look identical to the original ORUC values set in terms of specific humidity by the WMO. However, their units are in *absolute percent of relative humidity* (%RH) rather than in *relative percents of specific humidity* (% g kg^{-1}).

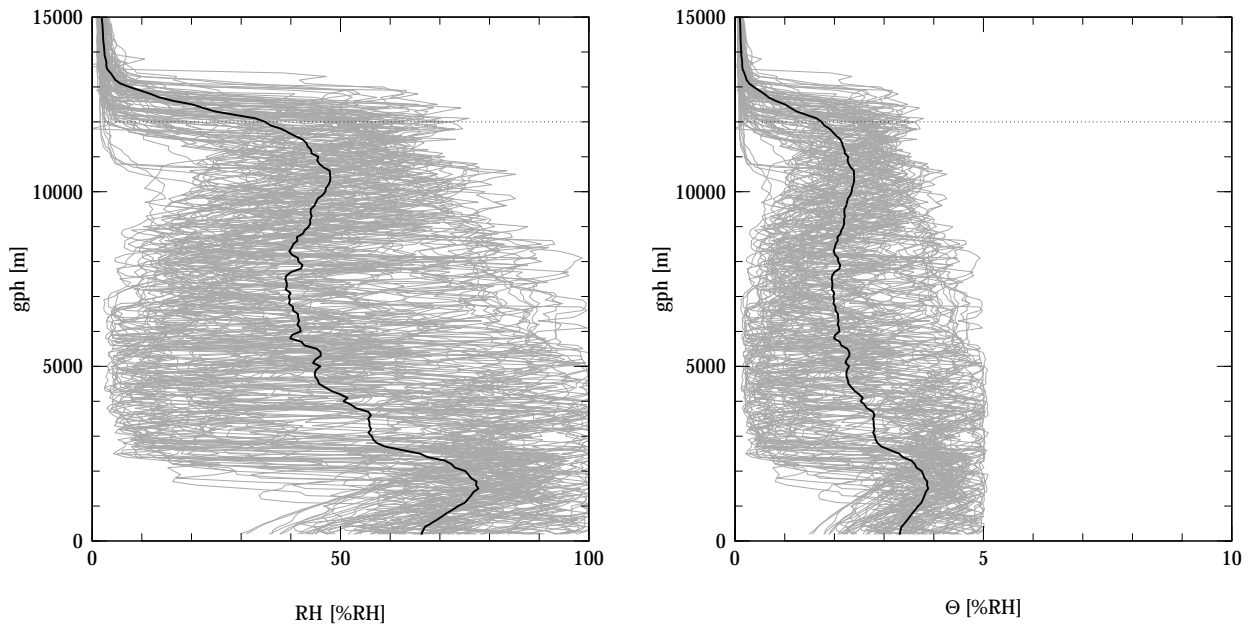


Figure K.1: Left: individual CWS profiles of relative humidity measured during the UAI 2022 field campaign (grey lines), and associated mean profile (black line). A wide range of relative humidity conditions have been sampled at all altitudes up to the tropopause. Right: Distribution of the ORUC values $\Theta_{RH,\mathcal{L}}$ for each individual measurement according to Equation (K.10) (grey lines) and associated mean profile (black line), for the example of $\Theta_{q[\%],\mathcal{L}} = 5\%$ of g kg^{-1} . The cap at $\Theta_{RH,\mathcal{L}} = 100 \cdot \frac{\Theta_{q[\%],\mathcal{L}}}{100} = 5\%$ RH is clearly visible, and corresponds to the conservative assessment level we use in our analysis. The median geopotential height of the tropopause during the UAI 2022 field campaign is indicated using a horizontal dotted line at 12.0 km in both panels.

L INDIVIDUAL $\Lambda_{c,\mathcal{L}}$ DIAGNOSTIC DIAGRAMS

L.1 ATMS-3710

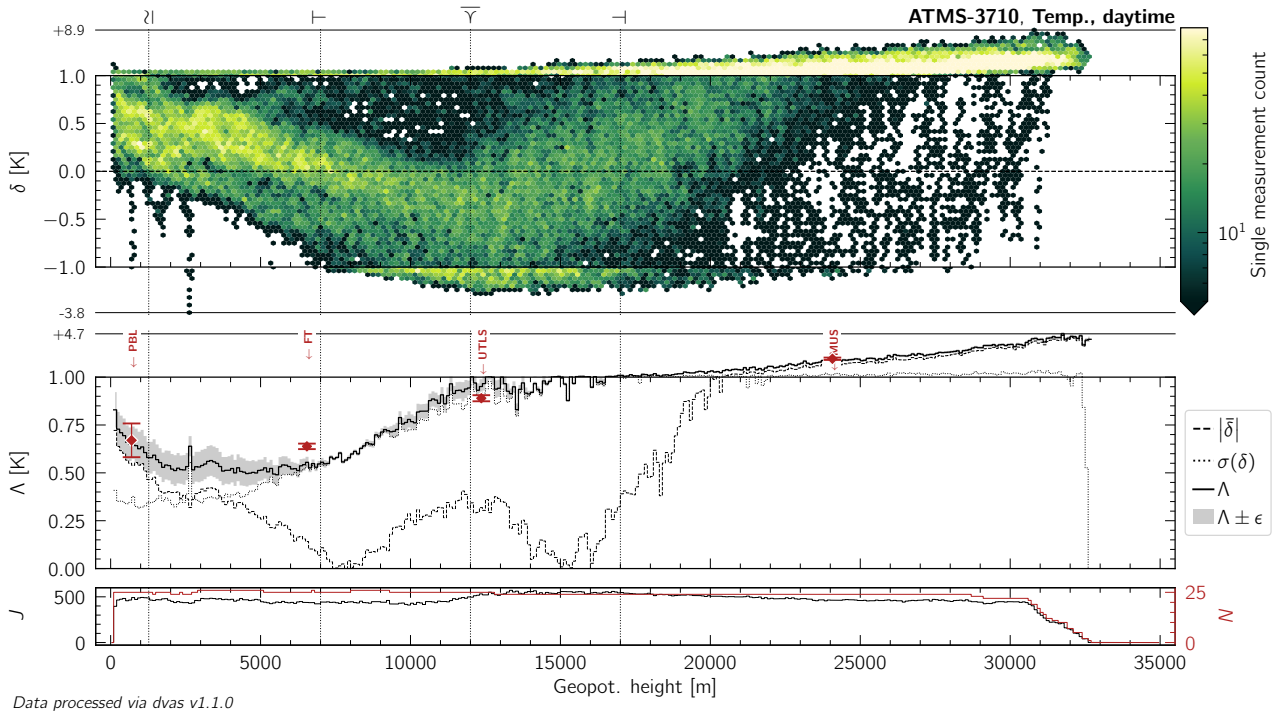


Figure L.1: Same as Figure 10.13.

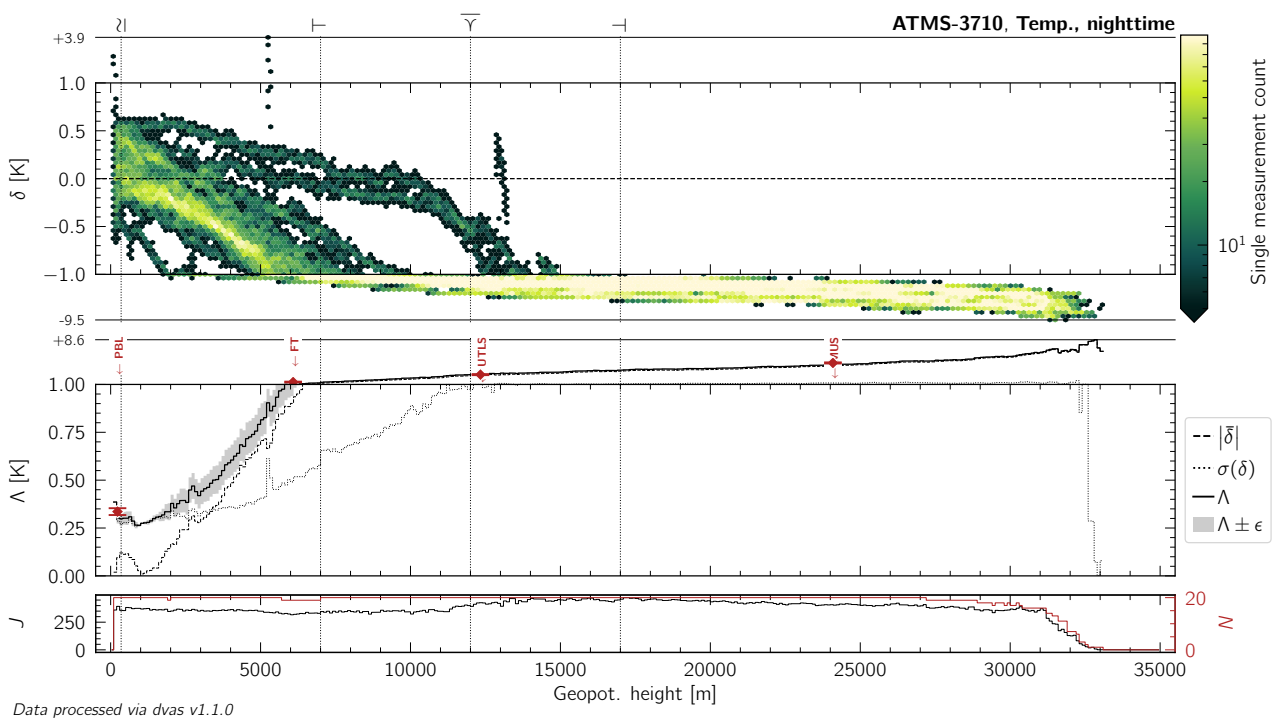


Figure L.2: Same as Figure 10.13, but for nighttime measurements of atmospheric temperature by the ATMS-3710 radiosonde.

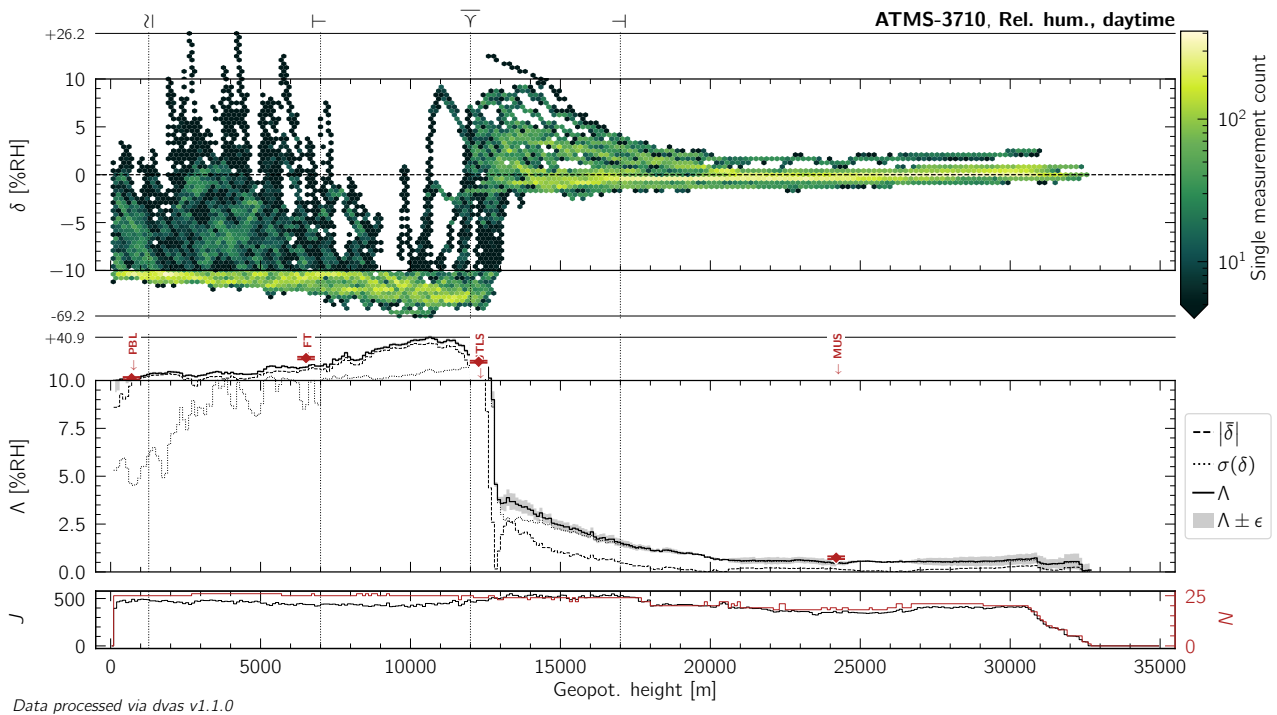


Figure L.3: Same as Figure 10.13, but for daytime measurements of relative humidity by the ATMS-3710 radiosonde.

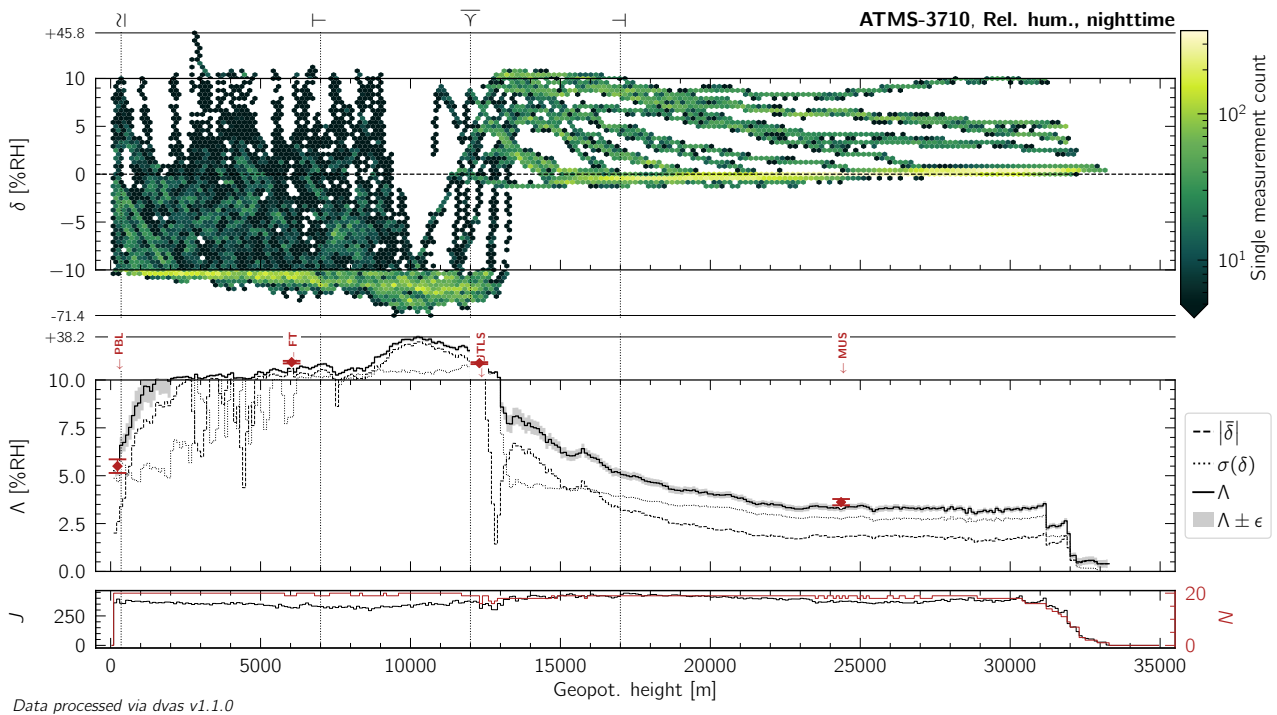


Figure L.4: Same as Figure 10.13, but for nighttime measurements of relative humidity by the ATMS-3710 radiosonde.

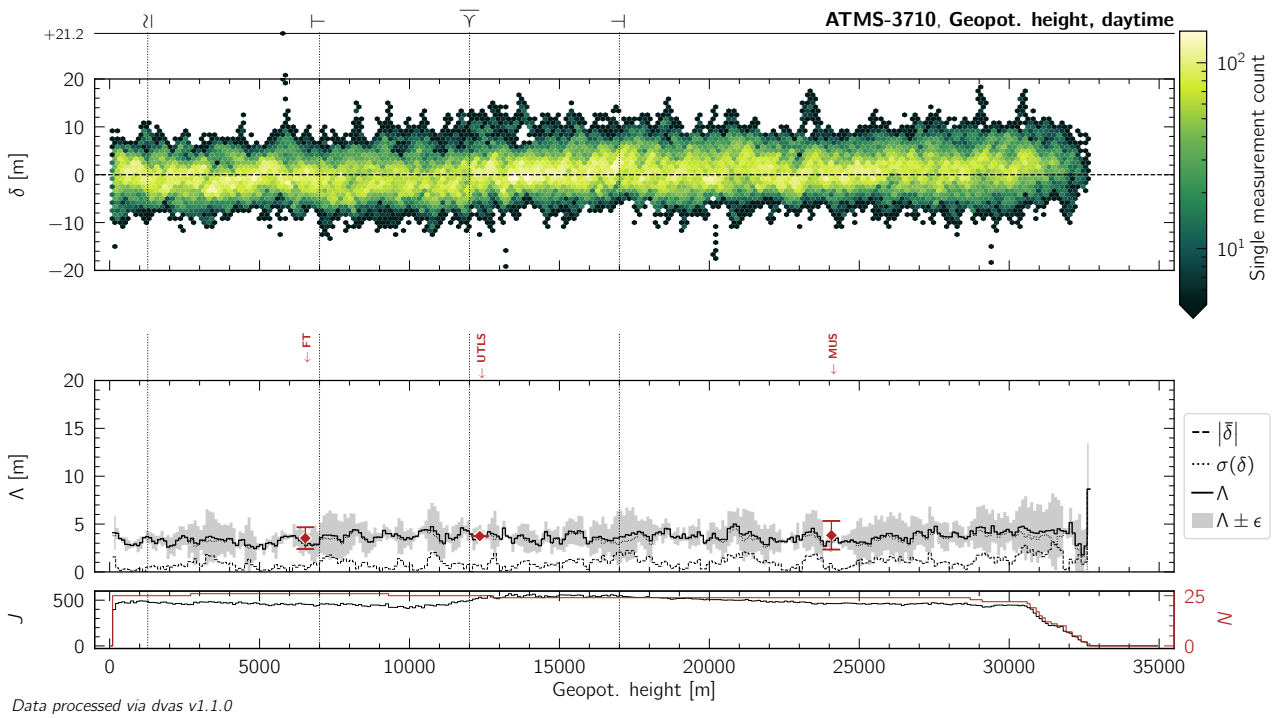


Figure L.5: Same as Figure 10.13, but for daytime measurements of geopotential height by the ATMS-3710 radiosonde.

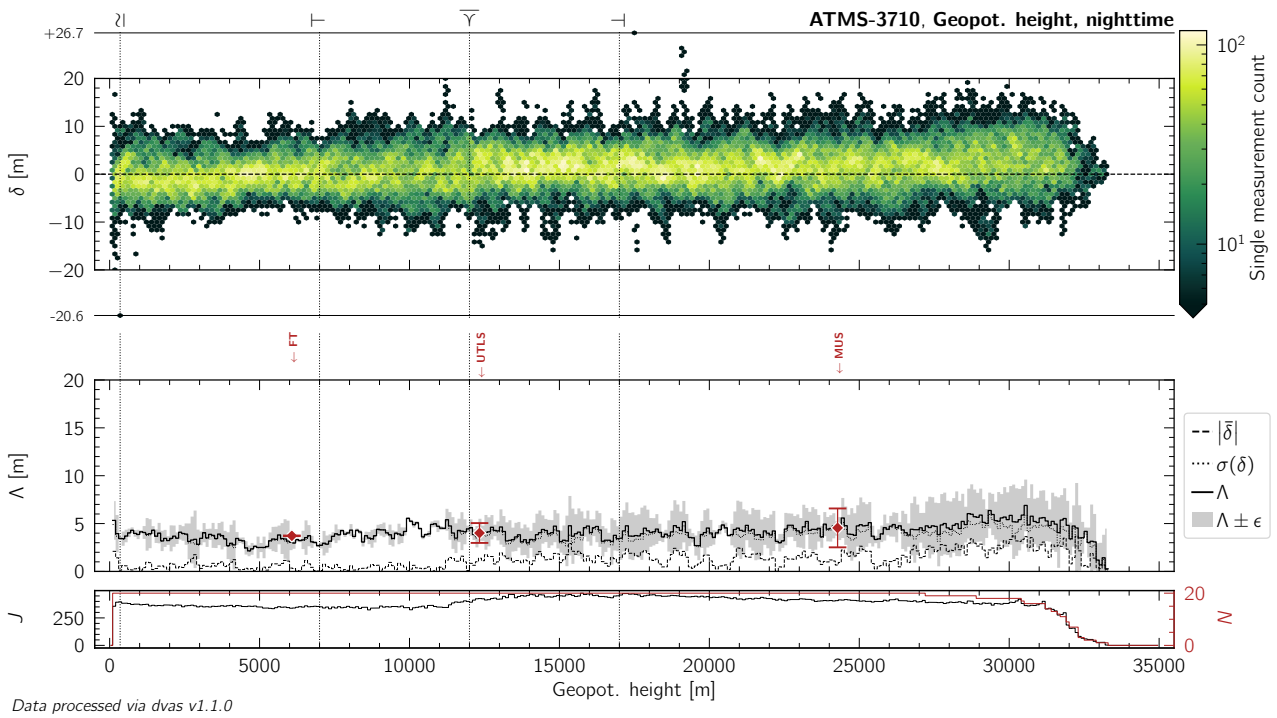


Figure L.6: Same as Figure 10.13, but for nighttime measurements of geopotential height by the ATMS-3710 radiosonde.

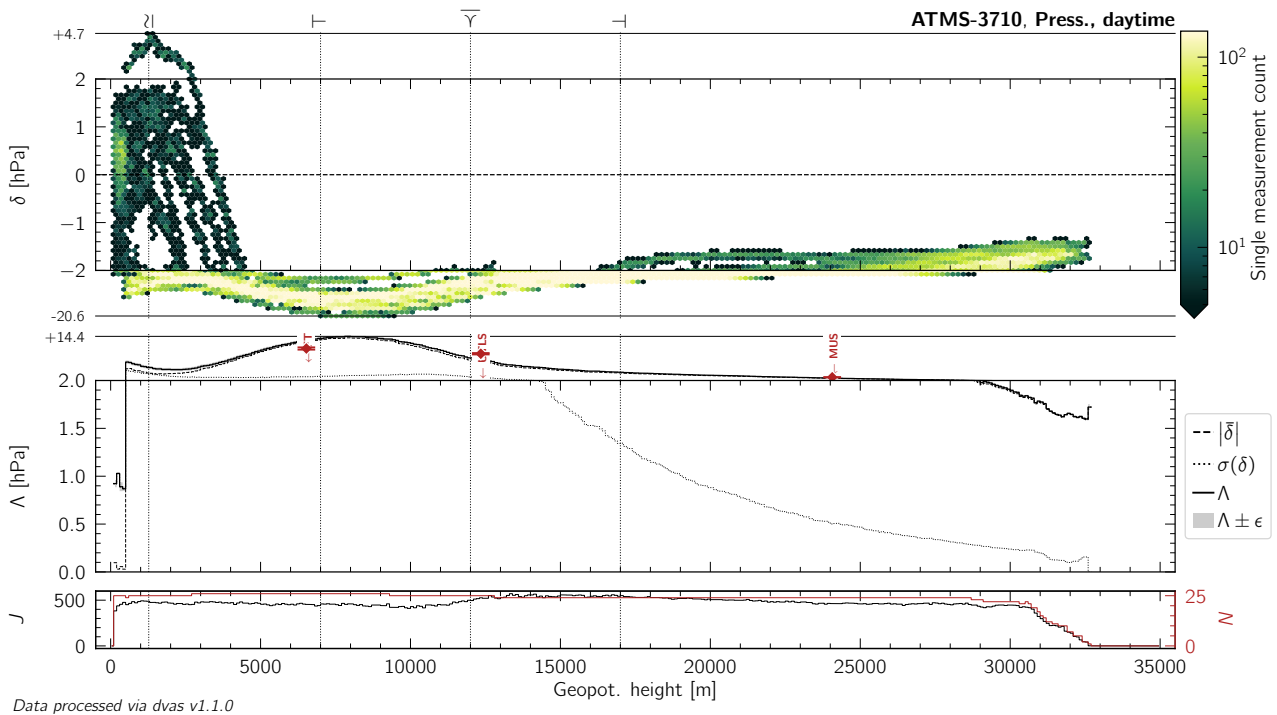


Figure L.7: Same as Figure 10.13, but for daytime measurements of atmospheric pressure by the ATMS-3710 radiosonde.

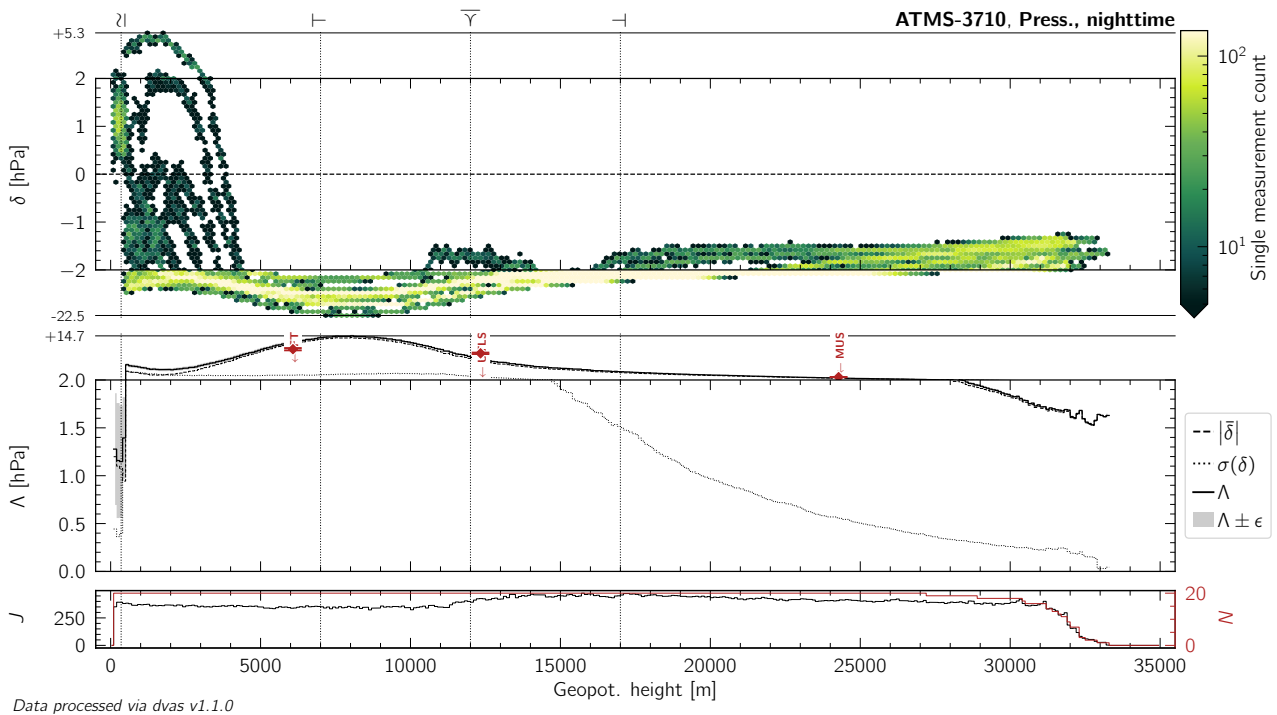


Figure L.8: Same as Figure 10.13, but for nighttime measurements of atmospheric pressure by the ATMS-3710 radiosonde.

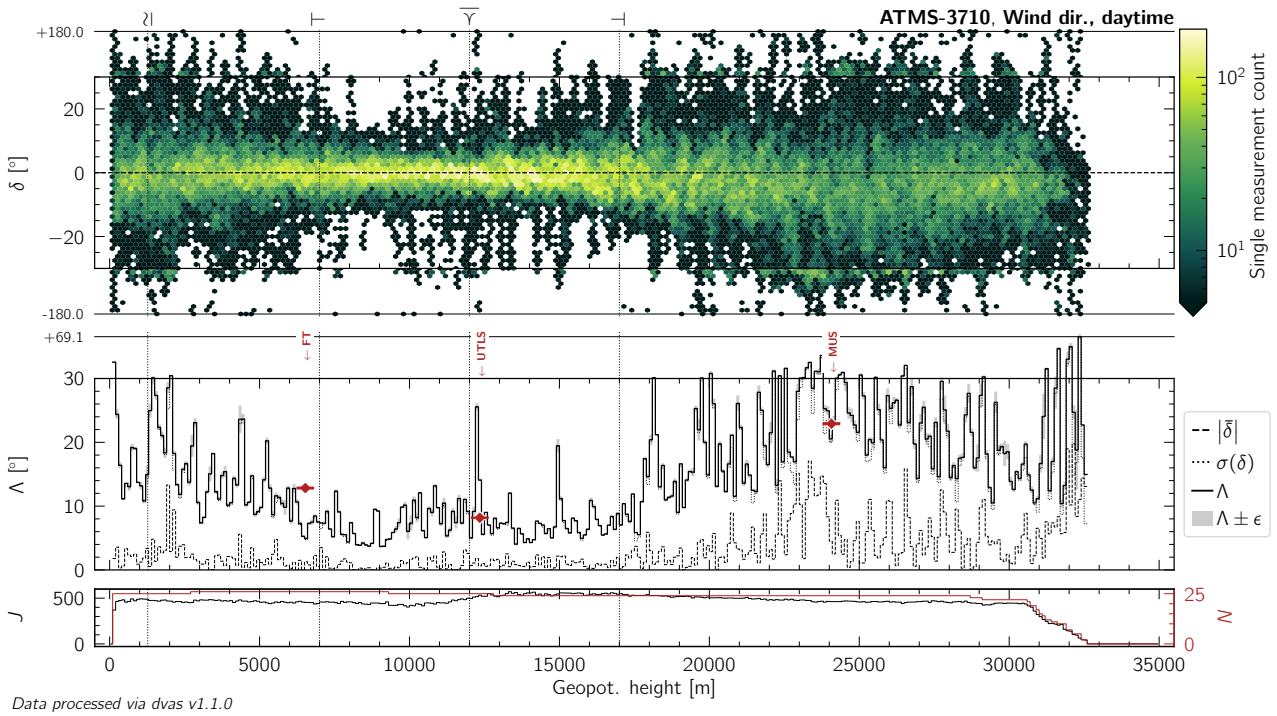


Figure L.9: Same as Figure 10.13, but for daytime measurements of wind (horizontal) direction by the ATMS-3710 radiosonde.

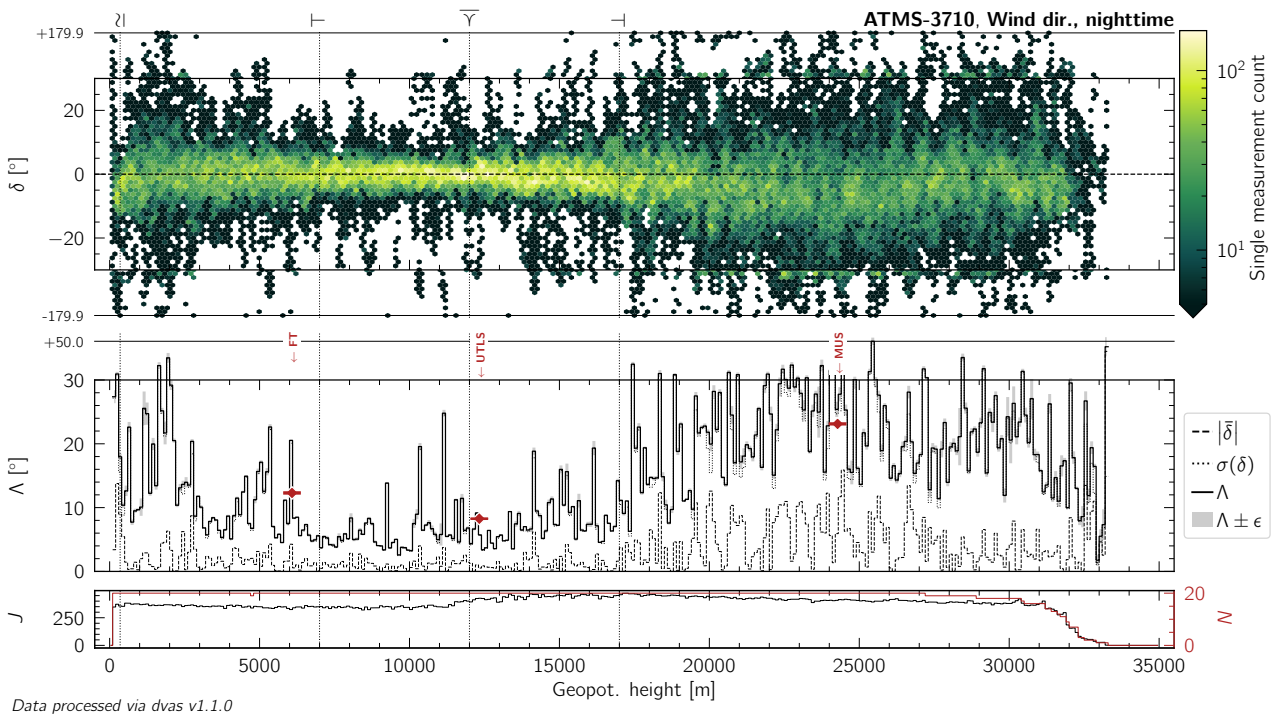


Figure L.10: Same as Figure 10.13, but for nighttime measurements of wind (horizontal) direction by the ATMS-3710 radiosonde.

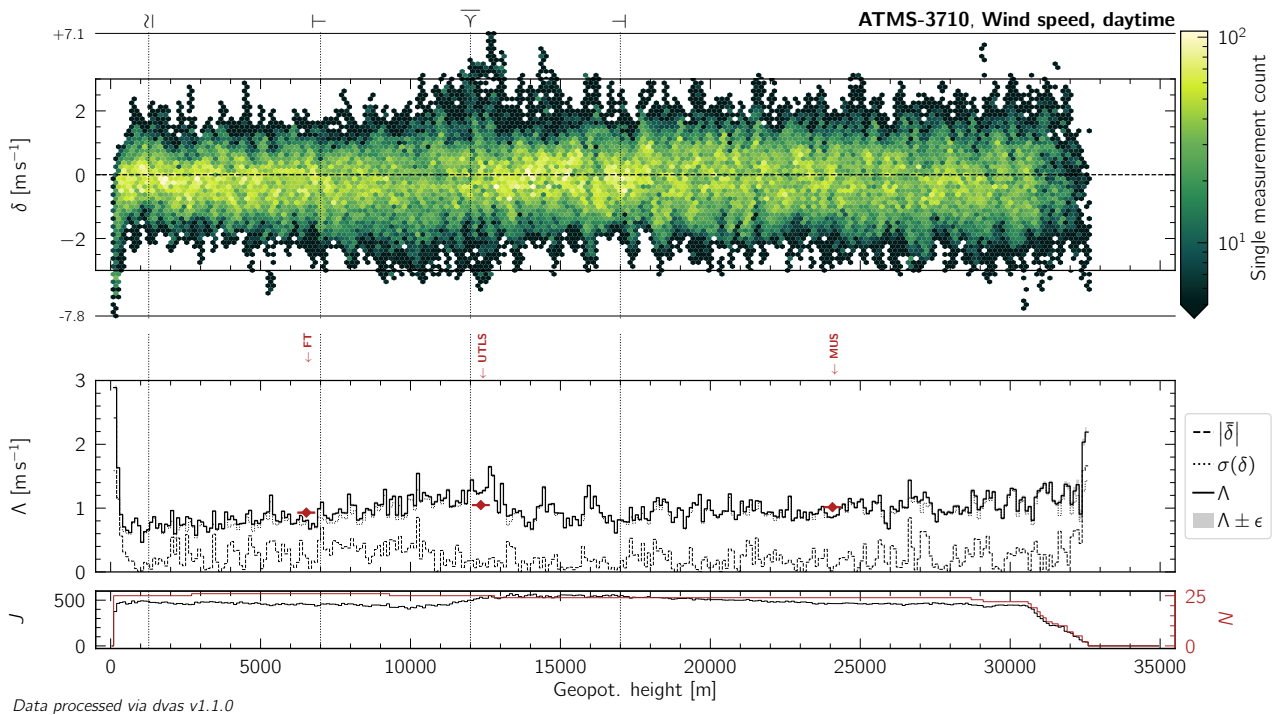


Figure L.11: Same as Figure 10.13, but for daytime measurements of wind (horizontal) speed by the ATMS-3710 radiosonde.

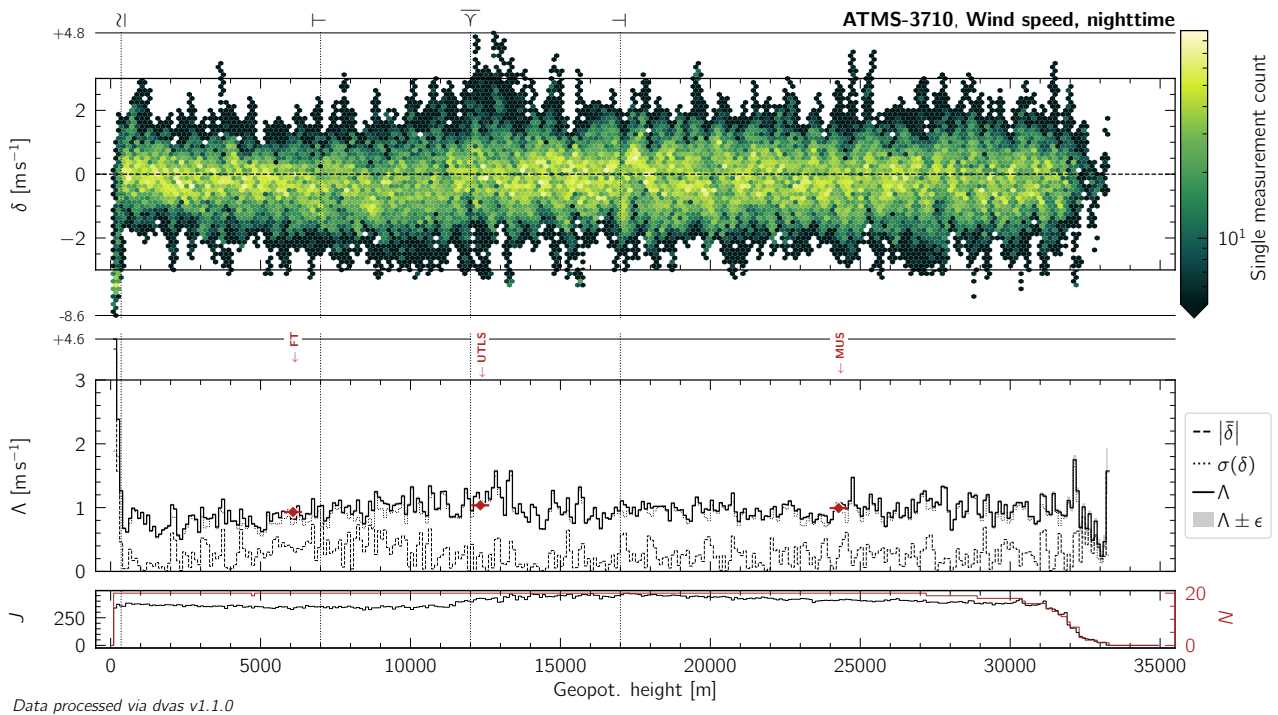


Figure L.12: Same as Figure 10.13, but for nighttime measurements of wind (horizontal) speed by the ATMS-3710 radiosonde.

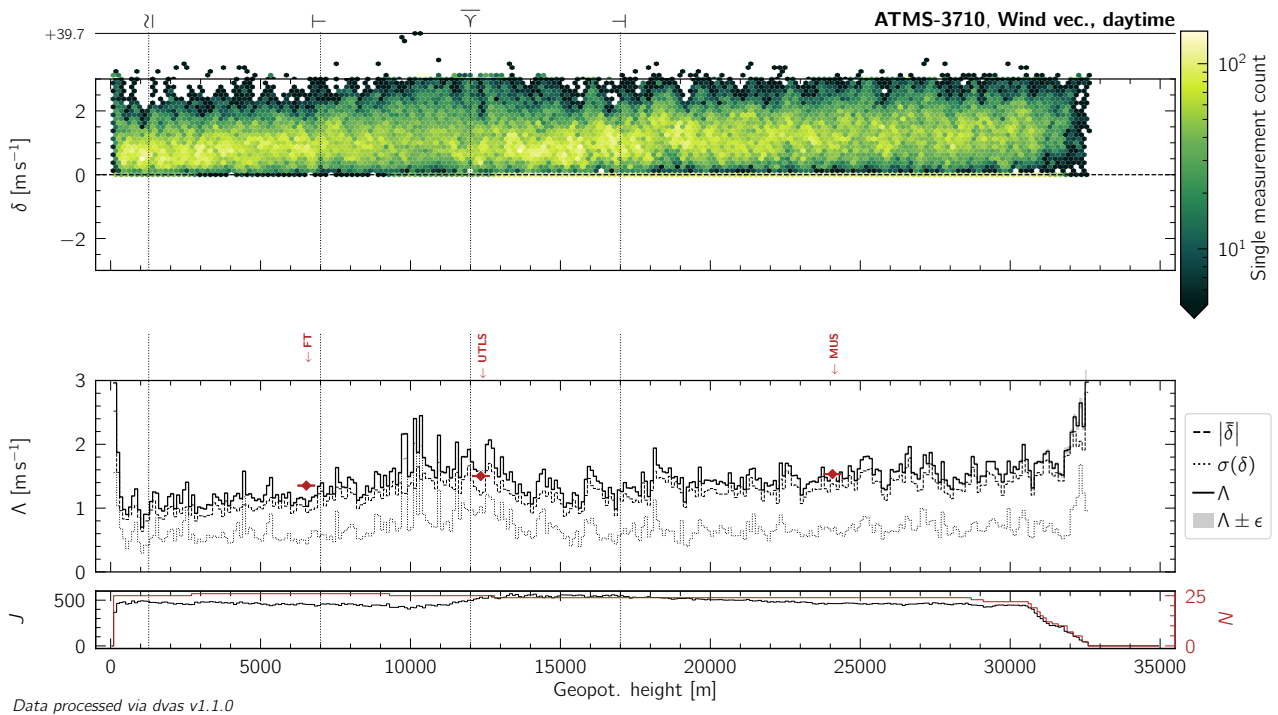


Figure L.13: Same as Figure 10.13, but for daytime measurements of the wind (horizontal) vector by the ATMS-3710 radiosonde.

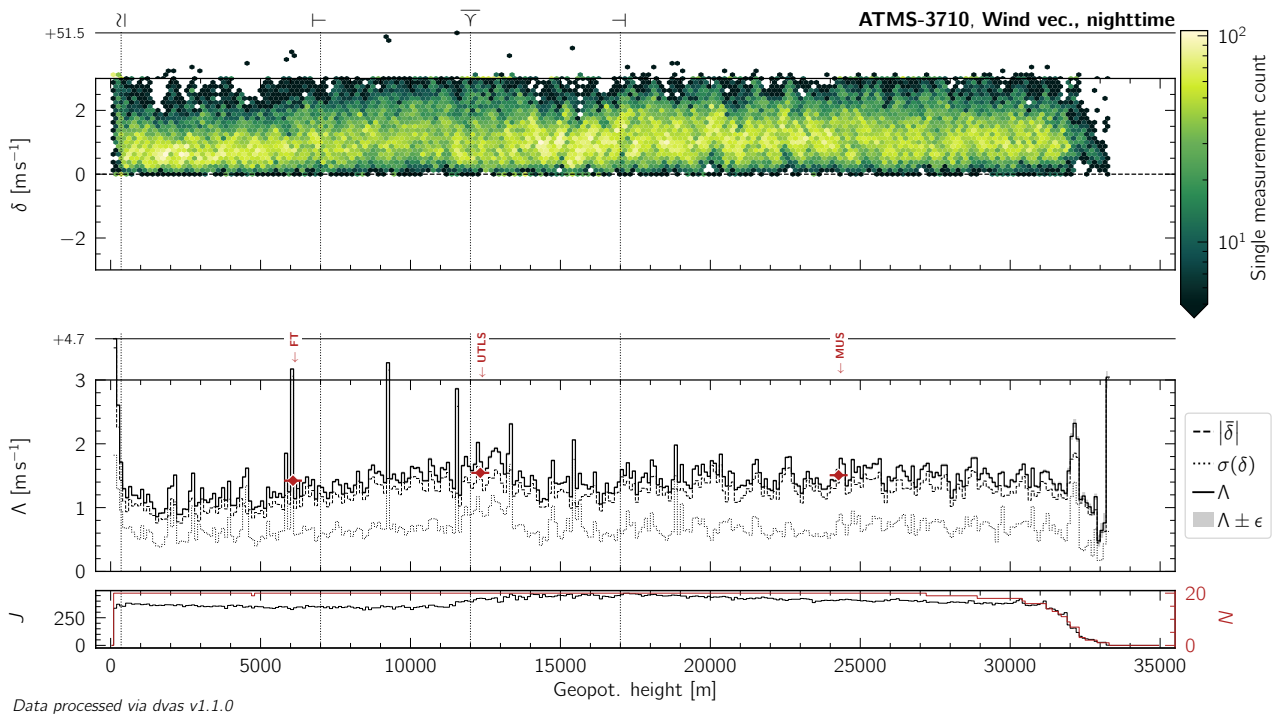


Figure L.14: Same as Figure 10.13, but for nighttime measurements of the wind (horizontal) vector by the ATMS-3710 radiosonde.

L.2 CF-06-AH

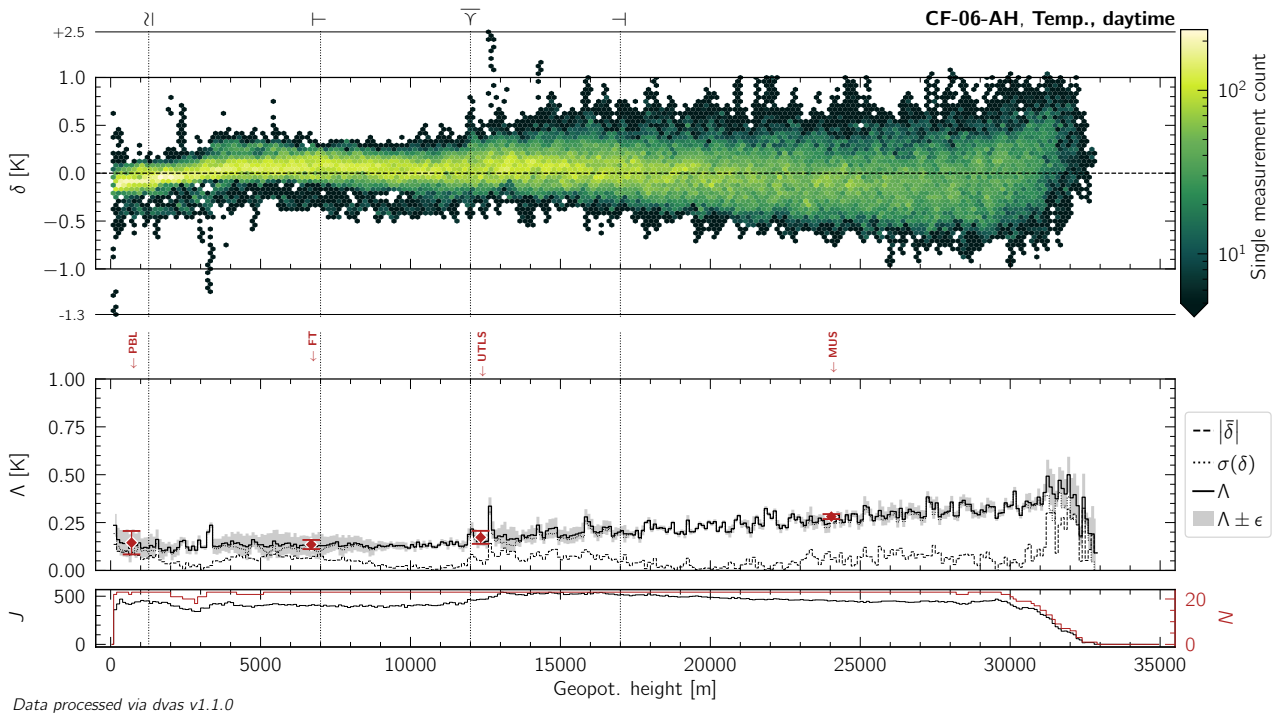


Figure L.15: Same as Figure 10.13, but for daytime measurements of atmospheric temperature by the CF-06-AH radiosonde.

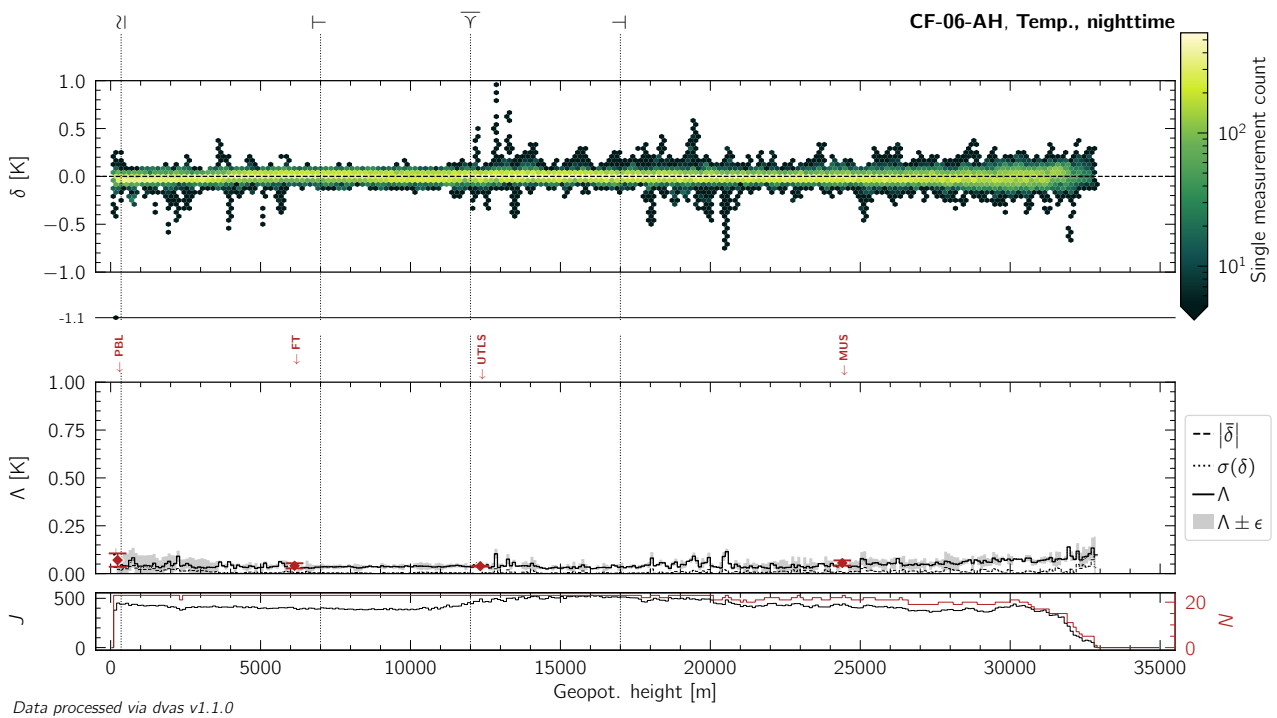


Figure L.16: Same as Figure 10.13, but for nighttime measurements of atmospheric temperature by the CF-06-AH radiosonde.

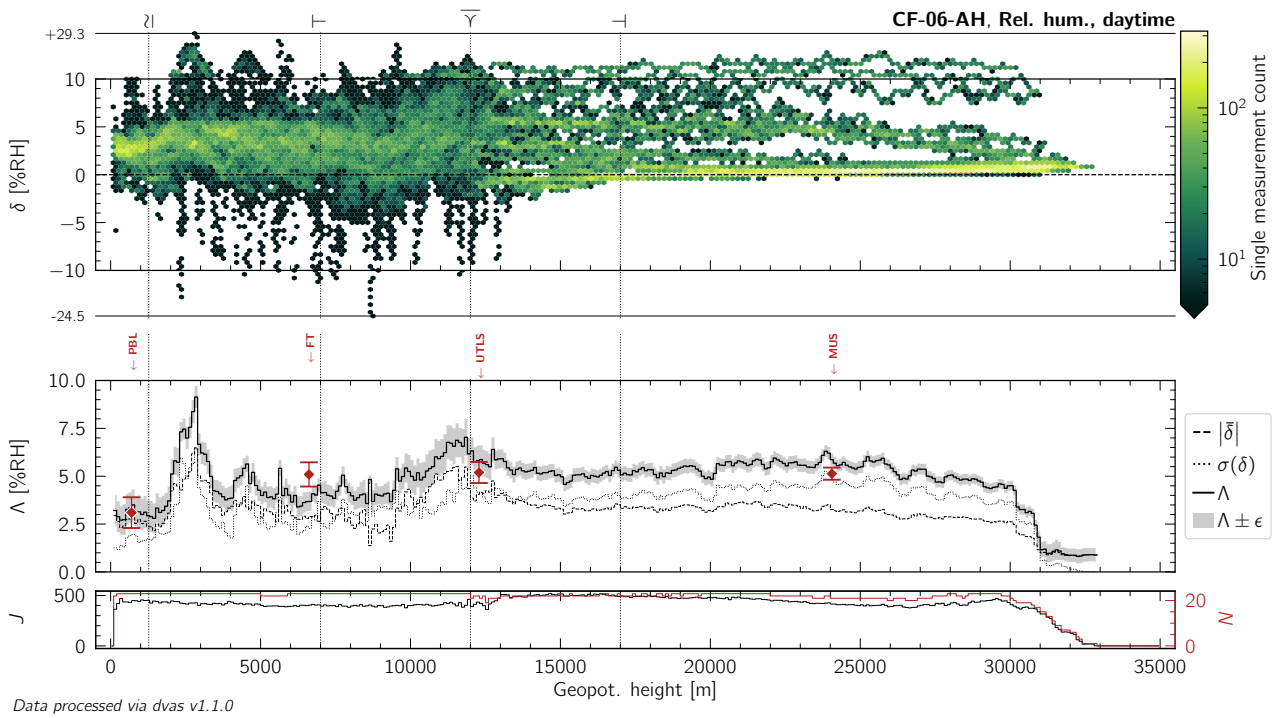


Figure L.17: Same as Figure 10.13, but for daytime measurements of relative humidity by the CF-06-AH radiosonde.

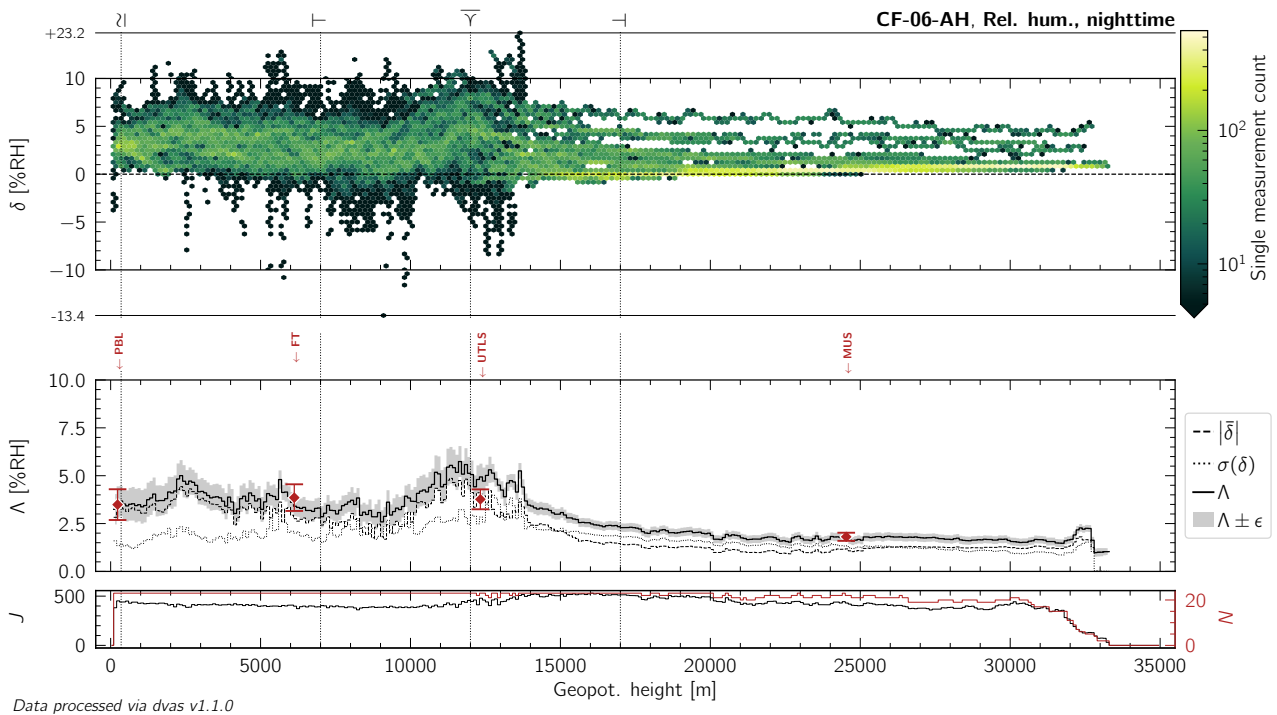


Figure L.18: Same as Figure 10.13, but for nighttime measurements of relative humidity by the CF-06-AH radiosonde.

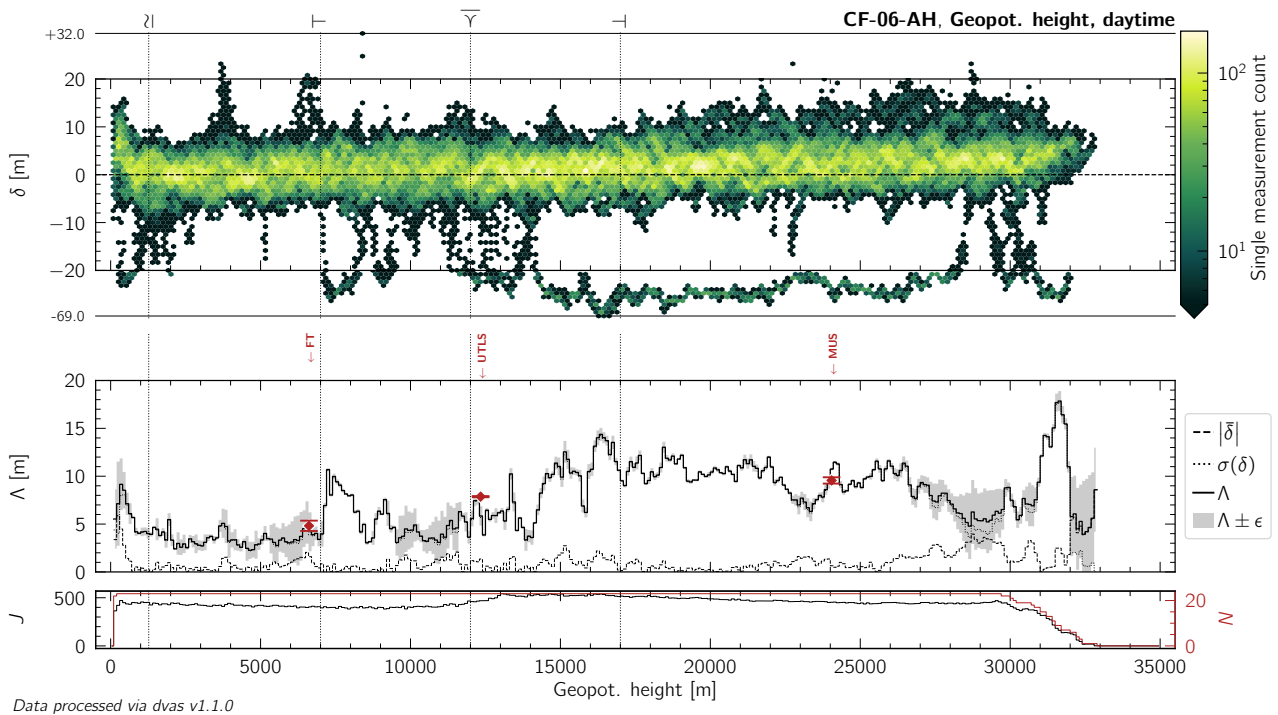


Figure L.19: Same as Figure 10.13, but for daytime measurements of geopotential height by the CF-06-AH radiosonde.

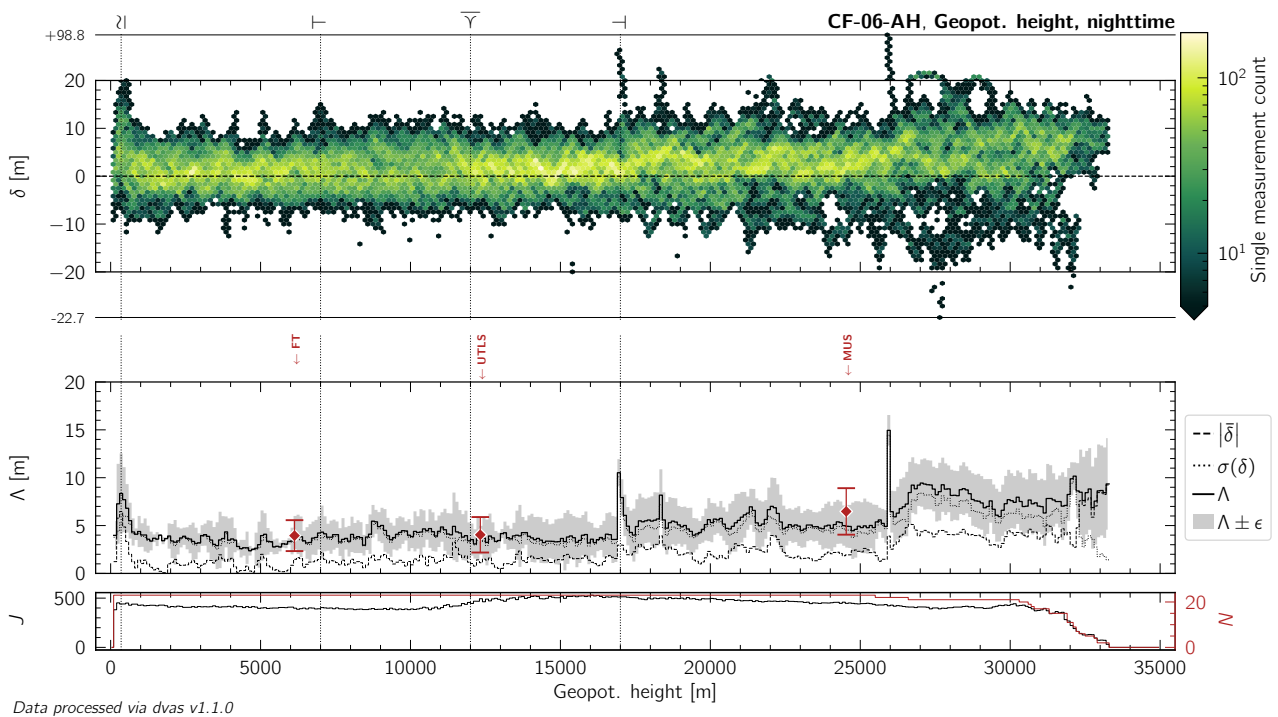


Figure L.20: Same as Figure 10.13, but for nighttime measurements of geopotential height by the CF-06-AH radiosonde.

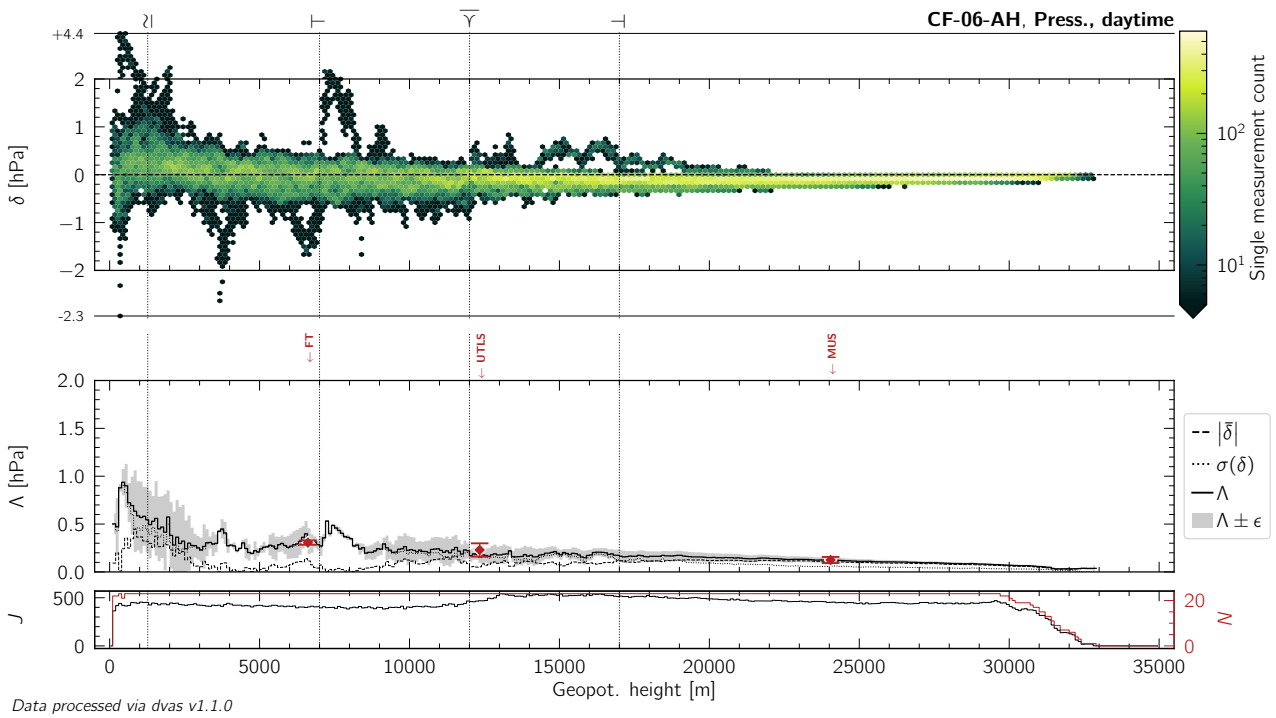


Figure L.21: Same as Figure 10.13, but for daytime measurements of atmospheric pressure by the CF-06-AH radiosonde.

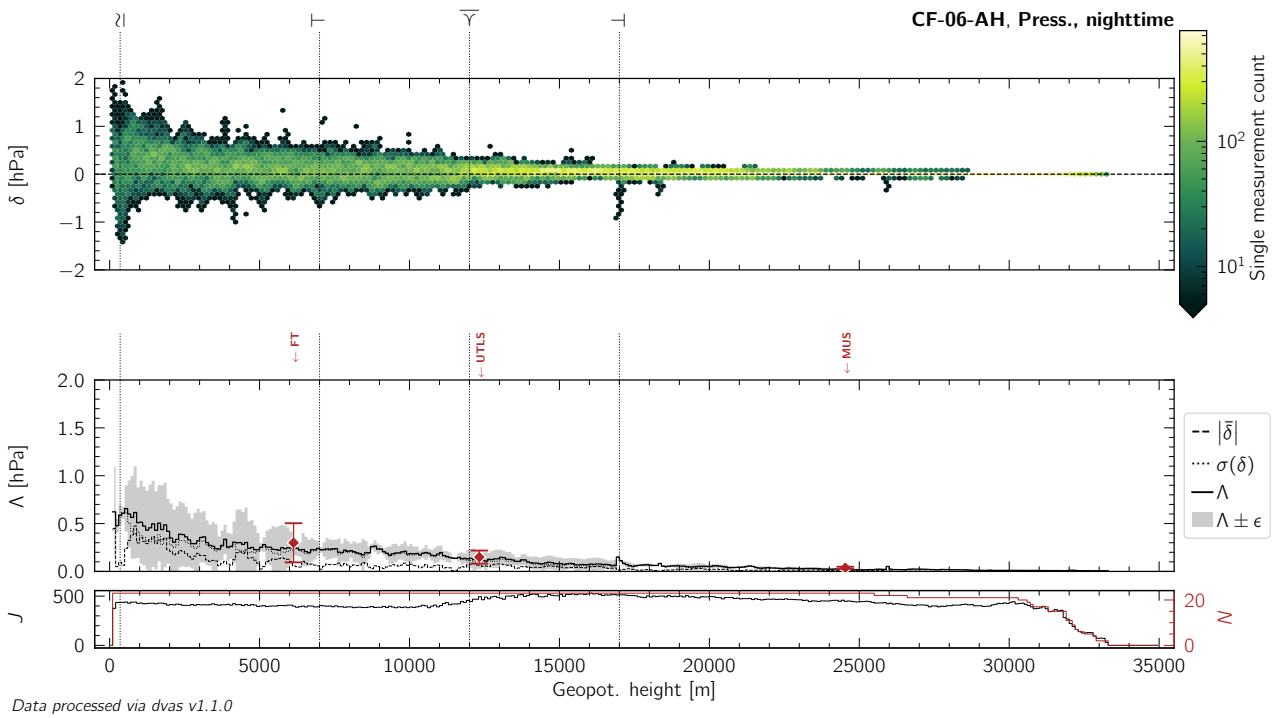


Figure L.22: Same as Figure 10.13, but for nighttime measurements of atmospheric pressure by the CF-06-AH radiosonde.

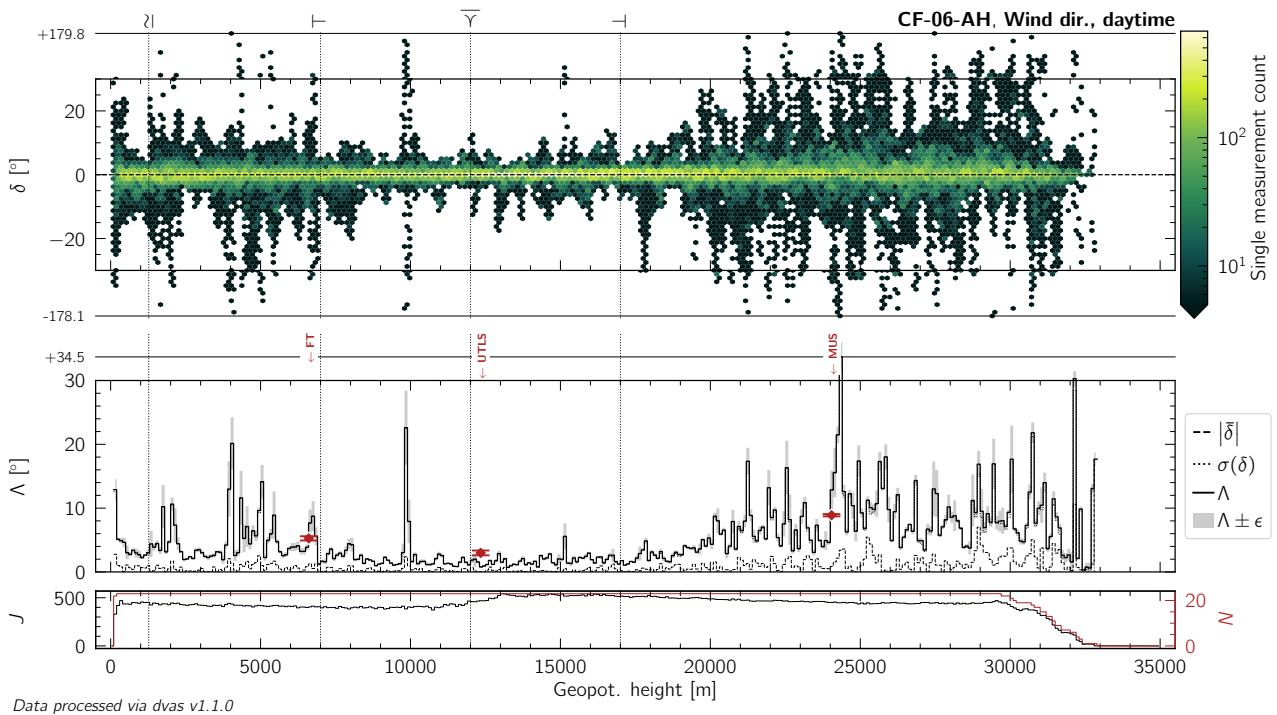


Figure L.23: Same as Figure 10.13, but for daytime measurements of wind (horizontal) direction by the CF-06-AH radiosonde.

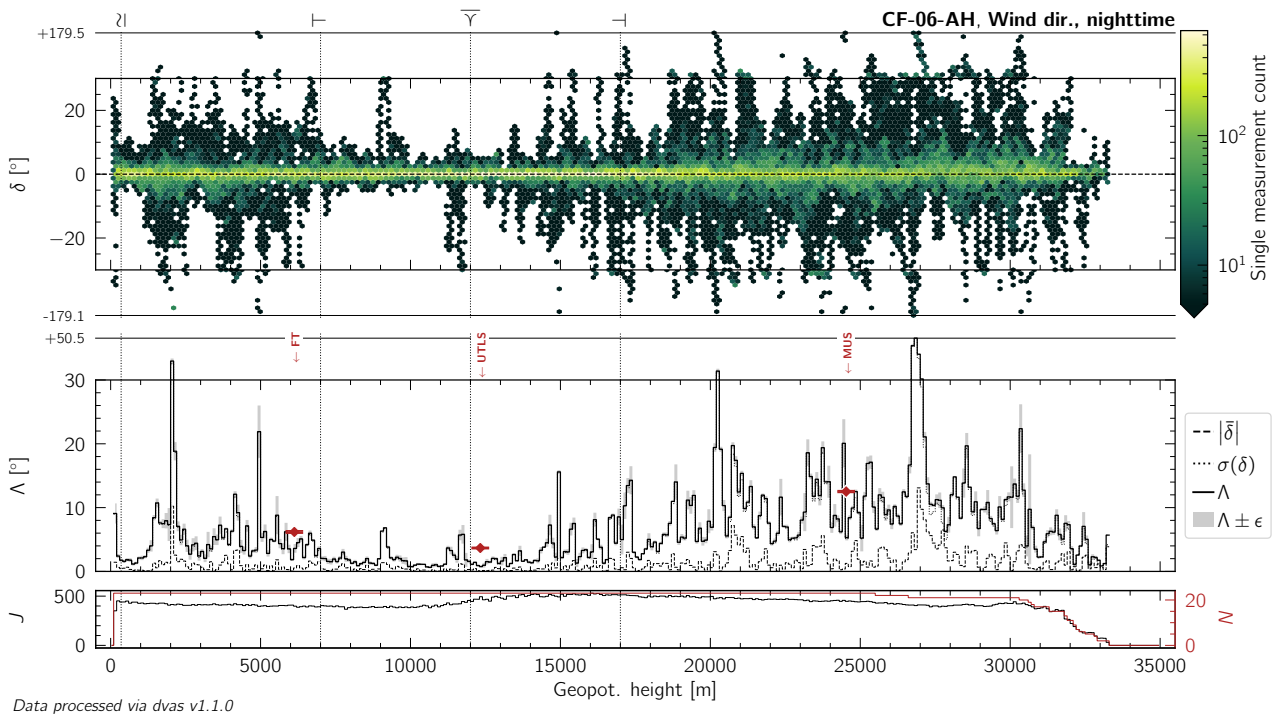


Figure L.24: Same as Figure 10.13, but for nighttime measurements of wind (horizontal) direction by the CF-06-AH radiosonde.

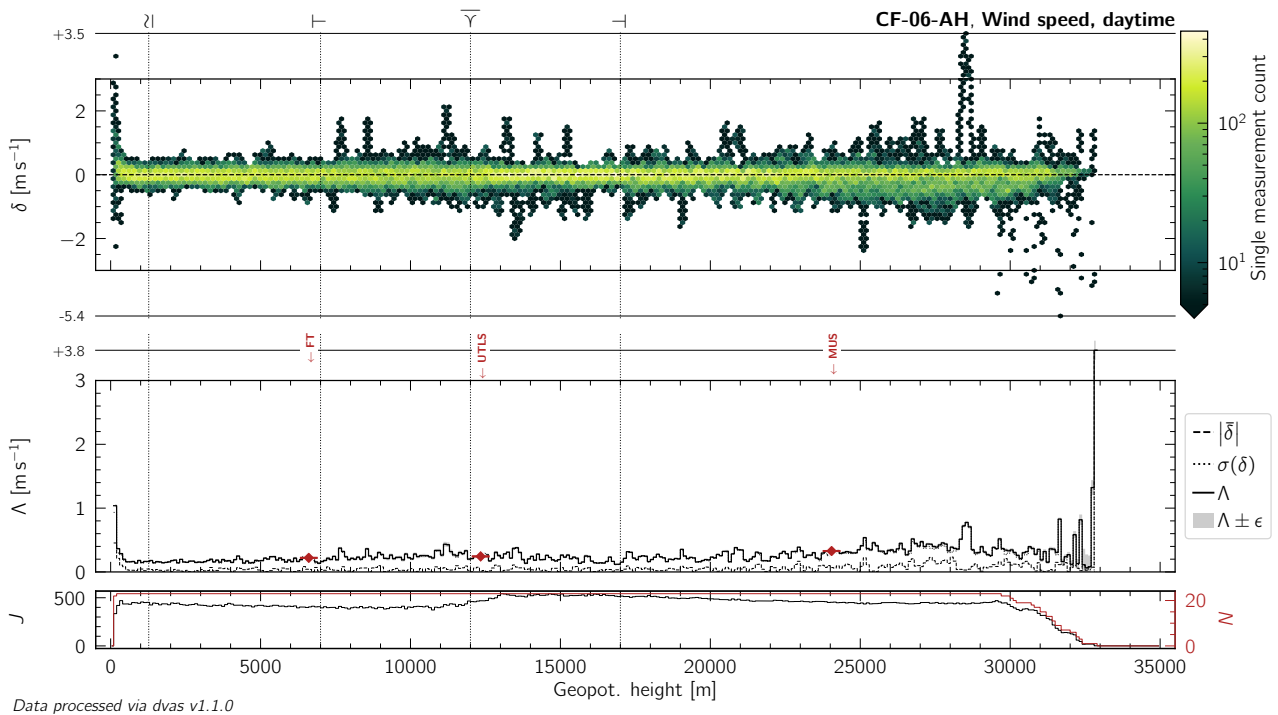


Figure L.25: Same as Figure 10.13, but for daytime measurements of wind (horizontal) speed by the CF-06-AH radiosonde.

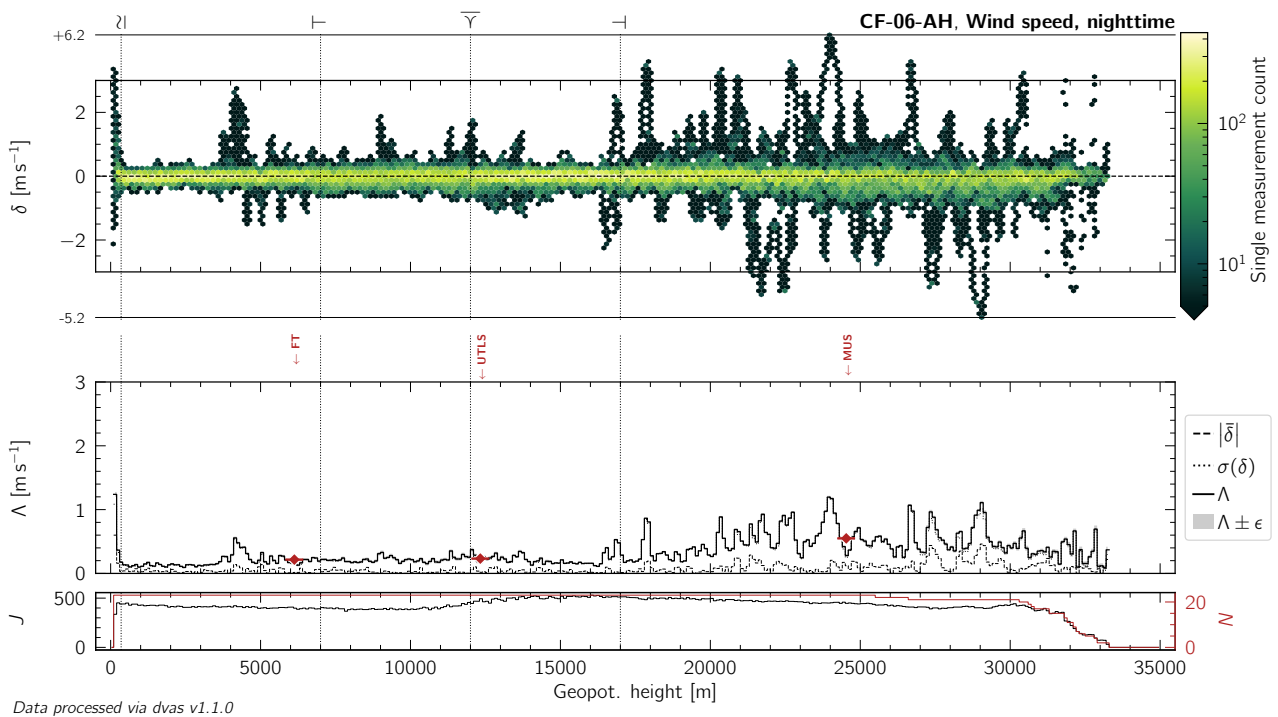


Figure L.26: Same as Figure 10.13, but for nighttime measurements of wind (horizontal) speed by the CF-06-AH radiosonde.

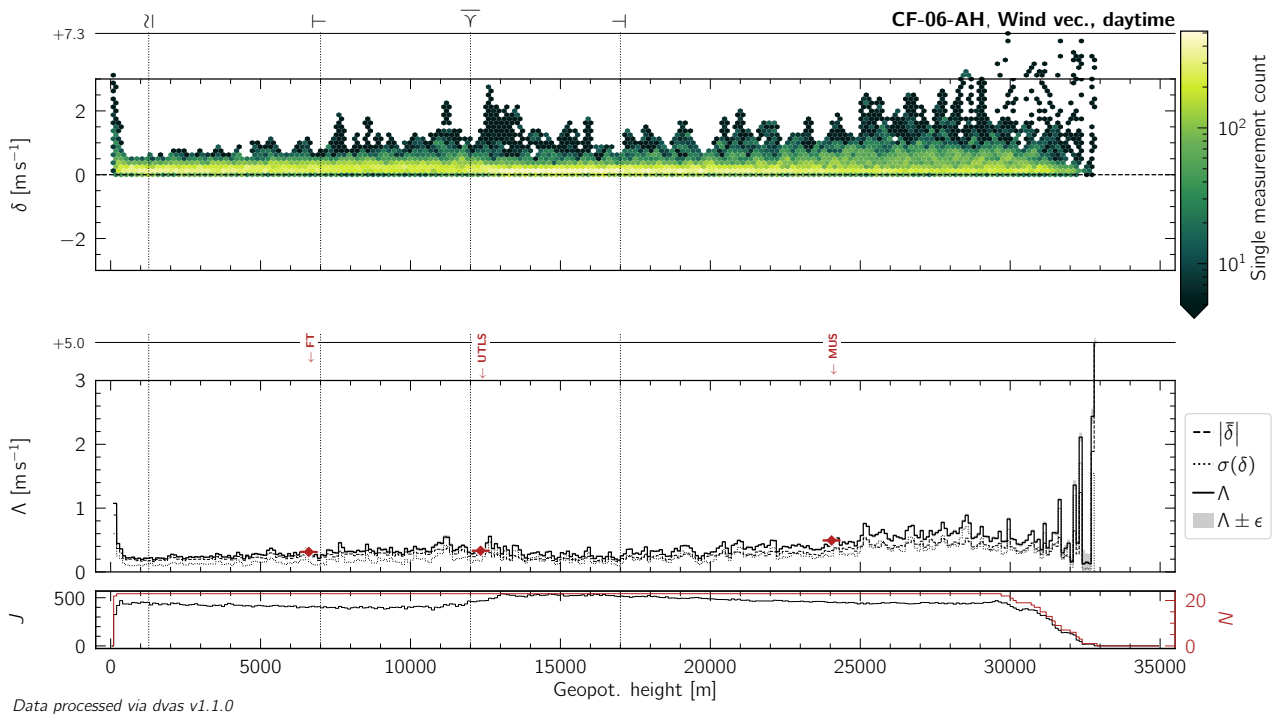


Figure L.27: Same as Figure 10.13, but for daytime measurements of the wind (horizontal) vector by the CF-06-AH radiosonde.

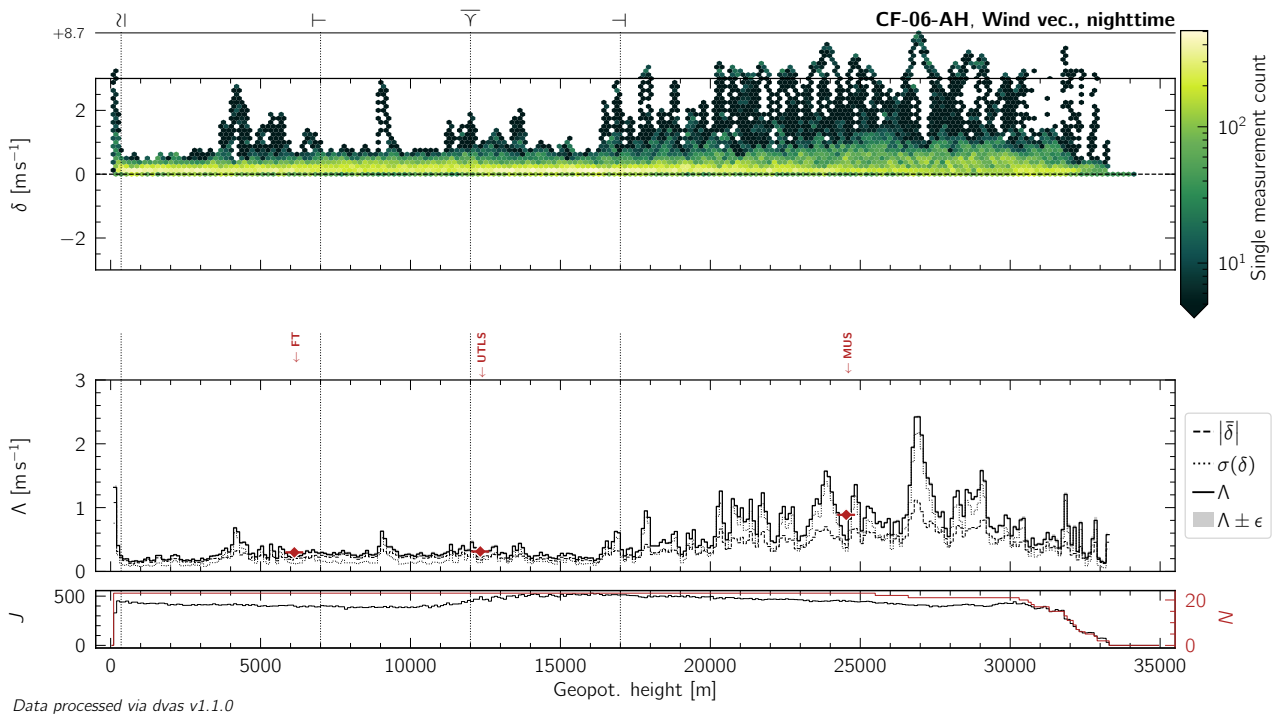


Figure L.28: Same as Figure 10.13, but for nighttime measurements of the wind (horizontal) vector by the CF-06-AH radiosonde.

L.3 DFM-17

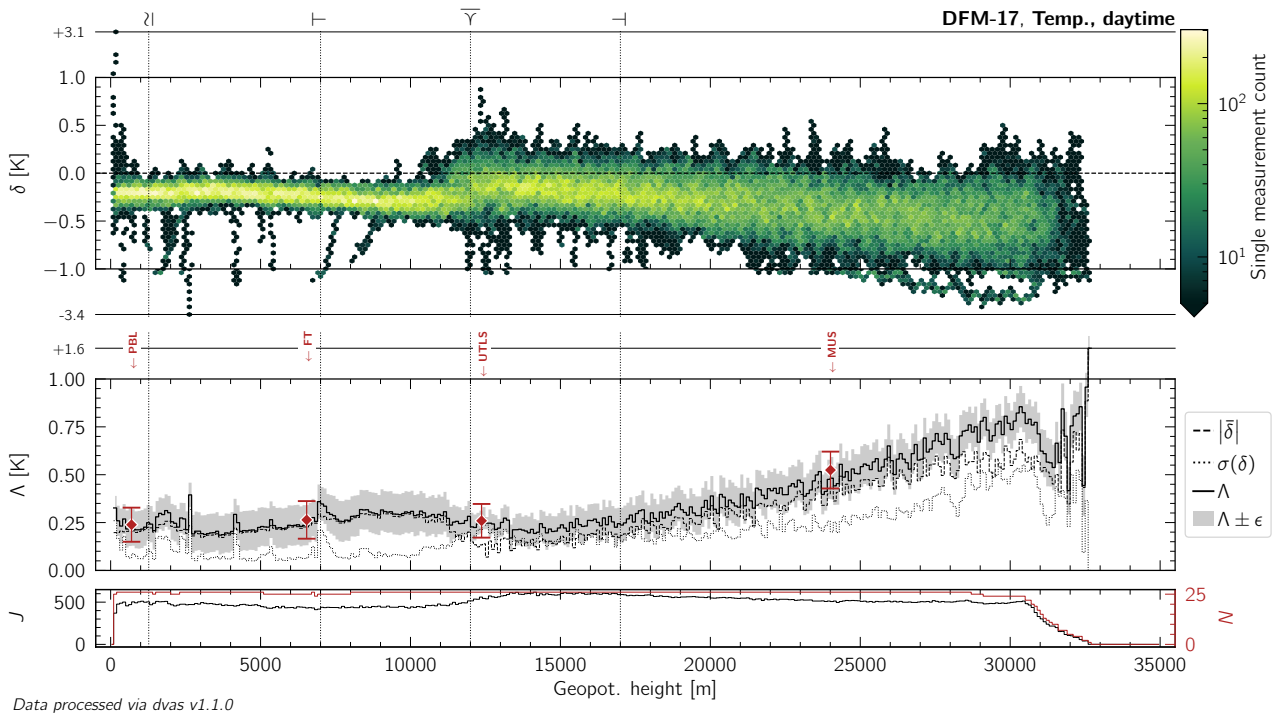


Figure L.29: Same as Figure 10.13, but for daytime measurements of atmospheric temperature by the DFM-17 radiosonde.

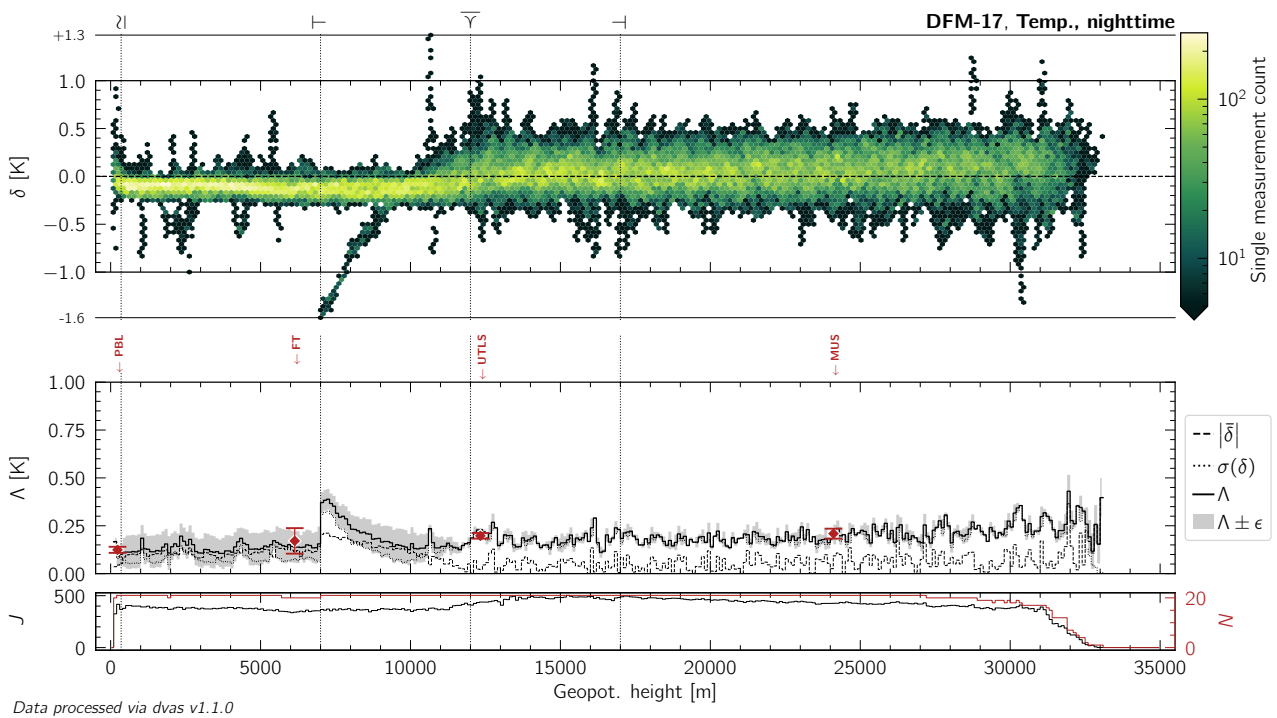


Figure L.30: Same as Figure 10.13, but for nighttime measurements of atmospheric temperature by the DFM-17 radiosonde.

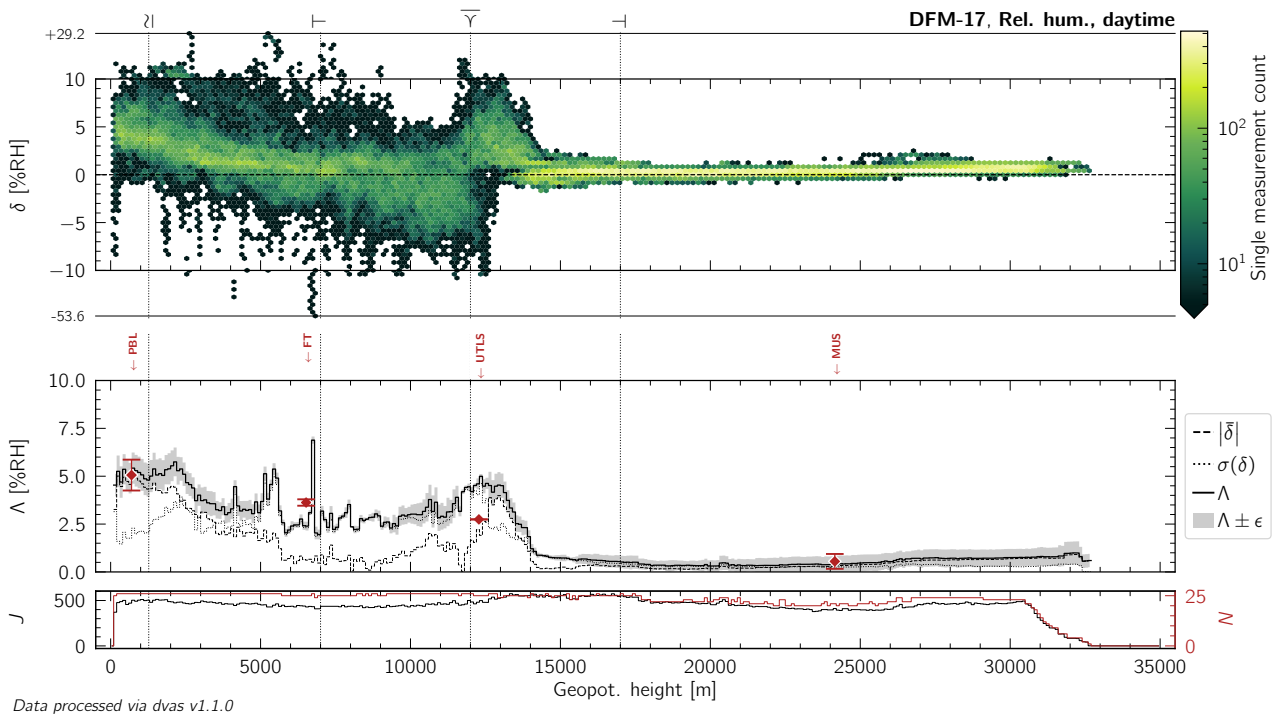


Figure L.31: Same as Figure 10.13, but for daytime measurements of relative humidity by the DFM-17 radiosonde.

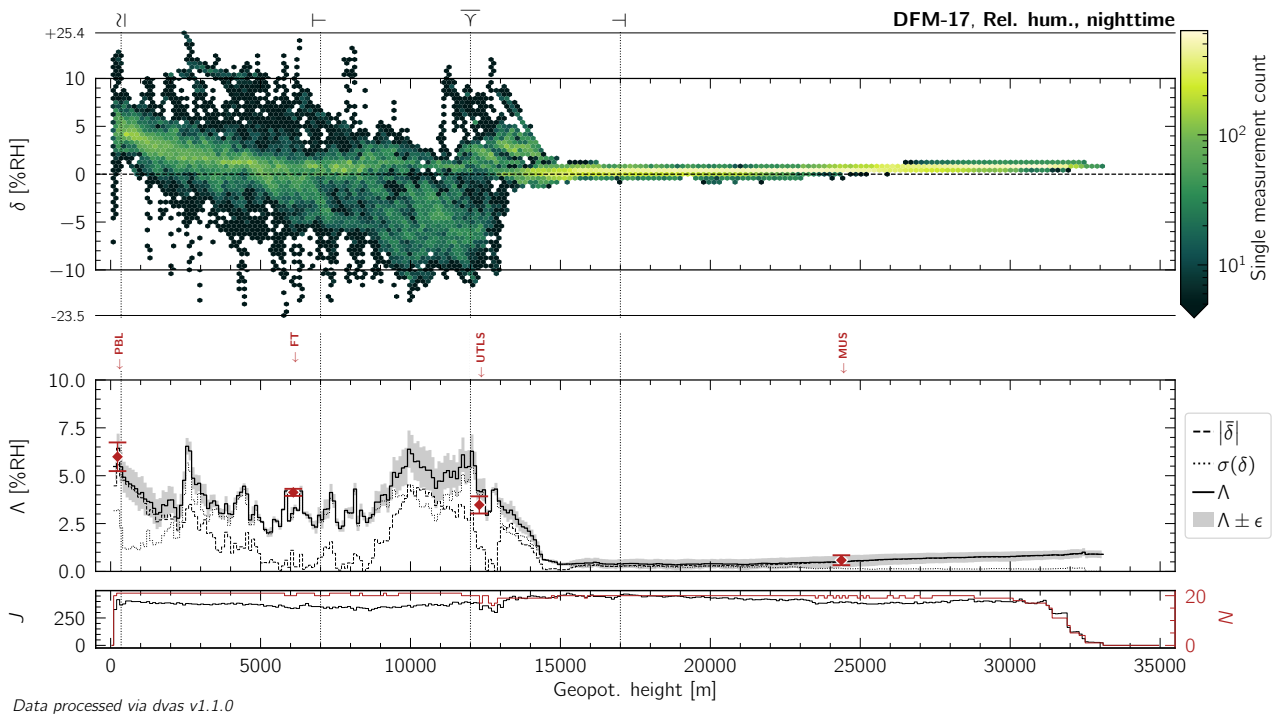


Figure L.32: Same as Figure 10.13, but for nighttime measurements of relative humidity by the DFM-17 radiosonde.

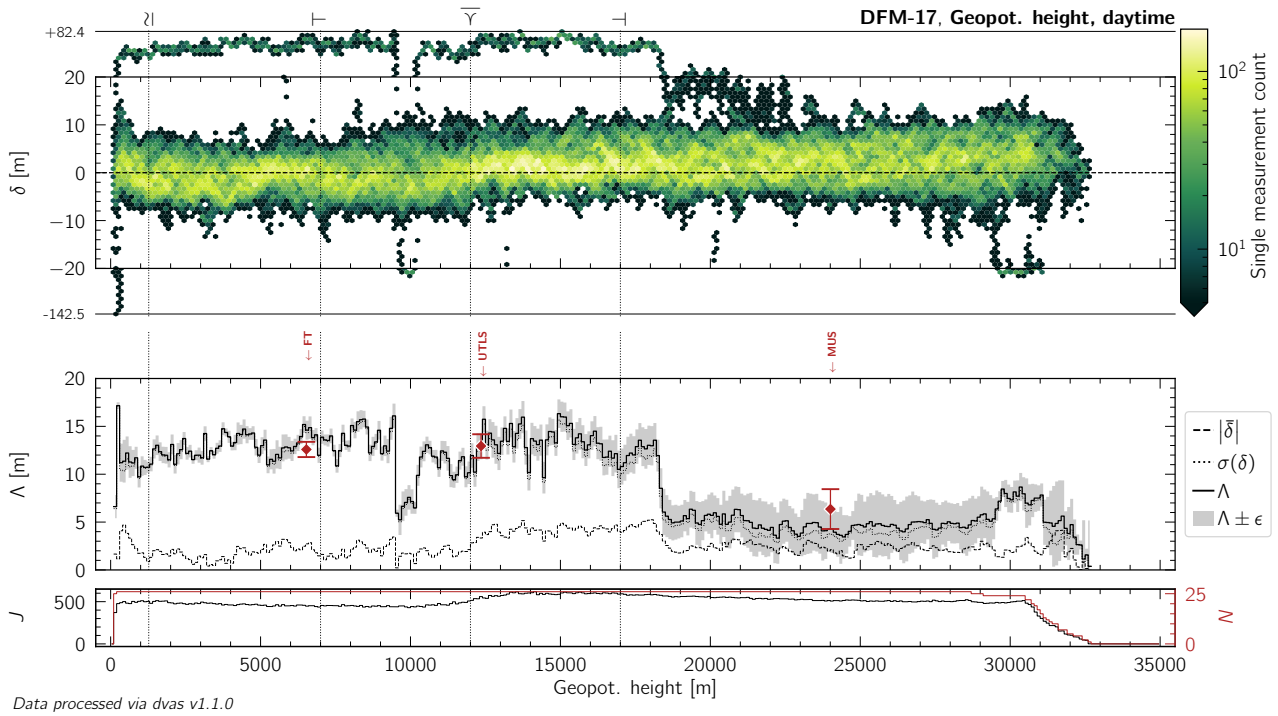


Figure L.33: Same as Figure 10.13, but for daytime measurements of geopotential height by the DFM-17 radiosonde.

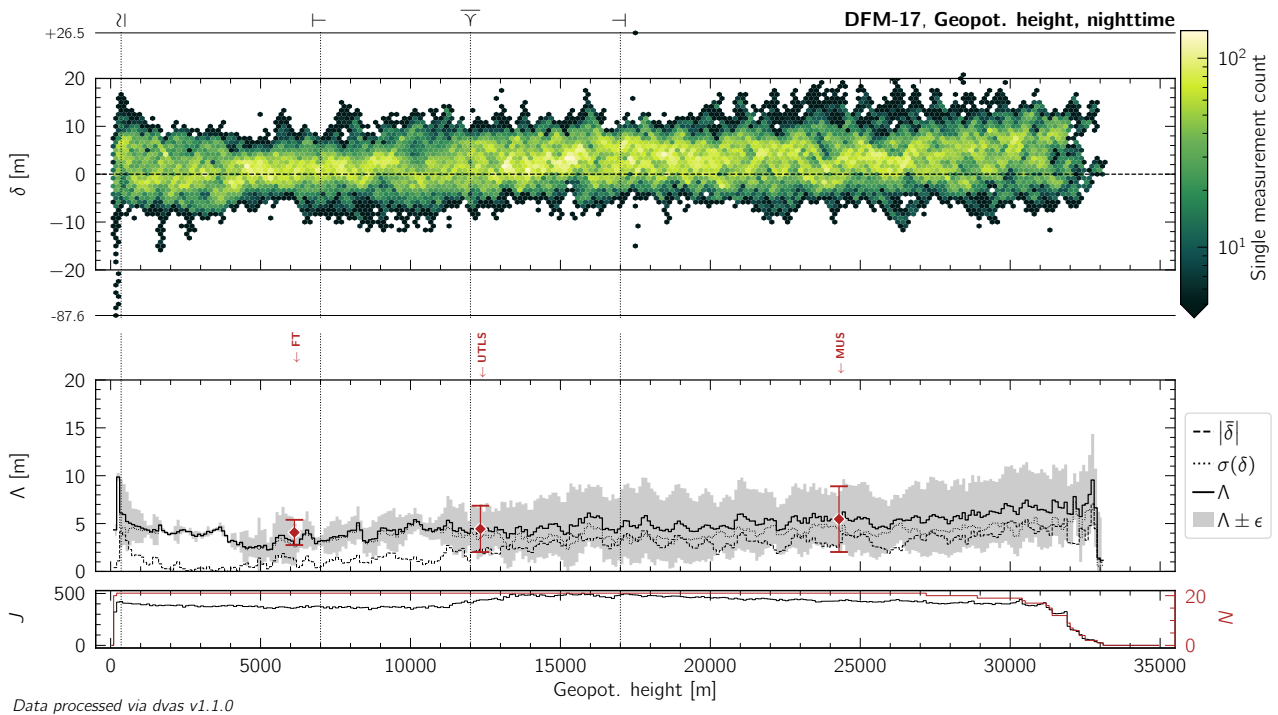


Figure L.34: Same as Figure 10.13, but for nighttime measurements of geopotential height by the DFM-17 radiosonde.

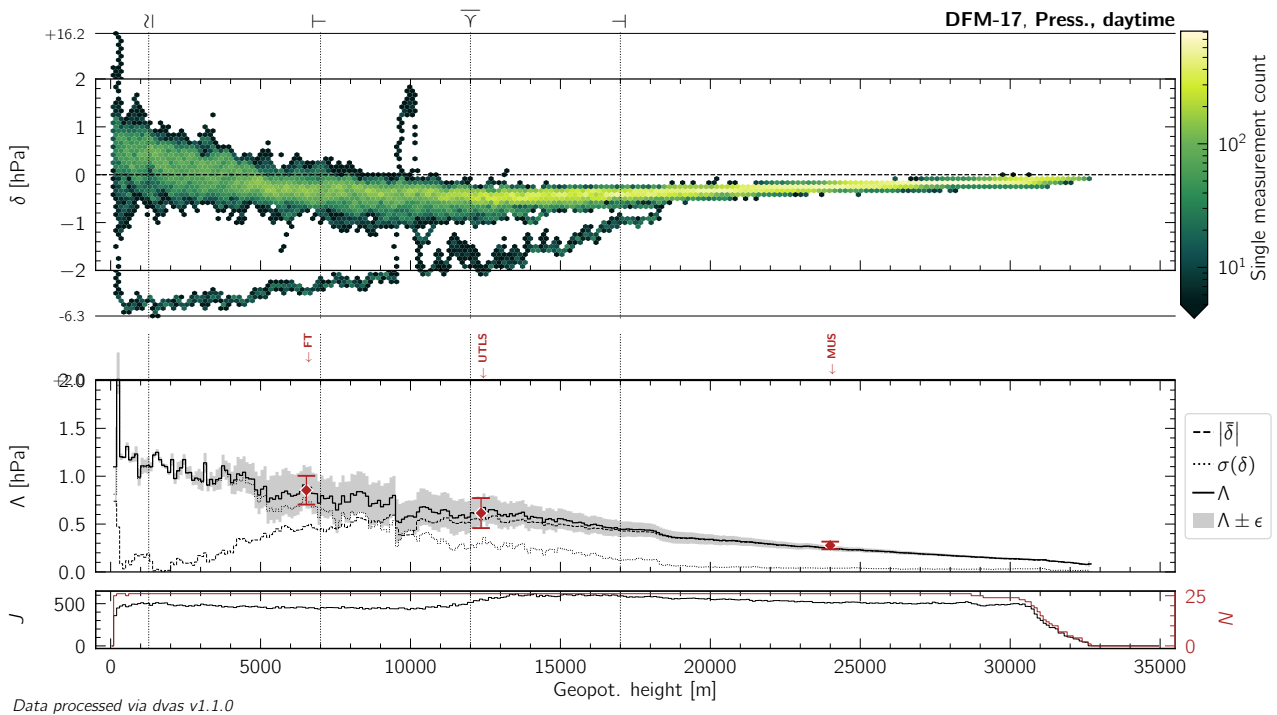


Figure L.35: Same as Figure 10.13, but for daytime measurements of atmospheric pressure by the DFM-17 radiosonde.

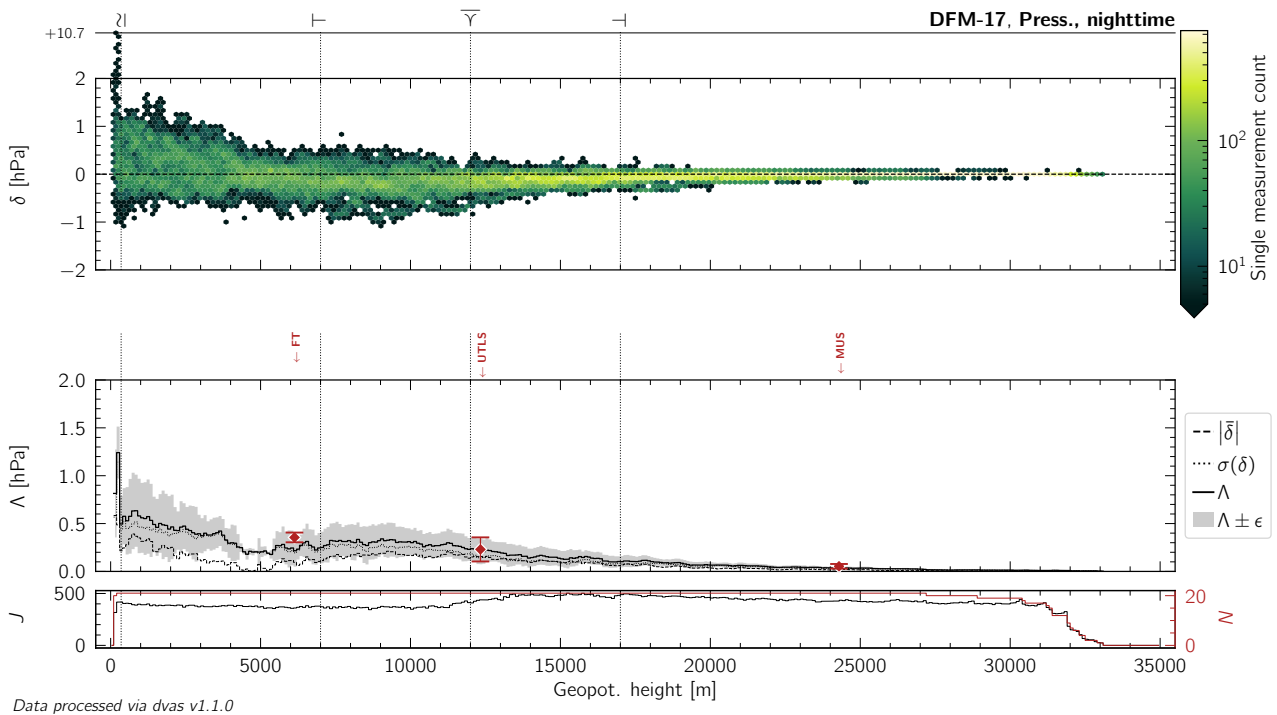


Figure L.36: Same as Figure 10.13, but for nighttime measurements of atmospheric pressure by the DFM-17 radiosonde.

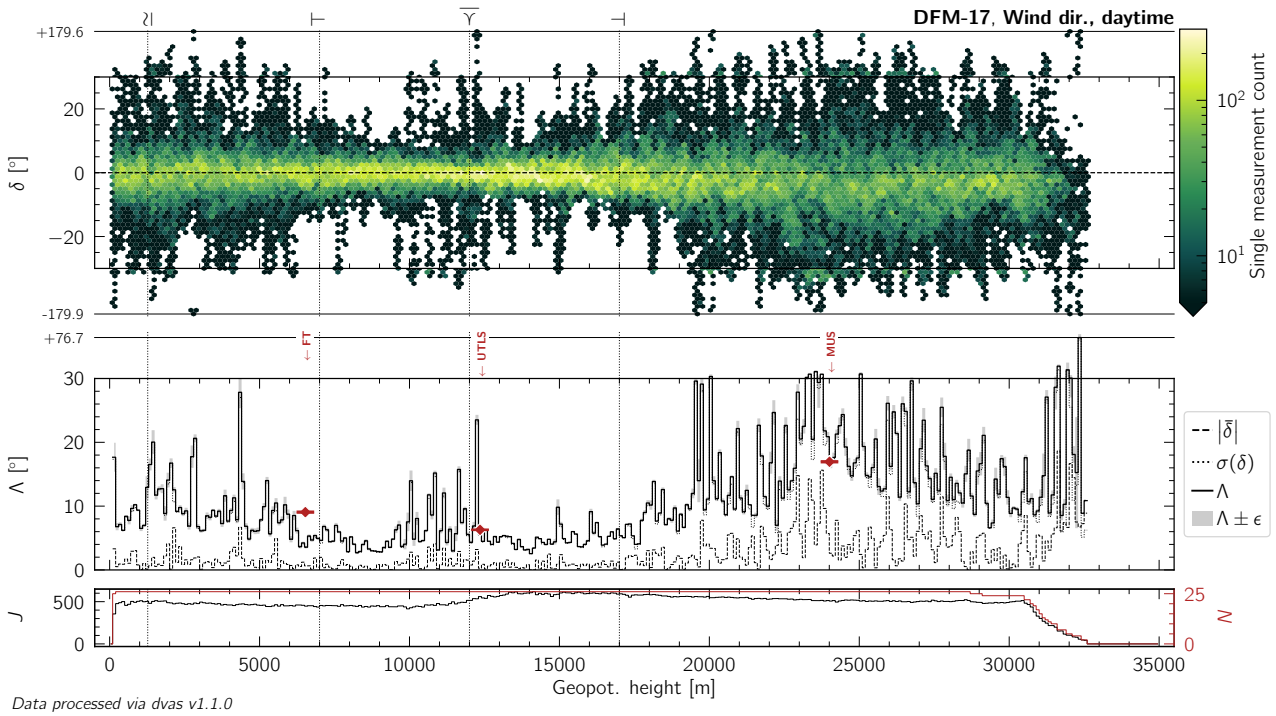


Figure L.37: Same as Figure 10.13, but for daytime measurements of wind (horizontal) direction by the DFM-17 radiosonde.

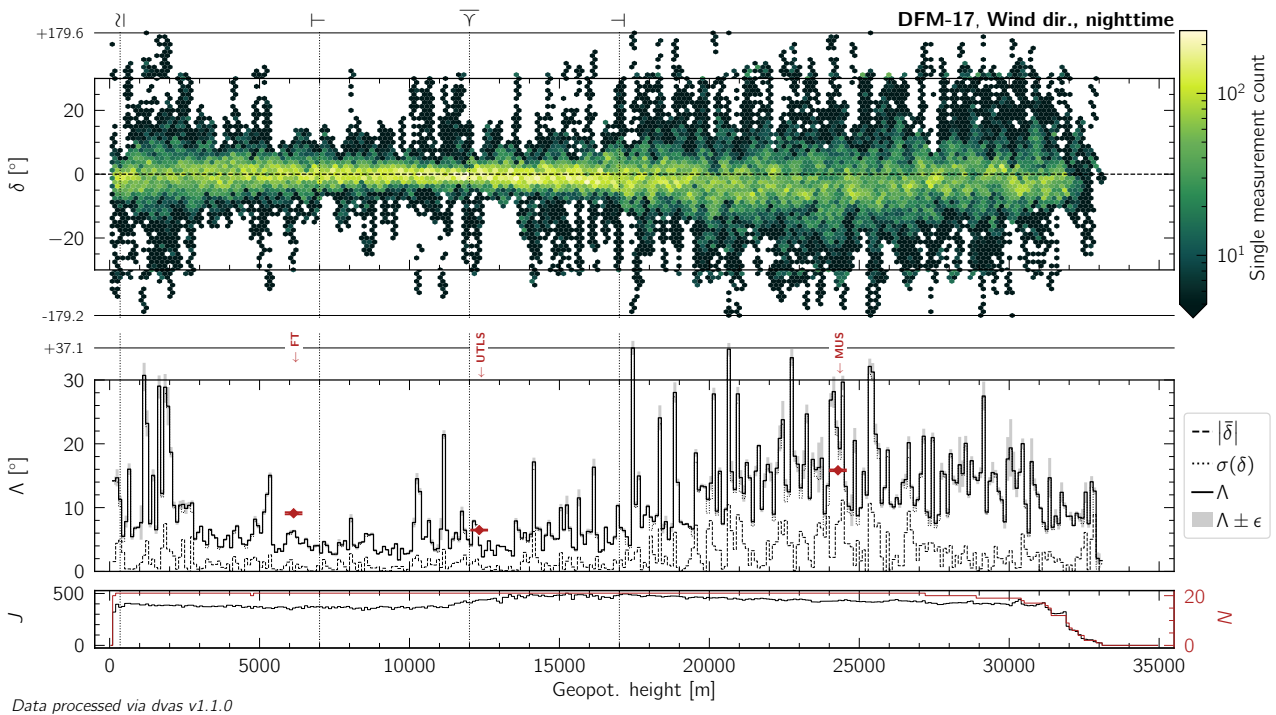


Figure L.38: Same as Figure 10.13, but for nighttime measurements of wind (horizontal) direction by the DFM-17 radiosonde.

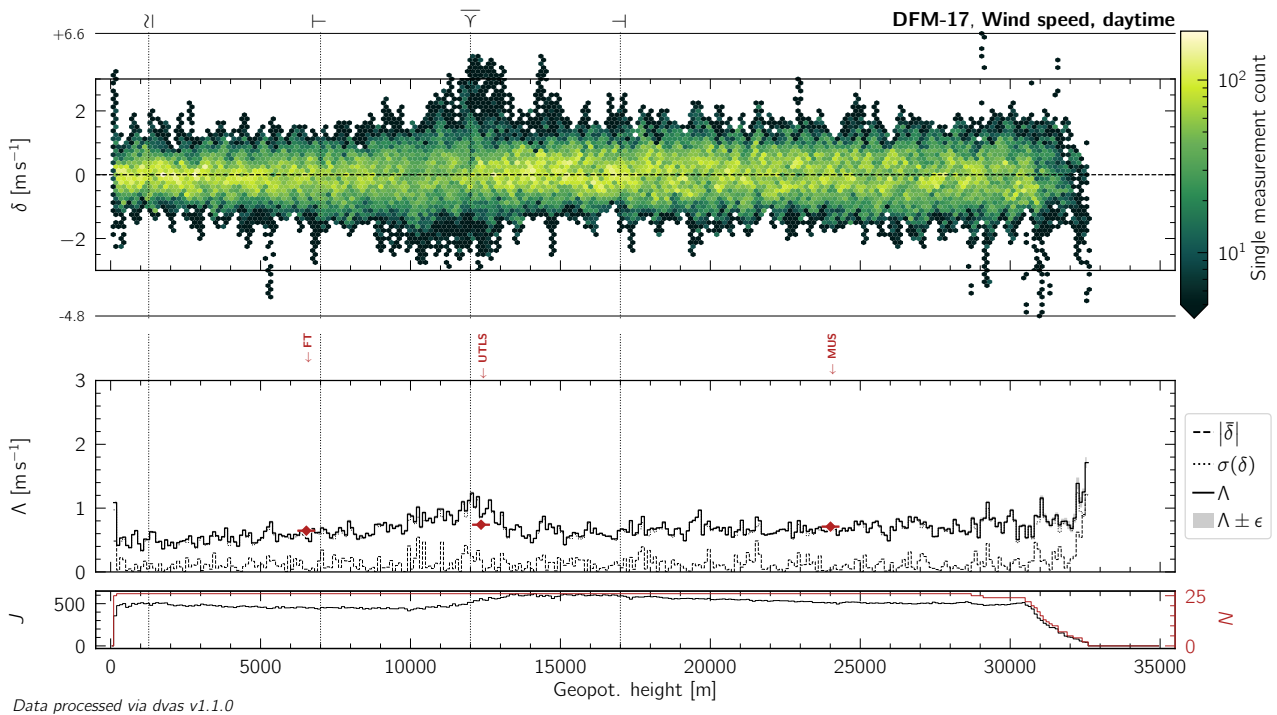


Figure L.39: Same as Figure 10.13, but for daytime measurements of wind (horizontal) speed by the DFM-17 radiosonde.

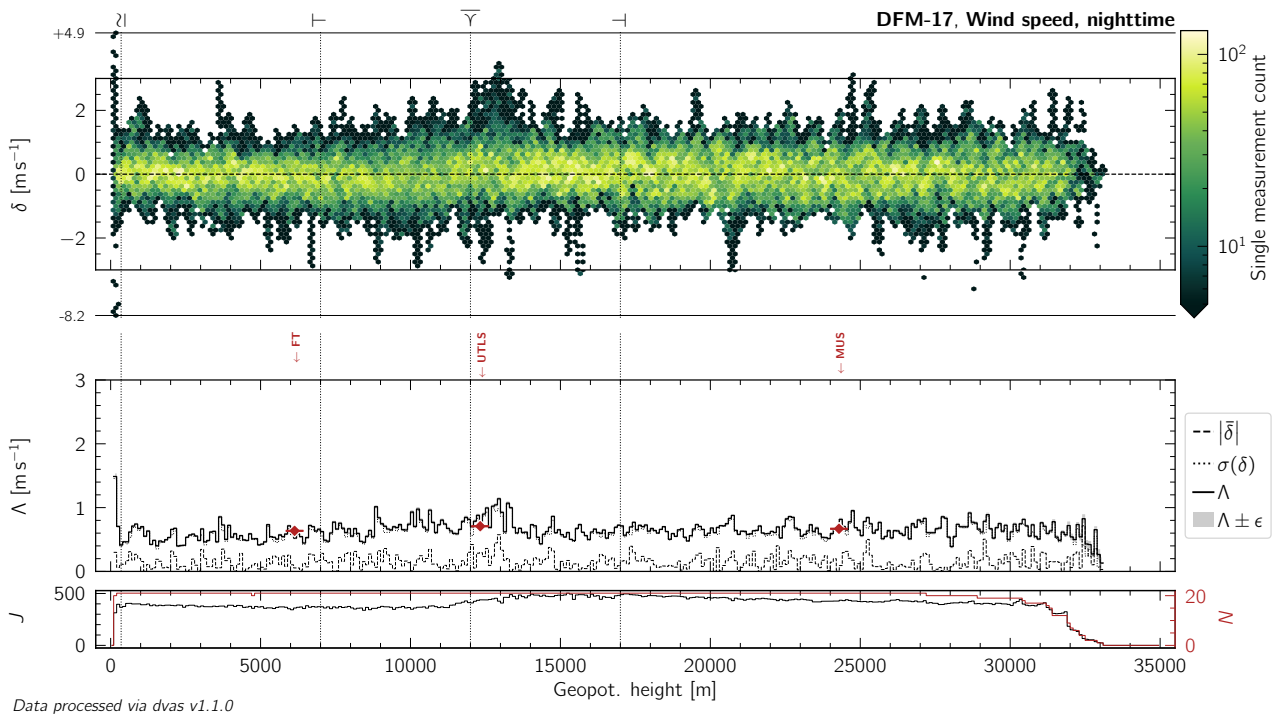


Figure L.40: Same as Figure 10.13, but for nighttime measurements of wind (horizontal) speed by the DFM-17 radiosonde.

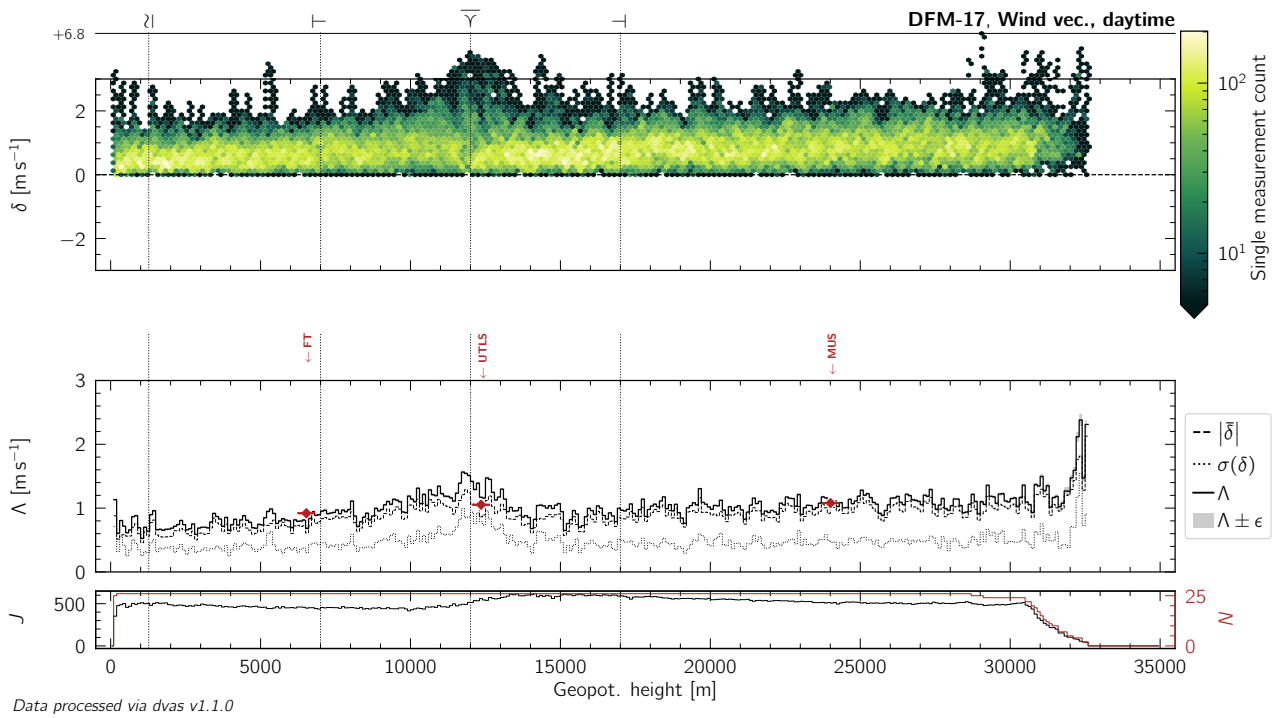


Figure L.41: Same as Figure 10.13, but for daytime measurements of the wind (horizontal) vector by the DFM-17 radiosonde.

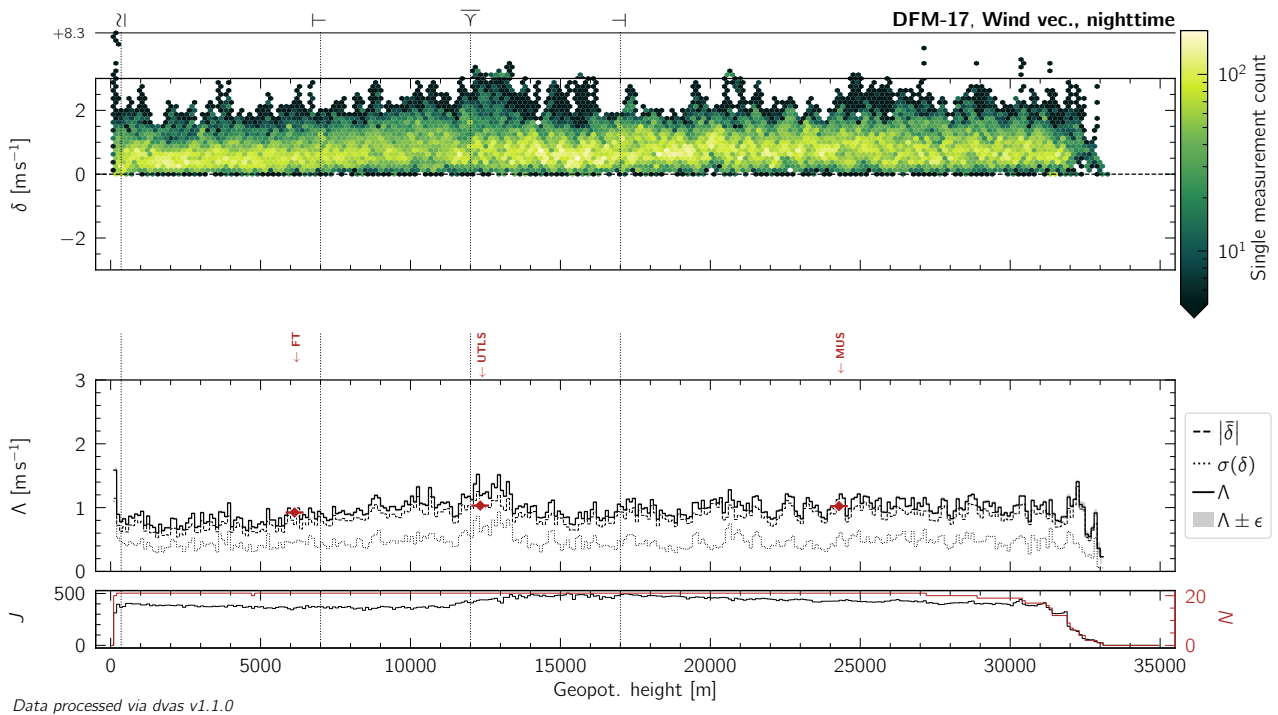


Figure L.42: Same as Figure 10.13, but for nighttime measurements of the wind (horizontal) vector by the DFM-17 radiosonde.

L.4 GTH3

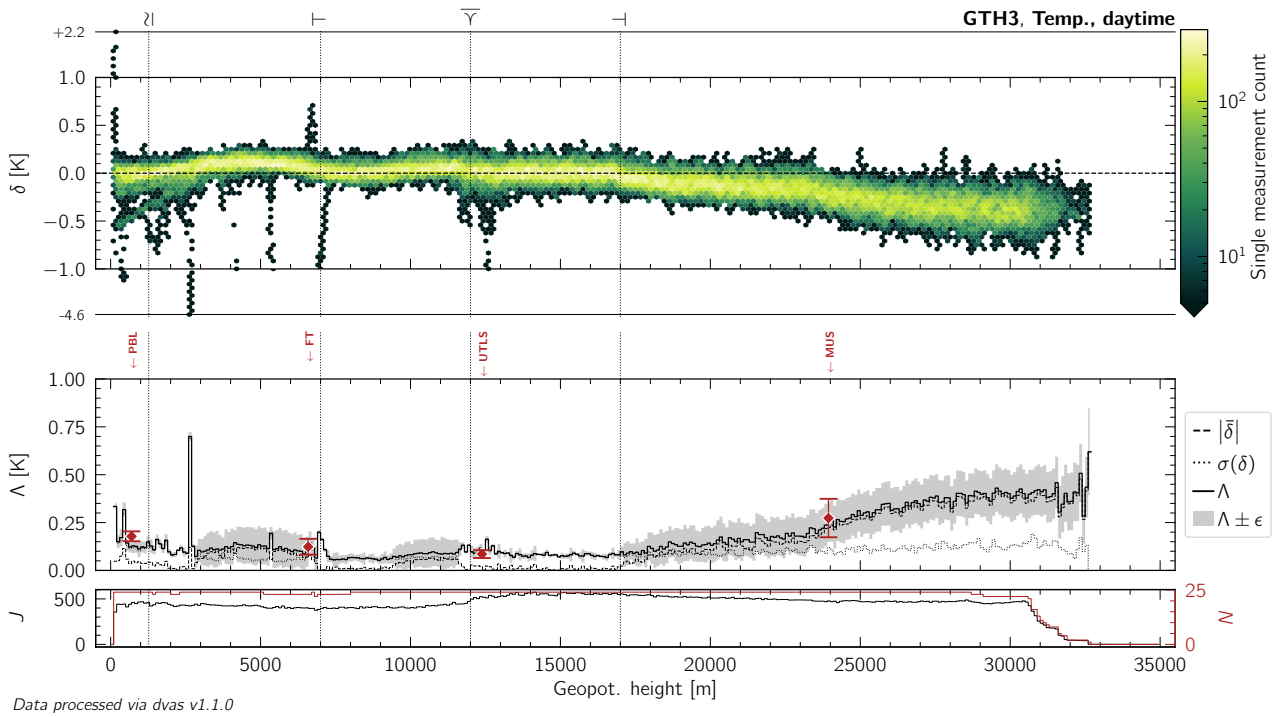


Figure L.43: Same as Figure 10.13, but for daytime measurements of atmospheric temperature by the GTH3 radiosonde.

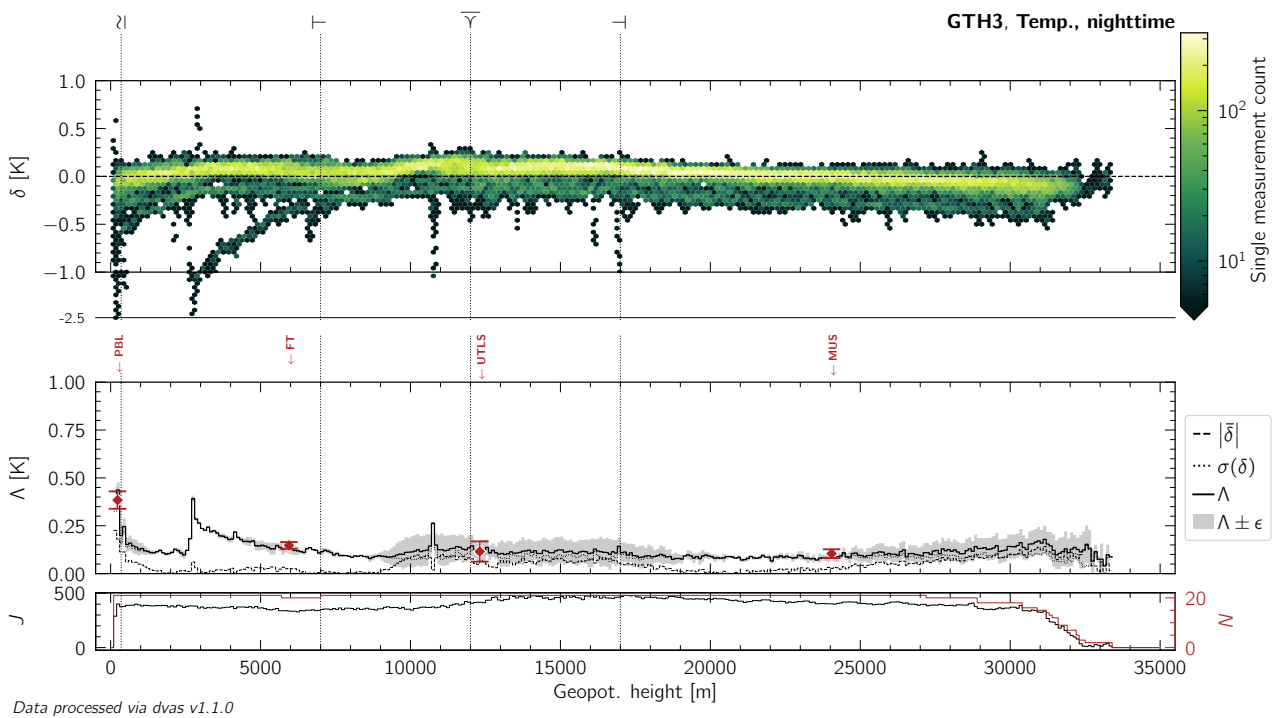


Figure L.44: Same as Figure 10.13, but for nighttime measurements of atmospheric temperature by the GTH3 radiosonde.

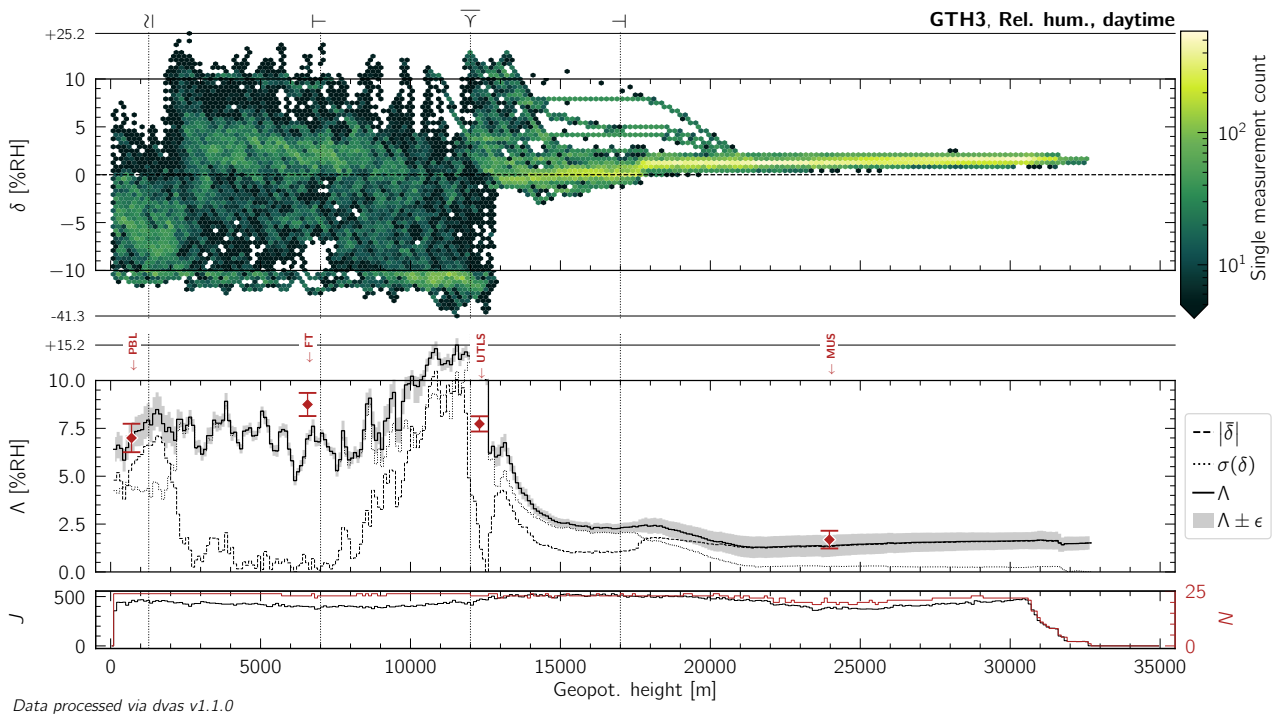


Figure L.45: Same as Figure 10.13, but for daytime measurements of relative humidity by the GTH3 radiosonde.

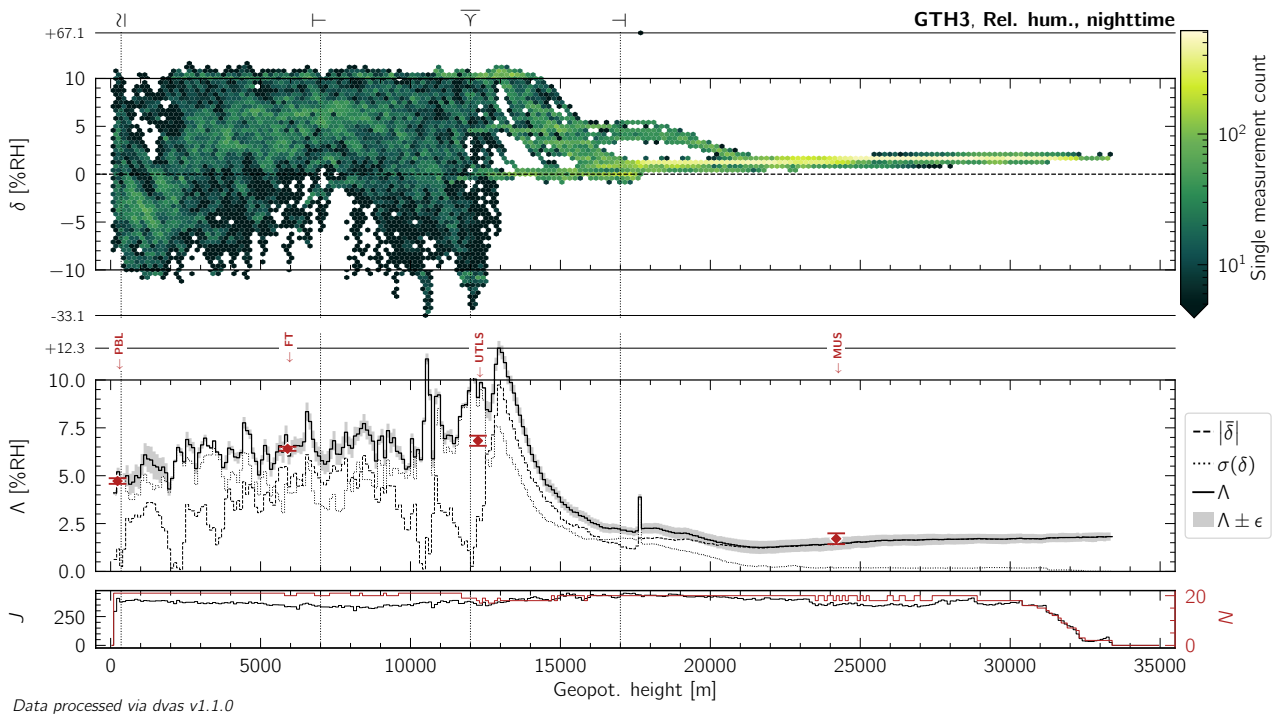


Figure L.46: Same as Figure 10.13, but for nighttime measurements of relative humidity by the GTH3 radiosonde.

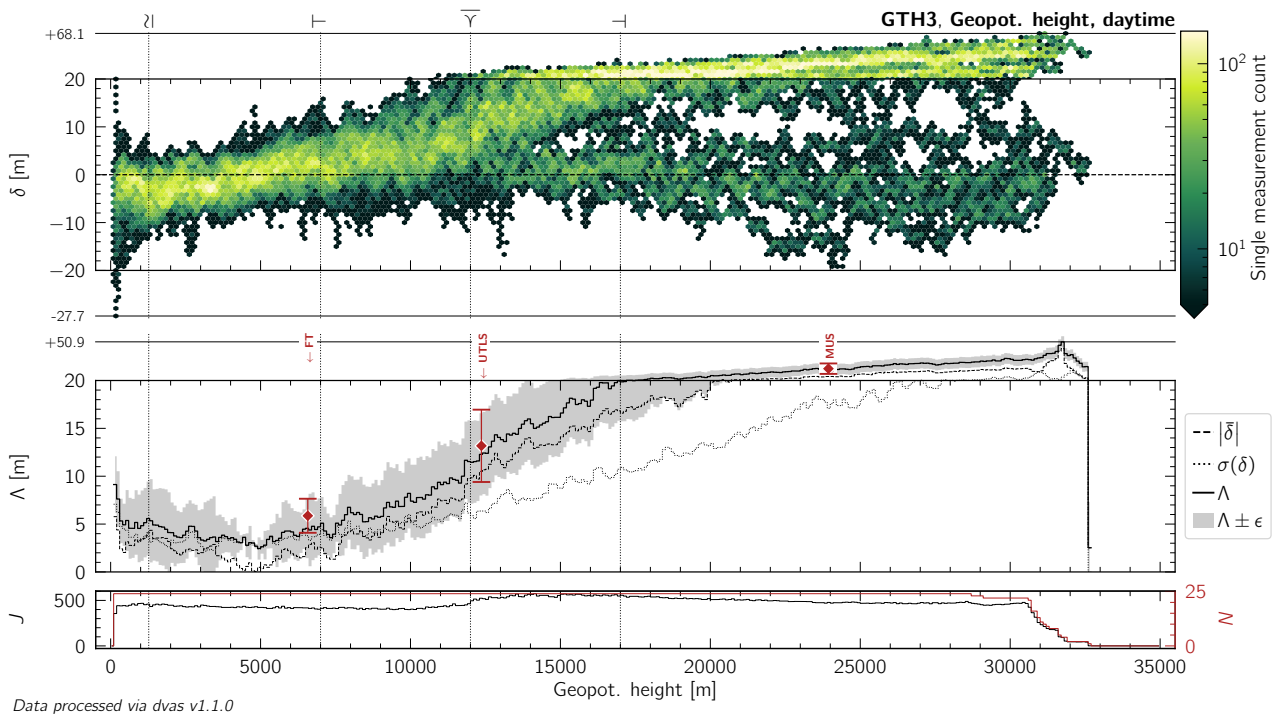


Figure L.47: Same as Figure 10.13, but for daytime measurements of geopotential height by the GTH3 radiosonde.

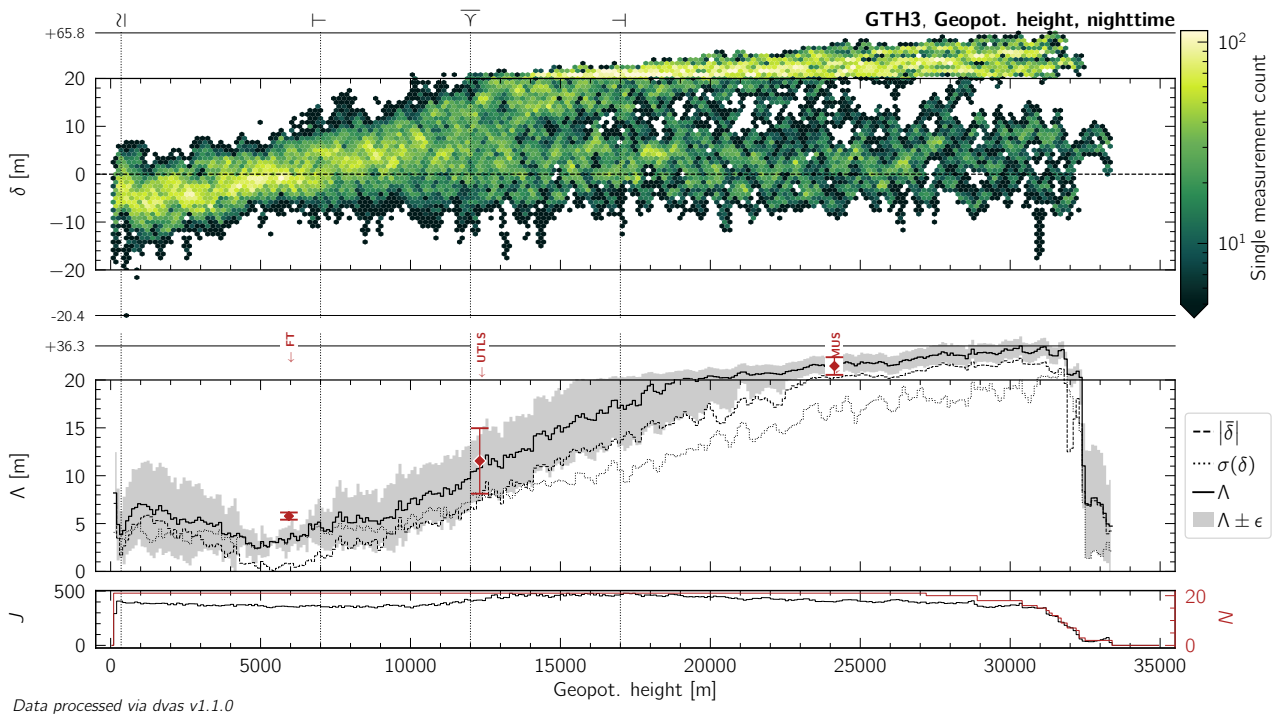


Figure L.48: Same as Figure 10.13, but for nighttime measurements of geopotential height by the GTH3 radiosonde.

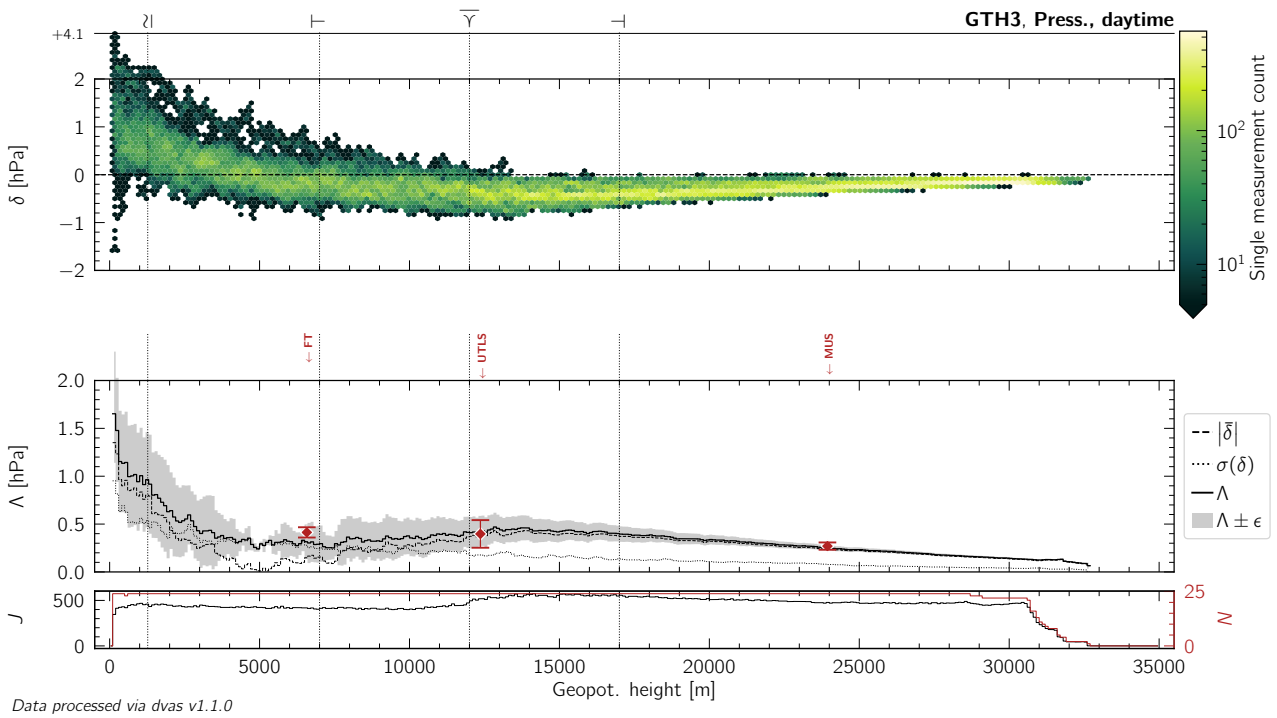


Figure L.49: Same as Figure 10.13, but for daytime measurements of atmospheric pressure by the GTH3 radiosonde.

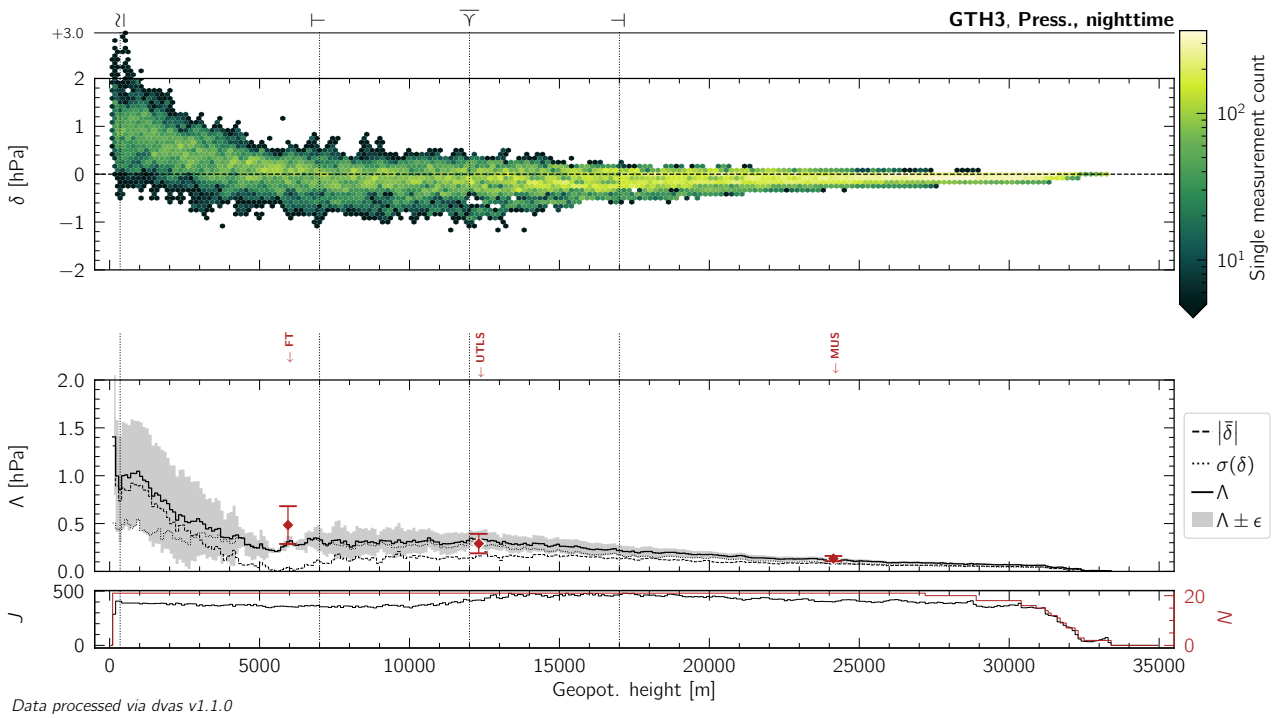


Figure L.50: Same as Figure 10.13, but for nighttime measurements of atmospheric pressure by the GTH3 radiosonde.

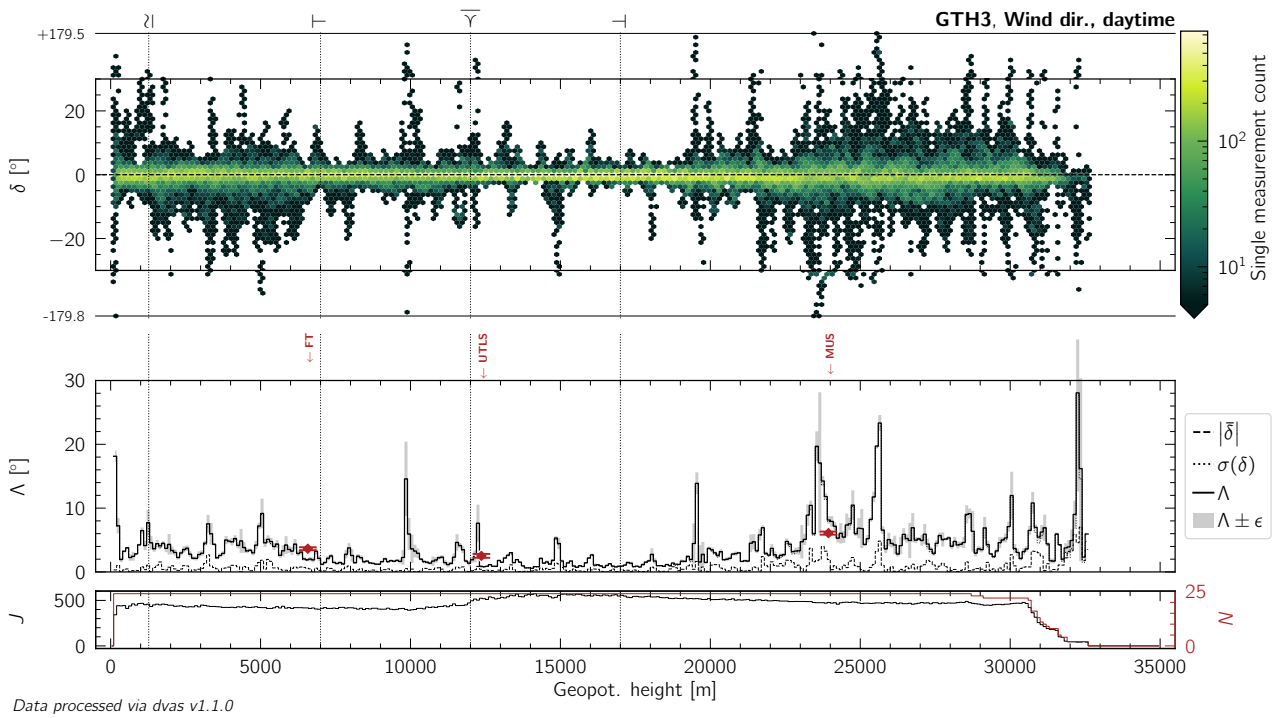


Figure L.51: Same as Figure 10.13, but for daytime measurements of wind (horizontal) direction by the GTH3 radiosonde.

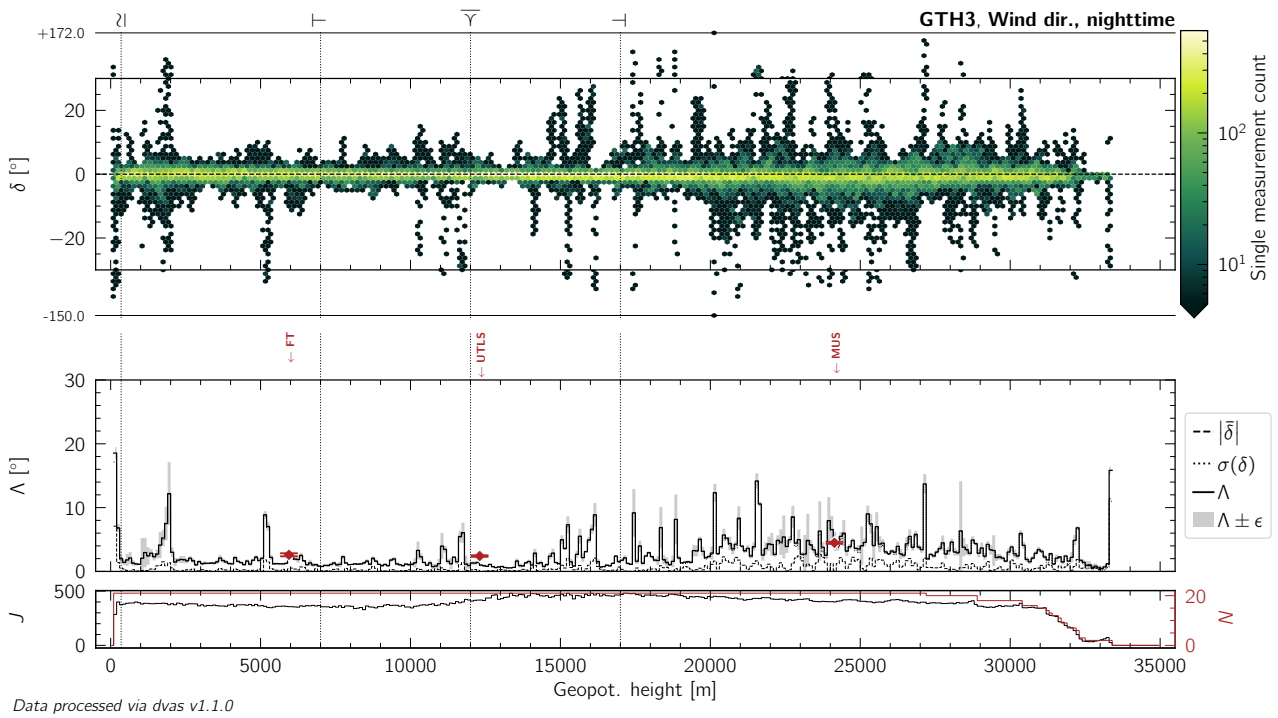


Figure L.52: Same as Figure 10.13, but for nighttime measurements of wind (horizontal) direction by the GTH3 radiosonde.

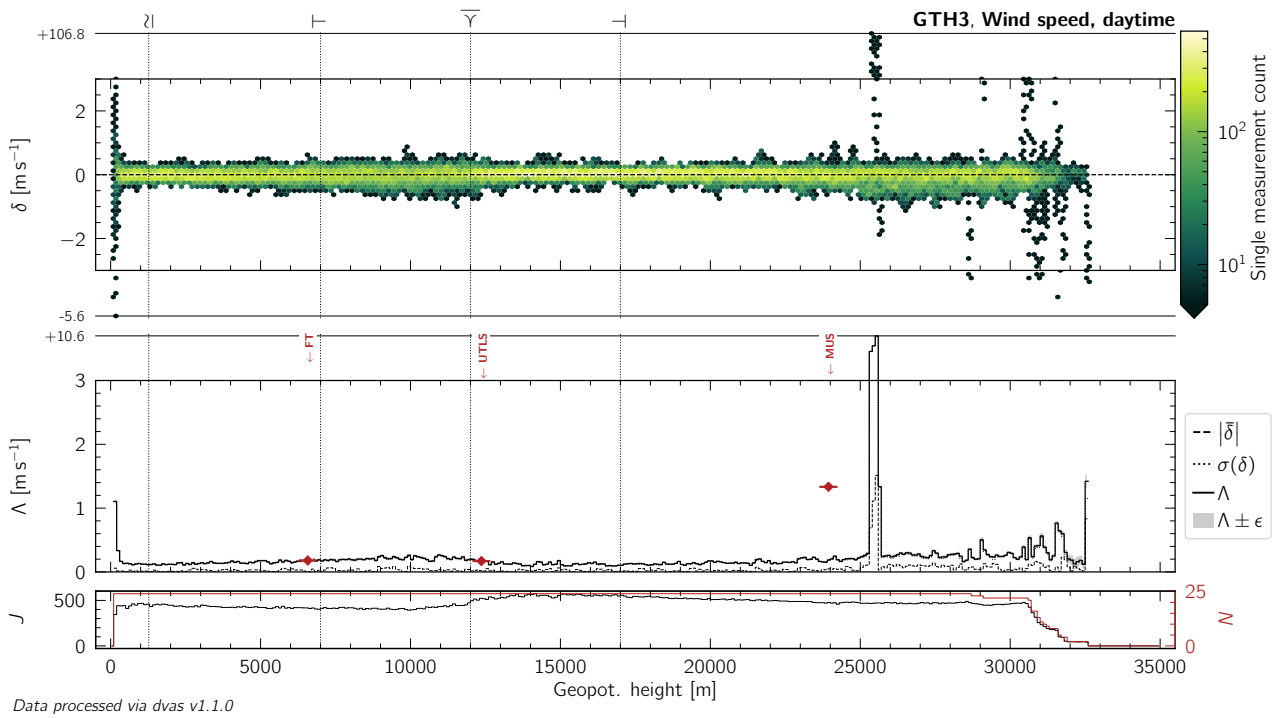


Figure L.53: Same as Figure 10.13, but for daytime measurements of wind (horizontal) speed by the GTH3 radiosonde.

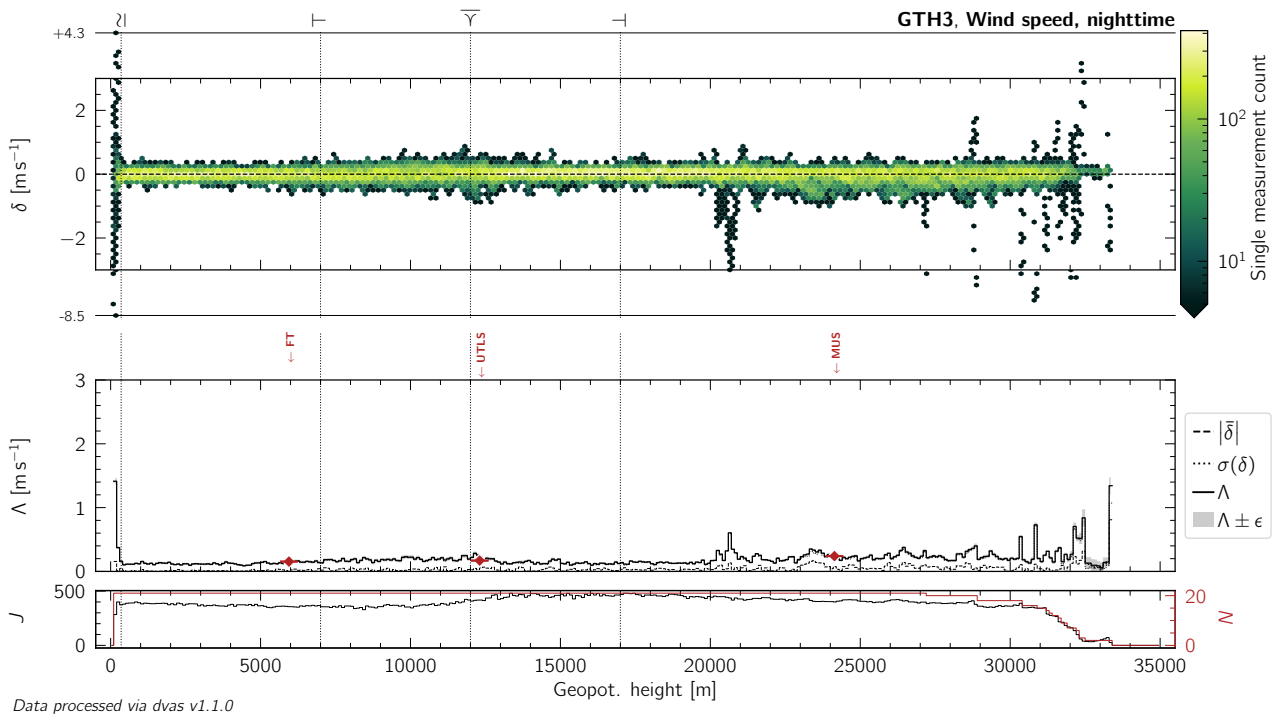


Figure L.54: Same as Figure 10.13, but for nighttime measurements of wind (horizontal) speed by the GTH3 radiosonde.

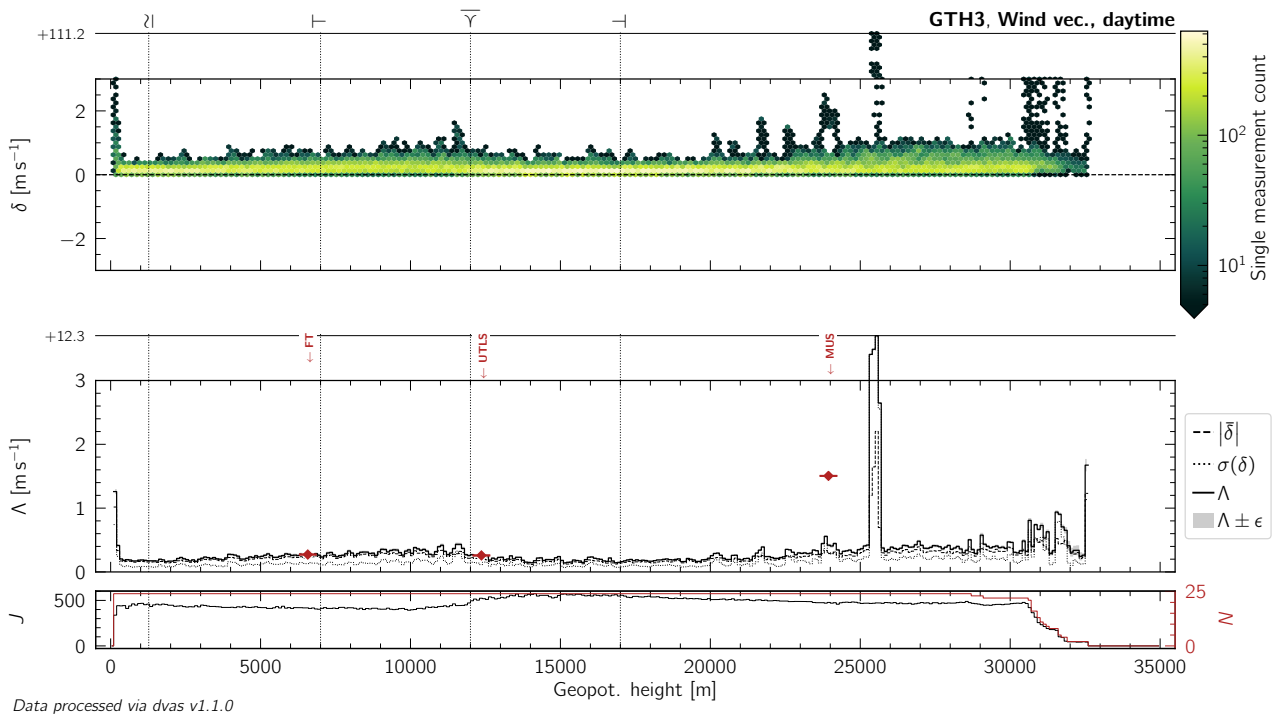


Figure L.55: Same as Figure 10.13, but for daytime measurements of the wind (horizontal) vector by the GTH3 radiosonde.

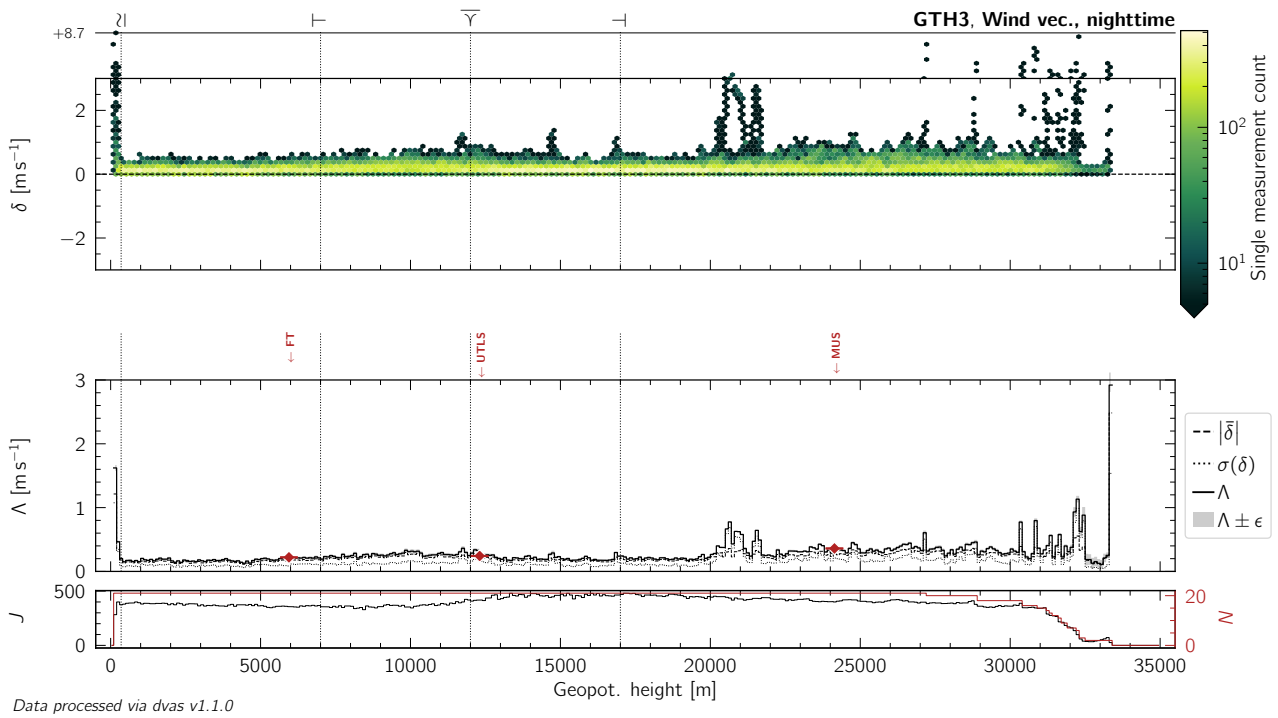


Figure L.56: Same as Figure 10.13, but for nighttime measurements of the wind (horizontal) vector by the GTH3 radiosonde.

L.5 IMET-54

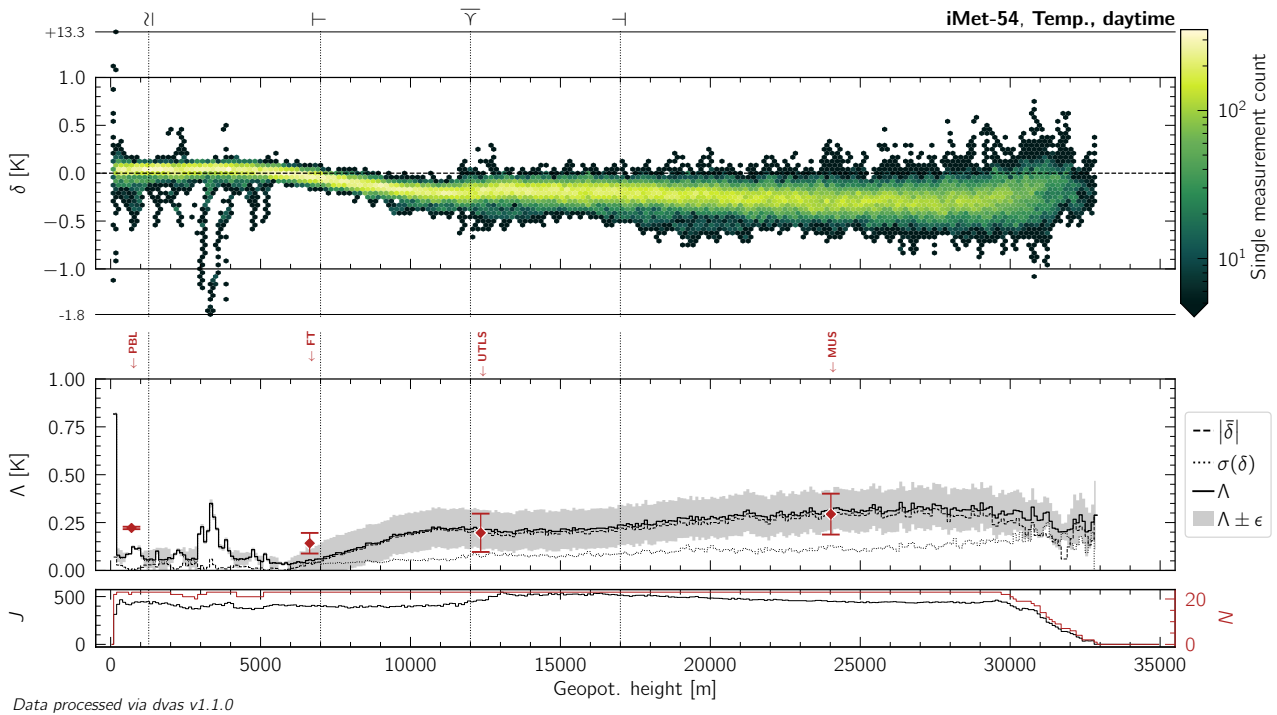


Figure L.57: Same as Figure 10.13, but for daytime measurements of atmospheric temperature by the iMet-54 radiosonde.

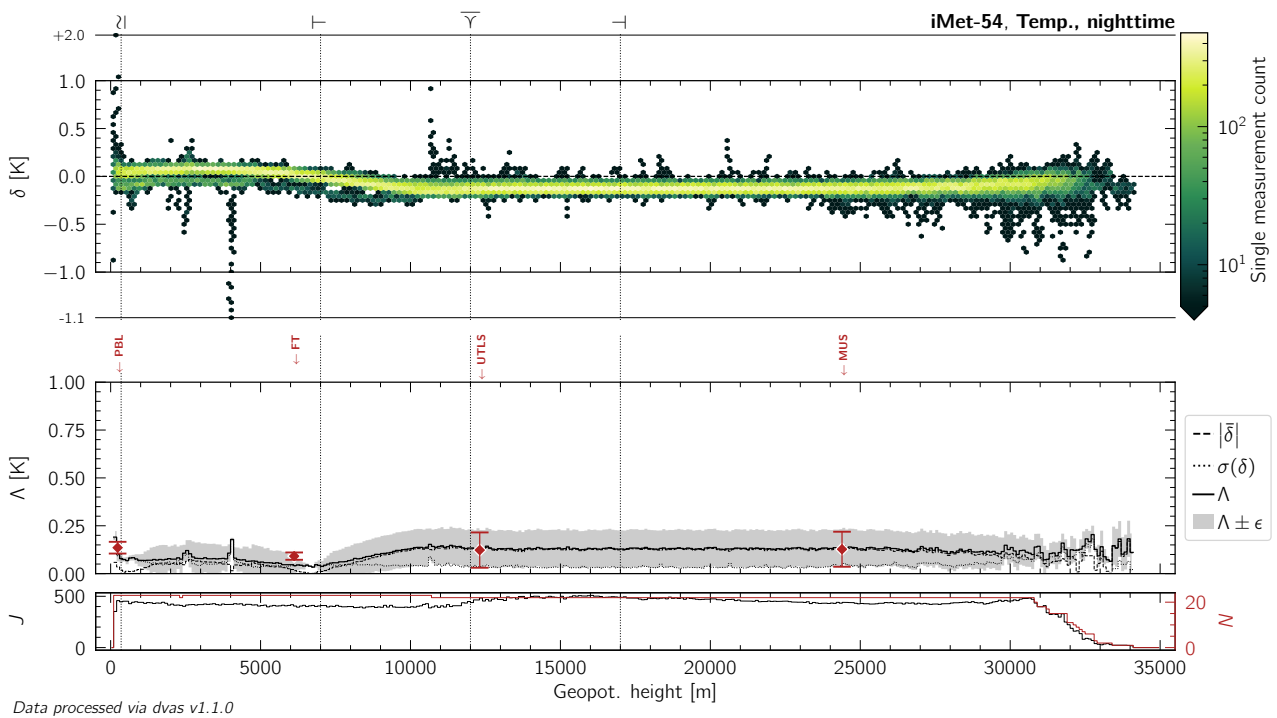


Figure L.58: Same as Figure 10.13, but for nighttime measurements of atmospheric temperature by the iMet-54 radiosonde.

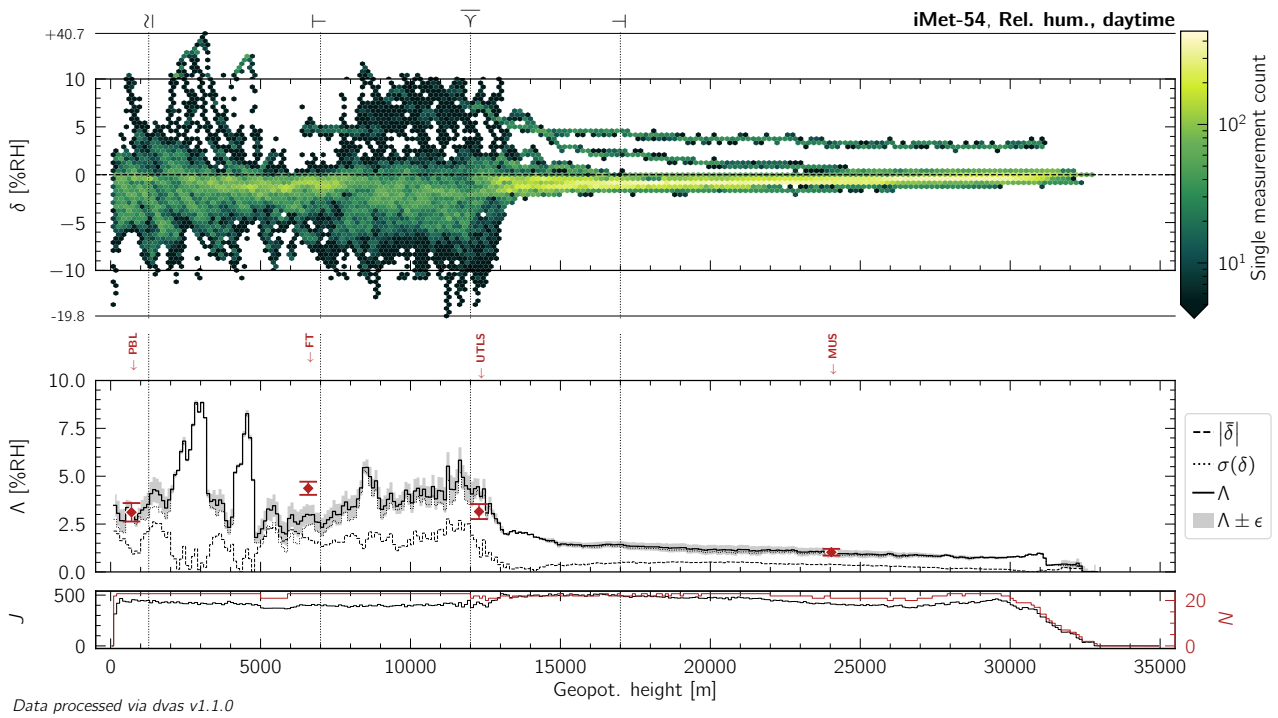


Figure L.59: Same as Figure 10.13, but for daytime measurements of relative humidity by the iMet-54 radiosonde.

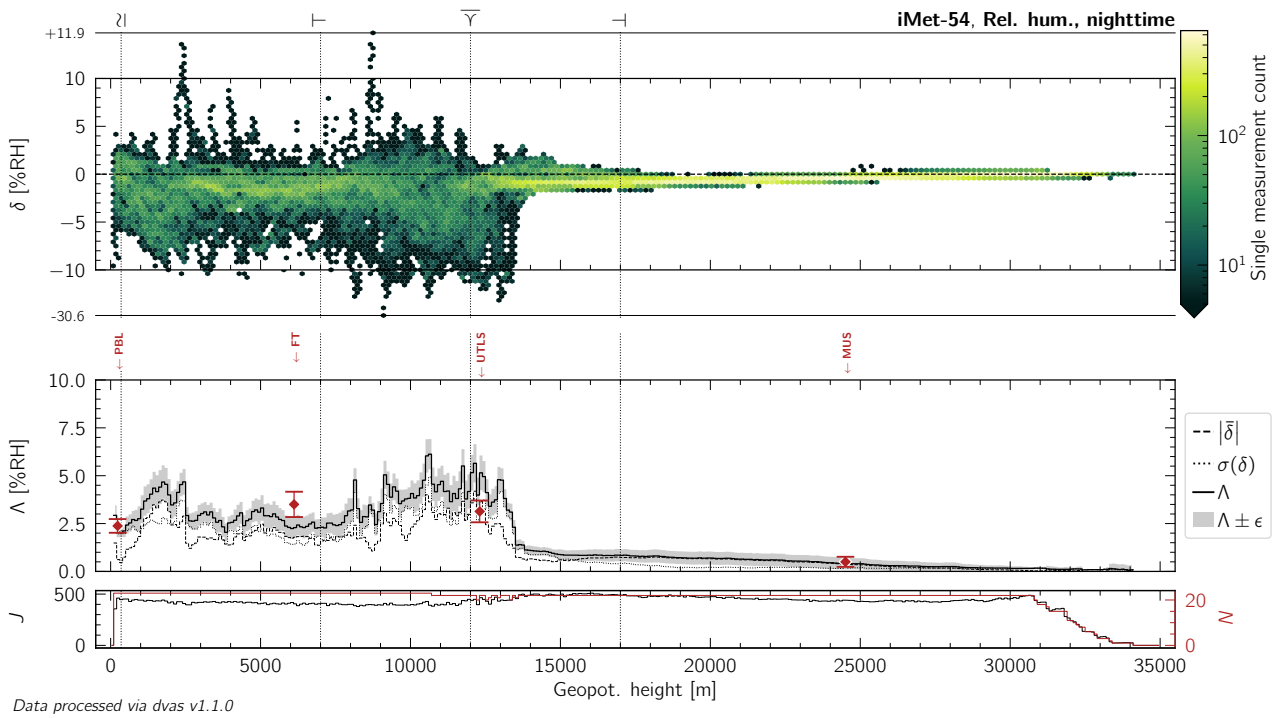


Figure L.60: Same as Figure 10.13, but for nighttime measurements of relative humidity by the iMet-54 radiosonde.

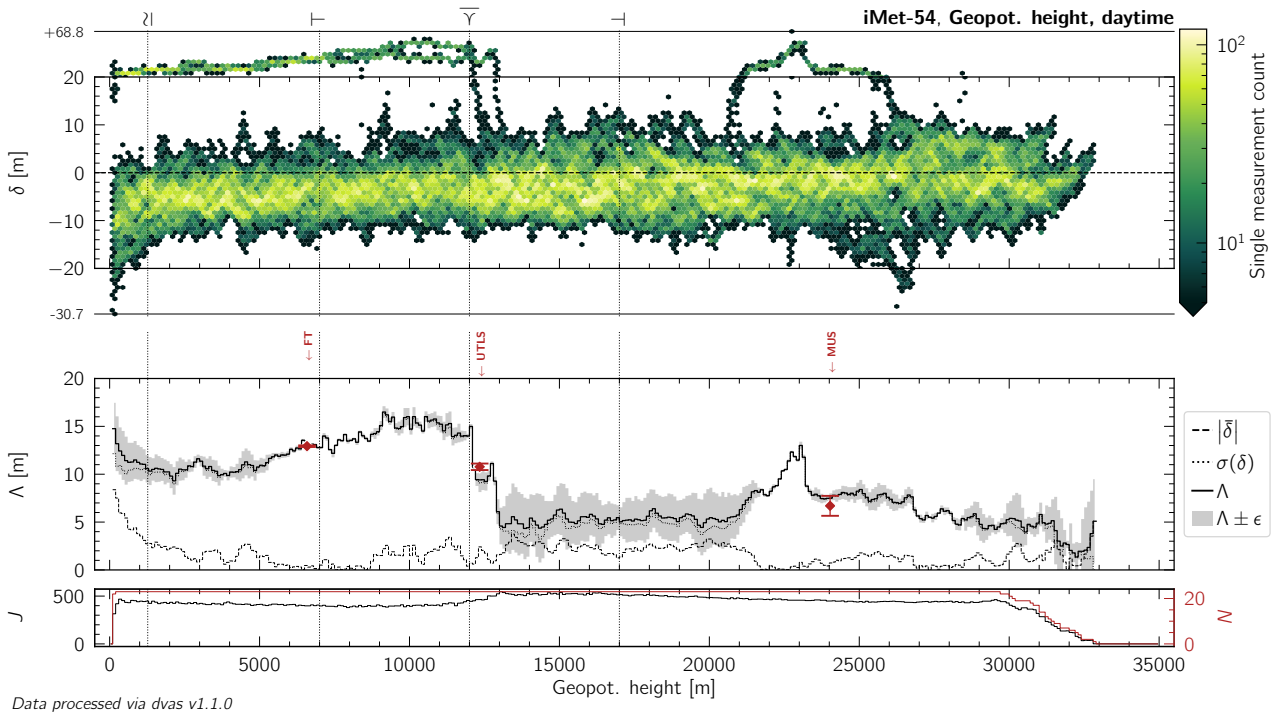


Figure L.61: Same as Figure 10.13, but for daytime measurements of geopotential height by the iMet-54 radiosonde.

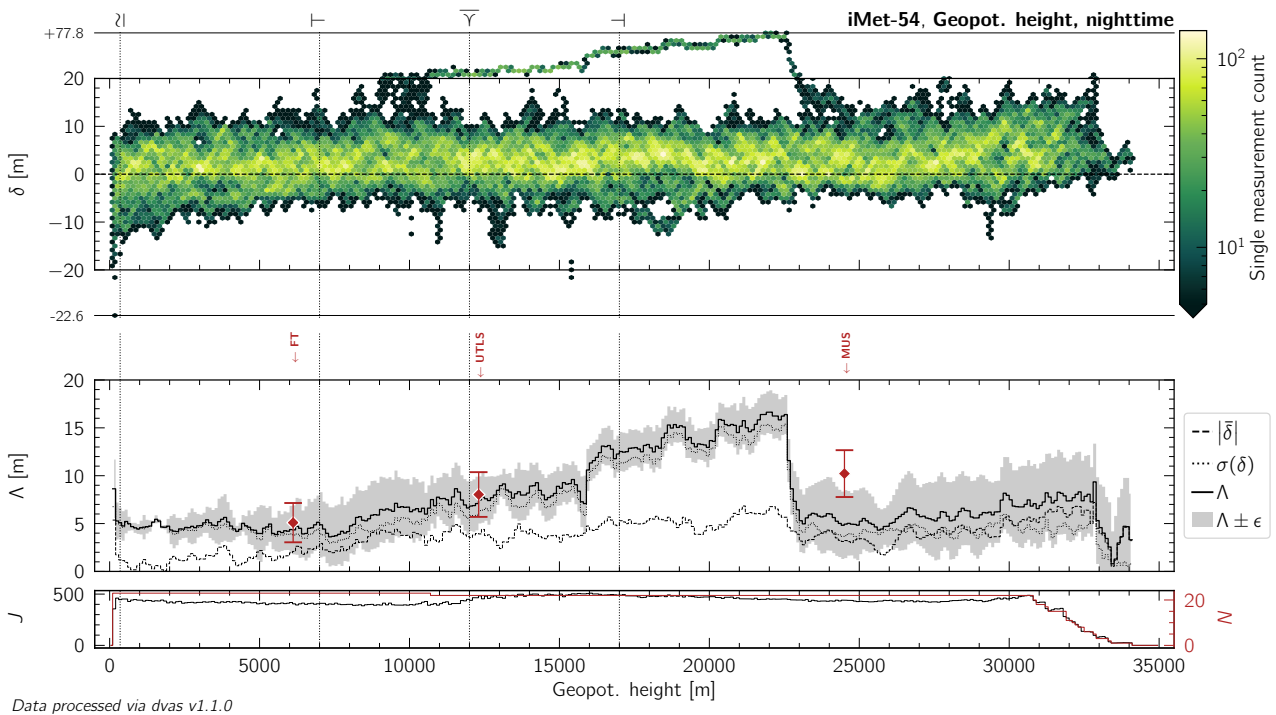


Figure L.62: Same as Figure 10.13, but for nighttime measurements of geopotential height by the iMet-54 radiosonde.

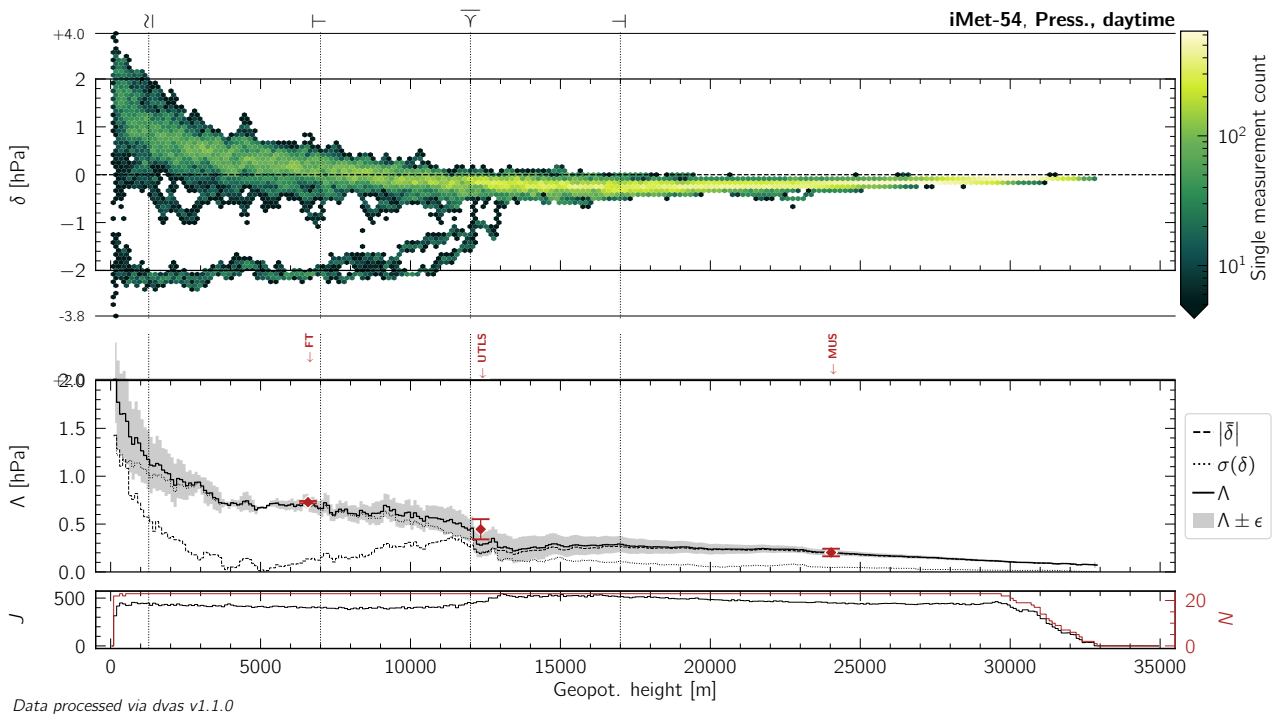


Figure L.63: Same as Figure 10.13, but for daytime measurements of atmospheric pressure by the iMet-54 radiosonde.

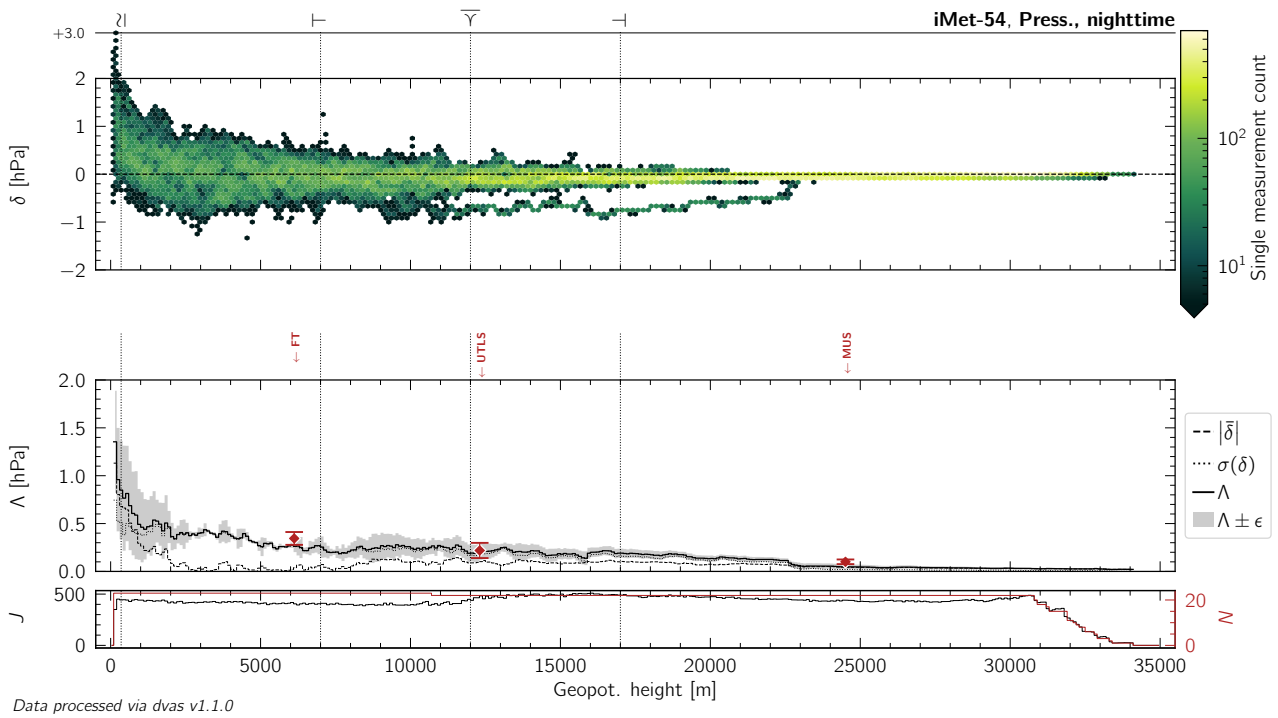


Figure L.64: Same as Figure 10.13, but for nighttime measurements of atmospheric pressure by the iMet-54 radiosonde.

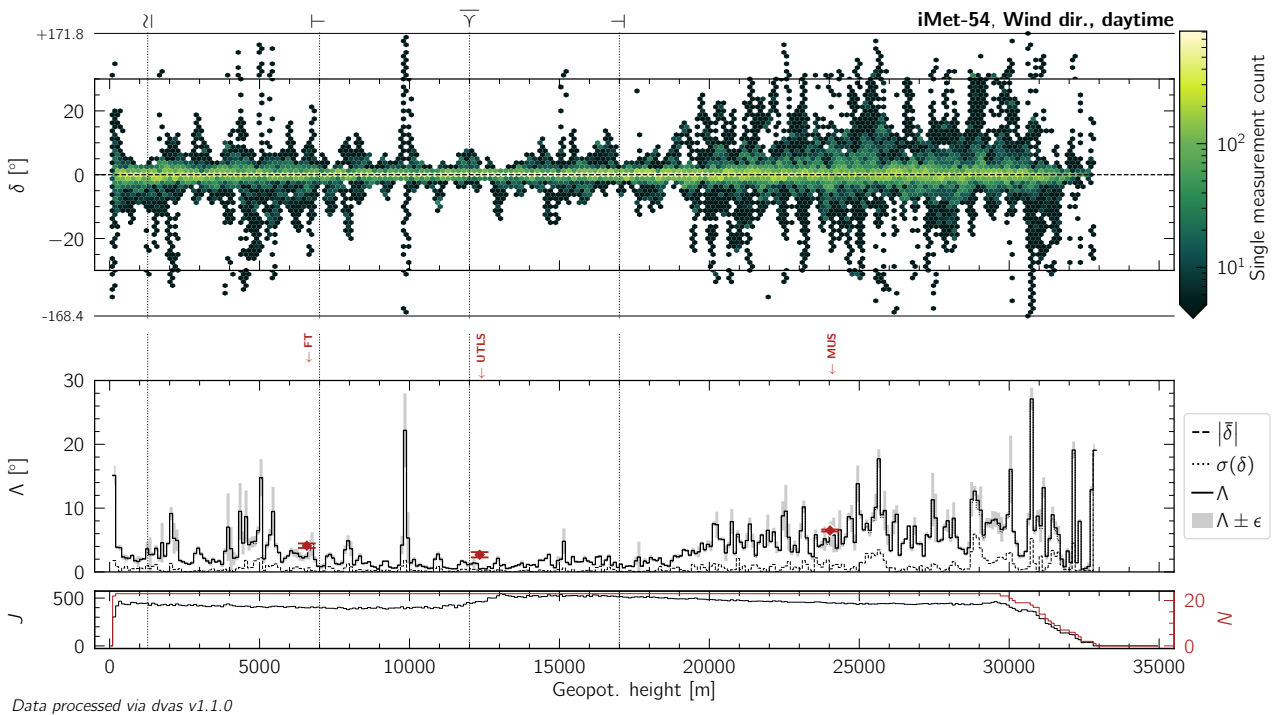


Figure L.65: Same as Figure 10.13, but for daytime measurements of wind (horizontal) direction by the iMet-54 radiosonde.

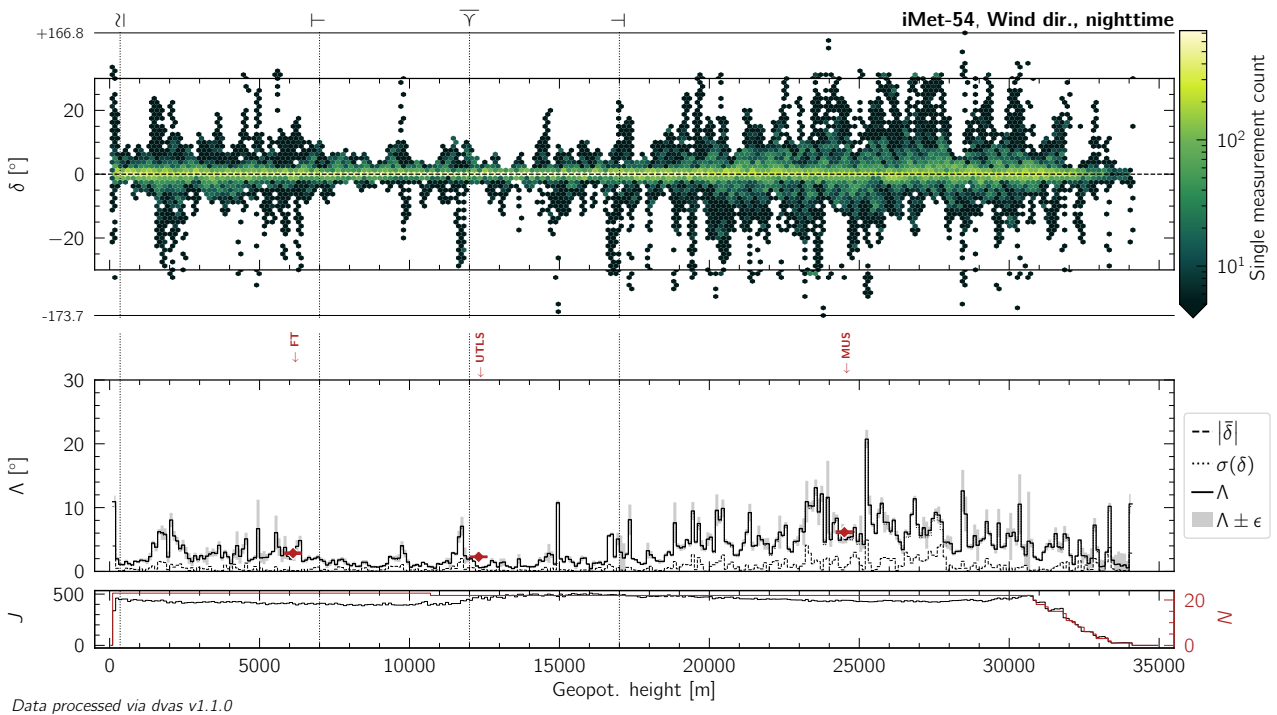


Figure L.66: Same as Figure 10.13, but for nighttime measurements of wind (horizontal) direction by the iMet-54 radiosonde.

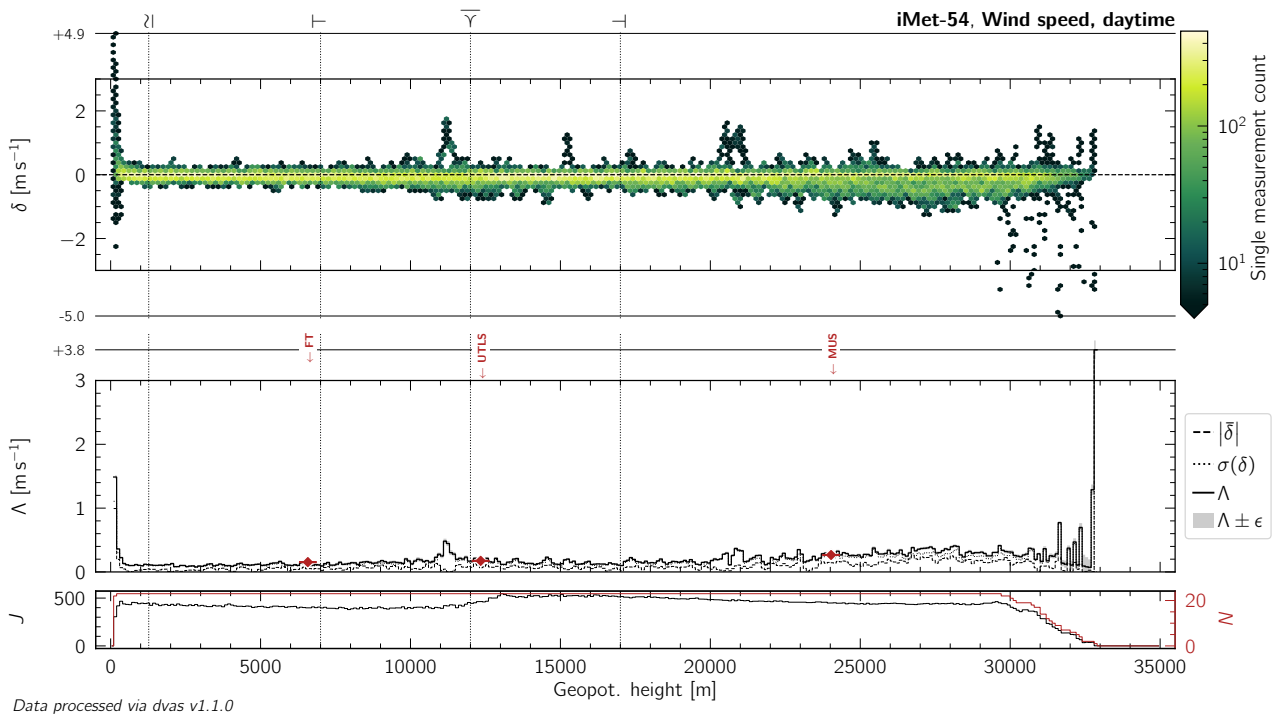


Figure L.67: Same as Figure 10.13, but for daytime measurements of wind (horizontal) speed by the iMet-54 radiosonde.

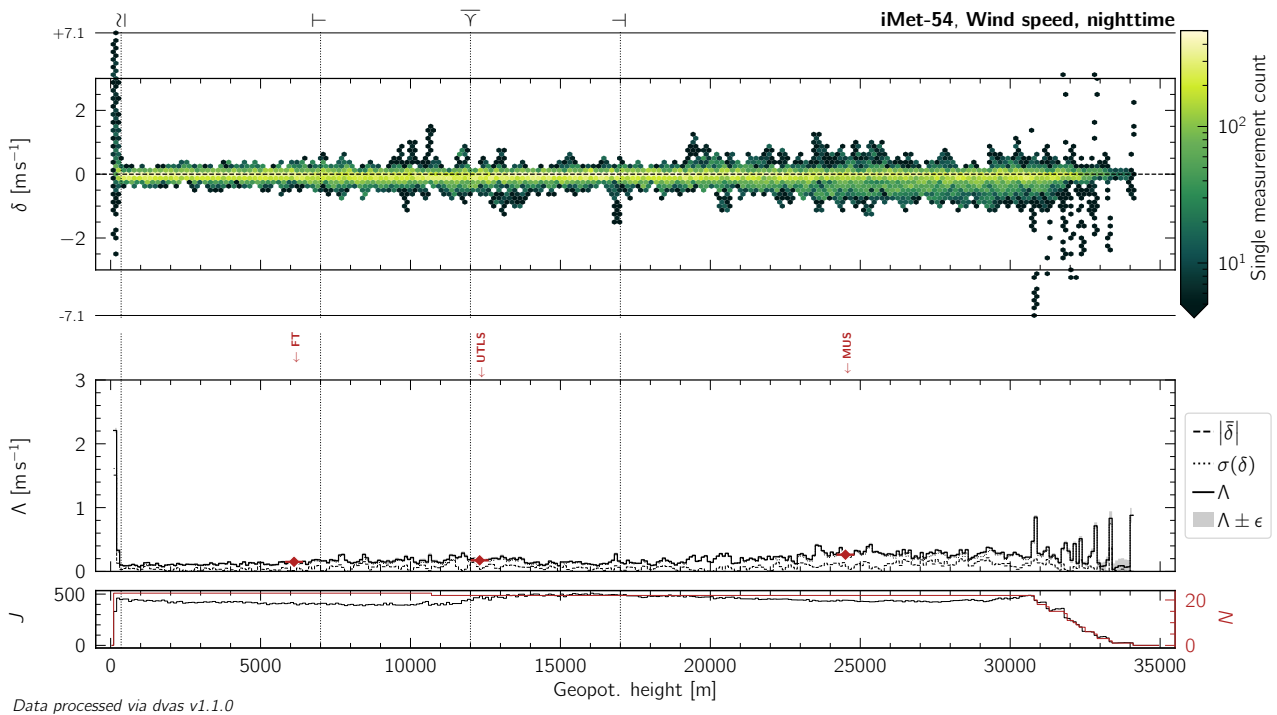


Figure L.68: Same as Figure 10.13, but for nighttime measurements of wind (horizontal) speed by the iMet-54 radiosonde.

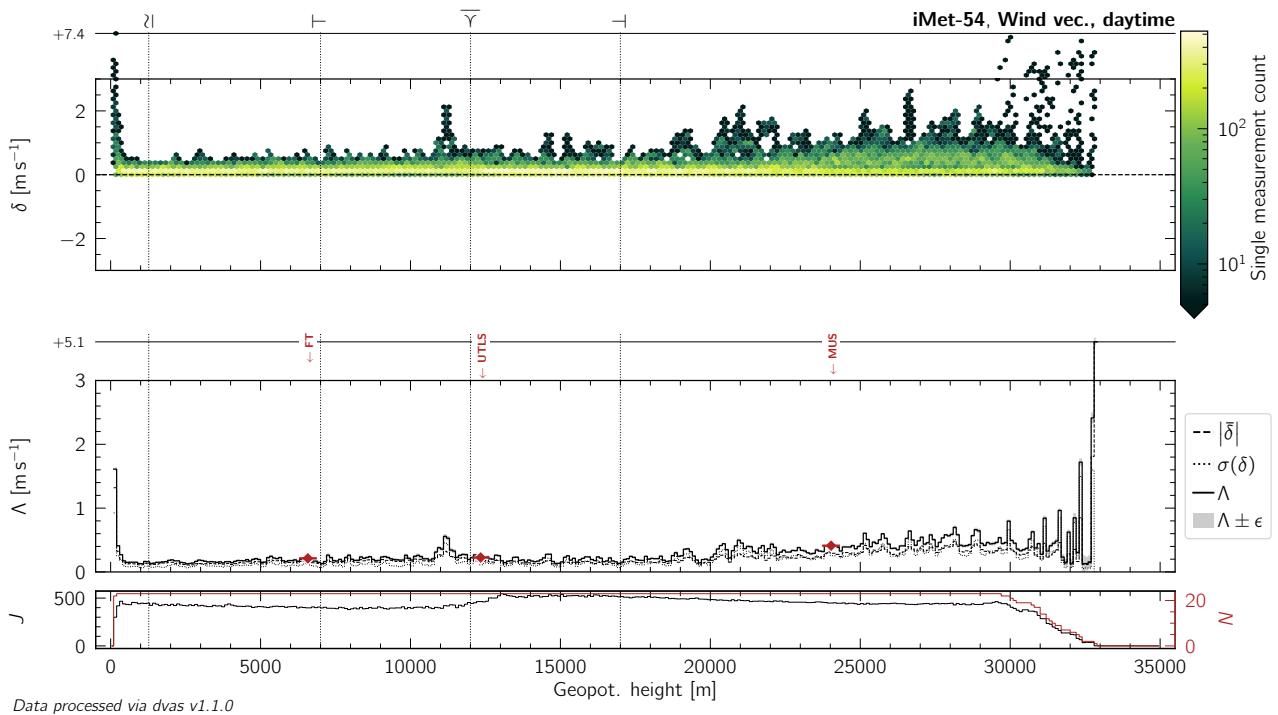


Figure L.69: Same as Figure 10.13, but for daytime measurements of the wind (horizontal) vector by the iMet-54 radiosonde.

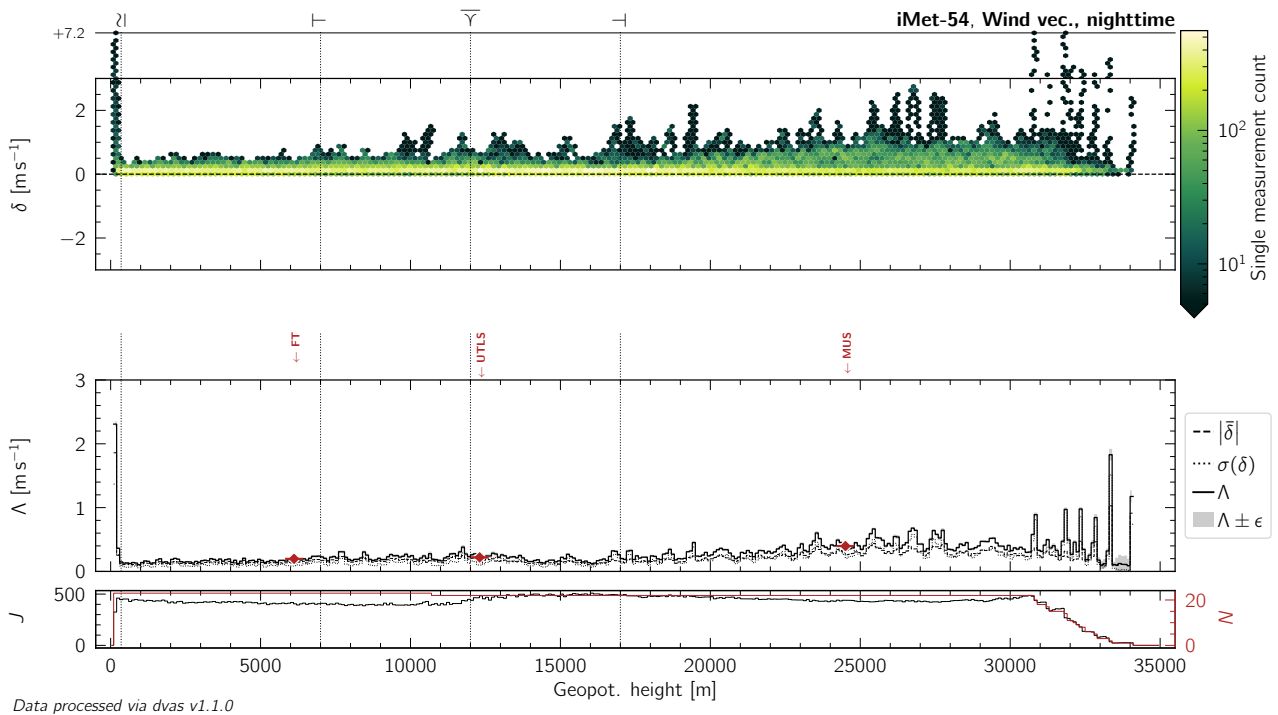


Figure L.70: Same as Figure 10.13, but for nighttime measurements of the wind (horizontal) vector by the iMet-54 radiosonde.

L.6 IMS-100

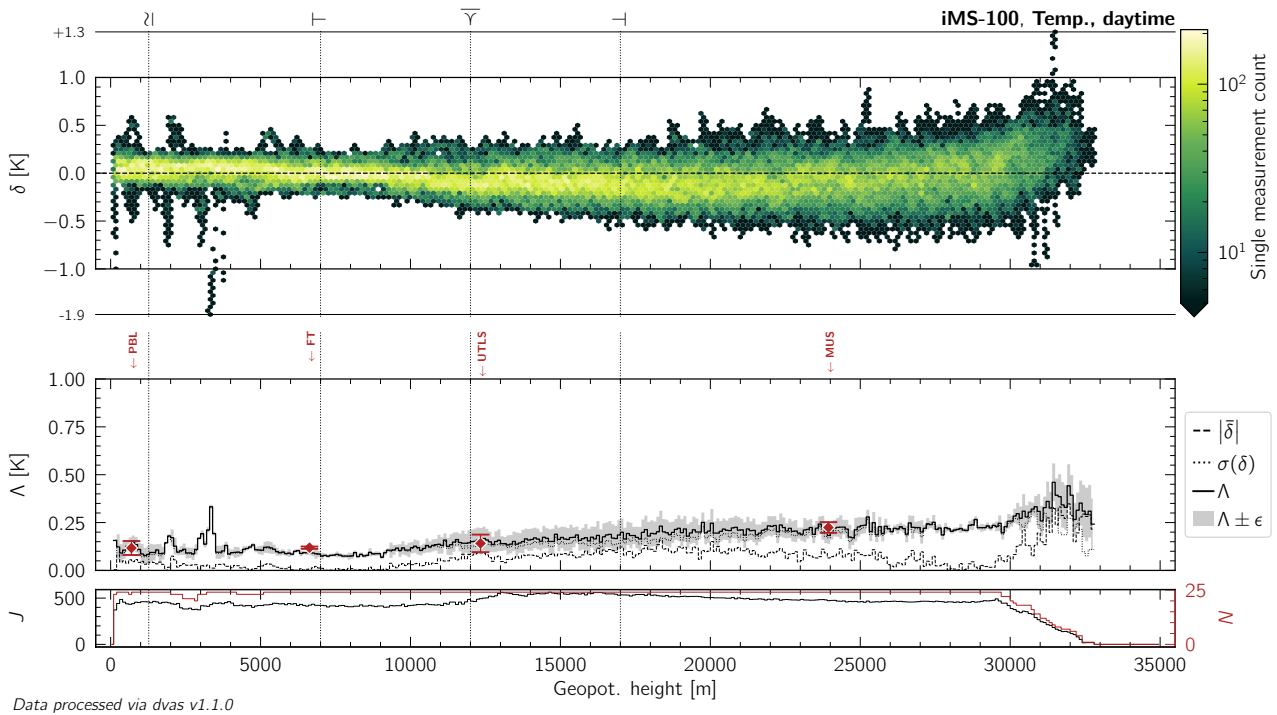


Figure L.71: Same as Figure 10.13, but for daytime measurements of atmospheric temperature by the iMS-100 radiosonde.

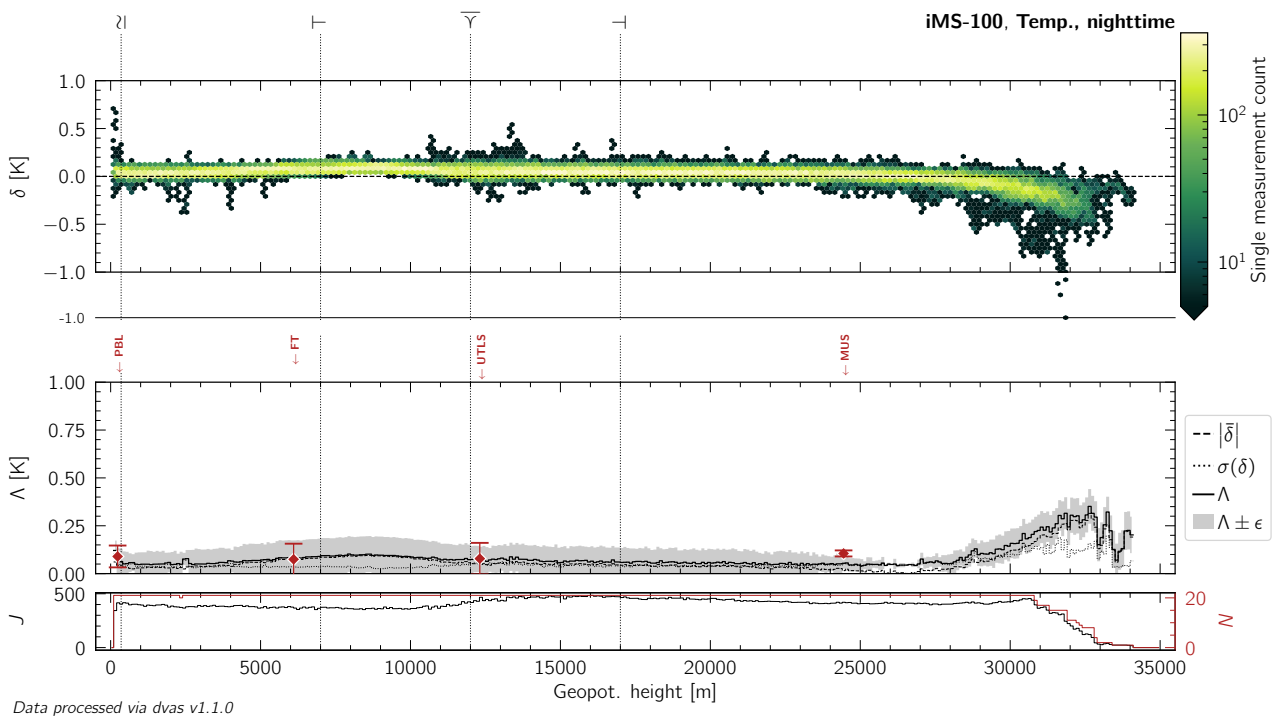


Figure L.72: Same as Figure 10.13, but for nighttime measurements of atmospheric temperature by the iMS-100 radiosonde.

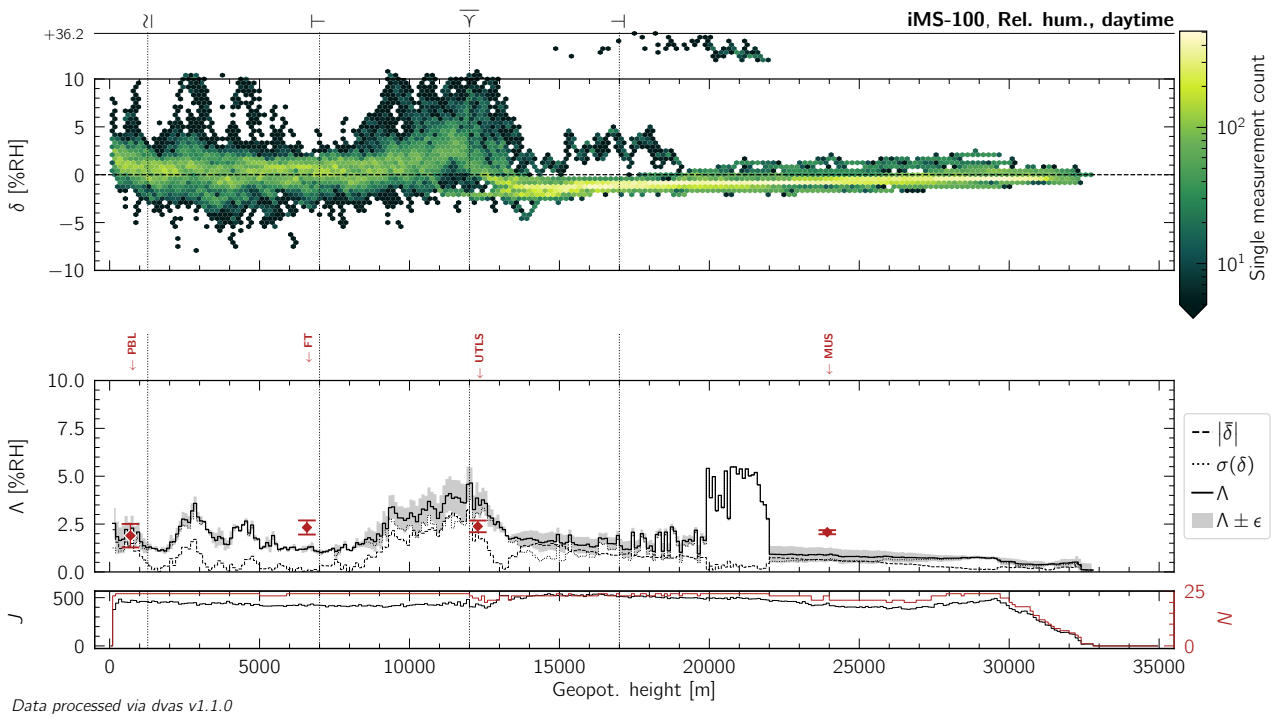


Figure L.73: Same as Figure 10.13, but for daytime measurements of relative humidity by the iMS-100 radiosonde.

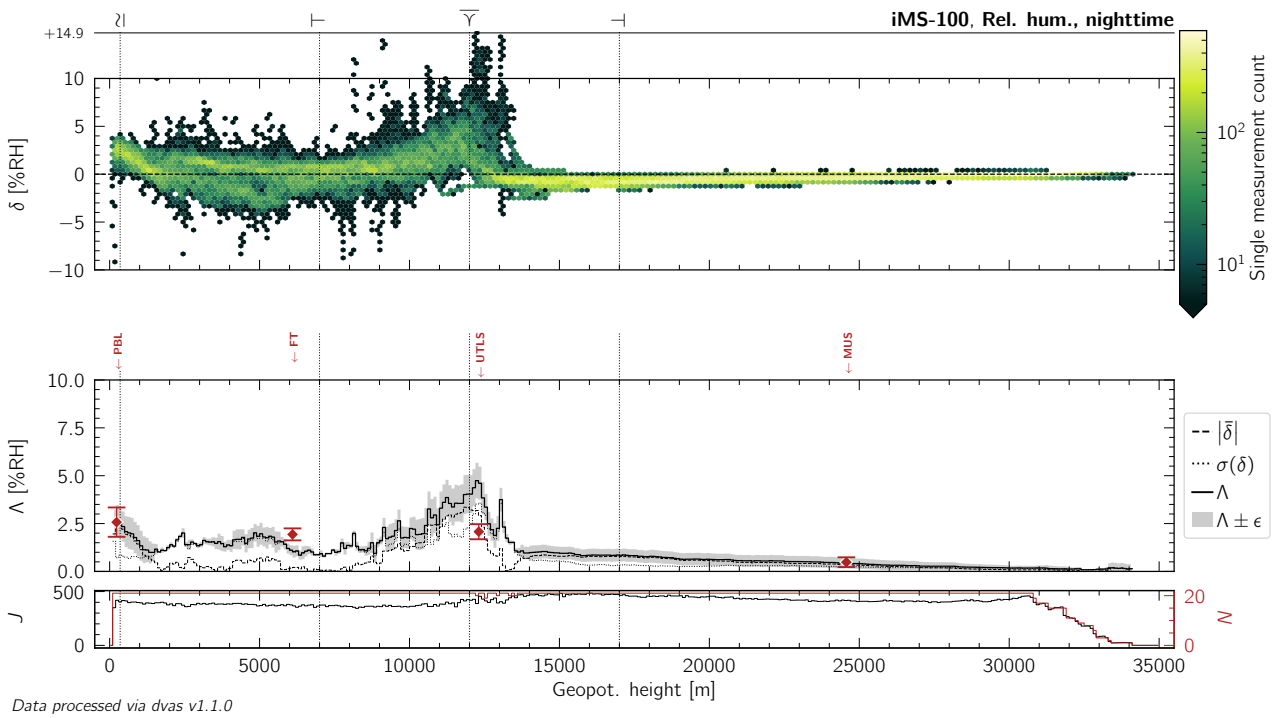


Figure L.74: Same as Figure 10.13, but for nighttime measurements of relative humidity by the iMS-100 radiosonde.

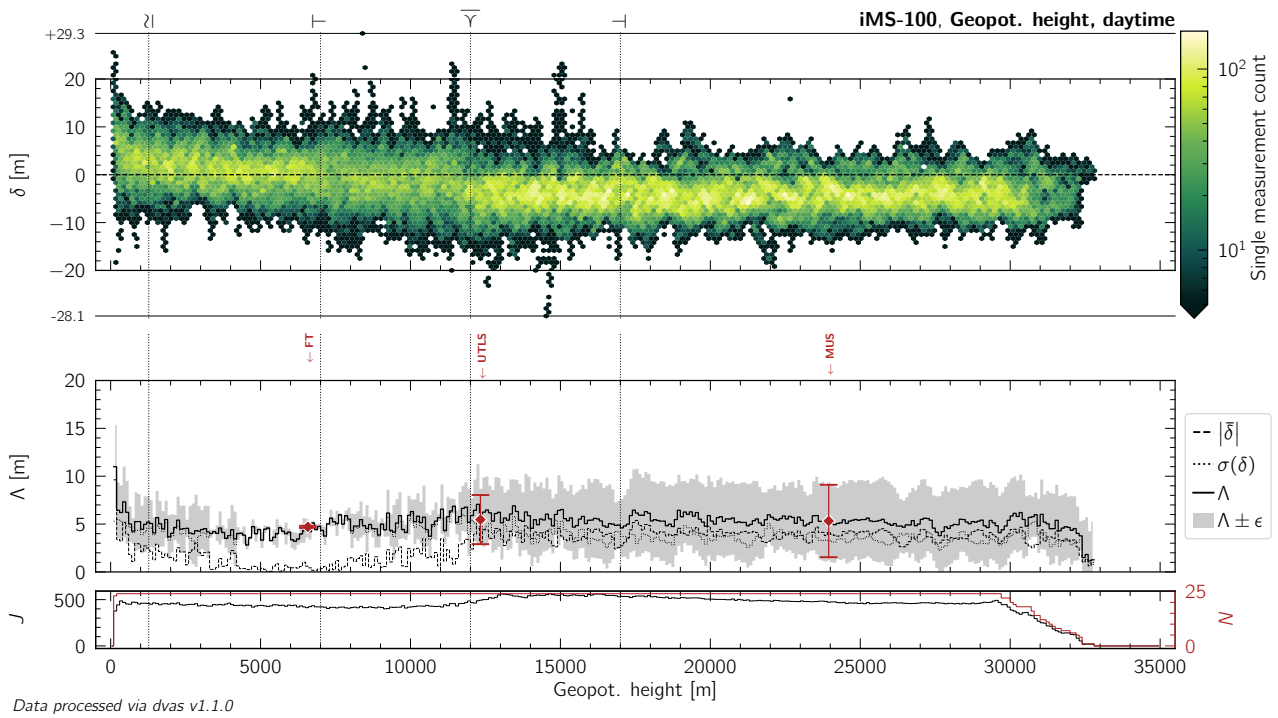


Figure L.75: Same as Figure 10.13, but for daytime measurements of geopotential height by the iMS-100 radiosonde.

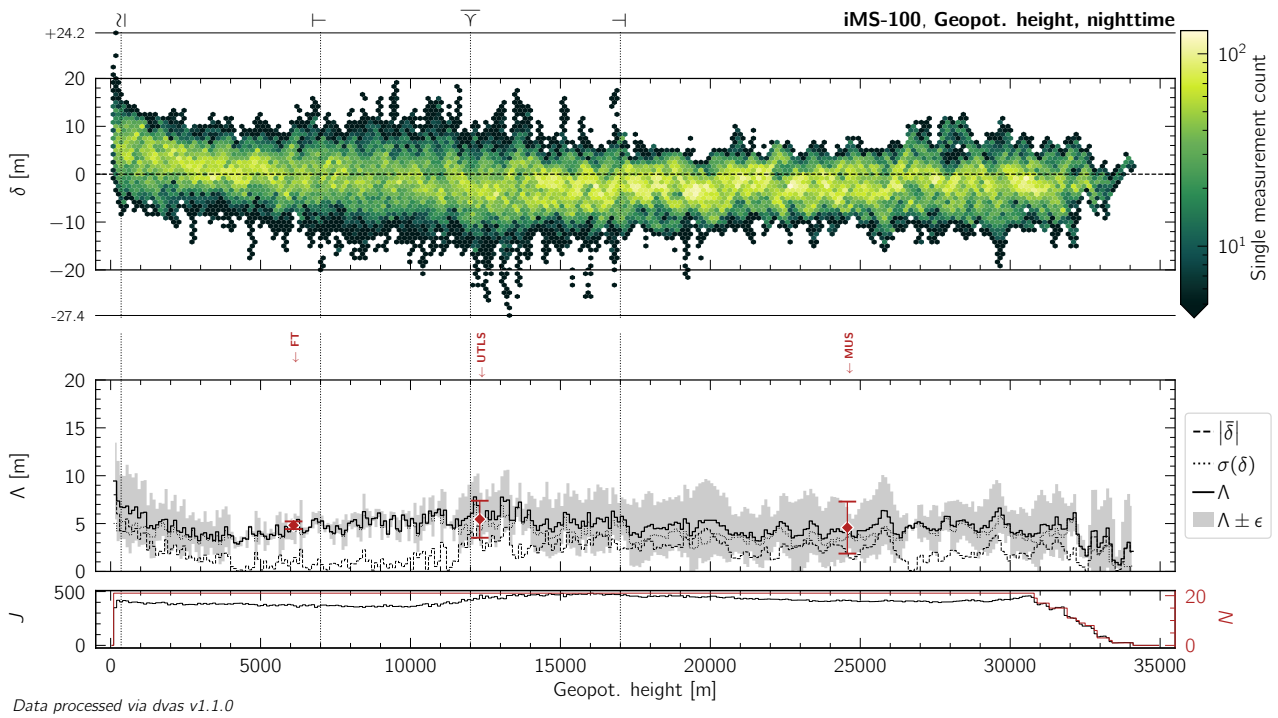


Figure L.76: Same as Figure 10.13, but for nighttime measurements of geopotential height by the iMS-100 radiosonde.

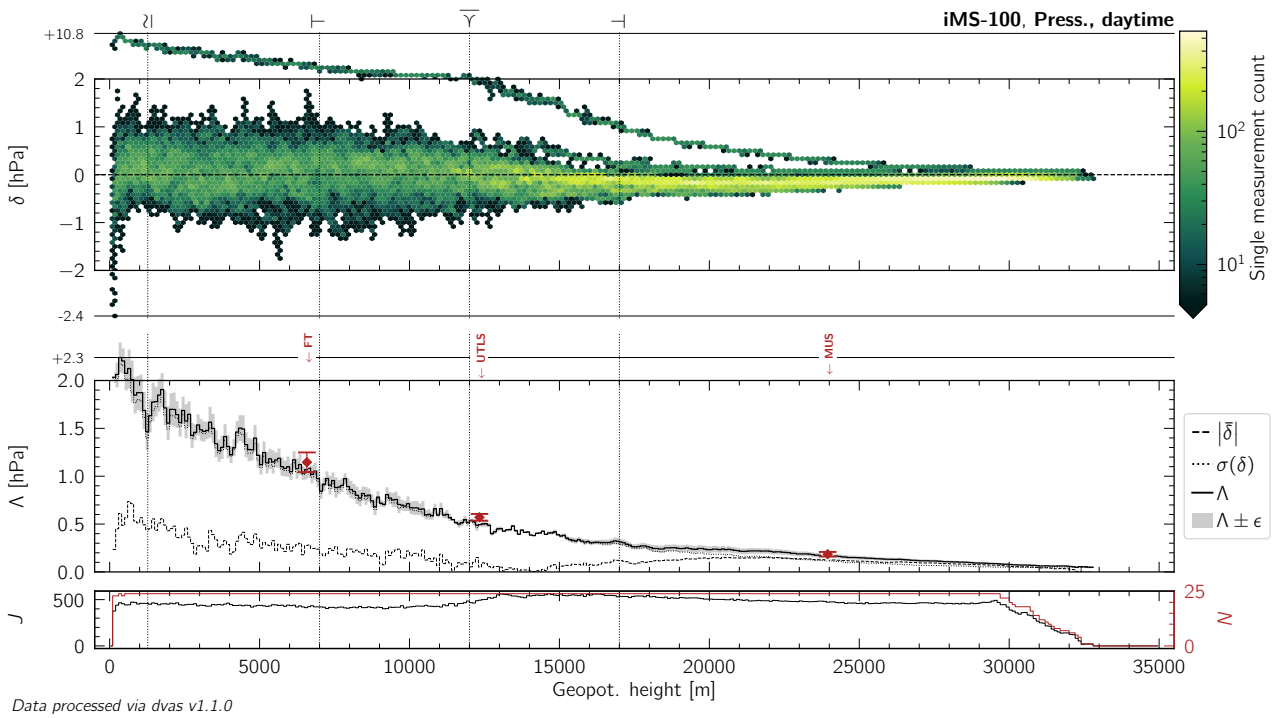


Figure L.77: Same as Figure 10.13, but for daytime measurements of atmospheric pressure by the iMS-100 radiosonde.

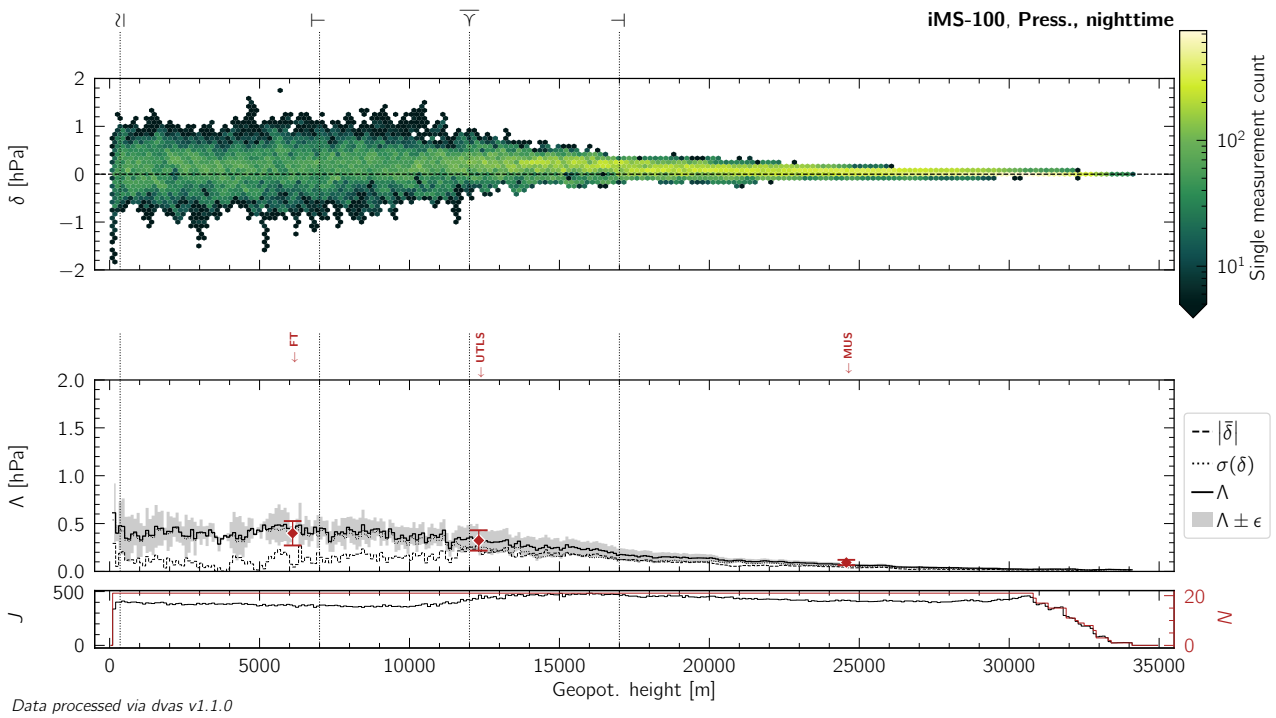


Figure L.78: Same as Figure 10.13, but for nighttime measurements of atmospheric pressure by the iMS-100 radiosonde.

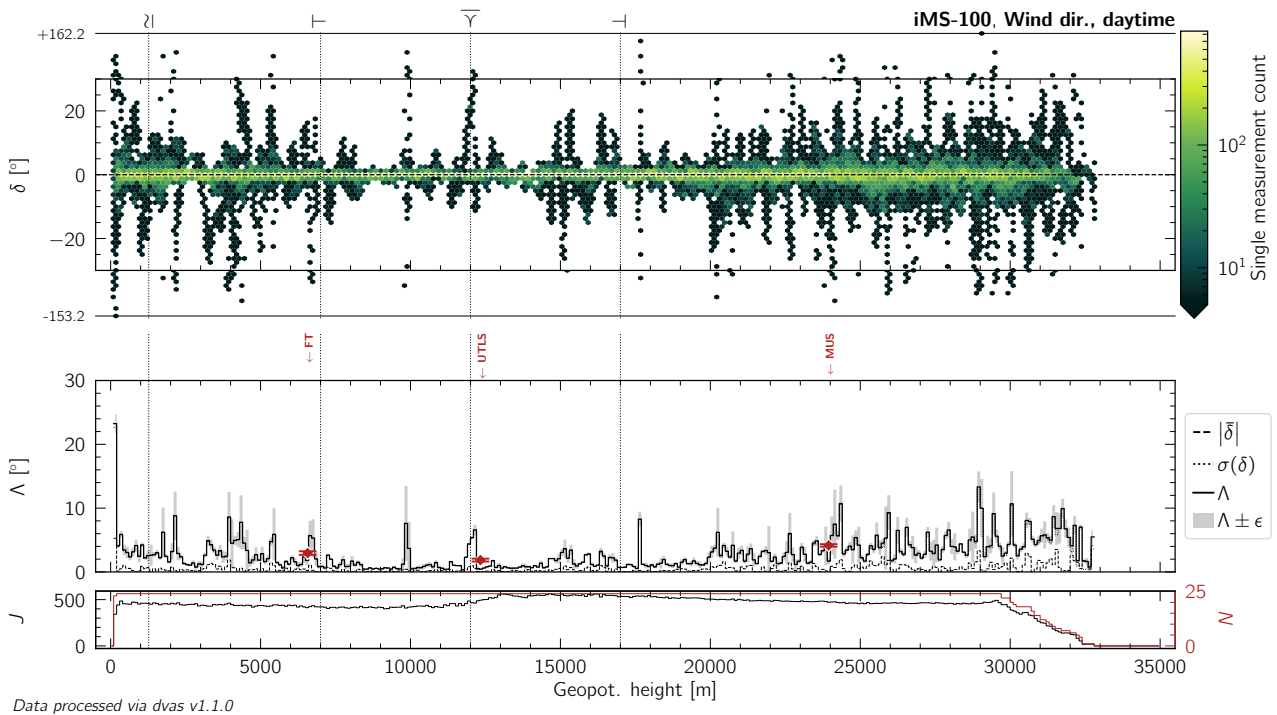


Figure L.79: Same as Figure 10.13, but for daytime measurements of wind (horizontal) direction by the iMS-100 radiosonde.

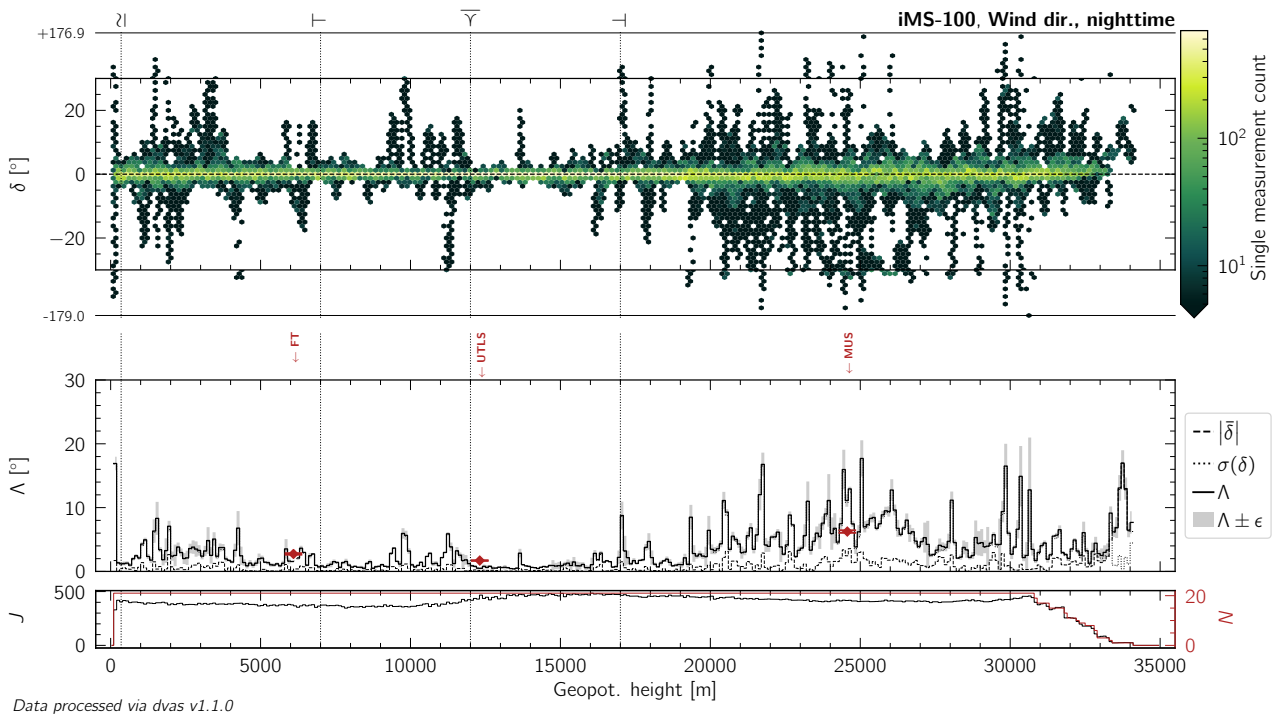


Figure L.80: Same as Figure 10.13, but for nighttime measurements of wind (horizontal) direction by the iMS-100 radiosonde.

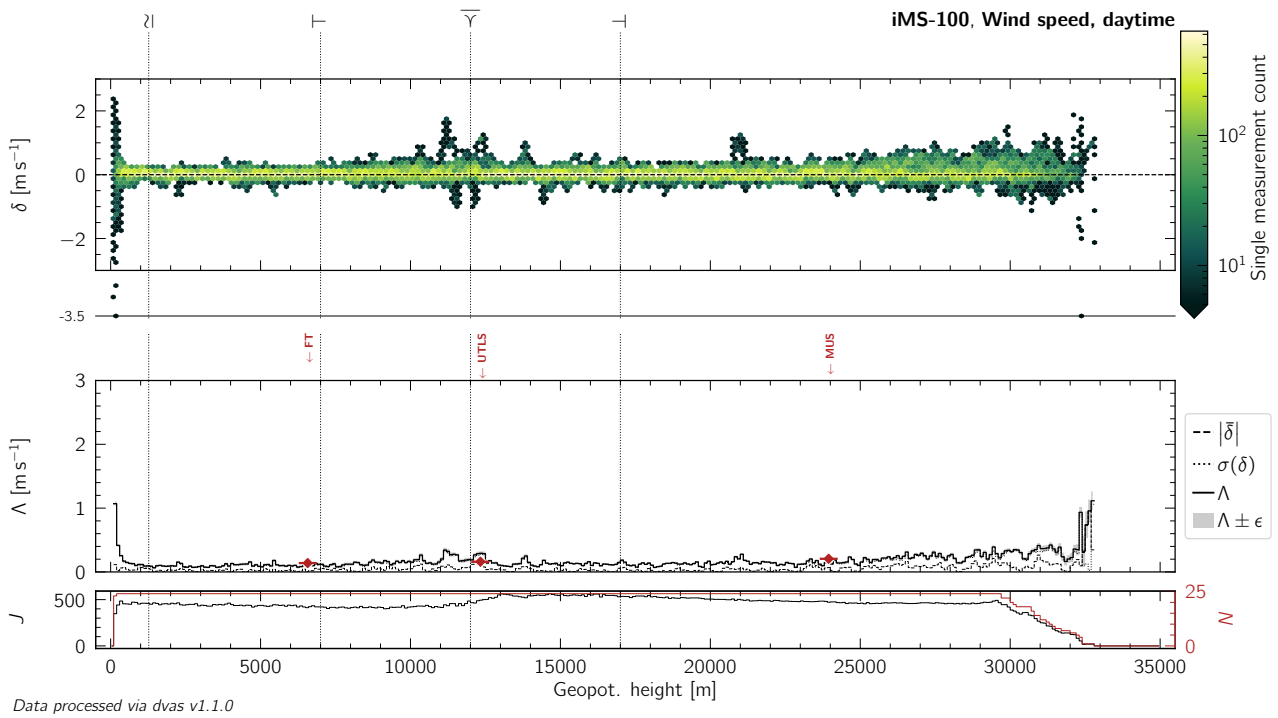


Figure L.81: Same as Figure 10.13, but for daytime measurements of wind (horizontal) speed by the iMS-100 radiosonde.

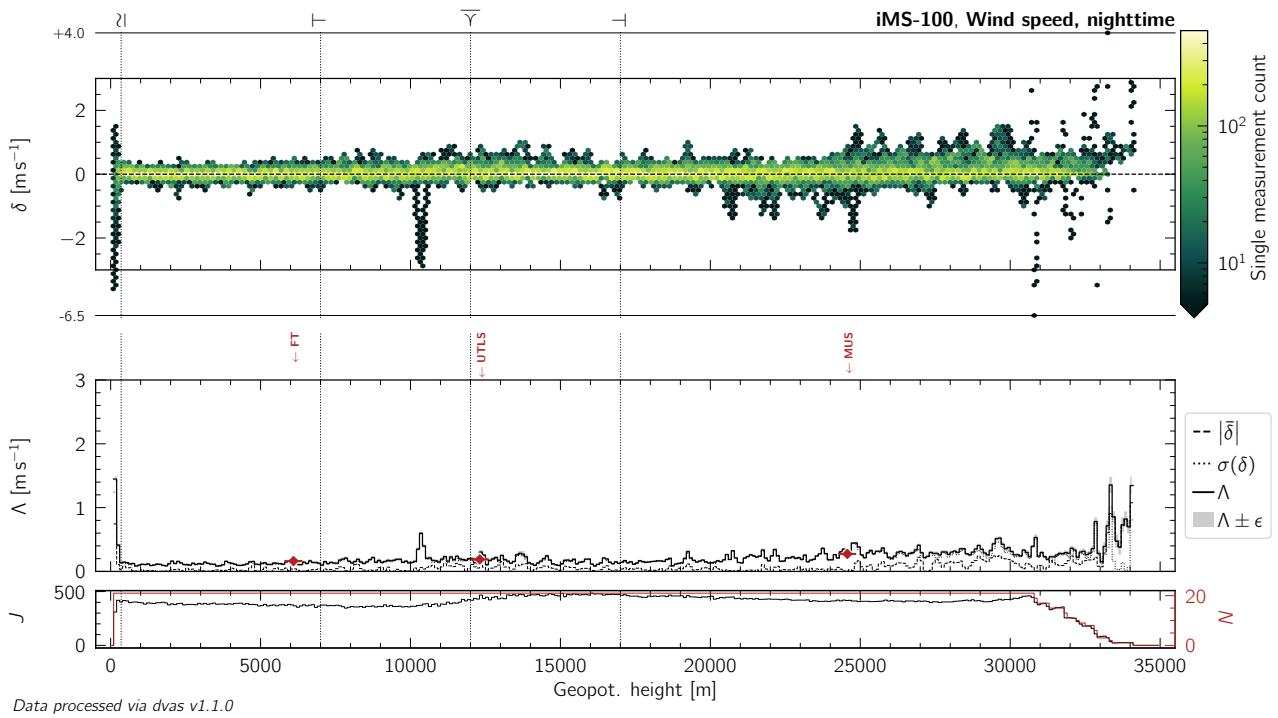


Figure L.82: Same as Figure 10.13, but for nighttime measurements of wind (horizontal) speed by the iMS-100 radiosonde.

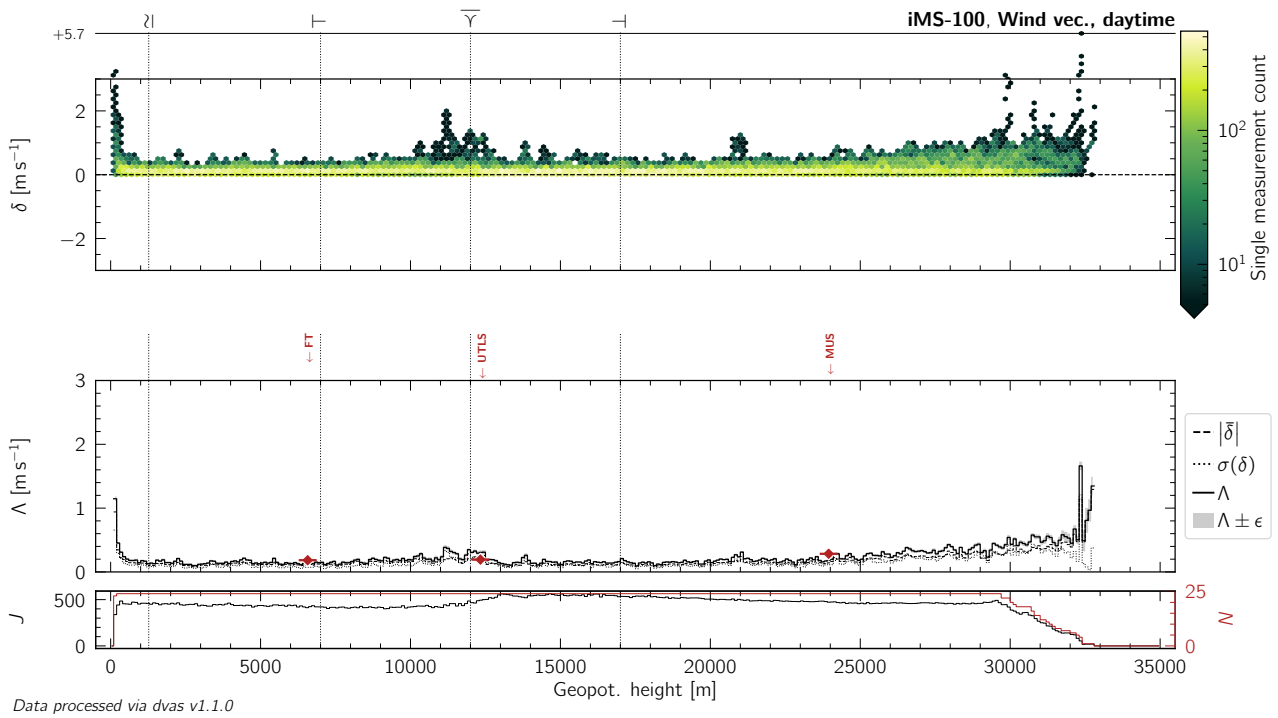


Figure L.83: Same as Figure 10.13, but for daytime measurements of the wind (horizontal) vector by the iMS-100 radiosonde.

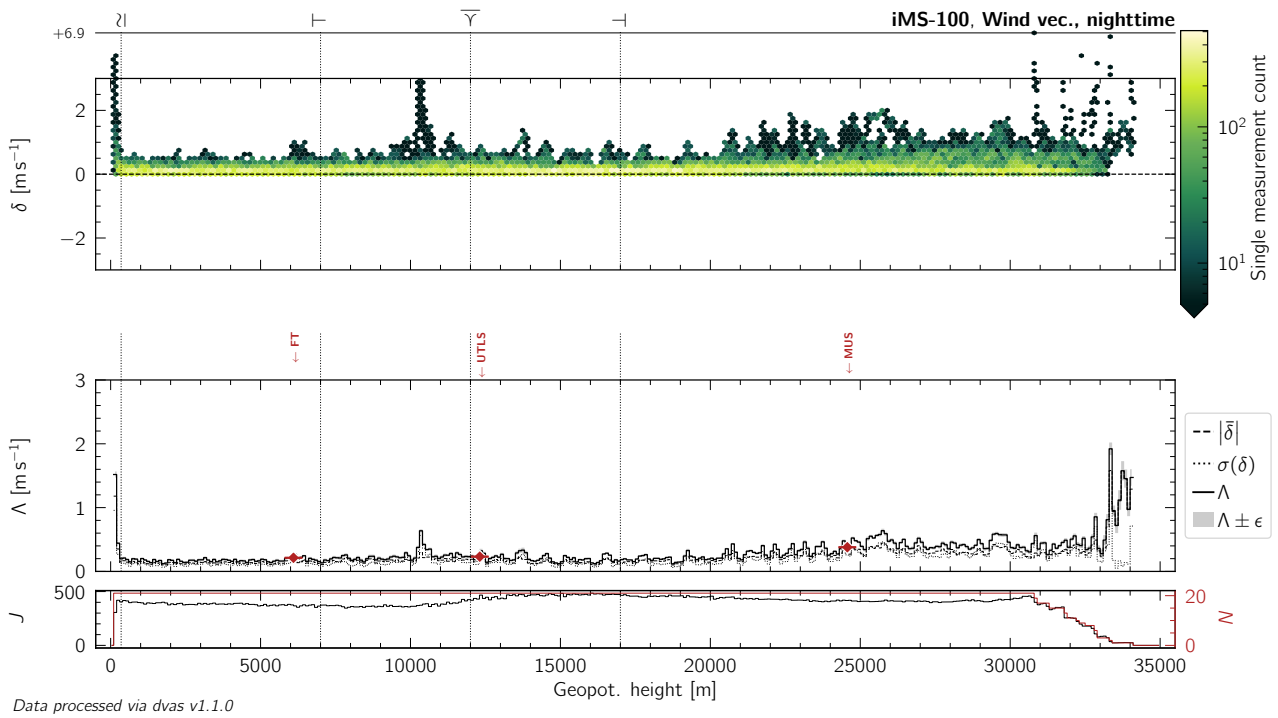


Figure L.84: Same as Figure 10.13, but for nighttime measurements of the wind (horizontal) vector by the iMS-100 radiosonde.

L.7 M20

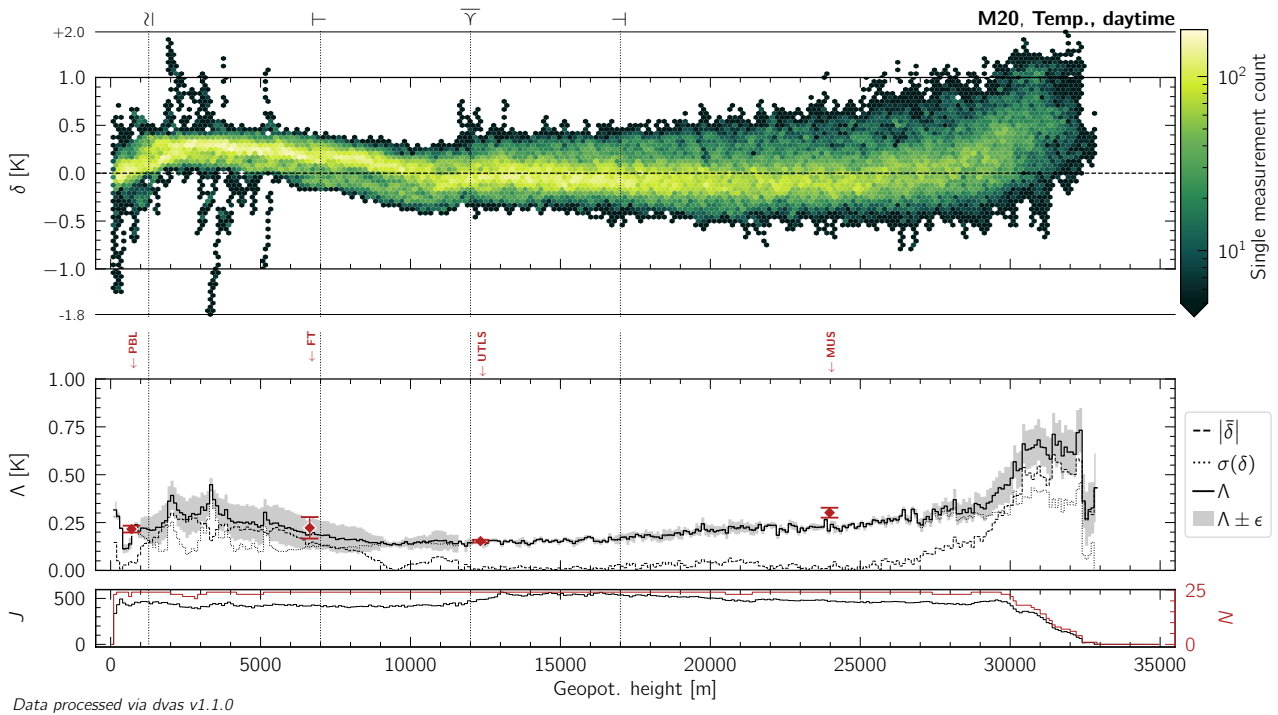


Figure L.85: Same as Figure 10.13, but for daytime measurements of atmospheric temperature by the M20 radiosonde.

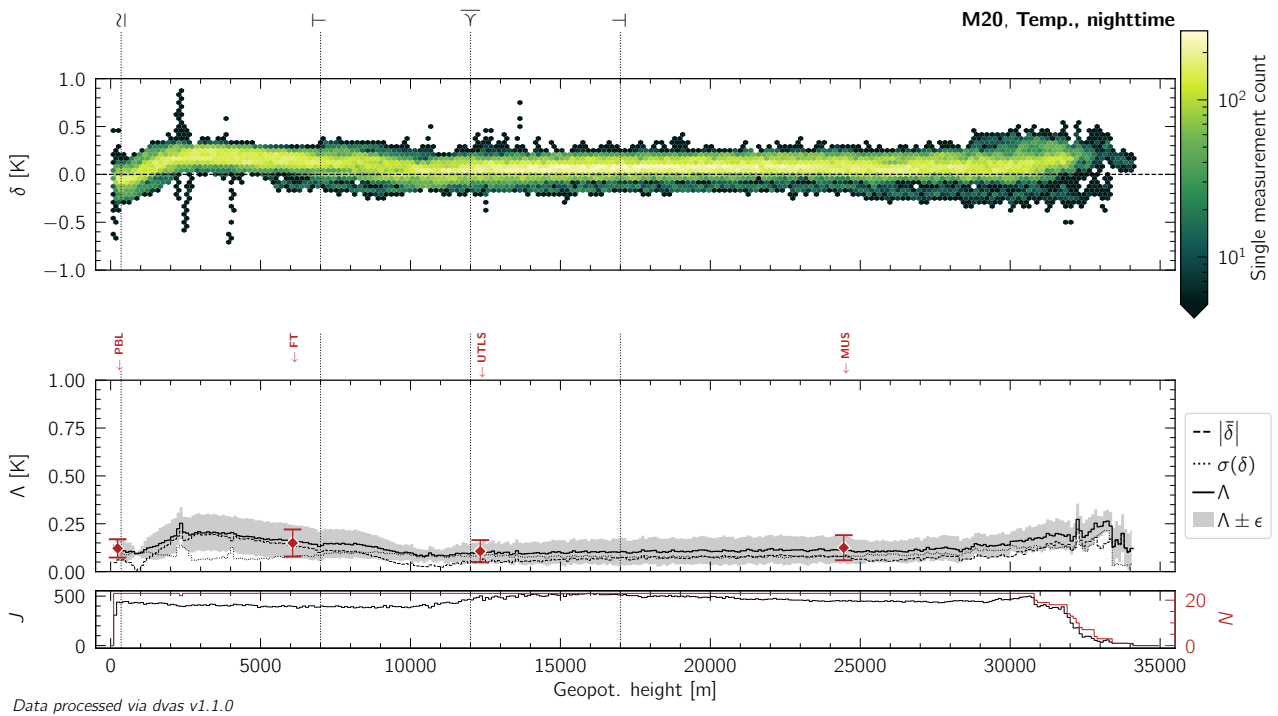


Figure L.86: Same as Figure 10.13, but for nighttime measurements of atmospheric temperature by the M20 radiosonde.

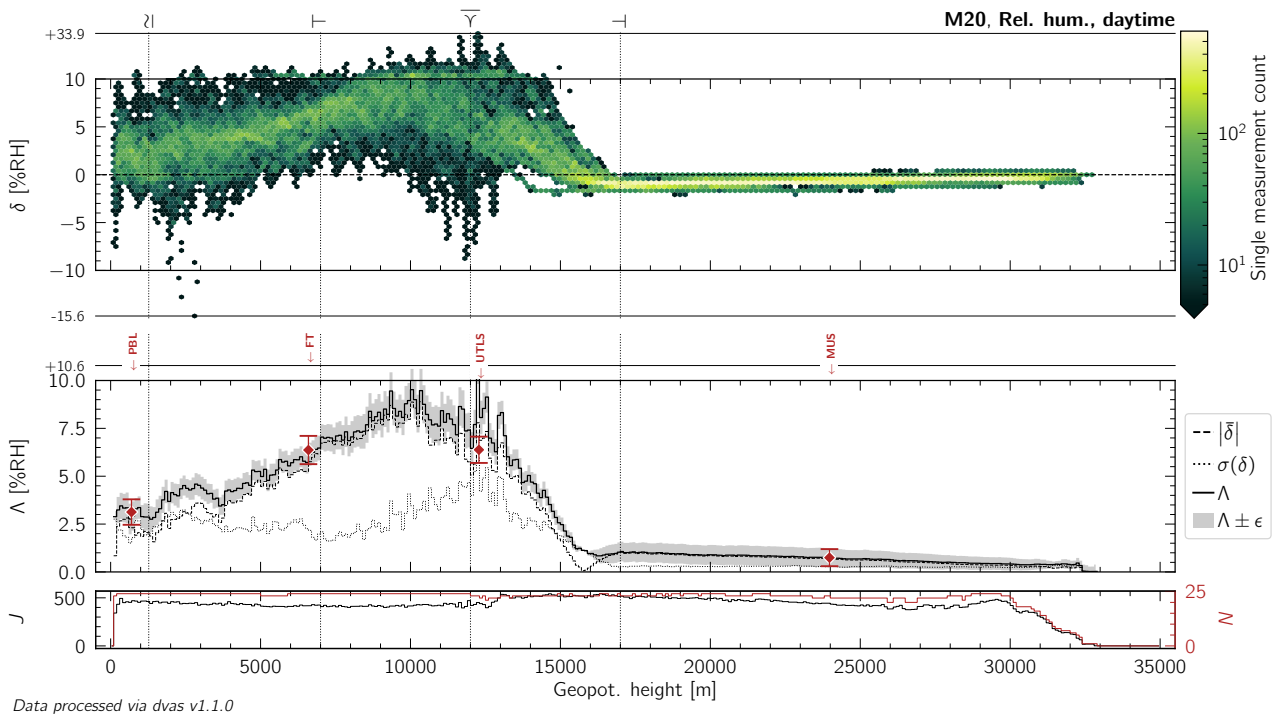


Figure L.87: Same as Figure 10.13, but for daytime measurements of relative humidity by the M20 radiosonde.

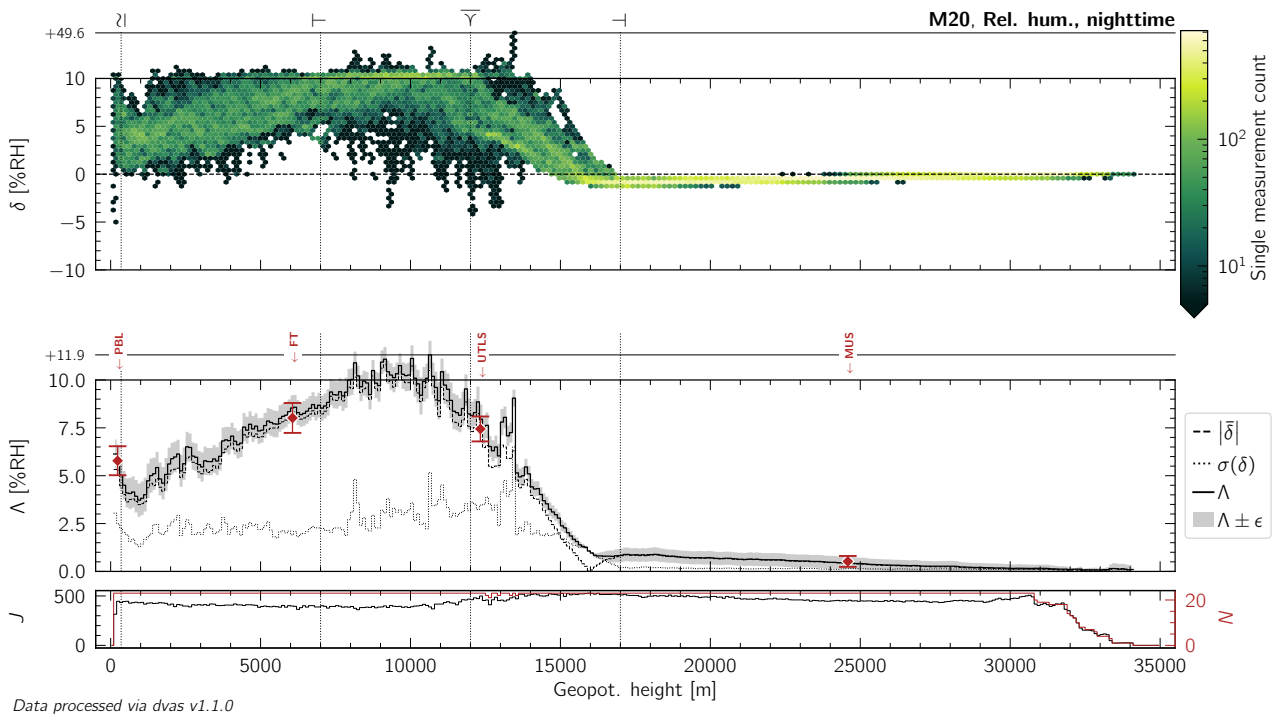


Figure L.88: Same as Figure 10.13, but for nighttime measurements of relative humidity by the M20 radiosonde.

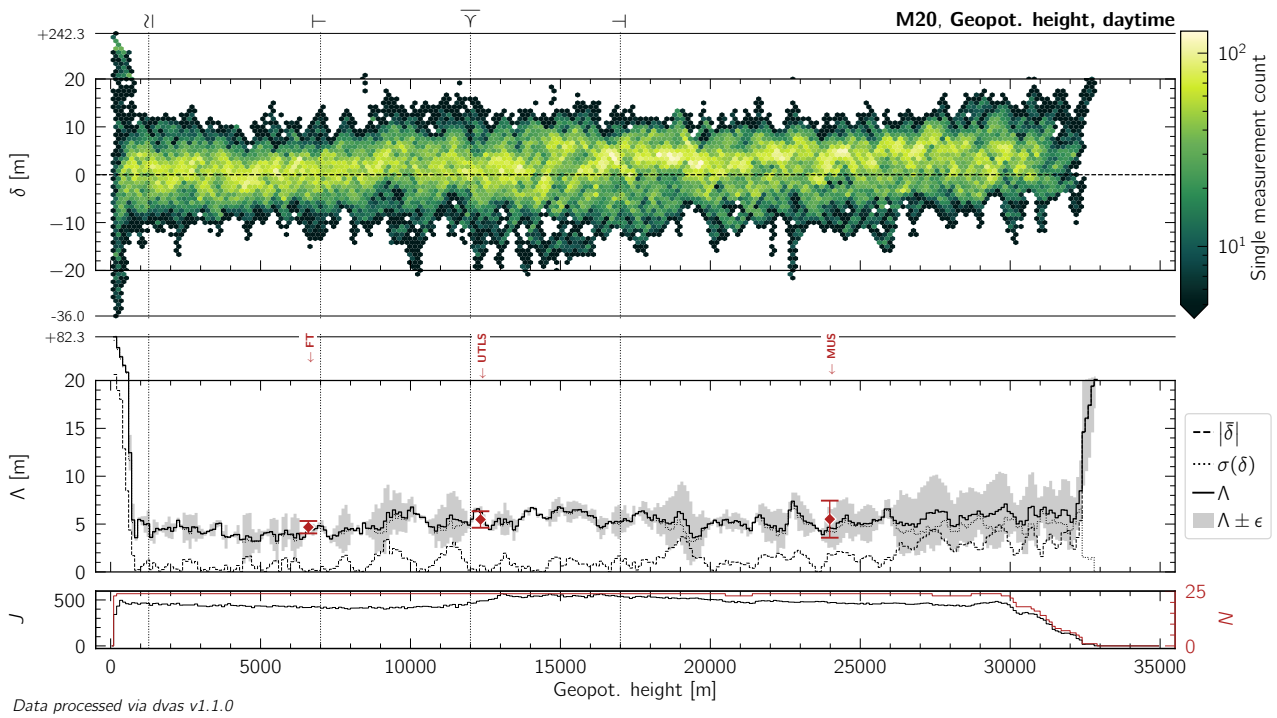


Figure L.89: Same as Figure 10.13, but for daytime measurements of geopotential height by the M20 radiosonde.

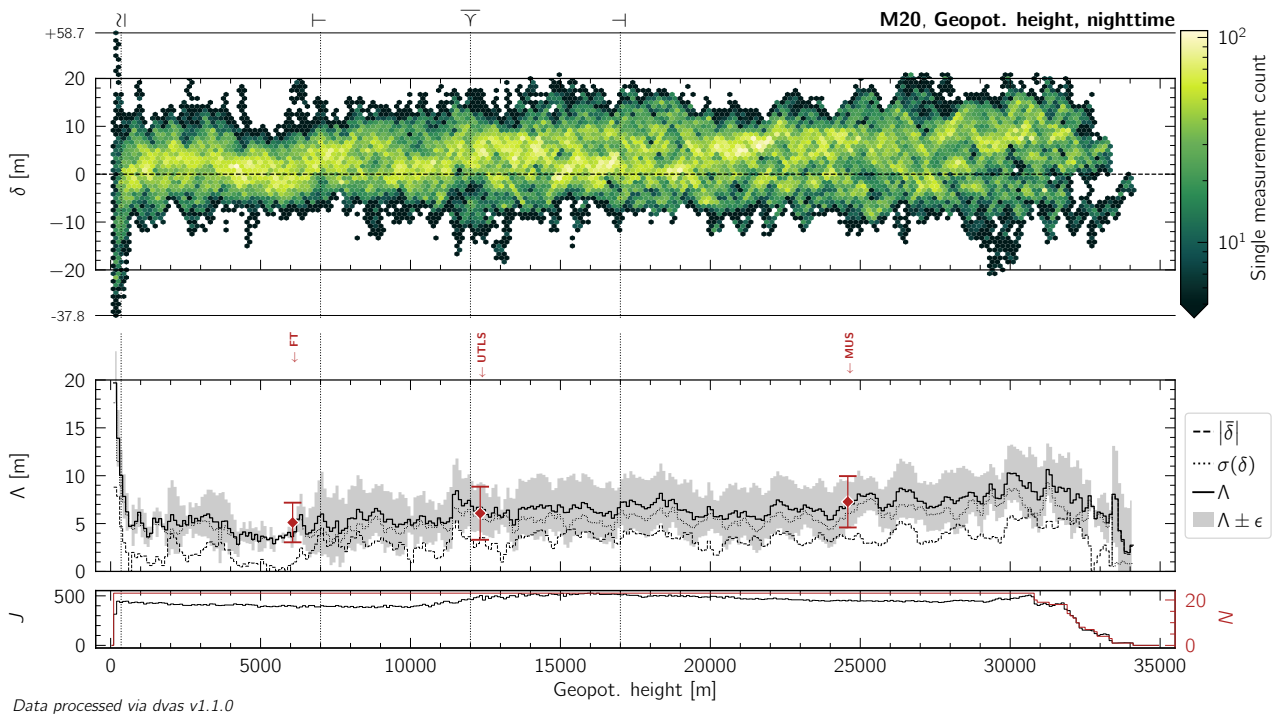


Figure L.90: Same as Figure 10.13, but for nighttime measurements of geopotential height by the M20 radiosonde.

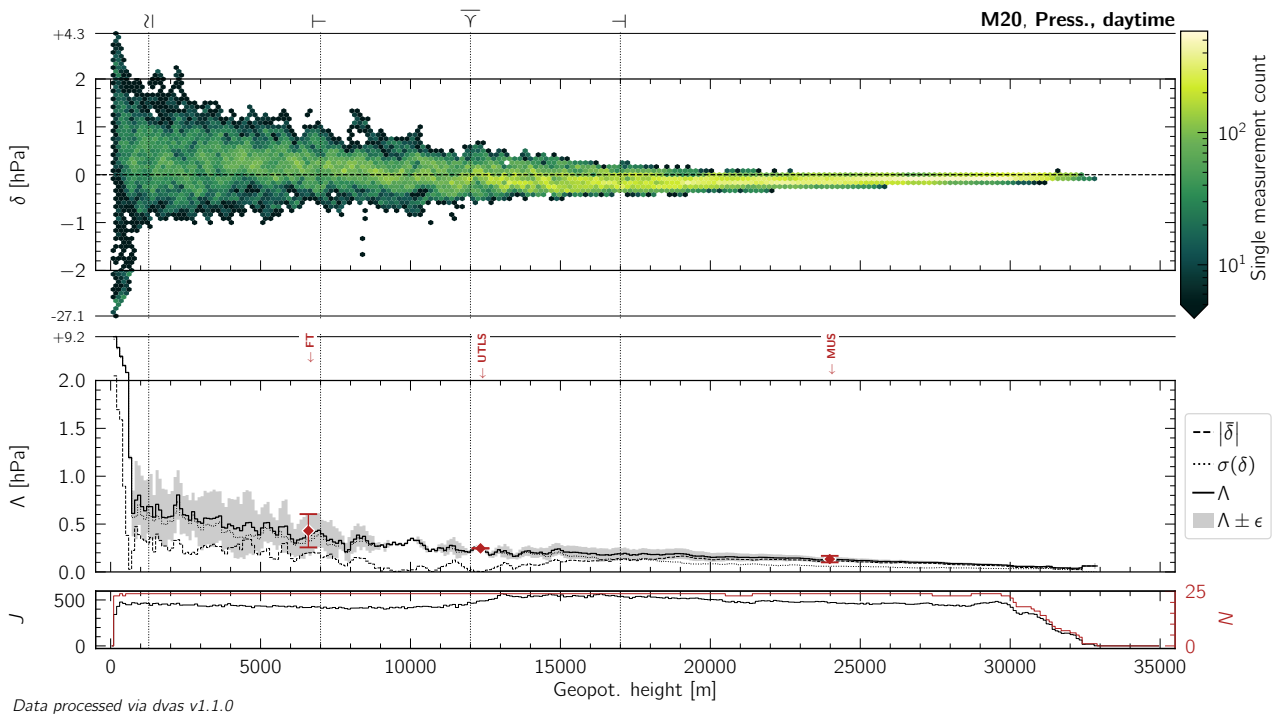


Figure L.91: Same as Figure 10.13, but for daytime measurements of atmospheric pressure by the M20 radiosonde.

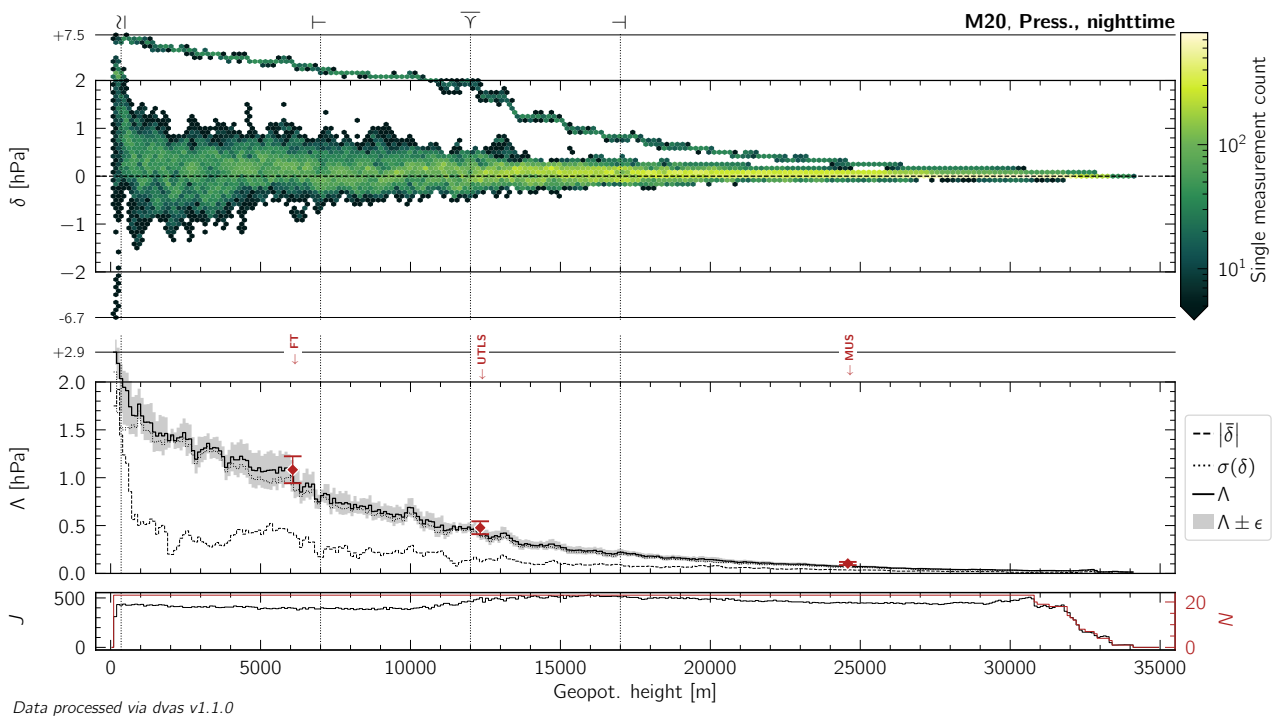


Figure L.92: Same as Figure 10.13, but for nighttime measurements of atmospheric pressure by the M20 radiosonde.

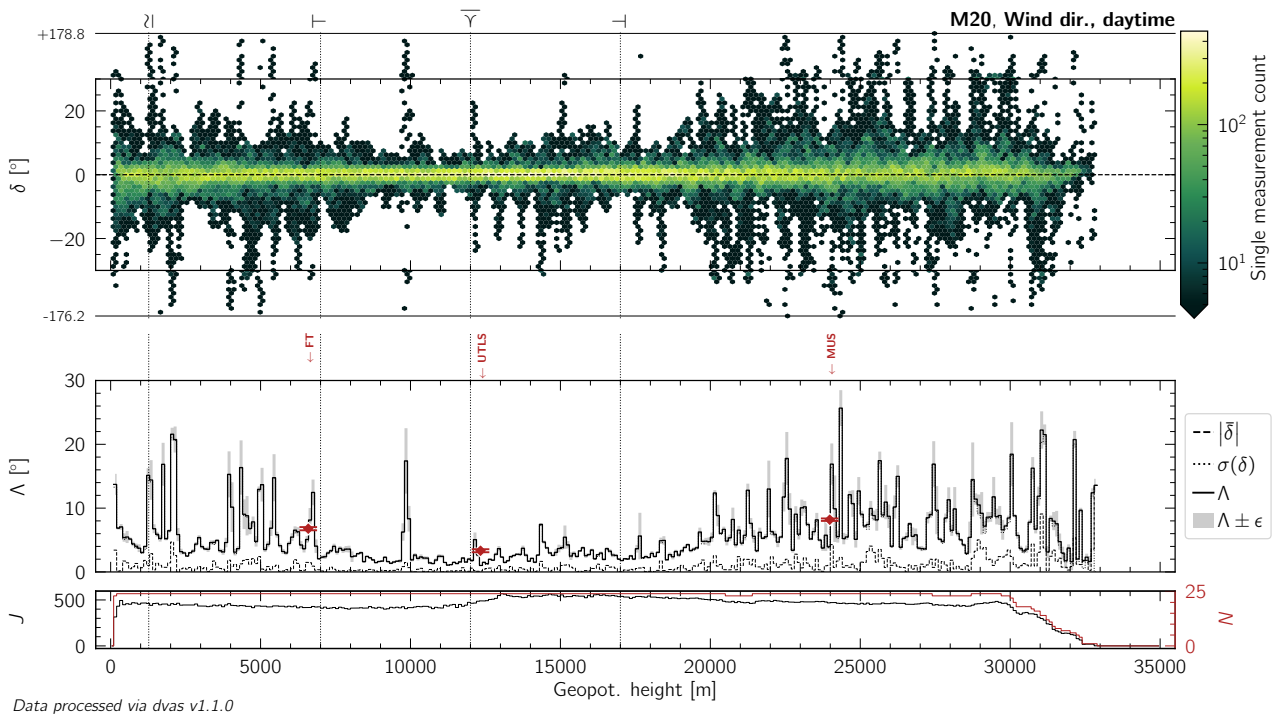


Figure L.93: Same as Figure 10.13, but for daytime measurements of wind (horizontal) direction by the M20 radiosonde.

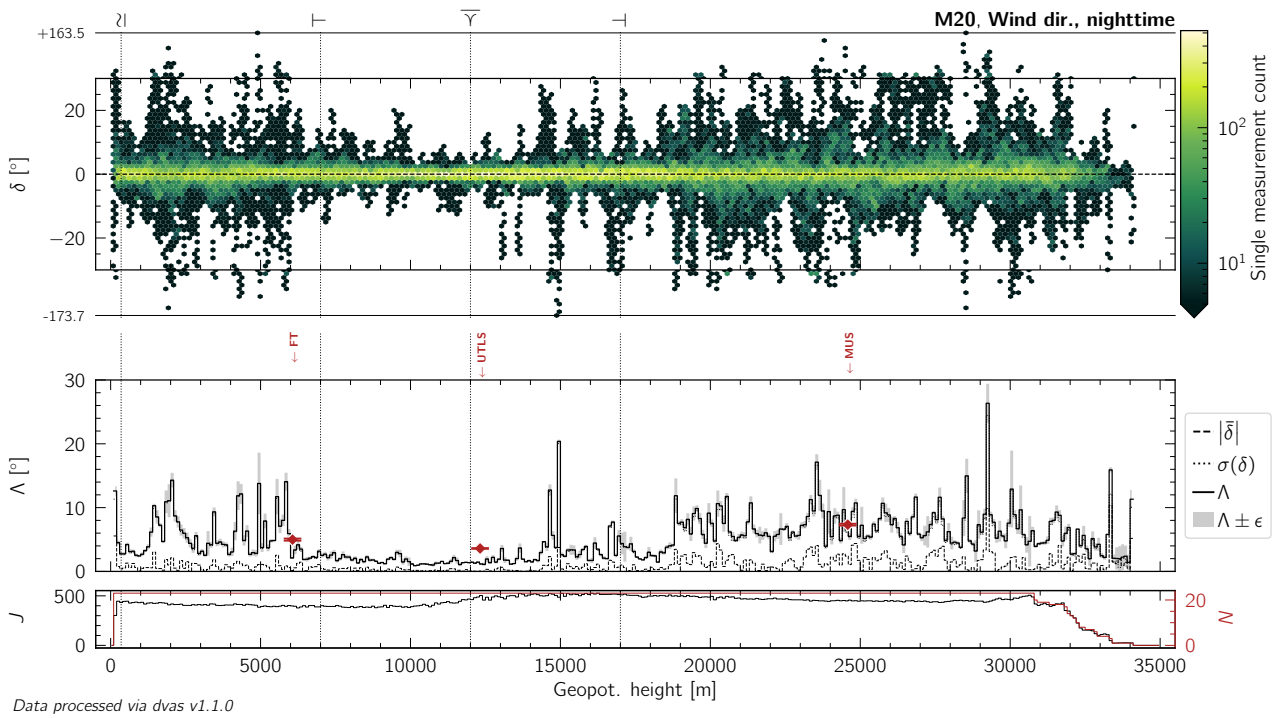


Figure L.94: Same as Figure 10.13, but for nighttime measurements of wind (horizontal) direction by the M20 radiosonde.

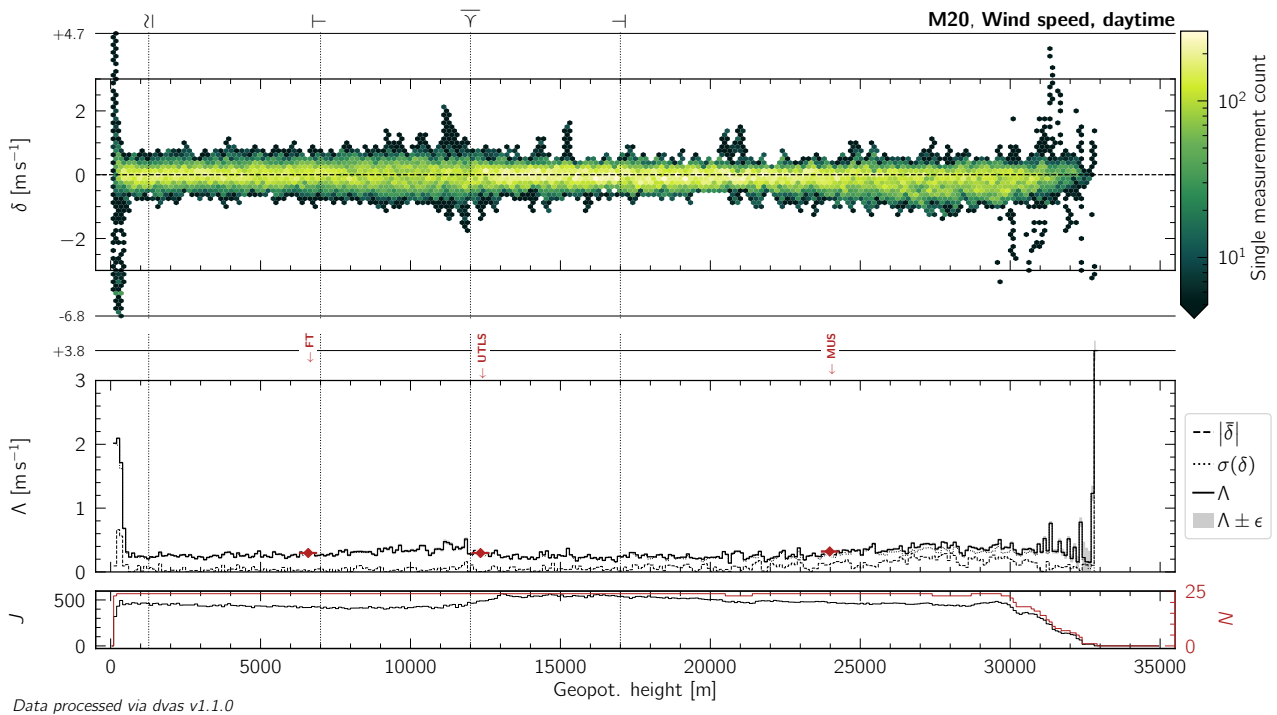


Figure L.95: Same as Figure 10.13, but for daytime measurements of wind (horizontal) speed by the M20 radiosonde.

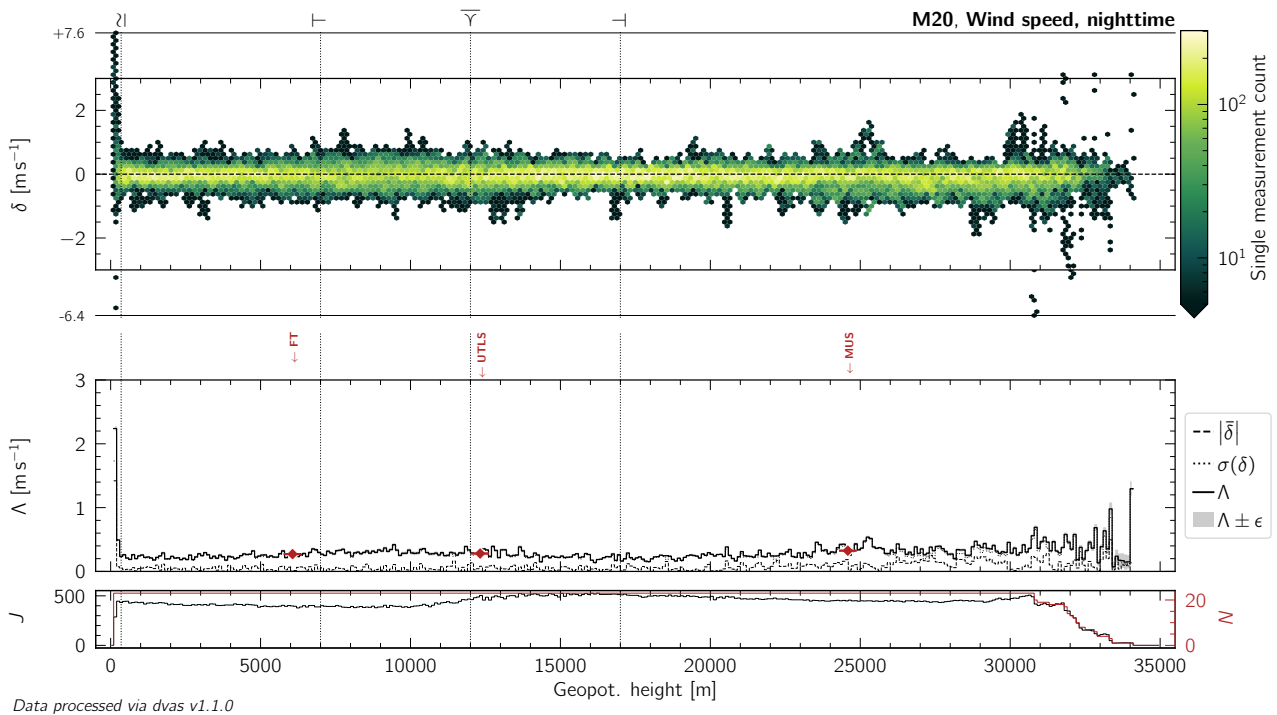


Figure L.96: Same as Figure 10.13, but for nighttime measurements of wind (horizontal) speed by the M20 radiosonde.

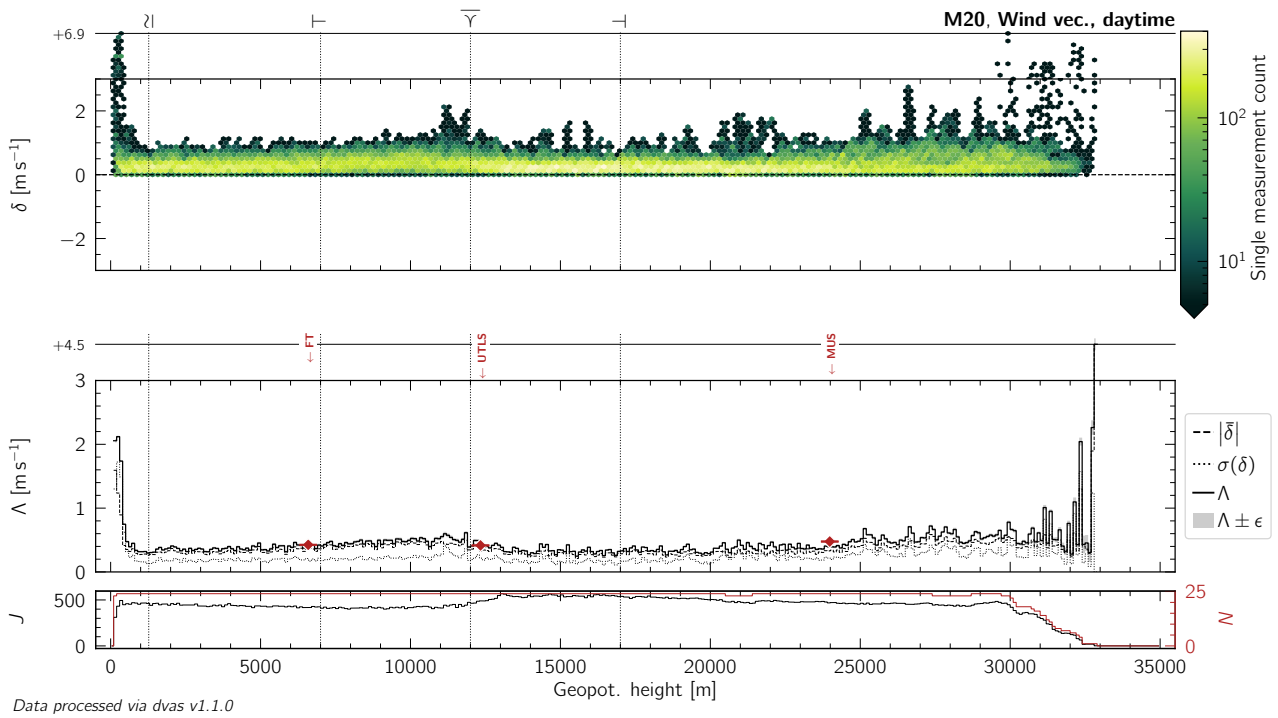


Figure L.97: Same as Figure 10.13, but for daytime measurements of the wind (horizontal) vector by the M20 radiosonde.

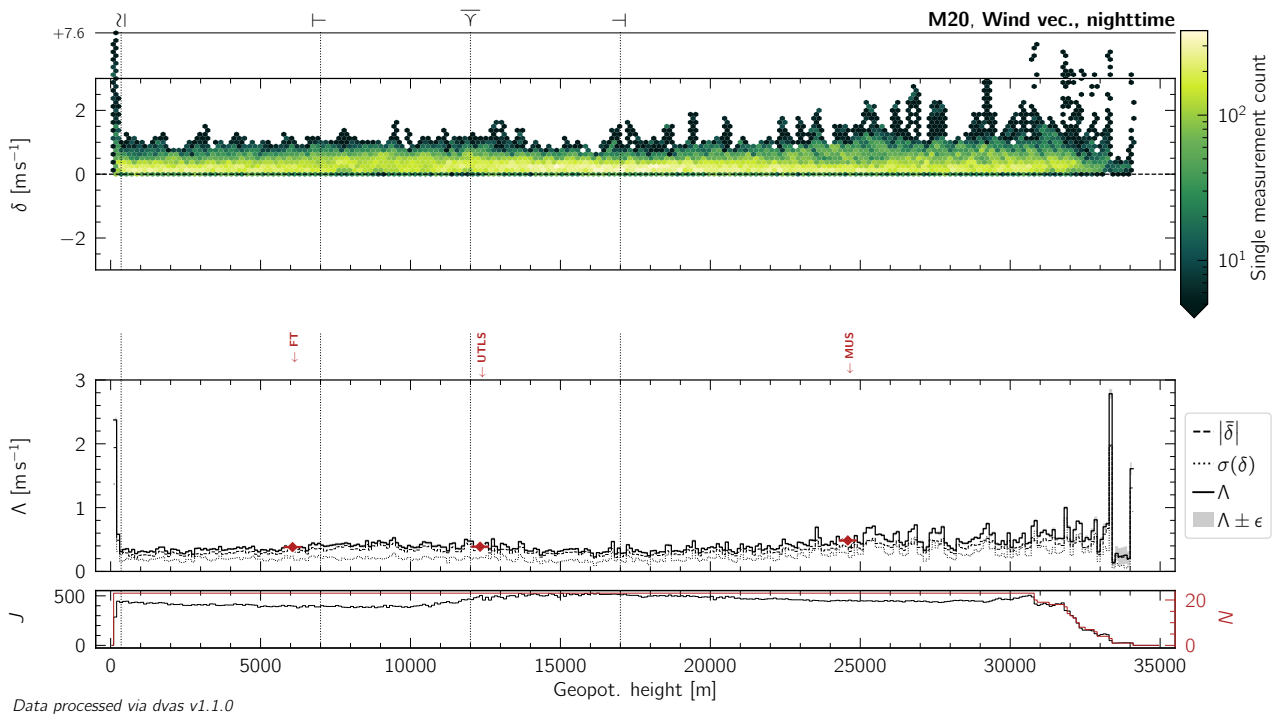


Figure L.98: Same as Figure 10.13, but for nighttime measurements of the wind (horizontal) vector by the M20 radiosonde.

L.8 PS-B3

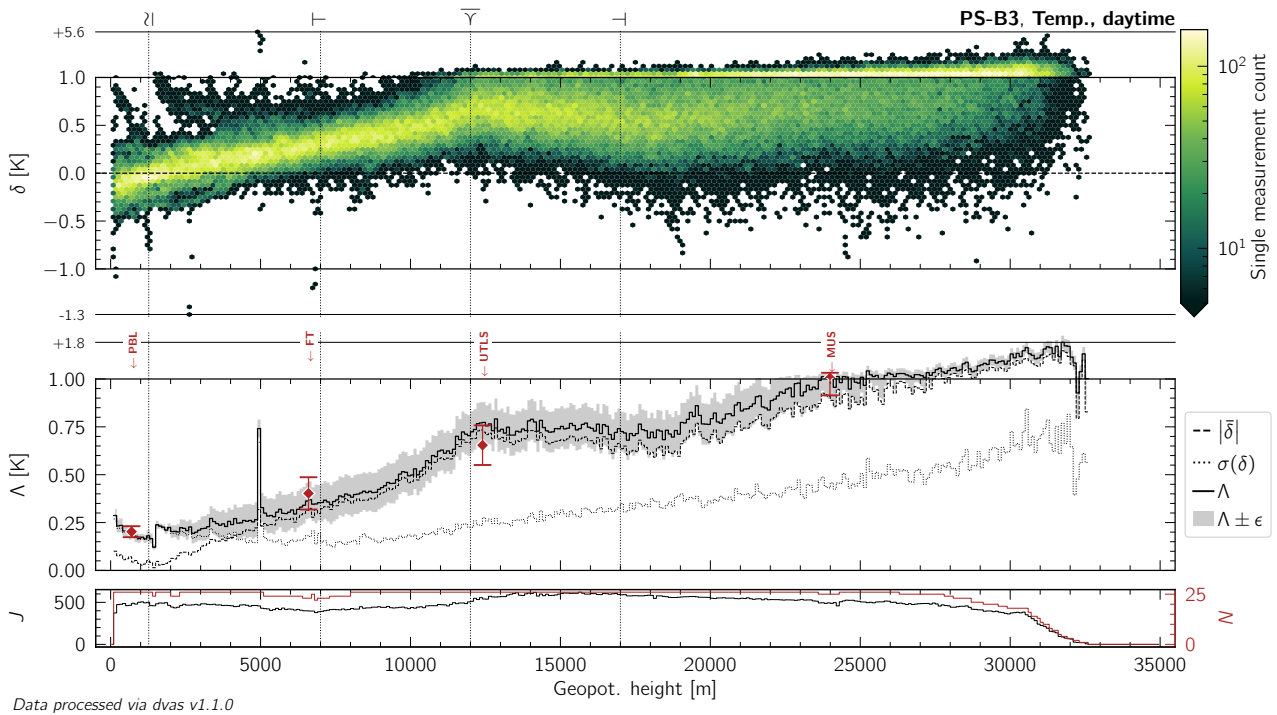


Figure L.99: Same as Figure 10.13, but for daytime measurements of atmospheric temperature by the PS-B3 radiosonde.

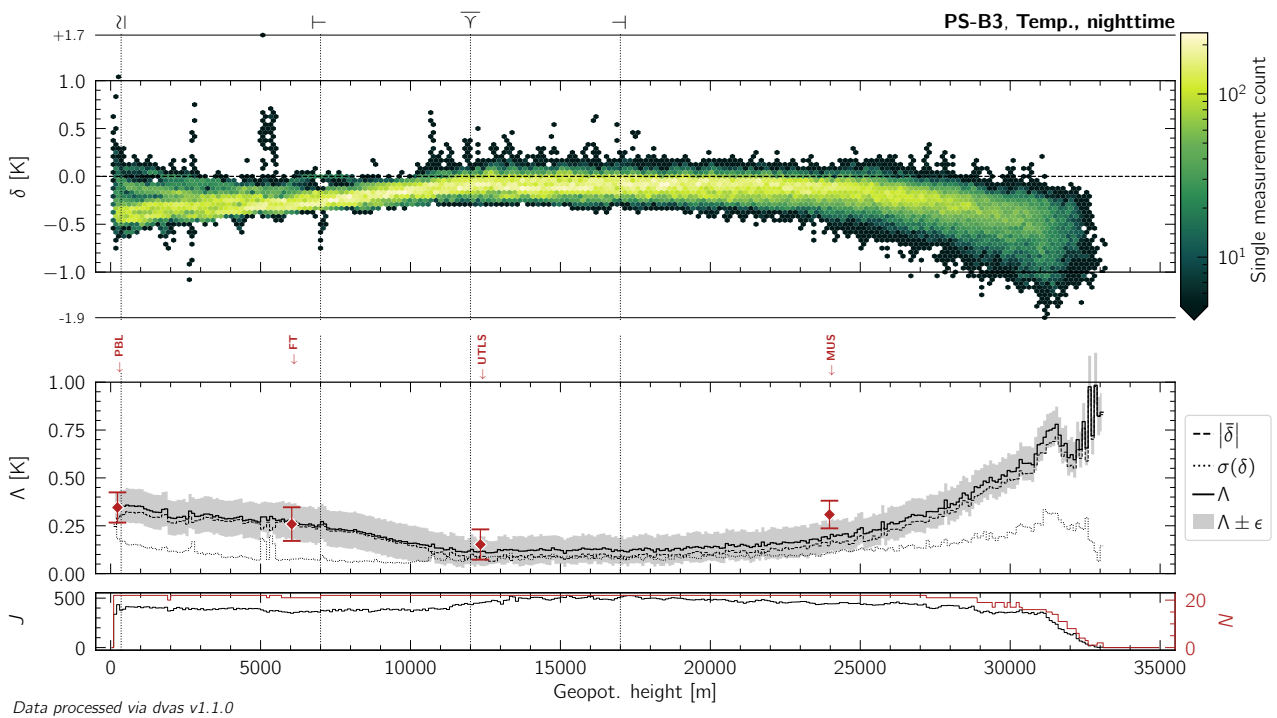


Figure L.100: Same as Figure 10.13, but for nighttime measurements of atmospheric temperature by the PS-B3 radiosonde.

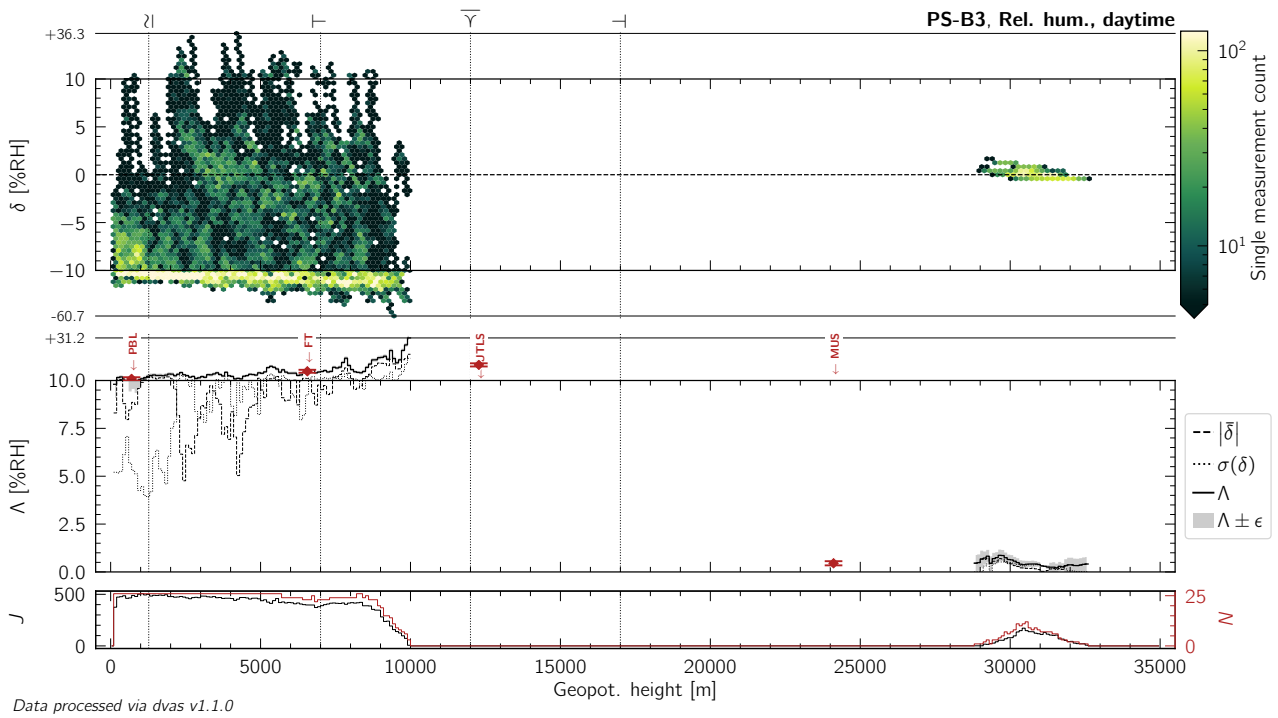


Figure L.101: Same as Figure 10.13, but for daytime measurements of relative humidity by the PS-B3 radiosonde.

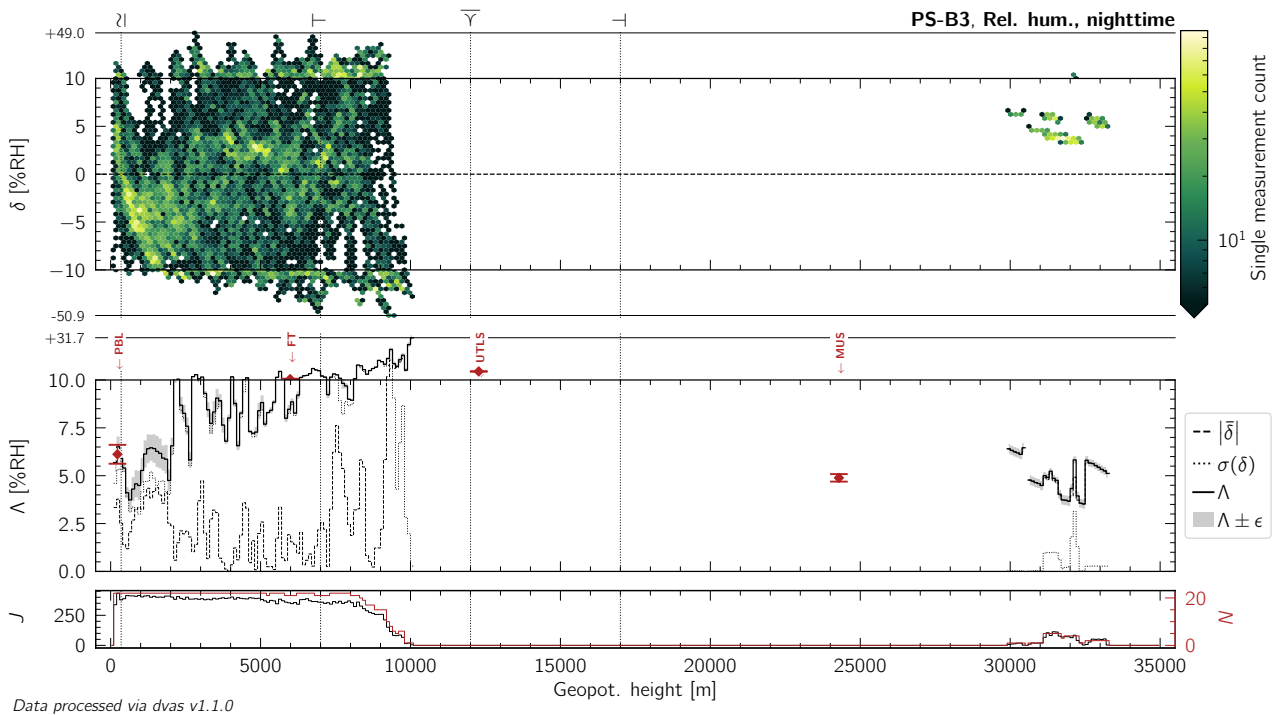


Figure L.102: Same as Figure 10.13, but for nighttime measurements of relative humidity by the PS-B3 radiosonde.

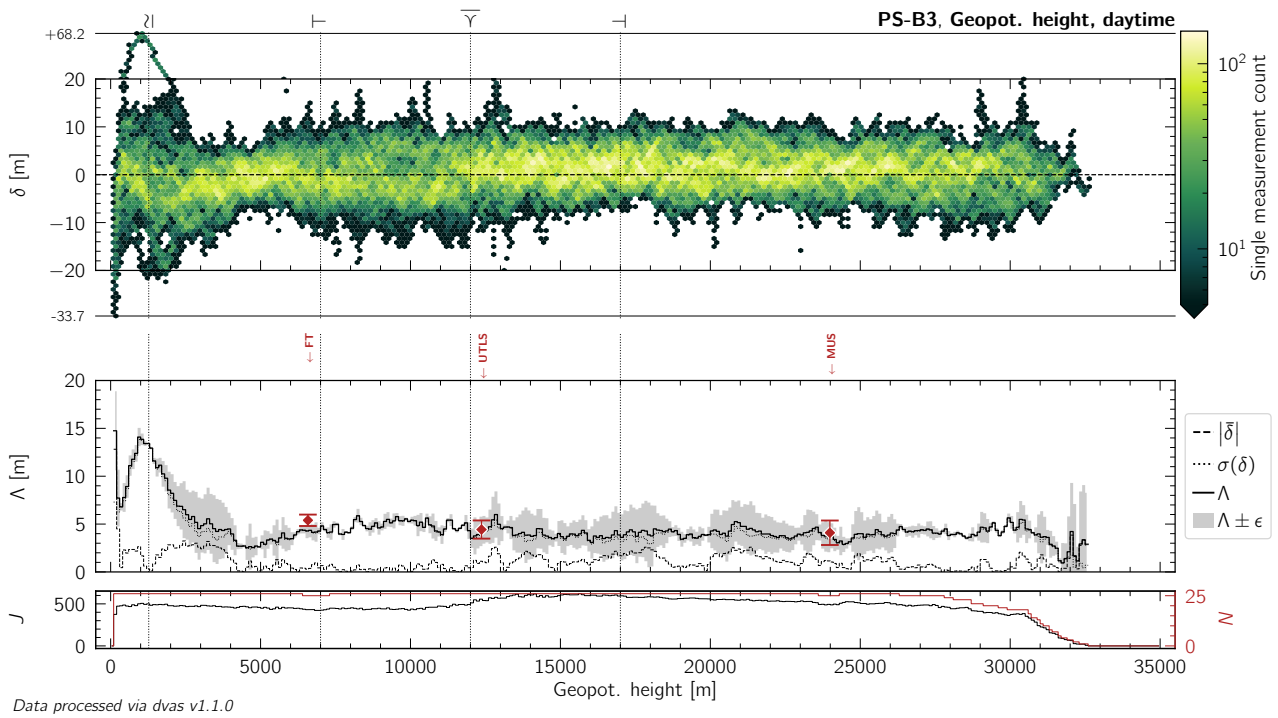


Figure L.103: Same as Figure 10.13, but for daytime measurements of geopotential height by the PS-B3 radiosonde.

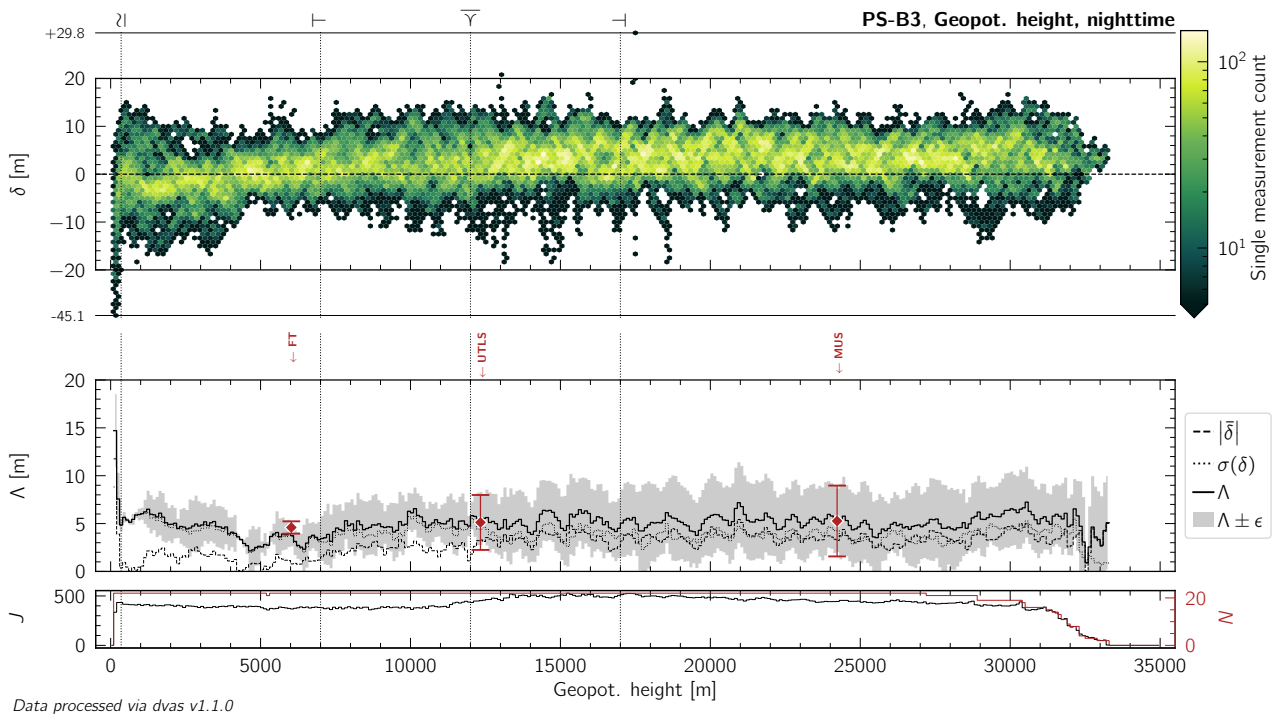


Figure L.104: Same as Figure 10.13, but for nighttime measurements of geopotential height by the PS-B3 radiosonde.

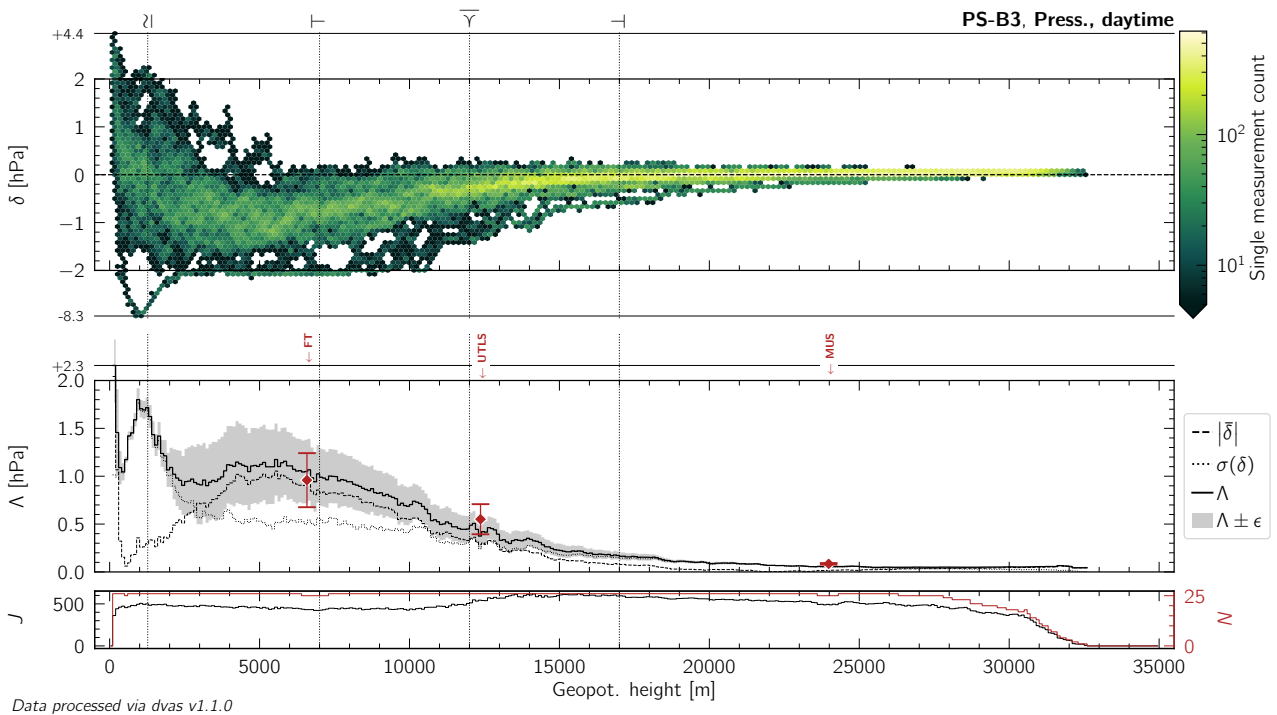


Figure L.105: Same as Figure 10.13, but for daytime measurements of atmospheric pressure by the PS-B3 radiosonde.

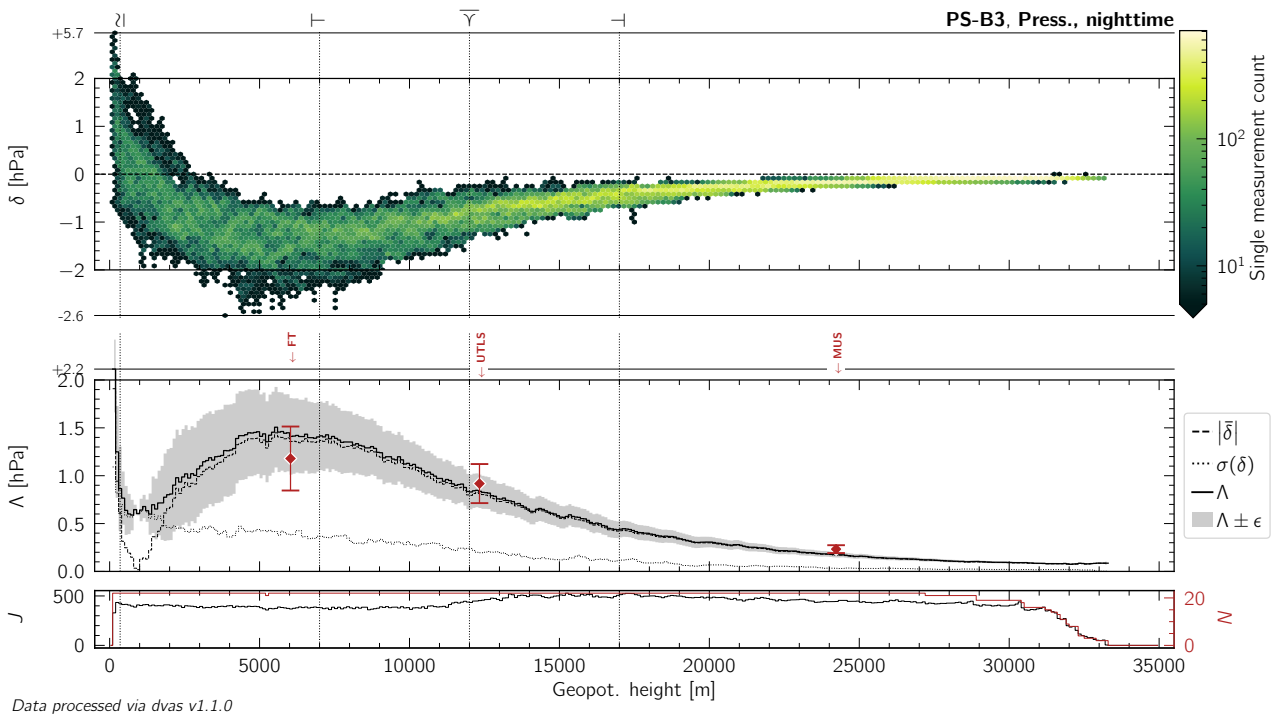


Figure L.106: Same as Figure 10.13, but for nighttime measurements of atmospheric pressure by the PS-B3 radiosonde.

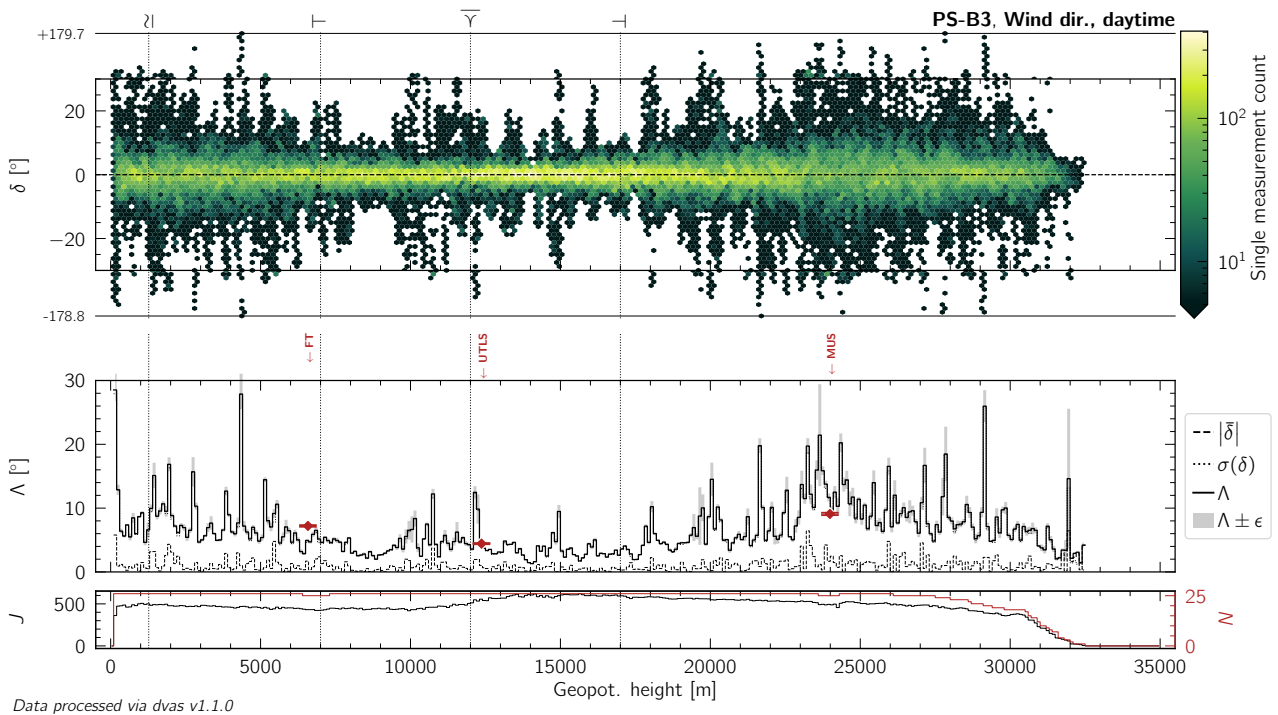


Figure L.107: Same as Figure 10.13, but for daytime measurements of wind (horizontal) direction by the PS-B3 radiosonde.

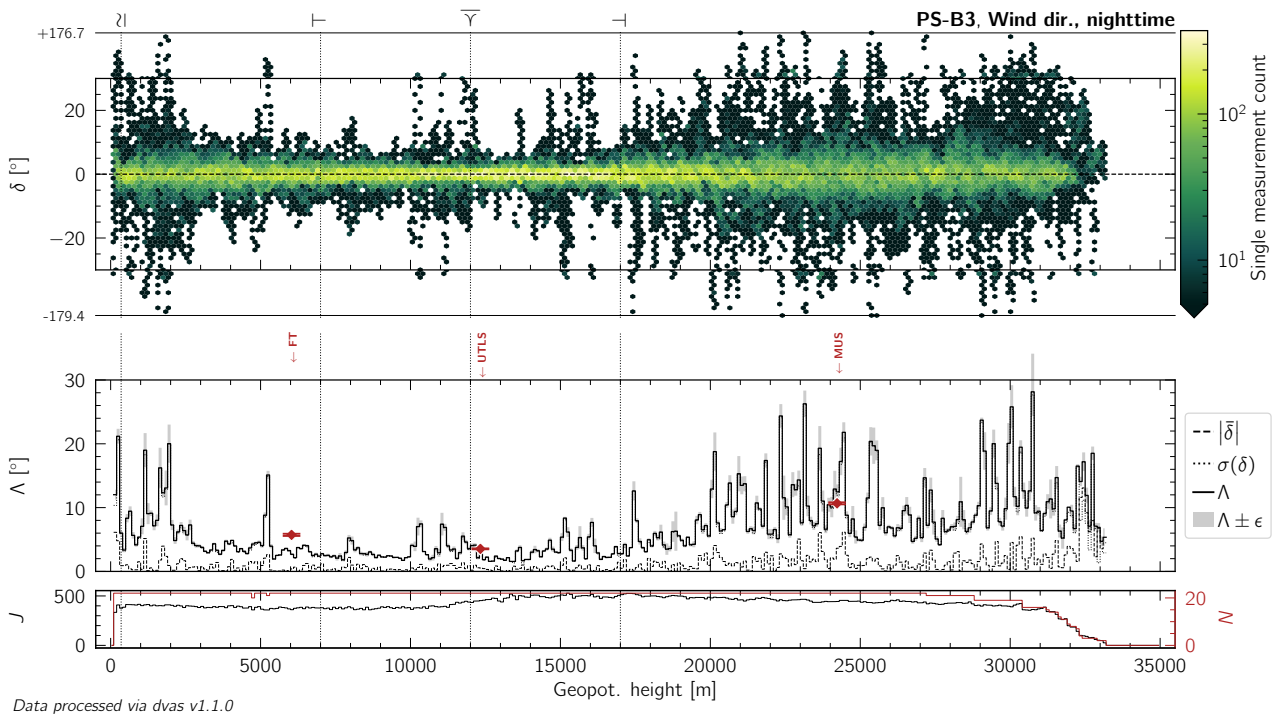


Figure L.108: Same as Figure 10.13, but for nighttime measurements of wind (horizontal) direction by the PS-B3 radiosonde.

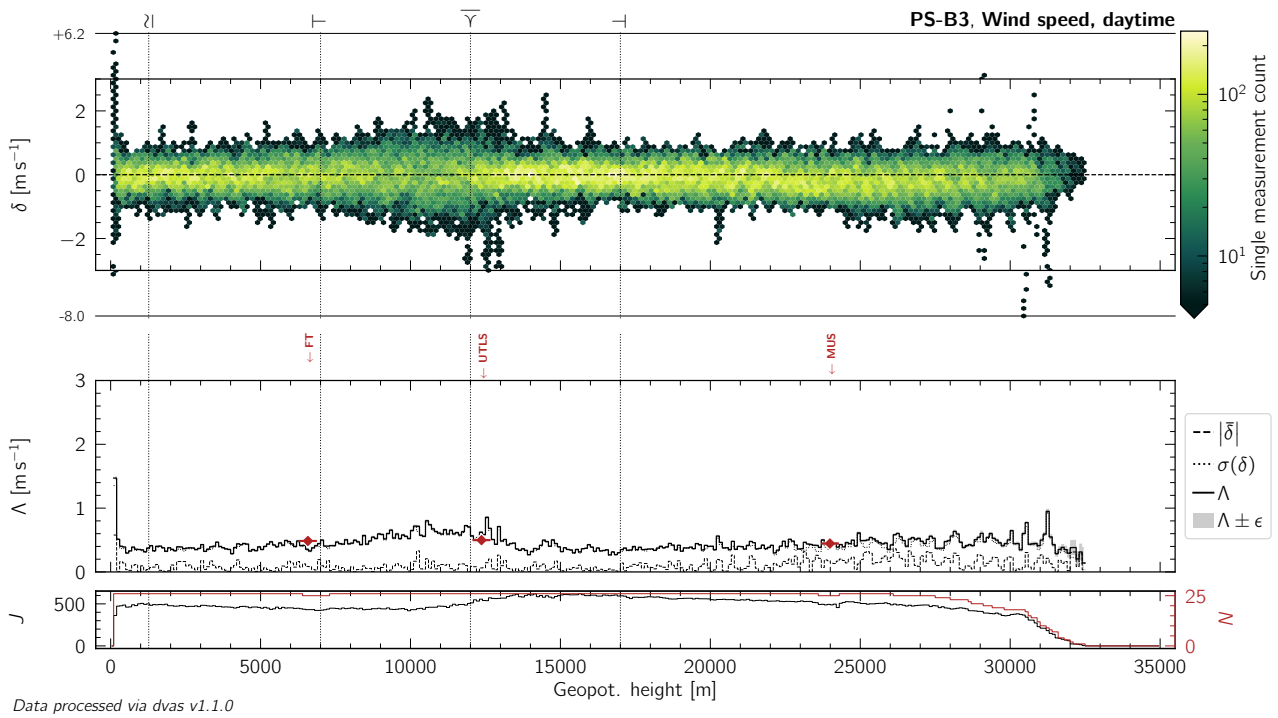


Figure L.109: Same as Figure 10.13, but for daytime measurements of wind (horizontal) speed by the PS-B3 radiosonde.

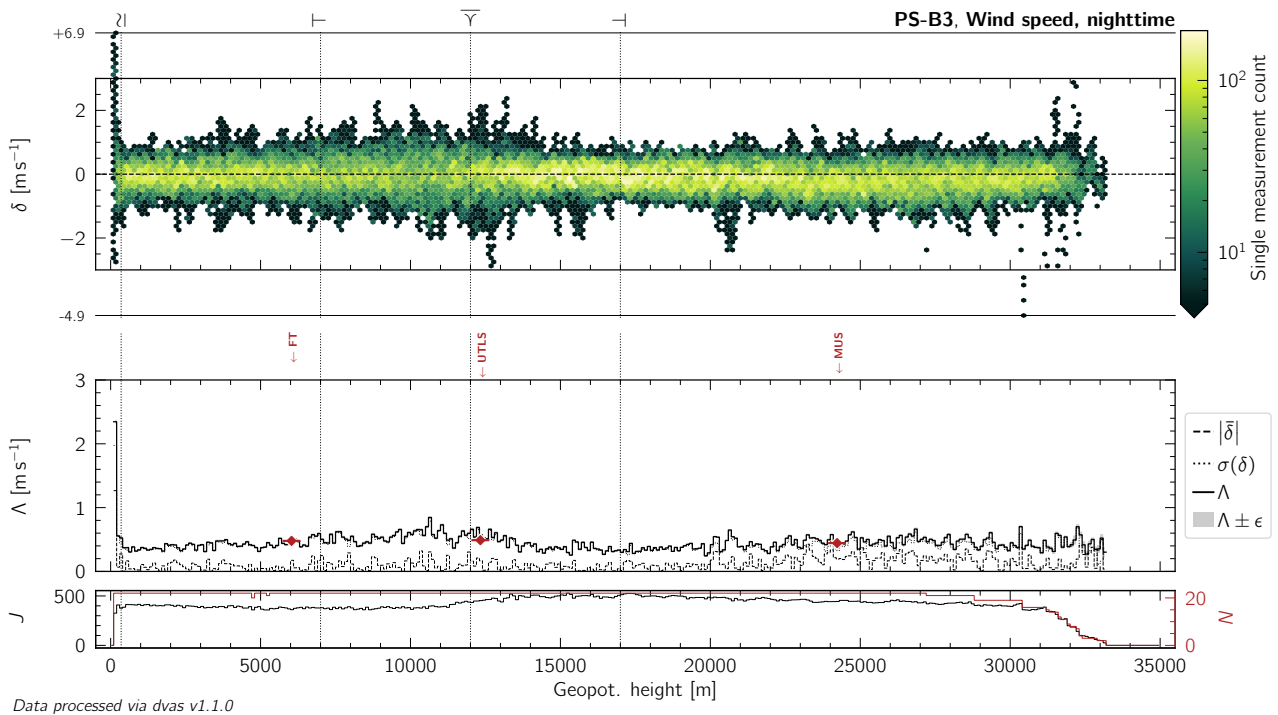


Figure L.110: Same as Figure 10.13, but for nighttime measurements of wind (horizontal) speed by the PS-B3 radiosonde.

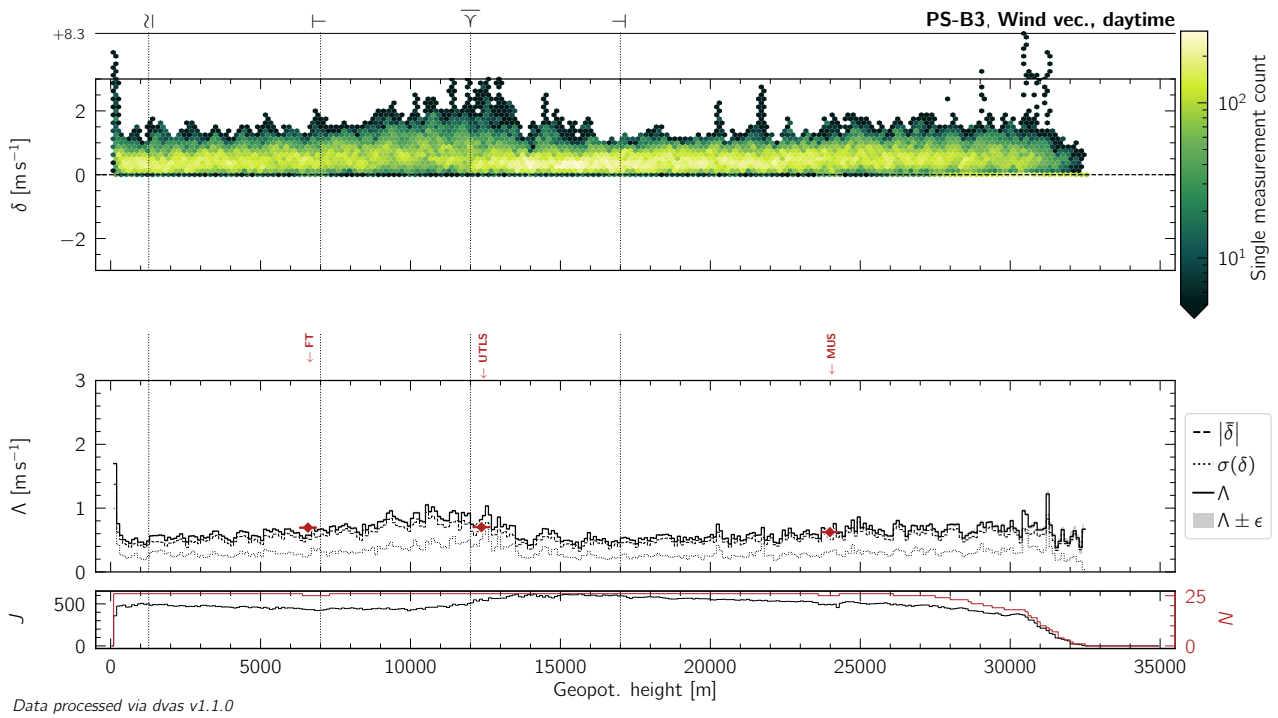


Figure L.111: Same as Figure 10.13, but for daytime measurements of the wind (horizontal) vector by the PS-B3 radiosonde.

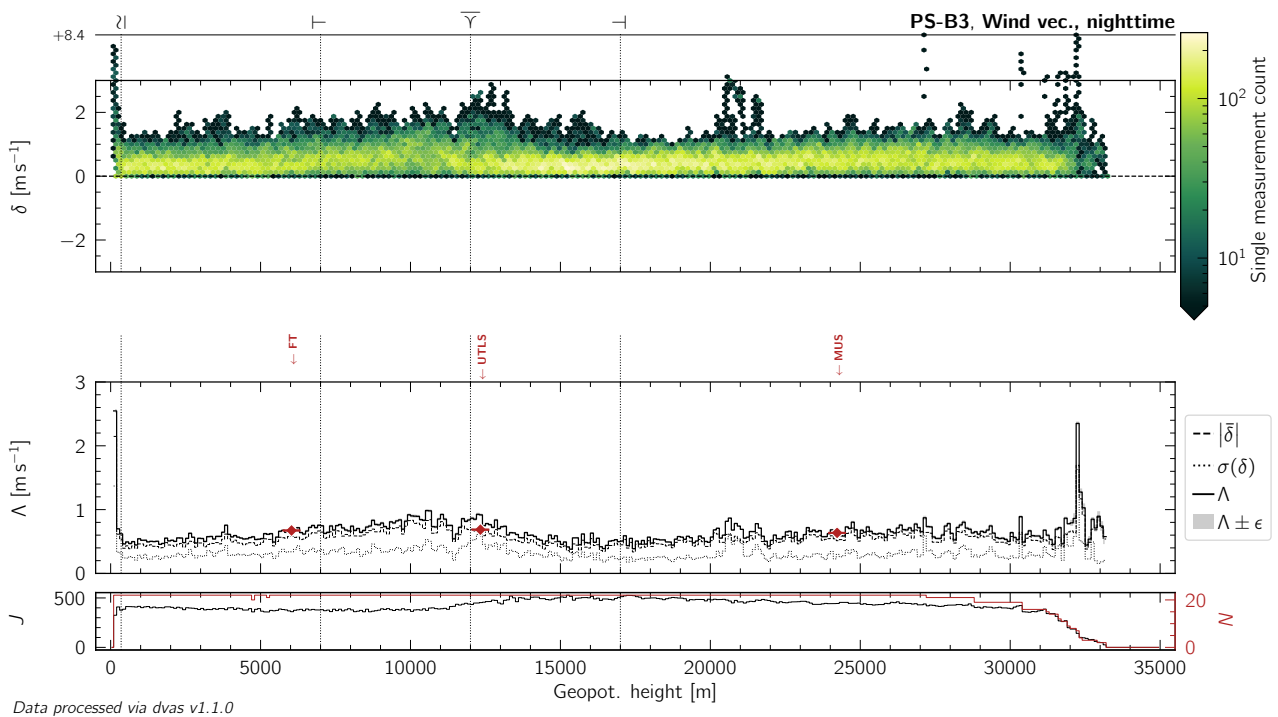


Figure L.112: Same as Figure 10.13, but for nighttime measurements of the wind (horizontal) vector by the PS-B3 radiosonde.

L.9 RS41

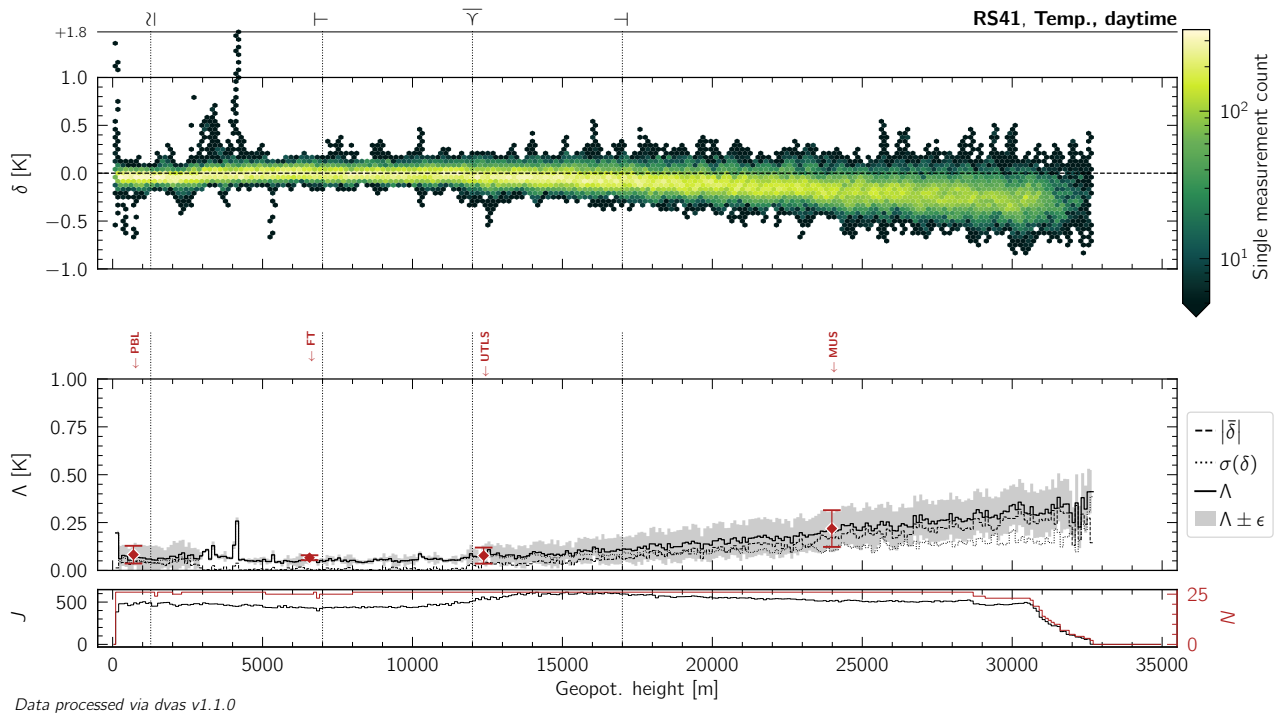


Figure L.113: Same as Figure 10.13, but for daytime measurements of atmospheric temperature by the RS41 radiosonde.

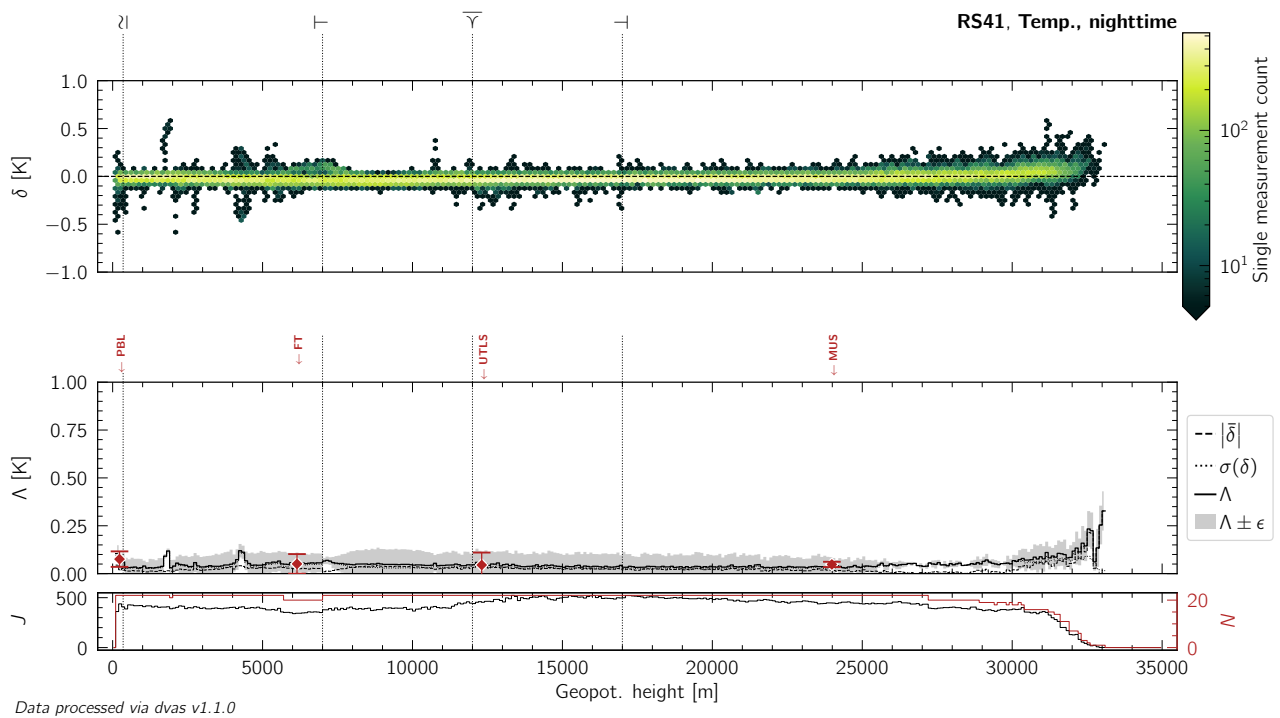


Figure L.114: Same as Figure 10.13, but for nighttime measurements of atmospheric temperature by the RS41 radiosonde.

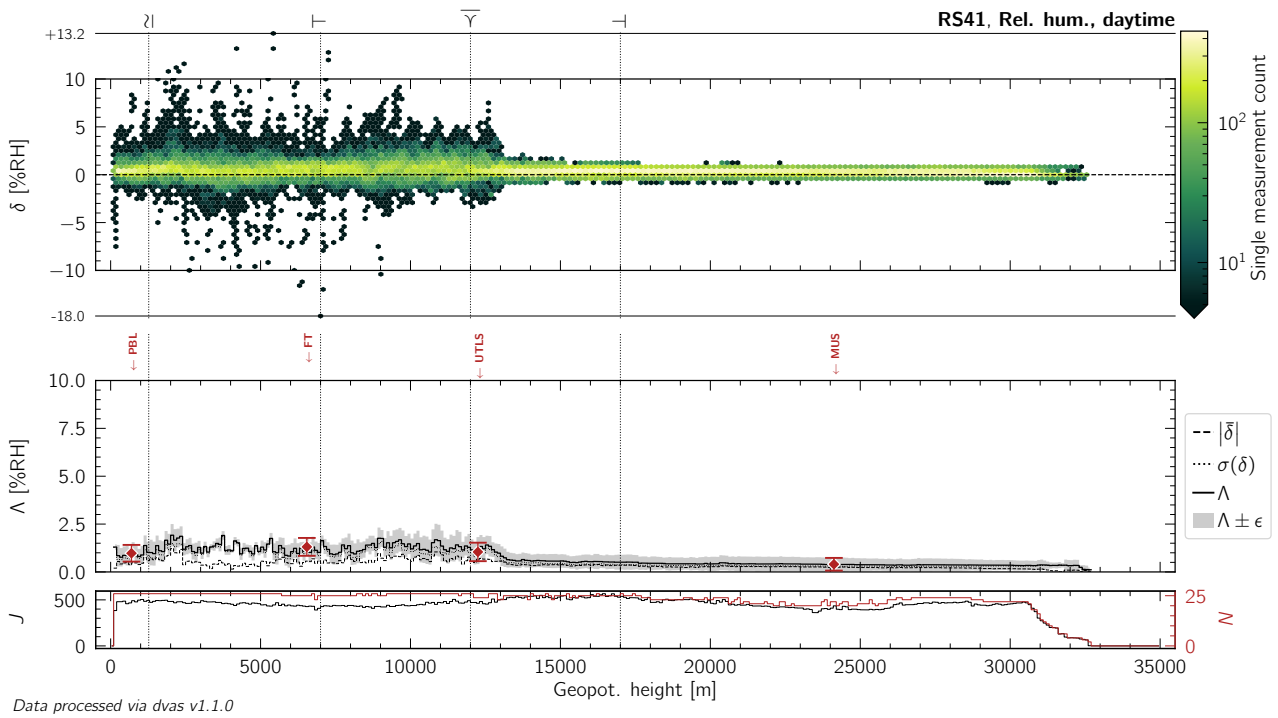


Figure L.115: Same as Figure 10.13, but for daytime measurements of relative humidity by the RS41 radiosonde.

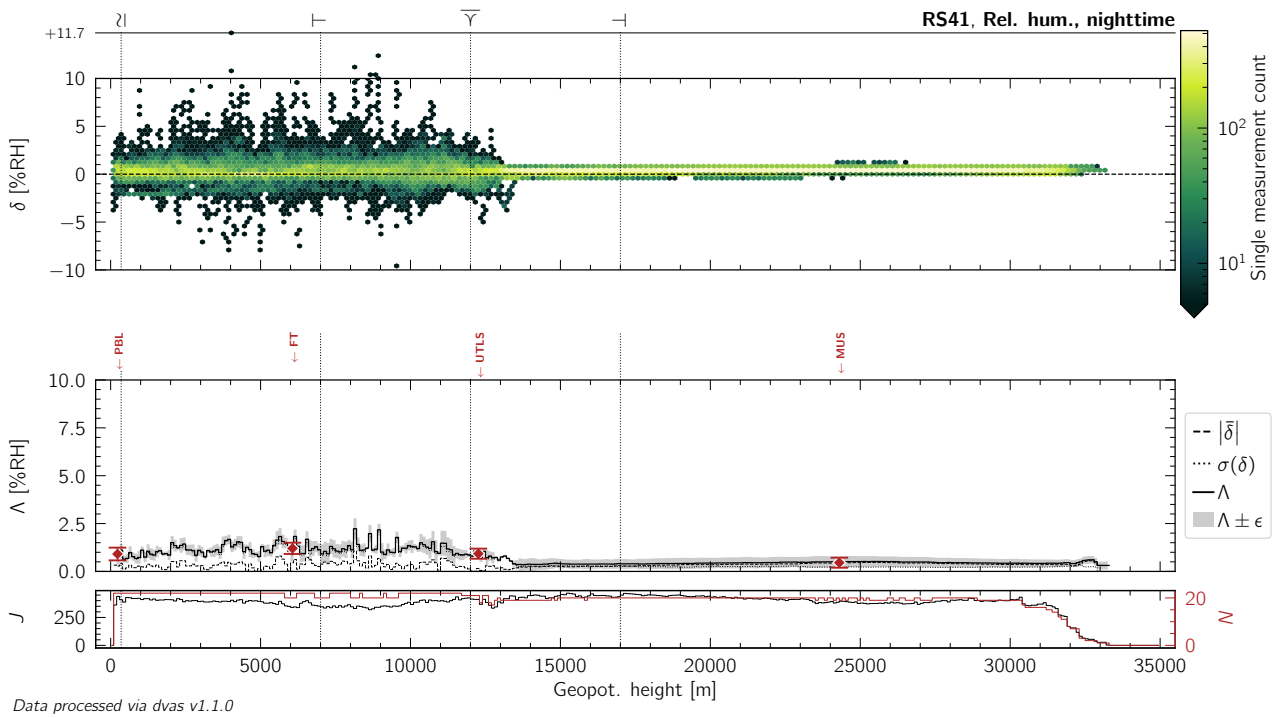


Figure L.116: Same as Figure 10.13, but for nighttime measurements of relative humidity by the RS41 radiosonde.

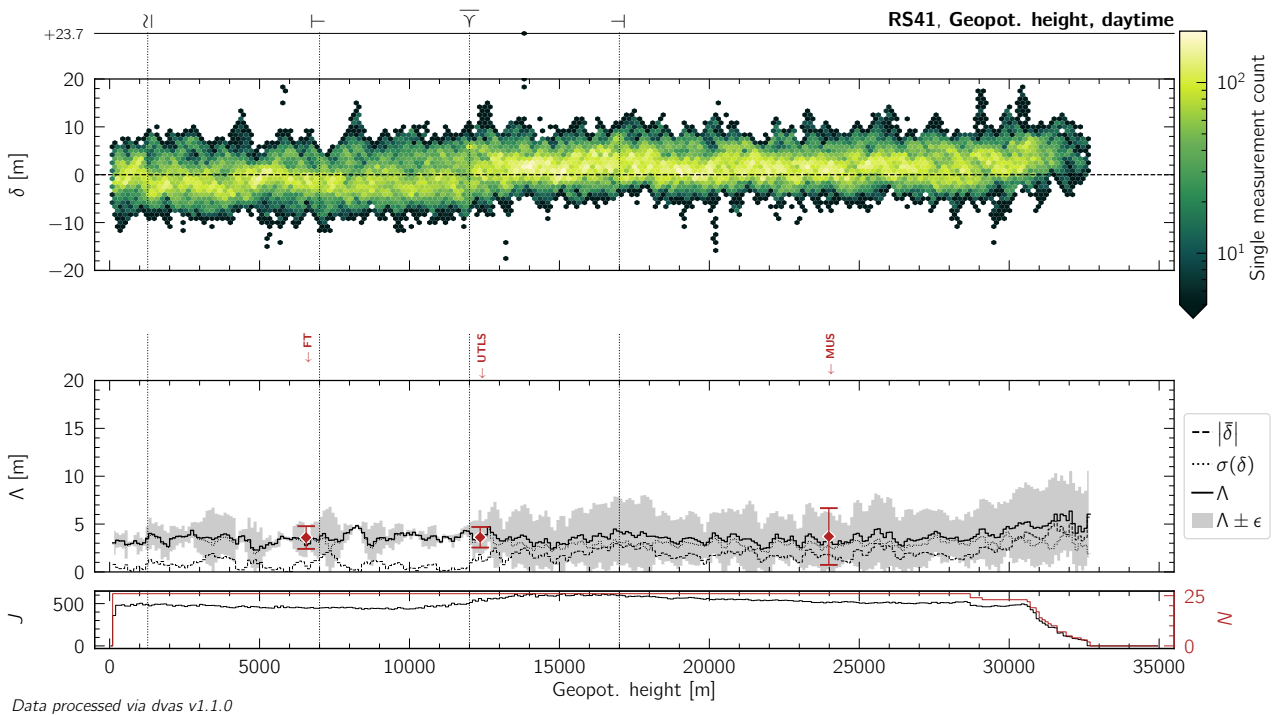


Figure L.117: Same as Figure 10.13, but for daytime measurements of geopotential height by the RS41 radiosonde.

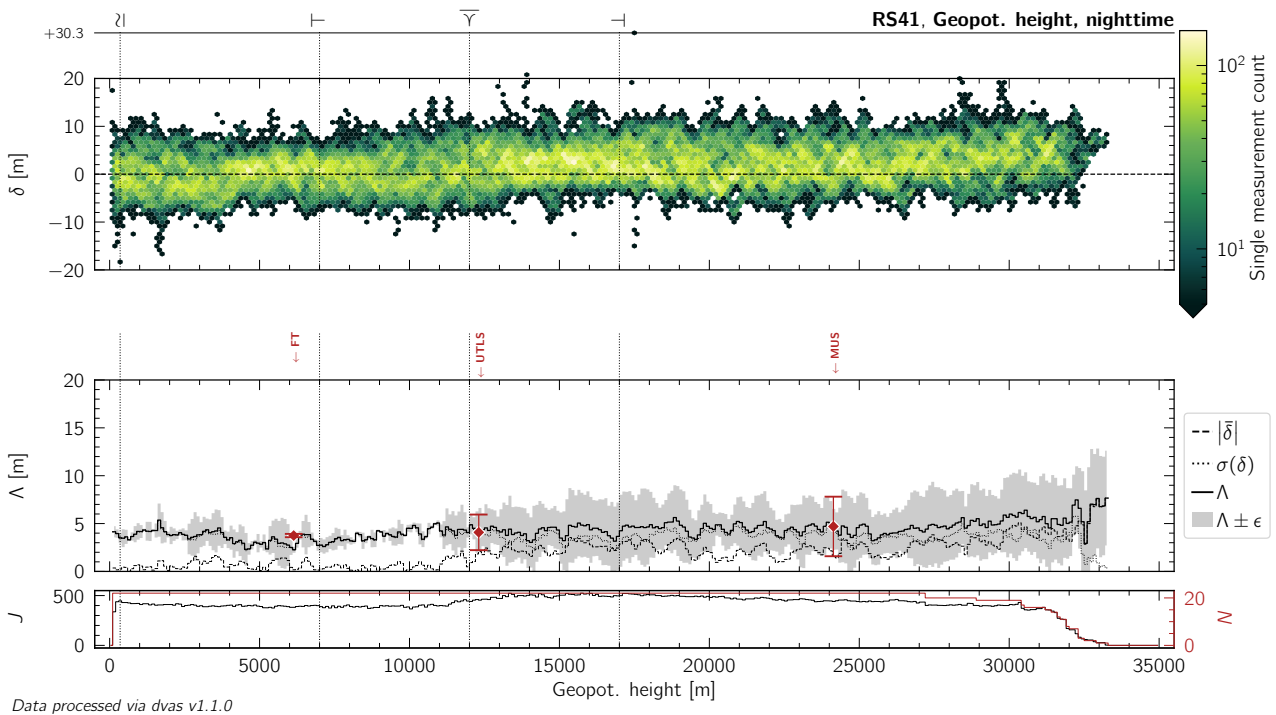


Figure L.118: Same as Figure 10.13, but for nighttime measurements of geopotential height by the RS41 radiosonde.

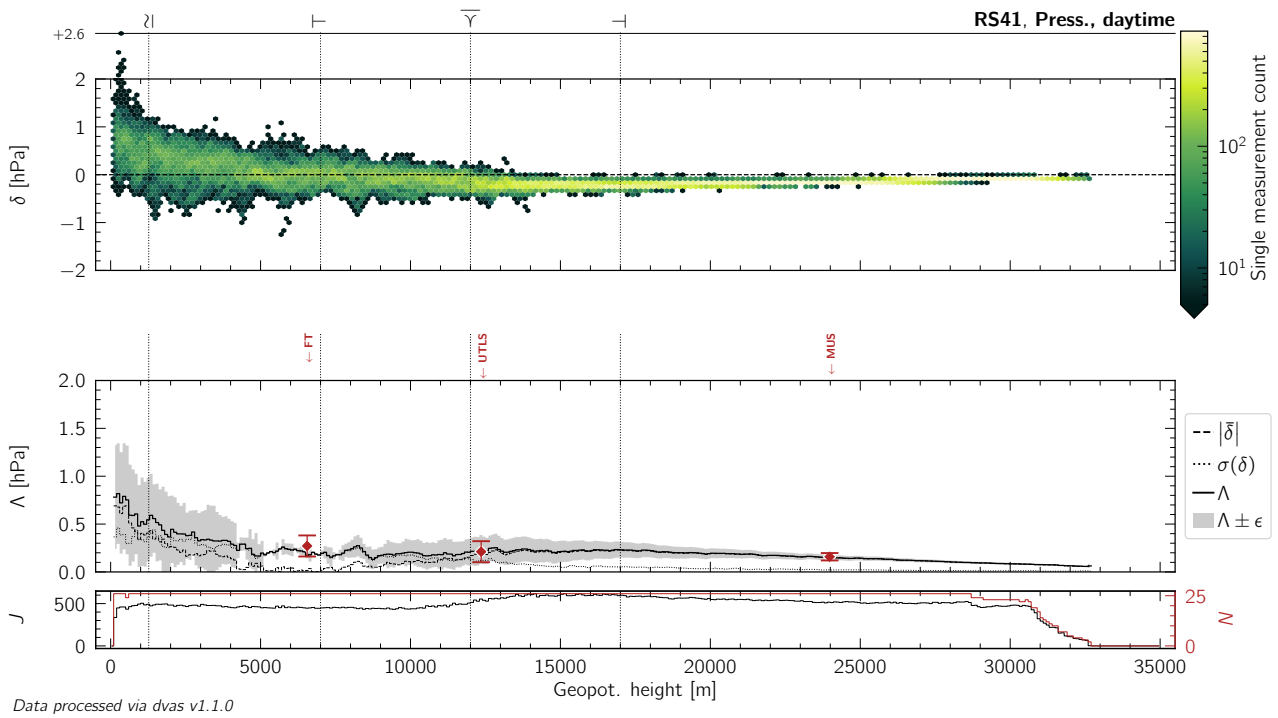


Figure L.119: Same as Figure 10.13, but for daytime measurements of atmospheric pressure by the RS41 radiosonde.

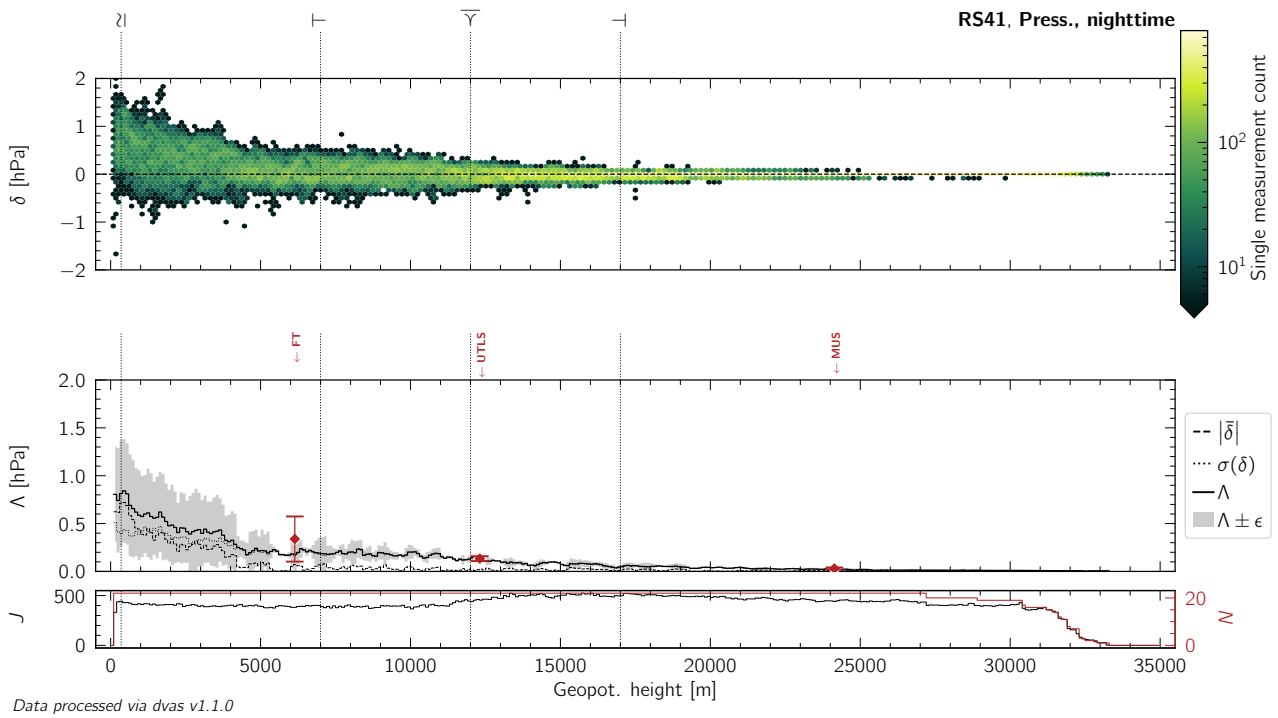


Figure L.120: Same as Figure 10.13, but for nighttime measurements of atmospheric pressure by the RS41 radiosonde.

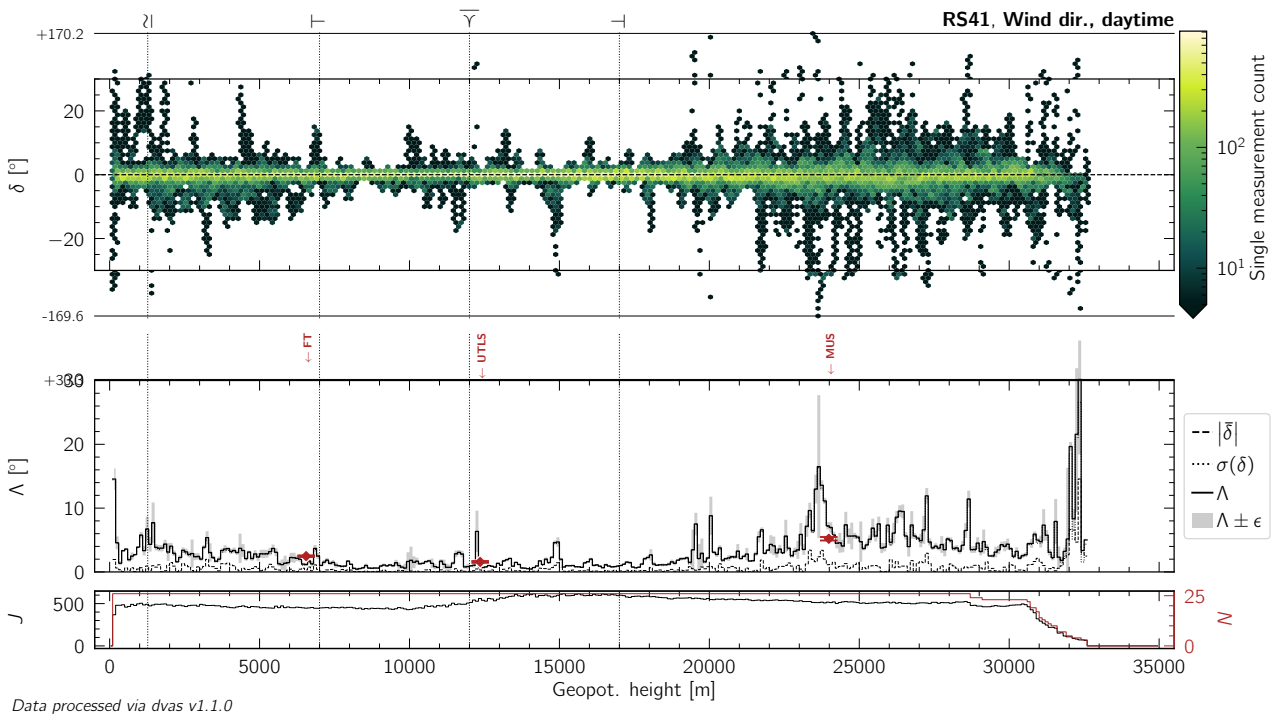


Figure L.121: Same as Figure 10.13, but for daytime measurements of wind (horizontal) direction by the RS41 radiosonde.

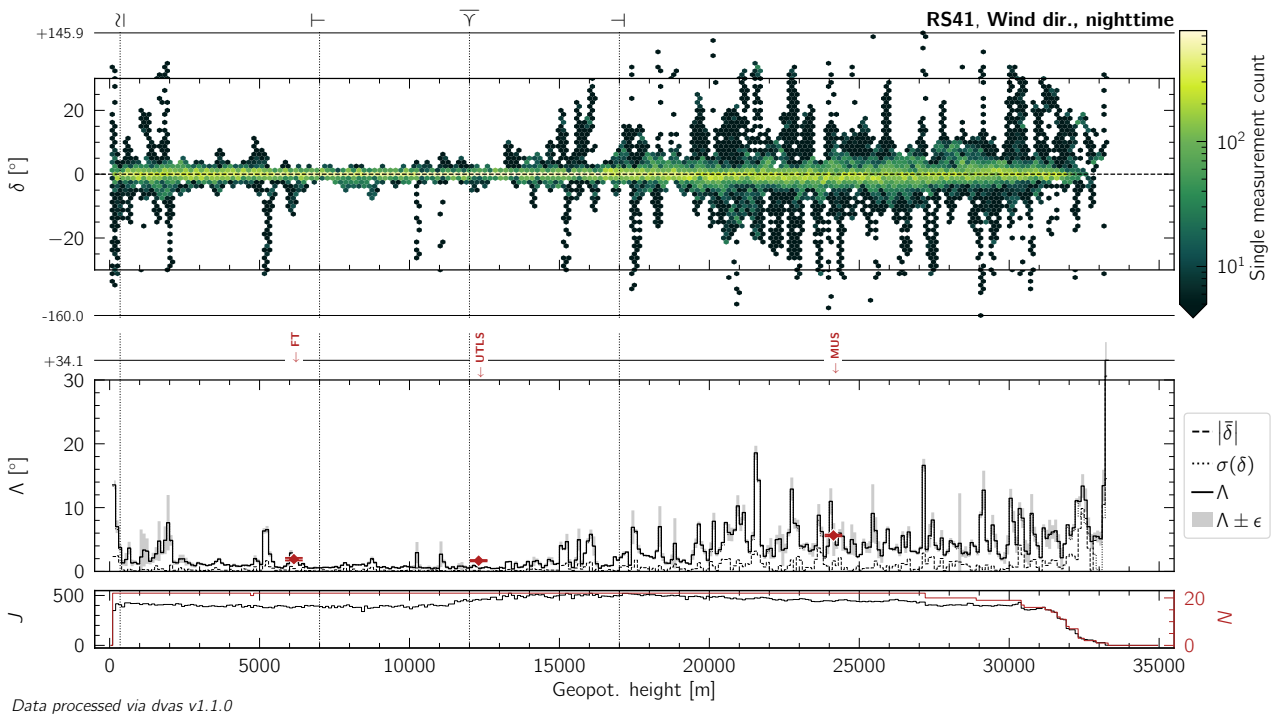


Figure L.122: Same as Figure 10.13, but for nighttime measurements of wind (horizontal) direction by the RS41 radiosonde.

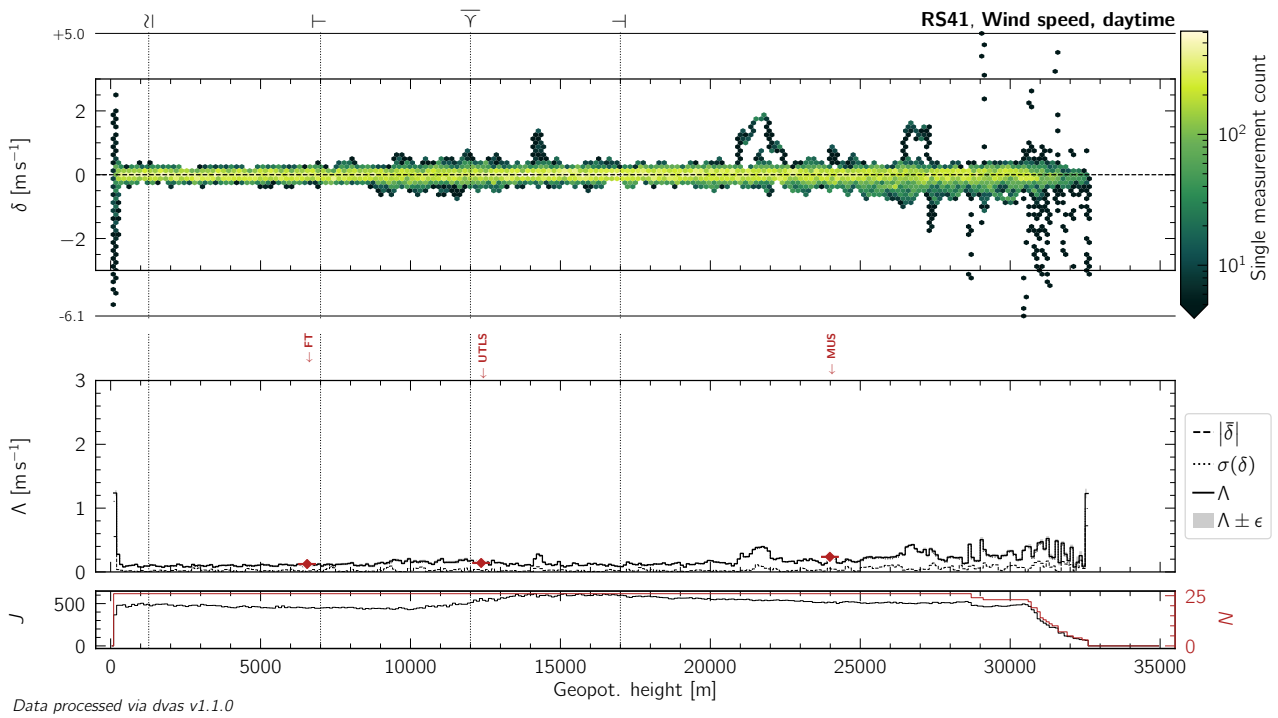


Figure L.123: Same as Figure 10.13, but for daytime measurements of wind (horizontal) speed by the RS41 radiosonde.

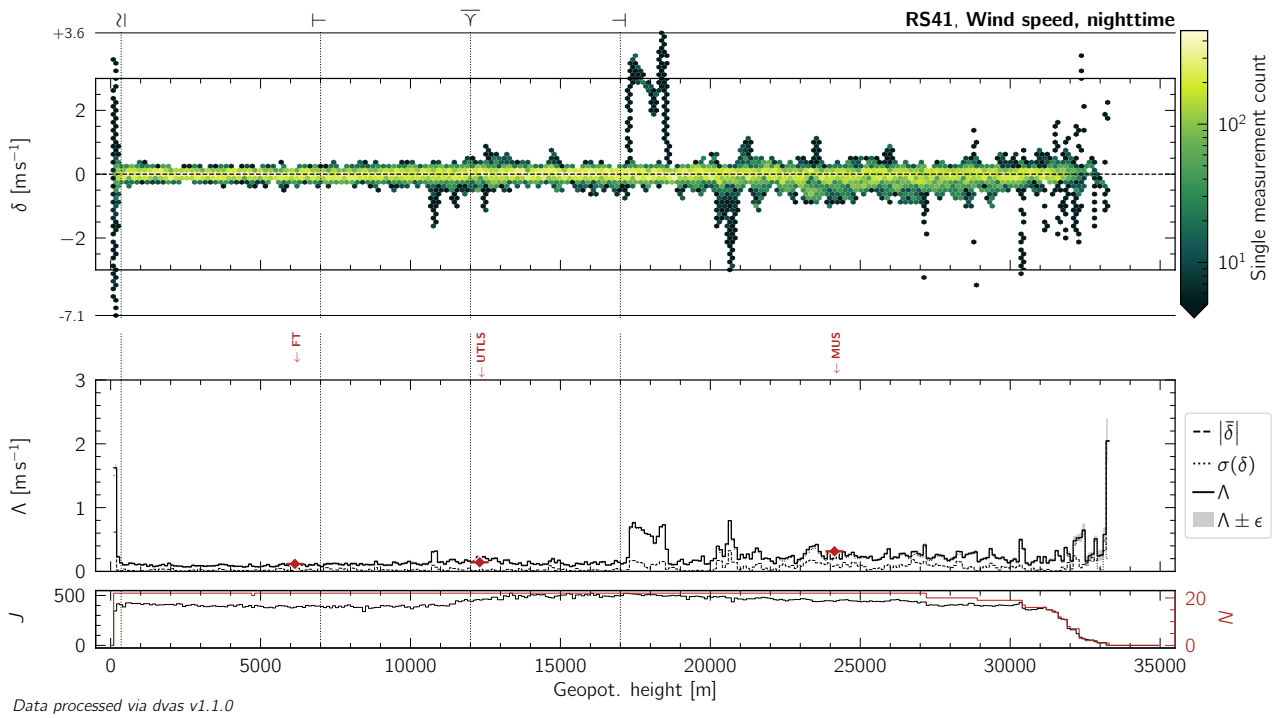


Figure L.124: Same as Figure 10.13, but for nighttime measurements of wind (horizontal) speed by the RS41 radiosonde.

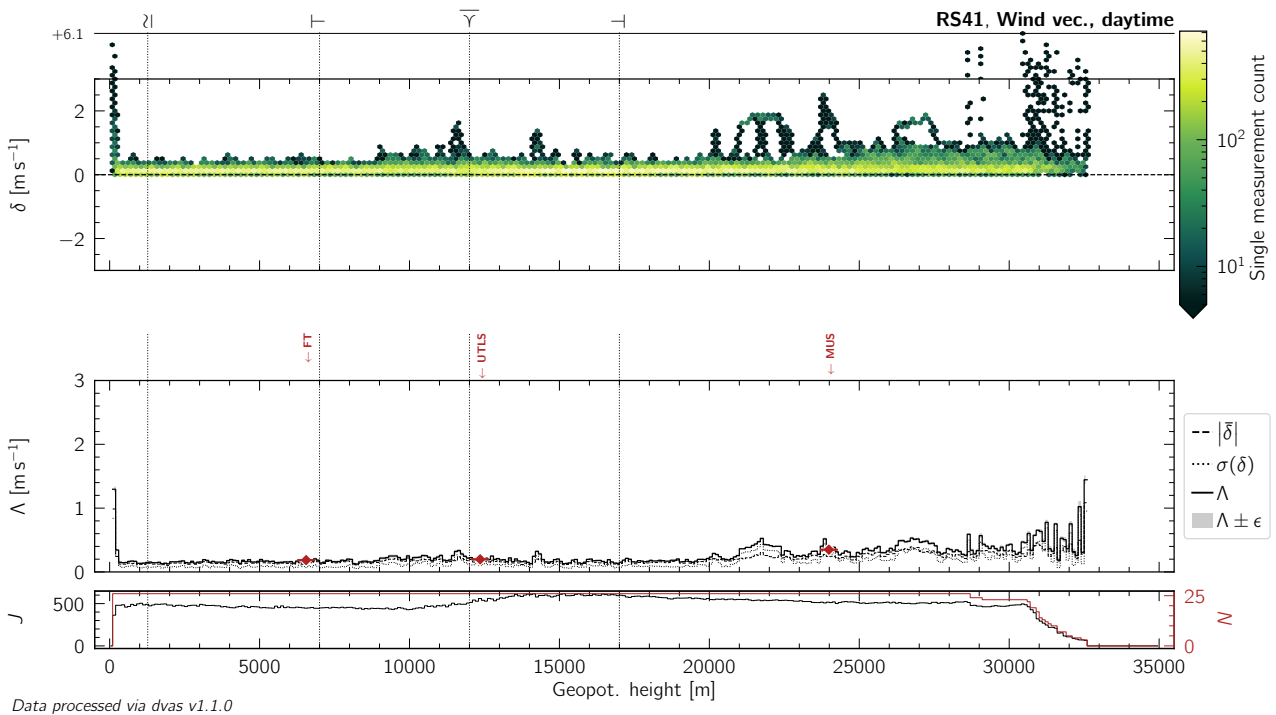


Figure L.125: Same as Figure 10.13, but for daytime measurements of the wind (horizontal) vector by the RS41 radiosonde.

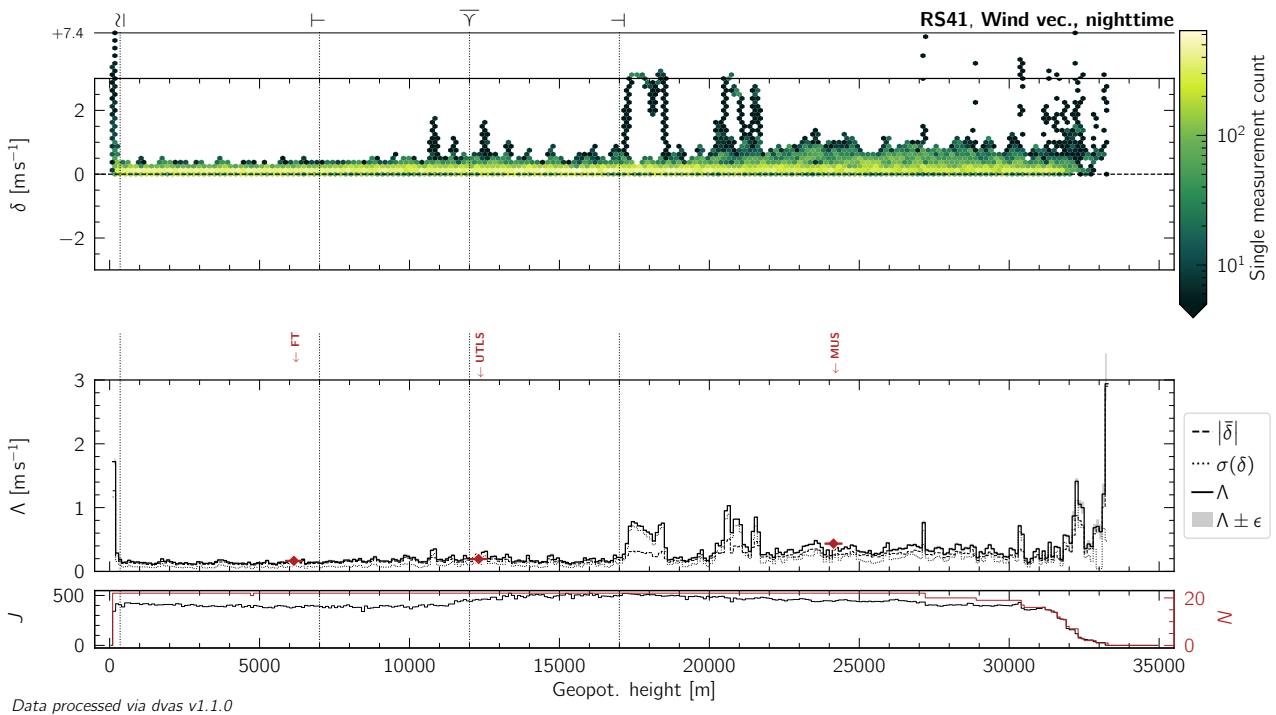


Figure L.126: Same as Figure 10.13, but for nighttime measurements of the wind (horizontal) vector by the RS41 radiosonde.

L.10 WXR-301D

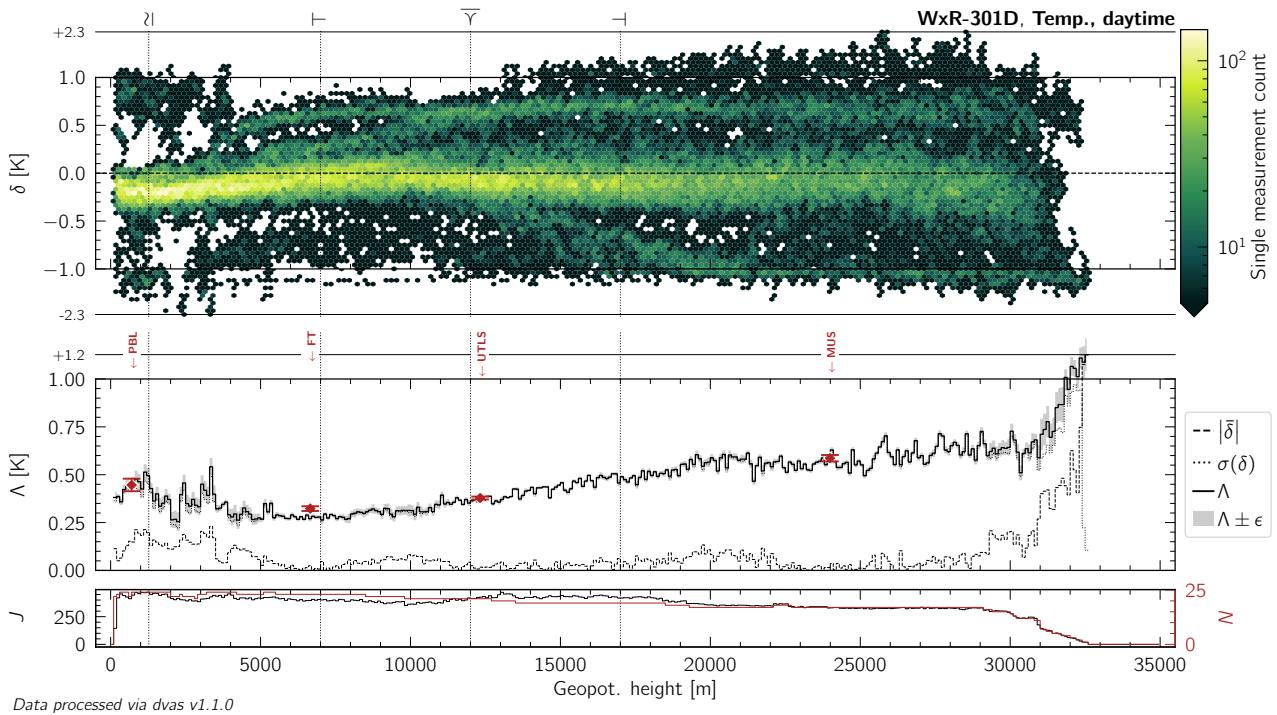


Figure L.127: Same as Figure 10.13, but for daytime measurements of atmospheric temperature by the WxR-301D radiosonde.

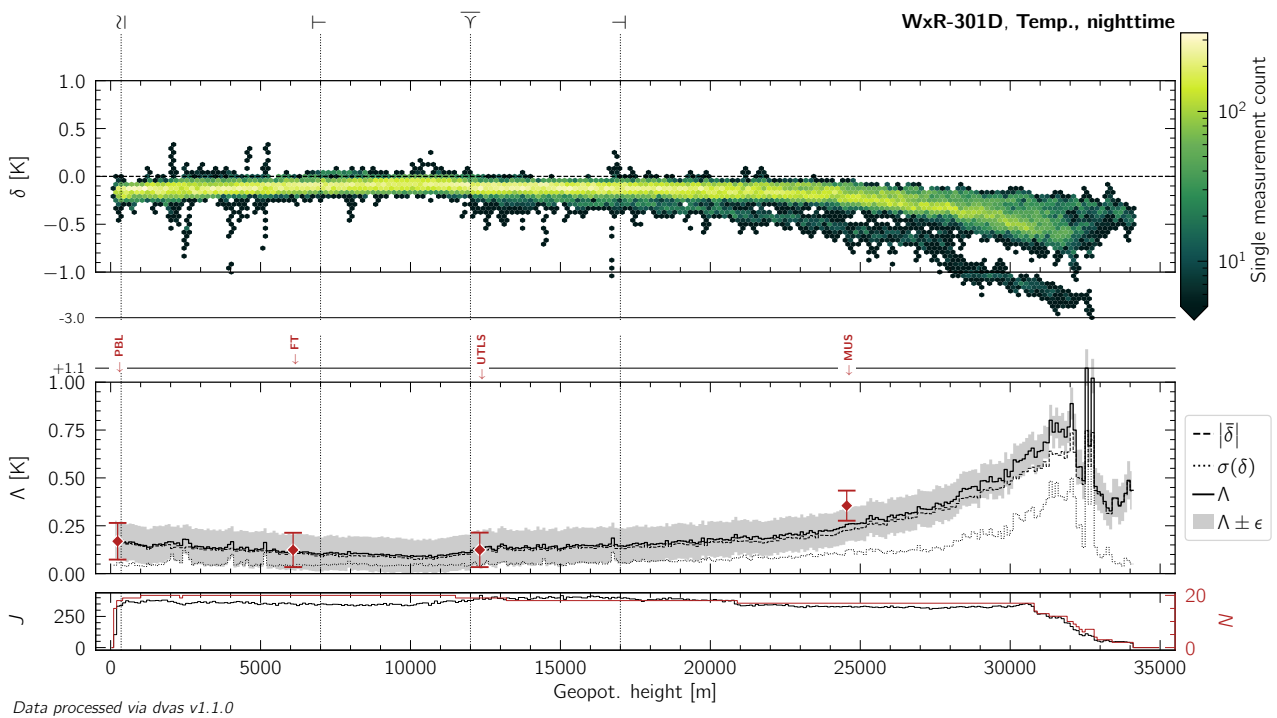


Figure L.128: Same as Figure 10.13, but for nighttime measurements of atmospheric temperature by the WxR-301D radiosonde.

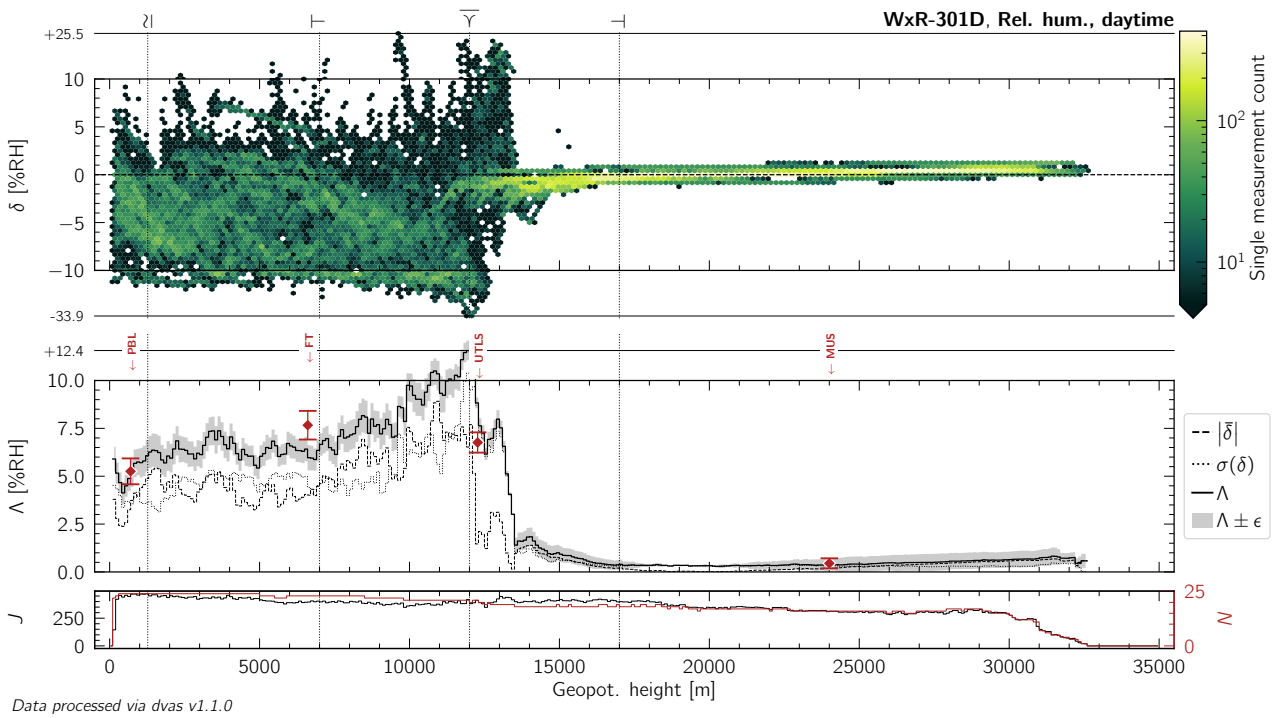


Figure L.129: Same as Figure 10.13, but for daytime measurements of relative humidity by the WxR-301D radiosonde.

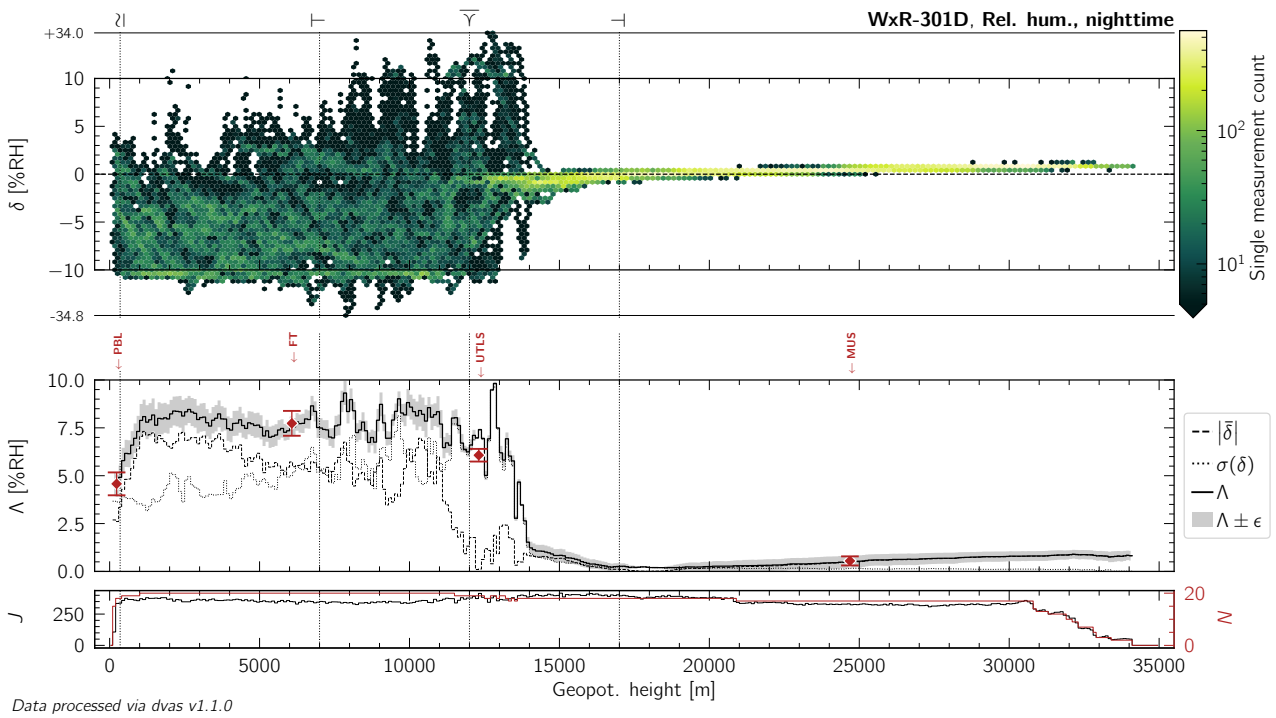


Figure L.130: Same as Figure 10.13, but for nighttime measurements of relative humidity by the WxR-301D radiosonde.

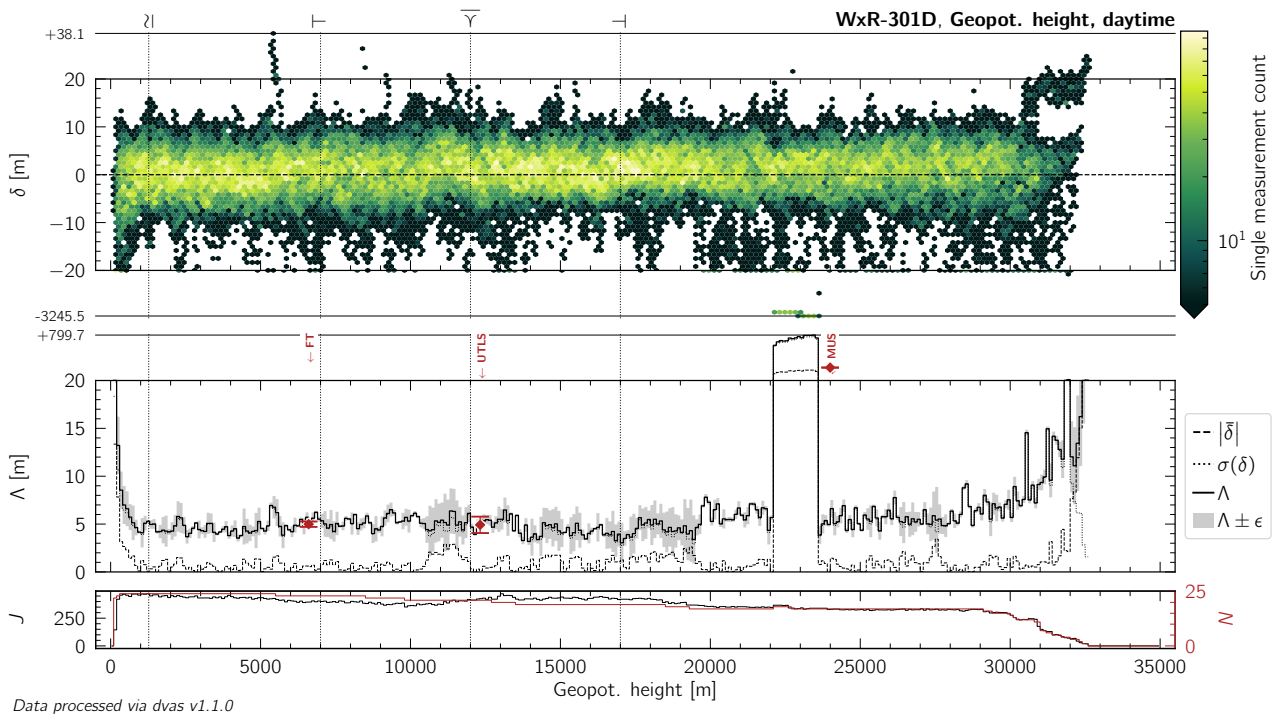


Figure L.131: Same as Figure 10.13, but for daytime measurements of geopotential height by the WxR-301D radiosonde.

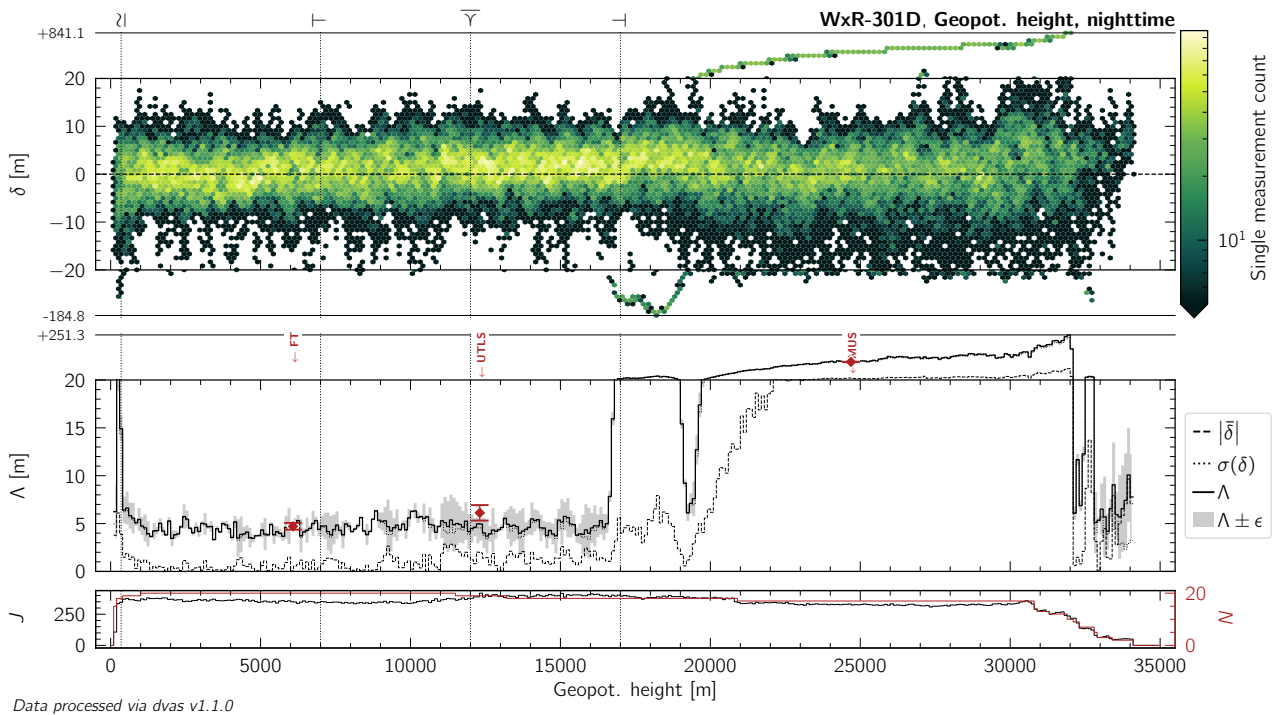


Figure L.132: Same as Figure 10.13, but for nighttime measurements of geopotential height by the WxR-301D radiosonde.

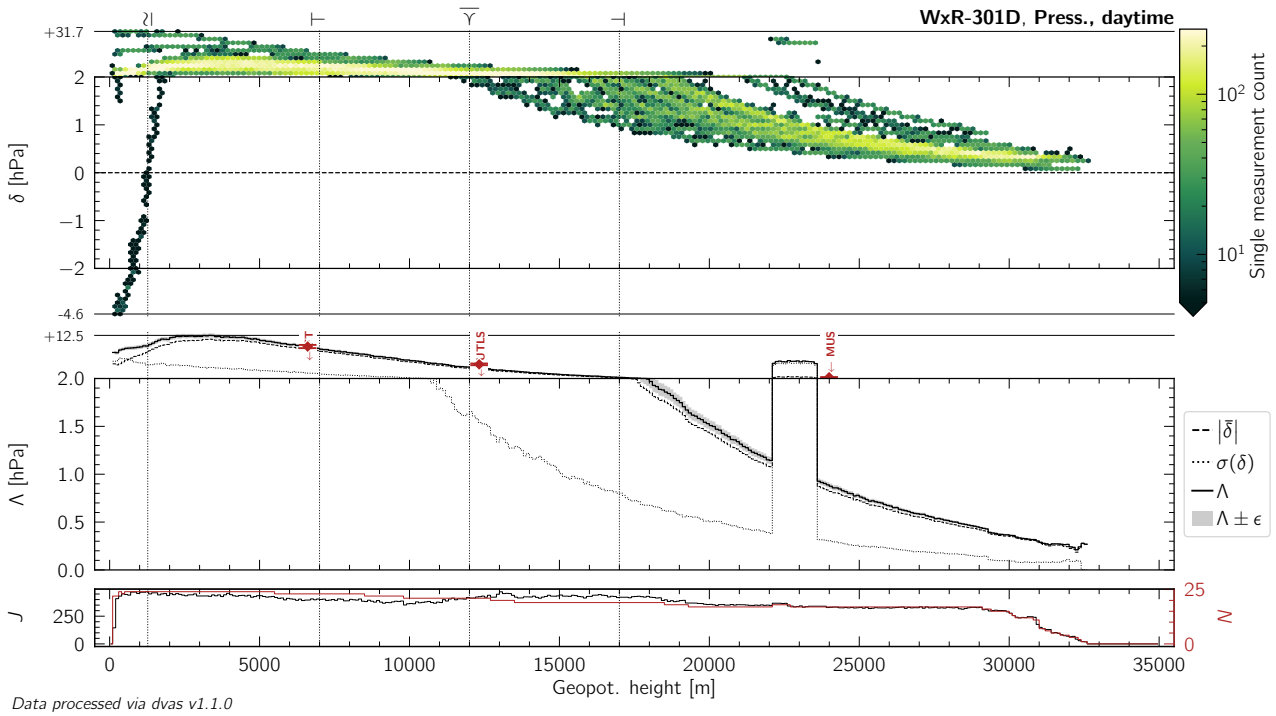


Figure L.133: Same as Figure 10.13, but for daytime measurements of atmospheric pressure by the WxR-301D radiosonde.

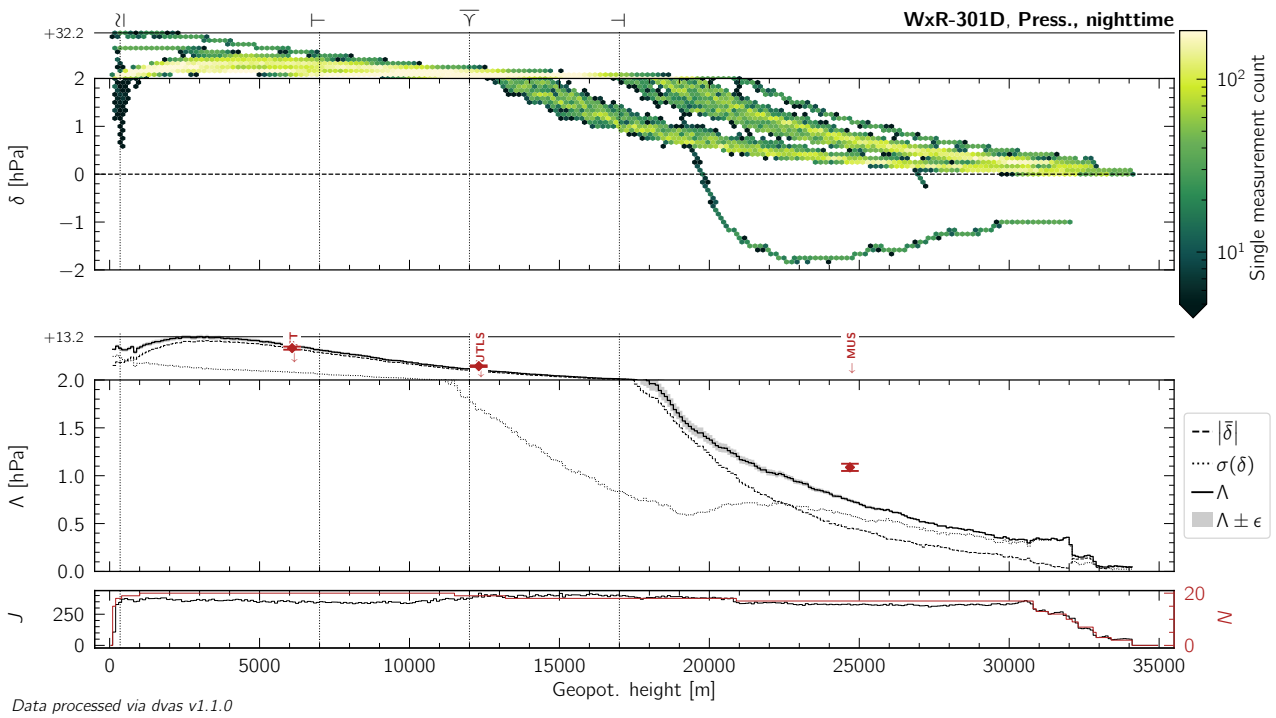


Figure L.134: Same as Figure 10.13, but for nighttime measurements of atmospheric pressure by the WxR-301D radiosonde.

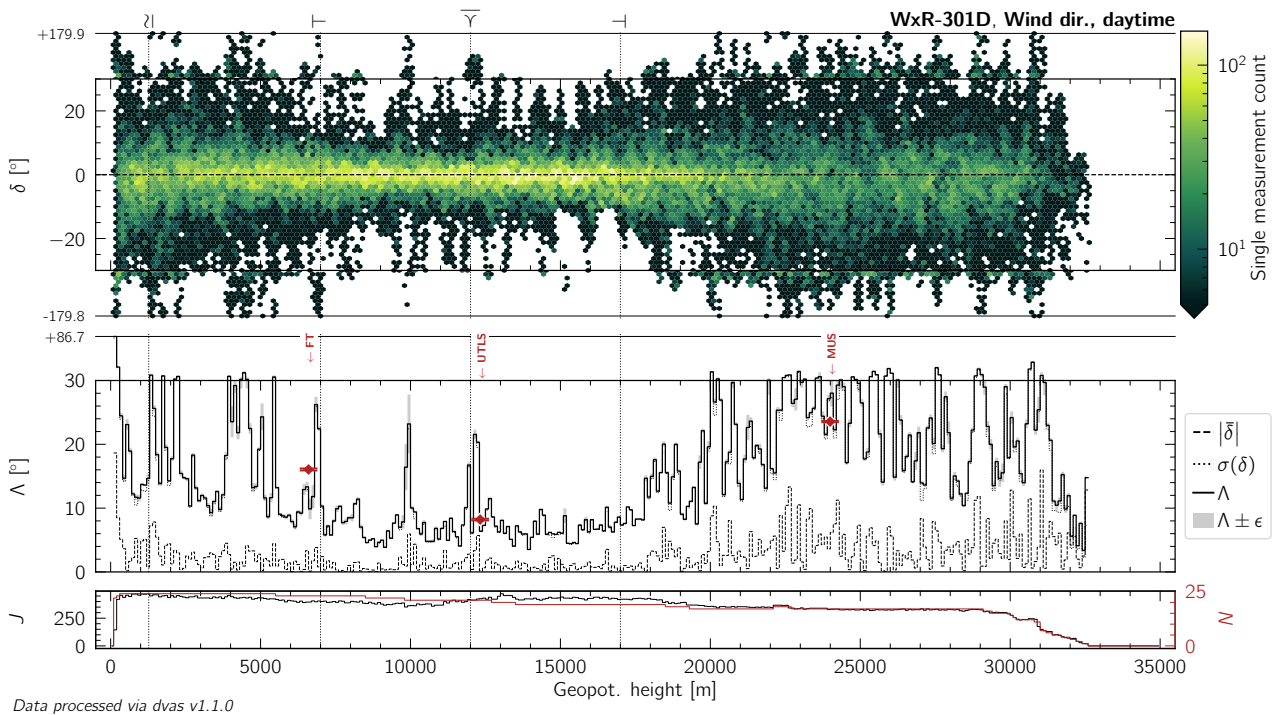


Figure L.135: Same as Figure 10.13, but for daytime measurements of wind (horizontal) direction by the WxR-301D radiosonde.

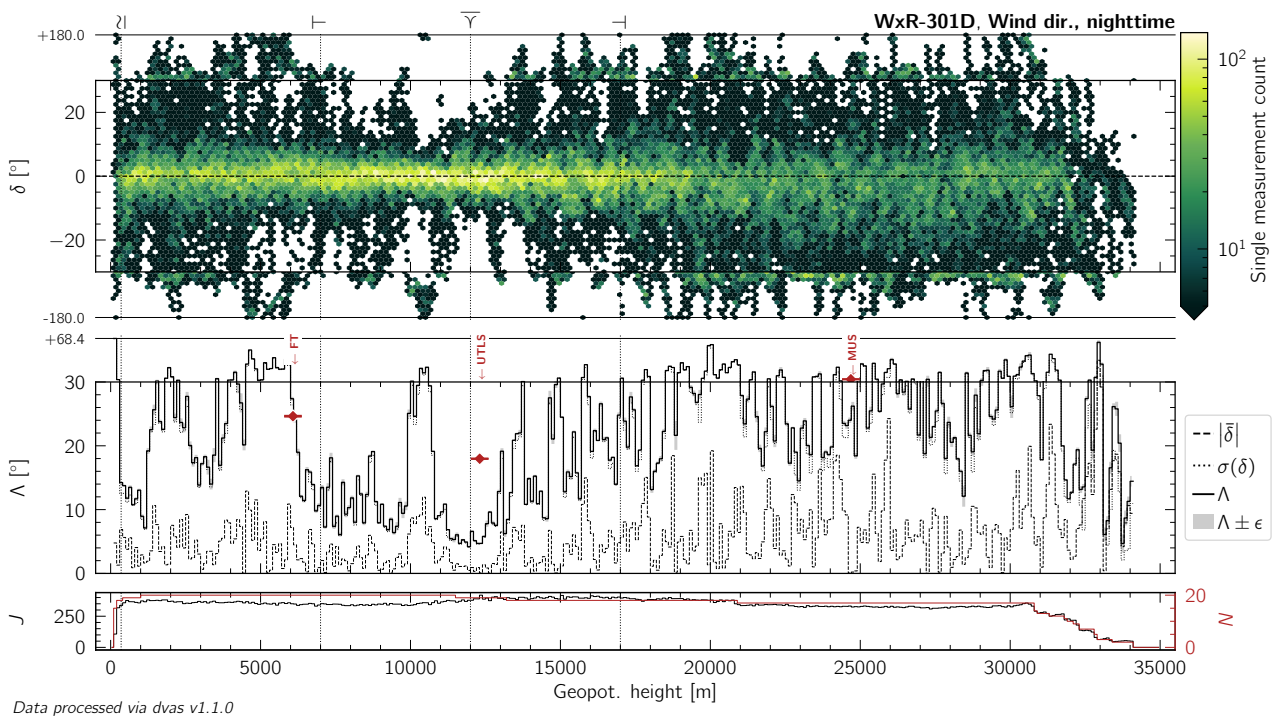


Figure L.136: Same as Figure 10.13, but for nighttime measurements of wind (horizontal) direction by the WxR-301D radiosonde.

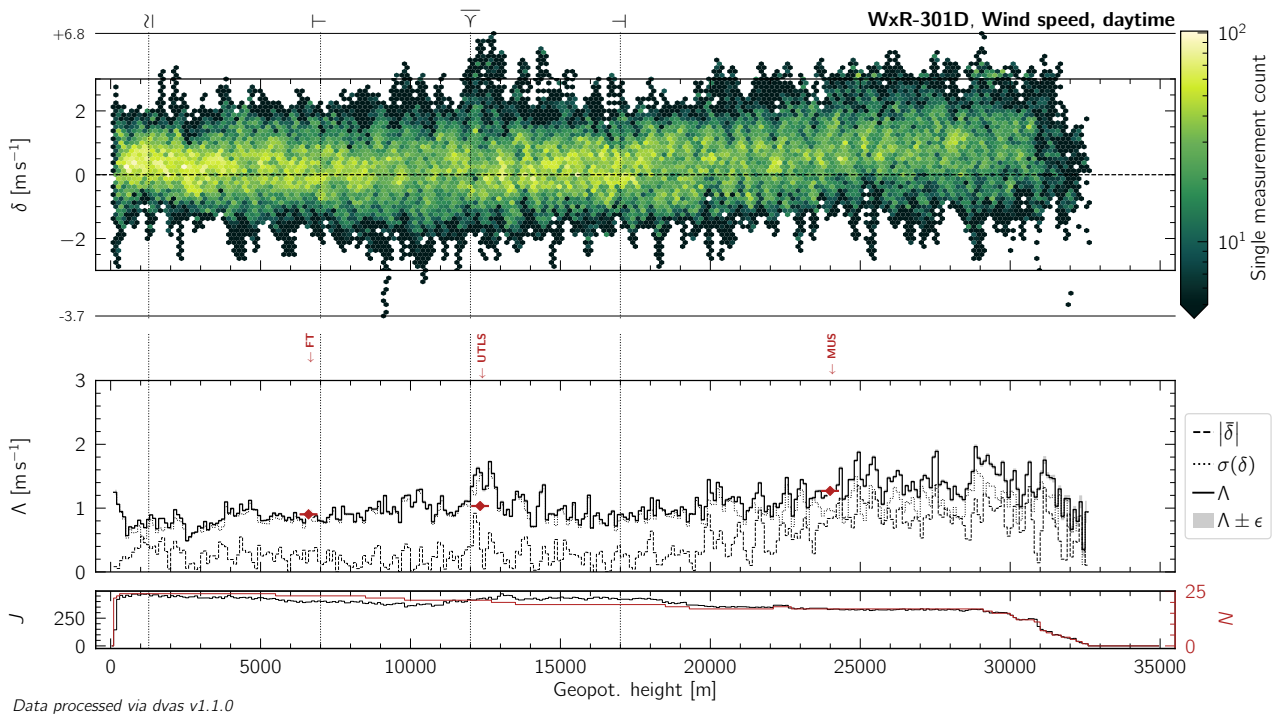


Figure L.137: Same as Figure 10.13, but for daytime measurements of wind (horizontal) speed by the WxR-301D radiosonde.

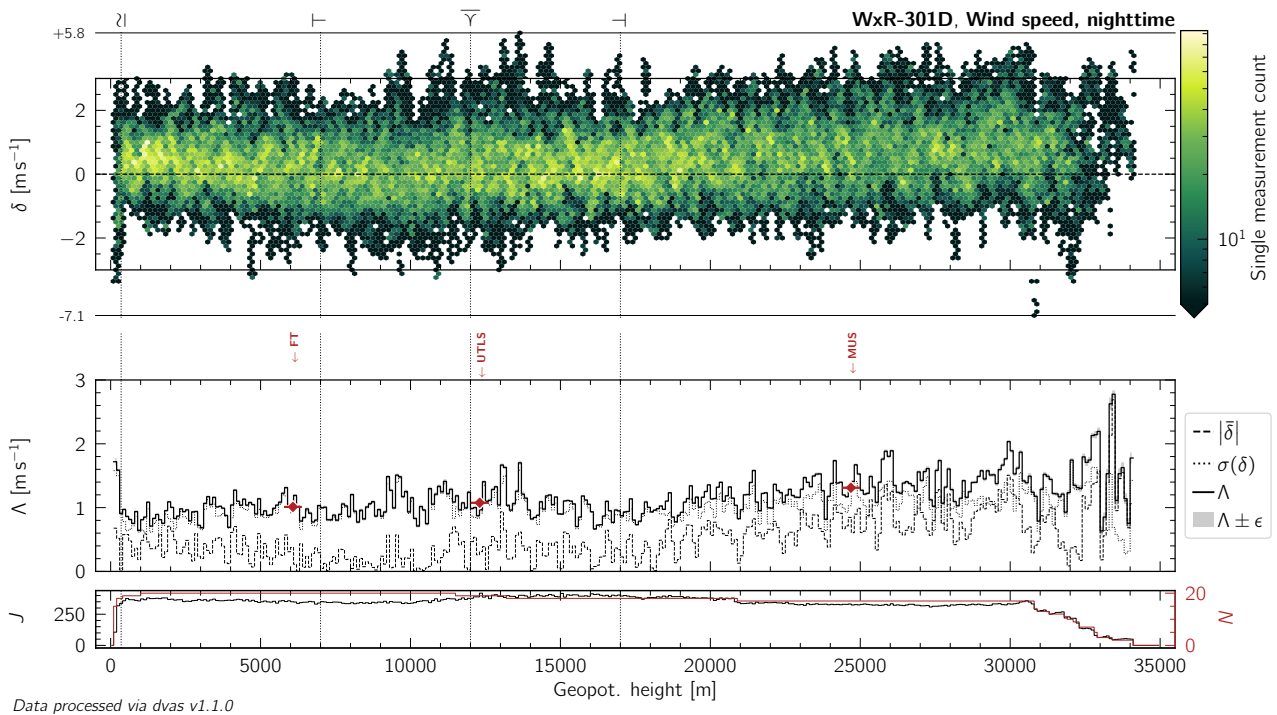


Figure L.138: Same as Figure 10.13, but for nighttime measurements of wind (horizontal) speed by the WxR-301D radiosonde.

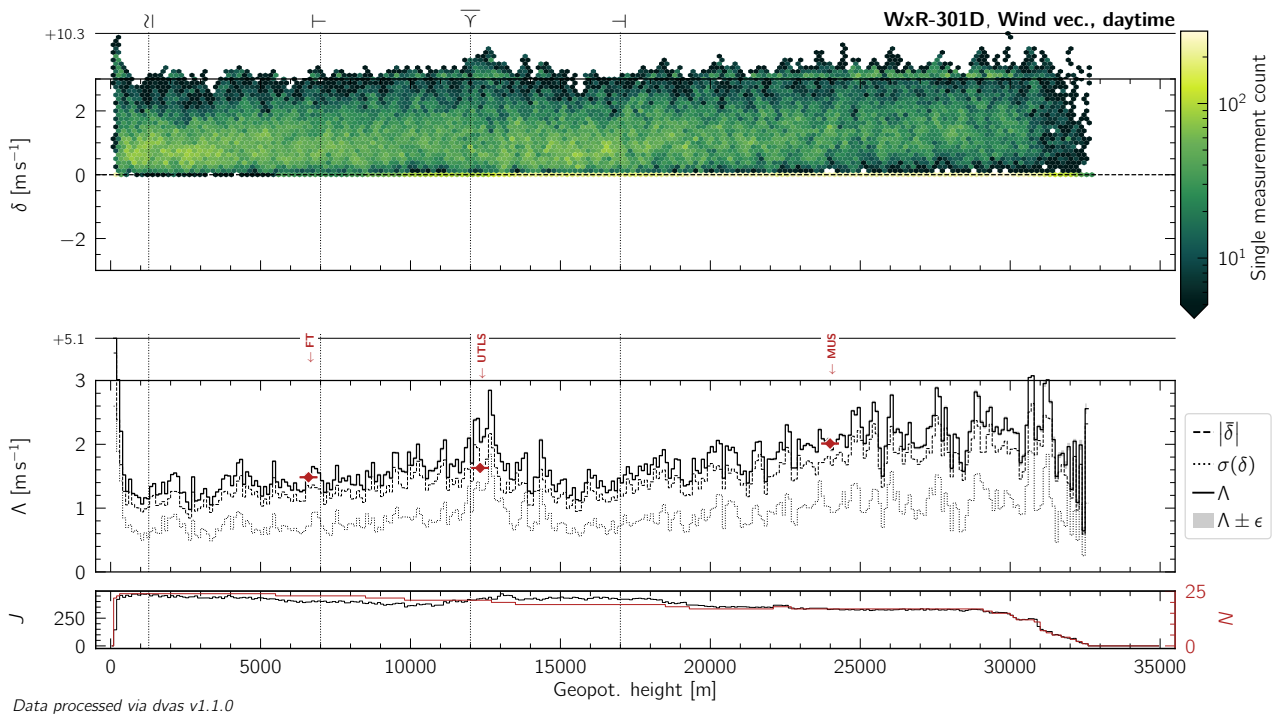


Figure L.139: Same as Figure 10.13, but for daytime measurements of the wind (horizontal) vector by the WxR-301D radiosonde.

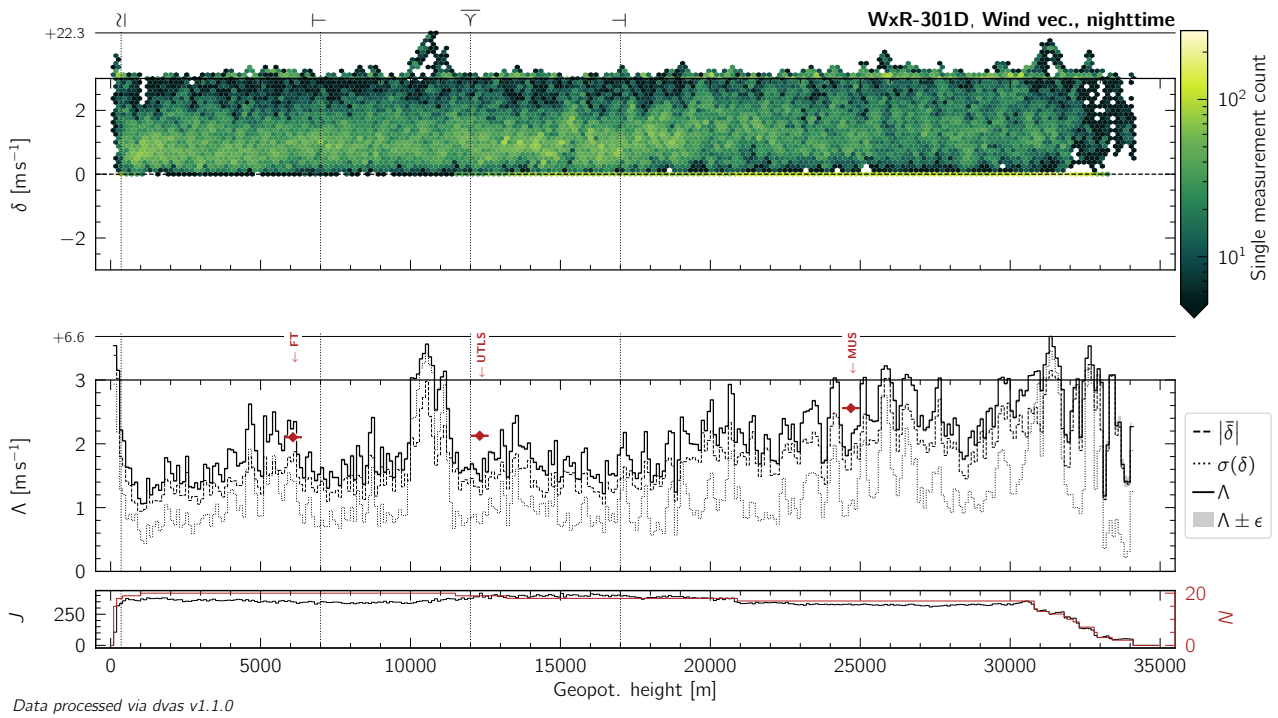


Figure L.140: Same as Figure 10.13, but for nighttime measurements of the wind (horizontal) vector by the WxR-301D radiosonde.

M COMBINED $\Delta_{c,\mathcal{L}}$ PERFORMANCE DIAGRAMS FOR GEOP. HEIGHT, ATMOSPHERIC PRESSURE, AND WIND (HORIZONTAL) SPEED & DIRECTION

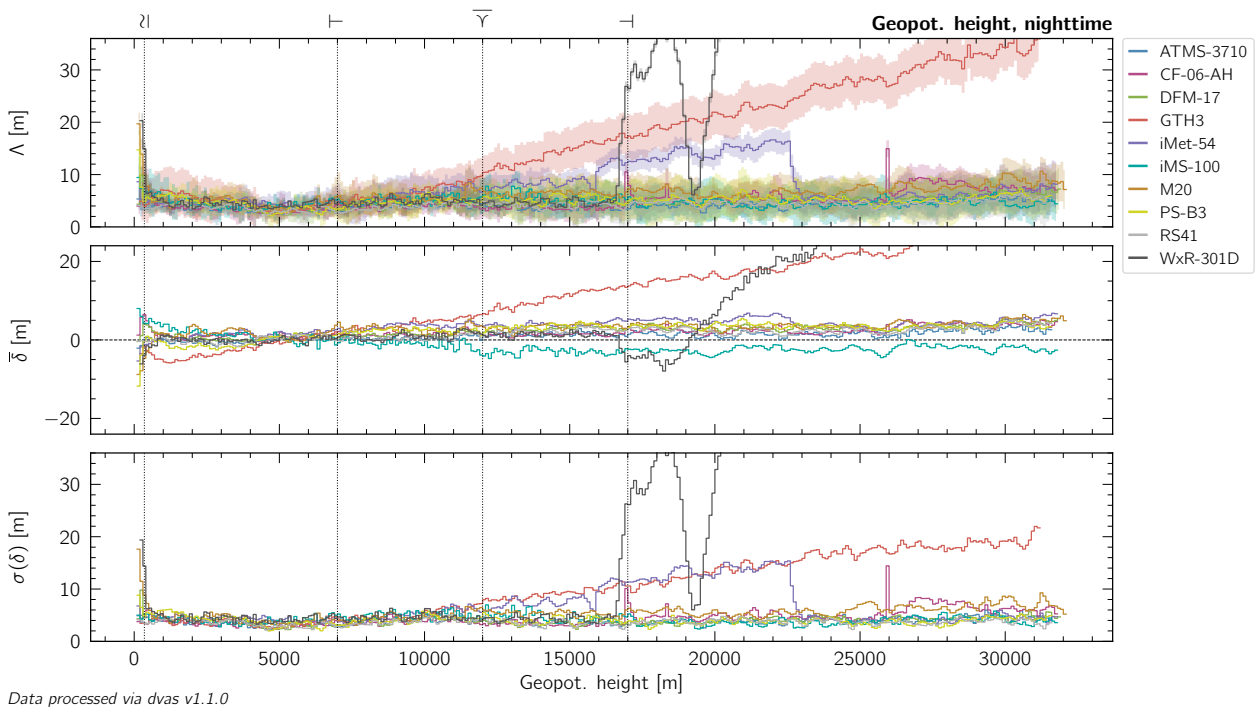
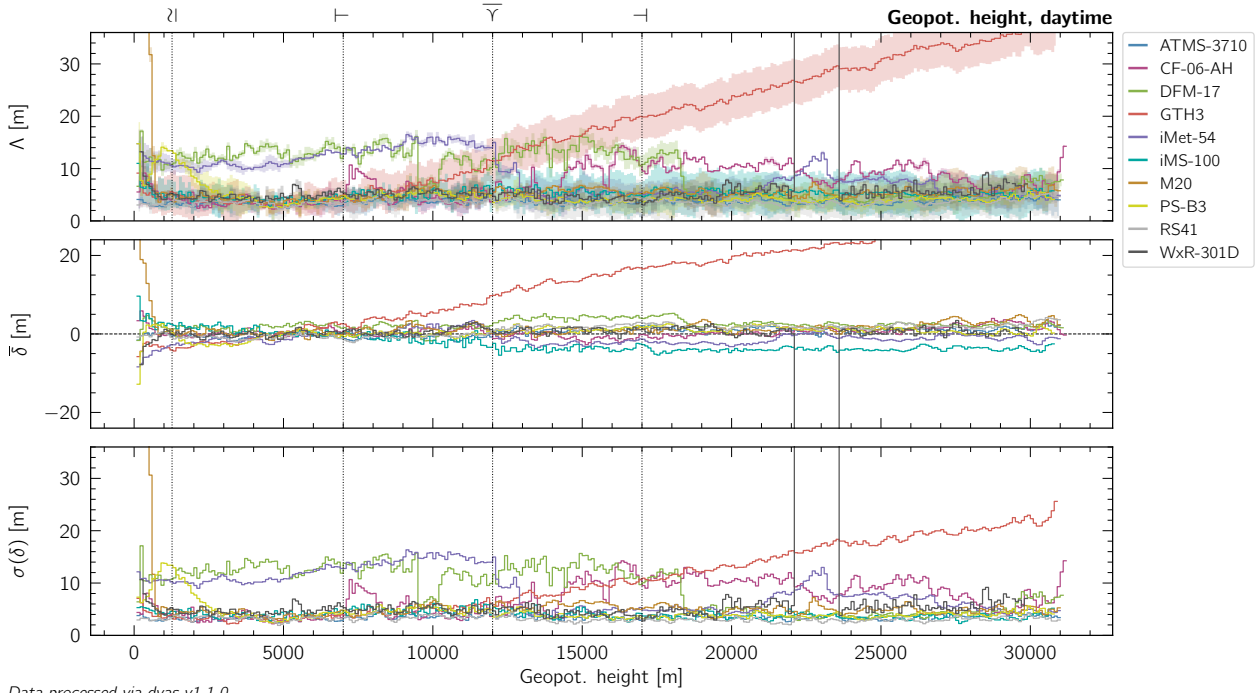


Figure M.1: Same as Figure 11.1, but for the geopotential height.

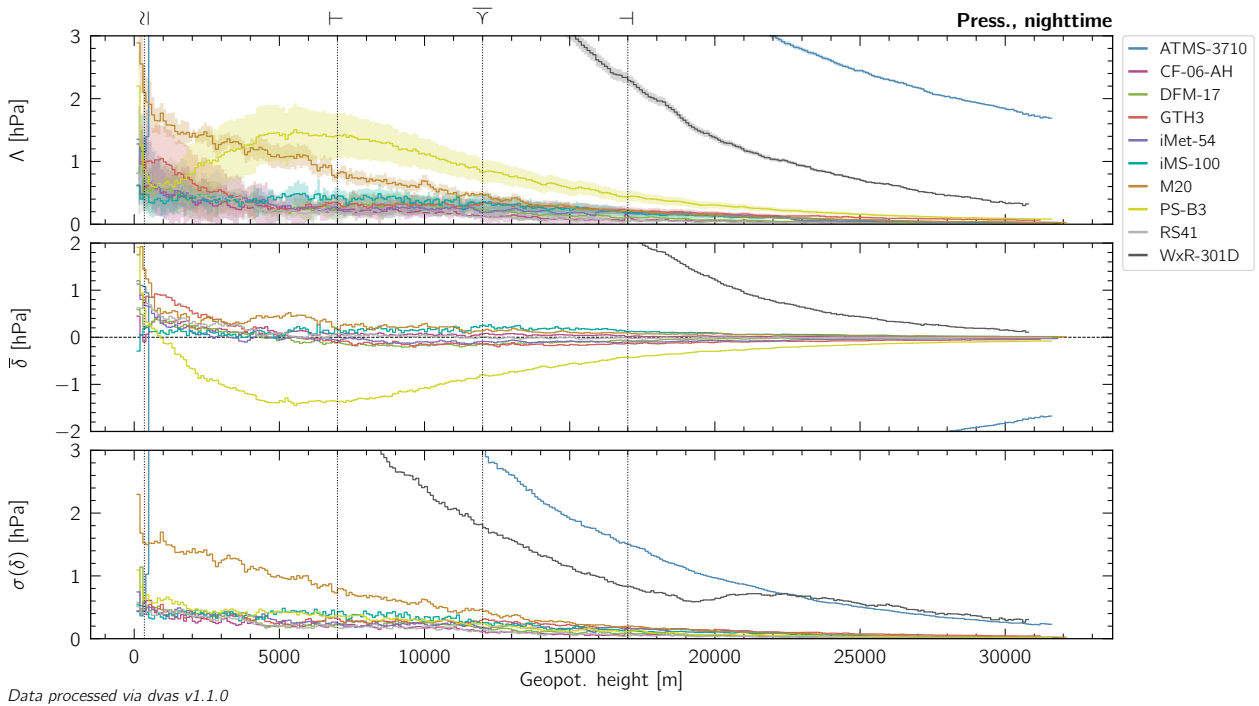
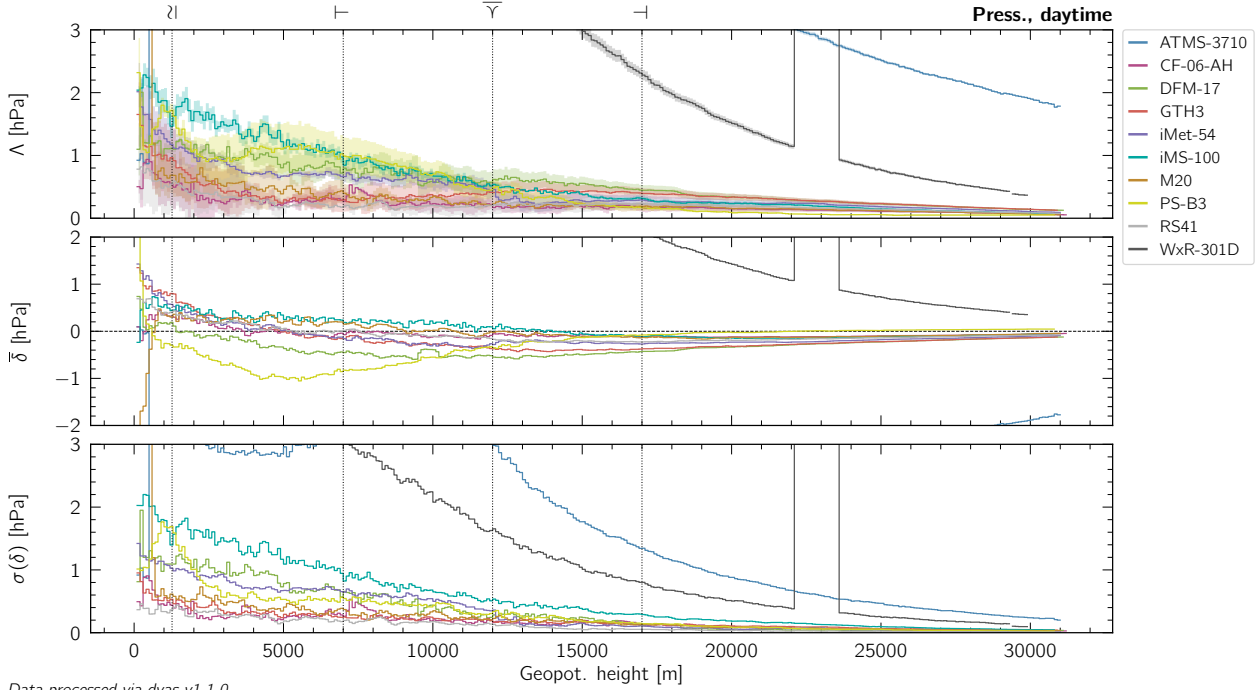
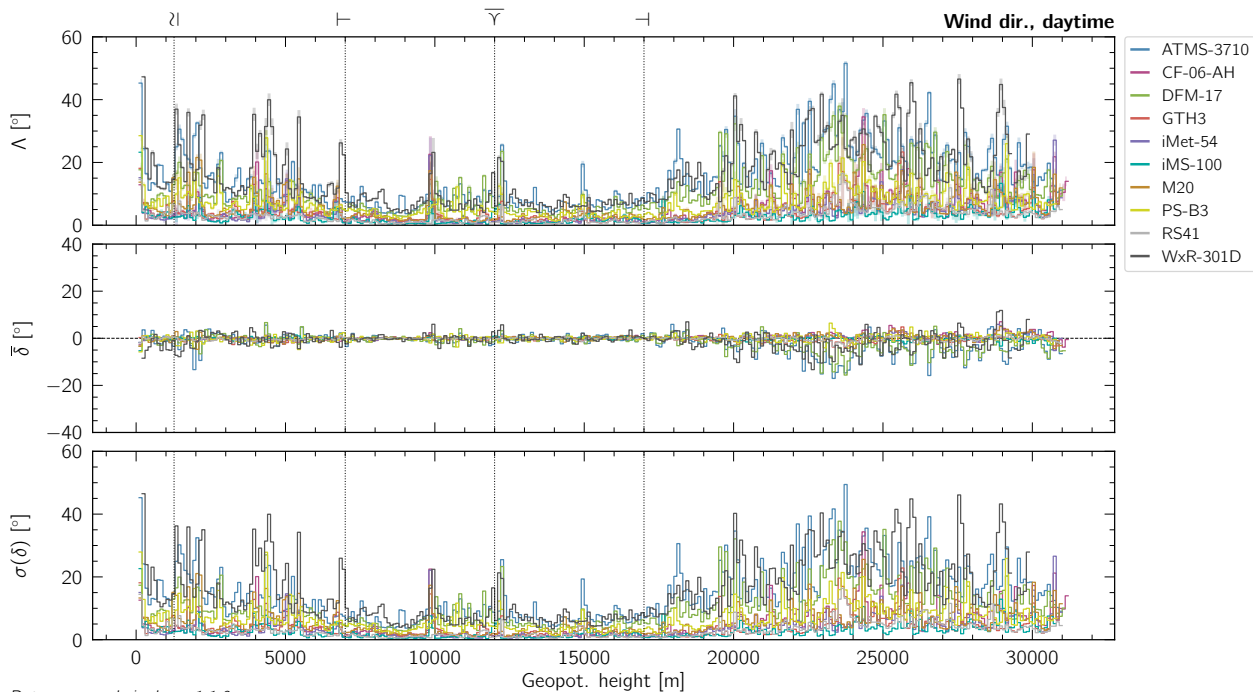
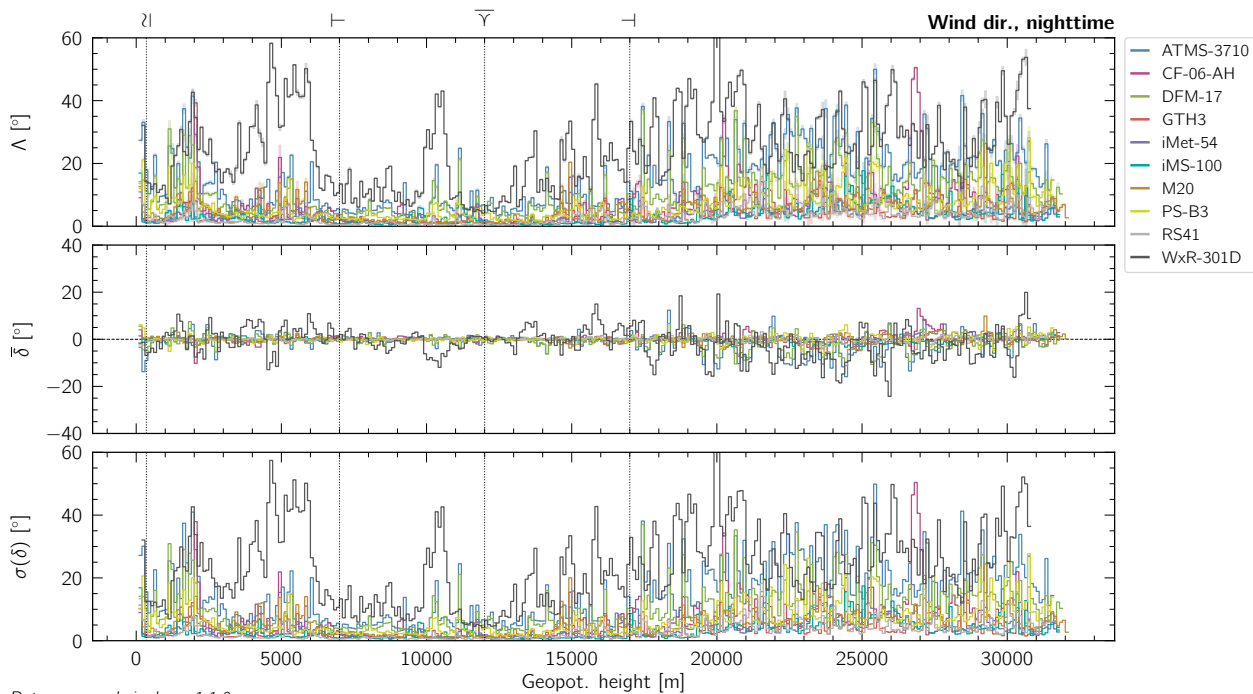


Figure M.2: Same as Figure 11.1, but for the atmospheric pressure.

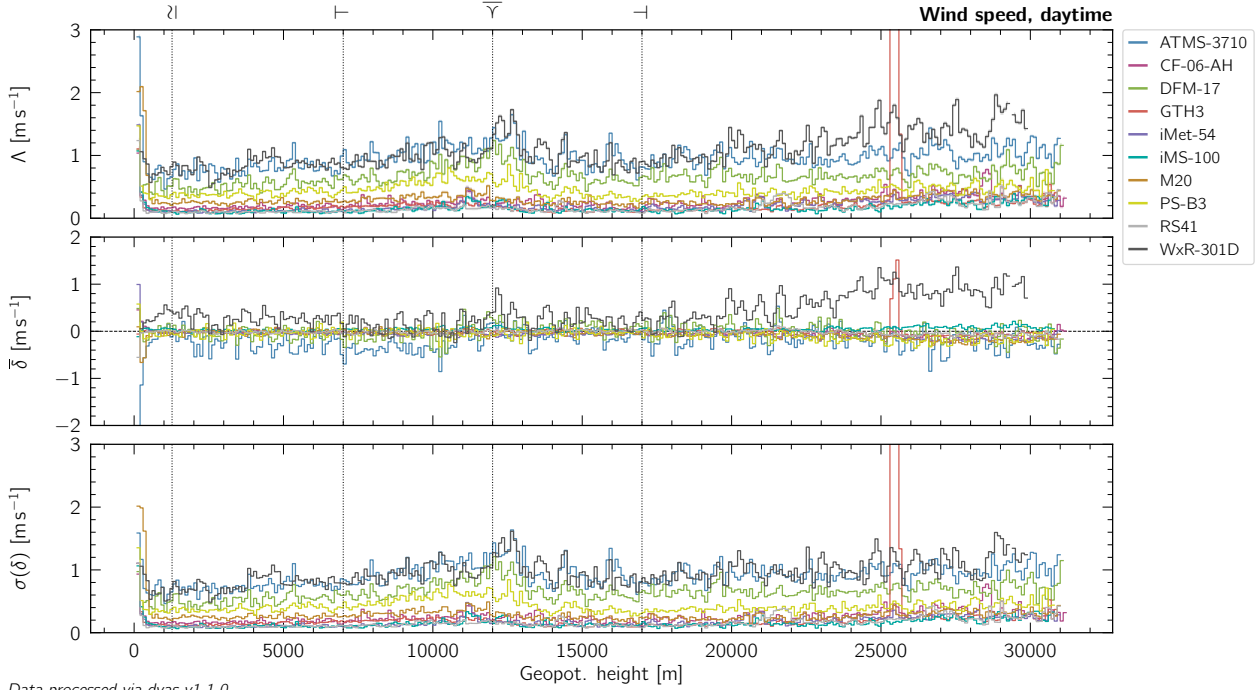


Data processed via dvas v1.1.0

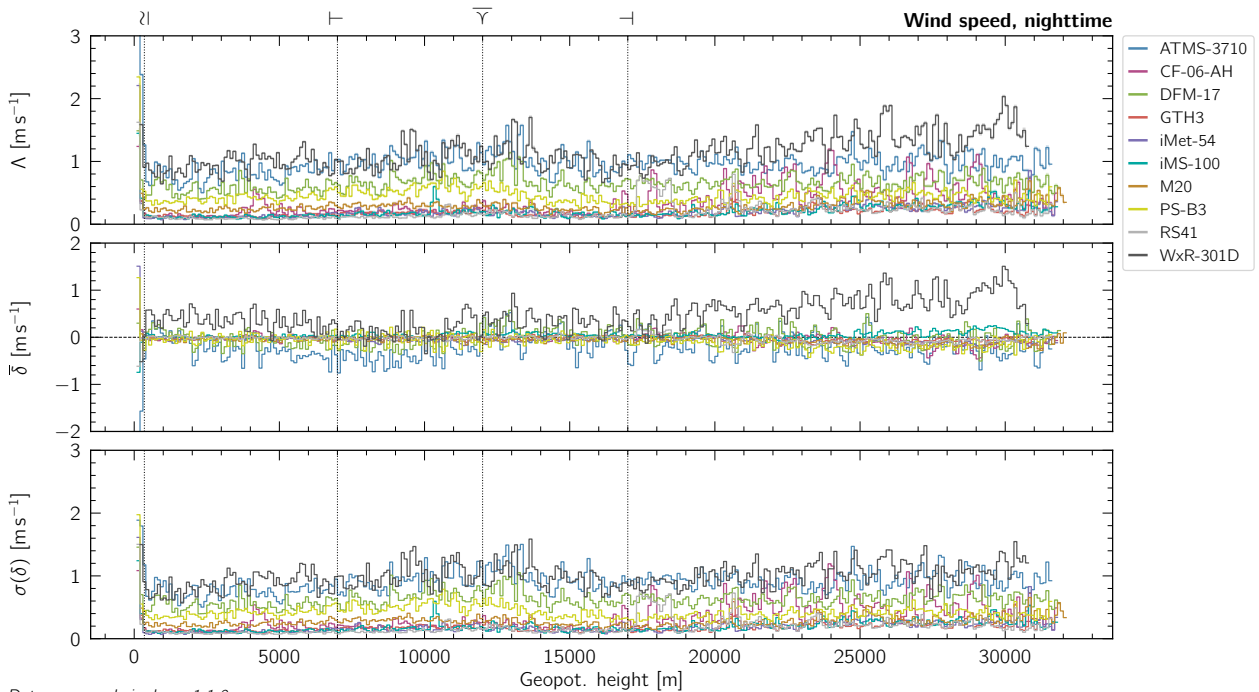


Data processed via dvas v1.1.0

Figure M.3: Same as Figure 11.1, but for the wind (horizontal) direction.



Data processed via dvas v1.1.0



Data processed via dvas v1.1.0

Figure M.4: Same as Figure 11.1, but for the wind (horizontal) speed.

N RIG CONSTRUCTION GUIDE

This guide describes the construction of a rig for parallel launching of up to 10 radiosondes on one balloon (see Figure N.1). Only worldwide available and inexpensive materials are used for this purpose.

The final rig will have a large diameter of approximately 360 cm. This size of rig was used during the UAII campaign. Of course, a different target size, as well as a different number of attachment points for radiosondes could also be selected. But then the lengths and dimensions should be adjusted accordingly.

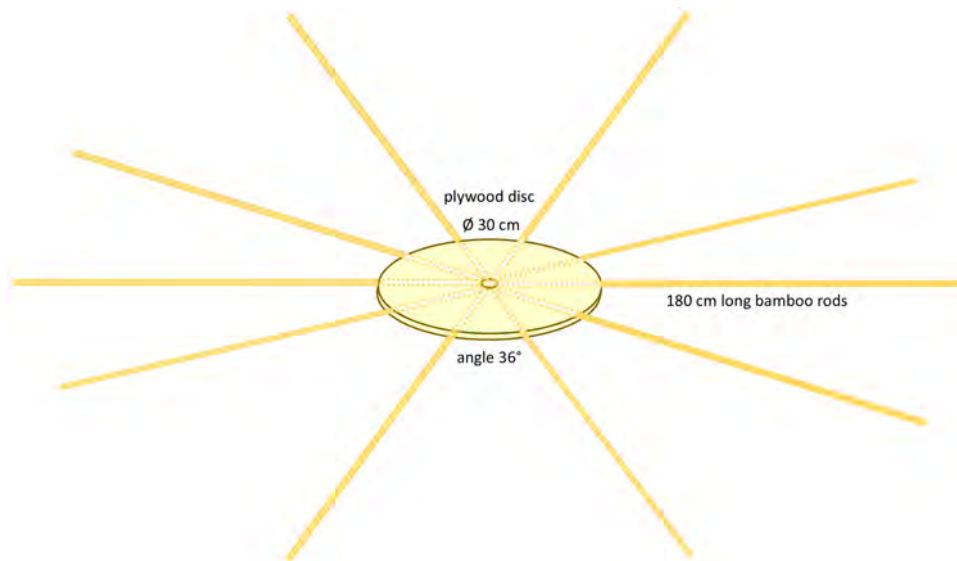


Figure N.1: Scheme of rig construction

Complete list of required tools and materials: Plywood plates (2 pieces, \varnothing 30 cm, approx. 3 mm thick (thinner possible)), bamboo rods (10 pieces, 180 cm), thin string (approx. 12 m with 0.6 mm thickness), thicker string (approx. 10 m with 1.5 mm thickness), thin strap (6.4 m with 10 mm width) and cord (4.20 m with 4 mm thickness), double-sided adhesive tape (3 m), paper tape, stick, ruler, scissors, expanding foam, cutter, drill, saw, screw clamps (4 x). (see Figure N.2)



Figure N.2: Overview about required materials and tools

N.1 PREPARATION

In order to build such a rig, several preparatory steps should first be carried out.

Required: Plywood plates, and bamboo rods.

Step 1.1:

Procure all necessary materials in sufficient quantity and procure all necessary tools.

Step 1.2:

Prepare two circular center plates (discs) of plywood so that they have a diameter of 30 cm and a central hole of 1 cm.

Step 1.3:

Select ten bamboo sticks, which are as straight and uniform as possible and have few side shoots only. Remove any side shoots and bring all the rods to the same length of 180 cm.

Step 1.4:

Weigh the plywood plates and bamboo rods individually and label them with their weight (see Figure N.3).

Important: This is done to calculate the weight of the rig that must be known in order to determine the correct amount of gas for the balloon filling and at the same time comply with the upper limit of the total weight of the balloon chain.

Step 1.5:

Have a sufficiently large and dry working area ready.

Important: When assembled, the total size of the rig is approx. 360 cm. Thus, an area of at least 4 m × 4 m should be available.



Figure N.3: Weighing a plywood plate

N.2 PREPARING THE SURFACE OF THE PLYWOOD PLATES

Required: Circular plates of plywood with \varnothing 30 cm with a central hole of \varnothing 1 cm (2 x), double-sided adhesive tape (3 m), pen, ruler, protractor, and scissors (see Figure N.4a).

Step 2.1:

Make 10 marks (e.g. lines from centre to edge) at an angular distance of 36° each to align the tape and later the bamboo rods (see Figure N.4b).

Step 2.2:

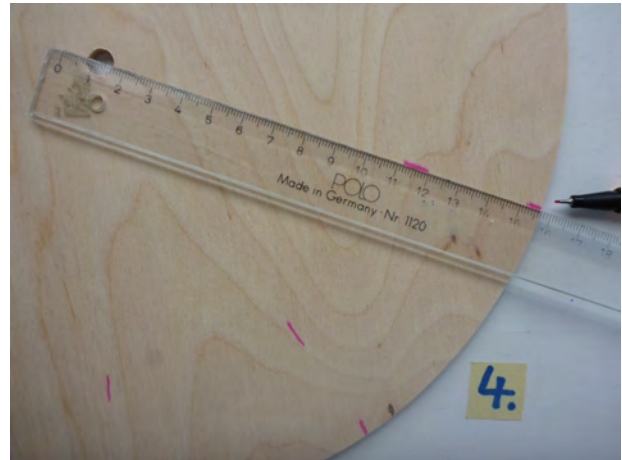
Attach the double-sided adhesive tape to the mark on the two plates of plywood (see Figures N.4c, N.4d).

Step 2.3:

The tape is adjusted and cut to the shape of the plywood.



(a) Raw plywood disc



(b) Marking



(c) Attaching double-sided adhesive tape



(d) 10 strips attached

Figure N.4: Preparing steps of the surface of the plywood plates

N.3 ATTACHING THE BAMBOO RODS AND FINISHING THE WORK ON THE MAIN RIG

Required: Bamboo rods 180 cm long (10x, straighten, minor "hooks" removed), screw clamps (4x), expanding foam, cutter, and drill.

Step 3.1:

Align and press firmly the bamboo rods on the first plate of plywood and tape (see Figures N.5a, N.5b).

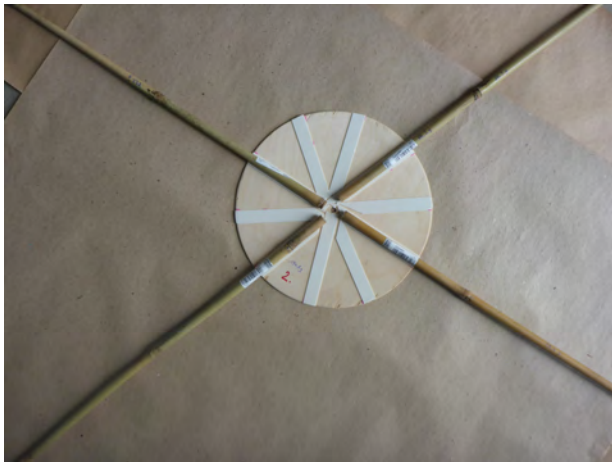
Step 3.2:

Align the second sheet of plywood with the tapes facing inward on the bamboo sticks (sandwich, see Figures N.5c, N.5d). Screw clamps are used to retain the specified depth/height of the resulting unit.

Attention: Care must be taken to ensure that the tape, bamboo rods and again the tape are layered on top each other well aligned (sandwich).

Step 3.3:

Fill in the resulting cavities with expanding foam, thus connecting the layers with each other



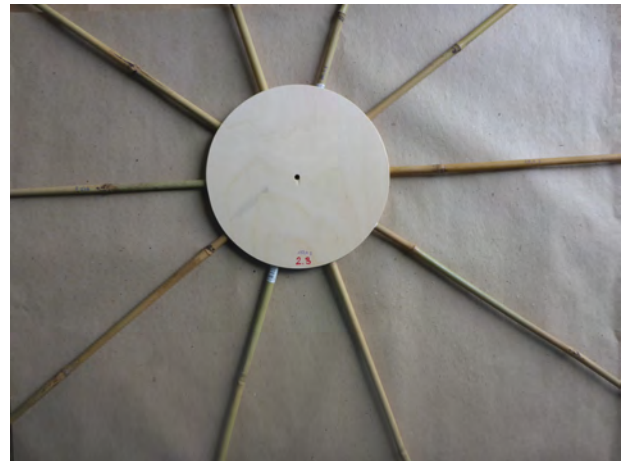
(a) Align bamboo rods individually



(b) All ten bamboo rods aligned



(c) Align the second plate of plywood



(d) Second plate of plywood aligned

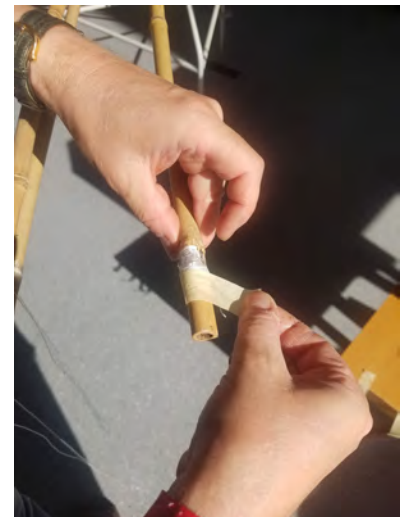


(e) Fill in expanding foam



(f) Remove excess material with the cutter

Figure N.5: Joining the bamboo rods with the central plywood panels

**(a)** Attach thin string**(b)** Wrap each individual string**(c)** Fix string with paper tape**(d)** Spider web for rig stability**(e)** Fasten as taut string**(f)** Using super glue**Figure N.6:** Attaching the strings

(see Figure N.5e).

Step 3.4:

Remove the screw clamps after the construction foam has hardened.

Step 3.5:

Remove excess material with the cutter, obtaining the shape of the plywood panels (see Figure N.5f).

Step 3.6:

Use a drill to free the central hole from the construction foam.

N.4 ATTACHING THE STRINGS AND STABILISING THE RIG

Required: 120 cm long strings (10x, 0.6 mm thick), string (10 m, 1.5 mm thick), paper tape, pen, super glue or tape.

Step 4.1:

Attach 120 cm long thin strings for the attachment of the radiosondes on the tips of the 10 bamboo rods (see Figure N.6a). Fix each string with knots and tape.

Step 4.2:

Place a mark on the string at 70 cm from the rod to ensure the same height of the sensor boom when mounting each radiosonde.

Step 4.3:

Wrap each individual string around the bamboo stick and fix it with paper tape to ensure an easier transport of the rig to the launch site (see Figures N.6b, N.6c).

Step 4.4:

Fasten a taut string similarly to a spider web, first with knots and finally with super glue (or alternatively tape) at a distance of approx. 70 cm from the plywood composite (for stability within the rig (see Figures N.6d, N.6e, N.6f).

N.5 ATTACHING THE BALLOON ATTACHMENT CORD

Required: 160 cm long straps (4 x, 10 mm width), 420 cm long cord (4 mm thick).

Step 5.1:

Distribute evenly the four straps and tie in the middle around the four bamboo rods facing each other (see Figure N.7a).

Step 5.2:

Take the 8 strap ends together and tie a knot approx. 40 cm above the plywood plate to balance the rig (see Figure N.7b).

Step 5.3:

Set another knot 10 cm above the first fixed point.

Step 5.4:

Pull a stable approx. 420 cm long security cord through the central hole in the plywood composite, the lower part of the cord should reach over the stabilisation line (spider web, see Figure N.7c).

Information: Use this security cord for attaching the rig to the launch stamp (see Figure N.7i).

Step 5.5:

Set a very large and firm knot of the security cord between the balloon attachment knot and the top side of the plywood plate (see Figure N.7d).

Important: This knot must not be able to be pulled through the hole.

Step 5.6:

Tension and attach the remaining cord to the balloon attachment knot (first fixed point, see Figure N.7e).

Step 5.7:

Place of two tight knots at the end of the cord, a larger eyelet is formed (see Figure N.7f).

Note: The 60 m long line for releasing the balloon or a proper unwinder (e.g. special Graw unwinder UW1 with 60 m) is hooked into this eyelet using a carabiner.

If necessary: Attach a finder's letter and unique number to the rig (for logging) (see Figure N.7g, N.7h).

N.6 BALANCING THE RIG DURING LAUNCH PREPARATION

Necessary: Preferably two persons to balance a rig.



(a) Attach first strap



(b) Knot all four straps



(c) Cord reaches the spider web



(d) Large knot of cord



(e) Attach cord to first knot



(f) Formed eyelet of cord



(g) Central disc with strings



(h) Finder's letter and number



(i) Launch stamp during UAII

Figure N.7: Attaching the balloon attachment cord



(a) Hanging rig at working height



(b) Labelling a bamboo rod

Figure N.8: Prepare a rig for usage at a specific launch



(a) Attaching a sonde dummy



(b) One radiosonde dummy

Figure N.9: Using radiosonde dummies to balance the rig



(a) Unbalanced rig



(b) Finally balanced rig

Figure N.10: Balancing the rig

Step 6.1:

Fastening the rig to the hook in the balloon hangar at a suitable working height (see Figure N.8a).

Step 6.2:

Labelling the bamboo rods (A to L, without I and J) according to the supervisor's plan. (see Figure N.8b)

Step 6.3:

Attachment of radiosonde dummies (made with rice as weight according to weight specification of original radiosondes including batteries) to their designated place (A to L) on the rig. (see Figures N.9a and N.9b)

Step 6.4:

Balancing the now equipped rig with additional weight (at ends of rods) if necessary to have the rig in balance. (see Figures N.10a and N.10b)

Step 6.5:

Removing the dummies, removing the paper tape from the bamboo rods to be equipped and unwinding the suspension string for the radiosondes.

Empty rods: Fixation of the suspension string remains, because no radiosondes will be attached.

N.7 LAUNCH PROCEDURE

Necessary: Three persons are needed to perform the launch procedure, the supervisor (person in charge of the whole launch), the rig manager (the person in charge of the rig), and the balloon manager (person in charge of the balloon).



(a) Rig at launch stamp



(b) 60 m balloon string laid out

Figure N.11: Rig placed on the launch stamp at the launch site

Step 7.1:

Lowering the prepared rig and transferring it to the launch site respectively launch stamp.

Step 7.2:

Fixation of the rig to the launch stamp by means of the "retaining line" (see Figure N.11a).

Step 7.3:

Checking the suspension strings, aligning if necessary.

Step 7.4:

Depending on the supervisor's decision, the balloon is launched with (a) a 60 m Graw unwinder or (b) a 60 m line laid out. In case (b) the 60 m string should be properly laid out beforehand (this prevents knots or similar). In both cases, the end of string will be attached to the eyelet by means of a carabiner (see Figures N.7f and N.11b).



(a) Attaching a radiosonde



(b) Attaching a radiosonde

Figure N.12: Attaching radiosondes on the rig which is already placed on the launch stamp at the launch site



(a) Slowly release the balloon



(b) Launch team at launch site

Figure N.13: Launch team during launching procedure: balloon manager slowly releases the balloon on the 60 m long line, the rig manager holds the last part of string, so that it does not tangle with the rig, and the supervisor keeps the overview and gives the commands.

Step 7.5:

After the preparation of all radiosondes is completed, the radiosondes (which are marked with letters A to L) are attached to their designated place (bamboo rods A to L) by means of fixed knots. The operators are assisted in attaching radiosondes by the person in charge of the rig (rig manager). The radiosondes are attached in such a way that the temperature sensor of the sensor boom is approximately at the height of the 70 cm mark on the suspension lines (see Figures N.12a and N.12b).

Step 7.6:

The person in charge of the balloon (balloon manager) will bring the filled balloon to the launch site.

Step 7.7:

The rig manager hooks the balloon into the 60 m launch line.

Step 7.8:

The supervisor checks everything again and asks all involved again if everything is OK.

Step 7.9:

If everything is OK, slowly release the balloon on the 60 m long line (see Figures N.13a and N.13b).

Important: Essential is to use gloves because of strong heat generation.

Step 7.10:

The rig manager detaches the retaining line of the rig at the launch stamp.

Step 7.11:

Launch is performed at supervisor command.

Attention: Note the current wind situation (including wind speed, direction and gust).

Step 7.12:

Exact launch time is detected by supervisor from independent validated timing source.

O PHOTO GALLERY OF THE UAI 2022

A collection of photos taken during the field campaign is shown in Figures O.1, O.2 and O.3. A large part of the photos is also presented at: <https://www.gruan.org/community/campaigns/uai2022>.

Figures O.4 and O.5 show snapshots from two videos taken by an action camera attached to the rig. The photos document a variety of cloud situations at different altitudes.

All photos in this gallery as well as the two videos are accessible as part of the supplementary material (see Section 1.6).



(a) Site introduction for manufacturers



(b) Training of operators on sounding systems in balloon hall



(c) Practise attaching radiosondes on the rig



(d) Campaign UAII2022 Lindenberg



(e) Lindenberg background team



(f) Operator training



(g) Operator training



(h) Operator training

Figure O.1: Photo collection of field campaign, page 1



(a) Rig manufacturing team



(b) Supervisors during sounding campaign



(c) Lindenberg workshop and facility management team



(d) Team for operation of reference humidity measurements (CFH)



(e) Visit of the president of DWD and the director of MeteoSwiss at UAII2022 in Lindenberg



(f) Attaching radiosondes for an evening/night flight



(g) Routine launch procedure



(h) Operational night shift during the campaign

Figure O.2: Photo collection of field campaign, page 2



(a) Balloon brought for an evening/night flight



(b) Receiving antenna field alongside the launch site



(c) Discussions in a data debriefing session



(d) Attaching radiosondes for a day flight



(e) Standard humidity chambers (SHC) for 100% ground checks



(f) Pre-launch briefing



(g) Sounding team One during day shift



(h) Sounding team Two during night shift

Figure O.3: Photo collection of field campaign, page 3



(a) 145 m, short after launch



(b) 2500 m



(c) 5500 m



(d) 8000 m, cloud base



(e) 9500 m, cloud top



(f) 12500 m, tropopause



(g) 15000 m



(h) 20000 m



(i) 25000 m



(j) 30000 m

Figure O.4: Flight snapshots (F68, 2022-09-09T08) taken from action camera video. Visible radiosondes (from left to right): IMS-100, DFM-17, PS-B3, RS41, GTH3, ATMS-3710 and WxR-301D.



(a) 135 m, short after launch



(b) 2500 m



(c) 5500 m



(d) 8000 m



(e) 9500 m, cloud base



(f) 11000 m, cloud top



(g) 15000 m



(h) 20000 m



(i) 25000 m



(j) 30000 m

Figure O.5: Flight snapshots (F56, 2022-09-06T08) taken from action camera video. Visible radiosondes (from left to right): (iMS-100,) M20, iMet-54, RS41, CF-06-AH, WxR-301D, iMS-100 (and iMet-54).

P PERSONS INVOLVED IN THE UAI

Table P.1: List and details of persons involved

Full name	Roles & functions	Organisation & country
<i>Independent operators</i>		
DURI, Norman	field	Meteorological Services Department of Zimbabwe, Zimbabwe
FAHMY, Zeinab	field	Egyptian Meteorological Authority, Egypt
GANGADEEN, Savitri	field	Trinidad and Tobago Meteorological Service, Trinidad and Tobago
JHABEEMISSUR, Josette	field	Seychelles Meteorological Authority, Seychelles
KÖRNER, Sven-Olaf	field	DWD, Germany
LAJNEF, Bassem	field	National Institute of Meteorology (INM), Tunisia, Tunisia
LANGA, Nontobeko	field	South African Weather Service, South Africa
NGUYEN THI, Quyen	field	Vietnam Meteorological and Hydrological Administration (VNMHA), Vietnam
PAJARILLA, Sonny	field	Philippine Atmospheric, Geophysical and Astronomical Services Administration (PAGASA), Philippines
PENE, Wayne	field	Fiji Meteorological Service, Fiji
<i>Manufacturers</i>		
HU, Jianqiao	lab & field	Aerospace Newsky, China
HUANG, Xiaojie	lab & field	Aerospace Newsky, China
KUAI, Mei Lin	lab & field	Aerospace Newsky, China
SHAH, Niraj	lab & field	Azista, India
SOLANKI, Narendra	lab & field	Azista, India
VEDAM, Raghavendran	lab	Azista, India
FRIELINGS DORF, Johannes	lab & field	Graw, Germany

This table is continued on the next page.

Table P.1 – *Continued from previous page*

Full name	Roles & functions	Organisation & country
KOTIK, Alexander	lab & field	Graw, Germany
SEIFERT, Jens	field	Graw, Germany
PANZER, Yvonne	lab & field	Graw, Germany
SPENCER, Andrew	lab & field	Intermet, South Africa
TALBOT, Michael	field	Intermet, South Africa
WENTZEL, Shaun Patrick	lab	Intermet, South Africa
NAGAHAMA, Norio	field	Meisei, Japan
SHIMIZU, Kensaku	field	Meisei, Japan
SUGIDACHI, Takuji	lab	Meisei, Japan
CHARPENTIER, Benjamin	field	Meteomodem, France
FARAH, Antoine	lab & field	Meteomodem, France
FINOT, Benjamin	lab & field	Meteomodem, France
GAUTIER, Rémy	field	Meteomodem, France
MESMIN, Samuel	field	Meteomodem, France
RAUX, Christophe	field	Meteomodem, France
CHEN, Wanzhen	lab & field	Tianjin Huayuntianyi, China
CHEN, Zhong	lab	Tianjin Huayuntianyi, China
XU, Jie	lab	Tianjin Huayuntianyi, China
DEY, Arup	field	Vaisala, Finland
JAUHAINEN, Hannu	lab & field	Vaisala, Finland
KESKINEN, Lauri	field	Vaisala, Finland
LEHMUSKERO, Matti	field	Vaisala, Finland
SAARINEN, Johannes	lab & field	Vaisala, Finland
SURVO, Petteri	lab	Vaisala, Finland
GIRIJA, J.	lab	VSSC, India
KINGSTONE, Eden Evans Samuel	field	VSSC, India
SRINIVAS, Potnuru	lab	VSSC, India
THANKAPPANNAIR SUMANGALABAI, Binilroy	field	VSSC, India
JEONG, Ui Jin	lab & field	Weathex, Rep. of Korea
SO, Jae Won	lab & field	Weathex, Rep. of Korea
<i>Members of TT-UAI</i>		
ANSARI, Mohd. Imran	participant selection; field: visitor	WMO, India

This table is continued on the next page.

Table P.1 – *Continued from previous page*

Full name	Roles & functions	Organisation & country
DIRKSEN, Ruud	campaign lead; field: supervisor; lab: LABH scientist	DWD, Germany
EDWARDS, David	consultant	MetOffice, United Kingdom
FELIX, Christian	field: operator	MeteoSwiss, Switzerland
GARDINER, Tom	consultant	NPL, United Kingdom
HAEFELE, Alexander	campaign lead; field: supervisor	MeteoSwiss, Switzerland
MARTUCCI, Giovanni	field: GDP operator; remote sensing scientist	MeteoSwiss, Switzerland
OAKLEY, Tim	participant selection	WMO; MetOffice, United Kingdom
ROMANENS, Gonzague	data manager; field: GDP operator	MeteoSwiss, Switzerland
SOMMER, Michael	data manager; field: supervisor; lab: LABH scientist	DWD, Germany
VOGT, Frédéric	dvas development; field: data processing manager	MeteoSwiss, Switzerland
VON ROHDEN, Christoph	field: GDP operator; lab: RADI + TLAG + LOWT scientist	DWD, Germany
VÖMEL, Holger	field: manager of operator training	NCAR EOL, USA
<i>Host joint venture (DWD & MeteoSwiss)</i>		
DIETZE, Stella	field: assistant, GDP operator	FU Berlin, Germany
DIRKSEN, Ruud	campaign lead; field: supervisor; lab: LABH scientist	DWD, Germany
FIEDLER-KRÜGER, Marion	field: rig and balloon manager; lab: LABH operator	DWD, Germany
FRIEDRICH, Helge	field: rig and balloon manager; lab: RADI operator	DWD, Germany
GÖRSDORF, Ulrich	field: photographer	DWD, Germany
HÜLSKÖTTER, Jens	field: local organisation, equipment return	DWD, Germany
JANTZE, Dirk	field: local organisation, driver, equipment return	DWD, Germany
JANTZE, Kathrin	field: local organisation	DWD, Germany
KAMINSKI, Madlen	field: local organisation	DWD, Germany
KARPINSKY, Jörg	lab: RADI operator	DWD, Germany
KONOPKA, Sabrina	field: local organisation	DWD, Germany
KÖRNER, Susanne	field: rig and balloon manager; lab: LABH + TLAG + LOWT operator	DWD, Germany

This table is continued on the next page.

Table P.1 – *Continued from previous page*

Full name	Roles & functions	Organisation & country
KÖRNER, Sven-Olaf	field: operator; lab: TLAG + LOWT operator	DWD, Germany
KNIST, Christine	field: remote sensing group	DWD, Germany
KNÖFEL, Andre	field: local organisation, equipment return	DWD, Germany
LEINWEBER, Ronny	field: remote sensing group	DWD, Germany
LEHMANN, Volker	field: remote sensing group	DWD, Germany
NAEBERT, Tatjana	field: assistant; lab: assistant	DWD, Germany
OELSNER, Peter	field: GDP operator, meteorological advisor; lab: TLAG + LOWT scientist	DWD, Germany
SCHMIDT, Andreas	field: local organisation	DWD, Germany
SCHROBITZ, Karsten	field: local organisation	DWD, Germany
SCHWEBE, Michael	field: local organisation	DWD, Germany
SCHWEBE, Karsten	field: local organisation	DWD, Germany
SIMEONOV, Tzvetan	field: supervisor, meteorological advisor; lab: RADI scientist	DWD, Germany
SOMMER, Michael	data manager; field: supervisor; lab: LABH scientist	DWD, Germany
TIETZ, Rico	field: rig and balloon manager; lab: TLAG + LOWT operator	DWD, Germany
VIETZKE, Karla	field: local organisation	DWD, Germany
VON ROHDEN, Christoph	field: GDP operator; lab: RADI + TLAG + RADI scientist	DWD, Germany
WALLRODT, Kerstin	field: local organisation	DWD, Germany
WEBER, Stefan	field: local organisation, equipment return	DWD, Germany
FELIX, Christian	field: operator	MeteoSwiss, Switzerland
HAEFELE, Alexander	campaign lead; field: supervisor	MeteoSwiss, Switzerland
MARTUCCI, Giovanni	field: GDP operator; remote sensing scientist	MeteoSwiss, Switzerland
MODOLO, Luca	dvas development	MeteoSwiss, Switzerland
ROMANENS, Gonzague	data manager; field: GDP operator	MeteoSwiss, Switzerland
VOGT, Frédéric	dvas development; field: data processing manager	MeteoSwiss, Switzerland
<i>WMO</i>		
PREMEC, Krunoslav	WMO Secretariat	WMO, Switzerland
RUEDI, Isabelle	WMO Secretariat	WMO, Switzerland

NOMENCLATURE

$\bar{\delta}_{\mathcal{C},\mathcal{L}}$	Mean measurement error with respect to the Combined Working measurement Standard (CWS), computed from the flights of the category \mathcal{C} over the atmospheric layer \mathcal{L} (see Section 10.1.5)
ΔT	Temperature sensor heating due to solar irradiation (RADI laboratory tests)
$\delta_{e,i}$	Individual measurement error with respect to the Combined Working measurement Standard (CWS) for the time step i of the flight e ($= x_{e,i} - \Omega_{e,i}$)
$\epsilon_{\mathcal{C},\mathcal{L}}$	Measurement uncertainty associated with the OSCAR requirement uncertainty criterion (ORUC) assessment function $\Lambda_{\mathcal{C},\mathcal{L}}$
$\Lambda_{\mathcal{C},\mathcal{L}}$	OSCAR requirement uncertainty criterion (ORUC) assessment function (see Equation 9.1)
$\Lambda_{\mathcal{C},100\text{m}}$	OSCAR requirement uncertainty criterion (ORUC) assessment function computed for the flights in the category \mathcal{C} with a vertical resolution of 100 m
\dashv	Upper limit of the UTLS
\mathcal{C}	Flight category (either day, or night)
\mathcal{L}	Atmospheric layer
$\Omega_{e,i}$	Combined Working measurement Standard (CWS) data point for the time step i of the flight e
$\bar{\gamma}$	Median tropopause during the UAII 2022 field campaign (=12 km)
ζ	Planetary Boundary Layer Height (PBLH)
σ	Standard deviation
$\sigma(\delta)_{\mathcal{C},\mathcal{L}}$	Standard deviation of the individual measurement errors with respect to the Combined Working measurement Standard (CWS), computed from the flights of the category \mathcal{C} over the atmospheric layer \mathcal{L} (see Section 10.1.5)
τ	Sensor response time (TLAG laboratory tests)
$\Theta_{x,\mathcal{L}}^B$	Breakthrough (B) level of a specific OSCAR requirement uncertainty criterion (ORUC), for a given geophysical variable x over a given atmospheric layer \mathcal{L}
$\Theta_{x,\mathcal{L}}^G$	Goal (G) level of a specific OSCAR requirement uncertainty criterion (ORUC), for a given geophysical variable x over a given atmospheric layer \mathcal{L}
$\Theta_{x,\mathcal{L}}^T$	Threshold (T) level of a specific OSCAR requirement uncertainty criterion (ORUC), for a given geophysical variable x over a given atmospheric layer \mathcal{L}
Υ	Tropopause
\vdash	Lower limit of the UTLS
dT	Temperature difference (LOWT laboratory tests)
k	Coverage factor
k_{eff}	Effective confidence level (see Equation 9.6)
p	Pressure, hPa or Pa
T	Temperature, °C or K
t	Time, s
U	Relative humidity, %RH
u	Uncertainty
$x_{e,i}$	Individual measurement of the geophysical variable x at the time step i of the flight e
$\text{NC}_L\text{hC}_M\text{C}_H$	Synop cloud code, with N the total cloud coverage (in oktas), h the code specifying the height of the lowest cloud layer, and C_L, C_M, C_H the codes describing low, medium and high clouds.

ACRONYMS

AMSL	Above Mean Sea Level
AGL	Above Ground Level
ASCII	American Standard Code for Information Interchange
AWS	Automatic Weather Station
BKG	Bundesamt für Kartographie und Geodäsie (the German Federal Agency for Cartography and Geodesy)
BSRN	Baseline Surface Radiation Network
BUFR	Binary Universal Form for the Representation of meteorological data
BT	Brightness Temperature
CEST	Central European Summer Time
CFH	Cryogenic Frost point Hygrometer
CIMO	Commission for Instruments and Methods of Observation
CWS	Combined Working measurement Standard
DOI	Digital Object Identifier
dvas	Data Visualization and Analysis Software
DWD	Deutscher Wetterdienst
DWL	Doppler Wind Lidar
ECV	Essential Climate Variable
EPS	Expanded Polystyrene
FPH	Frost Point Hygrometer
FT	Free Troposphere
GCOS	Global Climate Observing System
GDP	GRUAN Data Product
GFZ	GeoForschungsZentrum Potsdam (the German Research Centre for Geosciences)
GNSS	Global Navigation Satellite System
GPS	Global Positioning System
GRUAN	GCOS Reference Upper-Air Network
GUI	Graphical User Interface
GTS	Global Telecommunication System
INFCOM	Commission for Observation, Infrastructure and Information Systems
IOVR	Instrument Optimal Vertical Range
ISO	International Organization for Standardization
IPTS-68	International Practical Temperature Scale of 1968
ITS-90	International Temperature Scale of 1990
IWV	Integrated Water Vapour
KS	Kolmogorov-Smirnov
LC	Lead Centre
LAN	Local Area Network
LABH	Humidity sensor performance at room conditions
LDA	Laser Doppler Anemometry
LOWT	Temperature sensor performance at low temperatures
LOS	Line Of Sight
LRSS	Lindenberg Remote Sensing Suite
MCH	MeteoSwiss
MDP	Manufacturer Data Product
MEMS	Micro-Electro-Mechanical Systems
MOL-RAO	Lindenberg Meteorological Observatory – Richard Assmann Observatory
MoU	Memorandum of Understanding
MUS	Mid-Upper Stratosphere
MWR	Micro-Wave Radiometer
NaN	Not a Number
NetCDF	Network Common Data Format

NDACC	Network for the Detection of Atmospheric Composition Change
NMHS	National Meteorological and Hydrological Services
NOAA	National Oceanic and Atmospheric Administration
NTP	Network Time Protocol
NWP	Numerical Weather Prediction
ORUC	OSCAR requirement uncertainty criterion
OSCAR	Observing Systems Capability Analysis and Review Tool
PBL	Planetary Boundary Layer
PBLH	Planetary Boundary Layer Height
PID	Proportional Integral Derivative
PRF	Pulse-Repetition Frequency
QC	Quality Control
RADI	Radiation sensitivity of air temperature measurement
RASS	Radio Acoustic Sounding System
REMI	REMOte sensing Intercomparison
RMSE	Root-Mean Square Error
Ri	Richardson Number
RSI	Radio Sounding Intercomparison
RSSA	Remote Sensing Software Analysis
RSDP	Remote Sensing Data Product
RWP	Radar Wind Profiler
SC-MINT	Standing Committee on Measurements, Instrumentation and Traceability
SHC	Standard Humidity Chamber
SI	International System of Units
SISTER	Simulator for Investigation of Solar Temperature Error of Radiosondes
SNR	Signal-to-Noise Ratio
TLAG	Time lag behaviour of the humidity sensors
TT	Task Team
UAI	Upper-Air Instrument Intercomparison
UHF	Ultra High Frequency
UPS	Uninterruptible Power Supply
USB	Universal Serial Bus
UTC	Coordinated Universal Time
UTLS	Upper Troposphere / Lower Stratosphere
UV	Ultra Violet
VAD	Velocity Azimuth Display
WGS84	World Geodetic System 1984
WMO	World Meteorological Organization

Bibliography

- Barlow, R., *Statistics: A Guide to the Use of Statistical Methods in the Physical Sciences* (John Wiley & Sons, Chichester, 1997), ISBN 0-471-92295-1.
- Bevis, M., *et al.*, Gps meteorology: Remote sensing of atmospheric water vapor using the global positioning system, *Journal of Geophysical Research: Atmospheres*, **97**(D14), 15,787–15,801, <https://doi.org/https://doi.org/10.1029/92JD01517>, 1992, URL <https://agupubs.onlinelibrary.wiley.com/doi/abs/10.1029/92JD01517>.
- Beyrich, F. and J.-P. Leps, An operational mixing height data set from routine radiosoundings at Lindenberg: Methodology, *Meteorologische Zeitschrift*, **21**(4), 337–348, <https://doi.org/10.1127/0941-2948/2012/0333>, 2012.
- Bolton, D., The computation of equivalent potential temperature, *Monthly Weather Review*, **108**, 1046–1053, 1980.
- Browning, K. A. and R. Wexler, The Determination of Kinematic Properties of a Wind Field Using Doppler Radar, *Journal of Applied Meteorology and Climatology*, **7**(1), 105–113, [https://doi.org/10.1175/1520-0450\(1968\)007<0105:TOKPO>2.0.CO;2](https://doi.org/10.1175/1520-0450(1968)007<0105:TOKPO>2.0.CO;2), 1968.
- Buck, A. L., New equations for computing vapor pressure and enhancement factor, *J. Appl. Meteor.*, **20**, 1527–1532, 1981.
- Carr, J. L., A. Horváth, D. L. Wu, and M. D. Friberg, Stereo plume height and motion retrievals for the record-setting hunga tonga-hunga ha'apai eruption of 15 january 2022, *Geophysical Research Letters*, **49**, e98,131, <https://doi.org/10.1029/2022GL098131>, 2022, ISSN 0094-8276.
- Cimini, D., *et al.*, Temperature and humidity profile retrievals from ground-based microwave radiometers during tuc, *Meteorologische Zeitschrift*, **15**(1), 45–56, <https://doi.org/10.1127/0941-2948/2006/0099>, 2006, URL <http://dx.doi.org/10.1127/0941-2948/2006/0099>.
- Coy, L., *et al.*, Stratospheric circulation changes associated with the hunga tonga-hunga ha'apai eruption, *Geophysical Research Letters*, **49**, e2022GL100,982, <https://doi.org/10.1029/2022GL100982>, 2022, ISSN 0094-8276.
- Dirksen, R. J., *et al.*, Reference quality upper-air measurements: GRUAN data processing for the Vaisala RS92 radiosonde, *Atmospheric Measurement Techniques*, **7**, 4463–4490, <https://doi.org/10.5194/amt-7-4463-2014>, 2014.
- GCOS-245, The 2022 GCOS ECVs Requirements, Technical report, GCOS, 2022, URL https://library.wmo.int/index.php?lvl=notice_display&id=22135.
- Gottelman, A., *et al.*, The extratropical upper troposphere and lower stratosphere, *Reviews of Geophysics*, **49**(3), <https://doi.org/doi.org/10.1029/2011RG000355>, 2011.
- Goff, J. A. and S. Gratch, Low-pressure properties of water from -160 to 212 f, *Trans. Am. Soc. Heat. Vent. Eng.*, **51**, 125–164, 1946.
- Greenspan, L., Humidity fixed points of binary saturated aqueous solutions., *Journal of Research of the National Bureau of Standards. Section A, Physics and Chemistry*, **81A**(1), 89–96, <https://doi.org/10.6028/jres.081A.011>, 1977, ISSN 2376-5704, 0022-4332.
- Hardy, B., ITS-90 Formulations for Vapor Pressure, Frostpoint Temperature, Dewpoint Temperature, and Enhancement Factors in the Range -100 to +100 °C, in *Proceedings of the Third International Symposium on Humidity & Moisture, Teddington, London, England, April 1998* (1998).

- Hoshino, S., *et al.*, Comparison of GRUAN data products for Meisei iMS-100 and Vaisala RS92 radiosondes at Tateno, Japan, *Atmospheric Measurement Techniques*, **15**(20), 5917–5948, <https://doi.org/10.5194/amt-15-5917-2022>, 2022.
- Hurst, D. F., *et al.*, Stratospheric water vapor trends over Boulder, Colorado: Analysis of the 30 year Boulder record, *Journal of Geophysical Research: Atmospheres*, **116**(D2), D02,306, <https://doi.org/10.1029/2010jd015065>, 2011.
- Hyland, R. and A. Wexler, Formulations for the thermodynamic properties of the saturated phases of H₂O from 173.15 K to 473.15 K, *ASHRAE Trans.*, **89**, 500–519, 1983.
- Imfeld, N., L. Haimberger, A. Sterin, Y. Brugnara, and S. Brönnimann, Intercomparisons, error assessments, and technical information on historical upper-air measurements, *Earth System Science Data*, **13**(6), 2471–2485, <https://doi.org/10.5194/essd-13-2471-2021>, 2021, URL <https://essd.copernicus.org/articles/13/2471/2021/>.
- Immler, F. J., *et al.*, Reference Quality Upper-Air Measurements: guidance for developing GRUAN data products, *Atmospheric Measurement Techniques*, **3**(5), 1217–1231, <https://doi.org/10.5194/amt-3-1217-2010>, 2010.
- JCGM, *The international vocabulary of metrology—basic and general concepts and associated terms (VIM)*, JCGM 200:2012 (JCGM, 2012), 3rd edition, URL <http://www.bipm.org/en>, last accessed: May 25, 2021.
- Khaykin, S., *et al.*, Global perturbation of stratospheric water and aerosol burden by hunga eruption, *Communications Earth and Environment*, **3**, 316, <https://doi.org/10.1038/s43247-022-00652-x>, 2022.
- Kizu, N., *et al.*, Technical characteristics and GRUAN data processing for the Meisei RS-11G and iMS-100 radiosondes, GRUAN Technical Document 5, GRUAN, 2018a, URL <https://www.gruan.org/documentation/gruan/td/gruan-td-5/>.
- Kizu, N., *et al.*, Technical characteristics and GRUAN data processing for the Meisei RS-11G and iMS-100 radiosondes, GRUAN Technical Document 5 (GRUAN-TD-5), GRUAN Lead Centre, 2018b, URL <https://www.gruan.org/documentation/gruan/td/gruan-td-5>, v1.0 (2018-02-21).
- Lehmann, V., Optimal gabor-frame-expansion-based intermittent-clutter-filtering method for radar wind profiler, *Journal of Atmospheric and Oceanic Technology*, **29**(2), 141 – 158, <https://doi.org/10.1175/2011JTECHA1460.1>, 2012.
- Löhnert, U., D. D. Turner, and S. Crewell, Ground-based temperature and humidity profiling using spectral infrared and microwave observations. part i: Simulated retrieval performance in clear-sky conditions, *Journal of Applied Meteorology and Climatology*, **48**(5), 1017 – 1032, <https://doi.org/https://doi.org/10.1175/2008JAMC2060.1>, 2009, URL <https://journals.ametsoc.org/view/journals/apme/48/5/2008jamc2060.1.xml>.
- Massaro, G., I. Stiperski, B. Pospichal, and M. W. Rotach, Accuracy of retrieving temperature and humidity profiles by ground-based microwave radiometry in truly complex terrain, *Atmospheric Measurement Techniques*, **8**(8), 3355–3367, <https://doi.org/10.5194/amt-8-3355-2015>, 2015.
- Millán, L., *et al.*, The hunga tonga-hunga ha’apai hydration of the stratosphere, *Geophysical Research Letters*, **49**, e99,381, <https://doi.org/10.1029/2022GL099381>, 2022, ISSN 0094-8276.
- Miloshevich, L. M., A. Paukkunen, H. Vömel, and S. J. Oltmans, Development and Validation of a Time-Lag Correction for Vaisala Radiosonde Humidity Measurements, *Journal of Atmospheric and Oceanic Technology*, **21**(9), 1305–1327, [https://doi.org/10.1175/1520-0426\(2004\)021<1305:DAVOAT>2.0.CO;2](https://doi.org/10.1175/1520-0426(2004)021<1305:DAVOAT>2.0.CO;2), 2004.
- Nash, J., Measurement of upper-air pressure, temperature and humidity, Technical report, World Meteorological Organization (WMO), 2015, URL https://library.wmo.int/doc_num.php?explnum_id=7366, Instruments and Observing Methods Report No. 121.

- Ning, T., *et al.*, The uncertainty of the atmospheric integrated water vapour estimated from gnss observations, *Atmospheric Measurement Techniques*, **9**(1), 79–92, <https://doi.org/10.5194/amt-9-79-2016>, 2016, URL <https://amt.copernicus.org/articles/9/79/2016/>.
- Päschke, E., R. Leinweber, and V. Lehmann, An assessment of the performance of a 1.5 μm Doppler lidar for operational vertical wind profiling based on a 1-year trial, *Atmospheric Measurement Techniques*, **8**(6), 2251–2266, <https://doi.org/10.5194/amt-8-2251-2015>, 2015.
- Preston-Thomas, H., The International Temperature Scale of 1990 (ITS-90), *Metrologia*, **27**, 3–10, 1990.
- von Rohden, C., M. Sommer, T. Naebert, V. Motuz, and R. Dirksen, Laboratory characterisation of the radiation temperature error of radiosondes and its application to the GRUAN data processing for the Vaisala RS41, *Atmospheric Measurement Techniques*, **15**(2), 383–405, <https://doi.org/10.5194/amt-15-383-2022>, 2022.
- Schoeberl, M. R., *et al.*, Analysis and impact of the hunga tonga-hunga ha’apai stratospheric water vapor plume, *Geophysical Research Letters*, **49**, e2022GL100,248, <https://doi.org/10.1029/2022GL100248>, 2022, ISSN 0094-8276.
- Sommer, M., C. von Rohden, and T. Simeonov, User Guide for the RS41 GRUAN Data Product Version 1 (RS41-GDP.1), GRUAN Technical Note 13 (GRUAN-TN-13), GRUAN Lead Centre, 2022, URL <https://www.gruan.org/documentation/gruan/tn/gruan-tn-13>, v1.0 (2022-11-21).
- Sommer, M., *et al.*, GRUAN characterisation and data processing of the Vaisala RS41 radiosonde, GRUAN Technical Document 8 (GRUAN-TD-8), GRUAN Lead Centre, 2023, URL <https://www.gruan.org/documentation/gruan/td/gruan-td-8>, v1.0 (2023-06-28).
- Sonntag, D., Important new values of the physical constants of 1986, vapour pressure formulations based on the ITS-90 and psychrometer formulae, *Zeitschrift für Meteorologie*, **40**, 340–344, 1990.
- Stull, R. B., An introduction to boundary layer meteorology, *Springer Netherlands eBooks*, <https://doi.org/10.1007/978-94-009-3027-8>, 1988.
- Sugidachi, T., *Studies on the tropospheric and stratospheric water vapor measurements for climate monitoring*, Ph.D. thesis, Hokkaido University, Sapporo, Japan, 2014, URL <http://hdl.handle.net/2115/55416>.
- Taha, G., *et al.*, Tracking the 2022 hunga tonga-hunga ha’apai aerosol cloud in the upper and middle stratosphere using space-based observations, *Geophysical Research Letters*, **49**, e2022GL100,091, <https://doi.org/10.1029/2022GL100091>, 2022, ISSN 0094-8276.
- Teschke, G. and V. Lehmann, Mean wind vector estimation using the velocity–azimuth display (VAD) method: an explicit algebraic solution, *Atmospheric Measurement Techniques*, **10**(9), 3265–3271, <https://doi.org/10.5194/amt-10-3265-2017>, 2017.
- Tinney, E. N., *et al.*, A Modern Approach to a Stability-Based Definition of the Tropopause, *Monthly Weather Review*, **150**(12), 3151–3174, <https://doi.org/10.1175/MWR-D-22-0174.1>, 2022, ISSN 1520-0493, 0027-0644.
- Vömel, H., D. E. David, and K. Smith, Accuracy of tropospheric and stratospheric water vapor measurements by the cryogenic frost point hygrometer: Instrumental details and observations, *Journal of Geophysical Research: Atmospheres*, **112**(D8), D08,305, <https://doi.org/10.1029/2006jd007224>, 2007.
- Vömel, H., S. Evan, and M. Tully, Water vapor injection into the stratosphere by hunga tonga-hunga ha’apai, *Science*, **377**, 1444–1447, <https://doi.org/10.1126/science.abq2299>, 2022, ISSN 0036-8075.
- Vömel, H. and P. Jaennet, Balloon-borne frostpoint-hygrometry, in N. Kämpfer, ed., *Monitoring Atmospheric Water Vapour, ISSI Scientific Report Series*, volume 10, pp. 39–53 (Springer New York, 2013), ISBN 978-1-4614-3908-0, https://doi.org/10.1007/978-1-4614-3909-7_2.

- Vömel, H. S. J. O., D. J. Hofmann, T. Deshler, and J. M. Rosen, The evolution of the dehydration in the antarctic stratospheric vortex, *Journal of Geophysical Research: Atmospheres*, **100**(D8), 13,919–13,926, <https://doi.org/10.1029/95JD01000>, 1995.
- Wang, J., *et al.*, Global Navigation Satellite System (GNSS) - Precipitable Water (PW) Omnibus, GRUAN Technical Document 6 (GRUAN-TD-6), GRUAN Lead Centre, 2019, URL <https://www.gruan.org/documentation/gruan/td/gruan-td-6>, v2.0 (2019-08-21).
- Wexler, A., Vapor pressure formulation for ice, *Journal of Research of the national bureau of standards*, **81A**(1), 5–20, 1977.
- WMO, Project plan for the wmo upper-air instrument intercomparison campaign 2021, 2020, URL https://wmoomm.sharepoint.com/:b:/s/wmocpdb/EdWADOzS679KhYaLj1pTNAkbtIeaennTulk1Kz5Xpd_0xA?e=9dY8Wh, [Accessed 8 December 2023].
- WMO Bulletin, vol. IV, no. 4, Meteorology - A three-dimensional science: Second session of the Commission for Aerology, Technical report, World Meteorological Organization (WMO), 1957, URL https://library.wmo.int/doc_num.php?explnum_id=6960.
- WMO-No.306, Manual on Codes - International Codes, Volume I.2, Annex II to the WMO Technical Regulations: Part B – Binary Codes, Part C – Common Features to Binary and Alphanumeric Codes, Technical report, World Meteorological Organization (WMO), 2022, URL https://library.wmo.int/?lvl=notice_display&id=10684.
- WMO-No.8-Vol.I, Guide to Instruments and Methods of Observation Volume I – Measurement of Meteorological Variables, Technical report, World Meteorological Organization (WMO), 2021, URL https://library.wmo.int/index.php?id=12407&lvl=notice_display.

For more information, please contact:

World Meteorological Organization

7 bis, avenue de la Paix – P.O. Box 2300 – CH 1211 Geneva 2 – Switzerland

Strategic Communications Office

Tel.: +41 (0) 22 730 83 14 – Fax: +41 (0) 22 730 80 27

Email: cpa@wmo.int

public.wmo.int